NUREG/CP–0127
NEA/CSNI/R(93)8

Proceedings of the CSNI Specialists Meeting on Fuel-Coolant Interactions

Held in
Santa Barbara, California, USA
January 5–8, 1993

Organized by

OECD Nuclear Energy Agency

Center for Risk Studies and Safety
University of California, Santa Barbara

Sponsored by
Office of Nuclear Regulatory Research
U.S. Nuclear Regulatory Commission

NOTICE

These proceedings have been authored by a contractor of the United States Government. Neither the United States Government nor any agency thereof, or any of their employees, makes any warranty, expressed or implied, or assumes any legal liability or responsibility for any third party's use, or the results of such use, of any information, apparatus, product or process disclosed in these proceedings, or represents that its use by such third party would not infringe privately owned rights. The views expressed in these proceedings are not necessarily those of the U.S. Nuclear Regulatory Commission.

Available from

Superintendent of Documents
U.S. Government Printing Office
Mail Stop SSOP
Washington, DC 20402-9328

and

National Technical Information Service
Springfield, VA 22161

NUREG/CP-0127
NEA/CSNI/R(93)8

Proceedings of the CSNI Specialists Meeting on Fuel-Coolant Interactions

Held in
Santa Barbara, California, USA
January 5–8, 1993

Manuscript Completed: January 1994
Date Published: March 1994

Organized by
OECD Nuclear Energy Agency

Center for Risk Studies and Safety
University of California, Santa Barbara, CA

Sponsored by
Division of Systems Research
Office of Nuclear Regulatory Research
U.S. Nuclear Regulatory Commission
Washington, DC 20555–0001

ABSTRACT

A specialists meeting on fuel-coolant interactions was held in Santa Barbara, CA from January 5-7, 1993. The meeting was sponsored by the United States Nuclear Regulatory Commission in collaboration with the Committee on the Safety of Nuclear Installation (CSNI) of the OECD Nuclear Energy Agency (NEA) and the University of California at Santa Barbara.

The objectives of the meeting are to cross-fertilize on-going work, provide opportunities for mutual check points, seek to focus the technical issues on matters of practical significance and re-evaluate both the objectives as well as path of future research

PROCEEDINGS OF THE
CSNI SPECIALISTS MEETING ON FUEL-COOLANT INTERACTIONS
January 5-8, 1993

CONTENTS

CONTENTS (Cont'd)

CONTENTS (Cont'd)

ACKNOWLEDGMENTS

- The individuals responsible for the review effort (each was charged to arrange for one review of each paper submitted) were: M. Akiyama, R. Hall/N. Buttery, H. Jacobs and T.G. Theofanous. Their contribution was decisive to the value of these proceedings.
- The individuals responsible for guiding the technical discussions as session chairs and for developing the Meeting Summary were: M. Akiyama, M.L. Corradini, H.K. Fauske, D.F. Fletcher, R.E. Henry, H. Jacobs, B.D. Turland and T.G. Theofanous. Their contribution was decisive to setting the tone of the meeting and steering the discussions toward useful conclusions.
- The CSNI secretary responsible for this meeting was H. Holmström, and the CSNI PWG2 (past) chair that promoted this meeting was E. Hicken. The meeting has benefitted significantly from their support and active participation, including the preparation of the Meeting Summary. The meeting was also actively supported by the secretary and the chairman of the CSNI PWR4.
- All administrative aspects of the meeting organization, from the call for papers, through the review process, to the actual meeting arrangements, and the preparation of these Proceedings, were handled by Ms. E. Horton, Administrative Assistant to UCSB's Center for Risk Studies and Safety. Her efforts were essential to the success of all these key areas.
- F. Eltawila and T.G. Theofanous served as the General and Technical Program Chairs, respectively. Financial support for this meeting was provided by the U.S. Nuclear Regulatory Commission.

ORGANISATION FOR ECONOMIC CO-OPERATION AND DEVELOPMENT

Pursuant to Article 1 of the Convention signed in Paris on 14th December 1960, and which came into force on 30th September 1961, the Organisation of Economic Co-operation and Development (OECD) shall promote policies designed:

- to achieve the highest sustainable economic growth and employment and a rising standard of living in Member countries, while maintaining financial stability, and thus to contribute to the development of the world economy;
- to contribute to sound economic expansion in Member as well and non-member countries in the process of economic development; and
- to contribute to the expansion of world trade on a multilateral, non-discriminatory basis in accordance with international obligations.

The original Member countries of the OECD are Austria, Belgium, Canada, Denmark, France, Germany, Greece, Iceland, Ireland, Italy, Luxembourg, the Netherlands, Norway, Portugal, Spain, Sweden, Switzerland, Turkey, the United Kingdom and the United States. The following countries became Members subsequently through accession at the dates indicated hereafter: Japan (28th April 1964), Finland (28th January 1969), Australia (7th June 1971) and New Zealand (29th May 1973). The Commission of the European Communities takes part in the work of the OECD (Article 13 of the OECD Convention).

NUCLEAR ENERGY AGENCY

The OECD Nuclear Energy Agency (NEA) was established on 1st February 1958 under the name of the OEEC European Nuclear Energy Agency. It received its present designation on 20th April 1972, when Japan became its first non-European full Member. NEA membership today consists of all European Member countries of OECD as well as Australia, Canada, Japan, the Republic of Korea and the United States. The Commission of the European Communities takes part in the work of the Agency.

The primary objective of NEA is to promote co-operation among the governments of its participating countries in furthering the development of nuclear power as a safe, environmentally acceptable and economic energy source.

This is achieved by:

- encouraging harmonization of national regulatory policies and practices, with particular reference to the safety of nuclear installations, protection of man against ionising radiation and preservation of the environment, radioactive waste management, and nuclear third party liability and insurance;
- assessing the contribution of nuclear power to the overall energy supply by keeping under review the technical and economic aspects of nuclear power growth and forecasting demand and supply for the different phases of the nuclear fuel cycle;
- developing exchanges of scientific and technical information particularly through participation in common services;
- setting up international research and development programmes and joint undertakings.

In these and related tasks, NEA works in close collaboration with the International Atomic Energy Agency in Vienna, with which it has concluded a Co-operation Agreement, as well as with other international organisations in the nuclear field.

CSNI

The NEA Committee on the Safety of Nuclear Installations (CSNI) is an international committee made up of scientists and engineers who have responsibilities for nuclear safety research and nuclear licensing. The Committee was set up in 1973 to develop and co-ordinate the Nuclear Energy Agency's work in nuclear safety matters, replacing the former Committee on Reactor Safety Technology (CREST) with its more limited scope.

The Committee's purpose is to foster international co-operation in nuclear safety amongst the OECD Member countries. This is done in a number of ways. Full use is made of the traditional methods of co-operation, such as information exchanges, establishment of working groups, and organisation of conferences. Some of these arrangements are of immediate benefit to Member countries, for example by improving the data base available to national regulatory authorities and to the scientific community at large. Other questions may be taken up by the Committee itself with the aim of achieving an international consensus wherever possible. The traditional approach to co-operation is reinforced by the creation of co-operative (international) research projects, such as PISC (Programmes for the Inspection of Steel Components), OECD/LOFT (Loss-of-Fluid Test), Halden, and the TMI-2 Sample Examination Programme, and by the organisation of the international standard problem exercises, for testing the performance of computer codes, test methods, etc. used in safety assessments. These exercises are now being conducted in most sectors of the nuclear safety programme.

Increasing attention is devoted to the collection, analysis and dissemination of information on safety-related operation experience in nuclear power plants; CSNI operates an international mechanism for exchanging reports on nuclear power plant incidents (NEA-IRS).

The greater part of the CSNI co-operative programme is concerned with safety technology for water reactors. The principal areas covered are operating experience and the human factor, reactor system response during abnormal transients and accidents, accident prevention and control, various aspects of primary circuit integrity, the phenomenology of radioactive releases in reactor accidents, and accident management. The Committee also studies the safety of the fuel cycle, and conducts surveys of reactors safety research programmes.

The Sub-Committee on Licensing, consisting of the CSNI Delegates who have responsibilities for the licensing of nuclear installations, examines a variety of nuclear regulatory problems and provides a forum for the review of regulatory questions, the aim being to develop consensus positions in specific areas.

MEETING SUMMARY

1. INTRODUCTION

More than ten years have passed since the last CSNI Specialists' Meeting on Fuel-Coolant Interactions and interest in the area is found to be undiminished, and indeed broadened. The continuing interest in the alpha-failure (steam-explosion-induced containment failure) is demonstrated by the significant new programs (in addition to the on-going one in the US) initiated in the UK, Germany, France, Italy, CEC and Japan. The broadening of interest has occurred because of increasing emphasis on accident management, where one is interested in mild behavior as well, especially from the hydrogen production and coolability standpoints. Moreover, this interest in both energetics and accident management is now broadening even further under the consideration of new designs [for the Advanced Light Water Reactors (ALWRs)]. Finally, we observe an increased emphasis on the fundamentals, clearly motivated by the breadth of the intended application, but also by the desire for a deeper understanding of the safety margins in the assessment of alpha-failure. The purpose of this meeting was to provide a frame for a comprehensive consideration of progress made to date in all above-mentioned respects, and to delineate directions in which further progress is deemed desirable. The timeliness of this purpose was judged to be high, both in terms of the current rapid advancements in technology, as well as design/regulatory needs for ALWRs in the immediate future.

The proposal for this meeting was initiated by the CSNI Principal Working Group 2 (PWG2), through its Task Group on In-Vessel Degraded Core Behavior (TG-IVDCB). The meeting was organized in cooperation with the US Nuclear Regulatory Commission (US NRC) and the University of California at Santa Barbara (UCSB). There were a total of 26 papers (plus 7 open forum presentations) and 54 specialists (including a few observers) from 12 countries attended the 4-day meeting.

The organization emphasized communication prior to, during, and after the meeting. The communications prior to the meeting were in the form of full-paper reviews conducted in the usual quality standards of meetings/proceedings organized by the Thermal Hydraulics Division of the American Nuclear Society (that is, 3 peer reviews, authors' responses including revisions, and re-reviews as appropriate). During the meeting, extensive communication was assured by the structure of the program: at the end of each 2-hour session, in which 4 (or 5) papers were presented, and after a break, one hour was allowed for discussion, under the direction of the session's chair. The individuals involved in this task were (in chronological order of the program): H.K. Fauske, B.D. Turland, D.F. Fletcher, M. Akiyama, M.L. Corradini, H. Jacobs, and R.E. Henry. Their contributions were decisive in setting the proper tone and steering the discussions toward useful conclusions. In addition, they initiated, individually, sets of proposed conclusions and recommendations which, after some initial feedback in a meeting among themselves, were discussed in a panel session at the close of the meeting. These conclusions/recommendations, as they evolved from these discussions, were submitted (including the chairs' summary of the session and short summaries of the papers presented) by respective chairs within a few weeks after the meeting. A first draft of a Meeting Summary could thus be collected and fine-tuned through two more iterations with all sessions chairs. At the end, the Meeting Summary was mailed to all those that participated in the meeting.

This Meeting Summary is organized in four parts. The first part is this general introduction. The second part provides some technical introductory remarks and comments, intended as a high-level summary of the meeting. Detailed conclusions and recommendations are summarized in the third part, and the fourth part contains the chairs' summary of sessions and short summaries of papers presented. The third and fourth parts are subdivided according to the major topics of the program; that is, "Premixing," "Propagation," "Miscellaneous Experiments and Open Forum" and "Integral and Risk Aspects."

2. GENERAL TECHNICAL REMARKS

The overall goal of Research and Development in the area of Fuel-Coolant Interactions is to develop high confidence estimates that reasonably bound the magnitude of potential energetics in severe reactor accidents, to determine the conditions under which such interactions occur, and to estimate the range of fuel-coolant configurations appropriate for coolability in the case of benign interactions (i.e., quenching "in flight"). The pouring mode of contact is of principal interest, and the premixing transient is of fundamental significance to both of the above aspects. By premixing transient, we understand the space-time evolution of fuel, steam and water volume fractions. An energetic event can be triggered during this process; thus, premixing provides the initial conditions for any postulated trigger event. Further, the relationship between the premixture and triggering events presumably affects the occurrence of a large scale explosion as well as the magnitude of the resulting energetics.

The degree of contact between fuel and water during premixing can be (has been) used to provide bounding estimates of work potential[a] without regard to triggerability or detail of the pressure pulse in the explosive interaction. This, together with energy partition aspects of subsequent collision (material impact dynamics) processes, has provided the means of assessing the likelihood of alpha-failure. For the mechanical consequences of direct loading of structures, such as the lower head or adjacent containment structures in ex-vessel explosions, the details of the generated pressure pulse are necessary. This requires consideration of the escalation from a given (or postulated) trigger, and the dynamics of development of the pressure waves propagating through the premixture zone and surrounding fluid media.

In the absence of energetic events, consideration of the premixing transient through its completion (i.e., settling of the fuel to the bottom of the premixing region) provides the means of assessing the coolability aspects of the resulting debris and thermal loading of the supporting structure.

In accordance with the above, the meeting program was structured with "Premixing" and "Propagation" as the two fundamental components, with one whole day devoted to each topic respectively. In addition, the program included a session for miscellaneous experiments and an open forum as a way of further gauging current trends (in terms of planned or programs still at an early stage) and especially any new aspects of potential importance. Finally, the last, but not least, component of the program was devoted to integral/risk assessment aspects, thus providing the connection between fundamentals and application.

The conclusions/recommendations in each of these four areas are summarized in Part 3 of this meeting summary. The following, general, high level observations can be made on these detailed conclusions and recommendations.

1. The technology in this area is in a stage of rapid development, with significant progress on key fundamental aspects. All new results confirm previous assessments that alpha-failure is highly unlikely and may be impossible.
2. Further progress at the fundamental level is expected in the near future, especially in the more detailed aspect on explosion effects on direct loading of structures. This is expected to be especially important in the treatment of the subject in advanced reactor designs and to add further depth in understanding the margins of alpha-failure in both existing and advanced reactors.
3. As technology is maturing, it is timely and important that the synergistic effect from the various national efforts be maximized. The CSNI can significantly contribute to this goal by organizing standard problems around key experimental results as well as for specific but generic reactor applications. It is also recommended that these activities culminate in a specialists' meeting within 3 to 5 years.

In closing these general remarks, it is important to observe that the meeting was conducted in a generally more cooperative (and less contentious) atmosphere than has been the case in such past meetings. This points very hopefully to reaching international consensus in the foreseeable future, and indeed it is the most clear indication that progress is significant and that the subject is maturing. That this is the case is further corroborated by the detailed conclusions and recommendations that follow.

3. DETAILED CONCLUSIONS AND RECOMMENDATIONS

3.1 Premixing and Quenching

1. The topic of premixing, based on the conjecture of water depletion limiting the amount of mass that can participate in a steam explosion, has been the focus of fuel-coolant interaction research in recent years. During this time a number of sophisticated multi-phase computer codes have been developed and experiments undertaken to provide validation data at small scale for these codes. The experiments have validated the water depletion phenomenon. Based on plant applications of the codes, the efficient extraction of mechanical energy from the thermal energy of the melt is likely to be restricted to the equivalent of ideal conversion for no more than a few tonnes of melt.
2. Continuing confirmatory studies are desirable. They should be guided by an iterative approach taking into account both the experimental database, the use of the models in application to (uncertain) plant scenarios, and scaling considerations that relate these two aspects. Validation requirements for the codes should be guided by the use made of them in plant assessments. Experiments already planned by the international community will expand the database for code validation to higher temperatures (above 1000°C) and larger masses including prototypic materials. Provided boundary conditions can be well-defined, an international standard problem based on one of these premixing tests is desirable, perhaps coupled with a plant application.
3. More work on determining what constitutes a potentially explosive premixture, in terms of melt and water volume fractions, is desirable. Alternatively, one may require validation of multi-dimensional propagation codes to produce firm upper limits on the pressurization and energy conversion.
4. Analyses or experiments to support the conjecture that large scale fuel-coolant interactions are not possible in the lower plenum of a BWR (because of the extensive structures found in it) are desirable.
5. More emphasis now needs to be placed on accident management (debris coolability) considerations. In particular, jet break-up studies, with experimental valida-

[a] Normally expressed by the "conversion ratio"; that is, the fraction of the melt "thermal energy" converted to "mechanical work."

tion, should be continued to delimit better the conditions under which coolable debris will form in a melt-water interaction.

6. Experiments and analyses to characterize the sensitivity of premixing to available vent pathways would facilitate screening of current designs and guide future design efforts.

3.2 Propagation and Energetics

1. The study of propagation (both by experiments and modelling) is important because it provides a means of calculating the mechanical energy release from a given premixture (assuming a suitable trigger) and the pressure loading on structures (e.g., the lower head or a cavity wall).

2. The understanding of propagation is less well developed than that of premixing but current experimental and modelling programmes should allow significant progress to be made over the next two years. A variety of propagation models/codes have been developed. These have been used to perform numerical experiments and to analyse the KROTOS tests. There is little agreement on the chosen constitutive physics in the models. It is recommended that the available data (from UCSB, McGill and IKE) together with any additional data should be used to develop best-estimate constitutive relations for fragmentation and microinteractions. [The concept of microinteractions was introduced in this meeting by Yuen and Theofanous (see paper II.10).] Then the KROTOS tests should be re-analysed using the available models and the best-estimate constitutive physics to determine the current capabilities of such models. Following this, analysis of data from 2-D tests performed under controlled conditions is desirable to allow the multi-dimensional aspects of the process to be checked. In general, comparative studies with existing codes on available experiments and scalability of code results to reactor conditions are to be encouraged.

3. It is also desirable to extend the database for explosive interactions with prototypic reactor materials in both one- and multi-dimensional geometries. It is understood that 2-D modelling is essential for the evaluation of problems in reactor scale and geometry.

4. Triggering cannot be ruled out in reactor accidents but it is generally agreed that it becomes more difficult at higher pressures. Where possible existing and future experimental programmes should investigate the effect of pressure on triggering for *realistic* triggers. The ALPHA facility in Japan is ideally suited for this task.

5. It is possible that many propagation events seen to date are not true propagations but simply a sustained (or amplified) trigger pulse. Experimenters should provide full details of the triggers used so that the relevance to reactor applications can be determined and the hypothesis regarding the effect of trigger strength on propagation can be checked. Systematic and detailed studies on the role of external triggering are recommended.

6. More progress in measuring techniques and more investment on advanced measuring systems will be desirable for further validation work and for better understanding of the fundamental behavior. In particular, time and space resolution of information obtained by experimental data should be improved further by using innovative measuring techniques such as those developed by Frost et al., and by Theofanous et al. toward the goal of further reduction of the empirical component in modeling.

7. A wide range of experimental studies using simulant materials have suggested that stratified explosions involve only small depths of melt, propagate relatively slowly and require sufficient inertial constraint to propagate. It is recommended that a simple model of this process be developed and applied to the existing database. Once validated it should be applied to reactor conditions to verify by comparison to those extensively premixed, if stratified explosions are rather benign.

3.3 Miscellaneous Experiments and Open Forum

1. In several national research plans, there is renewed interest in the deepest understanding of steam explosions. The aims of these activities are to further confirm present understanding and to develop each group's own capability in analyzing steam explosions.

2. Recent work has highlighted the potential augmentation of energetics of steam explosions by chemical effects (in which melt, a highly reactive metal such as aluminum, is oxidized). It is suggested that further experimental work with prototypic materials be performed to address this issue, together with model development efforts.

3. Theoretical studies have indicated in the past an important effect of energy dissipation by the above core structures. The group expects confirmative results from experiments being prepared at KfK. The topic of structural consequences of steam explosions should be included in the next FCI specialists' meeting.

4. There are some initial indications and claims that surfactants may significantly affect the occurrence and/or intensity of steam explosions. To the extent that these indications are derived from single-droplet experiments, they are viewed by many with caution. It is recommended that this topic receive some further attention with experiments specifically designed to address the impact (of surfactants) on triggering and on propagation of steam explosions.

5. In-pile work for power-transient-induced fuel-coolant interactions is currently focused on fuel-failure thresholds and short-range fuel failure propagation rather than on large-scale energetics. This is judged to be appropriate.

3.4 Integral Assessment and Risk Aspects

1. The integral assessments presented did not provide any information indicating that the SERG (1985) conclusions were overstated (optimistic). On the contrary, the available information provided at the meeting either (1) validated the opinions generated in the SERG or (2) demonstrated that there was substantial conservatism in the SERG assessments and reduced those conservatisms thereby providing substantial margin between the calculated mechanical energy release and that required for an alpha-mode failure condition.

4. CHAIRS' SUMMARIES OF SESSIONS AND OF PAPERS PRESENTED

4.1 Premixing and Quenching

4.1.1 Chairs' Summary of the Session

1. The conjecture of Henry and Fauske that water depletion would limit the amount of melt that can be premixed in the lower plenum has been the subject of considerable research over the last few years.

2. The favored approach has been to develop 2 or 3 dimensional multiphase flow codes (PM-ALPHA, CHYMES, IVA-3, TRIO-MC) based on standard conservation laws. There are differences in the constitutive physics used by the various codes, particularly at intermediate void fractions, where the flow regime with three phases is uncertain. Current versions of the codes assume a predispersed melt into droplets.

3. An experimental database for validation of these codes has been developed (Nuclear Electric's simulant tests, MAGICO, MIXA, and the FARO-LWR scoping tests). Further tests in MAGICO and FARO will be supplemented by data from BILLEAU (CEA, France) and experiments at Karlsruhe. It is a feature of the experimental database that the less prototypic tests are better characterised for code validation purposes. The more prototypic tests have mechanisms operating (melt break-up, penetrating thermal radiation) that are not a feature of most of the simulant test data.

4. The published validation of the codes varies. PM-ALPHA gives good comparisons with MAGICO data (saturated water, open system, mm-sized steel spheres up to 1000°C) and with reasonable assumptions matches the (limited) data from the first FARO scoping test. Both the IVA-3 and TRIO-MC codes produce reasonable fits to the FARO data, but the IVA-3 calculations showed that non-linearities in the system of equations (the coupling between fragmentation and steam production) can lead to enhanced steam production and pressurization. Since adequate breakup models are not available, it is currently necessary for the analysts to make rather arbitrary assumptions about the initial melt droplet radius to match FARO-LWR data. Comparison of CHYMES calculations with small-scale experiments show qualitative agreement, but usually the melt is more dispersive at this scale than predicted by the code.

5. Thus considerable progress has been made in validating the original water depletion conjecture of Henry and Fauske. Furthermore, experiments have directly validated, with both simulant and high temperature melts, the water depletion phenomenon.

6. There appears to be no clear consensus on what the definition (characterization) of an explosive premixture is for application to the plant. Taking a 'worse-case' with efficient local conversion of thermal energy to work, has indicated that this, by itself, is insufficient to make a water-tight case against α-mode failure. However, some workers argue that the mixture should contain a minimum amount of melt and water (typically a few percent of melt and at least 10% of water) to support propagation and the efficient conversion of thermal into mechanical energy. This conjecture has not been demonstrated. However, (i) the calculated structure of the melt-water interaction region (a steam void above the major part of the melt, indicating the absence of a slug to provide a coherently moving missile), (ii) the anticipated slow rates of melt delivery (implying that only a small fraction of the core is interacting with the water at any given time) and (iii) the conservatisms in the ideal efficiency calculations, all indicate that efficient extraction of mechanical energy from the thermal energy of the melt is likely to be restricted to the equivalent of full conversion for no more than a few tonnes of melt.

7. With this perspective, further work should be viewed as confirmatory, and the requirements for code validation should be considered carefully. This is only possible when there is an iterative cycle between plant applications and these more fundamental studies. For instance, it may be that the assumed large (and rapid) pour of melt into the lower head, which is the precondition for these studies, is itself an outlier and should not absorb all the available resources, when scenarios in which melt and coolant might be driven together are also possible.

8. While encouraging this iterative approach, it seems prudent to continue the confirmatory research for large pours, as alternative contact modes will have features in common with the large pour scenario. However, whether this effort is best devoted to improving the premixing codes *per se*, or in attempting to clarify the characteristics of a potentially explosive premixture and a more realistic determination of the likely energy yield of a given premixture, should be considered.

9. For plant applications and comparisons with the available experiments, the codes should, as a minimum, be able to scope the effects of coolant sub-cooling and melt break-up, as both mechanisms have important feedbacks on other processes.

10. The experiments planned by the international community should improve the database for code validation, particularly by extending it at intermediate temperatures (1000–2500°C) and providing integral data with

prototypic materials at a larger scale (FARO-LWR). It is important that there be as little ambiguity as possible in initial conditions for such tests, and that as much local information as possible (e.g., void fraction) should be obtained.

11. A significant conjecture of the meeting was that large melt-coolant interactions are not possible in the lower head of a BWR, because of the large amount of guide tube structures present (also incoherent relocation is anticipated). It is desirable to place this conjecture on a firmer basis, either by analysis or experiments.

12. The topic of jet break-up was considered in a number of papers in the session. The melt is likely to be delivered in the form of a single jet or as multiple jets with diameters ranging from a few centimeters up to possibly a few tens of centimeters (particularly for vessel breach). Although there are models for the break-up of such jets, there is no agreement on the dominant break-up process. However, calculations and the results of the FARO-LWR scoping tests indicate that 100 mm diameter melt jets may penetrate significant depths of water. If this can be demonstrated at larger scale (e.g., in the 150 kg FARO test), it would provide a further limitation on premixing. However, there is also an interest from an accident management perspective, where it would be desirable to show that (or whether) such interactions with sufficient depth of water lead to coolable debris. For these reasons it would be desirable to reduce uncertainties in this area. With the current database and modeling uncertainty, a parametric approach to jet break-up for the premixing codes is favored.

4.1.2 Summary of Papers in the Session

Magallon (JRC Ispra) described the results of the first two FARO-LWR scoping tests. In these tests 18 kg and 44 kg respectively of melt (80% UO_2, 20% ZrO_2) entered water through a nominal 100 mm nozzle. The water was in a closed container, with about 70% free volume pressurised to 5 MPa. There was a small amount of initial sub-cooling that became more significant as the pressure increased during the interaction (the pressure rose significantly due to radiative heating of the cover gas prior to the melt-water interaction). This sub-cooling produced a significant heat sink (in the experiments the mass ratios of water to fuel were 7.5 and 5.7, respectively, compared with values less than 1 for a large pour in a reactor). There was only limited level swell measured in the experiments. The increases in pressure were 1.6 MPa and 1.8 MPa respectively; there were no steam explosions. In both tests about one-third of the melt formed a conglomerate on the debris catcher; the remainder was fragmented into particles with a median mass diameter of about 3.5 mm. The maximum heat flux to the debris catcher was 0.8 MW/m^2; there was no erosion of the catcher. Simulant tests of the melt release mechanism indicated that the initial portion of the melt jet is likely to be drawn to one side, and then to wander.

Jacobs (KfK) gave a brief description of the IVA-3 code, which has been developed at Karlsruhe to study premixing. The code includes 14 flow regimes, which are selected locally on the basis of phase volume fractions. IVA-3 has been used for both pre- and post-test analysis of the second FARO-LWR scoping test. A mesh with 6 radial and 20 axial nodes was used. The melt was assumed to be released over 4 times the area of the experimental nozzle. There was a tendency to underestimate the observed pressure rise when the initial particle size was set to 10 mm diameter; when this was reduced to 1 mm the pressure rise was overpredicted. An over-prediction also occurred in one case with the larger particles in which strong fragmentation occurred. This may well have been a numerical effect, but similar couplings between fragmentation and steam flow have been seen in other calculations. Jacobs also reported an analysis of the steam explosion that occurred in the BETA V6.2 experiment. IVA-3 calculated a rather benign pressure transient as a limited amount of melt entered the water in the annulus following melt through of the concrete. However, considerable level swell was predicted in the annulus, along with the melt levitation in the crucible. Jacobs speculated that the vent lines from the annulus, which turned to point down into the crucible, ejected water into the levitated melt causing a steam explosion in the upper part of the crucible.

Berthoud (CEA, Grenoble) presented a paper which includes a detailed description of the constitutive physics of the TRIO-MC premixing code. A key parameter used in the formulation is the void fraction when the melt no longer interacts directly with the liquid (above this value the convective film boiling contribution is zero, as is the corium-water drag). Regime maps also distinguish the cases of dense fuel packing, where debris bed models are used, and a dispersed fuel regime. The first FARO-LWR scoping test has been modelled with TRIO-MC using 10 radial and 28 axial nodes. On the basis of a liquid jet break-up regime map it was concluded that the initial pour was in the atomization regime. Further, using a Weber number criterion the initial particle diameter was set to 10 mm. The pressurisation following melt-water contact was reproduced reasonably well, as was the final particle size. In discussion, the assumption that the melt jet would break-up before reaching the water surface was queried. Berthoud stressed the need for a break-up model; one is being developed for later versions of TRIO-MC.

Sienicki (ANL, USA) described work carried out in collaboration with the Swedes on jet fragmentation for deep water pools (ex-vessel). Scoping energy balance calculations indicate that limited flooding beneath the vessel could quench the debris, but it is unclear whether, in practice, sufficient heat transfer would occur. The THIRMAL-1 code had been used to address this issue. Except for the initial transient the dominant fragmentation mechanism assumed is the erosion of molten droplets from the surface of the melt stream due to Kelvin-Helmholtz instability. Further melt-water interactions can generate steam around the melt-jet and influence the dynamics of the stripped particles. As the leading edge thins (in the model), it is subjected to capillary break-up, thus limiting the depth of penetration of the jet. Although the main calculation showed the vast majority of a 106 tonnes melt pour falling through 6.9 m of water being

fully quenched, sensitivity calculations indicated that there may be circumstances in which unquenched melt droplets could reach the base. For smaller depths of water (e.g., 4 m) the melt stream may reach the base for a larger range of parameters. It was concluded that further experimental validation is desirable.

Bürger (IKE, Stuttgart) described model developments for jet break-up. He said that jet break-up was not treated sufficiently in the current premixing codes, but remarked that, although models have been developed for break-up, there is not yet agreement even on the relevance of the basic physical models. As in the Argonne work, described above, Bürger has based his model on application of the Kelvin-Helmholtz instability. Bürger considered both a classical Kelvin-Helmholtz instability, where there is a discontinuity in velocity at the interface and a shear layer formulation. In these models the fragment size is determined by an energy balance principle. The models had been compared with data from experiments using molten Woods metal and water, and with ANL experiments using corium and water. These comparisons showed some discrepancies with the models: the Kelvin-Helmholtz approach for the simulant tests gave much too rapid fragmentation, while both approaches produced too small fragment sizes (although coalescence may occur in the experiments). Applying the shear layer formulation to corium jets results in much longer coherent jets with relatively little fragmentation; no final conclusions can be drawn from the Argonne corium tests. In discussion the use of linear stability analysis to provide a quantitative model was queried by a number of participants; the debate was vigorous, but inconclusive.

Hall's (NE, UK) simulant experiments for CHYMES validation were presented by Turland. The paper described tests, mainly performed in a slab geometry, with isothermal simulants (glass ballotini, glass balls, steel balls, mercury) and molten tin (single and multiple jets) into water, besides a preliminary experiment in which 3.5 kg of iron, generated from thermite, was poured through a 4 x 4 array into water. The slab geometry experiments were compared with CHYMES calculations. Calculations were reported with both a standard value of the drag coefficient (0.55) and an enhanced value (2.0), which had been found to give a better fit to isothermal simulant tests with steel balls entering water. The general picture was that while CHYMES predicted the qualitative behaviour reasonably well, it underpredicted radial dispersion at this scale. The agreement was least satisfactory for the multiple tin jets into water, where the code's prediction of little effect of vapour generation on the melt dynamics was not supported by the experimental data (however the 2-D geometry here may be unrepresentative, as the steam must break the jets up to escape). It was concluded that the experiments indicated that turbulence processes, not included in the code, were important for small particles in isothermal test, while CHYMES current drag laws may underestimate coupling between hot particles and the vapour. However, a full understanding of these effects is probably only required if the code is to be validated for detailed fuel/coolant/steam ratios, rather than used to confirm the gross features of the interaction. The scoping test with pre-dispersed iron-thermite had similar qualitative features to those observed in the MIXA tests.

Fletcher (AEA Technology, UK) described the validation of CHYMES, concentrating on data from the MIXA 06 test. He also referred to the verification work in which CHYMES calculations had been compared with FEAT and FLOW3D for a laminar jet, and with PM-ALPHA for melt dynamics. In the MIXA 06 test a ~120 mm jet of pre-fragmented ~6 mm droplets was poured into water at the saturation temperature at ambient pressure. The melt consisted of 3 kg of UO_2–Mo formed by a thermite interaction at 3600 K. CHYMES reproduced some features of the experiment well (the steam chimney, the melt fall rate after the initial deceleration, and the steam flow rate to within a factor of 2) but it did not predict some features of the mixture development (the initial melt deceleration and the radial spreading). Use of alternative drag laws (those in PM-ALPHA) led to excessive melt levitation. It was concluded that CHYMES is very valuable for providing a picture of the mixing process and the global conditions in the water pool prior to any explosion; however it has not been sufficiently well validated for use in a 'limits to mixing role.'

Theofanous (UCSB, USA) presented an update on the premixing studies being performed at the University of California at Santa Barbara. He noted that the boiling/condensation model in the PM-ALPHA code had been modified, but said that this had a minimal effect on predictions. The constitutive physics used in PM-ALPHA is fully described in an appendix to the paper. Various simulations for the MAGICO experiments, in which tens of kilogrammes of mm-sized steel balls are heated to temperatures up to 1000°C and then poured into water, were reported. In the tests the steel particles fall with little radial dispersion. The steaming rate often shows a significant increase after ~0.8 s of the interaction. This effect is reproduced in the PM-ALPHA calculations, where it arises from water outside the pour region reversing its direction of flow as its gravitational head builds up and re-entering the region of hot particles. The paper also describes verification of the local void fraction measurements made with the FLUTE device. A flash of soft X-rays was used to take an image of the mixing zone; in cross-sections where there are no particles present, the line density of water can be evaluated. Results are in good agreement with the FLUTE values (5–10% differences in void) and PM-ALPHA predictions. The PM-ALPHA has also been applied to the first FARO-LWR scoping test. The radiative heating of the cover gas prior to interaction with the melt was matched in a parametric manner, and the simulation then used a fixed particle size (7 mm) for the melt-water interaction. The experimental data were reasonably well matched by the simulation.

4.2 Propagation and Energetics

4.2.1 Chairs' Summary of the Session

Triggering

A suitable triggering event is required to start the mechanical energy release process following premixing. Trig-

gering is a complex physical process which can occur in the reactor case via, e.g. structural impact, cold water injection or entrapment of water within melt. A key issue is the effect of pressure on triggering, since establishment of a pressure threshold above which explosions cannot be triggered by the sources available in an accident would be very useful.

In experiments, a wide range of triggers have been used and their strengths vary greatly. It was proposed that these should be classified according to whether they are weak (i.e., have a small energy compared with that required to involve more melt droplets), intermediate, or strong (in which the trigger fragments sufficient melt for the trigger pulse to be sustained or amplified but at relatively low rates compared to a true propagating event).

Propagation

On the experimental side, the KROTOS tests have demonstrated that supercritical propagation can occur in 1-D in the aluminum oxide/water system. Progress has been made in measuring the initial conditions prior to an explosion but additional diagnostics which provide local measurements of the void fraction in the premixture and some form of visualization would be very helpful.

On the modelling side, the aim is to perform calculations to determine the possible energy conversion from the premixture and to provide pressure-time histories for structural loading calculations. The framework suggested by Board and Hall has been developed to the point that transient models now allow for finite fragmentation and heat transfer rates. The models developed include CULDESAC, IDEMO and TEXAS-III which are 1-D and ESPROSE which is 2-D. Comprehensive studies have been performed to check the numerical aspects of these calculations, to ensure that they reproduce known two-phase flow behaviour and to investigate parameter studies. However, the degree of validation against experimental data is low.

The important inputs to these models are the initial mixture configuration and the constitutive relations for heat transfer and fragmentation. It has been recognized that thermal disequilibrium in the water phase (because the fragments are not in contact with all of the water) is very important. Recent experiments in the SIGMA facility at UCSB have illustrated the extent of fragment mixing with water and the term 'microinteractions' has been coined to describe the zone containing a mixture of fragments and heated water.

Attempts to model the KROTOS tests have yielded results in broad agreement with the experimentally observed pressure levels and propagation speeds but have required 'artificial' assumptions to overcome the lack of modelling of the micro-interactions described above. Recent work at UCSB has suggested a means by which the micro-interactions can be included in a propagation model (their modified code is ESPROSE.m) and initial results are promising.

Two-dimensional scoping calculations performed using ESPROSE have shown the importance of the void in the premixture and two-dimensional effects in determining the pressure load on the boundaries of the mixing vessel and the pressure field in the mixing system.

Stratified Explosions

A wide range of small-scale experiments using simulant materials have been performed to investigate stratified explosions. From these it can be concluded that the velocity of propagation is low ($\sim$50 m s^{-1}), that the mixing depth (i.e., the thickness of melt involved in the explosion) is of the order of 5 mm and that without sufficient inertial constraint (provided by the upper layer of fluid) a propagation does not occur. On the basis of these data stratified explosions are of no importance in the α-mode failure issue but may be relevant ex-vessel where a large pool of melt could collect. Some workers are also concerned that a stratified explosion could premix more material but although such secondary explosions are observed in experiments using simulant materials there is no evidence that this mixing process is particularly efficient.

Chemical Reactions

Considerable interest has been shown recently in the use of aluminum clad fuels for the New Production Reactor project. The energy potentially available from melts containing aluminum (from oxidation and hydrogen combustion) greatly exceeds the thermal energy. Experiments using single droplets and kilogramme quantities of melt have shown that this reaction is potentially important and is scale-dependent. A simple model suggests that the local void fraction in the premixture is also very important. Additional data would be required to validate this model.

The same type of reaction potentially could occur with zirconium. Although the rapid release of chemical energy has been observed in the aluminum/water system there is no direct evidence that it can occur in the zirconium/water system. In the latter case, it is likely that the zirconium would be mixed with oxidic phases (reducing the likelihood of a 'runaway reaction') and it is believed that a significant interaction would be required to initiate the chemical reaction by finely fragmenting some melt locally.

4.2.2 Summary of Papers in the Session

There were a total of ten papers presented in the session entitled "Propagation and Energetics." These dealt with the issues of triggering, propagation and combined chemical reaction. A brief summary of each paper is given below.

McCahan (Univ of Toronto) presented a paper, coauthored with Shepherd, on the calculation of possible end-states for aluminum-water interactions. The usual shock Hugoniot analysis was performed, but allowing for the chemical reaction of the aluminum, and CJ detonation and deflagration end-states were calculated. It was stressed that both end-states should be considered and it was suggested that propagating explosions may correspond to the CJ deflagration.

Fauske (Fauske and Associates Inc) presented a paper coauthored with Epstein on the requirements for energetic

molten aluminum-water interaction. A heuristic model was presented which was based on the assumption that the reaction zone behind the shock front is of the order of a few centimetres wide and that its length is independent of the premixture configuration and the oxidation kinetics. With this assumption, together with relationships for shock speeds and relative velocities in two-phase mixtures they were able to show that the fraction of metal oxidised was very sensitive to the initial void fraction. Making reasonable assumptions for the initial void fraction in both the SL-1 incident and for the large-scale pouring test performed at Sandia allowed the difference between the two cases in the fraction of metal oxidised to be reproduced.

Gabillard (Gaz de France) presented a paper coauthored by Sainson and Williams on experiments performed to study stratified explosions in the liquid nitrogen/water system. Propagation was not observed in their system when the liquids were fully stratified. Instead they observed propagating triggers which rapidly died away. If they triggered an interaction soon after the liquid nitrogen was poured onto the water, while the interfaces were still 'wavy', a propagating explosion was obtained.

Frost (McGill University) gave a paper on stratified tin/water explosion studies which was coauthored by Bruckert and Ciccarelli. Results were presented from studies of stratified explosion experiments performed in three different geometries, namely (i) linear propagation in a narrow channel open at the top, (ii) propagation in a narrow channel with vertical confinement, and (iii) radial propagation in a cylindrical tank. The experiments resulted in propagations with a speed of 40-50 m/s, an effective mixing depth of less than 2 mm and low conversion efficiencies (less than 1% of the ideal maximum). In addition, a minimum degree of inertial confinement (represented by the overlying water layer depth) was identified for a propagation to occur. In some circumstances a second interaction was observed when the tin and water mixed as they fell back under gravity after the initial stratified explosion had occurred.

Henry (Fauske and Associates Inc) described a proposed methodology for determining where an observed explosion was simply a propagating trigger pulse or a real propagation event. His ideas are based on the observation that the initial premixture is a meta-stable state, so that inputting energy from a trigger will result in the release of more energy without propagation necessarily occurring. He proposed a quantification of this effect using mixing energy fomulae developed by Cho et al. It was concluded that the propagating events observed in the FITS tests were propagating triggers rather than true propagations. He stressed the importance of using realistic triggers in explosion experiments if they are to be applied to the reactor situation.

Fletcher (AEA Technology) presented a paper describing recent results obtained from the CULDESAC propagation model. He gave a brief description of the equations and constitutive physics used in the model. He then went on to describe calculations performed to examine numerical aspects of the computations (e.g., effect of grid size), the effect of varying the heat transfer rate, the initial mixture conditions and allowing for non-uniform mixtures. His calculations showed the rapid attenuation of pressure pulses in regions of high void fraction even in 1-D. In addition, he presented calculations which showed a deflagration-like mode of propagation, obtained using a thermal fragmentation model.

Hohmann (JRC Ispra) presented a paper, coauthored with Magallon, Schins and Yerkess, describing the latest propagation experiments performed in the KROTOS facility. Experiments have been performed using 1.5 kg of $A\ell_2O_3$ melt at a temperature of 2300-2400°C released into water subcooled by 10, 40, and 80 K. In the nearly saturated system, steam explosions could be externally triggered and resulted in supercritical explosion pressures. In the two tests performed with the water subcooled by 80 K self-triggered explosions occurred and gave rise to pressures above 100 MPa. An energy conversion ratio of 1.25% was estimated (based on the mass of material less than 250 μm).

Corradini (Univ. of Wisconsin) presented a paper, coauthored by Tang, describing the TEXAS-III integral model for FCIs. The model is 1-D and treats the steam and water as Eulerian phases but treats the melt in a Langrangian manner. The model contains a hydrodynamic fragmentation model (used for mixing and propagation calculations) and a thermal fragmentation model (based on film collapse and subsequent coolant jet penetration into the melt) which is used during propagation calculations and is believed to be necessary during the escalation stage. The model has been applied to the KROTOS-21 test and fair agreement with the data was obtained.

Bürger (Univ. of Stuttgart) presented a paper, coauthored by Buck, Müller and Schatz, on the stepwise validation of thermal detonation models. He presented a brief description of the IDEMO model and discussed validation philosophy. He showed that IDEMO gave predictions for the tin/water experiment KROTOS-21 which were in similar agreement with the experimental data to those calculated using ESPROSE.a. In order to obtain this agreement a strong additional contribution of thermal fragmentation was assumed in IDEMO. An initial calculation for the experiment KROTOS-28 was presented and was shown to reproduce the essential features of the experiment (the peak pressure and propagation velocity).

Theofanous (Univ. of California at Santa Barbara) presented a paper, coauthored by Yuen, on the prediction of 2-D thermal detonations and their resulting damage potential. He described the development of the ESPROSE model with time from a basic model using 3 fluids (fuel, steam, and water and debris) via ESPROSE.a (in which thermal fragmentation and direct vaporization of the water were allowed) to the current version, ESPROSE.m, which has three fields: fuel particles, microinteraction zone and water. The microinteraction zone contains the fragments and the water they heat, with data to describe this region being obtained from the SIGMA facility. Calculations were presented for KROTOS tests, an explosion in the lower plenum of a reactor and in the cavity. The importance of allowing for microinteractions and multi-dimensional effects (due to spatial

variations in the melt and void fraction) was demonstrated. The importance of the void in reducing peak pressures was noted.

4.3 Miscellaneous Experiments and Open Forum

4.3.1 Chair's Summary of the Session

In many contributions an important renewed interest in a deeper understanding of steam explosions was demonstrated. The aims of these activities are to confirm present indications to the degree required (according to the needs of the task) and to develop (improve) own capabilities in analyzing steam explosions.

The large number of *experimental* studies recently begun or in preparation indicates a serious need of data for better understanding mechanisms, verify hypothesis, and validate models. Statistically significant results of experiments using prototypical materials under conditions relevant for accident scenarios are most useful to answer safety questions. While data obtained with simulant materials can be quite useful to study individual reaction mechanisms or separate effects, the applicability of such data to the reactor case is not guaranteed.

Since most experiments are at small or intermediate scales, application to reactor safety questions requires the use of models (analytical or numerical) and concern about effects of scale. Computer codes need to be validated by comparison of the final code version with relevant experimental data. With more relevant data becoming available, it would be useful to identify a set of experiments to be analyzed by proposed mixing and explosion models in a way organized by CSNI and to develop a scaling rationale.

4.3.2 Summary of Papers in the Session

4.3.2.A Miscellaneous Experiments

1. The third day's sessions began with a paper describing work by researchers at Georgia Tech on the effect of surfactants on the likelihood and severity of energetic FCI. A series of experiments was performed with differing concentrations of surfactant in water at atmospheric pressure. Molten tin (~10 gm) at 800 degrees C was dropped into the water (~20°C). The authors conclude that, "Regarding the use of surfactants for practical applications, at the present time, insufficient data exists regarding the effects of surface tension to propose any firm recommendations."

2. The next paper, by Lloyd Nelson at Sandia, reported on experiments in which single drops of aluminum were dropped into water. This recent work was done in connection with safety studies of one of the proposed new production reactors, and has little direct relationship to commercial power reactors. The phenomena focused on the aluminum ignition temperature threshold important to FCIs in aluminum-water interactions. He suggested that the ignition threshold decreases as the mass of the aluminum is increased.

3. A Japanese group at JAERI has been conducting experiments in which the interaction of molten thermite material, simulating fuel, interacting with water. The multipurpose ALPHA facility was used in these experiments to investigate larger scale explosions and the effect of subcooling, ambient pressure, interposing structure and contact mode. This work in some ways extends the work of Sandia in the FITS facility and to date the results are qualitatively similar.

4. This same group reported experiments meant to simulate the expulsion of hot fuel into coolant by a severe RIA. Although the SL1 accident appears to have demonstrated that when this occurs the resulting SE can be severe, it is not clear that this is relevant to US power reactors. The presentation by the Japanese researchers was a complete review of these past experiments and associated analyses.

4.3.2.B Open Forum

1. Peppler (KfK Karlsruhe) reported on experiments with respect to melt/coolant premixing and to energy conversion that are in preparation at KfK. Premixing will be studied in an open geometry with optical observation while energy conversion will be measured in a strongly confined geometry. In both cases the corium melt will be simulated by molten Al_2O_3. Exploratory tests have been conducted but are not yet evaluated.

2. Meyer (KfK Karlsruhe) reported on planned experiments in which the melt/water premixing process is studied replacing the melt by a multitude of hot spheres. The sphere temperature shall range up to 2600 K and dense jets of spheres shall be studied. In preparatory tests single instrumented spheres of 15 mm diameter have been quenched in saturated water.

3. Cenerino (IPSN/CEA France) described the IPSN sponsored steam explosion research within CEA. Besides the development of the multifield code TRIO-MC (see Session I) experiments with spheres in place of the melt are in progress at Grenoble. The experimental program consists of three phases: isothermal tests that are finished, intermediate temperature (up to 1300 K) tests beginning 1993, and high temperature (up to 2500 K) tests beginning 1994. The mechanical effects of steam explosions on the reactor vessel are studied with the PLEXUS code at Fontenay-aux-Roses. So far scoping calculations have been performed in which the heat addition to the water has been described parametrically.

4. Bürger (IKE Stuttgart) reported on experimental and theoretical studies of drop fragmentation in thermal detonation waves. He concluded that it is not yet clear which fragmentation mechanisms are relevant in which situation. Similarly there are no agreed upon mathematical descriptions of these mechanisms.

5. Cho (ANL) reported on an aluminum/water FCI experiment in which a violent interaction has been observed. In this experiment a strong trigger has been used and the thermal interaction has partly been clouded by a chemical interaction of dispersed aluminum with the atmosphere.

6. Frost (McGill U, Montreal) reported on experiments to study thermal fragmentation of single drops, i.e. with cycles of bubble growth and collapse. Metal drops have been observed to fragment by ejecting filaments. It is thought that the coolant vapor pressure plays an important role in this. The 'fuel' surface tension may strongly influence the second bubble growth.

7. Venart (U New Brunswick) reported on experiments in which explosive vaporization of superheated liquids was observed. He stressed that recompression of already expanded bubbles was required to produce these explosions.

8. Theofanous (UCSB) reported on recent results of the SIGMA experiments in which fragmentation of molten metal drops is studied in a shock tube. The main point was that aluminum did blow up into a porous but still coherent body in contrast with tin for which production of individual fragments of micrometer size had been observed.

4.4 Integral Assessment and Risk Aspects

4.4.1 Chair's Summary of the Session

In summary, the assessments provided by Turland and Theofanous clearly show that the assessments of in-vessel steam explosions since the Steam Explosion Review Group report (NRC, 1985) have resulted in a reduction in the conservatisms initially imbedded in the SERG report with the major implication being that these assessments have shown a substantially reduced potential to intermix large quantities of molten fuel with water as the debris drains into the lower plenum. The major reason for this is water depletion in the interaction zone due to the substantial heat transfer from the particulated debris to the water and the influence of the subsequent high steaming rates on the surrounding water pool. Further initial explosion loading results presented by Theofanous indicate that accounting for the voiding within the mixing zone and for 2-D propagation may provide adequate relief to eliminate concerns about lower head failure. The discussion provided by Jacobs shows that additional work will be done and can potentially further reduce the conservatisms in the analyses for the likelihood of such events, potentially resulting in the conclusion that steam explosions sufficient to fail an RPV are impossible. Lastly, the considerations provided by Okkonen show that, while the issues related to alpha-mode failure may be moving toward a general consensus, there are other issues related to accident management considerations that should be included so that these issues can be technically evaluated and incorporated into the accident management training given to utility personnel.

4.4.2 Summary of Papers in the Session

Four papers were presented in this session, the first focused on issues related to fuel-coolant interactions in BWRs, the second provided a quantification of the conditional probability for containment failure resulting from an in-vessel steam explosion, the third reported on steam explosion assessments at Karlsruhe and the fourth updated the probability for an alpha-mode containment failure from a previous assessment. This spectrum of topics provides a sound foundation for assessing the applicability of the Steam Explosion Review Group (NRC, 1985) conclusions in light of new information.

1. The first paper on FCIs in BWRs presented by Okkonen (STUK, Finland) concludes that in-vessel steam explosions of sufficient strength to damage the reactor pressure vessel and containment "is estimated even less likely in a BWR than is indicated by the studies focused on PWRs." This is principally attributed to the dense packing of control rod guide tubes in a BWR lower plenum, thereby preventing a coherent melt relocation and coarse premixing of sufficient quantities to create an explosion as envisioned in the "alpha-mode" failure discussed in the Reactor Safety Study (NRC, 1975). Other potential issues related to less energetic events, but nonetheless significant for evaluating accident management behavior were raised in this paper. These include the potential for inducing a fuel coolant interaction when a BWR core, which may have experienced melting relocation of control material, is reflooded as a result of a fuel coolant interaction in the lower plenum. Order of magnitude analyses were performed assuming that a low void fraction "slug" of water could be pushed into the core region as a result of an FCI in the lower plenum. These estimates assume that fuel coolant interactions could occur in the lower plenum and propel a one-dimensional, two-phase mixture into the core, and indicate concerns of recriticality and neutron power peaks in core regions without control material. However, it was concluded that a more detailed study of phenomena should be undertaken. Additional considerations were discussed with respect to the oxidation of Zircaloy as a result of FCIs and the potential pressurization of the smaller volume BWR containments. Lastly, accident management considerations with respect to conditions within the reactor pressure vessel and containment relating to accident management measures and procedures were also discussed. In particular, the actions considered and briefly evaluated were (1) primary system depressurization, (2) core cooling recovery, (3) flooding of the pedestal region, and (4) containment flooding.

2. The second paper presented by Turland (AEA Technology, UK) discussed a methodology for quantifying the conditional probability of alpha-mode failure. The specific reactor analyzed was the Sizewell B PWR and the methodology focused on the areas of:

- the melt relocation rate and the time to first contact of the base as a means of assessing the amount of molten material mass in the lower plenum,
- the likelihood of initiating a trigger,
- the extent of the mass involved in the explosion once an event has been initiated,
- the likelihood that the lower head could be failed if an explosion was initiated,
- the kinetic energy that a postulated slug would have if it was propelled upward by an explosion in the lower plenum,
- the potential distribution of energy of the slug impacting on the upper head, and

- the likelihood that a missile created by rupturing the RPV upper head would threaten containment integrity.

Distribution functions were applied to all of these elements in the analysis and a Monte Carlo sampling technique was used to develop the probability density distributions and to calculate the likelihood that an alpha-mode failure could occur. Discussions were provided with respect to the information examined for each of the processes and how this was used for the distribution functions. For example, the pressure dependence for triggering of explosive events was considered to be more difficult at elevated pressure. Assumed were a 70% probability of occurrence if the pressure was essentially 0.1 MPa, a 20% probability of occurrence if the pressure was 6 MPa and a 10% chance if the pressure was 15 MPa. Once these distribution functions were formulated and inputted to the Monte Carlo method, the conditional probability of an alpha-mode failure given melt relocation to the lower plenum was assessed as a few parts in 10,000. It was stated that the Sizewell B evaluaton is the first to consider the likelihood that elevated RCS pressures would reduce the chance of explosions, with the results suggesting only modest sensitivity to system pressure. However, this was essentially dictated by the relatively insensitive distribution function developed to describe the pressure dependence for the trigger.

With the assessment for Sizewell B, at a few parts in 10,000, alpha-mode failure has an essentially negligible contribution to the risk of the plant. It is also noted that several of the assessments carried out, such as the potential for slug formation and transmittal were conservative in assuming that such overlying slugs could occur. Mitigating effects such as leakage by an overlying slug were evaluated, but even though several reasons were given for why it was hard to identify coherent slug overlying the explosion region, a slug was still assumed in the analysis. The bypass leakage was used to represent all of the reasons why an overlying slug tamping the explosion would likely be difficult to achieve.

3. In the third paper Jacobs (KfK, Germany) discussed the ongoing research at Karlsruhe, including alternate containment designs to specifically prevent the alpha-mode failure as conceived in WASH-1400. These are considered because of the *perceived* results of an in-vessel steam explosion. This is based on the conclusions that past steam explosion research has

- only provided a broad qualitative understanding,
- has not provided sufficient quantitative information, and
- has not developed a simple physical argument to exclude containment failure altogether.

To further develop the understanding of steam explosions, the specific activities at KfK include the following.

- Experiments on melt/water premixing,
- experiments on energy conversion,
- experimental determination of loads on the vessel head,
- theoretical analysis of premixing,
- theoretical analysis of energy conversion in steam explosions,
- theoretical analysis of core melt progression, and
- theoretical analysis of mechanical behavior of pressure vessel and core components under steam explosion loads.

4. The last paper in Session V (presented by Theofanous, UCSB) was devoted to an update of the assessment of the probability of alpha-mode failure. Specifically, this updated the assessment provided by T.G. Theofanous, et al., in 1987 using the Risk Oriented Accident Analysis Methodology (ROAAM). In particular, this paper focused on the mass of core material that could be effectively premixed with water as the melt drains into the lower plenum. This assessment was developed through a computer code, designated as PM-ALPHA, which addresses the potential for water depletion in the interaction zone as the melt is fragmented and attempts to intermix with the lower plenum water. This computer model compares favorably with experiments (Angelini, et al., 1993) as well as with the results of another computer code, CHYMES, recently published by Fletcher (1992). While further experimental validation is desirable, the results of plant calculations showed that the premixing for a depressurized reactor system was limited to $\sim$ 1500 kg at the time that the melt front would reach the RPV lower head. It was concluded that this shows that there was a large degree of conservatism embodied in the assessment provided in NUREG/CR-5030 (Theofanous, et al., 1989).

References

1. Angelini, S., Yuen, W.W. and Theofanous, T.G., 1993, "Premixing-Related Behavior of Steam Explosions," CSNI Specialists' Meeting on Fuel-Coolant Interactions, Santa Barbara, California, January 5-8, 1993.
2. Fletcher, D.F., 1992, "Comparison of Coarse Mixing Predictions Obtained from the CHYMES and PM-ALPHA Models," *Nuclear Engineering and Design*, 135, 419-425.
3. Nuclear Regulatory Commission (NRC), 1975, "Reactor Safety Study," WASH-1400.
4. Steam Explosion Review Group (1985) "A Review of Current Understanding of the Potential for Containment Failure Arising from In-Vessel Steam Explosions," NUREG-1116, U.S. Nuclear Regulatory Commission.
5. Theofanous, T.G., Najafi, B. and Rumble, E., 1987, "An Assessment of Steam-Explosion-Induced Containment Failure. Part I: Probabilistic Aspects," *Nuclear Science and Engineering*, 97, 259-281, also published as NUREG/CR-5030, 1989.

HIGH PRESSURE CORIUM MELT QUENCHING TESTS IN FARO

D. Magallon and H. Hohmann
Commission of the European Communities
Joint Research Centre, Safety Technology Institute
21020 Ispra (Va) - Italy
Telephone +39-332-789361, Fax +39-332-785412

ABSTRACT

The paper presents and discusses the first of a kind experimental data concerning the quenching of large masses of corium melt of realistic composition when poured into pressurized water at reactor scale depths. The tests involved 18 and 44 kg of a molten mixture 80 w% UO_2 - 20 w% ZrO_2, which were delivered by gravity through a nozzle of diameter 100 mm to 1m depth nearly saturated water at 5.0 MPa (i.e. around 263°C). The objective was to gain early information on the melt/water quench process previous to tests that will involve larger masses of melt (150 kg of mixtures UO_2-ZrO_2-Zr). Particularly, pressures and temperatures were measured both in the gas phase and in the water. The results show that significant quenching occurred during the melt fall stage with 35% of the melt energy transferred to the water and 15% used for steam generation. About 2/3 of the melt fragmented in particles of mean size of the order of 4.0 mm. The remaining 1/3 collected still molten in the debris catcher but did not produce any damage to the bottom plate. The maximum downward heat flux was 0.8 MW/m^2. The maximum vessel overpressurization, i.e. 1.8 MPa, was recorded with 44 kg of melt poured into 255 kg of water and a cover gas volume of 0.875 m^3. No steam explosions occurred.

I. INTRODUCTION

The general background of the present FARO-LWR Test Series has been previously reported (Fasoli-Stella and Hohmann, 1991; Corradini and Hohmann, 1992). It is summarized here. The reference situation is that of a postulated core melt down accident when jets of molten corium penetrate into the lower plenum water pool. This issue suffers a lack of data on the water quenching potential that determines whether the thermal loading on the bottom head structures is mitigated. In past analyses it had been assumed that this sequence of events would have result in either settling of most of the fuel unquenched on the lower head with eventual RPV wall failure, or steam explosion. During the TMI-2 accident, although twenty tons of corium did pour into the water lower plenum, neither of these two possible scenarios actually occurred. Consequently, safety aspects of the FCI issue needed to be reconsidered and it has been found of fundamental importance to carry out tests involving large amounts of prototypical corium poured into water at reactor scale depth, in order to characterize the melt/water mixing and quenching process, and melt /structure interaction.

The JRC-Ispra FARO plant (Hohmann et al., 1986) is used for such a purpose. It is a multi-purpose test facility in which Severe Accidents can be simulated out-of-pile under a variety of conditions. Basically, a maximum quantity of the order of 150 kg of UO_2-ZrO_2 fuel type melts (up to 3000°C) can be produced in the FARO furnace, possibly mixed with metallic components (e.g. Zr), and delivered to a test section of interest. The plant has been used previously for LMFBR safety problems such as melt relocation and molten fuel/sodium interaction. The 1.5 m^3 test vessel TERMOS used for MFCI experiments can withstand 10 MPa at 300°C, which makes it particularly suitable for simulating high pressure accident sequences. It can contain up to approximately 1 m^3 of coolant over a height of 2.5 m and a diameter of 0.71 m.

The objective of the test series is to determine: -1) the melt quenching rate associated to the melt/water penetration, -2) the hydrogen production associated to the zirconium oxidation, -3) the thermal load on the bottom structures, and to -4) characterize the debris structure. It must be noted that these tests are not steam explosion experiments and, consequently, are not intended to produce data for this issue. The first

part of the test matrix, which deals with high pressure and nearly saturation conditions (Fasoli-Stella and Hohmann, 1991), should further limit the risk of a steam explosion and allow to concentrate on the quenching phenomena. Nevertheless, the possibility of occurrence of a steam explosion has been taken into account and the instrumentation chosen accordingly (fast pressure transducers in the water).

In the absence of previous work under the conditions mentioned above, it had been decided to proceed by step towards the target corium quantity of 150 kg. Two tests has been performed at constant volume with a pure oxide mixture 80w%UO_2-20w%ZrO_2, which was delivered by gravity through a nozzle of diameter 100 mm to a 1.0 m depth nearly saturated water pool at 5.0 MPa. The melt quantity, the water mass, the vessel diameter were 18 kg, 120 kg, 0.47 m and 44 kg, 255 kg, 0.71 m for the first and the second test, respectively. The paper summarizes and discusses the findings from these experiments. A simple assessment of the steam generation during the melt fall stage is made. The heat fluxes through the debris catcher bottom plate are calculated from the thermocouple data. The most relevant and recent experimental study on the fragmentation and quenching of corium melts in water is the CCM series (Wang et al., 1989). Particularly, the CCM-5 and CCM-6 tests dealt with approximately 13 kg of a 60w%UO_2-16w%ZrO_2-24w% steel mixture poured into 510 kg of 45°C-subcooled and saturated water at 0.1 MPa through a nozzle of diameter 51 mm. Results from these tests are briefly compared with ours.

II. EXPERIMENT DESCRIPTION

A. Test Arrangement and Procedure

The experimental arrangement is shown in Fig.1. The interaction vessel TERMOS is connected to the FARO furnace via the release tube, the intersection/isolation valve unit and the melt catcher.

The corium is melted at low pressure (i.e. 0.1-0.2 MPa), while the pressure in TERMOS is as required by the test (e.g. 5 MPa). The melt catcher closing flap is the barrier between the low pressure and the high pressure regions. Nevertheless, the main isolation valve SO2 remains closed during corium melting for the sake of safety. The temperature in TERMOS up to the SO2 valve corresponds to the saturation conditions of TERMOS (e.g. 263°C).

At the end of the corium melting phase, the SO2 is opened, the melt released from the furnace to the catcher, and the SO2 closed again. The melt

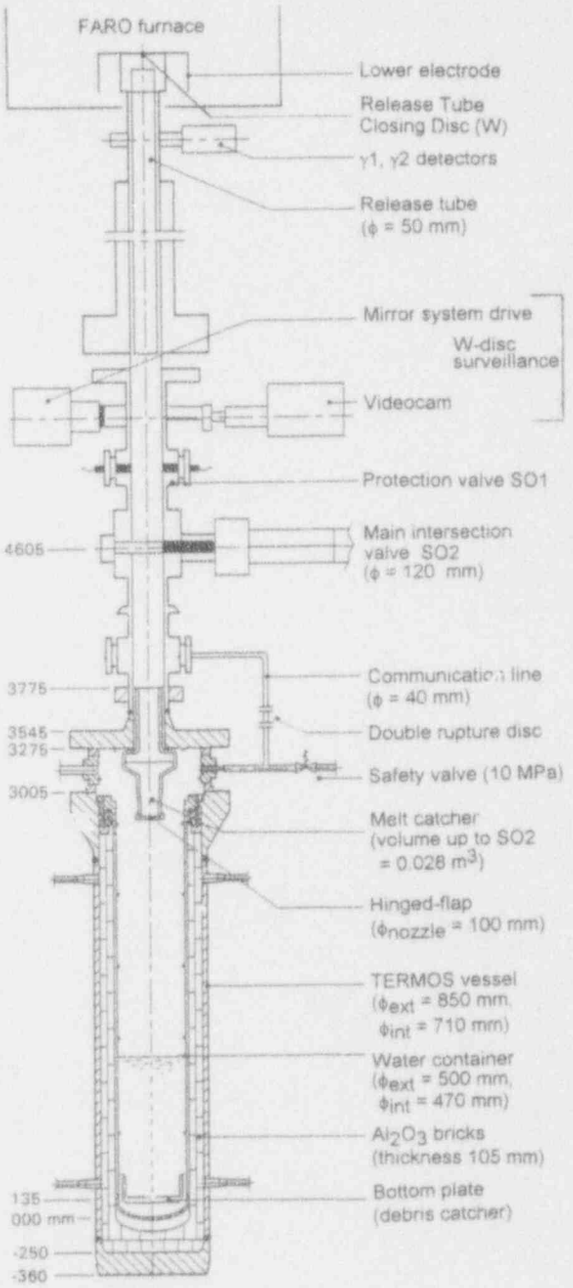

Figure 1. Scoping test arrangement

catcher volume is used as a lock-chamber for pressure equalisation. This is obtained by bursting a double disc mounted on the communication line, which acts as a quick opening valve. Upon pressure balancing, the melt catcher hinged-flap automatically opens, and the melt is delivered by gravity to the water.

B. TERMOS Test Section

1. Scoping Test (ST). The TERMOS test section included the pressure vessel (10 MPa, 300°C) and an

internal water stainless steel container separated from the pressure vessel by Al_2O_3 bricks for thermal insulation. The main dimensions are given in Fig.1. From the upper flange of the pressure vessel to the lower flange of the SO2 valve, a thermal insulator was installed externally. The heating of the space inside the water container was provided by means of four heater rods of total power 90 kW. The space above the upper flange of the pressure vessel up to the lower flange of the SO2 was heated by means of trace-heaters (21 kW) sticked on the outer surface of the components.

The debris catcher was supported by three adjustable legs put on the bottom of the water container. The debris catcher bottom plate had a thickness of 40 mm. Its upper face was distant 135 mm from the bottom of the container. The catcher was provided with trace-heaters (3.5 kW) sticked on its lower face.

2. Quenching Test 2 (QT2). For this test the internal vessel of diameter 470 mm and the Al_2O_3 bricks were removed, thus increasing the diameter of the water pool to the diameter of the TERMOS vessel, i.e. 710 mm. To account for the increase of steel mass to be heated with respect to the Scoping Test (the pressure vessel itself 45 mm thick, i.e. about 7 tons), additional trace-heaters for a total power of 17.5 kW were sticked on the lower part of the TERMOS outer wall. The vessel was thermally insulated from outside. The same debris catcher as for the Scoping Test was used with a funnel to account for the change in diameter of the test section.

C. Test Instrumentation

The principal quantities measured during the corium quenching were pressures and temperatures both in the gas region and in the water, and temperatures in the debris catcher bottom plate. The distribution and types of the probes reported in Fig. 2 and 3 correspond to the Scoping Test configuration. They remained essentially the same for the Quenching Test 2.

Four KELLER pressure transducers (piezoresistive, 5-kHz frequency response) measured the vessel pressurisation. They were installed at the end of 12-mm-diam, 400-mm-long straight tubes emerging in the gas phase region at the levels reported in Fig.2, and water cooled. Prior to the test, the uppermost ones were used to monitor the pressure in the melt catcher and in the chamber between the double disc, respectively. Four VIBRO-METER's (piezoelectric, 15-kHz frequency response) were located in the water as indicated in Fig.2 (radial position: 195 mm from the vessel centreline) for rapid transient records in case of an FCI. They were protected by stainless steel grids.

The eight steam K-thermocouples were installed in such a way that they could not "see" a centred melt jet. 14 thermocouples were fixed on the structures by means of clamps. They were fixed to the internal vessel for ST and to the pressure vessel for QT2 at the same axial positions. The 25 water K-thermocouples were essentially sacrificial thermocouples used to determine the downward progression and radial extension of the melt jet. Those not destroyed during melt penetration recorded the long time water temperature history. They were attached on thin (0.2 mm) stainless steel wires crossing the test section.

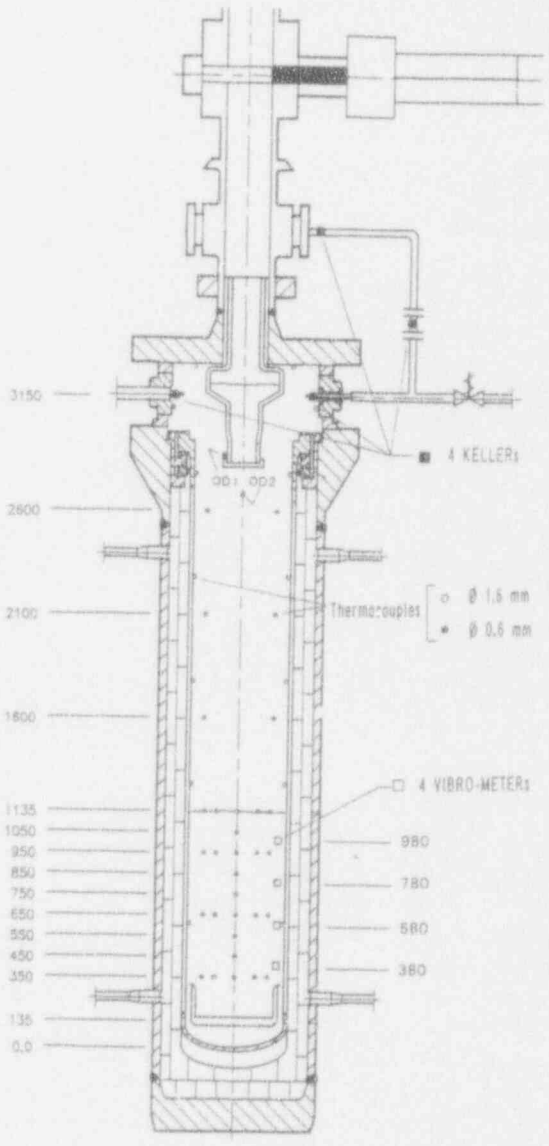

Figure 2. Scoping test instrumentation

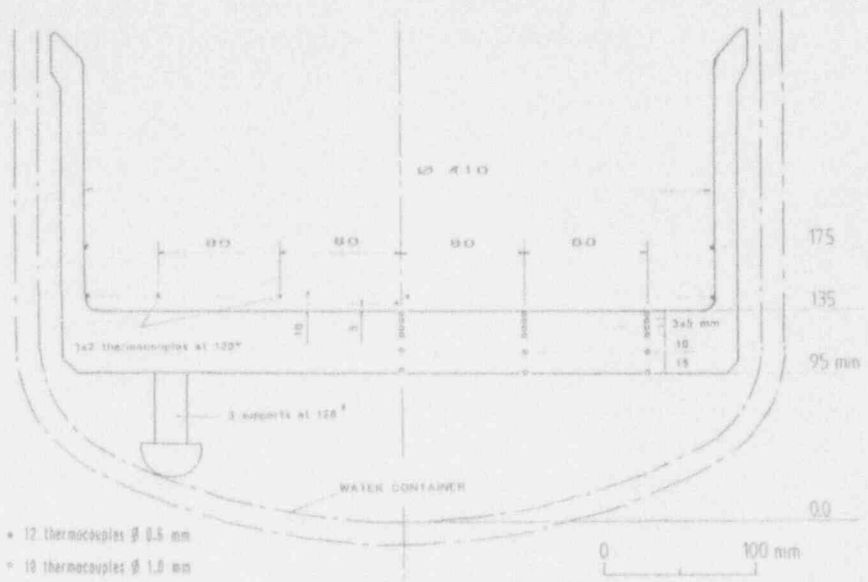

Figure 3. Debris catcher instrumentation

The opening of the melt catcher was indicated by the rupture of a 0.5 mm K-thermocouple (OD1) mounted opposite to the hinge, and fixed both to the melt catcher lower flange and to the flap. Another 0.5 mm K-thermocouple (OD2) was placed on the centreline of the vessel, 250 mm below the lower face of the flap, for detecting the passage of the melt.

In addition to the instrumentation reported in Fig.2, four resistance probes for measuring the level swell in QT2 were installed 250, 500, 750 and 1000 mm above the initial water level, respectively (radial position: 160 mm from the vessel centreline).

III. EXPERIMENTAL CONDITIONS

The conditions are summarized in Table 1 for both tests. The interacting melt mass corresponds to the quantity of debris found in the debris catcher. The melt temperature is a data inferred from ultrasonic temperature sensor measurements performed in previous similar melting and release tests in FARO. An attempt for measuring the temperature of the melt in the melt catcher was made in QT2, but was unsuccessful. The delivery times have been deduced from the OD1 and OD2 signals as follows. The OD1 rupture was taken as the melt release start (time 0). The OD2 thermocouple was not destroyed by the melt (in both tests) even though it indicated temperature jumps above 1400°C. One reason for that was the off-centring of the melt jet induced by the hinged flap. The time corresponding to the start of temperature decerase after the maximum has been taken as the end of the melt catcher discharge, thus giving the delivery time. As noted in Table 1, the durations (280 ms and 370 ms, respectively for ST and QT2) are higher than the theoretical values (110 ms and 235 ms, respectively for ST and QT2) due to crust formation in the delivery tube and start-end of release disturbances. The relative larger difference noted for ST is explained by the formation of an abnormally thick crust in the nozzle (5 mm) and above the melt (~10 mm), probably favoured by the small quantity and the poor overheating. Melt streams rather than a coherent mass release is likely for this test. The vessel pressure, and water temperature and level indicated in Table 1 needs further explanation.

A. Scoping Test.

The pressure in TERMOS at 80°C was 0.4 MPa (essentially argon). Heating was pursued up to reaching a water temperature of 266°C and a vessel pressure of 5.3 MPa without further addition of argon (pressurisation due to steam generation only in boiling regime). Then, the heating power was reduced just to maintain these conditions. This residual power was swiched-off a few seconds before the melt to water release. The water height counted from the debris catcher bottom plate upper face was 0.87 m. Upon bursting the communication line rupture disc, the pressures in both TERMOS and the melt catcher equalised to 5.0 MPa. This little blow-down of TERMOS enhanced water boiling and induced a level swell. The temperature of the water did not exhibit significant changes. While the melt crossed the gas space, the pressure increased up to reaching approximately 5.4 MPa when the melt leading edge arrived near the water surface (contact time deduced from thermocouples). As a consequence, boiling should

Table 1. Summary of Experimental Conditions

	SCOPING TEST	QUENCHING TEST 2
Melt		
Composition, w%	80 UO_2 + 20 ZrO_2	idem
Mass, kg	18	44
Temperature, °C	2650	2750
Delivery nozzle, mm	100	100
Delivery time, s	0.280	0.370
Flow Rate, kg/s	64	119
Free Fall in Gas, m	1.83	1.7
Water		
Mass, kg	120	255
Depth, m	0.87	1.00
Temperature, °C	266 (230 bottom plate)	263 (255 bottom plate)
Subcooling at melt contact, °C	2 (38 bottom plate)	12 (20 bottom plate)
Fuel to Coolant Mass Ratio	0.15	0.17
Gas Phase		
Composition, w%	83 steam + 17 Ar	70 steam + 30 Ar
Volume, m^3	0.464	0.875
Temperature at OD1 rupture (release start), °C	270	263
Test Vessel		
Diameter, m	0.470	0.710
Overall volume, m^3	0.640	1.3
Pressure at OD1 Rupture, MPa	5.0	5.8
Pressure at Melt/ Water Contact, MPa	5.4	6.1

had completely ceased at that time, and the water resumed its original depth of 0.87 m. Note that water was about 38°C subcooled near to the debris catcher (referred to 5.4 MPa) because of an unaware switch off of the power of the catcher heater. The decrease from 266°C to 230°C was localised within 250 mm above the debris catcher bottom plate.

B. Quenching Test 2.

The pressure in TERMOS was 0.2 MPa at 70°C (essentially argon). The heating of the test section was pursued up to reaching 263°C and 5.0 MPa in the same way as for the Scoping Test. To supress boiling of the water during the pressure equalisation between TERMOS and the melt catcher, argon was blown into TERMOS just before bursting the communication line rupture disc. Due to this argon addition, the pressure at the time the melt started flowing down was 5.8 MPa. It increased to 6.1 MPa as the melt crossed the cover gas. Consequently, the subcooling of the water at melt/water contact was 12°C in the bulk against 20°C at the bottom plate level.

IV. EXPERIMENTAL RESULTS AND DISDUSSION

The experimental curves presented in this section are also used as a basis for discussing the timings of the melt fall stages and for suggesting some interpretations of the facts that occurred. In order to avoid any ambiguity, each sub-section starts with a short introduction presenting just the related experimental curves. The different times indicated in the figures and in the data summary Table 2 were deduced from the thermocouple signals. This method does lead to some uncertainties. In particular, one does not know exactly whether the bulk leading edge of the melt or some preceding lumps contacted the probe first. For this reason, the data deduced from the thermocouples form part of the discussions. For all the data reported, time zero corresponds to the OD1 rupture (melt catcher hinged-flap opening, i.e. start of melt release).

A. Melt Fall Stage

1. Experimental data. The cover gas pressure traces corresponding to the first 1.4 second of both tests are reported in Fig.4. The values are normalized to the value at time zero, i.e. 5.0 MPa for ST 5.8 MPa for QT2. The water pressure transducers (not reported) gave exactly the same signals as the cover

Table 2. Summary of Experimental Results (time t = 0 = release start)

	SCOPING TEST	QUENCHING TEST 2
Melt		
Mean velocity in cover gas, m/s	4	5
Mean velocity in water, m/s	2.3	3.7
Fragmented, kg	12	30
Molten on bottom plate, kg	6	14
Mean size of fragments, mm	4.5	3.8
Melt/Debris fluidization	no	no
Delivery nozzle, mm	100	100
Bottom Plate		
Maximum temperature increase,°C	-	275 (contact face)
Maxi downward heat flux , MW/m^2	-	0.8
State	intact	intact
Pressure Increase		
From release start to end of fragmentation, MPa	1.1 (at t = 1.2 s)	1.8 (at t = 1.2 s)
From melt/water contact to end of fragmentation, MPa	0.7	1.5
Maximum long term, MPa	1.6 (at t = 12 s)	1.8 (at t = 22 s)
Steam explosion	no	no
Temperature increase		
Steam (maxi measured), °C	86	83
Steam (mean value at t=10 s), °C	~43	~30
Water	15 (maxi at t = 12 s)	23 (at t = 25 s)*
Level Swell		
Level swell, mm	130**	250 (~maxi)

* maximum not reached at that time - data not available beyond

** from thermocouples - not necessarily the maximum

gas transducers, except the classical late drift due to heating. In Fig.5 has been reported the signal from the resistance probe located 250 mm above the initial water level for QT2. Only this probe signal moved from rest, which gives an indication of the maximum level swell. The early steam temperature increases are presented in Fig. 6 for QT2. They were very similar for ST.

2. Discussion of melt fall stage data. The curves of Fig. 4 indicate that the fragmentation process was essentially the same for both tests. The pressure increase after melt/water contact (MWC) was 0.7 MPa for ST and 1.5 MPa for QT2. It is interesting for the discussion to keep in mind the following relationships between the tests: in QT2, the gas volume was 1.9 times the ST one while the melt mass was 2.4 times higher, resulting in a total overpressurisation 1.6 times higher in QT2 than in ST. The end of fragmentation time (EOF) reported in the figures means that the unfragmented part of the trailing edge should have reached the bottom plate at that time. It has been calculated by adding the delivery time to the time at which the leading edge touched the bottom (MBC).

Before penetrating into the water, the melt crossed the gas space (height 1.83 m for ST and 1.7 m for QT2). Let us first analyse in Fig.4 the pressure increases measured before the melt contacted the water. The ST pressure increase during that period (0.4 MPa) should have resulted from heating of the gas mixture by the melt and from steam generation due to the "disequilibrium" created at the time of pressure equalisation between TERMOS and the melt catcher. On the contrary, the QT2 pressure increase (0.33 MPa) should have been due only to gas heating (see the different equalisation procedures reported in the previous section). Considering that superheated steam behaves as a perfect gas and that condensation is negligible during this short time period (0.345 s), the temperature increase corresponding to the QT2 pressure increase is 36 °C. (The same method applied to ST would give a temperature increase of 41°C, which clearly suggest that vaporisation occurred at

the same time as steam heating). The steam temperature traces reported in Fig.6 for QT2 (they are very similar for ST) do not indicate such an increase for the time period of interest. One reason is that classical thermocouples can hardly measure transient steam superheating. Another reason is that the steam heating was more localized around the melt path. One thermocouple in Fig. 6 indicate a limited temperature increase before melt/water impact but it is not known whether it had been directly heated by radiation or not (due to off-centred melt).

According to the discussion above, the pressure increases observed before all the melt was in the water are a consequence of both cover gas heating by the melt, and steam generation due to melt quenching. Only beyond the trailing melt penetration time (AMIW time in the figures) are the increases resulting from steam generation alone. At that point it is interesting to look at the rate of pressure increase curves plotted in Fig.7. These curves have been obtained by differentiating the spline smoothed pressure histories. It is seen that the slope became negative very soon after melt impact, which, a priori, is not consistent with the start of quenching. One explanation is that the steam produced at first was colder than the cover gas mixture previously heated by the melt. If this explanation is valid, one can conclude that the steam produced was overheated less than the 36°C corresponding to the cover gas heating by the melt. Further ahead in the fragmentation, the fluctuations can be due also to an irregular melt penetration.

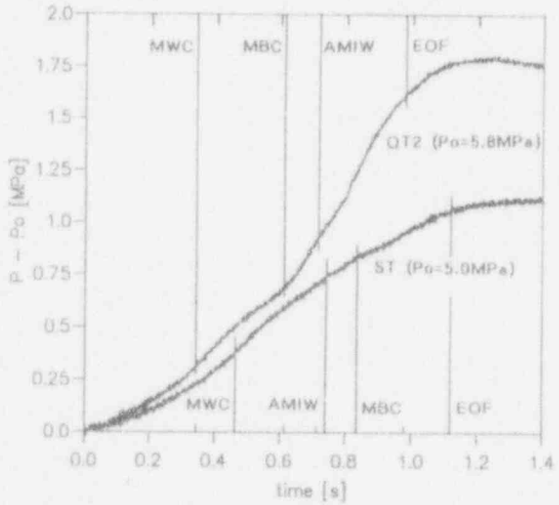

Figure 4. Early vessel pressure increase (ST: Scoping Test, QT2: Quenching Test 2, t = 0: release start, MWC: Melt Water Contact, MBC: Melt Bottom Contact, AMIW: All Melt In Water, EOF: End Of Fragmentation)

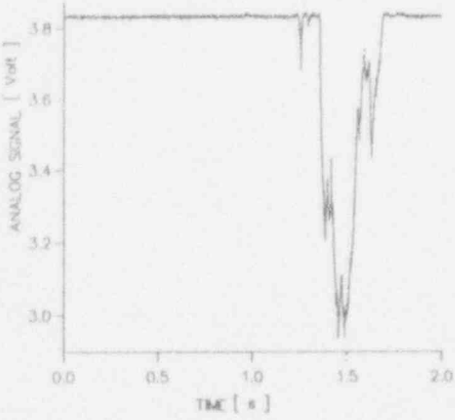

Figure 5. Signal from the QT2 level indicator located 250 mm above the initial water level

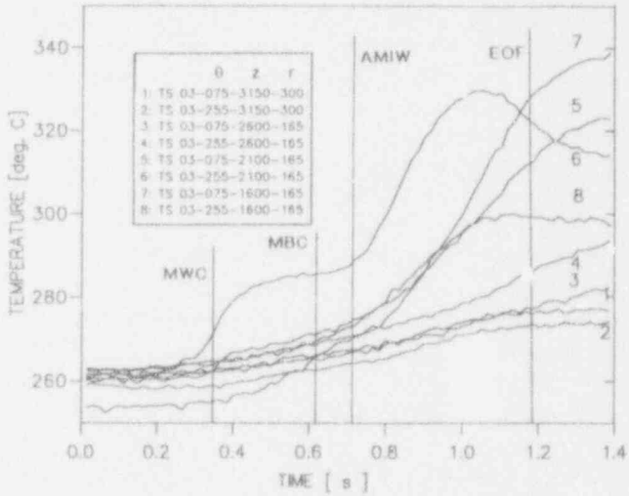

Figure 6. QT2 early steam temperature increase (for legend, see Figure 4)

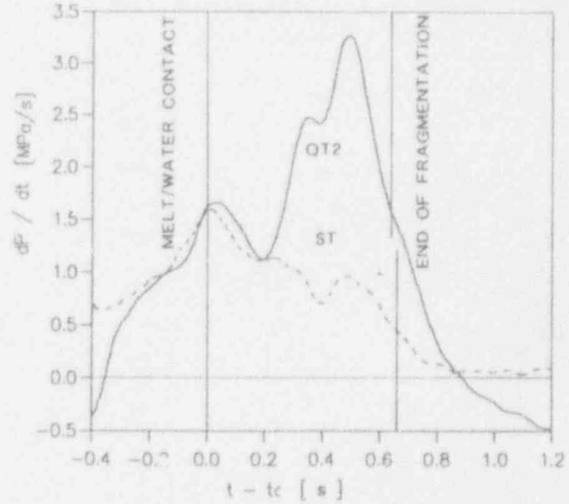

Figure 7. Pressure increase rates during the melt fall stage (tc=contact time)

The fact that the short term steam temperature measurements are difficult to interpret makes arduous an attempt for quantifying the steam generation rate, which otherwise could have been approximated multiplying the pressure increase rate by the quantity MV/R_uT_g, where M is the steam molecular weight, V the cover gas volume, T_g the cover gas temperature, and R_u the universal gas constant. Trying nevertheless to apply the method to the major peak of the QT2 dp/dt, corresponding to a time where the effects discussed above might have been of secondary importance, one find a peak steam generation rate of 11 kg/s for T_g = 300°C, which has to be considered as an upper bound. An estimate of the amount of steam produced during the melt fall stage can be made by using the steam table at the partial pressures of the steam corresponding to the pressure increases after melt/water contact (i.e. between 4.8 and 6.1 MPa for ST, and between 4.9 and 6.4 MPa for QT2). One finds 1.7 kg for ST and 7.4 kg for QT2 at T_g = 300°C, which corresponds to an energy of 2.5 MJ for ST and 10 MJ for QT2.

From the water thermocouple signals, only a broad picture of the melt penetration history could be established. Mainly the times of melt /water impact and melt arrival on the bottom plate could be determined as reported in the Figs. 4 and 6. For ST, all other thermocouples in between appeared contacted by the melt in a rather stochastic way as the result of the not coherent release as explained before. For QT2 it could be established that only an off-centring effect from the hinged-flap was present. The melt flowed down laterally but coherently, probably impacted first the debris catcher funnel and then spread on the bottom plate from one side. In both cases, only few water thermocouples were damaged.

B. Longer Term Stage.

1. Experimental data. In Fig. 8 is presented the steam temperature distribution over the first ten seconds of the Scoping Test. The signals for QT2 are very similar. The pressure histories over a period of time of 25 s are reported in Fig.9. The long term maximum pressure was reached after approximately 12 s for ST and 22 s for QT2. In Figs. 10 and 11, the cover gas, water and saturation temperatures are plotted.

2. Discussion. As can be seen in Fig. 8, the steam temperature is largely not uniform, especially soon after the end of the jet fall. Although radiation from small melt pieces remaining attached to structures in the cover gas region might have affected some of the signals (see n.5 and 7), it is believed that this map represents the reality of the steam generation and mixing with the cover gas. When quiet steaming from the debris bed dominates, temperatures tend to equalize as Fig. 8 shows.

Figs 9 to 11 indicate that similar vaporization/condensation scenarios developed at two different time scales for both tests: the melt fragmentation time scale and the long term debris cooling time scale. The pressure evolution at the transition between the two periods suggest the following interpretation. During the melt fragmentation stage, production of steam was very fast and intense, inducing a fast pressurization of the vessel up to a level that was higher than the saturation pressure corresponding to the cover gas temperature (see Fig.11). As a consequence, as soon as the fragmentation stopped, condensation dominated steam production from the debris cooling (mainly steam to steam condensation). The higher the steam generation during the melt fall quenching stage, the higher the pressure decrease at the transition phase. Then, the contrary occurred up to the second maximum. Later on, condensation definitively dominated. Previous to the second pressure maximum, steam generation due to debris cooling is evidenced by the fact that the steam temperature decreased as the pressure increased. Boiling in the debris region is further evidenced by the wiggly signal from the water thermocouples located just above the debris (see Fig. 12 and compare to Fig. 10).

When comparing Figs. 10 and 11 one remarks that the temperatures are of the same order for both tests. This is not so surprising considering that homogenisation rapidly occurred after the melt fall stages (within the first 5 seconds in the water). Proportionally to the melt quantity, more steam was produced in QT2 during the melt fall stage (see discussion in section B), inducing a higher pressurisation and a subcooling of the water. As a consequence, part of the steam produced in the debris catcher region condensed while rising through the water, increasing the water temperature. Less steam than in saturated water conditions could reach the cover gas, which cooled down more rapidly than in ST.

Assuming that the 20°C temperature jump observed early in Fig.11 is the result of the melt quenching during the fall stage, one calculates an energy of 25 MJ transferred to the water during that phase. Proportionally to the melt quantity, this value is comparable to the CCM values (Wang et al., 1989), where 10 MJ in subcooled water (CCM-5) and 3.5 MJ

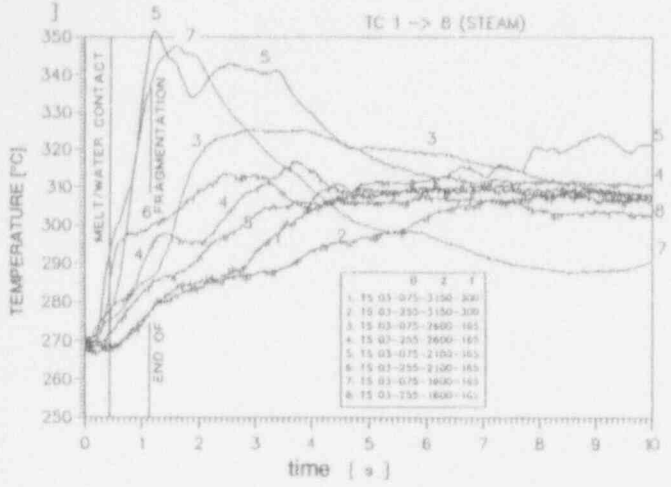

Figure 8. Scoping Test steam temperature histories for the 10 first seconds after release start

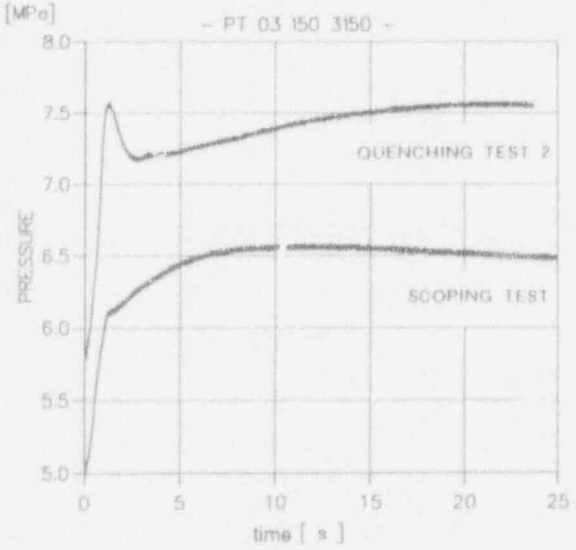

Figure 9. Long term pressure histories

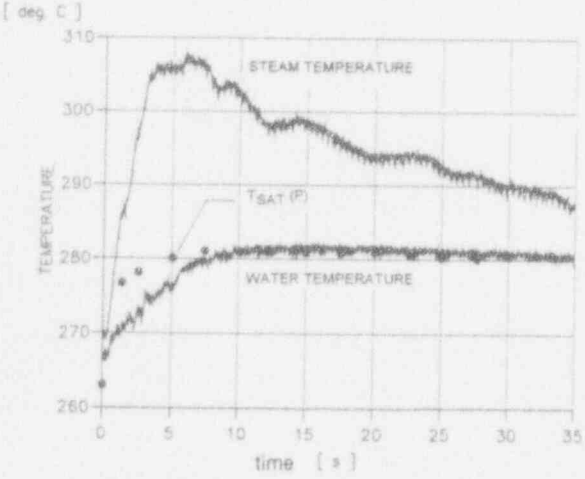

Figure 10. Scoping Test steam and water temperatures compared to the saturation temperature

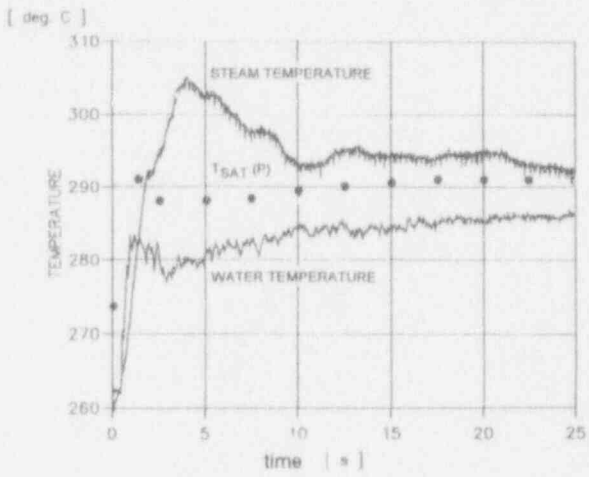

Figure 11. Quenching Test 2 steam and water temperatures compared to the saturation temperature

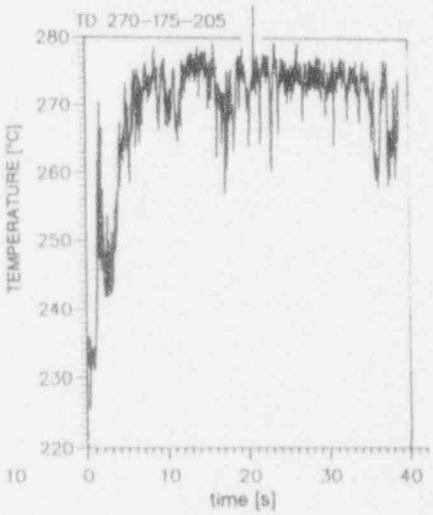

Figure 12. Scoping Test water temperature just above the debris (at level 175 mm)

in saturated water (CCM-6) for 13 kg of melt were calculated. By adding these 25 MJ to the estimate of the energy transferred to the steam (10 MJ), one arrives to about 50% of energy transferred to the steam/water system during the melt fall stage, which globally corresponds to the CCM-6 estimates.

C. Debris Catcher Data.

The debris structures were very similar for both tests. Fig.13 shows a view of the ST debris surface as found in the catcher. Fig.14 shows a view of a part of the conglomerate in contact with the bottom plate. This part was certainly still molten when it contacted the plate. As can be seen, the plate did not

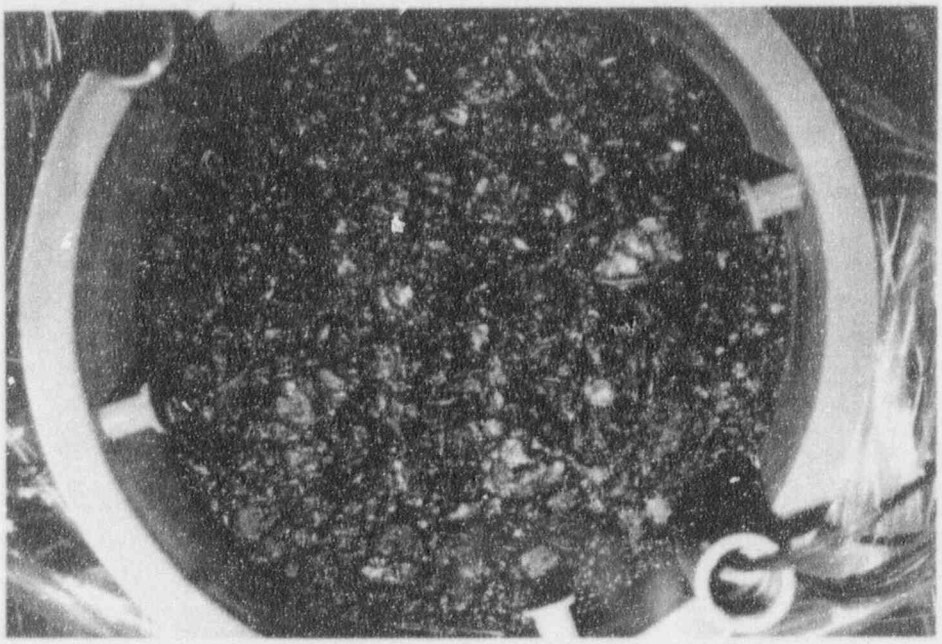

Fig.13: View of the debris bed from above

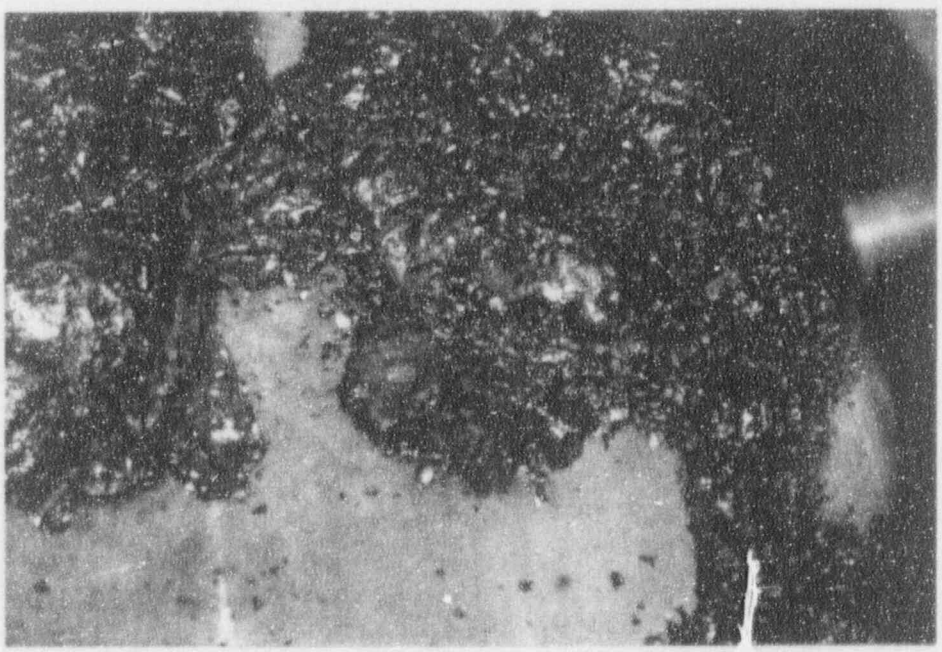

Fig.14: View of the melt spread on the botto n plate

suffer any damage. This is not surprising using a pure oxide melt because we knew already, from the BLOKKER Series performed in FARO in the frame of the LMFBR programme (Hohmann et al., 1989; Magallon et al., 1990), that jets of 100 kg of pure UO_2 around 3000°C interacting in dry conditions with 40 mm thick plates preheated to 400°C did not induce any erosion even though the plates reached 1000°C.

Some samples of the ST debris are shown in Fig.15. They were very irregular in shape and aspect. Only a few spheres as that in the figure were present. Contrarily to pure UO_2, these particle were very brittle and great care had to be taken in manipulating them in order not to alter the analysis. In general, particles up to a dimension of the order of 10 mm presented a fine granular internal structure, nor-

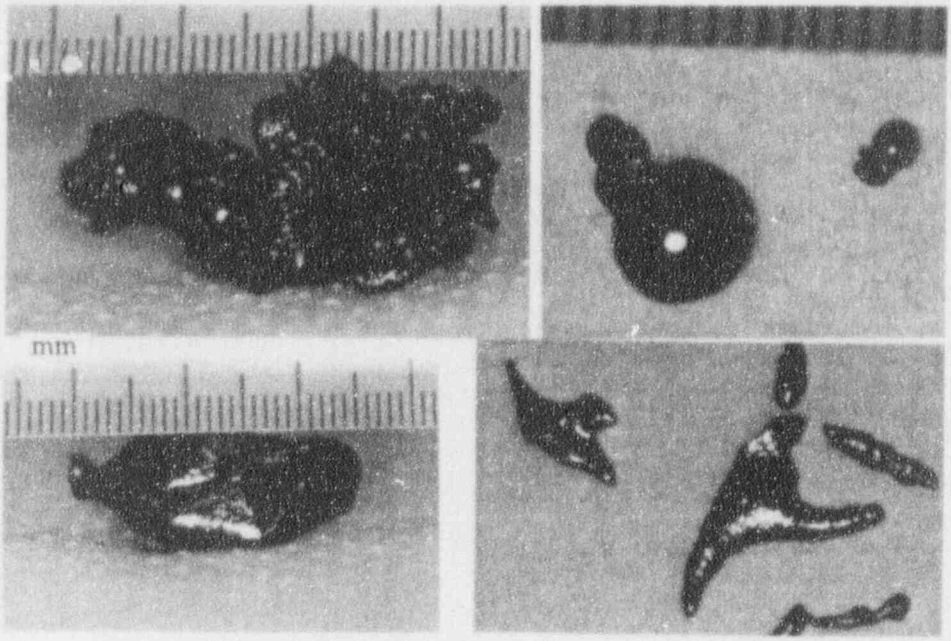

Fig.15: Debris samples

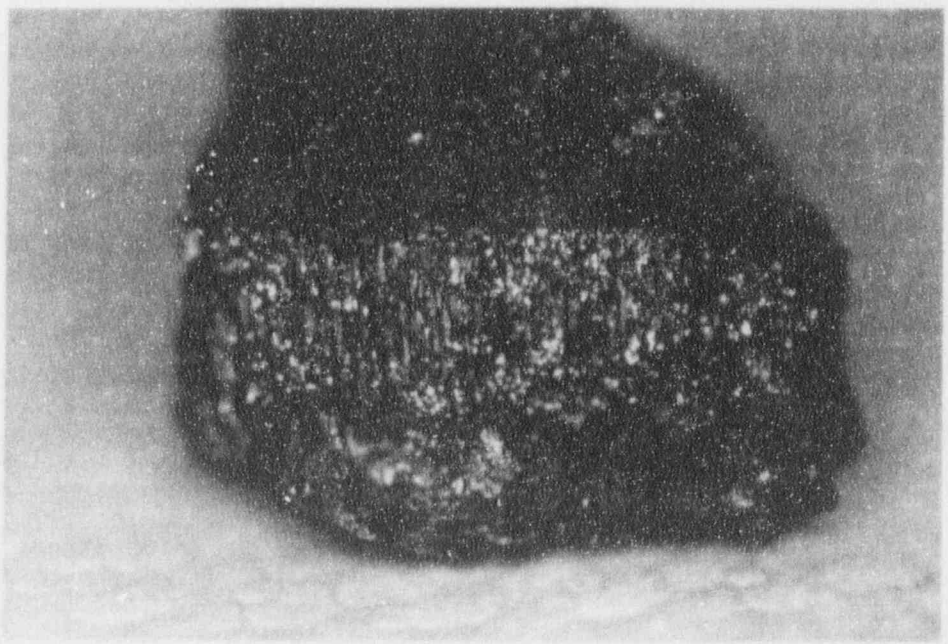

Fig.16: View of the internal part of a 4 cm particle from the debris

mally a sign of rapid quenching. Larger particles (a few particles of some centimetres were part of the debris) presented an internal structure as that shown in Fig.16. The central grain growth structure is typical of slow quenching.

The particle size distributions are given in Fig.17 and compared with that of CCM-5 and CCM-6. The difference in the mean particle size between ST and QT2 can be explained by the higher penetration velocity observed in QT2. The mean particle sizes of both FARO tests lie in between those of CCM, which agrees with the fact that the degree of subcooling of the water in FARO was in between that of CCM tests. It should be noted that in neither of the two CCM tests of concern, signs of a reagglomerated molten corium were evidenced. This happened only in CCM-2 where the water depth was 0.64 m instead of 1m.

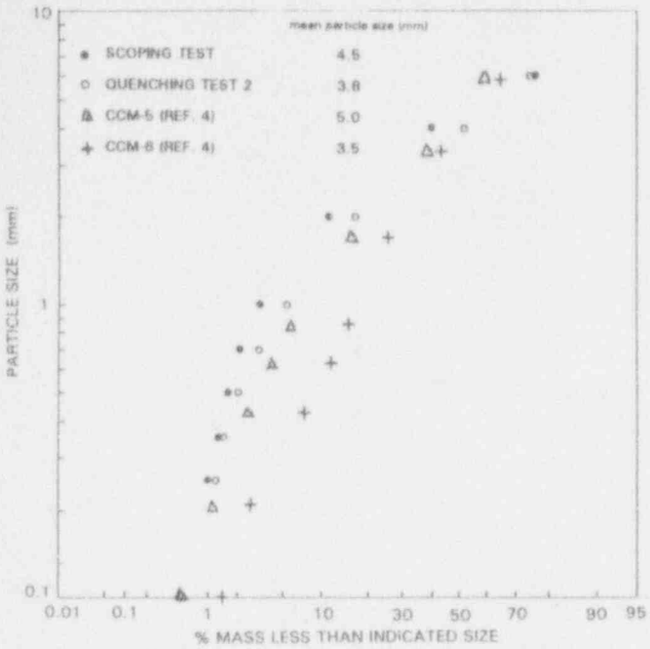

Figure 17. Particle size distributions (total debris for CCM; fragmented debris, i.e. 2/3 of total, for ST and QT2)

Most of the thermocouples located just above the surface of the bottom plate were destroyed during melt impact. Contact temperatures and temperatures 5 mm below the bottom plate surface are shown in Fig.18 for different radial locations (QT2 test). They reflect the fact that the melt did not spread uniformly on the plate. Downward heat fluxes calculated from these temperatures are reported in Fig.19. A maximum value of 0.8 MW/m^2 is obtained. The time integrals of these curves gives the energy released to the plate (Fig.20), which reached a maximum around 9 MJ/m^2 at time 20s.

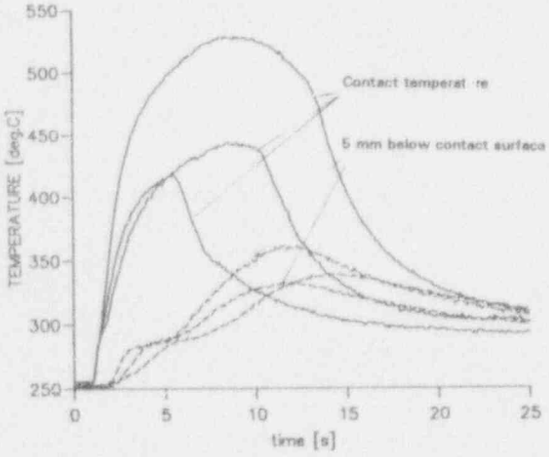

Figure 18. Melt/bottom plate contact temperatures and temperatures in the plate 5 mm below the contact surface

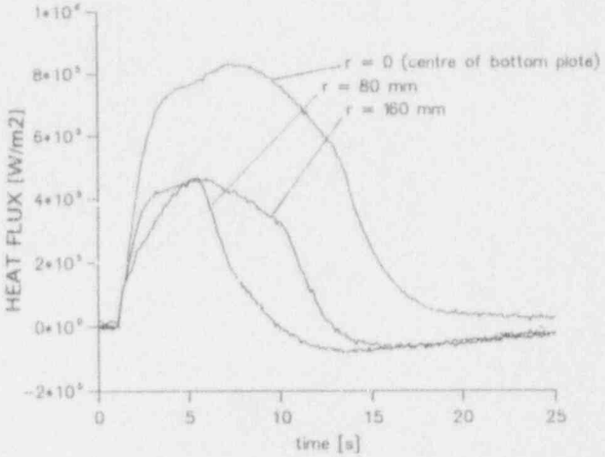

Figure 19. Downward heat fluxes at different radial locations

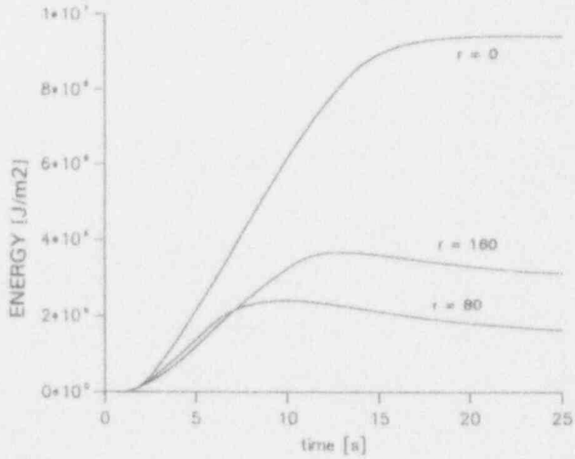

Figure 20. Energy transferred to the bottom plate

IV. CONCLUDING REMARKS

The essential objectives of the two first tests of the FARO quenching series have been achieved. Estimates of the melt quenching rates and of the thermal loads on the bottom structures, and characterization of the debris have been made. It has been found that the melt loosed more than 50% of its energy during the fall through water stage. Despite the fact that about 30% of the corium collected still molten on the bottom plate where the water was up to 38°C subcooled, no steam explosions occured and the plate remained intact. Maximum downward heat fluxes of the order of 0.8 MW/m^2 have been calculated from the thermocouple data.

With respect to past quenching experiments using smaller quantities of thermite generated melt at ambient pressure, there were found no fundamental differences, but some correlation between test pressure and steam generation on one hand, and water depth and molten mass that reached the bottom plate on the other hand, could be further evidenced. This justifies to pursue by using larger amounts of melt. As well, the influence of the presence in the melt of a percentage of a metallic compound still have to be evaluated. It is recommended to perform at least one test of the larger melt mass series with boundary conditions as close as possible to that of the preliminary tests reported in this paper (closed volume), in order to facilitate comparisons and code validation.

Some problems arose when trying to assess the steam generation rate from the pressure and temperature data. They were essentially due to the heating of the cover gas by the melt itself previous to the melt/water interaction, and to the difficulty in measuring transient steam overheating by using classical thermocouples. On the other hand, one can hardly eliminate these problems working with high pressure and necessarily limited volumes. Consequently, it is important for the interpretation of the experiments by the fragmentation codes and for the validation of these codes, that they include good models for the melt fall through and heat transfer to the cover gas previous and during the melt/water interaction.

ACKNOWLEDGEMENTS

This work was performed in collaboration with the US Nuclear Regulatory Commission in the frame of a Technical Exchange Agreement. The authors greatly acknowledge the work and efforts of the whole FARO experimental team.

REFERENCES

CORRADINI M.L. and H. HOHMANN, Multi-Phase Flow Aspects of Fuel-Coolant Interactions in Reactor Safety Research, OECD/CSNI, Specialist Meeting on Transient Two-Phase Flow held in Aix-en-Provence, 6-8 April 1992.

FASOLI-STELLA P. and H. HOHMANN, Planning for FARO-LWR Experiments, CSARP Meeting, Washington, May 1991.

HOHMANN H., D. MAGALLON, A. BENUZZI, A.V. JONES AND A. YERKESS, Results of the FARO Programme, Proc. of the Seminar on the Commission Contribution to Reactor Safety Research held in Varese (Italy) on 20-24 Nov. 1989, Elsevier Applied Science, p. 837.

HOHMANN H. , D. MAGALLON, H. SCHINS, R. ZEYEN, H. LAVAL and A. BENUZZI, Contribution to FBR Accident Analysis: The JRC-Ispra FARO Programme, Proc. of the Int. Conf. on Fast Reactor Safety held in Guernsey on 12-16 May 1986, BNES, Vol. 2, pp 139-144.

MAGALLON D. , R. ZEYEN and H. HOHMANN, 100 kg-scale Molten UO2 Out-of-Pile Interactions with LMFBR Structures: Plate Erosion and Fuel Freezing in Channels, Int. Conf. on Fast Reactor Core and Fuel Structural Behaviour held in Inverness on 4-6 June 1990, BNES.

WANG S.K., C.A. BLOMQUIST, B.W. SPENCER, L.M. MAC UMBER and J.P. SCHNEIDER, Experimental Study of the Fragmentation and Quench Behavior of Corium Melts in Water, Nat. Heat Transfer Conf., ANS, 1989.

ANALYSIS OF LARGE-SCALE MELT-WATER MIXING EVENTS

H. Jacobs
Kernforschungszentrum Karlsruhe, Institut für Neutronenphysik und Reaktortechnik
Postfach 3640, D-7500 Karlsruhe 1, ☎ +49 (7247) 82-2443

ABSTRACT

The transient multiphase multicomponent threefield hydrodynamics code IVA3 that is being developed at KfK Karlsruhe is used to analyse large-scale melt-water mixing events that have been observed in the FARO LWR facility at JRC Ispra and the BETA facility at KfK Karlsruhe. In the case of the FARO tests encouraging agreement between experiment and calculations is found.

I. INTRODUCTION

In case of a core melt accident in a pressurized water reactor, a large-scale steam explosion might occur in the lower head of the reactor pressure vessel (RPV) and might conceivably rupture the RPV and even the reactor containment. Such explosions are often considered to develop through four stages: premixing, triggering, propagation, and expansion. Here, the premixing stage is thought to set the stage for the explosion and at the same time is expected to inherently limit the amounts of melt and water that can finally interact. This autocatalytic limitation of the interacting masses is expected to result from the enormous vapour production that is driven by the heat transfer from the quickly increasing melt surface (Henry and Fauske, 1981). Initially this effect has been studied by zero-dimensional (0D) steady-state models. Today it is widely accepted that a reasonable description of premixing requires the use of a multiphase multicomponent hydrodynamics code with at least two spatial dimensions and three velocity fields for describing the separate motions of melt, liquid water, and steam (Amarasooriya and Theofanous, 1991; Fletcher and Thyagaraja, 1991).

II. THE IVA3 CODE

A new member in the family of multifield codes that are suitable to describe premixing (and potentially propagation and expansion) is the IVA3 code developed recently at KfK (Kolev, 1991a). This is a 3D transient code describing 3 fields that can be in complete thermal and dynamic disequilibrium, but have a common pressure locally. Field number 1 is gas, i. e. steam and possibly noncondensable gas (presently modelled as air). Field number 2 is liquid water and, of course, fields 1 and 2 can exchange mass by evaporation or condensation. Field number 2 can also contain microscopic particles of the material in field number 3 that are large enough so that they don't change the water equation of state and which are in perfect thermal and dynamic equilibrium with the water. Field number 3 contains one further material that is liquid or consists of (partially) solid particles and does not vapourize. As long as its chemical nature is undetermined it is called melt or corium. All three fields can be continuous or discontinuous so that 14 different and distinct flow regimes are being modeled. The required exchange terms for mass, heat, and momentum are modeled using engineering correlations as far as possible. The flow regimes and the associated heat and mass transfer models are listed in more detail in Appendix A. Although the modelling in less important flow regimes is occasionally not yet fully developed or even provisional, this large choice of flow regimes obviously enables the code to reasonably describe a large variety of situations.

IVA3 also solves an extra set of differential equations for the three particle number densities from which the particle size can be obtained. (Here the term particle is used for any discontinuous structure in any of the fields, i. e. bubbles, water or corium droplets, or solid corium particles. In addition, the term particle is used if it is undetermined whether a corium globule is liquid, in the melting or freezing transition, or solid.) The local instantaneous particle production rate is obtained from the present and the ultimate particle sizes and the breakup time. For droplets of water or liquid corium, the stable (ultimate) size is derived from a critical Weber number $We_{cr} = 12$, where $We = \rho_d |\vec{V}_d - \vec{V}_c|^2 d_d/\sigma_d$ (for the meaning of the symbols see the nomenclature). The breakup time τ_b is determined by one of the two following models. One possibility is to use the Taylor type correlation

$$\tau_b = c_b \sqrt{\rho_d/\rho_c}\, d_d |\vec{V}_d - \vec{V}_c|^{-1} Bo^{-0.25}$$

as given e. g. by Simpkins and Bales (1972) but based on the diameter. Here the Bond number is approximated by $Bo = 1.5\, We$ and the constant c_b is taken to be 32.5 after the data of Reinecke and

Waldman (see Simpkins and Bales, 1972) if the continuous field is gas and $c_b = 2.5$ is assumed with reference to Patel and Theofanous (1981) when the continuous field is liquid. The other possibility is to use the correlations given by Pilch and Erdman (1987). At present IVA3 does not describe the production of a separate fraction of microscopic melt particles that might e. g. be stripped from larger drops by surface layer stripping. Therefore, the code in its present state does not seem to be prepared to model propagation and true explosions. However, as mentioned above, the code offers already the possibility to describe microscopic corium particles that make part of the second (water) field. Only the corresponding mass source terms are missing and are on the list of foreseen further improvements.

The code is still in its developmental stage. The first aim is to qualify the code for assessing the premixing phase of steam explosions. Above all this requires comparison of code predictions with real data. But very few of the required three phase data are available. Therefore two types of such experiments are in preparation at KfK. In one of them a large number ($\approx 10^5$) of hot (typically 2500 K) but solid spherical particles will be mixed with water. In the other, large quantities (up to 50 kg) of molten alumina will be used for the same purpose. Before those data become available, it is interesting to test the code by comparison with actual melt-water mixing events. To this end some analysis of experiments in the FARO LWR facility at JRC Ispra and of the BETA experiment V6.2 conducted at KfK have been performed and are reported here. Besides the varying modelling assumptions that are indicated, all the results presented in some detail have been obtained using the same code except for the corium equation of state for which one that is expected to describe the Ispra corium mix ($T_m = 2747$ K) is used for the FARO cases and one describing iron for the BETA case. All calculations have been 2D assuming cylindrical symmetry.

III. THE ISPRA FARO LWR EXPERIMENTS

In the FARO LWR tests that are being performed at JRC Ispra large quantities of simulated corium are dropped into water within a vessel that can withstand about 100 bar pressure at 300°C. In order to avoid much higher interaction pressures as far as possible, 50 bar initial pressure and saturated water have been used so far. In the so-called quenching tests to be discussed here, the vessel was closed so that the melt-water interaction caused a characteristic pressure rise which is the observation that can most easily be compared with the calculation. Already in 1991, prior to the first quenching test, and in July 1992, prior to the second quenching test (with a larger vessel and more melt and water), the results of absolutely blind precalculations have been communicated to JRC Ispra. Unfortunately, in both cases, the actual experiment parameters differed so much from those assumed in the calculations that a detailed intercomparison is useless. Also, some heat transfer models that had already been used in the first case could not be used in the second case, because they caused numerical difficulties that could not be overcome in the time left until the performance of the test. However, the calculations agreed quite well with the experiments in predicting a gradual pressure rise of the order of some ten bars (26 bar in the first and 16 bar in the second case). In the meantime the above mentioned difficulties have been overcome and further corrections and additions to the code have been made. Therefore, the 'precalculation' has been repeated and is presented here as a starting point.

A. 'Precalculation' of Second Quenching Test

This calculation actually was performed after the test but without taking into account the information available on the actual parameters and the results. The assumed geometry and initial material distributions are shown in Figure 1. In this type of plot which will be used also later the geometry is shown on scale and the calculational mesh is indicated by dotted lines. All three volume fractions are shown as the corresponding area fractions of the cell. At the bottom of each cell, the corium fraction is shown in black, above it the water fraction as a shaded area, and on top the gas fraction as blank area. The observer should always keep in mind that

Figure 1: FARO LWR 2nd Quenching Test; geometry, calculational mesh and intial material distributions assumed for the calculations. The radius of the vessel is 35.5 cm.

this type of figure doesn't show the arrangement of the fields within the cell (which are always assumed to be fully intermixed) but only their distribution within the field of calculation. The full lines in the lower right corner indicate impermeable walls that form a trough of the size of the debris catcher. The four mesh cells behind them do not contribute to the calculational result. The water fills the vessel up to a hight of 1 m above the bottom of the debris catcher. The void fraction is assumed to be only 0.5 %. This gives (above the debris catcher) a water volume of 1.17 m^3 or a mass of 247 kg at the initial temperature of 537.1 K. The intermediate corium catcher from which the corium is released into the interaction vessel is modeled as a tube of 20 cm diameter. Its bottom is 1.7 m above the water surface. In order to simulate the outflow opening of only 10 cm diameter, the permeability of the lower cell boundary is set to 25 %. (The top is assumed to have a permeability of 10%.) The corium melt is assumed to have a temperature of 3000 K and to fill the mesh cell by 95 %, the remaining space being occupied by (bubbles of) gas. This results in a mass of 53 kg. The free gas space amounts to 0.85 m^3. Assuming a mass concentration of noncondensable gas (modeled as air) of 20 % in all the gas present, this results in an initial gas (steam and air) mass of 21.55 kg. At time zero all materials are at rest such that the fall of the melt towards the water is fully modeled by the code.

The most interesting result, the pressure history, is shown in Figure 2. (For better comparison with the real case calculations and the experiment, the curve is shifted upwards by 8 bar.) In this like in all FARO cases the pressure at the top of the gas space is shown. But as there are no fast pressure transients, this pressure is fully representative. The typical result is that a gradual pressure rise leads to a pressure increase of 11.2 bar within about 1.2 sec. After 1.3 sec the pressure starts to rise slowly again.

B. Real Case Calculations

In the actual experiment only about 44 kg of melt have been released into the water. The mass was adjusted by reducing the corium volume fraction in the one cell occupied by corium initially. The initial water temperature was 536 K. But as the initial pressure was raised to 58 bar by adding Argon, the water was effectively subcooled by 10 K. Still, assuming the presence of 20 % (by mass) of air, the observed initial pressure of 58.0 bar could be modelled. As is shown in Figure 2 the pressure in real case 1 (label RC1) rises only by 9.0 bar until 1.1 sec. Compared with the experimental result that is shown in the Figure as well, the timing seems to be about correct but the pressure increase is too low by a factor of two.

Besides the pressure level, there is not much difference between the 'precalculation' and the real case calculation. After the first contact of tiny corium masses with the water at about 0.3 sec, the pressure rises a little bit more slowly in real case 1

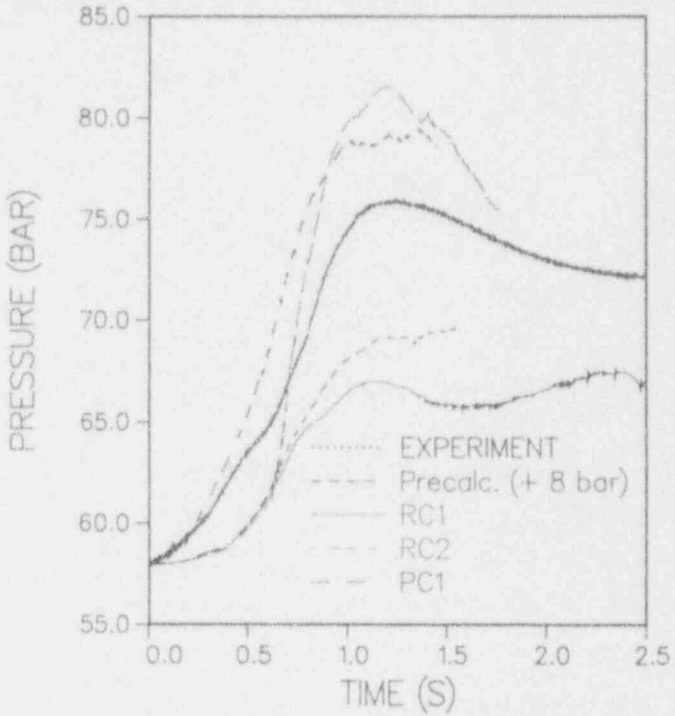

Figure 2: FARO LWR 2nd Quenching Test; pressure histories of experiment, 'precalculation,' real case calculations (label RCx), and a parametric calculation (label PC1). Due to the many data points the experiment appears as the thick irregular line.

which could be due to the slightly lower melt delivery rate. However, until about 0.8 sec the total pressure increments of both cases are very similar although the melt mass within the water pool is 20 % lower in real case 1. Only after that the pressure at first continues to rise steeply in the 'precalculation' and then approaches asymptotically a pressure increment of 12 bar while it rises more slowly in real case 1, reaches a maximum with a total increment of 9 bar already at 1.1 sec and then starts to oscillate slowly. The latter is probably a consequence of the water subcooling.

Figure 2 also shows results of further calculations. In real case 2 (label RC2) the Pilch and Erdman (1987) correlations for drop fragmentation time are used instead of the Taylor type correlation (Simpkins and Bales, 1972), see above. In this case something qualitatively new is happening. At time 0.62 sec the pressure rise rate suddenly increases. Actually, a small but fast pressure transient like those that are always present in cells containing water and melt occurs in the cell in which the corium first hit the water surface (originally the uppermost water filled cell). This event might be a parallel to (a miniature edition of) the sometimes observed surface eruptions. It suddenly inverts the gas velocity and thus causes an early strong fragmentation of the melt. Due to this, the pressure quickly rises to such an extent that even the experimental rise is

exceeded. The total corium surface jumps from 5 to 11 m^2 within 60 msec, continues to grow quickly until it reaches about 23 m^2 at 0.66 sec, and then increases more gradually until it reaches a value slightly below 30 m^2 shortly after 0.7 sec. Still at this time the typical particle diameters at some distance from the intermediate catcher are in the range of 0.6...1.1 mm. Before the sudden fragmentation event at 0.62 sec they have been 6...8 mm and during the event a small amount of corium has been fragmented into particles of less than 0.4 mm diameter. (Mean particle radii can be obtained by dividing 6 times the corium volume, e. g. 0.033 m^3, by the total surface.) Because the corium droplets start to freeze in this state, the melt surface remains essentially constant until the present end of the calculation at 1.8 sec. The final total corium surface is about 3 times as large as in real case 1. This means that the mean particle radii are about 3.9 mm in real case 1 and about 1.1 mm in real case 2. In this respect, real case 1 does better agree with the experiment which gave a mean particle size of 3.8 mm (Magallon and Hohmann, 1993). As will be discussed below, the qualitatively different behaviour of real case 2 cannot be explained straight forward by the use of a different breakup time correlation.

Figure 3 shows the system pressure and the saturation pressure of the hottest liquid water for a few selected points in time. This combination of data reveals that the faster pressure increase after 0.4 sec is driven by an increase of the highest available saturation pressure of liquid water. This finding seems to be reasonable because in the calculated slow transient the water-steam system should always stay close to saturation conditions locally so that effectively the hottest liquid water in the system defines a lower limit to the system pressure. During the essential part of the period covered in Figure 3, the hottest water masses are droplets that are combined with corium particles in three-phase droplet

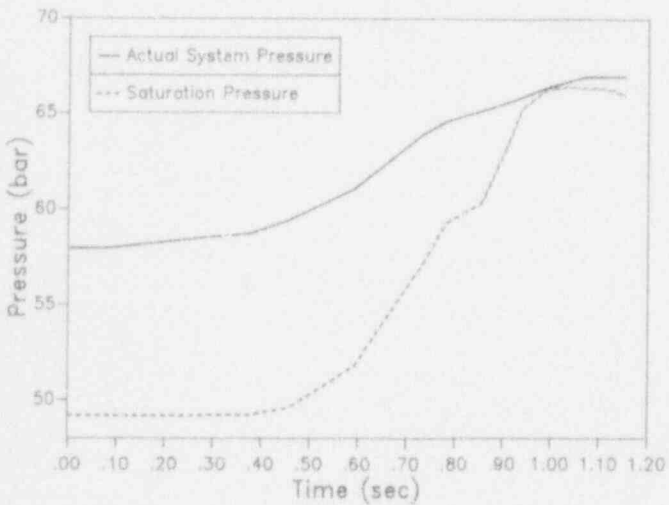

Figure 3: FARO LWR 2nd Quenching Test: system pressure and saturation pressure of the hottest water in the real case calculation RC1.

flow. The agreement between the two pressures shortly before 1.0 sec indicates that at that time there is no noncondensable gas present in the atmosphere surrounding the hottest water drops. That this occurs seems also to be reasonable because the strongest evaporation should occur where the saturation pressure of the liquid water is highest and there any noncondensable gas should be swept away. Before this time and later on the compression of noncondensable gas or the addition of its partial pressure to the local vapour pressure contribute to the system pressure.

As to the corium delivery it is reported (Magallon and Hohmann, 1993) that the melt contacted the water at 0.345 sec and the trailing edge entered the pool at 0.71 sec. In the calculation(s) sizable amounts of melt start to enter the water pool at 0.34 sec in good agreement with the experiment but the corium needs more time for entering the pool than in the experiment. It is only at 0.92 sec that 90 % of the total melt have entered the (original) pool volume. And it takes another 0.5 sec before the remaining part of the corium has arrived in the pool. More details of the movement of the corium in real case 1 can be observed in the sequence of volume fraction plots that are shown in Figure 4. Initially the melt is perfectly concentrated to the innermost cells. After reaching the debris catcher, the corium first piles up in the center (see 0.78 sec) and then sloshes first out and, after about 1.22 sec, back to the center. (In these plots the 'weight' of any area element increases with the radius of its position because the volume that it represents increases. So, to the eye, the total amount of melt seems to decrease when it moves radially outwards because the total black area decreases.) The vapour is initially concentrated around the corium jet but at the end of the calculation (2.5 sec) the initial steam channel is completely filled with liquid water and the void is close to the periphery. It is interesting to note that Figure 4 indicates that a lot of water is raised into the cell extending to 1.32 m while very little (only a few droplets) enters the next cell extending beyond 1.5 m. This is in agreement with the experimental observation that the level swell exceeded 1.25 m but did not reach 1.5 m (Magallon and Hohmann, 1993).

The unrealistically protracted melt delivery to the water pool clearly will contribute to the underestimate of the pressure rise. It may be caused by the way in which the intermediate melt catcher and the corium stream towards the water surface are modelled. In earlier calculations, the innermost column of cells (and thus the intermediate melt catcher) had been assumed to have a diameter of 10 cm so that no decreased permeability was required at the 'orifice' of the melt catcher and there was a higher hydrostatic pressure head in it. In these calculations the melt stream penetrated the gas space and the water pool with very little material being displaced radially and a stronger pressure rise during the fall of the melt towards the water had been obtained. However, in order to avoid the concern that the purely vertical corium motion might have been produced or accentuated by choosing just the right cell dimension, the present calculations have

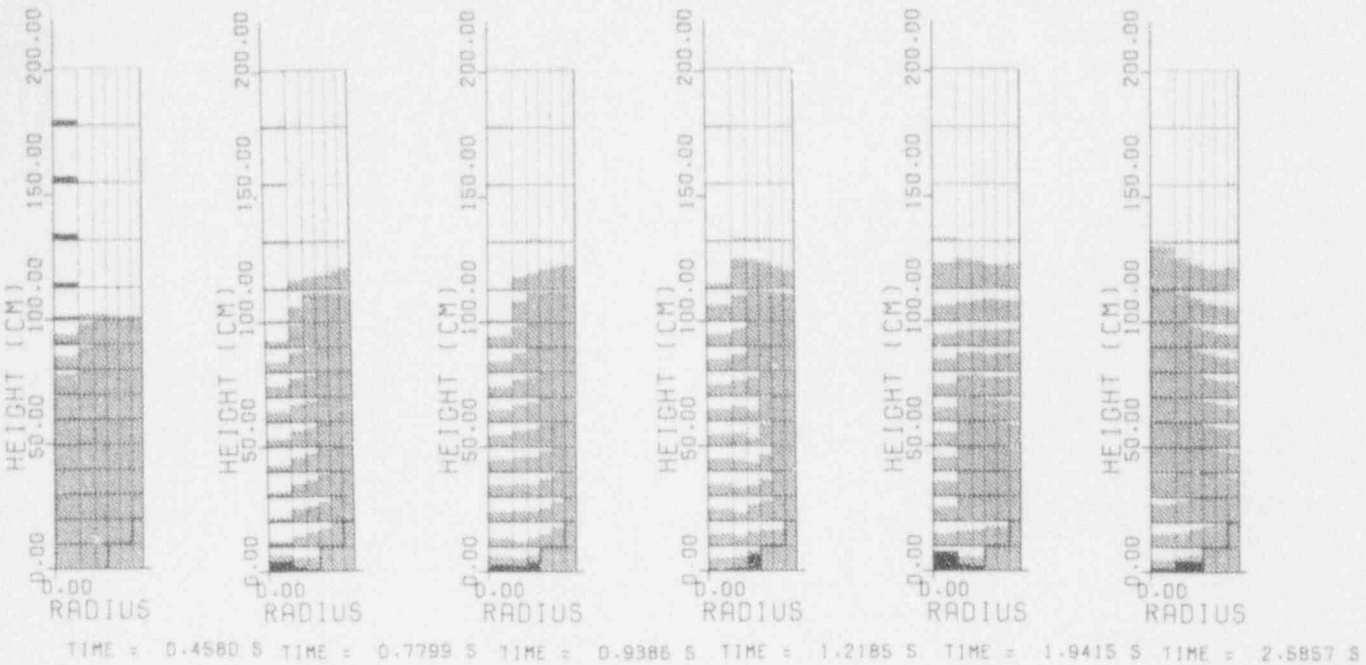

Figure 4: FARO LWR 2nd Quenching Test, real case calculation RC1. Volume fraction plots of the lower 15 rows of cells.

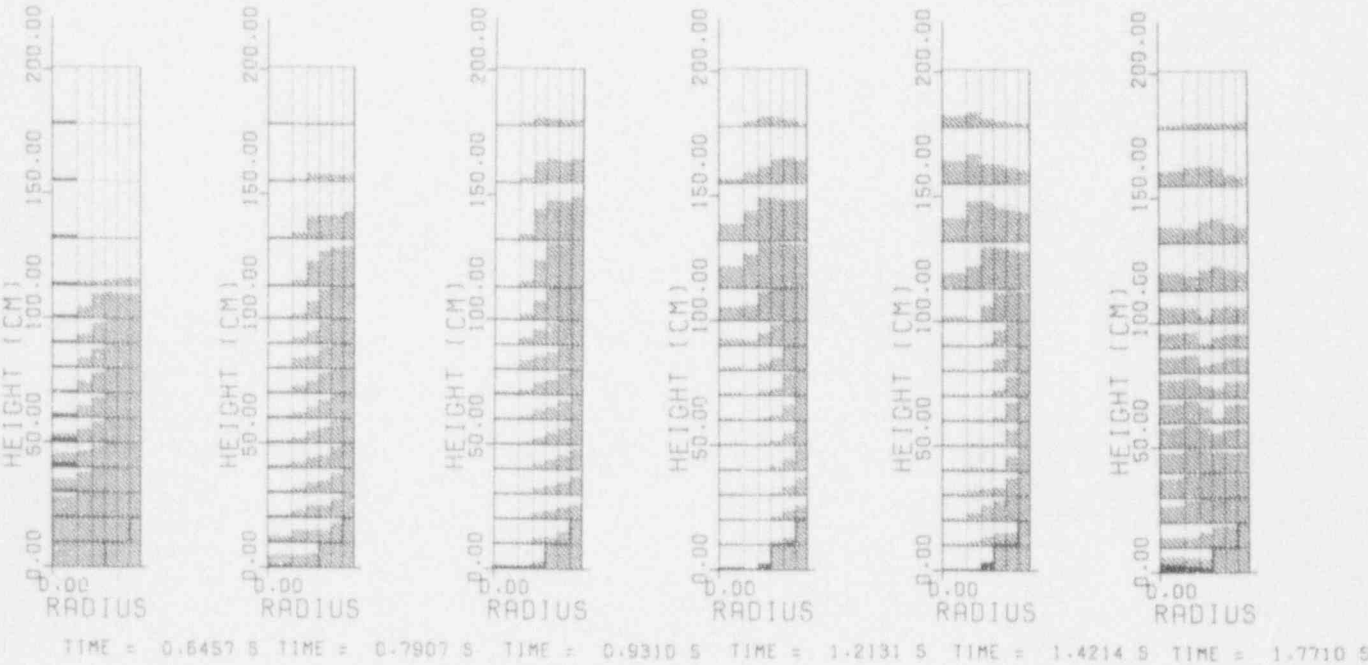

Figure 5: FARO LWR 2nd Quenching Test, real case calculation RC2. Volume fraction plots of the lower 15 rows of cells.

been performed with the inner cells having 20 cm diameter and the assumptions concerning the intermediate melt catcher described above. It turned out that still the corium moved essentially vertically dowmwards. So, the concern mentioned might have been in vain. But now the concern araises that the different model of the melt catcher might be responsible of the protracted melt release. In this situation it might be prudent to move into the other direction and even use two radial meshes within the 10 cm diameter of the orifice. This still remains to be done. But in any case one has to keep in mind that the code cannot describe (with its three velocity fields) a melt jet emerging from the orifice that subsequently disintegrates into droplets. Because the corium volume fraction in the mesh cells below the 'orifice' always stays below 50 %, the corium in these cells is always modeled as droplets. In the special case of the FARO LWR experiments in which the corium jet is to be expected to fully disintegrate during the fall towards the water surface, this modelling does not seem to be too bad.

Similar volume fraction plots of real case 2 are shown in Figure 5. In this case the corium motion is virtually the same until the sudden fragmentation event at 0.62 sec. But this fragmentation leads to a stronger radial dispersion of the corium jet and thus also to a radially more extended voiding (compare e. g. the situations shortly before 0.8 sec). Also it takes much longer until the corium settles in the debris catcher and in comparison with the above cited experimental finding the water is too far thrown up.

Both calculations so far discussed strongly understimate the pressure rise during the period in which the corium falls toward the water surface. It amounts to almost 0.8 bar only as compared to the experimentally observed 3.3 bar. Most probably this is due to a too small heat transfer from the corium to the gas phase and/or the water surface. One possible explanation for that is that radiation plays a major role in this phase but radiative heat transfer is not modeled in the flow regime ascribed to corium droplets in contunuous gas. Also, a corresponding correlation does not seem to be available in the literature. So, just in order to see what consequences increased heat transfer has, the model was modified in such a way that the corium droplets emerging from the intermediate catcher assumed a diameter of 1 mm instead of the 1 cm in the previous calculations. Both of these values are parametrical as the fragmentation model would predict much larger corium drops due to the small velocity difference present. The argument for limiting the diameter to 1 cm (actually 1/10 of the radial width of the cell) had been that the code inherently assumes dispersed flow so that the dimensions of the flow structures (here the droplets) should be smaller than the cell width. Even smaller diameters (such as the here parametrically assumed 1 mm) might e. g. result from a mechanical disturbance of the corium jet by the release mechanism (flap) or from turbulence or enclosed gases in the jet. (This is only to say that diameters at or even below 1 cm might not be completely out of range.) The consequences of this ten times larger initial corium surface are about the correct initial pressure increase and a pressure maximum about 3 bar above the experimental value. (see curve PC1 in Figure 2). Actually this parametric calculation gives the closest similarity with the experiment. No attempt was made at optimizing the droplet diameter. Such an exercise would make no sense at the present state of modeling.

Figure 6 shows the pressure histories obtained in another set of calculations with only slightly modified conditions, i. e. initial pressure and water subcooling. All of them have been performed with the Taylor type breakup time correlation. The only thing varied was the water subcooling. In parameter case 2 (label PC2) the water in the two lowest rows of cells was assumed to have a temperaure of 505 K (41 K subcooled) and the temperature was assumed to increase lineraly from 534 K to 541 K (5 K subcooled) from row number 3 to row number 10 (all of these cells are 10 cm high). (These temperatures but not the initial pressure level correspond to the first, the so-called scoping test in the FARO LWR facility.) In parameter case 3 (label PC3) the water temperature in the two lowest rows of cells was raised to 534K. This, quite reaonably, resulted in higher pressures at later times. In parameter case 4 (label PC4) all of the water was assumed to have a temperaure of 541 K (only 5 K subcooled). This case shows no deviation initially, but at 0.58 sec the pressure rise rate suddenly increases due to the same reason as (slightly later) in real case 2 above. This calculation demonstrates that it is not the different choice of breakup time correlation that caused

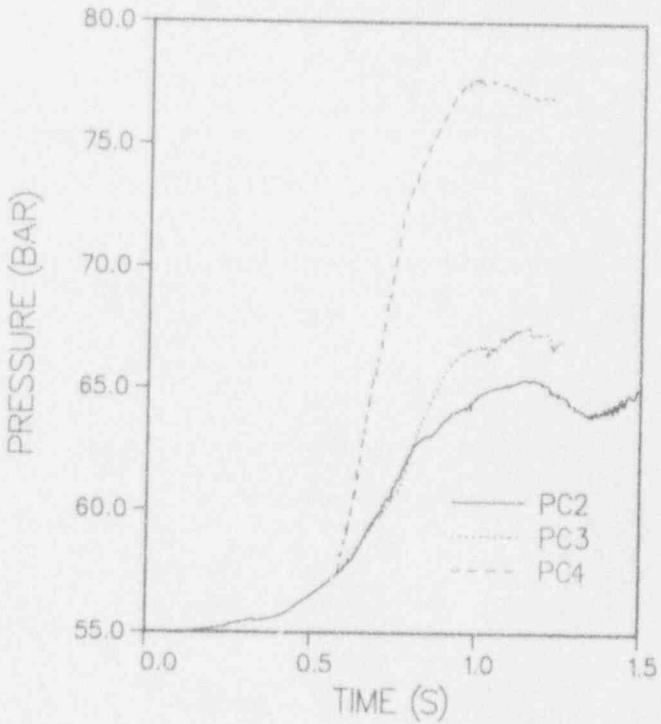

Figure 6: FARO LWR 2nd Quenching Test; pressure histories of parametric calculations at 55 bar initial pressure and varied subcooling of the water.

the calculation of real case 2 to differ so markedly from real case 1. In this case it is slightly reduced subcooling of the water that happened to cause the occurrence of the above described miniature surface eruption.

That such small eruptions happen in this type of calculation is not too astonishing. After all, steam explosions as well as their milder forms like surface eruptions are (or at least can be) a largely autocatalytic process: Evaporation and local pressure rise lead to larger velocity differences between melt drops and vapour which leads to additional fragmentation and thus to increased heat transfer and evaporation, etc. Actually, smaller sudden fragmentation events occur in almost every calculation. It appears to be consistent that in the above described set of calculations it was the reduction of subcooling (favouring evaporation) that produced a larger one. On the other hand, in the set of real case calculations presented in Figure 2 it was the choice of a different breakup time correlation that had the same effect, while calculations will be presented further below that show almost no difference between the two correlations for breakup time. So, we have to accept that there is no clear causal dependence between model assumptions or initial conditions and the occurrence of unrealistically strong fragmentation events. Conceivably they might be avoided by just choosing a finer calculational mesh. This question will have to be studied further.

C. Precalculations of First Base Case Test

The next test to be performed in the FARO LWR facility is called first base case and (according to the present planning) shall involve 150 kg of corium and slightly over 600 kg of water at saturation temperature at the initial pressure of 50 bar. The distance between the corium release orifice with still 10 cm diameter and the water surface is reduced to 1 m because the water pool is 2 m deep. In order to limit the pressure increase, an additional free volume of 0.5 m^3 is connected with the FARO vessel via a 14 cm wide pipe.

With the aim to obtain conservative results with respect to total pressure rise, all the precalculations have been performed assuming that the corium breaks up into droplets of 1 mm diameter when leaving the intermediate melt catcher. The pressure histories obtained are shown in Figure 7. In the first of these (label BC1) the additional volume has not been modeled. Obviously the pressure becomes much too high for the facility. The other two calculations have taken into account the additional volume and have been performed with the two available correlations for breakup time. These two calculations give virtually the same result and indicate that the design limit of 100 bar might be exceeded in spite of the additional volume. As it is not clear how conservative these calculations are (to what degree of conservatism the artificially reduced corium particle diameter leads in this case), it cannot be excluded that the integrity of the facility will have to be ensured by controlled pressure relief before reaching 100 bar.

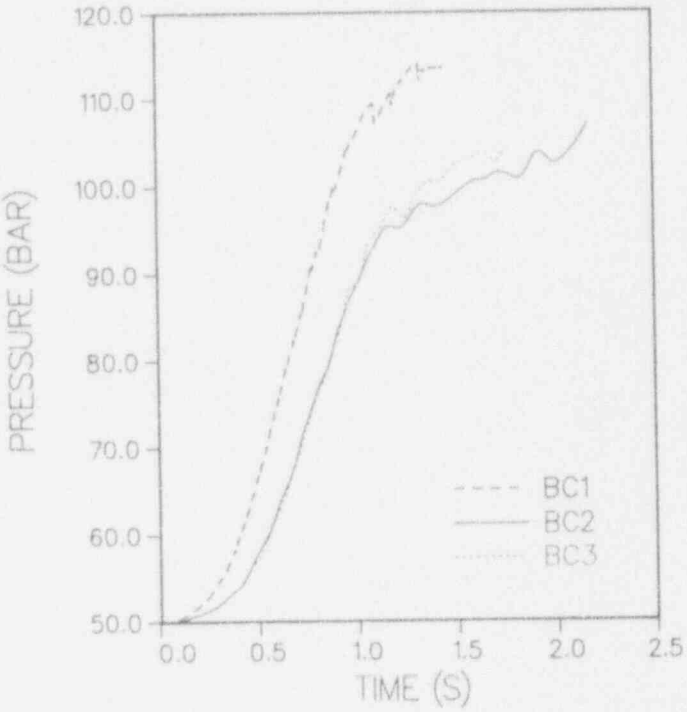

Figure 7: FARO LWR 1st Base Case Test; pressure histories of different blind precalculations.

IV. THE KFK BETA EXPERIMENTS

In the BETA experiments that have been performed at KfK since several years, the corium-concrete interaction is studied. To this end about 300 kg of molten iron and some alumina that result from an aluminium thermite reaction are poured into a concrete crucible and the iron is heated by high frequency induction heating while it erodes the concrete. In experiment V6.1 it was intended to test whether stagnant water in contact with the concrete could stop the radial erosion (Alsmeyer, 1992). Obviously this was not the case and as a result of direct contact between melt and water a mild pressurization was observed. The test was repeated as experiment V6.2 with a slightly modified geometry, see Figure 8. This time a more violent interaction occurred that caused some damage to the test rig. Unfortunately there are almost no data available of these events. In the first case, the pressure records went into saturation at 1 bar overpressure. The second event was so fast that the experiment was destroyed within one measuring interval of 0.4 sec. Only from the damage one can deduce that the pressure must have exceeded 20 bar for some period.

This second experiment was modeled using the same code as in the above FARO cases and with a very rough geometrical model (only one radial mesh cell for the crucible, the concrete w[illegible], and the

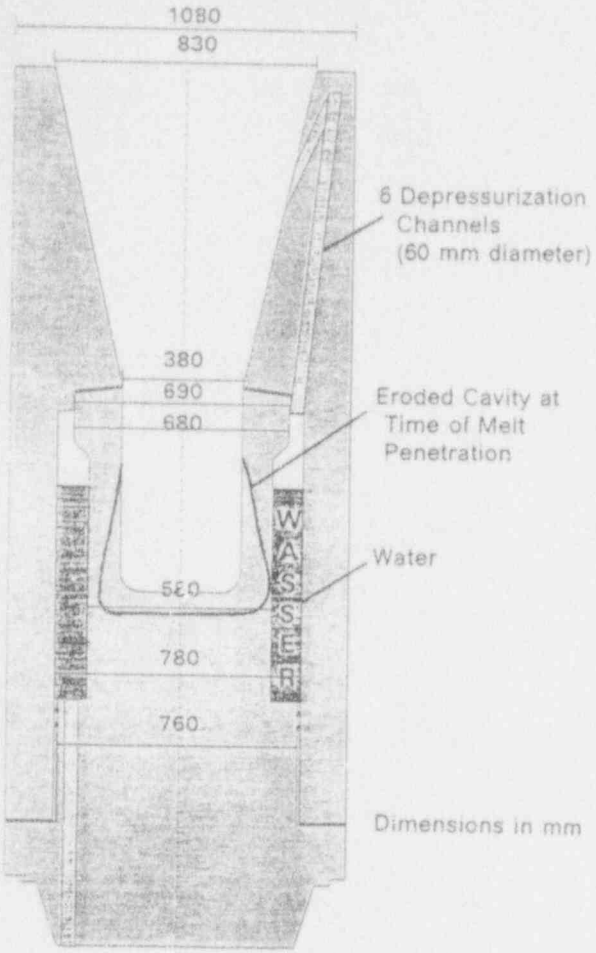

Figure 8: BETA V6.2; crucible geometry. Above this is a large head providing a large free volume and connection to an offgas line.

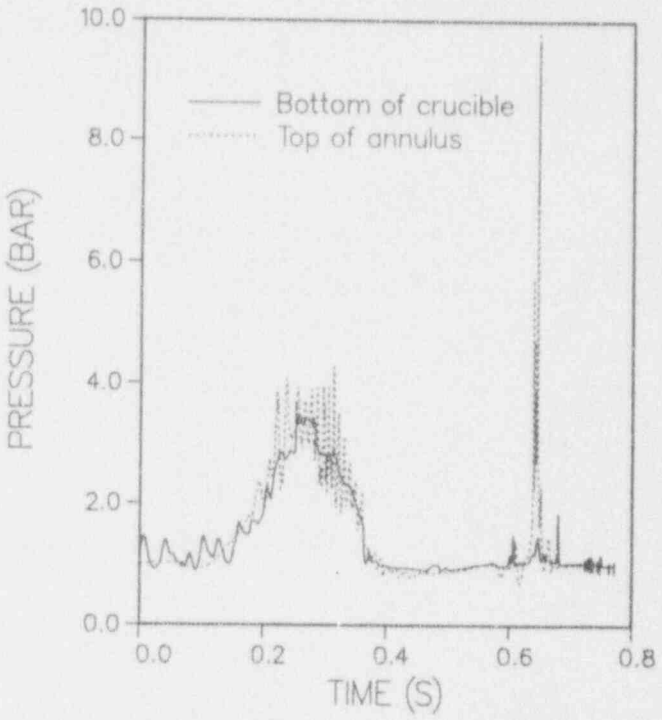

Figure 9: BETA V6.2; pressure histories obtained at the bottom of the crucible and the top of the water annulus (case 06C).

water annulus, respectively). It is assumed that initially a 7 cm high (circumferential) gap that is already filled with melt connects the crucible with the water annulus as a result of the concrete erosion. So, due to the higher hydrostatic pressure in the melt, initially some melt penetrates into the water annulus. As a consequence, the pressure in the annulus starts to rise after about 0.15 sec. This can be seen from Figure 9 which shows the pressures at the bottom of the crucible and at the top of the water annulus. This pressure rise inverts the pressure difference and the flow direction in the gap so that now water is squeezed into the gap and the crucible proper. This in turn leads to a pressure rise within the crucible to about 3.5 bar that throws the melt upwards. From 0.28 sec on, the pressure drops again, returns to about 1 bar, and remains there during the remainder of the calculation. The pressure in the upper gas space is always very close to 1 bar because of the offgas line that is modeled by a long cell (omitted in Figure 9) and a boundary condition prescribing 1 bar pressure.

The early end of the pressure rise is somewhat astonishing, because, as can be seen from the volume fraction plots in Figure 10, there are, e. g. at 0.36 sec, considerable masses of iron and water in close proximity as well in the crucible as in the water annulus and they are in vigorous motion towards the top. At around 0.28 sec there are even more than 50 kg of molten iron contained within liquid water in the film boiling state. This flow regime is normally considered to be most dangerous with respect to steam explosions. And certainly the explosion of 50 kg would be sufficient to involve also the remaining material into a steam explosion. But no initiating event is calculated and the small pressure event calculated instead cannot account for the observed damages. The latter remains true if the melt is (parametrically) assumed to fragment into drops of 1 mm diameter when entering the water annulus, like in the FARO parameter case 1 above. In the case of the BETA test, such smaller particle sizes could be due to thermal fragmentation of the melt in the water pool. With these smaller particles the whole process is more violent. The pressure in the crucible reaches about 7 bar and spikes up to about 12 bar are to be observed at the top of the water annulus. But already after 0.1 sec the pressures start to die away and the transient is over after 0.18 sec. Again nothing like a steam explosion is predicted.

It might be that the absence of a strong explosion in these calculations is simply due to the lack

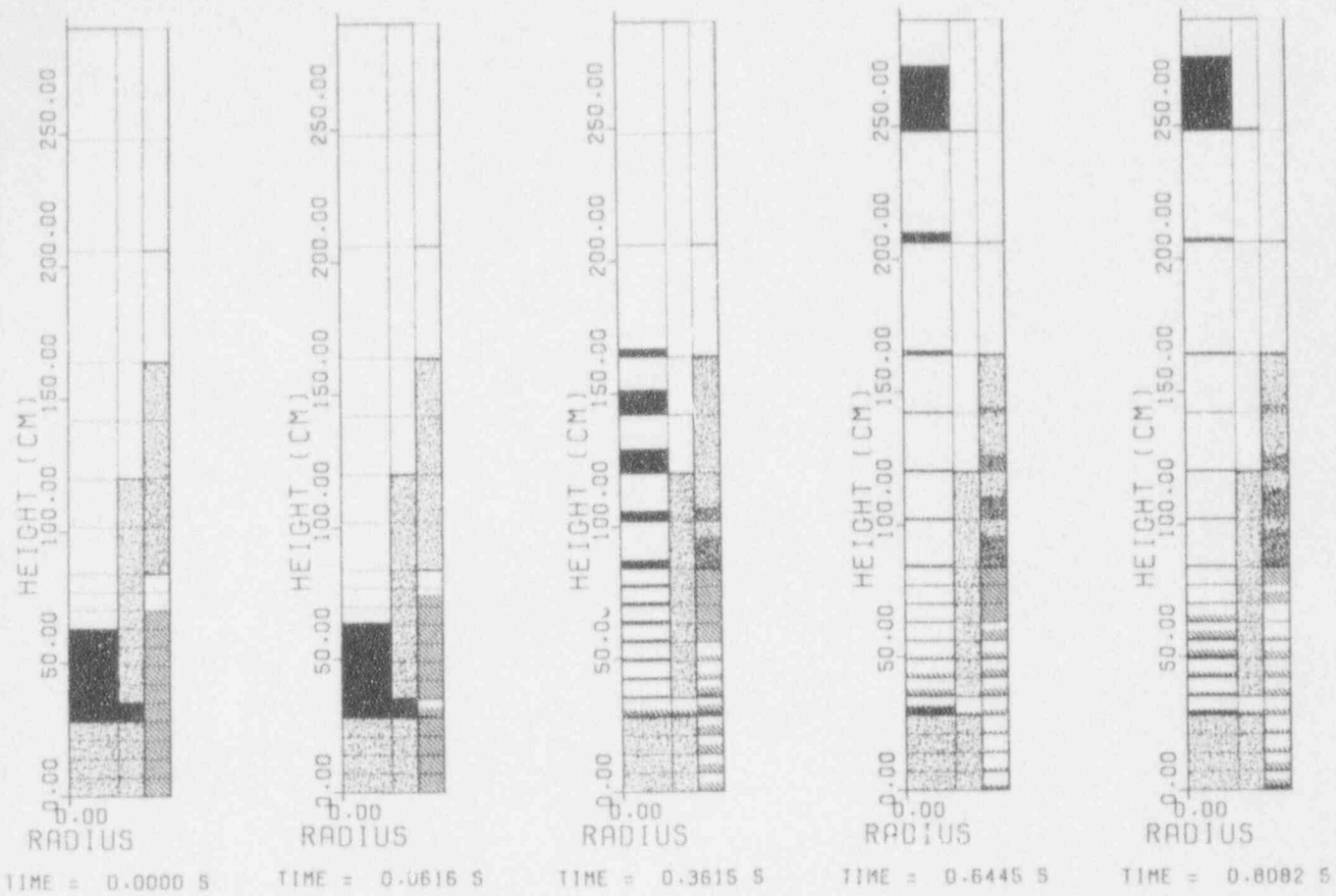

Figure 10: BETA V6.2; volume fraction plots (case 06C). The outer radius of the water annulus is 39 cm. (The cells occupied by concrete are dotted.)

of some important model in the code. But there is still another possibility. As can be inferred from the pressure history at the roof of the annulus (Figure 9) and the volume fraction plots (Figure 10), the pressure transient throws upwards not only the melt in the crucible but also the water above the level at which the melt penetrates into the water annulus. This water may contain bubbles or not - after impact with the roof of the annulus it will be pure liquid. A similar process must have taken place in the experiment. (Actually one would not have needed calculations with a multiphase code to infer that a pressure build up in the lower part of the water annulus caused by melt penetration must cause a water hammer hitting the roof of this annulus.) Now, in the real roof of the annulus there have been the openings of the six depressurization channels that are embedded in the concrete and lead first upwards, then turn, and have openings pointing towards the bottom of the crucible (see Figure 8). It is inevitable that the water hitting the roof of the annulus also penetrated these channels and it cannot be excluded that quite some amount of water was consequently injected in downwards direction into the already upwards moving melt mass. (It is as well quite obvious that a few bars of overpressure are sufficient to throw the melt upwards within the crucible.) And if such counterflow of molten iron and liquid water really occurred, it must almost certainly have lead to a benign steam explosion or steam spike. An additional explosive event must have resulted because melt and water have been mixed in a way that forced intimate contact and fine fragmentation of both materials. But at the same time this explosion must have remained benign because there has already been a lot of void present in the interaction volume. As the special arrangement of the depressurization channels was the only essential change between experiments V6.1 and V6.2, it occurs that the second experiment might (unintentionally) have been designed to almost certainly produce a mild steam explosion and this could explain the different outcomes of the two experiments. That even mild loads could do a lot of damage to the test rig is due to the fact that this one was not designed to resist any sizable internal pressures.

Unfortunately it is difficult to model the above described sequence of events by the present version of IVA3. The flow area of the depressurization channels could readily be modeled by assuming a small (8 %) permeability of the annular roof and the

cell boundaries within the concrete above. It could, however, not be modeled that only narrow channels are available to the water within the concrete (let alone their complicated shape). The concrete structures are just modelled by impermeable walls, but if there are penetrations assumed like those for the channels, the structures appear to be empty to the system and a lot of water is transferred into them. This explains the apparently absurd presence of water in the concrete that can be observed in Figure 10. At least this large amount of water indicates how vigorous water is squeezed through the small openings in the annular roof. Obviously, BETA V6.2 remains to be modeled by improved versions of IVA3 using a more refined geometrical model.

Even in the calculation shown in Figure 7 that gives the more benign results, the velocity with which water penetrated into the (poor model of the) depressurization channels reached 15 m/sec at 0.29 sec. Assuming that the roughly 1.4 m long channels might have been passed through with a mean velocity half as high, water would have been injected into the melt before 0.4 sec, i. e. less than 0.4 sec after the start of the event at about 0.15 sec. And of course, with higher reaction pressures in the water annulus, everything would have proceeded faster. So, the here proposed sequence of events would have had a good chance to destroy the test rig within less than 0.4 sec and thus escape registration.

V. DISCUSSION OF RESULTS

The calculations presented show that the present version of IVA3 which is far from being complete is able to describe melt-water mixing under quite different conditions. The parameter variations performed for the FARO case show that normally the results depend in a reasonable way on the input parameters. However, real case 2 (RC2) and parameter case 4 (PC4) also show that there is an additional influence on the results that is due to sudden fragmentation events that occasionally become so important that they drastically change the predicted description of a process. Such decicive influence of local events on the whole calculation might be a numerical artefact and should be avoided. Possibly this can be done by using smaller cells in the calculational mesh.

Analysis of the calculational results indicates that the observed pressure rise is essentially due to an increase of the saturation pressure of the hottest liquid water present.

Comparing the calculations to the data from the FARO experiments reveals encouraging agreement but also important discrepancies. Most importantly, gradual pressure rises on the time scale of a second are obtained like in the experiments. But the size of the total pressure rise is seriously underestimated in real case 1. On the other hand, real case 2 and parameter case 1 even overestimate the pressure increase. However, comparing level swell (i. e. void formation) and final particle sizes with the experiment, one finds that real case 1 better fits the data. So, the corium fragmentation predicted in real case 1 seems to be superior over that predicted in real case 2 and that assumed in parameter case 1. Still, in real case 1, there is quite obviously too little heat transfer during the corium fall towards the water surface and later on too little heat transfer to the liquid water (which would drive pressure build up, see above). This in turn may have two reasons: Either simply the fact that the melt is not delivered fast enough to the water pool (possibly not released fast enough from the intermediate catcher) or not effective enough heat transfer mechanisms. So, if the pressure increase should continue to be understimated after fixing the unrealistically protracted melt delivery, it will have to be studied whether radiative heat transfer from corium droplets to steam and (directly) to water droplets (in three-phase droplet flow) are sufficient to resolve the problem.

For the experimentors it might be reassuring that in none of these calculations including those producing suddenly or assuming from the beginning strong fragmentation, the pressure rose sharply beyond the load limits of the FARO facility. One should, however, not forget that the models that allow for the description of real steam explosions are almost certainly still missing in the code. Much work remains to be done before this code can be used to reliably exclude the occurrence of steam explosions.

For the BETA experiment a rather benign pressure transient is predicted that cannot account for the observed damages. This may well be due to the above mentioned deficiency or lack of models in the code. Besides that, the calculational results suggest that due to the special geometrical conditions of the test already such benign pressure transient must almost certainly lead to a more pronounced steam spike by countercurrent injection of water into the upwards accelerated melt mass.

REFERENCES

Alsmeyer, H. (1992) Melt Attack and Penetration of Radial Concrete Structures Cooled by Outside Water, 20th Water Reactor Safety Information Meeting, Bethesda, MD, October 21 - 23

Amarasooriya, W. H. and T. G. Theofanous (1991) Premixing of steam explosions: a three-fluid model, Nuclear Engineering and Design **126**, 23 - 39

Dhir, V. K., and G. P. Purohit (1978) Subcooled Film-Boiling Heat Transfer From Spheres, Nuclear Engineering and Design **47**, 49 - 66

Dhir, V. and J. Lienhard (1971) Laminar Film Condensation on Plane and Axisymmetric Bodies in Nonuniform Gravity, Trans ASME C: J Heat Transfer **C93**, 97 - 100

Fletcher, D. F. and A. Thyagaraja (1991) The CHYMES coarse mixing model, Progress in Nuclear Energy **26**, 31 - 61

Henry, R. E. and H. K. Fauske (1981) Required Initial Conditions for Energetic Vapor Explosions, in: Fuel Coolant Interactions, ASME Report HTD - Vol. 19, pp. 99 - 107

Holman, J.P. (1972) *Heat Transfer*, McGraw-Hill

Hunt, D. L. (1970) Effect of Delayed Bubble Growth on the Depressurisation of Vessels Containing High Temperature Water, UKAEA Report AHSB(S) R 189

Isenberg, J. and S. Sideman (1970) Direct contact heat transfer with change of phase: bubble condensation in immiscible liquids, Int J Heat Mass Transfer, **13**, 997 - 1011

Kolev, N. I. (1991 a) IVA3: A Transient 3D Three-Phase, Three-Component Flow Analyzer, Proc Int Topcl Mtg on Safety of Thermal Reactors, Portland, OR, July 21 - 25, pp. 171 - 180

Kolev, N.I. (1991 b) A Three-Field Model of Transient 3D Multiphase, Three-Component Flow for the Computer Code IVA3; Part 2: Models for the Interfacial Transport Phenomena. Code Validation, Kernforschungszentrum Karlsruhe Report KfK 4949

Labuntsov, D. A. and A. P. Kryukov (1977) Process of Intensive Evaporation, Thermal Engineering (Teploenergetika), **24** (4), 8 - 11

Magallon, D. and H. Hohmann (1993) High pressure corium melt quenching tests in FARO, this conference

Miropolskii, Z. L. (1963) Heat Transfer in Film Boiling of a Steam-Water Mixture in Steam-Generating Tubes, Teploenergetika, **10** (5), 49 - 52 (AEC-tr 6252)

Nigmatulin, R. I. (1978) *Fundamentals of the Mechanics of Heterogeneous Fluids*, Moskva, Nauka (In Russian)

Patel, P. D. and T. G. Theofanous (1981) Hydrodynamic fragmentation of drops, J Fluid Mech **103**, 207 - 223

Pilch, M. and C. A. Erdman (1987) Use of Breakup Time Data and Velocity History Data to Predict the Maximum Size of Stable Fragments for Acceleration-induced Breakup of a Liquid Drop, Int J Multiphase Flow **13**, 741 - 757

Ranz, W. and W. Marschal Jr. (1952) Evaporation from Drops, Chemical Engineering Progress, **48**, 141 - 146

Rohsenow, W. M., J. P. Hartnett, and E. N. Ganic Eds. (1985) *Handbook of Heat Transfer Fundamentals*, Mc Graw Hill

Simpkins, P. G. and E. L. Bales (1972) Water-drop response to sudden accelerations, J Fluid Mechanics **55**, 629 - 639

Tanaka, M. (1980) Heat Transfer of a Spray Droplet in a Nuclear Reactor Containment, Nuclear Technology **47**, 268 - 281

Nomenclature

Bo	Bond number (-)
c_b	breakup time constant (-)
C_1	concentration of air in field 1 (-)
d_d	diameter of particles (m) in discontinuous field
$P_{1,v}$	partial pressure (Pa) of steam in field 1
$P_{sat,2}$	saturation pressure (Pa) corresponding to the water temperature T_2
$\dot{q}''_{cr}$	critical heat flux density (W/m^2) (depends on coolant subcooling)
$\dot{q}''_{nb}$	heat flux density (W/m^2) due to nucleate boiling
T_1	gas temperature (K)
T_2	water temperature (K)
T_3	corium temperature (K)
T_{crit}	critical temperature (K)
T_{inb}	minimum wall temperature (K) required for inception of nucleate boiling (depends on coolant subcooling)
T_{ifb}	minimum wall temperature (K) required for film boiling (depends on coolant subcooling)
T_m	melting temperature (K)
T_{sat}	saturation temperature (K) corresponding to the local system pressure
$T_{sat,1}$	saturation temperature (K) corresponding to the steam partial pressure $P_{1,v}$
T_{sup}	superheat (K) required for flashing (depends on decompression rate)
$\vec{V}_c$	velocity of continuous field (m/sec)
$\vec{V}_d$	velocity of discontinuous field (m/sec)
We	Weber number (-)
We_{cr}	critical Weber number (-)
ρ_c	density of continuous field (kg/m^3)
ρ_d	density of discontinuous field (kg/m^3)
σ_d	surface tension of discontinuous field (N/m)
τ_b	dimensional breakup time (sec)

Appendix A: Flow regimes and related heat and mass transfer modes in IVA3

1. Introduction

In this Appendix only the physical content of the heat and mass transfer (HMT) correlations is described and the most important references are given. More details can be found in Kolev (1991b).

2. One field only

2.1 Velocity field 1 (gas) only

No heat or mass transfer.

2.2 Velocity field 2 (water) only: Check for inception of field 1.

If $T_2 > T_{crit}$: put all water into gas field.

If $T_2 > T_{sat} + T_{sup}$: bubble nucleation; an assumed number of nuclei (per volume) reaches the critical radius (Labunzov and Krukov, 1977).

2.3 Velocity field 3 (corium) only

No heat or mass transfer.

3. Two fields

3.1 Bubbly flow: Gas bubbles in water

3.1.1 Supercritical water

If $T_2 > T_{crit}$: put all water into gas field.

3.1.2 Subcritical water: Check for condensation

If $T_{sat,1} > T_2$: condensation depending on bubble motion (Hunt, 1970; Isenberg and Sideman, 1970)

3.1.3 Subcritical water, no condensation: Check for evaporation

If $T_2 > T_{sat} + T_{sup}$: thermally controlled bubble growth (Labunzov and Krukov, 1977).

If $C_1 > 0$ and $T_2 > T_{sat,1}$: modified thermally controlled bubble growth.

3.2 Churn turbulent flow: discontinuous gas in continuous water

Until now the same HMT models as in bubbly flow (3.1).

3.3 Droplet flow: Water droplets in gas

3.3.1 Supercritical water ($T_2 > T_{crit}$)

Put all water into gas field.

3.3.2 Superheated water ($T_2 > T_{sat}$)

If $P_{sat,2} - P_{1,v} - \frac{P_{sat,2}}{2T_2}(T_2 - T_1) > 0$:

flashing (modified Hetz-Knudsen-Langmuir, see Rohsenow et al., 1985)

3.3.3 Subcooled water, gas is pure steam ($T_2 < T_{sat}$, $C_1 = 0$)

Thermally controlled laminar condensation (Dhir and Lienhard, 1971).

3.3.4 Subcooled water, gas is air/steam mixture ($T_2 < T_{sat}$, $0 < C_1 < 1$)

If $T_2 < T_{sat,1}$: diffusion controlled condensation (Ranz and Marshall, 1952; Tanaka, 1980).

If $T_2 > T_{sat,1}$: diffusion controlled evaporation (Ranz and Marshall, 1952; Tanaka, 1980).

3.3.5 Subcooled water, gas is pure air or superheated steam ($T_2 < T_{sat}$, $\{C_1 = 1$ or $T_{sat,1} > T_{sat}\}$)

convective heat transfer to water (Ranz and Marshall, 1952)

3.4 Corium particles in water

3.4.1 Superheated water ($T_2 > T_{sat}$)

Check for flashing like in 2.2 above irrespective of corium temperature. (number of nuclei = number of corium particles).

3.4.2 Low temperature corium ($T_3 < T_{inb}$)

Convective heat transfer (Nigmatulin, 1978)

3.4.3 Medium temperature corium ($T_{inb} \leq T_3 < T_{ifb}$ and $\dot{q}''_{nb} < \dot{q}''_{cr}$)

If $T_2 \geq T_{sat}$: saturated nucleate boiling.

If $T_2 < T_{sat}$: subcooled nucleate boiling.

(Thom, see Miropolskij, 1963)

3.4.4 High temperature corium ($T_3 \geq T_{ifb}$ or $\dot{q}''_{nb} \geq \dot{q}''_{cr}$)

If $T_2 \geq T_{sat}$: saturated film boiling.

If $T_2 < T_{sat}$: subcooled film boiling.

Both include forced convection and radiation (Dhir and Purohit, 1978)

If flashing and boiling occur both, the evaporation rates are added.

3.5 Water droplets in continuous corium

3.5.1 Low temperature corium ($T_3 < T_{sat}$)

Convective heat transfer (Nigmatulin, 1978)

3.5.2 Medium temperature corium ($T_{sat} \leq T_3 < T_{ifb}$)

Saturated nucleate boiling. (Thom, see Miropolskij, 1963)

3.5.3 High temperature corium ($T_3 \geq T_{ifb}$)

Film boiling including radiation and with evaporation as allowed by acceleration controlled bubble growth.

3.6 Gas bubbles in continuous corium

Convective heat transfer (Nigmatulin, 1978) assuming natural convection in the bubble (Holman, 1972).

3.7 Corium particles in continuous gas

Convective heat transfer (Nigmatulin, 1978).

4. *Three fields*

4.1 Three-phase bubble flow: Gas bubbles and corium particles in water

The bubbles interact with water like in 3.1 above and the particles interact with water like in 3.4 above. The respective HMT rates are added.

4.2 Three-phase droplet flow: Water droplets and corium particles in gas

The droplets are treated like in 3.3 above and the particles exchange heat with the gas like in 3.7 above. (There is no direct heat transfer between droplets and particles.)

4.3 Water droplets within gas channels in continuos corium

4.3.1 Low or medium temperature corium

If $T_3 \leq T_{ifb}$: no HMT.

4.3.2 High temperature corium

If $T_3 > T_{ifb}$: simplified model of film boiling. All transferred heat is used to create vapour except for 20 % of the radiative heat transfer which is (parametrically) used to heat the water droplets.

4.4 Gas bubbles within water channels in continuos corium

Until now no HMT.

CALCULATIONS OF THE PREMIXING PHASE OF AN FCI WITH THE TRIO MC CODE

G. Berthoud, M. Valette
Commissariat à l'Energie Atomique, C.E.N.G. - Département de Thermohydraulique et de Physique
85 X - 38041 Grenoble cedex, France
Telephone (33) 76 88 32 44 - Fax (33) 76 88 51 77

ABSTRACT

A transient, three-dimensional, four field model is under development to deal with the premixing of large amounts of molten corium falling down in the lower plenum of a PWR. Calculation of the FARO Scoping test are presented with the two-dimensional, three field version of TRIO MC.

I. INTRODUCTION

In the frame of PWR Severe Accident Studies sponsored by the Nuclear Safety Institute of CEA (IPSN), it has been recognized that an energetic vapour explosion could take place when large amounts of molten corium fall into the lower plenum of the Reactor Pressure Vessel or, in the case of the breach in the RPV, when the corium falls in the Reactor Cavity which may be filled with cold water. The hypothetical vapour explosion that can developpe will largely depend on the way the fuel will fragment and disperse under the action of the large amounts of vapour which are produced. To solve this problem, we decided to build a model that can describe :

- the transformation of melt jets into globules
- the fragmentation and dispersion of these globules under the action of the vapour production
- the desequilibrium between the vapour and liquid coolant.

Many other premixing models exist in the literature : TEXAS [1], PM ALPHA [2], CHYMES [3], IFCI [4] and IVA3 [5] but none of them include the jet fragmentation which can be a serious factor in order to limit the mixing of corium and coolant. At this point, it must be mentionned that the fact of using fuel droplets of constant diameter may not be considered as conservative from a safety point of view. In fact, by assuming this, we favour the premixing by suppressing the fragmentation sequence but we reduce the explosibility by overestimating the vapour production.

For this reason we think that a premixing code should include the progressive fragmentation of the melt in its sequence.
Besides the evident physical consequence of the overestimated vapour production, this assessment is supported by at least two experimental observations :

- in the experimental FITS program performed in Sandia [6], it has been shown that in order to developpe an FCI, the mixture should not be too poor (nor too rich) in fuel. In the MD Series for example, the apparent density of fuel in the mixture should belong to the interval 0.12 g/cm3 to 0.17 g/cm3 (see fig. 1). So, if the vapour production is overestimated, the consequence is a reduction in the apparent density of the fuel. This behaviour is also observed in chemical explosives for which the efficiency of the reaction reaches a maximum for a certain amount of oxygen,

- in the ALPHA program [7], explosions which are observed when 20 kg of aluminium thermite are dropped into water are suppressed when the melt is delivered through a grid which transforms this melt into a population of droplets. In this case, we can also suspect that the larger amount of vapour in the mixture is responsible of the non-explosivity.

Up to now, the jet fragmentation modelling is rather poor but in order to calculate the FARO Experiment [8], we think that during its fall in the vapour, the corium jet will undergo complete fragmentation. So, we will restrict the presentation to the three fields version of TRIO MC.

II. MATHEMATICAL DESCRIPTION

TRIO MC consists in an eulerian description of the behaviour of fuel droplets, water and steam. Thus, we have three continuity equations, three momentum equations and three internal energy equations. Each field can exchange momentum and energy with the other fields, the exchange

of mass being limited in this version between water and steam. The corium droplet population will undergo fragmentation which is described through an interfacial area transport equation (which is very useful when we deal with jet fragmentation).

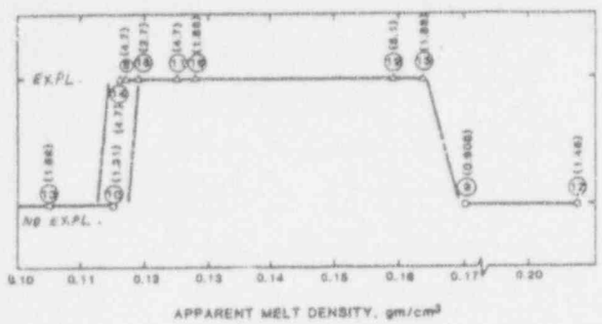

Figure 1 Explosivity as a function of the apparent density of the melt in the FITS MD Series

With the variables described in the nomenclature, the equations are the following :

- Continuity equations

$$\frac{\partial}{\partial t}(\alpha_L \rho_L) + \vec{\nabla}.\alpha_L \rho_L \vec{V}_L = -G_{ec}$$

$$\frac{\partial}{\partial t}(\alpha_V \rho_V) + \vec{\nabla}.\alpha_V \rho_V \vec{V}_V = +G_{ec}$$

$$\frac{\partial}{\partial t}(\alpha_d \rho_d) + \vec{\nabla}.\alpha_d \rho_d \vec{V}_d = 0$$

- Momentum equations

$$\frac{\partial}{\partial t}(\alpha_V \rho_V \vec{V}_V) + \vec{\nabla}.\alpha_V \rho_V \vec{V}_V \vec{V}_V + \alpha_V \vec{\nabla} P = K_{LV}(\vec{V}_L - \vec{V}_V) + K_{dV}(\vec{V}_d - \vec{V}_V) + \alpha_V \rho_V \vec{g} + G_{ec} \vec{V}_L$$

$$\frac{\partial}{\partial t}(\alpha_L \rho_L \vec{V}_L) + \vec{\nabla}.\alpha_L \rho_L \vec{V}_L \vec{V}_L + \alpha_L \vec{\nabla} P = K_{LV}(\vec{V}_V - \vec{V}_L) + K_{dL}(\vec{V}_d - \vec{V}_L) + \alpha_L \rho_L \vec{g} - G_{ec} \vec{V}_L$$

$$\frac{\partial}{\partial t}(\alpha_d \rho_d \vec{V}_d) + \vec{\nabla}.\alpha_d \rho_d \vec{V}_d \vec{V}_d + \alpha_d \vec{\nabla} P = K_{dV}(\vec{V}_V - \vec{V}_d) + K_{dL}(\vec{V}_L - \vec{V}_d) + \alpha_d \rho_d \vec{g}$$

Using this form of the equation implies that the pressure is uniform within one cell and that the diffusion terms are negligable. We also neglect, up to now, the added mass term for the vapour momentum equation.

- Internal energy equations

$$\frac{\partial}{\partial t}(\alpha_V \rho_V e_V) + \vec{\nabla}.\alpha_V \rho_V e_V \vec{V}_V = -P\left(\frac{\partial \alpha_V}{\partial t} + \vec{\nabla}.\alpha_V \vec{V}_V\right) + Q_{dV} + Q_{VI} + G_{ec} H_{VSAT}$$

$$\frac{\partial}{\partial t}(\alpha_L \rho_L e_L) + \vec{\nabla}.\alpha_L \rho_L e_L \vec{V}_L = -P\left(\frac{\partial \alpha_L}{\partial t} + \vec{\nabla}.\alpha_L \vec{V}_L\right) + Q_{IL} + Q_{LI} - G_{ec} H_{LSAT}$$

$$\frac{\partial}{\partial t}(\alpha_d \rho_d e_d) + \vec{\nabla}.\alpha_d \rho_d e_d \vec{V}_d = -P\left(\frac{\partial \alpha_d}{\partial t} + \vec{\nabla}.\alpha_d \vec{V}_d\right) - Q_{dV} - Q_{dL} - Q_{dI}$$

- Interfacial area transport equation for the fuel droplets

$$\frac{\partial}{\partial t} A_d + \vec{\nabla}.A_d \vec{V}_d = S_g$$

We will now describe the different exchange laws wich are needed for closure.

III. EXCHANGE LAWS

Every exchange term will be written under the form of the product of a transfer coefficient, an interfacial area and a driving difference. To do so, it is necessary to describe the different flow patterns we are dealing with. We will then distinguish between the falling phase where the fuel is dispersed within the coolant and the phase where the fuel is accumulating at the bottom of the vessel.

A. Falling phase

In this phase we will distinguish two extreme configurations : the one where the water is the continuous phase for the coolant from the one where it is the vapour which is the continuous phase as it can be seen on fig. 2.

1. Heat Transfer Laws

1.1. Film boiling flow configuration

In this configuration, the fuel froplets are surrounded by a (thin) vapour film from which vapour bubbles escape. This configuration will be assumed if the void fraction $\alpha = \frac{\alpha_V}{\alpha_V + \alpha_L}$ is smaller than α_f (~ 0.3).

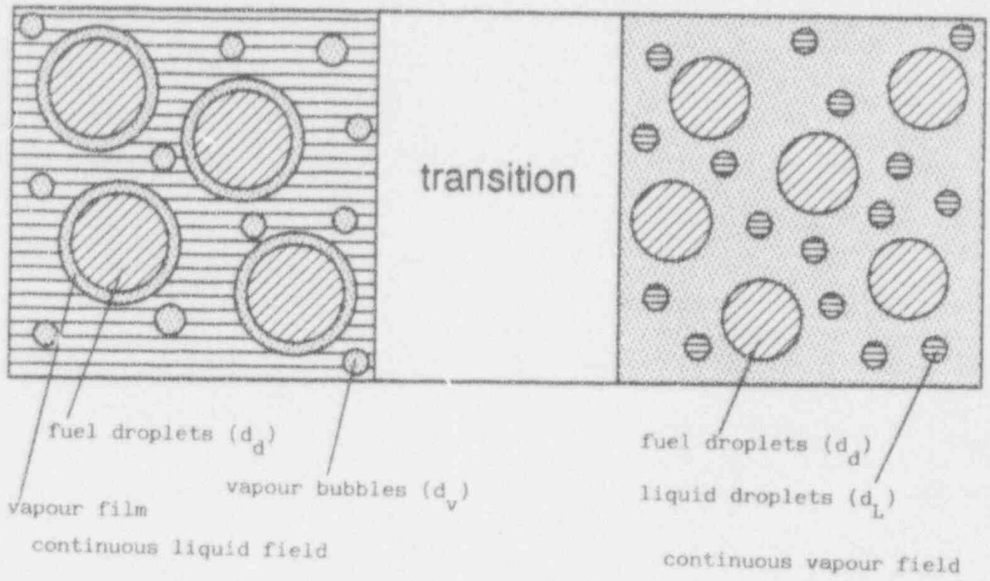

Figure 2. The two extreme flow patterns in the falling phase

In this configuration, heat is transferred directly from the fuel to the liquid-vapour interface in order to produce vapour. This Q_{di} term is made of two terms :

- A forced convection film boiling term which is described by the Epstein Hauser correlation [8] ie :

$$\frac{\beta Nu}{(\mathrm{Re})^{1/2}} = 2{,}5\left[\frac{1}{24A} + \left(\frac{2}{\pi}\right)^2\left(\frac{B}{A}\right)^4\right]^{1/4}$$

with

$$\beta = \left[\left(\frac{\rho_f}{\rho_L}\right)^{1/2}\left(\frac{\nu_f}{\nu_L}\right)\right]^{1/2}$$

$$Nu = \frac{h d_d}{k_f}$$

$$\mathrm{Re} = \frac{|V_d - V_L|\, d_d}{\nu_L}$$

$$A = \frac{C_{pf}(T_d - T_{SAT})}{\mathrm{Pr}_f\, h_{LV}}$$

$$B = \beta \frac{k_L}{k_f} C_{pf} \frac{(T_{SAT} - T_L)}{\mathrm{Pr}_f\, h_{LV}} (\mathrm{Pr}_L)^{1/2}$$

- a radiative contribution : a fraction C_{rad} of the radiative heat flux is "absorbed" at the interface instead of going into the liquid.
We then have

$$Q_{di} = hA_d(T_d - T_{SAT}) + C_{rad} Q_{rad}$$

with $Q_{rad} = \dfrac{\varepsilon_d \varepsilon_L}{\varepsilon_d + \varepsilon_L - \varepsilon_d \varepsilon_L} \sigma A_d (T_d^4 - T_L^4)$

and $A_d = \dfrac{6\alpha_d}{d_d}$ where the droplet diameter will be given by the fragmentation law (sec 4.13)
Heat will also be transfered directly to the liquid i.e.

$$Q_{dL} = (1 - C_{rad}) Q_{rad}$$

and we will consider the vapour as a transparent medium i.e $Q_{dV} = 0$

As for the liquid-vapour heat transfer, we have :
$Q_{Li} = h_c A_B (T_{SAT} - T_L)$ for subcooled water
with h_c given by a convective heat transfer correlation of the type

$Nu = 2 + 0{,}6\, \mathrm{Re}_B^{1/2}\, \mathrm{Pr}_L^{1/3}$ and $A_B = \dfrac{6\alpha_V}{d_B}$ where d_B comes from a Weber criteria

or
$Q_{Vi} = 10^7 (T_{SAT} - T_L)$ for superheated water to avoid too large superheat

As for Q_{Vi} we also chose $Q_{Vi} = 10^7 (T_{SAT} - T_V)$ for the same reason

The resulting evaporation rate is then given by :

$Q_{di} - Q_{Vi} - Q_{Li} = G_{ec} h_{LV}$

1.2. Droplet flow configuration $\alpha > \alpha_f$

This droplet configuration should only be reached when the void fraction α reaches a value α_{lim} close to 0.7. But, in order to have continuous exchange laws, we extrapolate the expected exchange in droplet flow configuration to the value obtained at the end of the film boiling flow pattern (when $\alpha = \alpha_f$). Thus, the exchange laws are the following.

In this configuration, the expression of the heat transfer between the corium and the liquid vapour interface is modified in such a way :

- the convective film boiling rapidly disappears when α moves from α_f to α_{ff} (α_{ff} : end of film boiling contribution ; if $\alpha_f \sim 0.3$ $\alpha_{ff} \sim 0.4$)

- the radiative heat transfert becomes $C_{rad}\, Q_{rad}\, p_1$ where p_1 is a ponderation factor taking into account the fact that this contribution must disappear when the liquid disappears i.e. vhen α --> 1. In the present version, p_1 is chosen in such a way that radiative component decays linearly from its value for $\alpha = \alpha_f$ to zero for $\alpha = 1$.

In this configuration there is also a convective heat transfer from the corium to the vapour which can be written an :

$$Q_{d\text{-}v} = h_c A_d (T_d - T_v) p_2$$

At elevated pressure, part of the radiant heat leaving the fuel can also be absorbed by steam. This is ignored in the present version of TRIO MC.

h_c comes from a classical convective heat transfert correlation and p_2 being another ponderation factor varying linearly from 0 for $\alpha = \alpha_f$ to 1 for $\alpha = 1$.

The radiant heat transfert from the corium to the liquid is also modified to take into account the progressive disappearance of the water :

$$Q_{d\text{-}L} = (1 - C_{rad}) \varnothing_{rad}\, p_3$$

p_3 varying linearly from 1 when $\alpha = \alpha_f$ to 0 when $\alpha = 1$ ($\alpha_L = 0$).

At the liquid-vapour interface, we have the following terms :

$Q_{Vi} = 10^7 (T_{SAT} - T_v)$ is kept up to $\alpha = \alpha_{lim}$ (~ 0.7) and for $\alpha > \alpha_{lim}$ we retain the Lee and Ryley [9] correlation

$$Nu = 2 + 0,738\, Re_L^{1/2}\, Pr_{V,sat}^{1/3}$$

$$with\ Re_L = \frac{\rho_V |V_V - V_L| d_L}{\mu_V}$$

d_L coming from a Weber stability criteria, so

$$Q_{Vi} = h A_L (T_{SAT} - T_V) \qquad where \quad A_L = \frac{6\alpha_L}{d_L}$$

For the liquid side heat transfer, we chose a transient conduction estimation in the liquid droplets so :

$$Q_{Li} = \frac{k_L}{\delta_L} A_L (T_{SAT} - T_L)$$

when δ_L is thermal boundary layer thickness = a d_L ($0.01 \leq a \leq 0.1$)

2. Momentum exchange laws :

They come from the ISHII, MISHIMA work [10]

2.1. Corium-water exchange (K_{dL}) :

This term only exists when $\alpha < \alpha_{ff}$ and we distinguish between two patterns for the fuel :

- dispersed fuel when $\alpha_d < 0.3$

$$K_{dL} = 0.166\, A_d C_D \rho_L |V_d - V_L|$$

$$where \quad C_D = \left(\frac{g(\rho_d - \rho_L)}{\sigma} \right)^{1/2} \frac{d_d}{3} \left[\frac{1 + (17.6B)^{6/7}}{18.6B} \right]^2$$

$$B = f(\alpha_{dispersed}) = (1 - \alpha_d)^{2.25}$$

- dense fuel configuration $\alpha_d > 0.4$

$$K_{dL} = \frac{150 \alpha_L^2 \alpha_d^2 \mu_L}{(1 - \alpha_d)^3 d_d^2} + \frac{1.75 \alpha_L \alpha_d \rho_L |V_L - V_d|}{(1 - \alpha_d)^3 d_d}$$

- when $0.3 < \alpha_d < 0.4$ linear interpolation

2.2. Corium-vapour exchange [K_{dV}] :

It is only taken into account when $\alpha > \alpha_{ff}$

- dispersed fuel ($\alpha_d < 0.3$)

$$K_{dV} = 0.166\, A_d C_D \rho_V |V_d - V_V|$$

$$with \quad C_D = \left(\frac{g(\rho_d - \rho_V)}{\sigma} \right)^{1/2} \frac{d_d}{3} \left[\frac{1 + (17.6B)^{6/7}}{18.6B} \right]^2$$

$$and \quad B = (1 - \alpha_d)^3$$

- dense fuel configuration : same formula as K_{dL} if subscript L is replaced by subscript V.

2.3 Liquid-steam exchange (K_{LV})

Again we distinguish between film boiling and droplet configurations.

- film boiling configuration ($\alpha < \alpha_{ff}$)

$$K_{LV} = 0.166\, A_B C_D \rho_L |\vec{V}_L - \vec{V}_V|$$

$$with \quad C_D = \left(\frac{g(\rho_L - \rho_V)}{\sigma_L}\right)^{1/2} \frac{d_B}{3}\left[\frac{1+(17.6B)^{5/7}}{18.6B}\right]^2$$

$$and \quad B = \left(\frac{\alpha_L}{\alpha_L + \alpha_V}\right)^{1/2}$$

- droplet flow configuration ($\alpha > \alpha_{lim}$)

$$K_{LV} = 0.166\, A_L C_D \rho_V |\vec{V}_L - \vec{V}_V|$$

C_d coming from above but with d_L but with

$$B = \alpha^3 = \left(\frac{\alpha_v}{\alpha_v + \alpha_L}\right)^3$$

- $\alpha_f < \alpha < \alpha_{ff}$

the film boiling drag drops to zero when $\alpha \longrightarrow \alpha_{lim}$

the drop flow drag drops to zero when $\alpha \longrightarrow \alpha_{ff}$

3. Corium droplet fragmentation

It is described with the law deduced by YOUNG for IFCI [4] from the work of PILCH [11]. So we use :

$$\frac{dD_d}{dt} = -0.245\,|V_r|\varepsilon^{1/2}$$

$$with \quad |V_r| = \left|\vec{V}_d - \frac{\alpha_V \vec{V}_V + \alpha_L \vec{V}_L}{\alpha_V + \alpha_L}\right|$$

$$\varepsilon = \frac{\alpha_V \rho_V + \alpha_L \rho_L}{(\alpha_V + \alpha_L)\rho_d}$$

but we put $\frac{dD_d}{dt} = 0$ when D_d becomes smaller than the value given by a Weber criteria or if T_d becomes smaller than the solidification temperature.

We then have the source term S_g for the interfacial area transport equation

ie : $$S_g = 6\alpha_d \frac{d(1/D_d)}{dt} = 6\alpha_d \frac{0.245\,|V_r|\varepsilon^{1/2}}{D_d^2}$$

When corium accumulates at the bottom of the vessel, we no longer use these equations as soon as α_d becomes greater than $\alpha_{d(bed)} = 0.7$.

B. Settling phase

Up to now, we use the same laws as in the falling phase but we know that we have to use for momentum and heat exchange special laws coming from debris bed analysis.

When α_d reaches 0.7 in a cell, we do not allow corium to enter or to leave the cell anymore (by increasing the friction coefficient).

IV. NUMERICAL ASPECTS

The set of continuity, momentum and energy equations is solved by a semi-implicit ICE-type method on either 3D cartesian or axisymetric domain.

The energy and mass source terms are totally implicit except for heat transfer coefficients depending on Reynolds number.

The interfacial area transport equation is solved explicitly.

Basic time step cannot be greater than 1 ms and sometimes must decrease to 0,1 ms to ensure convergence with strong evaporation rates.

V. DESCRIPTION OF THE FARO SCOPING TEST : INITIAL CONDITIONS OF THE CALCULATION

This test is presented in another paper of this meeting [12]. In our calculation the FARO vessel is described as a cylinder of the same volume (609 liters) with a radius of 0.235 m and a height of 3.51 m. The meshing is the following (see fig.3)

- radially 10 meshes
- axially : 11 meshes in the water (10 with 8 cm plus a 7 cm one)

18 meshes in the vapour space

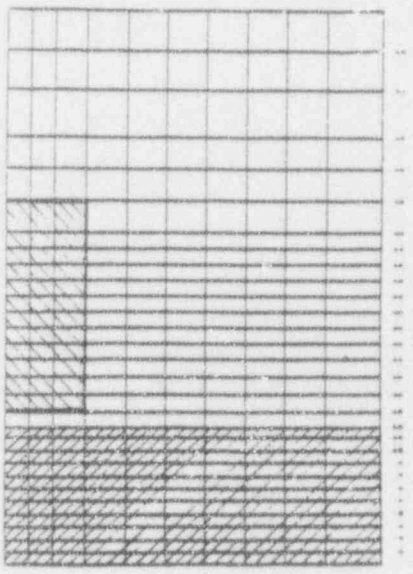

Figure 3. FARO Scoping Test Meshing

The calculation is initialized when the corium is entering the water pool so we have to provide informations for the volumetric flow rate of corium $(\alpha_{d(z)}, V_{d(z)}, D_{d(z)})$ at this time. From the experiment we have the following informations :

- initial velocity of the jet = 1.4 m/s
- initial diameter of the jet ≤ 0.1 m
- fall height : 2 m
- duration of the fall : $\Delta t = 0.280$ s

We have then to estimate the jet behaviour during its fall in the vapour space and we will obtain informations from isothermal jet fragmentation behaviour. The velocity at entrance after a 2 m fall is 6 m/s so we have to deal with a 10 cm jet accelerated from 1.4 m/s to 6 m/s through steam at 5MPa ($\rho_V = 25$ kg/m^3). Jet behaviour in isothermal conditions is often defined as a function of Weber and Ohnesorge numbers or Reynolds and Ohnesorge numbers

$$We_{jet} = \frac{\rho_V V_{rel}^2 D_{jet}}{\sigma}$$

$$\mathrm{Re}_{jet} = \frac{\rho_{jet} V_{rel} D_{jet}}{\mu_{jet}}$$

$$On = \frac{\mu_{jet}}{\sqrt{\rho_{jet} D_{jet} \sigma}}$$

The relative velocity is increasing from 1.4 m/s to 6 m/s so

$$9.8 \le We_{jet} \le 180$$

$$1.5\,10^5 \le \mathrm{Re}_{jet} \le 6.4\,10^5$$

$$On = 4.10^{-4}$$

$$D_{jet} = 0.1m \;\forall z$$

$$\sigma_{jet} = 0.5$$

$$\mu_{jet} = 8.10^{-3}$$

$$\rho_{jet} = 8.5\ 10^3$$

From the literature [13, 14] we found that we are very close of the atomization regime as it can be seen on fig.4 from [13] or from the criteria for atomization extracted from [14] ie $We_{jet} \ge 13$. So we decided to transform the continuous jet into a dispersed droplet jet.

The evaluation of the droplet diameter then comes from an hydrodynamical stability criteria ie in a gradually applied relative velocity the critical Weber number is about 17 ($\sqrt{2}$ higher than the well known $We_{cr} = 12$ for suddenly applied relative velocity). This leads to $D_d \sim 1$ cm.
We are then able to distribute the corium along the z axis according to the total mass delivery law ie $M_{total} = \alpha S|_z \rho V_{(z)} \Delta t$

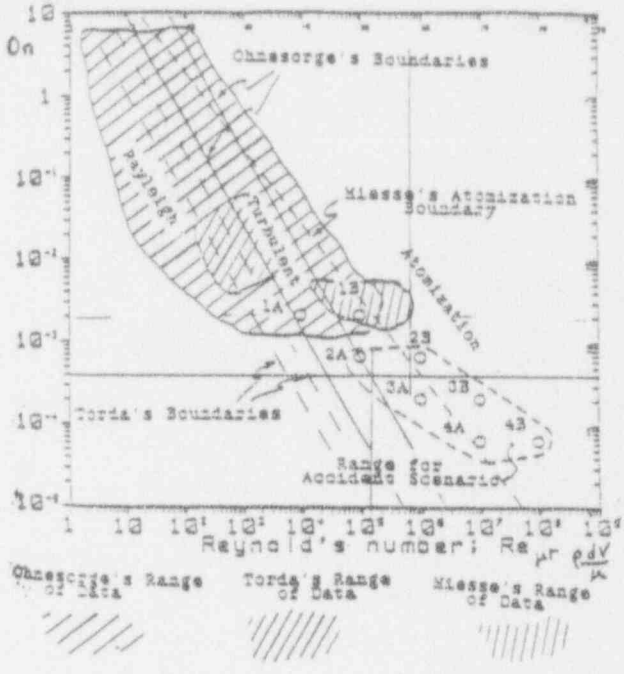

Figure 4. Liquid jet breakup regime map

Assuming a jet cross section at the water interface of 10 cm diameter, we then provide the corium jet volumetric concentration in the different cells.

The initial temperature of the water is described as in the experiment ie we take into account the measured subcooling at the bottom of the tank.

VI. CALCULATION RESULTS

Parameters have been set as following :

Crad = 0,1
αf = 0,2
αff = 0,3
αlim = 0,7

It must then be recalled that our initial time corresponds to the arrival of the melt at the water surface, time which is referred as MWC (Melt Water Contact) on the FARO results [12, see fig 4). In the experiment, during the melt fall in the vapour space, heat is transferred to he vapour by radiation (at this pressure absorption by steam is not negligible) and convection. This leads to an increase of the pressure which is of the order of 4 bars in the experiment. This heating of the vapour is not calculated in this study so, we will only calculate the steam pressure increase after the melt penetration in the water.

Comparison between the calculated steam pressure and the experimental results is shown on fig. 5. The underprediction in the early times would be at least partly corrected if the direct radiative heat transfer between the corium and the vapour during the late fall stage of the fall in the vapour sky (between MWC and end of melt penetration : AMIW on fig. 5) had been taken into account.

In the settling phase, our constitutive laws are overestimating the heat transfer (they are not changed) and this can explain the overestimated vapour pressure).

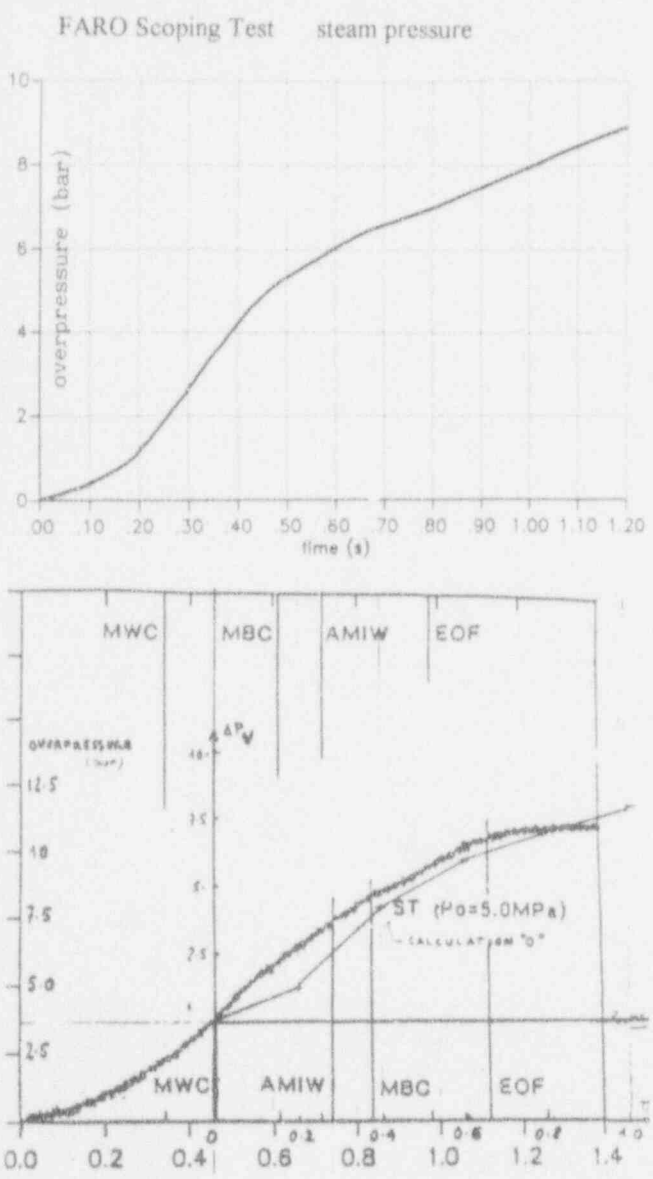

Figure 5. Calculated steam pressure and comparison with experiment result

Evolutions of the different volumetric concentrations of droplet, liquid and steam are given on fig. 6, 7 and 8. At 0.5 s most of the corium has reached the bottom of the vessel : 4.9 kg lies in the bottom cells under the 8 cm level, 7.25 kg are under the 16 cm level and 8.75 under the 24 cm level. A vapour chimney is formed around the corium jet axis and at around 0.6 s the liquid motion which was counter clock wise changes to a clock wise motion as observed in MAGICO calculations by Theofanous et al [15].

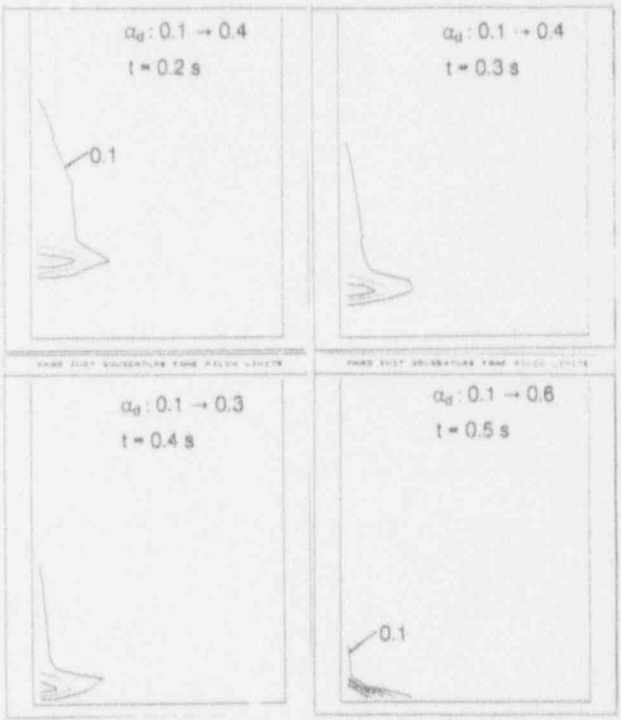

Figure 6 Evolution of the volumetric concentration of droplets

At the end of the calculation, most of the corium is under the form of droplets of 3 to 4 mm in diameter.

Evolutions of temperatures in the initial subcooled water in the lower part of the tank and in the vapour space are also shown in fig. 9.

At the end of our calculation the subcooled water has reached saturation condition while the steam has a little superheat (~ 6°C)

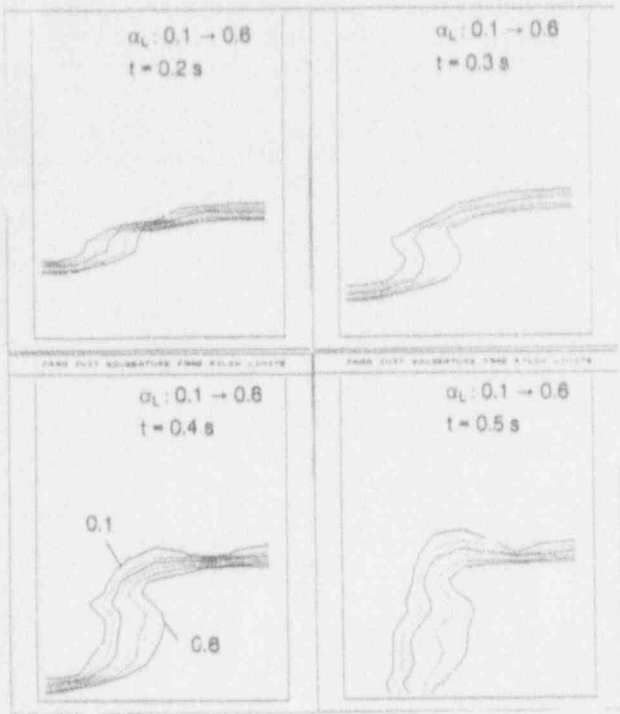

Figure 7 Evolution of the volumetric concentration of liquid

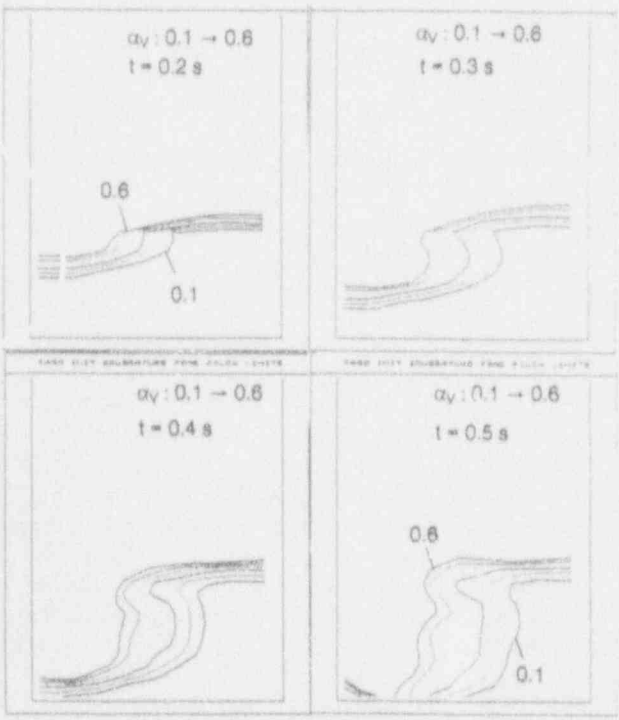

Figure 8 Evolution of the volumetric concentration of steam

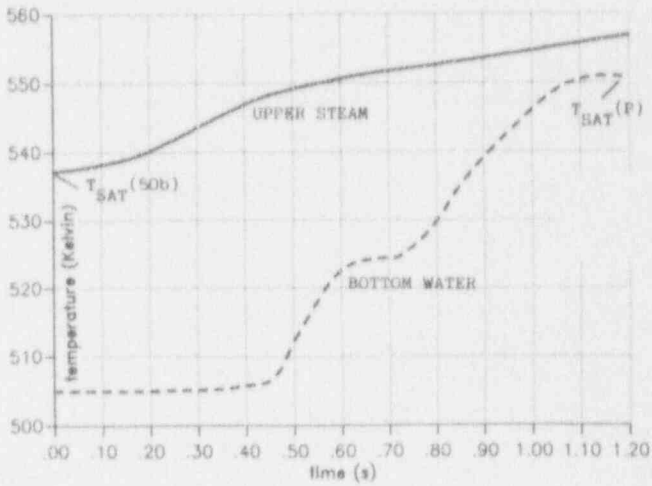

Figure 9 Scoping test
Initial drop diameter 9 mm water and steam temperatures

VII. CONCLUSIONS

This paper presents the first attempt to test the TRIO MC Premixing Code against experimental data. Our ongoing work will be to validate the friction and heat transfer laws against experimental results obtained with solid spheres in our BILLEAU facility and in other experiments of the same type performed in Europe. Global validation against FARO data will also be performed. We are also developping a jet fragmentation model whose results will be used as source terms for the droplet population in the four field version of TRIO MC.

NOMENCLATURE

α_i volumetric concentrationi

e_i specific internal energy

ρ_i density

k_i thermal conductibility

υ_i cinematic viscosity

ε_i emissivity

V_i velocity

G_{ec} net evaporation mass transfer kg/s.m^3

K_{LV} interfacial friction term for momentum exchange between liquid and vapour

K_{dV} interfacial friction term for momentum exchange between droplet and vapour

K_{dL} interfacial friction term for momentum exchange between droplet and liquid

g acceleration of gravity

Q_{dV} heat flux from corium to vapour (per unit volume)

Q_{dL} heat flux from corium to liquid (per unit volume)

Q_{di} heat flux from corium to liquid-vapour interface (per unit volume)

Q_{Vi} heat flux from interface to vapour (per unit volume)

Q_{Li} heat flux from interface to liquid (per unit volume)

P pressure

S_g interfacial area variation rate per unit volume (m^2/s x m^3)

α_f limiting value of the relative void fraction α for the film boiling flow configuration

A_B interfacial area between the vapour-bubbles and water (per unit volume) in the film boiling configuration

A_L interfacial area between water droplets and stream (per unit volume) in the droplet flow regime

v vapour

i = L water

d corium droplet

f vapour tum at $T_f = \frac{T_d + T_{SAT}}{2}$

REFERENCES

1. Chu, C.C., Corradini, M.L., 1989, NSE, **101**, pp 38-71
"One dimensional transient fluid model for FCI analysis"

2. Medhekar, S., Amarasooriya, W.H., Theofanous T G., 1989, Proc. 4th International Topical Meeting on Nuclear Reactor Thermal hydraulic, Karlsruhe, Oct.10-13, p 319
"Integrated Analysis of Steam Explosions"

3. Fletcher, D.F., Thyagaraja, A., 1988, ANS Proc.of the 25th Nat.Heat Transfer Conf. Houston, July 24-27, HTC 3
"A mathematical model of premixing"

4. Young, M.F., 1987, NUREG/CR - 5084
"IFCI : an integrated code for calculation of all phases of FCI"

5. Kolev, N.I., 1992, KfK 4948
"A three-field model for transient 3D multiphase three-component flow for the computer code IVA3"

6. Mitchell,D.E., Corradini, M.L., 1981, NUREG/CR-2145-, SAND 81-012F
"Intermediate le Steam Explosion Phenomena : Experiments nalysis"

7. Yamano, N., Sugimoto, J., Maruyama Y., Soda K., 1993, this conference
"Studies of FCI during Core Melt Accident of Nuclear Power Plants"

8. Epstein, M., Hauser, G.M., 1980, Int.J.Heat Mass Transfer, **23**, p 179-189
"Subcooled forced-convection film boiling in the forward stagnation region of a sphere or cylinder"

9. Lee, K., Ryley,D.J., 1968, J.of Heat transfer, Nov., p 445
"The evaporation of water droplets in superheated steam"

10. Ishii, M., Mishima, K., 1984, N.E.D., 82, p 102-126
"Two fluid model and hydrodynamic constitutive relations"

11. Pilch, M., 1981, Ph.D Thesis - U.of Virginia
"Acceleration induced fragmentation of liquid drops"

12. Magallon, D., Hohmann, H., 1993, this conference
"High pressure corium quenching in FARO : Results of the scoping test"

13. Winquist, S.C., 1986, Master of Science, University of Wisconsin
"Modelling the atomization of a liquid jet and application of the model to large diameter molten corium jets"

14. Ranz ,W.E., 1956, Dept. Eng. Penn. State University Bulletin, **65**
"On sprays and spraying"

15. Theofanous, T.G., Angelini, S., Yuen, W.W., 1993, this conference
"Premixing-related behaviour of steam explosions"

EX-VESSEL MELT-COOLANT INTERACTIONS IN DEEP WATER POOL: STUDIES AND ACCIDENT MANAGEMENT FOR SWEDISH BWRs

J. J. Sienicki, C. C. Chu and B. W. Spencer
Argonne National Laboratory
9700 S. Cass Avenue
Argonne, Illinois 60439
(708) 252-6564

W. Frid
Swedish Nuclear Power Inspectorate
Sehlstedtsgatan 11, Box 27106
S-102 52 Stockholm, Sweden
46-8-6654460

and

G. Löwenhielm
Vattenfall AB
S-162 87 Vällingby, Sweden
46-8-7395342

ABSTRACT

In Swedish BWRs having an annular suppression pool, the lower drywell beneath the reactor vessel is flooded with water to mitigate against the effects of melt release into the drywell during a severe accident. The THIRMAL code has been used to analyze the effectiveness of the water pool to protect lower drywell penetrations by fragmenting and quenching the melt as it relocates downward through the water. Experiments have also been performed to investigate the benefits of adding sufactants to the water to reduce the likelihood of fine-scale debris formation from steam explosions. This paper presents an overview of the accident management approach and surfactant investigations together with results from the THIRMAL analyses.

I. INTRODUCTION

By the end of 1988, the Swedish Reactor Accident Mitigation Program, initiated after the accident in TMI-2, reached its conclusion. Engineered measures and prepared emergency procedures, aimed at mitigating the consequences of accidents with severe core damage, have been fully implemented at all reactor sites (Högberg, 1988). The program was supported by the research projects FILTRA and RAMA (Reactor Accident Mitigation Analysis) conducted jointly by the Swedish nuclear safety authorities and the utilities. Final reports are now available from the RAMA project.

In order to protect the integrity of BWR containments, the following mitigation measures have been implemented and in operation since the end of 1988 (valid forall BWR plants except Barsebäck 1 and 2 which have had a gravel bed filter vent system since 1985):

i) Enhanced, high reliability containment spray system;

ii) Filtered venting to prevent late containment failure;

iii) Unfiltered venting to prevent early containment overpressurization for accident sequences involving a large LOCA combined with malfunction of the pressure suppression system but operability of the normal ECCS systems. The system consists of a large capacity pressure release line comprising a rupture disc and valves for reclosure after activation. As core melt is not envisaged for this accident sequence, an unfiltered release is considered acceptable.

iv) Flooding of the lower drywell compartment in BWRs of second generation (i.e., with an annular suppression pool) using the suppression pool water on indication of core damage.

To further explain the last accident management strategy, the second generation of BWRs in Sweden have an annular suppression pool which means that there is no water below the reactor pressure ves-

sel during normal operation. Special measures are therefore needed to prevent early meltthrough of the containment floor. In a core melt accident, following reactor vessel lower head failure, the molten core materials would relocate into the lower drywell. Electrical and mechanical penetrations in the lower part of the drywell would then be exposed to and most probably damaged by the hot core debris opening a release path from the containment. In order to prevent this from occurring and to provide a means to cool the core debris, a system for flooding the lower drywell has been installed. The system will allow water from the suppression pool to flow by gravity force into the drywell when the isolation valve in the connecting line is opened (Figure 1).

The success of the chosen strategy will depend, to a great extent, on the character and efficiency of the processes of melt fragmentation and quenching in a deep pool of subcooled water. The depth of the water pool in the flooded lower drywell will be between 4 and 12 meters, depending on the particular plant and accident scenario. Steam explosions could negatively affect the coolability of core debris on the containment floor by generation of very small debris particles. The possibility of major destructive steam explosions has been rated remote enough to justify taking advantage of the strategy.

The issues of ex-vessel melt fragmentation, quenching, and core debris coolability have received great attention in the Swedish research (Frid, 1991). Thus, experimental studies were conducted of coolability limits in stratified beds, methods for protecting the penetrations in the lower drywell of BWRs were developed and tested, a method to suppress or mitigate fine-scale fragmentation and steam explosions (to avoid very small debris particles) by adding small amounts of surfactants to the water has been investigated, and calculations of melt stream breakup and debris formation in a deep pool of subcooled water have been performed.

In this paper we describe and discuss the results of experimental studies into the effects of adding surfactants to the water and the results of calculations of melt stream breakup and debris formation using the THIRMAL melt/water interaction code developed at Argonne National Laboratory. However, the surfactant studies are described very briefly as most of the results have been presented and reported earlier (Becker and Lindland, 1981, 1991). It should be noted here that the potential influence of surfactants on the process of melt stream breakup has not been considered in the THIRMAL calculations. It is possible that such an effect exists but it is probably small (Frid, 1991a).

II. SUPPRESSING OF FINE-SCALE FRAGMENTATION AND STEAM EXPLOSIONS BY SURFACTANTS

Becker suggested that fine-scale fragmentation and steam explosions could be mitigated or prevented by adding small amounts of surface active agents (surfactants) to the suppression pool water just prior to vessel meltthrough (Becker and Ölander, 1988). The idea is based on the hypothesis that the surfactant molecules stabilize the water-vapor interface by forming a layer of molecules at the interface.

According to the theory of steam explosions, the destabilization of the vapor film surrounding the melt droplets during the coarse mixing stage is a necessary, but not sufficient, condition for triggering and propagation of an explosion through the melt-water mixture.

The stabilizing effect of surfactants on disturbances at a water-vapor interface is supported by some evidence from the metallurgical and chemical industry (Becker and Ölander, 1988).

In order to explore the potential of using surfactants in severe accident mitigation, the RAMA project has sponsored small-scale experiments at the Royal Institute of Technology (KTH) in Stockholm, and at Sandia National Laboratories (SNL) in the USA. Most recently, the post-RAMA projects HAFOS and APRI (Accident Phenomena of Risk Importance) have sponsored small-scale experiments at the University of Wisconsin in the USA. (HAFOS is a Swedish acronym denoting cooperation on severe accident research between Swedish regulatory authorities and utilities.)

The objective of the experiments at KTH, carried out by Becker and Ölander (1988) was to select the surfactants and to find the optimal surfactant concentration in water for the single droplet experiments at SNL. This objective was achieved by measuring the rise velocity of nitrogen bubbles in water. The measurements were carried out at water temperatures of 20 degrees Centigrade and 50 degrees Centigrade. The surfactant concentrations were varied in the range between 0 and 200 ppm corresponding to the water surface tension in the range of 0.072 and 0.030 N/m. Becker and Ölander found that the behavior of the nitrogen bubbles in water is significantly affected by surfactant concentrations in water of about 1 ppm regardless of the kind of surfactants used (or their mixture).

At this concentration, the oscillations of the bubble surface during the rise were completely eliminated and the bubble rise velocity was significantly decreased. The observed effect of the surfactants was explained by the well-known properties of surface active substances, namely their ability to form a layer of molecules at the

water-vapor interface. According to Becker and Lindland, the stabilization of the gas-water interface is a result of the Marangoni effect.

The effects of small concentrations of surfactants in water on spontaneous and triggered single droplet explosions were investigated at SNL in a joint project with KTH. The study is briefly described by Becker and Lindland (1989, 1991). The spontaneous explosions were studied in a tin-water system using, in most cases, 12 g of tin at 650 degrees Centigrade and ethoxilated - nonyle - fenole (available as Emulgator U-9) solutions. The water temperature was 20, 35, 40 and 50 degrees Centigrade and the surfactant concentration was in the range of 0 to 40 ppm. The triggered explosions were carried out in the thermite-water system for 4.5 g of thermite at 2700 degrees Centigrade and with water at 20 degrees Centigrade. Three experiments were performed for pure water and three experiments with 5 ppm of Emulgator U-9 in water.

Becker and Lindland concluded that the tin-water experiments seemed to support the hypothesis that small concentrations of a surfactant in water mitigate against a steam explosion. However, it should be noted that at the water temperature of 40 degrees Centigrade, an enhancement of the explosion was observed at 5 ppm. With regard to the triggered thermite-water experiments, Becker and Lindland concluded that the surfactant had a strong mitigating influence on the steam explosions.

The mitigating and/or suppressive effects of adding small amounts of surfactants to the water coolant has been investigated in the single droplet explosion tests at the University of Wisconsin-Madison in a joint project with KTH. Molten 0.1 g iron-oxide droplets at about 2000 degrees Centigrade have been used. The water temperature was in the 20 to 50 degrees Centigrade range. The preliminary results from these tests are unclear with indication of the possibility of some suppressive effects.

Obviously, the currently existing database and theoretical foundations on the effects of surfactants in water on steam explosions and melt fragmentation phenomena are insufficient to allow a definite decision to be made as to the application of the proposed method during an accident.

III. ENERGY BALANCE QUENCHING ANALYSIS

It is necessary to establish that the water pool inventory provided beneath the reactor vessel is sufficient to quench the released corium mass. This can be demonstrated by means of a simple energy balance quenching analysis. The analysis was carried out for a water mass associated with the 8.4 meter diameter lower drywell of the Forsmark 3 BWR. For this particular plant, the water pool depth can vary from 4.1 meters corresponding to the maximum sustainable pressure difference between the drywell and wetwell to 6.9 meters corresponding to no drywell-wetwell pressure differential. The water pool depth was varied over a range of 4 to 12 meters. Greater depths up to 12 meters are also examined to further encompass the depths that may be attained in other Swedish plant designs (e.g., Forsmark 1 and 2). The water pool mass is assumed limited to that in the cylindrical lower drywell cavity beneath the vessel. Interaction of corium with the additional water inside the tunnel passageway that leads from the cylindrical cavity to the airlocks is presently ignored. The containment pressure (0.15 MPa), initial water temperature (321 K), and released melt composition are based upon MAAP 3.0B code calculations for a station blackout (SBO) accident sequence; these conditions are included in Table 1. A mass of 106000 Kg is assumed released representative of roughly half the full core inventory of fuel and structure. A released melt superheat of 50 K is assumed based upon the assessment of Theofanous et. al. (1991) that ascribes the greatest likelihood to the attainment of superheats between 25 and 50 K for sudden melt release from a large (3300 MWt) BWR.

Because the water is initially subcooled by a significant amount (64 K), it is assumed that all steam formed through the quenching process is initially condensed inside the pool such that the water temperature rises until the saturation temperature (385 K) is attained. The mass of melt which has entered the water and has been quenched at the onset of saturation is given by

$$M_{melt,sub} = M_{water} \frac{\Delta e_{water,sub}}{\Delta e_{melt}}. \qquad (1)$$

After the water becomes saturated, then quenching of the additional melt will result in vaporization of water giving rise to the formation of steam. Assuming that the steam formed is condensed by the containment pressure suppression systems such that the pressure remains constant, the mass of steam produced by quenching the remainder of the melt is given by

$$M_{steam} = (M_{melt} - M_{melt,sub}) \frac{\Delta e_{melt}}{\Delta e_{water,vap}}. \qquad (2)$$

Assuming that this steam mass is effectively lost from the water pool over the quench timescale, the pool water volume will decrease. The corresponding reduction in pool depth, however, will be diminished by thermal expansion of the remaining water in going from the initial temperature to saturation. The pool height will also tend to rise due to volume displacement by the corium and level swell. However, aside from these latter effects, the final effective water depth is given by

Table 1. CONDITIONS ASSUMED IN ANALYSES

Water Pool Depth, m	6.87
Water Pool Diameter, m	8.4
Water Pool Floor Area, m^2	55.4
Water Pool Volume, m^3	381
Initial Water Temperature, K	321
Containment Pressure, MPa	0.15
Water Saturation Temperature, K	385
Initial Water Subcooling, K	64
Water Pool Mass, Kg	377000
Water Specific Enthalpy Change Between Initial and Saturation Temperature, MJ/Kg	0.270
Water Heat of Vaporization, MJ/Kg	2.227
Water Density, Kg/m^3	
385 K	950
321 K	989
Released Melt Mass, Kg	106000
Released Melt Volume, m^3	14.4
Initial Melt Temperature, K	2723
Initial Melt Superheat, K	50
Melt Composition, wt %	
UO_2	55.2
ZrO_2	5.2
Zr	23.3
Stainless Steel	15.5
B_4C	0.8
Melt Specific Enthalpy Change Between Initial Temperature and Water Saturation Temperature, MJ/Kg	1.34
Chemical Oxidation Reactions	$Zr + 2H_2O \rightarrow ZrO_2 + 2H_2$ $2Cr + 3H_2O \rightarrow Cr_2O_3 + 3H_2$ $0.947Fe + H_2O \rightarrow Fe_{0.947}O + H_2$
Specific Chemical Energy Release from Zirconium Oxidation, MJ/Kg	1.57
Specific Chemical Energy Release from Stainless Steel Oxidation, MJ/Kg	0.205
Combined Specific Chemical Energy Release from Oxidation, MJ/Kg	1.77
Combined Melt Specific Enthalpy Change and Chemical Energy Release, MJ/Kg	3.11
Fall Height from Lower Head to Water Pool, m	6.6
Fall Height from Lower Head to Lower Drywell Floor, m	13.5
Lower Head Wall Thickness, m	0.186
Initial Failure Hole Diameter, cm	6.5
Lower Head Inner Radius, m	3.21
Initial Melt Depth Inside Lower Plenum, m	1.50
Reactor Vessel Pressure, MPa	1.0 to 0.5[a]

a) Pressure decreases linearly from 1.0 to 0.5 MPa during first 20 seconds following vessel failure and remains at 0.5 MPa until end of release.

$$h = \left[1 - \frac{M_{steam}}{M_{water}}\right] \frac{\rho_{water}(T_{initial})}{\rho_{water}(T_{sat})} h_{initial} \quad (3)$$

In writing Equation 3, use is made of the fact that expansion of the radially confined water is realized almost entirely in the vertical direction.

Figure 2 shows the corium mass that must be quenched down to the saturation temperature in order to saturate the initially subcooled water. Because of the high proportion of metallic zirconium and stainless steel in the corium, the additional energy release from chemical oxidation reactions is included with the extent of reaction treated as a parameter. It is observed that in the absence of steam formation, complete quenching of the released mass of 106000 Kg will raise the water temperature to saturation except when the pool depth exceeds 9 meters in the limit of negligible oxidation. The net steam mass formed is shown in Figure 3 where it is seen that more than sufficient water is present to completely quench the released melt over the relevant range of water depth. The effects of combined depletion of the water inventory from complete quenching and water thermal expansion upon the pool depth are shown in Figure 4.

The energy balance quenching analysis thus shows that more than sufficient water is available to fully quench the assumed released melt mass of 106000 Kg.

IV. THIRMAL-1 ANALYSIS OF MELT STREAM-WATER INTERACTIONS

A. Modeling Approach

Given that sufficient water is provided in the lower drywell to quench the released mass of molten fuel and structure, the question becomes whether natural physical processes will result in fragmentation and freezing to an extent sufficient to produce a coolable debris state. Analysis of this problem requires the modeling and calculation of a large number of interrelated process. It is therefore not surprising that different researchers in this area have developed diverse calculational capabilities. Sensitivities to basic model assumptions have never been determined in a comprehensive way such that it is difficult to attach uncertainty bounds to the results obtained using any of the current models and codes. The present analysis was carried out using the THIRMAL-1 code that calculates the nonexplosive fragmentation and quenching of a melt stream inside a water pool as well as the associated water heatup, net steam formation, oxidation, and hydrogen generation.

THIRMAL-1 treats the case of a circular melt stream entering the water pool with a time varying diameter, velocity, temperature, and composition. Except for the initial transient penetration of the melt stream into the pool, the dominant fragmentation mechanism is the erosion of molten droplets from the surface of the melt stream due to the formation of Kelvin-Helmholtz instabilities along the stream surface (Figure 5). Immediately behind the stream leading edge, the instabilities are driven by the upward flow of vapor inside a vapor film immediately surrounding the stream along part of its length. As the eroded fragments enter the surrounding water, heat transfer from the fragments gives rise to the local formation of steam which rises through the pool. This results in the formation of an interaction zone surrounding the stream containing melt droplets, melt particles, water, and steam. The radial extent of the interaction zone reflects the lateral migration of the droplets and particles and their temperatures that directly determine the vapor source.

Near the leading edge, the steam rises through water within the interaction zone in a bubbly flow regime. At increasing heights above the leading edge, the accumulation of steam increases the superficial vapor velocity through the interaction zone causing a transition to a churn turbulent flow regime. Dispersed flow typically develops in the overlying part of the interaction zone. Here, melt droplets and particles together with water droplets are dispersed in the upward flowing steam. Heat transfer from the melt droplets and particles in the dispersed flow region typically produces superheated steam that exits the interaction zone at the elevation of the top of the pool.

Interactions of the upward flowing steam with the melt stream also result in the erosion of droplets from the stream surface through the Kelvin-Helmholtz instability mechanism (Wang, Blomquist and Spencer, 1989, 1989a). Heat transfer to the water droplets and the water at the outer boundary of the interaction zone can occur at such a high rate in the upper part of the dispersed flow region that steam condensation effects are locally suppressed. Depending upon the droplet/particle diameter and the vapor flow conditions, melt droplets and particles in the dispersed region may be swept up out of the pool or may settle downward through a continuous vapor flow before encountering the continuous liquid churn turbulent and bubbly flow regions near the stream leading edge. In the present application, those droplets and particles that are swept out are assumed to rebound elastically off of the steel shield plate located above the pool and to reenter the interaction zone with downward directed momentum.

In addition to Kelvin-Helmholtz instabilities, fragmentation of the melt stream leading edge due to boundary layer stripping is modeled as the stream initially penetrates downward rapidly

through the water pool. However, this initial penetration phase involves only a negligible portion of the released mass in the present analysis. Subsequently, the effects of erosion cause the local stream diameter at the leading edge to decrease to sizes so small that breakup occurs from capillary effects. In the present application, this happens when the diameter locally decreases to about five millimeters. Intermittent capillary breakup at the leading edge is calculated according to a Weber number-based criterion.

The droplet diameter resulting from the Kelvin-Helmholtz mechanism is assumed to be equal to the inverse wavenumber of the fastest growing wavelength locally contributing to the Kelvin-Helmholtz instability. Because the conditions under which erosion occurs vary in space along the melt stream column as well as in time, a distribution of sizes is calculated reflecting the spatial and temporal variations in the conditions under which erosion occurs. The droplet diameter is determined at the instant of erosion from the melt stream. In particular, once a droplet is created, no further breakup of the droplet into smaller sized fragments is modeled. Likewise, no growth in the droplet size as the result of coalescence is modeled.

THIRMAL-1 accounts for the presence of distinct oxide and metal phases in the melt entering the water. In particular, individual droplets eroded from the melt stream are modeled as consisting wholly of either oxide or metal. This approach permits oxide and metal droplets to freeze at different temperatures representing the actual freezing range of each of the individual phases. Modeling distinct freezing transitions is important because the coincident release of oxide and metal at the same temperature will result in the metal having a much higher molten superheat above its liquidus temperature than the oxide. Thermophysical properties assumed for the oxide and metal phases as well as relevant properties for the heterogeneous oxide-metal melt mixture are shown in Table 7. In the present analysis, erosion of the melt stream and droplet formation are calculated using the heterogeneous mixture properties. In particular, the erosion rate and droplet diameter reflect the mixture surface tension. As a consequence, oxide and metal droplets formed at the same location along the column and at the same time are assumed to have the same diameter.

THIRMAL-1 models oxidation of the metallic droplets and particles as they relocate through the interaction zone and water pool. Oxidation of metal when it is still part of the melt stream is not calculated. Oxidation rate limitations from both steam diffusion through a vapor/hydrogen film or the dispersed flow continuum and parabolic ion diffusion through the droplet/particle itself are modeled. Reaction of zirconium and the stainless steel constituents is assumed to occur sequentially. The oxidation energy released is deposited in the droplet/particle as a heat source.

An approximate assumption made in THIRMAL-1 is that the water pool depth remains constant in time. Thus, the effects of water depletion resulting from net steam formation that would lower the water level are ignored. On the other hand, heatup of subcooled water is accompanied by thermal expansion of the water which is also not modeled. The resulting volume expansion of the radially confined water will be mainly realized as an increase in the water level tending to somewhat offset the effects of net steaming. A second approximation in THIRMAL-1 is to ignore the water pool heatup and net steam formation associated with heat transfer off of the debris that collects and spreads on the lower drywell floor. Thus, THIRMAL-1 presently predicts effects associated solely with melt fall stage relocation through the water pool.

B. Model Application

THIRMAL-1 was applied to the case of melt stream-water pool interactions during a station blackout sequence in the Forsmark 3 plant. Lower head failure is assumed to involve a single instrument/neutron flux measurement tube or tube penetration resulting in melt release through an initial 6.5 cm diameter pathway through the lower head wall. The water depth at the beginning of melt release is taken to be 6.9 meters. A melt mass of 106000 Kg is assumed released.

The RPV-to-drywell pressure difference was obtained from MAAP 3.0B. In particular, the pressure difference decreases from 0.85 to 0.35 MPa over the first 20 seconds following head failure and thereafter remains at 0.35 MPa until the release phase is finished. Other conditions are sumamrized in Table 1. The time dependent diameter and velocity of the stream exiting the lower head were calculated using a detailed melt release/hole erosion model that accounts for spatial variations in the thermal erosion-induced enlargement of the hole through the thickness of the lower head wall. These spatial variations arise from the local variations in the forced convection heat flux from the flowing melt. Gravitational acceleration and contraction of the stream as it falls to the water pool upper surface are significant and accounted for in calculating the melt entry conditions. This model is described in greater detail in Appendix A.

Thermophysical properties assumed in the analysis are contained in Tables 2 and 3.

The melt is assumed to relocate from the lower head to the water surface as a coherent circular stream. Interactions of the stream with shielding or CRD-related structures beneath the

RPV are currently neglected. Together with the assumption that the release involves only a single instrument tube, this is expected to represent a conservative assumption. In particular, these assumptions restrict all the melt to enter the water as a single stream and tend to increase ooth the entry diameter and velocity. This is expected to enhance the calculated melt stream penetration distance below the water surface and the potential for debris to collect on the floor in a molten state in the calculations.

Figures 6 through 9 show the calculated time dependent conditions of melt release from the lower head and melt entry into the water pool. The release phase is calculated to last 106 seconds during which the hole/stream diameter at the head increases from 6.5 to 17 cm. The release velocity decreases from 16 to 10 m/s. The corresponding melt stream entry velocity decreases from 20 to 16 m/s during the first 20 s and continues to decrease to 15 m/s thereafter. The stream entry diameter rises from 5.9 to 14 cm over the release phase duration.

Figure 10 shows the calculated time dependent penetration of the melt stream leading edge. The location of the leading edge is calculated to vary in an oscillatory manner. This is a result of the modeling assumption that allows the portion of the melt stream immediately behind the leading edge to break up according to a Weber number based criterion when the diameter becomes small. In the present application this happens when the stream diameter decreases to about 5 millimeters. Leading edge breakup suddenly decreases the length of the stream by a finite amount. However, because the stream now undergoes erosion over a somewhat shorter length and lesser surface area, the stream leading edge penetrates further downward into the pool. When the diameter of the new leading edge decreases sufficiently to break up, then the cycle is calculated to begin again.

After 25 seconds, the melt stream is calculated to intermittently impinge upon the lower drywell floor. Thus, a portion of the melt is calculated to arrive at the floor in a molten state. However, this is only a minor amount of the released corium mass as observed from Figure 11. By 115 seconds, nearly all of the corium is calculated to have settled out upon the floor. At this time, 94000 of the 106000 Kg released has collected as a particle bed. This corre- sponds to 89 percent of the collected corium mass (Figure 12).

The energy removed from the particles during quenching is mainly realized in the heatup of the water pool. Figure 13 shows the mean water pool temperature which is calculated to rise by 44 degrees Kelvin due solely to fall stage quenching of the melt. However, the water remains subcooled due to the high initial 64 degree Kelvin subcooling. A difference between the assumptions of the energy balance quenching analysis and the present results is that THIRMAL-1 calculates that superheated steam exits the pool while it is still in a global state of water subcooling.

The calculation also indicates that a large fraction of sub-millimeter sized particles could be formed and that a large amount of hydrogen (e.g., 1000 Kg) could be produced. However, these particular indications must currently be viewed as preliminary and require further investigation.

In summary, the THIRMAL-1 calculation for a SBO sequence predicts that 89 percent of the melt settles out as fully solidified particles together with 9 percent that impinges as a molten stream and 2 percent that collects as molten or partially frozen droplets.

V. SCOPING SENSITIVITY ANALYSIS

Prior to the conduct of the time dependent THIRMAL-1 calculations, THIRMAL-0 was used to scope the melt release and melt-water interaction behavior, and to investigate the sensitivities to the accident sequence, initial melt superheat, and total released melt mass. THIRMAL-0 (Wang, Blomquist and Spencer, 1989; 1989a; Sienicki, Wang and Spencer, 1992) was an earlier version of THIRMAL; differences between THIRMAL-1 and THIRMAL-0 are summarized in Appendix B. Because THIRMAL-0 did not treat the case of time varying melt entry conditions, the code was used to calculate the melt-water interaction behavior at snapshots in time during the release process. In particular, those times when 50 and just less than 100 percent of the cumulative melt mass have entered the water were selected. Assuming constant entry diameters calculated at these particular times, THIRMAL-0 was run until a quasi-steady solution was obtained. Because a full time dependent calculation was not performed, the effects of progressive heatup of the water were neglected such that the pool subcooling was assumed to remain unvarying over the release duration. In the previous section, the water temperature is calculated to rise by no less than 44 K when a mass of 106000 Kg enters the pool as a coherent melt stream.

To determine melt entry conditions, the scoping analysis did not incorporate the detailed multinode hole erosion model discussed in Appendix A. Instead, a simple single node erosion calculation was employed. The heat transfer coefficient was defined to be the maximum of that of Dittus and Boelter for fully developed pipe flow,

$$h_{conv} = 0.023\ Re_{hole}^{0.8}\ Pr^{0.4}\ \frac{k}{D_{hole}}, \qquad (4)$$

and a rough approximation of an entrance coefficient given by

$$h_{conv} = 2\,(Re_L\ Pr)^{1/2}\ \frac{k}{L_{head}}. \qquad (5)$$

The resulting hole and stream diameters calculated for the scoping analysis exceed those predicted with the more detailed model incorporated in THIRMAL-1 (Appendix A). In this regard, the larger melt entry diameters used in the scoping analysis are regarded as a conservative assumption. Another assumption concerns the melt entry velocity. This was not taken to be the calculated entry velocity at the 50 and 100 percent release times. Rather, the velocity exiting the head for the 50 percent cumulative release calculation was defined as that corresponding to the mean release rate over the first half of the release divided by the hole area at the 50 percent release time. Similarly, the velocity exiting the lower head for the 100 percent cumulative release calculation was taken to be that corresponding to the mean release rate over the second half of the release divided by the final hole area. The melt entry velocity is not strongly sensitive to this assumption due to the significant incremental velocity rise associated with the 6.6 m fall height from the lower head to the water pool surface.

Melt thermophysical properties assumed in the scoping analysis are presented in Table 4.

The definition of cases and results are shown in Tables 5 and 6, respectively. It is observed that for the LOCA cases (in which melt gravity drains from the lower plenum) the behavior involves melt steam fragmentation and freezing prior to collection upon the lower drywell floor. The melt stream diameter and breakup length calculated for the LOCA sequences are observed to be sensitive to the initial melt superheat.

For the SBO with an assumed initial molten superheat of 5 K, complete breakup and freezing are also calculated. However, when the initial superheat is increased to 50 K and the full core inventory is assumed released (i.e., 212000 Kg), some of the corium entering with the final stream diameter is calculated to arrive upon the floor in an unsolidified state. Forty-three percent of the corium entering the water at the very end of the release phase is calculated to collect as molten or partially frozen droplets together with two percent impinging as a molten stream that does not break up completely prior to reaching the floor. The remaining 55 percent settles out as fully solidified particles. In contrast, melt entering with the smaller diameter characteristic of the 50 percent cumulative release time is predicted to fully fragment and freeze. This suggests that the release of lower total masses somewhat below 212000 Kg would result in the calculation of particle bed formation throughout the release duration. This was demonstrated by Case 5 in which the released mass was reduced to half the core inventory.

The released melt mass, initial superheat, and composition for Case 5 are identical to those of the THIRMAL-1 calculation described in the previous section. This case thus serves to delineate differences in the predictions of the two code versions. One major difference already noted is that the THIRMAL-0 melt release/hole erosion model predicted larger melt stream diameters (e.g., 0.25 m at the end of the release) than the more detailed model incorporated into THIRMAL-1 (0.14 m at the end of release). Even though the stream diameters entering the water are significantly smaller, longer melt stream penetrations and a greater extent of melt collection in a molten state are calculated with THIRMAL-1. This indicates that the breakup/penetration lengths and extents of molten corium collection were underestimated in the scoping sensitivity analysis.

The scoping sensitivity calculations thus serve to reveal a sensitivity to the released melt superheat mainly through its effect on the stream diameter as well as a sensitivity to the accident sequence. In particular, the SBO sequence represents a more severe case than the LOCA with regard to melt fragmentation because of the higher melt stream velocities resulting from the RPV-to-drywell pressure difference and the lower drywell absolute pressure.

VI. CONCLUSIONS

A final conclusion with regard to the feasibility of using surfactants to mitigate ex-vessel steam explosions and fine-scale fragmentation cannot be reached on the basis of knowledge available thus far. A critical review of this subject will be made as soon as the experiments at the University of Wisconsin are evaluated. Decision as to the continuation of the research in this area will be made following this evaluation. One possibility which has been discussed is to investigate the effectiveness of surfactants in experiments involving larger melt masses.

The results of the THIRMAL calculations, which were chosen to include what are believed to be a number of conservatisms, raise some concern with regard to the effectiveness of the water pool in the lower drywell in Forsmark 3 to completely disintegrate and quench the molten stream prior to arrival on the containment floor. One important question in this context - besides of course the question of how good are the THIRMAL predictions - is how conservative are the calculations presented in this paper. This is a difficult problem since the initial and boundary conditions in the THIRMAL calculations are functions of the in-vessel accident progression

where the uncertainties are large. However, the assumption that one hundred metric tonnes of melt is available for release during a short period of time is likely to be conservative. Also, neglecting structures below the reactor pressure vessel is conservative, at least during the initial phase of melt release. With regard to the other important parameters, namely melt superheat and release rate, it is more difficult to make a judgement; it is possible that the values used in present calculations are not conservative.

The existing uncertainties and the importance of effective melt quenching for accident mitigation motivate continued research in this area. A need exists for experimental validation of the THIRMAL-1 code as well as other codes for melt-water interactions.

ACKNOWLEDGEMENTS

This work was sponsored by the APRI Project. The APRI participants are: Swedish Nuclear Power Inspectorate; Vattenfall AB; OKG Aktiebolag; and Sydkraft. The authors would like to acknowledge the contributions of the late Professor Kurt Becker of the Royal Institute of Technology in Stockholm in the area of surfactant investigations as well as for his continuing interest in the present work and his comments throughout its duration. The manuscript was prepared by L. J. Ondracek.

NOMENCLATURE

C = specific heat, J/(Kg·K)

C'_{fx} = skin friction coefficient

D = diameter, m

g = gravitational acceleration, m/s^2

H_{fall} = fall distance from bottom of lower head to water pool upper surface, m

h = depth, m

h_{conv} = forced convection heat transfer coefficient, $W/(m^2 \cdot K)$

k = thermal conductivity, W/(m·K)

L_{head} = lower head wall thickness, m

M_{melt} = released melt mass, Kg

$M_{melt,sub}$ = mass of melt quenched that removes water subcooling, Kg

M_{steam} = net steam mass formed, Kg

M_{water} = total water mass, Kg

Nu = Nusselt number

$$= \frac{h_{conv} D}{k}$$

Nu_x = Nusselt number based on x,

$$= \frac{h_{conv} x}{k}$$

Pr = Prandtl number

$$= \frac{C\mu}{k}$$

Re = Reynolds number

$$= \frac{\rho U D}{\mu}$$

$$Re_{hole} = \frac{\rho U_{hole} D_{hole}}{\mu}$$

$$Re_L = \frac{\rho U_{hole} L_{head}}{\mu}$$

Re_x = Reynolds number based on x

$$= \frac{\rho U x}{\mu}$$

$T_{initial}$ = initial water temperature, K

T_{sat} = water saturation temperature, K

t = time, s

U = velocity, m/s

U_{hole} = velocity of melt exiting at bottom of lower head wall, m/s

V = melt volume inside lower plenum, m^3

x = distance coordinate into channel, m

$$x^* = \frac{2\left[\frac{x}{D}\right]}{Re\ Pr}$$

Δe_{melt} = difference in melt specific enthalpy between initial melt temperature and water temperature, J

Δe_s = change in specific enthalpy of lower head steel in going from initial temperature to liquidus, J

$\Delta e_{water,sub}$ = difference in water liquid phase specific enthalpy between saturation and initial temperatures, J

$\Delta e_{water,vap}$ = water heat of vaporization, J

ΔT_{sup} = molten superheat of melt above oxide phase liquidus temperature, K

μ = viscosity, Kg/(m·s)

ρ = density, Kg/m^3

ent = subscript denoting melt entry conditions at water surface

hole = subscript denoting conditons at hole through lower head wall

REFERENCES

1. Andreussi, P. and B. J. Azzopardi (1983), "Droplet Deposition and Interchange in Annular Two-Phase Flow," *Int. J. Multiphase Flow*, Vol. 9, p. 681.

2. Becker, K. M. and H. Ölander (1988), "An Experimental Investigation of the Effects of Tensides on the Rise Velocity of Nitrogen Bubbles in Water," KTH-NEL-45 (May 1988).

3. Becker, K. M. and K. P. Lindland (1989, 1991), "The Effects of Tensides on Hydrodynamic Fragmentation and Steam Explosion," KTH-NEL-50 (December 1989, Revised Edition April 1991).

4. Frid, W. (1991), "Containment Severe Accident Thermohydraulic Phenomena, RAMA III Final Report," RAMA III 89-04, Studsvik Library, S-61182 Nyköping, Sweden (August 1991).

5. Frid, W. (1991a), Unpublished Information, Swedish Nuclear Power Inspectorate (1991).

6. Gnielinski, V. (1989), "Forced Convection in Ducts," *Heat Exchanger Design Handbook, Volume 2, Fluid Mechanics and Heat Transfer*, ed. E. U. Schlünder et. al., Hemisphere Publishing Corporation, New York.

7. Högberg, L. (1988), "The Swedish Programme on Severe Accident Management and Release Mitigation," *Severe Accidents in Nuclear Power Plants*, Sorrento, March 21-25, 1988, Vol. 1, p. 73, International Atomic Energy Agency, Vienna.

8. Schlichting, H. (1979), *Boundary Layer Theory*, Seventh Edition, McGraw-Hill Book Company, New York (1979).

9. Sienicki, J. J., S. K. Wang and B. W. Spencer (1992), "Analysis of Melt Arrival Conditions on the Lower Head in U. S. LWR Configurations," *Proceedings of the Fifth International Topical Meeting on Reactor Thermal Hydraulics*, Salt Lake City, September 21-24, 1992, Vol. II, p. 450, American Nuclear Society, Inc., La Grange Park.

10. Wang, S. K., C. A. Blomquist and B. W. Spencer (1989), "Modeling of Thermal and Hydrodynamic Aspects of Molten Jet/Water Interactions," *ANS Proceedings 26th National Heat Transfer Conference*, Philadelphia, PA, August 6-10, 1989, Vol. 4, p. 225, American Nuclear Society, La Grange Park.

11. Wang, S. K., C. A. Blomquist and B. W. Spencer (1989a), "Interfacial Instability Leading to Bubble Departure and Surface Erosion During Molten Jet/Water Interaction," *ANS Proceedings 26th National Heat Transfer Conference*, Philadelphia, PA, August 6-10, 1989, Vol. 4, p. 31, American Nuclear Society, La Grange Park.

12. Theofanous, T. G., W. H. Amarasooriya, H. Yan and U. Ratnam (1991), "The Probability of Liner Failure in a Mark-I Containment," NUREG/CR-5423, United States Nuclear Regulatory Commission (August 1991).

APPENDIX A

MODELING OF MELT RELEASE FROM THE LOWER PLENUM, LOWER HEAD WALL HOLE ENLARGEMENT, AND MELT ENTRY CONDITIONS

Lower head failure is assumed to occur in a localized fashion as the result of formation of a single flowpath for melt flow through the lower head wall thickness. In the current analysis, the formation of a hole through the head wall is assumed to involve failure of a single instrument/neutron flux measurement tube or tube penetration. It is further assumed that a melt pool has collected to its full depth upon the lower head at the time of failure.

The velocity of melt flowing from the lower head is assumed to be given by

$$U_{hole} = \left[\frac{2(\rho g h + \Delta P)}{\rho}\right]^{1/2} \qquad (A1)$$

and the melt volume inside the lower plenum decreases with time as

$$\frac{dV}{dt} = - U_{hole} \frac{\pi}{4} D_{hole}^2. \qquad (A2)$$

The melt volume is related to the melt depth through a functional relationship specific to the lower plenum configuration and dimensions.

At the assumed molten superheats, melt flowing through the opening in the lower head wall will heat the surrounding lower head steel up to the melting temperature within a fraction of a second. Subsequently, the surrounding steel will be eroded away and the hole diameter enlarged

with time due to forced convection heat transfer from the superheated melt flowing past the steel surface. The increase in the local hole diameter with time is calculated from the equation,

$$\frac{dD}{dt} = \frac{2h_{conv}\,\Delta T_{sup}}{\rho_s \Delta e_s}. \qquad (A3)$$

The erosion rate represented by Equation A3 assumes that solid crusts of frozen oxidic material are present between the flowing melt and the steel wall substrate. For a corium flow containing molten oxide and having a superheat equal to the value assumed in the current study, a crust will form upon the carbon steel inner surface of the hole penetrating the lower head thickness. Following the inception of steel melting, the melted steel is subsequently expected to flow downward as a molten film between the corium and underlying solid steel. In this manner, the melted steel is removed and the hole enlarged in diameter. While steel melting is taking place, a crust will still be present again providing a temperature boundary condition for heat transfer. In this situation, the crust is expected to exist as islands that form and move on the melted steel wall film.

As melt drains from the lower plenum, fresh melt is continually transported over the eroding interface. The oxide material that freezes out to form the crusts is expected to have a composition that corresponds to freezing at the oxide phase liquidus temperature. The appropriate temperature difference for forced convection heat transfer is therefore the difference between the bulk melt temperature and the oxide phase liquidus temperature. This is identically equal to the molten superheat of the melt.

In addition to the temperature difference for heat transfer, an important component of Equation A3 is the selection of an appropriate forced convection heat transfer coefficient. Melt is expected to approach the hole through the lower head wall in a laminar flow regime. However, as the melt accelerates and flows through the hole, the velocities become high enough for local turbulence to develop in the vicinity of the eroding interface. The heat transfer coefficient is therefore largely based upon flow over a flat plate. This approach is employed in the analysis of entrance region heat transfer at high Reynolds numbers. In the present instance, it is noted that the diameter of the hole may exceed the thickness of the lower head wall.

The forced convection heat transfer coefficient for flow over a flat plate is a function of the distance along the plate. The present evaluation predicts an initial laminar flow region followed by a transition to turbulent heat transport. In the laminar section, the flat plate heat transfer coefficient is given by the Nusselt number relationship (Schlichting, 1979),

$$Nu_x = 0.332\, Re_x^{1/2}\, Pr^{1/3}. \qquad (A4)$$

It is convenient to rewrite Equation A4 in terms of Nusselt and Reynolds numbers based on the hole diameter,

$$Nu = \frac{0.332}{Pr^{1/6}} \left[\frac{2}{x^+}\right]^{1/2}. \qquad (A5)$$

When melt release begins, the instrument tube diameter is less than the lower head wall thickness. Recognizing that the flow may have aspects of tube entrance flow, the correlation (Gnielinski, 1989),

$$Nu = \begin{cases} 1.077 \left[\dfrac{2}{x^+}\right]^{1/3}, & \text{if } x^+ < 0.02 \\ 3.66, & \text{if } x^+ \geq 0.02, \end{cases} \qquad (A6)$$

appropriate for thermally developing laminar flow in a tube with a constant wall temperature is also considered. The release model selects the maximum laminar heat transfer coefficient between Equations A5 and A6. For the conditions of the current study, Equation A5 typically provides a greater heat transfer coefficient.

The flow in a layer immediately adjacent to the wall becomes turbulent and turbulent heat transfer begins at a distance, x_{crit}, where the Reynolds number

$$Re_{x,crit} = \frac{\rho U x_{crit}}{\mu} = 500000. \qquad (A7)$$

In the turbulent regime, the Nusselt number correlation of von Kármán (Schlichting, 1979) is used whereby

$$Nu_x = \frac{\frac{1}{2} Re_x C_{fx}'}{1 + 5\left[\frac{1}{2} C_{fx}'\right]^{1/2} \left\{Pr - 1 + \ln\left[1 + \frac{5}{6}(Pr - 1)\right]\right\}} \qquad (A8)$$

where

$$C_{fx}' = \frac{0.0576}{Re_x^{1/5}}. \qquad (A9)$$

The heat transfer coefficient depends upon the distance, x, downward into the hole. It follows that the local erosion rate of the head wall and the local diameter are functions of the distance into the hole. For this reason, the release model solves Equation A3 at a user specified number of locations through the head wall

thickness. In the present analysis, the time dependent diameter was calculated at twenty points through the head thickness.

The "hole diameter" in Equation A2 and the diameter of the released melt stream correspond to the minimum diameter calculated through the head thickness at any given time. The stream diameter thus tends to reflect more the erosion rate corresponding to the minimum heat transfer coefficient over the head thickness. The location of the minimum will be either: (i) the place where the transition from laminar to turbulent flow occurs with the minimum heat transfer coefficient given by the appropriate laminar expression; (ii) the bottom of the lower head with the heat transfer coefficient given by the turbulent expression; or (iii) the bottom of the lower head with the coefficient given by the appropriate laminar expression in the absence of the development of turbulence. After draining through the hole in the lower head wall, the melt stream will accelerate and contract under the influence of gravity. The melt stream velocity entering the water pool is thus given by

$$U_{ent} = \left(U_{hole}^2 + 2g\, H_{fall}\right)^{1/2} \qquad (A10)$$

and the stream water entry diameter is obtained from the mass conservation relationship,

$$D_{ent} = D_{hole} \left(\frac{U_{hole}}{U_{ent}}\right)^{1/2} \qquad (A11)$$

APPENDIX B
DIFFERENCES BETWEEN THIRMAL-1 AND THIRMAL-0 MODELS

Both the THIRMAL-1 and THIRMAL-0 codes have been used in carrying out the various analyses. THIRMAL-0 was the original version and has been described previously (Wang, Blomquist and Spencer, 1989; 1989a; Sienicki, Wang and Spencer, 1992). THIRMAL-1 represents a significantly improved version incorporating a number of recent modifications. The most important improvements that distinguish THIRMAL-1 from THIRMAL-0 are:

i) An extension to handle time dependent conditions of melt stream entry into the water, specifically time varying jet diameter, velocity, temperature, and composition. For example, the erosion of the hole through the lower head gives rise to a diameter that increases significantly with time. Concurrently, the velocity of the stream exiting the hole decreases with time as the melt depth inside the lower plenum decreases, especially during a LOCA sequence. The previous version required the definition of fixed (i.e., unvarying with time) melt entry conditions.

ii) An extension to treat the presence of distinct oxide and metal phases. This extension encompasses situations in which the melt is released in a stratified state (e.g., all the metal is released first followed by all of the oxide) or the melt stream consists of a heterogeneous oxide-metal mixture (ie., the oxide and metal are released together). The extent of mixing of oxide and metal is assumed to remain at such a level that individual droplets resulting from melt stream fragmentation are modeled as either all oxide or all metal in the new version. This is important because the metal freezes at a much lower temperature than the oxide. In the previous version, the melt was modeled as a homogeneous material having a single freezing temperature.

iii) An improved and more physical treatment of the hydrodynamic and heat transfer phenomena taking place in the mixing region containing melt droplets/particles, water, and steam. The one-dimensional vapor mass and energy equations were reformulated to enable an improved prediction of vapor void fractions and temperatures on the Eulerian pool grid. Local flow regimes within the zone are determined from a flow regime map that includes bubbly, churn turbulent, and dispersed regimes. Transitions between the different regimes are predicted using recognized criteria involving the appropriate Kutateladze group containing the superficial vapor velocity. The previous version modeled only bubbly and dispersed flow assuming a transition between the two at a fixed void fraction of 0.75. The new version solves a quasi-steady vapor momentum equation to obtain vapor velocities in dispersed regions whereas the old version assumed a constant dispersed flow steam velocity. The new version also incorporates improved modeling for heat transfer controlled vaporization/condensation of bubbles in the bubbly and churn turbulent regimes as well as for flowing vapor in dispersed flow regions. The modeling of the steam generation rate associated with heat transfer from melt droplets and particles in the mixing zone has been made more realistic and dependent upon the local flow regime and conditions.

iv) The Lagrangian treatment of droplet/particle relocation has been improved to account for drag effects associated with local conditions (e.g., void fraction) in the mixing zone and to provide a better representation of the lateral velocity with which fragments come off of the melt stream column. In particular, a correlation based upon the velocities with which droplets are

entrained from liquid films in annular flow (Andreussi and Azzopardi, 1983) is employed. The envelope of droplet/particle migration determines the boundaries of the mixing zone. The earlier version used a simplified treatment that ignored variations in local conditions and assumed high lateral velocities for eroded droplets.

v) Determination of the maximum Kelvin-Helmholtz wave growth rate and the corresponding wave number using a wave number spectrum analysis. The maximum growth rate and associated wave number are used to define the stream column erosion rate and fragment size. Previously, a most probable wave number was obtained from a simple approximate expression that ignored the effects of the vapor film thickness. The new approach could be further extended to predict a distribution of eroded fragment sizes representing a range of wave numbers.

vi) A much improved numerical solution methodology that better accounts for both time and spatial dependencies of the melt stream fragmentation rate, vapor film thickness, and film vapor velocity within the film. The melt stream is now also modeled in terms of Lagrangian cells that move through a fixed Eulerian grid in the pool. The previous version resolved the stream on the fixed Eulerian grid such that step changes in stream penetration and length were computed rather than a continuous penetration versus time.

vii) An extension to treat the time dependent pressurization of a closed volume system and the heatup of the water pool. The system pressurization and pool heatup models in the previous version were incomplete.

viii) The calculation of erosion-induced enlargement of the hole through the lower head wall and melt release from the lower plenum has been improved (Appendix A).

Table 2. CORIUM THERMOPHYSICAL PROPERTIES ASSUMED IN THIRMAL-1 ANALYSIS

Property	Oxide Phase	Metal Phase	Mixture
Liquidus Temperature, K	2673	2173	-----
Solidus Temperature, K	2613	2093	-----
Specific Enthalpy, MJ/Kg			
Liquidus	1.28	1.18	-----
Solidus	0.892	0.917	-----
298 K	0	0	-----
Liquid Specific Heat, KJ/(Kg·K)	0.513	0.563	0.534
Solid Specific Heat, KJ/(Kg·K)	0.385	0.511	0.479
Liquid Density, Kg/m^3	8370	6110	7320
Liquid Thermal Conductivity, W/(m·K)	3.4	31	9.6
Viscosity, Pa·s	4.2×10^{-3}	2.1×10^{-3}	3.7×10^{-3}
Surface Tension, N/m	0.52	1.60	1.02
Emittance	0.83	0.39	0.62

Table 3. LOWER HEAD WALL CARBON STEEL THERMOPHYSICAL PROPERTIES ASSUMED IN ANALYSIS

Property	Value
Freezing/Melting Temperature, K	1811
Specific Enthalpy, MJ/Kg	
Liquidus	1.29
Solidus	1.05
298 K	0
Solid Specific Heat, KJ/(Kg·K)	0.761
Solid Density, Kg/m^3	7320

Table 4. CORIUM THERMOPHYSICAL PROPERTIES USED IN SCOPING SENSITIVITY ANALYSIS

Property	Property Value
Freezing/Melting Temperature, K	2500
Specific Enthalpy, MJ/Kg	
Liquidus	1.30
Solidus	1.01
298 K	0
Liquid Phase Specific Heat, KJ/(Kg·K)	0.554
Solid Phase Specific Heat, KJ/(Kg·K)	0.459
Liquid Density, Kg/m^3	7250
Liquid Thermal Conductivity, W/(m·K)	17
Viscosity, Pa·s	3.62×10^{-3}
Surface Tension, N/m	0.72

Table 5. CONDITIONS OF SCOPING SENSITIVITY ANALYSIS[a]

Case No.	Accident Sequence	Released Melt Mass, Kg	Initial Melt Superh +. K	RPV Pressure, MPa	Containment Pressure, MPa	Initial Water Temperature, K	Initial Water Subcooling, K
1	LOCA	212000	5	0.43	0.43	321	98
2	LOCA	212000	50	0.43	0.43	321	98
3	SBO	212000	5	1.0 to 0.5[b]	0.15	321	62
4	SBO	212000	50	1.0 to 0.5[b]	0.15	321	62
5	SBO	106000	50	1.0 to 0.5[b]	0.15	321	62

a) Water depth = 6.87 m.

b) Pressure decreases linearly from 1.0 to 0.5 MPa during first 20 seconds following vessel failure and remains at 0.5 MPa until end of release.

Table 6. RESULTS OF SCOPING SENSITIVITY ANALYSIS

Case No.	Total Release Phase Duration, s	Cumulative Mass Entry into Water, %	Melt Stream Diameter Exiting Lower Head, m	Melt Stream Diameter at Water Surface, m	Melt Stream Velocity at Water Surface, m	Melt Stream Breakup Length, m	Corium Arrival State Particles/Droplets/Stream, %
1	485	50 100	0.14 0.17	0.075 0.090	11.9 11.9	3.3 3.6	100/0/0 100/0/0
2	138	50 100	0.28 0.34	0.13 0.18	11.7 11.9	4.1 5.3	100/0/0 100/0/0
3	174	50 100	0.16 0.19	0.11 0.15	13.1 14.5	4.2 5.4	100/0/0 100/0/0
4	44	50 100	0.32 0.39	0.22 0.31	12.9 14.4	5.2 >6.9	100/0/0 55/43/2
5	38	50 100	0.26 0.31	0.18 0.25	13.1 14.4	4.9 6.2	100/0/0 100/0/0

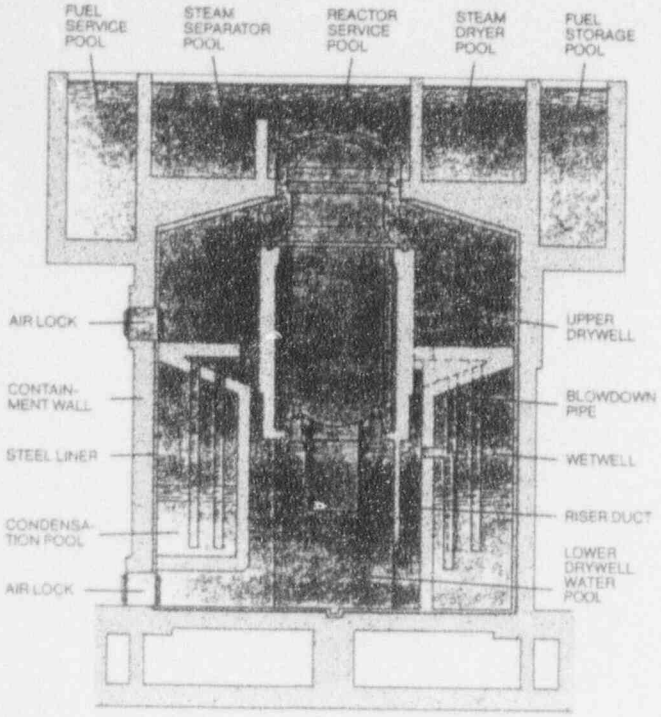

Figure 1. Schematic Illustration of Forsmark 3 BWR Containment.

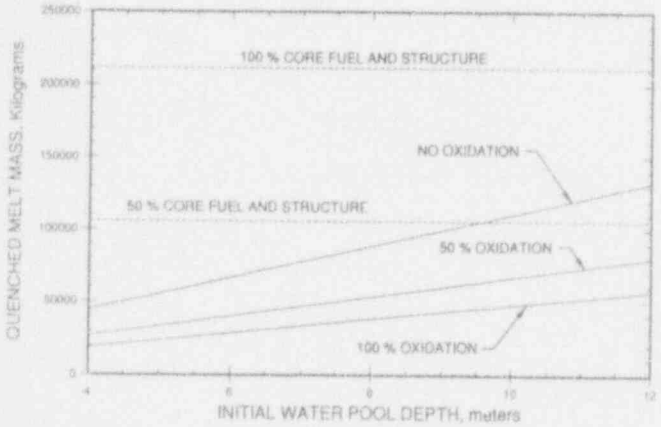

Figure 2. Corium Mass that Must be Completely Quenched to Saturate Lower Drywell Water Pool Initially Subcooled by 64 K.

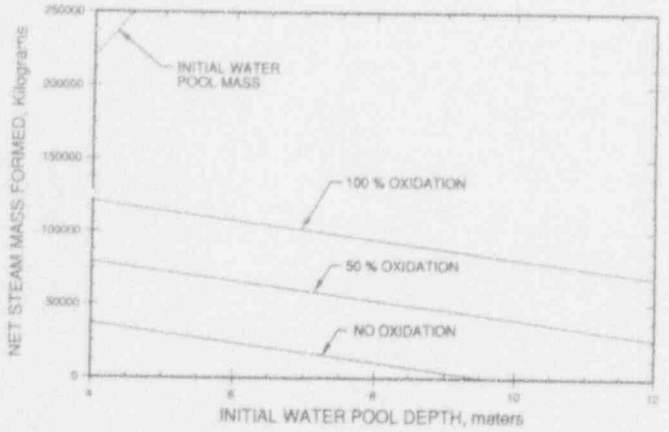

Figure 3. Net Steam Mass Formed from Complete Quenching of 106000 Kg of Corium in 64 K Initially Subcooled Lower Drywell Water Pool.

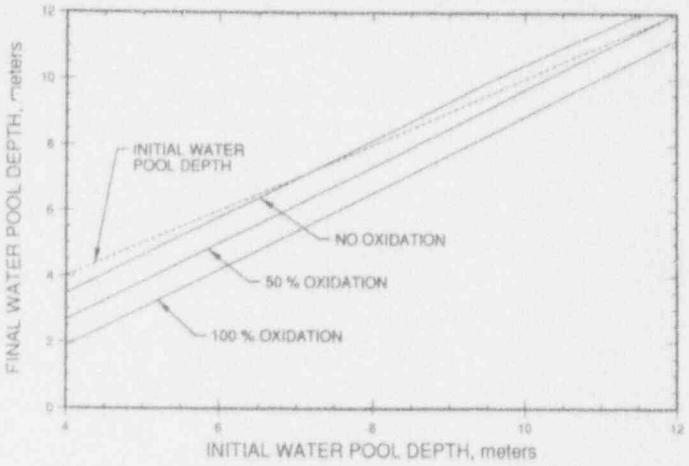

Figure 4. Water Pool Depth Following Complete Quenching of 106000 Kg of Corium in 64 K Initially Subcooled Lower Drywell Water Pool.

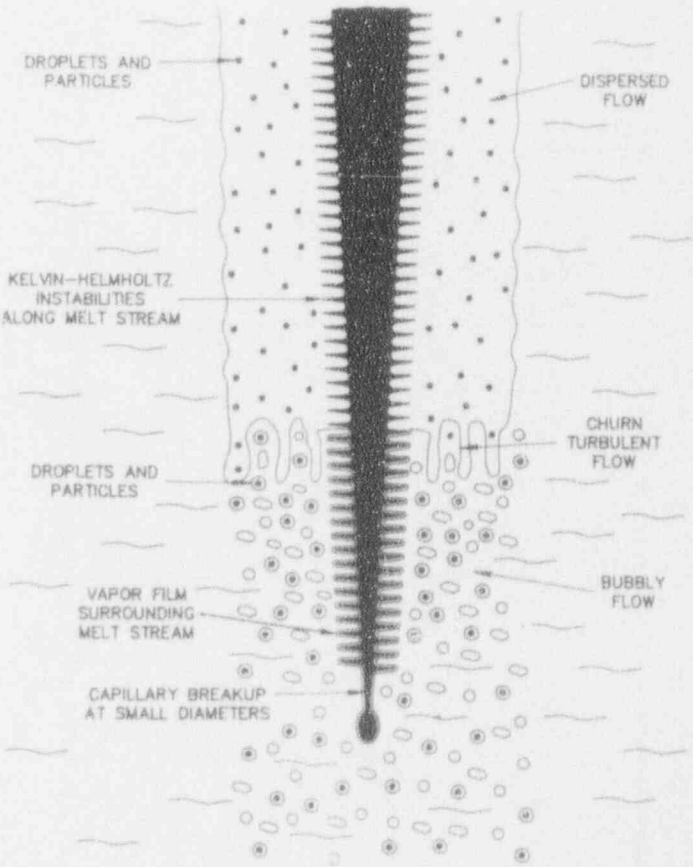

Figure 5. Schematic Illustration of Melt Stream Breakup from Kelvin-Helmholtz Instabilities Modeled in THIRMAL-1.

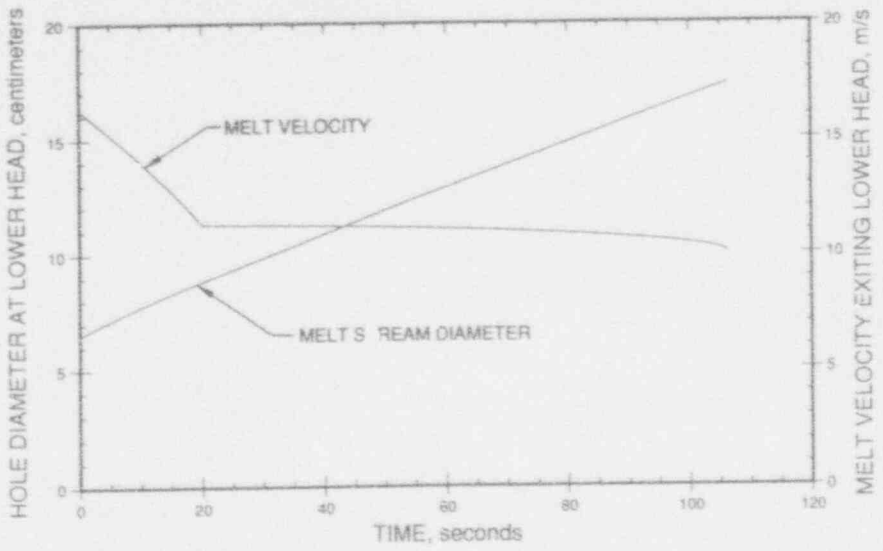

Figure 6. Melt Stream Diameter and Velocity Exiting Lower Head.

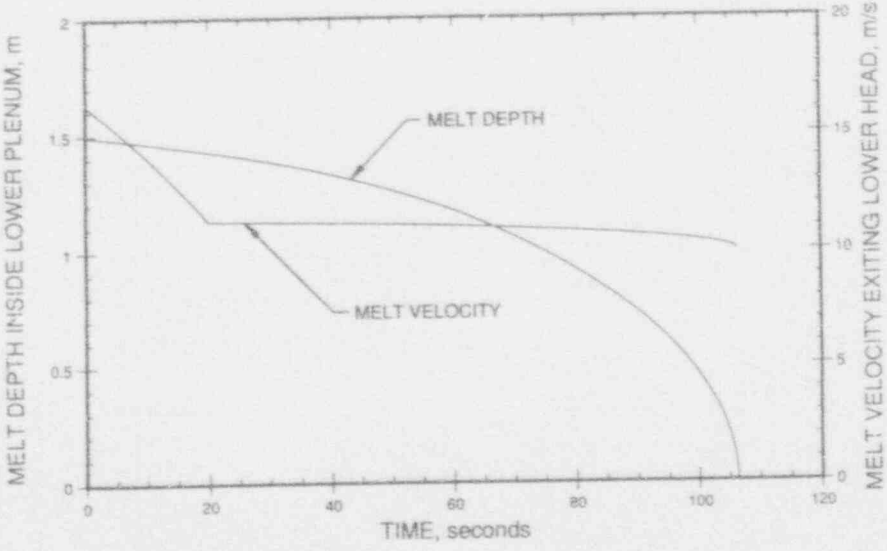

Figure 7. Melt Velocity Exiting L··er Head and Melt Depth Rema;ning Inside Lower num.

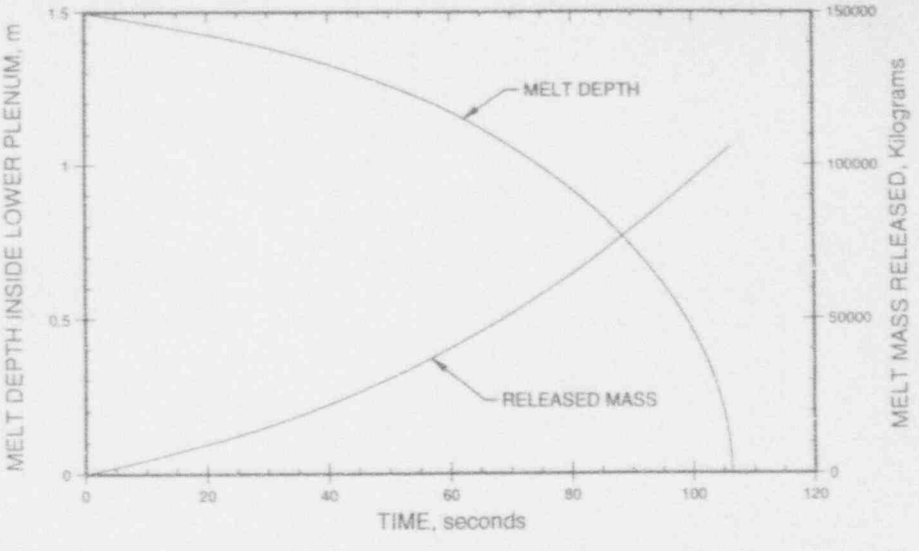

Figure 8. Cumulative Released Melt Mass and Melt Depth Remaining Inside Lower Plenum.

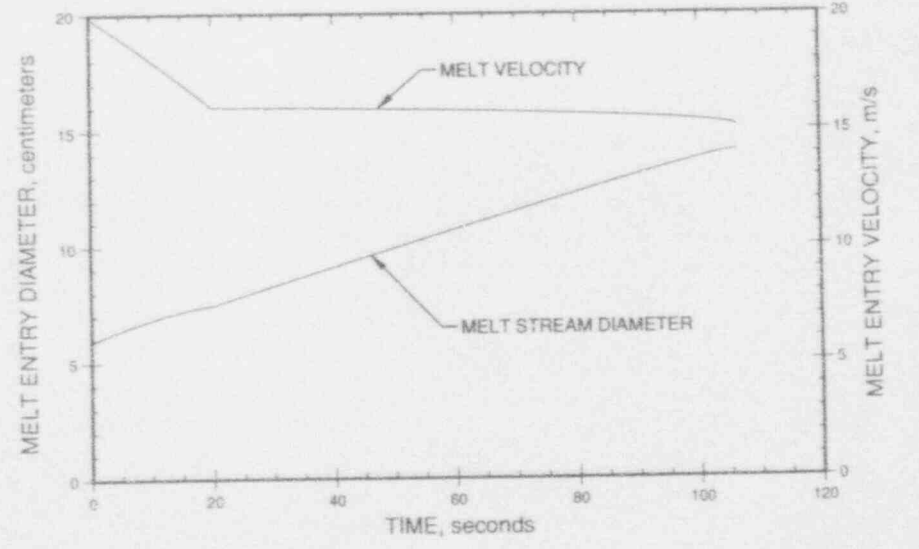

Figure 9. Melt Stream Diameter and Velocity Entering Surface of Water Pool.

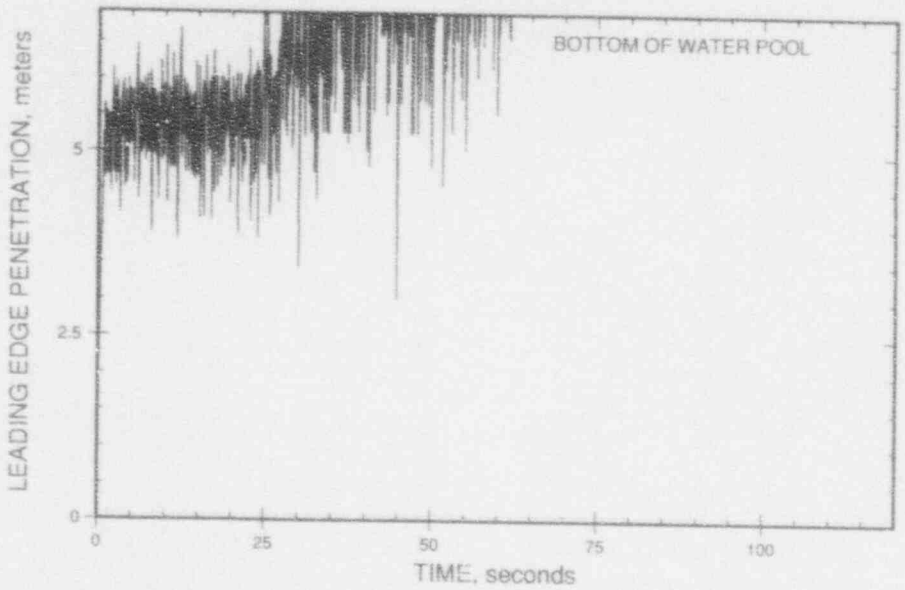

Figure 10. Penetration of Leading Edge of Coherent Melt Stream Column.

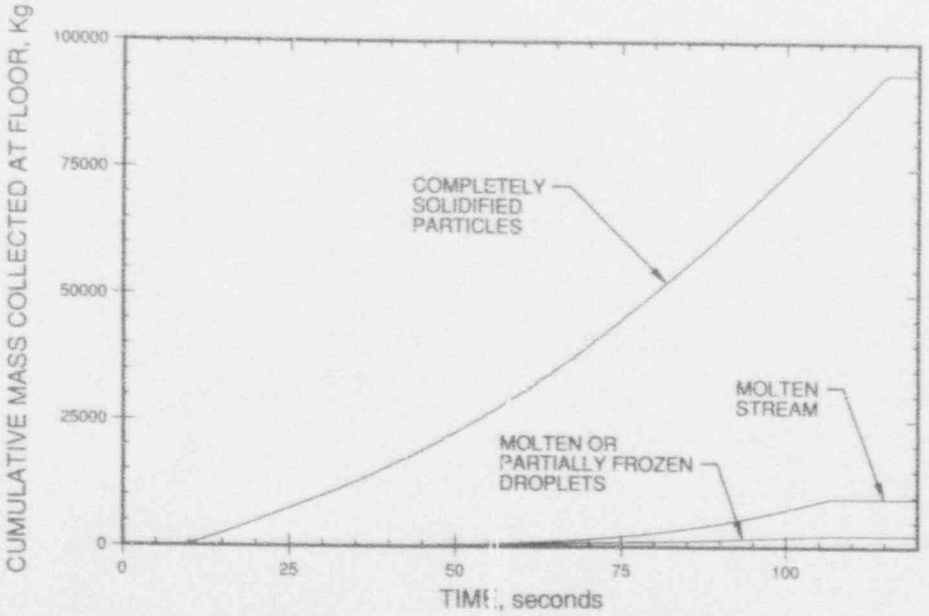

Figure 11. Cumulative Corium Collection at Lower Drywell Floor.

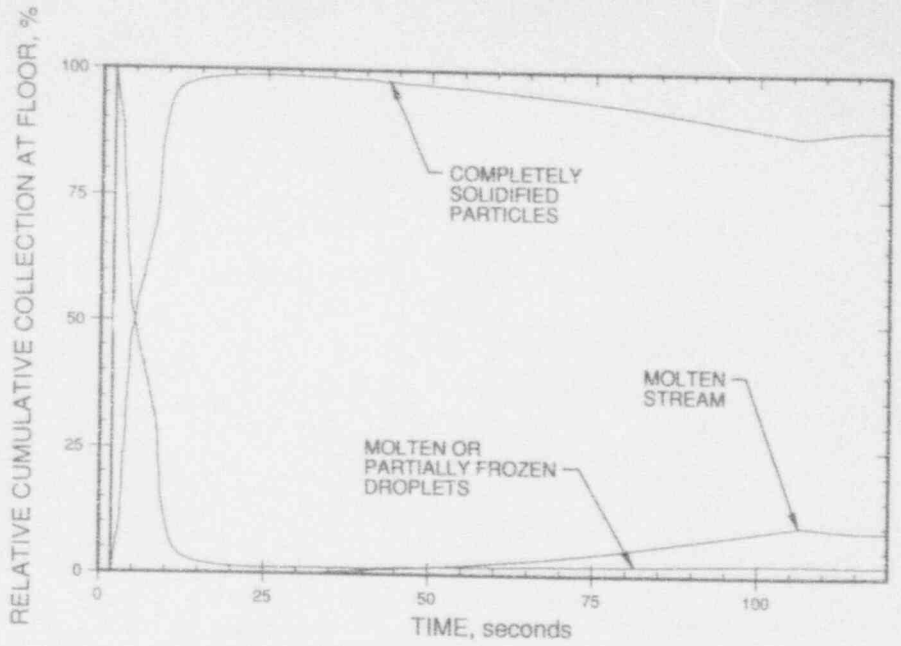

Figure 12. Cumulative Corium Relative Collection at Lower Drywell Floor.

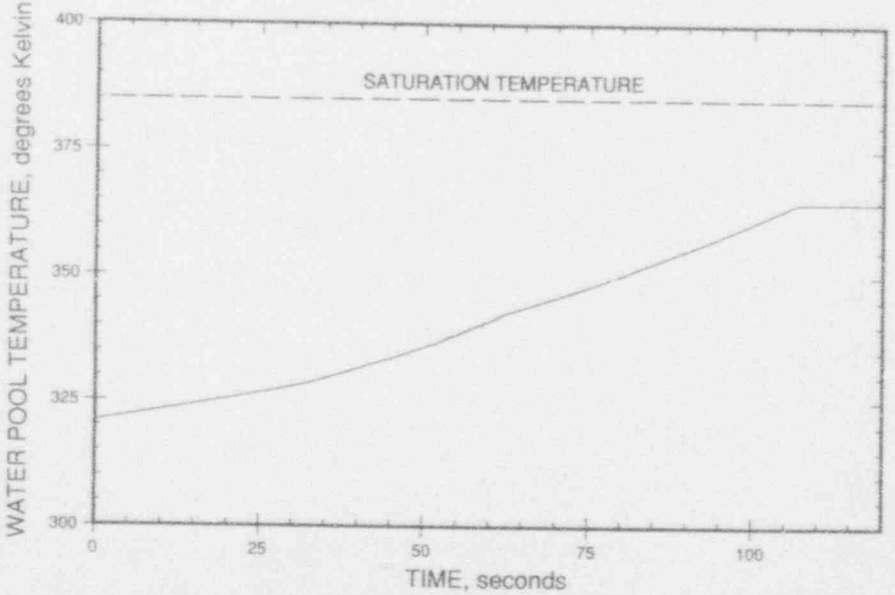

Figure 13. Water Pool Heatup Due Solely to Melt Fall Stage Quenching.

BREAKUP OF MELT JETS AS PRE-CONDITION FOR PREMIXING: MODELING AND EXPERIMENTAL VERIFICATION

M. Bürger, S.H. Cho, E. v. Berg, A. Schatz
Institut für Kernenergetik und Energiesysteme (IKE), University of Stuttgart,
Pfaffenwaldring 31, 7000 Stuttgart 80, Germany
Telephone ++49-711-685-2368 - FAX ++49-711-685-2010

ABSTRACT

The breakup of jets of melt in water pools constitutes a central problem in the frame of severe LWR accidents, influencing further accident progression. Especially, the mixing behavior of molten core material with water and thus the possibility of strong vapor explosions or the mode of contact of core material with the lower plenum structures are determined by this. For evaluating available modeling approaches on jet breakup the model developed at the IKE has been applied to experiments with jets of low melting Wood's metal in water performed at IKE, ANL and JRC Ispra. From variations of essential modeling features conclusions on different approaches are drawn. In principle, the mechanism of stripping at the jet column due to shear flow produced waves appears to explain the experiments, if based on the Miles formulation of the instability. Application to corium jets under vapor film boiling leads to much more stable coherent jet cores than based on the Kelvin-Helmholtz formulation and to much less fragmentation.

I. INTRODUCTION

During a severe core melt accident in a light water reactor (LWR) molten core material may be released into a remaining water pool in the lower plenum of the reactor pressure vessel (RPV). The interaction with the water yields fragmentation of the melt, mixing with the water, rapid steam production, pressure buildup and even explosive events or thermal detonations. All these effects influence the further accident progression. Even if strong thermal detonations threatening the integrity of the RPV may be excluded, steam generation and vessel pressurization influence the further core heatup, oxidation of metallic material with resulting hydrogen production, melting and the integrity of vessel internals. Of major safety concern however is the physical state of the molten material or of hot solid parts or refrozen material coming into contact with the vessel itself, especially at the bottom of the vessel. This determines the heatup of the vessel wall, physical and chemical interactions between the hot material and the wall and thus the failure conditions and the flow of corium into the reactor cavity.

Several models and computer codes (e.g. /1/ - /4/) have been developed or are under development which describe the motion of drops of melt within the water pool under vapor film boiling and strong vapor production, mixing with the water, cool-down during falling and settling at the bottom of the vessel. Such mixing models have earlier been developed mainly with respect to the analysis of thermal detonation conditions, but are now considered to be independently important for the question of lower head failure. These models appear to have reached a rather high level of sophistication, in spite of remaining strong uncertainties, e.g. due to the drag and heat transfer formulations in the multiphase approaches /5/. Even stronger uncertainties however exist concerning the breakup of the melt falling into and through the water. But, the breakup decides critically the subsequent behavior. Thus, it must be considered as a key process for modelling of mixing in the lower plenum.

As outlined by Spencer, Gabor and Cassulo /6/, the more probable mode of corium entry into the water is by relatively small (~ 10 cm) diameter pour streams or rivulets, not by coherent collapse of large melt mass. Thus, the breakup behavior of such streams or jets of melt in water has to be considered. Even with this specification large uncertainties remain, however. In the presently available mixing codes the jet breakup seems not to be treated sufficiently. Mostly, drop sizes are assumed and often taken as fixed. Although models on breakup of melt jets have been developed, there exists still no agreement even on the relevance of the basic physical mechanisms.

II. REVIEW OF BREAKUP MECHANISMS

Earlier analyses on liquid jet breakup have usually been done with small (millimeter) diameter jets of low density fluids, mostly in gas surroundings. Different regions of behavior have been identified with increasing injection velocity. Fig. 1 shows the typical qualitative behavior of jet breakup length with jet velocity or Weber number. The different breakup regimes range from axisymmetric, varicose breakup (AB) under the influence of surface tension at low velocities to the atomization regime at high velocities, characterized by intense spray production directly at the jet outlet (for a survey see e.g. /7/). In the latter regime a continuous liquid core is assumed to be surrounded by a spray cone. According to Ginsberg /7/ droplet stripping from the surface of the jet produces the spray, while also breakup of the

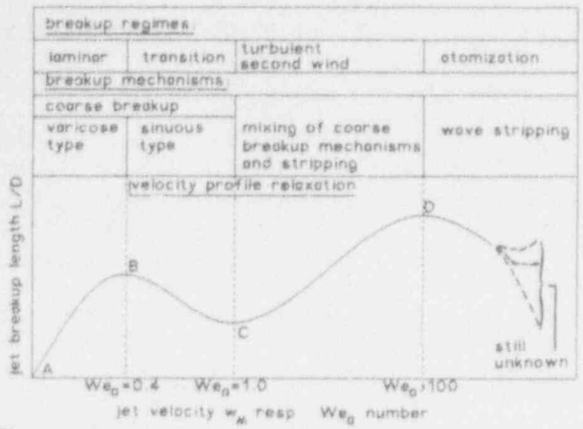

Fig. 1: Sketch of jet breakup length curve with related breakup regimes and mechanisms

liquid core into relatively large dorplets with subsequent secondary breakup is possible.

The transitions between are reflected in the curve of Fig. 1 by the changes in slope and especially by the formation of extrema. This is due to the increase of jet velocity, on one hand tending to increase the breakup length for unvaried fragmentation, but being counteracted by changes in the fragmentation process, on the other hand. In the range between the above extremes various phenomena are under discussion. With increasing velocity the axisymmetric disturbances are usually superposed by transverse, sinuous type disturbances of the jet. While with the varicose instability the surface tension is the main agent of the disturbance, it is here acting against the transverse instability which is due to relative flow of the surrounding medium. On the other hand, turbulence and nozzle design are considered as essential for breakup in this range and for formation of the first maximum in the L/D-curve. A 'bursting breakup' is considered to take place due to redistribution of velocity profiles in high speed laminar jets with parabolic profiles after release from long tubes /8/.

For even higher velocities (range CD in Fig. 1) a combination of stripping of droplets from the surface of the jet (at lower velocities via formation of long ligaments from surface waves and subsequent ligament breakup) with bulk jet breakup due to instabilities of transverse or helically transverse type occurs /7/. This regime starts for We > 1, according to /7/. The respective contributions may change, yielding finally dominance of more and more direct stripping of crests of waves in the atomization region. Thus, in the view of the present authors, the whole breakup curve may be explained by single or combined processes of coarse breakup, due to varicose or different types of transverse disturbances driven by surface tension and relative flow of the surrounding medium, in combination with stripping processes under the shearing flow. Other effects such as turbulence, profile rearrangement or cavitation are considered as only additional effects in most cases, perhaps influencing wave growth via induced initial disturbances. An ambient Weber number of ~ 100 may be taken as condition for entering the atomization range with intense spray production just beginning at the outlet /7/.

Additional aspects have to be taken into account with hot melt jets in liquid coolant. If the melt is hot enough, film boiling will occur and a thick vapor film will be formed. Then, the vapor flow should determine the breakup regime and acording to estimations of Ginsberg /7/ may establish the atomization regime for conditions relevant during a core-melt accident (see below). By means of Kelvin-Helmholtz instability analysis taking into account the thickness of the vapor film, Epstein and Fauske /9/ derive correlations for the jet penetration distance in the limits of thin and thick films. They show that in the thin film case the water density and in the thick film case the steam density determine the behavior. This underlines the above mentioned assumption that with thick films the vapor flow determines the breakup regime.

Further, thermal interactions may occur due to local vapor film collapses, especially at the leading edge of the jet. This can be caused by the thinning of the film at the leading edge due to increased pressure and especially by Taylor instabilities at the water/steam interface in this region if this interface is sufficiently accelelerated downwards due to the jet motion. Indications for the occurence of such interactions at the leading edge are found by Saito, Sato and Imahori /10/ from their experiments with hot water jets injected into Freon-11 and with water jets at room temperature into nitrogen. They emphasize the increased vapor production and flow along the jet columns due to this effect.

Marshall, Beck and Berman /11/ also conclude rapid jet fragmentation at the leading edge from their experiments under more reactor-typical conditions. They observe a rapid expansion of melt at jet entry. Further details of the jet behavior are however not given and the authors claim the necessity of further investigations as do also Saito et al., with emphasis on more typical conditions for the reactor case than in their experiments (higher density difference, higher heat transfer).

In contrast to the above authors, Wang et al /12/, /13/ do not mention such leading edge effects from their experiments with corium jets in water. A stable leading edge without significant fragmentation due to melt-water interaction is assumed in /12/, however with a leading vortex ball during the transient phase of jet penetration from which a considerable amount of relatively large particles is detached at its tail due to the relative steam flow. The high stability of the vapor film at the hot corium jets in spite of strong agitations during jet penetration may be taken as a support for this view. Furthermore, the conditions for Taylor instabilities to be effective at the leading edge need further justification concerning the determination of the required accelerations.

Schneider, Marciniak and Jones /14/ performed experiments with Cerrobend jets penetrating Freon-11. Both their motion pictures and X-radiographs show the jets to be completely enshrouded by a large diameter vapor chimney. They conclude that jet breakup at steady state may be presumed to be driven entirely by the vapor counterflow. Rayleigh-Taylor instablities are not observed. The X-ray pictures indicate a mixed type of jet breakup between atomization processes and coarse breakup behavior at the coherent core (varicose

or sinuous type bulges).

III. APPLICATION TO CORIUM STREAMS IN THE RPV WATER POOL

A. General Considerations

It remains an open question whether the above characterizations and especially quantifications on hydrodynamic breakup regimes are applicable to the conditions of streams of corium in water. Here, vapor film boiling has to be considered, as well as high densities and surface tensions of the jet material. Furthermore, the jets to be analysed in the present context are large in diameter. Nevertheless, because of the lack of alternatives, Ginsberg /7/ takes the above mentioned Weber number criteria for first evaluations on the breakup regime. An assumed relative velocity of the surrounding steam of 25 m/s, a jet diameter of 0.1 m, a Corium temperature of 3080 K and an ambient pressure of 0.1 MPa yield an ambient Weber number of ~ 20, i.e. the so-called turbulent or 'second wind' regime of breakup with probably still small stripping contribution. Higher steam velocities are however reached at the jet (see below) and thus the atomization regime may also be reached, especially for increased ambient pressures.

Most uncertainties in this respect appear to be related to the diameter effect. The much larger diameters to be considered here strongly increase the Weber number and thus tend to support atomization, i.e. an increased contribution of stripping in our view outlined above. Such an increased contribution with increased diameters may be due to the effect of thickness on the instabilities produced by shear flow of the surrounding fluid. However, the effect should be terminated at least if the wavelength of the growing waves becomes much smaller than the diameter. On the other hand, also the coarser breakup mechanisms mentioned above which work simultaneously at the liquid core depend on the diameter. They appear to be less effective for larger diameters, thus probably also favoring the conditions for stripping as the remaining mechanism.

But, it must also be taken into account that the diameter of the liquid core decreases spatially due to stripping of fragments. Therefore, the coarse breakup mechanisms may become effective at least in the region of the tip of the jet after sufficient thinning due to sideways stripping. This can even occur under conditions of pronounced stripping in the atomization regime.

B. Modeling Approaches

Thus, for modeling the breakup of the corium streams, a model of the stripping process due to relative steam flow as well as models of coarse breakup appear to be necessary. A combined treatment taking into account the changes in conditions along the jet core should give the respective contributions to breakup and may thus explain the essential features of the behavior for the regimes attributed to
We > 1.
The most advanced model appears to be that in the THIRMAL-0 code /13/, /15/. Two erosion mechanisms at the jet are modeled, stripping of fragments from the surface of the jet column due to Kelvin-Helmholtz instabilities produced by the relative steam flow and boundary layer stripping from the vortex ball assumed at the leading edge of the jet. Breakup due to some coarse breakup mechanism is not modeled. Also Taylor instabilites at the leading edge are not taken into account. A description on this mechanism has been given by Chu and Corradini /16/. It may be relevant in principle for the thicker jets, yielding large breakup, however only if sufficient deceleration of the melt jet in the water occurs. The experimental observations of Hopkins and Robertson cited in /13/ against this possibility seem not to be sufficient for this because of the much thinner jets and much smaller density differences between the jet materials and the surrounding fluid in this work.

Because of the present uncertainties in general, indicated by all the works cited above and also mentioned by the authors themselves (e.g. Schneider et al /14/: "These divergent modeling assumptions currently exist and are used because there are insufficient experimental observations for model validation"), the main task appears at present not to be to work out all aspects of the phenomena in an unified model. Instead, dominating mechanisms must be worked out in modeling approaches and checked against available experiments. Again, a generalised check seems not to be of priority. Checking the alternative approaches against single experiments with relatively defined conditions and results, especially with clear identification of the breakup phenomenology, i.e. the breakup regime, should be a first step. The present contribution aims to proceed in this sense.

In this respect, other uncertainties in the state of modeling the jet breakup must be considered concerning the description of the stripping process at the jet column. In THIRMAL the Kelvin-Helmholtz description is applied for wave growth. The rate of mass stripping is given by an erosion velocity which is set equal to the growth velocity c_i in the exponential growth law of the wave amplitude $\hat{\eta}_i = \hat{\eta}_{i0} \exp(kc_i t)$. For the stripped droplets a diameter of $1/k_m$ is assumed, with k_m denoting the dominant wave number.

A basic question is whether the Kelvin-Helmholtz approach is valid in principle. It assumes a jump in velocity between the fluids which leads to pressure oscillations with increased pressures in the troughs of the wavy melt surface. Taking into account the shear flow profile in the flowing steam leads to a modified description and a displaced pressure distribution over the wavy melt surface, i.e. increased pressures over the slopes of the wave. This approach is known as Miles' shear flow theory (for further details see /17/, /18/ and has been considered as main agency for the development of wind induced waves in the review of Ewing /19/. It must however be taken into account that this review stating also some experimental validation concerns gravity waves, not the capillary wave to be considered in the present context.

The IKE model on drop fragmentation in thermal detonation waves has been based on this description applying it for capillary waves (e.g. /18/). The same has been done for a

model on melt jet fragmentation developed with respect to technical gas atomization plants (e.g. /17/). This model has meanwhile been extended for application in the present context and will be described below. It contains also a description of the stripping process itself and the determination of the fragment sizes from more detailed considerations than in the THIRMAL model.

C. Specific Experimental Data Basis

As already mentioned above, the experimental basis with respect to the present problem and also the problem of melt stream breakup in general, especially with larger diameter jets and under vapor film boiling at high temperatures, is rather small and also uncertain (see e.g. /10/, /14/). There exists even no definitive knowledge on phenomenology and on the breakup regime depending on the conditions. The only experiments available with high-temperature corium or iron/alumina jets in water pools appear to be those performed at ANL and SNL (e.g. /11/-/13/). First tests have been undertaken in the FARO facility at JRC Ispra /20/. The available results suffer in general from uncertainties in characterization of the jet behavior as well as obviously too less mass input to reach steady state conditions of the jet flow and breakup process.

Further interesting simulation experiments are available from Saito et al /10/ and from the recent work of Schneider et al /14/. Especially the latter work gives some detailed view of the breakup process by means of X-ray photography. This recent work could however not yet be considered for calculations with our model.

Because of the uncertainties mentioned it appears to be worthwhile to take also other available experiments with melt jets at lower temperatures for model and code examination and validation. In any case this gives a larger range of conditions for checking the basic approaches. Such experiments have been performed especially with jets of the low-melting Wood's metal in water. Although the surrounding medium is in these cases water instead of steam, this should be of interest in the present context, since the much lower water than steam velocities are compensated or over-compensated here by the much higher density of the water. Thus, a comparable range of behavior may be observed or at least the range of conditions is strongly extended over the available data basis. Such experiments have been performed at IKE /21/ with jets of Wood's metal at low temperatures (< 373 K at 0.1 MPa) and at relatively small diameters (2-4 mm) as well as - more important for the present context - with diameters of ~ 2 cm at ANL /6/ and up to 5 cm at JRC Ispra /22/,/23/. The experiments at ANL and JRC Ispra have also been performed at higher melt temperatures but not for sure with stable film boiling.

D. Main Intentions of the Present Contribution

The present contribution serves mainly to check whether the available modeling can explain and quantitatively describe experimental results from the Wood's metal experiments at IKE, JRC Ispra and ANL as well as results from corium experiments at ANL. Open questions shall be identified for stimulating discussion and further work. Emphasis will be laid on the stripping process, asking to what extent it can explain the results. Especially, the different formulations of the wave growth according to Kelvin-Helmholtz or Miles will be checked. To some extent also considerations with respect to coarse breakup will be done. Taylor instabilities or thermal interactions due to melt/water contact at the leading edge of the jet are not taken into account, at present. At first, some more details on the IKE model are given.

IV. JET BREAKUP MODELING AT IKE

A. Transient Jet Behavior

The basic equations determining the transient jet behavior, i.e. jet flow and jet contour, are given in a one-dimensional approach as follows (for the configuration and coordinate system see Fig. 2a).

Mass balance:

$$\frac{\partial}{\partial t}\left(A_M \rho_M\right) + \frac{\partial}{\partial z}\left(A_M \rho_M w_M\right) = -\dot{M} \,, \tag{4.1}$$

Momentum balance:

$$\frac{\partial}{\partial t}\left(A_M \rho_M w_M\right) + \frac{\partial}{\partial z}\left(A_M \rho_M w_M^2\right) = g\left(\rho_M - \rho_K\right) A_M - c_{DM} \pi R_M \rho_K \left(w_M - w_K\right)^2 - w_M \dot{M} \,, \tag{4.2}$$

with $A_M = \pi R_M^2$.

Pressure forces on the jet are neglected and also cooldown of the jet material is assumed to be negligible. For w_K and ρ_K the values of the medium adjacent to the jet have to be taken, i.e. either for steam in the high-temperature case with film boiling or for water with direct contact of water. The existence of mixtures, steam with entrained water and fragments or water with steam bubbles and fragments, is not yet considered in the present model. For the local drag coefficient c_D between the column of the jet and the surrounding fluid flow a correlation for a completely rough surface is taken according to Schlichting /24/:

$$c_{DM} = \left(2.87 + 0.686 \ln \frac{L - z}{K_{ers}}\right)^{-2.5} \tag{4.3}$$

In Eq. (4.3) K_{ers} means an effective roughness height which is here due to the waviness of the jet surface induced by the relative flow. Thus, there exists in principle a feedback between the friction and the wave growth at the jet surface. The dependence on boundary layer development starting from the tip of the jet is expressed by L-z. In the present calculations however only a simplified approach with a chosen constant value of $c_{DM} = 0.05$ has been applied. This comparatively large value has been chosen to take into account the high roughness and friction effects at the jet surface due to the fragmentation process.

A separate model of a vortex ball at the leading edge of the jet as in THIRMAL has not yet been included. Also, a description of boundary layer stripping at the leading edge is not applied at present. However, as shown below, calculations have been performed with a parametrically increased drag coefficient at the leading edge to enable possible ball formation and to check the effects. Likewise, the fragmentation rate has been varied at the leading edge to consider enforced mass efflux due to stripping of melt layers.

According to the experimental observations in /6/, vortex ball formation and fragmentation at the leading edge may be dominant in the beginning, but should disappear if the jet reaches a steady state. This can also be expected since in the steady state the leading edge becomes fixed and thus the stagnation pressure and the drag must go to zero with the relative velocity. Fragmentation at the jet column must therefore dominate, ultimately, as observed in /6/. Coarse breakup of the coherent core after sufficient thinning due to lateral stripping may however also become important. Even oscillation behavior at the leading edge may then be possible.

B. Model of Vapor Film Boiling

At present, film boiling at the jet column has been modeled in a quasi-steady approach, assuming that the vapor film adapts instantaneously to a certain state of the jet. The model itself is similar to that of Han and Bankoff /25/ and also to that in /6/, however simplified in some aspects. Behind a short length of laminar film boiling, starting from the leading edge of the jet, turbulent flow is expected to set in. This point x_t as well as the subsequent separation surface between the laminar sublayer and the turbulent film region (see Fig. 2b) are characterized by the condition of transition

$$Re = \frac{\overline{\rho_{Vl}}\ \overline{w_{Vl}}\ \delta_l}{\overline{\mu_{Vl}}} > Re_t = 100 \ , \qquad (4.4)$$

where the superscript line means the mean values over δ_l.

For the laminar sublayer linear temperature and velocity profiles are assumed, for the turbulent layer due to ideal mixing constant values are taken. Approximating further the actual shape of the jet by a vertical surface, assuming $\delta_l \approx \delta_t$ after short distance, neglecting the fragments as well as entrainment of water droplets in the film and of vapor bubbles into the water and considering only the case of saturated water the mass and energy balances yield

$$\frac{d}{dx}\left(\rho_{Vl} w_{Vl} \delta_t\right) = \frac{1}{h}\left(\alpha_r + \frac{\overline{\lambda_{Vl}}}{\delta_l}\right)\left(T_M - T_S\right) \ , \qquad (4.5)$$

and the momentum balance

$$\frac{d}{dx}\left(\rho_{Vl} w_{Vl}^2 \delta_t\right) = \qquad (4.6)$$

$$g\left(\rho_W - \rho_{Vl}\right)\delta_t + w_M \dot{m}_V - \tau_W - \tau_M \ .$$

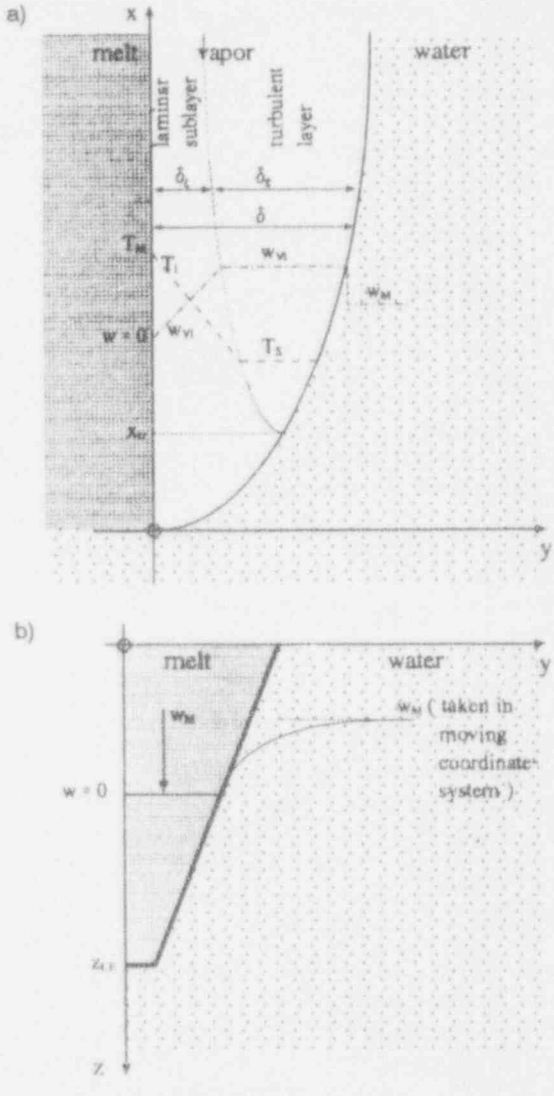

Fig. 2: Sketch of coordinate systems for jet breakup model
a) description of jet dynamics
b) film boiling model

with the evaporation mass rate

$$\dot{m}_V = \frac{d}{dx}\left(\rho_{Vl} w_{Vl} \delta_t\right) \ , \qquad (4.7)$$

the radiation heat transfer coeffficient

$$\alpha_r = \varepsilon_M \sigma_B \frac{T_M^4 - T_S^4}{T_M - T_S} \ , \qquad (4.8)$$

and the wall and water interface friction forces per surface area

$$\tau_M = \overline{\mu_{Vl}} \frac{w_{Vl}}{\delta_l} \ , \qquad (4.9)$$

$$\tau_W = \frac{1}{2}\, c_{DW}\, \rho_{VI}\, (W_{VI} - W_M)^2 \,. \qquad (4.10)$$

The drag coefficient is here chosen as $c_{DW} = 0.05$. No velocity profile is taken into account in the water, assuming the water velocity as zero.

The main result of this film boiling model with respect to the analysis of jet breakup is the vapor (steam) velocity w_{VI}, set for w_K in Eq. (4.2) and applied also in the breakup model itself under film boiling conditions.

C. Model of Wave Growth

As already mentioned above, the model of jet breakup is essentially based on the stripping of fragments from waves produced at the surface of the jet column due to the relative flow of the surrounding medium, either water or steam in the cases considered here. A first step is to model the wave growth starting from arbitrary initial disturbances at the surface. This is done in a linearized approach, yielding

$$\hat{\eta} = \hat{\eta}_0\, e^{k\, c_i\, t} \qquad (4.11)$$

for the amplitude of a disturbance with wavenumber k. Both the Kelvin-Helmholtz formulation and that of Miles are included for choice in the IKE model. While according to Kelvin-Helmholtz (without considering the effect of finite thickness of vapor film or jet)

$$c_i = \frac{\left[\rho_M \rho_K\, (W_M - W_K)^2 - \sigma_M\, k\, (\rho_K + \rho_M)\right]^{\frac{1}{2}}}{(\rho_M + \rho_K)} \,, \qquad (4.12)$$

the description of Miles yields

$$c_i = \beta_J\, \gamma\, \frac{(W_{rel} - c_r)^2}{2 c_r}\, k - \nu_M\, k^2 \,, \qquad (4.13)$$

with

$$W_{rel} = |W_M - W_K| \,, \qquad (4.14)$$

the relative velocity of the surrounding fluid at large distance, i.e. outside the boundary layer profile. This means w_{VI}-w_M for the case of steam flow under film boiling and w_M for the case of no net steam production with jet injection into stagnant water. For the wave speed c_r the expression

$$c_r^4 - \frac{1}{4}\, \beta_J^2\, \gamma^2\, (W_{rel} - c_r)^4 + \nu_M^2\, k^2\, c_r^2 - \qquad (4.15)$$

$$- \alpha_J\, \gamma\, (W_{rel} - c_r)^2\, c_r^2 \quad = \quad \frac{\sigma_M\, k}{\rho_M}\, c_r^2$$

or as approximately used here assuming $\varepsilon \to 0$ and $\nu_M \to 0$:

$$c_r = \left[\frac{\sigma_M\, k}{\rho_M}\right]^{\frac{1}{3}} \,, \qquad (4.16)$$

the free surface wave speed of capillary waves, can be derived.

Eqs. (4.13) and (4.15) result from the normal stress balance at the jet surface, using the solution of the Orr-Sommerfeld Equation for the jet region, with the coefficients α_J and β_J from the formal expression

$$\hat{P}_K = (\alpha_J + i \beta_J)\, \rho_K\, (W_{rel} - c_r)^2\, k\, \hat{\eta}_0 \qquad (4.17)$$

for the amplitude of perturbation pressure in the surrounding medium. With a special choice for α_J and β_J this leads back again to the Kelvin-Helmholtz formulation. An approximate solution of the Orr-Sommerfeld Equation in the surrounding medium taking into account a shear flow profile $w_{rel}(y)$ however yields (for more details see /17/)

$$\beta_J = -\frac{\pi\, k^2}{(W_{rel} - c_r)^2} \left(\frac{d^2 w_{rel}}{dy^2}\right)_c \left(\frac{dw_{rel}}{dy}\right)_c^{-3} \cdot \qquad (4.18)$$

$$\cdot \left[\int_{y_c}^{\infty} e^{-ky}\, (W_{rel} - c_r)^2\, dy\right]^2 \,.$$

Here, the index c means the distance $y = y_c$ with $w_{rel} = c_r$, causing a singularity in the Orr-Sommerfeld equation.

For closing the problem it remains to determine $w_{rel}(y)$. A logarithmic profile

$$w_{rel}(y) = \frac{w^*}{\kappa}\, \ln \frac{y}{y_{eff}} \qquad (4.19)$$

can be taken, assuming turbulent flow. The quantities w^* and y_{eff} depend on the roughness of the jet surface. An essential complication of the problem results because this roughness depends on the waviness of the jet surface produced by the instability. In a first approach empirical relations for fully rough conditions have been chosen according to /24/, with

$$y_{eff} = 0.033\, K_{eff} \qquad (4.20)$$

and the local friction coefficient

$$c_{DM} = (2.87 + 0.686\, \ln\, (x / K_{eff}))^{-2.5} \qquad (4.21)$$

in

$$w^* = \left(\frac{c_{DM}}{2}\right)^{\frac{1}{2}} W_{rel} \,. \qquad (4.22)$$

At present, the effective height of roughness K_{eff} has been simply set to the geometrical value of the wave amplitude,

although differences between the effective and the geometrical roughness must be noted in principle /24/.

D. Model of Jet Breakup

The above description of wave growth has been formulated with locally changing conditions along the jet column. The wavelength with maximum growth is calculated according to the local conditions as well as the mass stripped. Ring waves are considered which grow due to the instability caused by the shear flow. The crests of these waves are then assumed to be stripped by the flow after growing beyond a certain height proportional to the wavelength and taken here as half the wavelength. For determining the stripped mass as well as the radius of the fragments an energy balance is applied to the crest region beyond the above height. It states that the work done by the flow force on the crest, moving it along its width, together with kinetic energy from the wave growth must at least equalize the new surface energy produced by stripping (see Fig. 3 and for more details again /17/ and /18/). The final fragment size is then determined from breakup of the stripped wave crest of assumed ring-shape according to a criterion of minimum surface energy. By weighting the fragment sizes at a certain location and time with the rate of stripped mass and adding

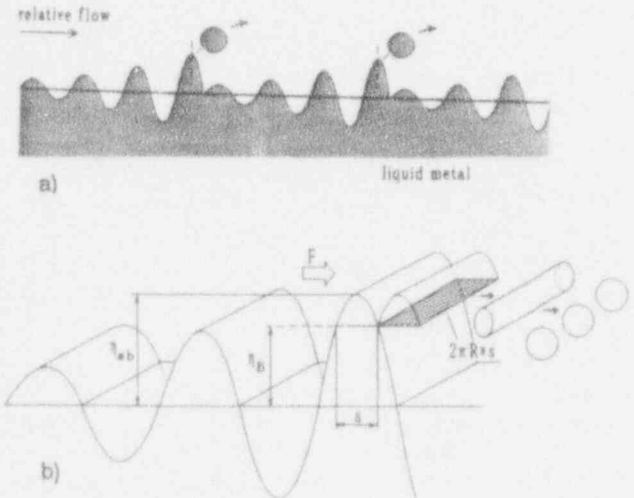

Fig. 3: Idealized picture of stripping mechanism
a) stripping pattern
b) wave crest stripping and decay into droplets

over location and time a deterministic part of fragment size distribution can finally be obtained.

Direct stripping of crests of waves without previous ligament formation as assumed here in an idealized model should become more and more realistic with increasing relative velocity. It may be taken as the dominant fragmentation process in the atomization region, while the model of the stripping process should be less adequate for lower velocities. In the case of small stripping contribution in the 'second wind' regime, ligament formation as part of the stripping process may still be relevant. By stripping of the crests of waves these are reduced to the critical height for beginning of stripping (Fig. 3). Due to the continued influence of the relative flow, they must grow and crests will be stripped again.

This process is modeled along the jet, leading to a local instantaneous pattern of multiple stripping events in a quasi-steady approach, i.e. assuming that this pattern establishes and changes according to the local and instantaneous conditions at the jet surface much more rapidly than these conditions change. The local, instantaneous rates of stripped mass are calculated by considering the waves travelling over the stripping locations. These rates are needed as $\dot{M}$ in Eq. (4.1) and (4.2). The change in jet cross-section due to this description of jet dynamics is taken into account in the stripping model.

The waves are assumed to start growing at each location on the jet column due to arbitrary initial disturbances or disturbances induced at the outlet. In accordance with the above assumption they are assumed to reach very quickly their critical height. Again, this appears only to be valid for the atomization regime. Moderating and checking this assumption can however be done by calculating the growth from initial disturbances. These can be taken as being initiated at the leading edge of the jet under film boiling and being driven upwards along the jet due to the steam flow. In the case without film boiling the jet moves more quickly than the surrounding medium. The waves are here finaliy transported downwards with the jet material although being driven upwards relative to the jet by the relative flow. Therefore, disturbances induced at the outlet grow traveling downwards with the jet.

The present model should only be applied for cases with dominant wavelengths sufficiently small against the jet diameter, due to the assumption of infinite lateral extensions of the jet and the surrounding medium in the instability model. In principle, however, the instability approach may also yield larger wavelengths responsible for coarse breakup of the jet core. This should also happen in the atomization regime after sufficient thinning of the jet core due to stripping. Therefore, in spite of the present restrictions of the instability approach, it is assumed that the remaining jet core breaks off if the calculated local wavelength reaches the jet diameter. Combined stripping at the jet column and coarse break-off in the tip region can thus be considered in a first approach.

V. EXPERIMENTAL RESULTS FROM THE WOOD'S METAL EXPERIMENTS IN COMPARISON WITH MODEL CALCULATIONS

A. Experimental Conditions and Observations

In the experiments performed at the IKE /21/, jets of molten Wood's metal (diameter 4 mm, temperature 363 K) are injected into water (293 K - 353 K) at velocities between ~3 m/s and 20 m/s. Typical jet appearances are shown in the photos of Fig. 4. In the case with 4 m/s ($We_s \sim 200$ in Fig. 4b), still some transition behavior, perhaps to be characterized as 'second wind' regime, can be seen with coarse

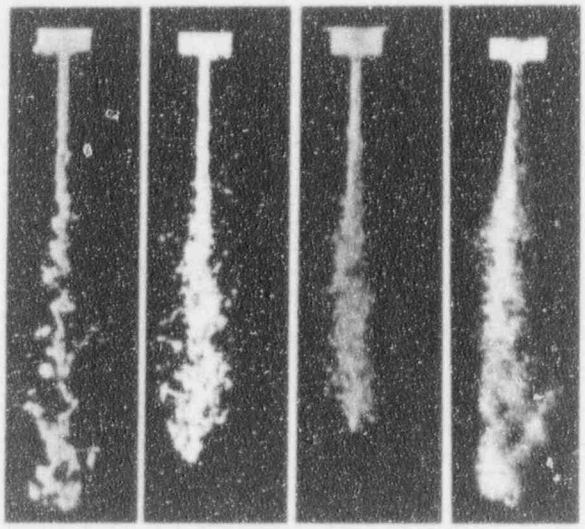

a) b) c) d)

Fig. 4: Appearance of disintegrating jet from IKE experiments (Woods metal into water, D = 4 mm)
a) jet velocity 2 m/s
b) jet velocity 4 m/s
c) jet velocity 6 m/s
d) jet velocity 15 m/s

breakup in the lower region of the jet and beginning of lateral stripping processes. The transition to stripping can be seen with more clearness in Fig. 4c) at a jet velocity of 6 m/s. Ligament stripping before breakup indicates limitations for the applicability of the above model. On the other hand, for 15 m/s ($We_a \sim 3000$) the jet appears to be fully in the atomization regime with direct formation of a dense spray or cloud of fragments.

Experiments with thicker jets of Wood's metal (diameter around 2 cm) falling into water at lower velocities of ~ 3 m/s have been performed at ANL /6/, partly also with temperatures excluding boiling effects. Tests # 20 and # 28 from /6/ may be taken as representative (temperature of Wood's metal: 373 K, of water: ~ 295 K). With $We_a \sim 400$ these experiments should also be in the atomization regime according to the criteria of Chapter 2, although the uncertainties mentioned with respect to the diameter effect must be noted. From the observations reported in /6/ a clear classification cannot be made. As dominant effects a sudden enlargement or vortex ball formation at the leading edge after entering the water is noted by Spencer, Gabor and Cassulo, with dominant mass efflux from this region in an inital phase. Simultaneously, a much less effective stripping due to irregularities at the jet column is reported, which however becomes dominant with increasing column length and reaching quasi-static conditions for which the vortex ball was observed to disappear.

A similar appearance may also be concluded from some experiments at JRC Ispra /22/, /23/ with Wood's metal jets of 2.8 cm and 5 cm in diameter and entry velocities of 2-5 m/s into the water pool. Again boiling effects were excluded within some of these series. The interpretation by vortex ball formation and fragmentation from the leading edge seems however not to be clear from high speed films of these experiments. Especially the large cloud region around the jet over a long distance may also indicate strong stripping at the jet column, perhaps somewhat pronounced at the leading edge - but not in all cases.

B. Calculations on Leading Edge Advance for Selected Experiments

Thus, since a final clarification on the dominant breakup processes cannot be achieved at present, calculations with the IKE model based mainly on the stripping mechanism have been performed for these experiments in order to check its applicability in principle and to identify open questions. For simplification and in order not to burden this exercise by the present uncertainties in calculating of β_j, a simplified instability calculation has been chosen here, by taking β_j as a parameter. For the IKE experiment with 16 m/s, which certainly shows the atomization regime, a variation of β_j between 0.05 and 0.3 has been performed, as can be seen in Fig. 5. The experimental result shows a change in the penetration velocity at L/D ~ 30, which is attributed to the loss of existence of a coherent jet core. Since the model does not contain the subsequent particle settling, a constant jet core length is obtained then from the calculations. Thus, the calculation with $\beta_j = 0.1$ yields the best approach.

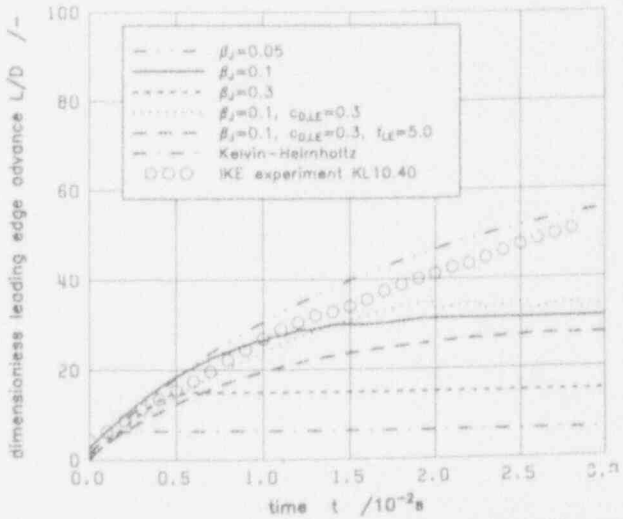

Fig. 5: Comparison of leading edge advance with different modelling approaches for IKE-experiments KL 10.40 (experimental conditions: Woods metal / water, temperatures: 363 K/353 K, inital jet diameter 4 mm, initial jet velocity 16 m/s)

An additional calculation has been performed with the Kelvin-Helmholtz formulation (however not applying the full stripping description outlined in Chapter 4, but simply assuming stripping of fragments with a diameter of half the dominant wavelength) in order to check this approach against that of Miles. As can be seen from Fig. 5, it yields a much too small steady jet core length and must therefore be

excluded as possible explanation. Further inspection shows that this is due to very strong mass stripping, not comparable with the experimental result.

Applying the IKE model with the Miles formulation and β_j = 0.1 to test # 20 from /6/ yields a too rapid penetration (with dimensionless distance: ~ 135/s from theory, ~ 100/s from experiment) and a significantly too long final coherent jet length (L/D ~ 37 instead of ~ 22 from experiment) as compared to the experimental result, according to Fig.6. But, again the Kelvin-Helmholtz result is much too low in the final jet length.

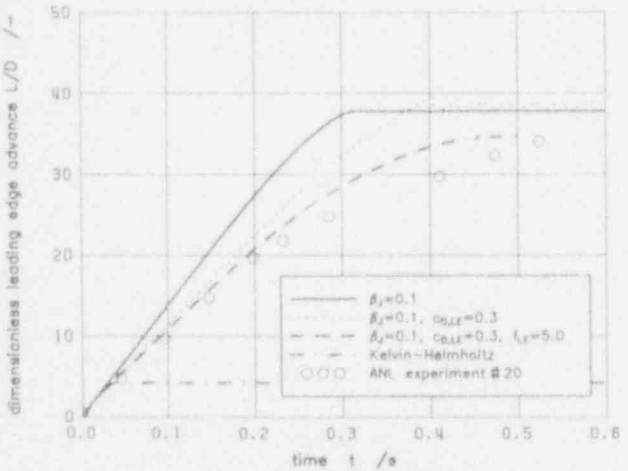

Fig. 6: Comparison of leading edge advance with different modelling approaches for ANL-experiment # 20 /6/ (experimental conditions: Woods metal/water, temperatures: 373 K/295 K, initial jet diameter 22 mm, initial jet velocity 2,7 m/s)

The same is true for an experiment from JRC Ispra with a diameter of 5 cm, as shown in Fig. 7. Furthermore, the penetration velocity of the coherent jet is again significantly higher from theory (with dimensionless distance: ~ 60 /s) than from the experiment (~ 40 /s), while the difference in the final length is not as high (experiment: L/D ~ 22, theory: 28) as with the ANL case.

In spite of the remaining differences the comparisons with the IKE, ANL and Ispra experiments can be considered as promising for the model with the choice of β_j = 0.1 in the Miles formulation. The large uncertainties in general existing at present must be taken into account. Thus, it seems to be possible to explain even the experiments at ANL and JRC Ispra to a large extent by stripping from the jet columns, especially concerning the length of jet core finally reached in the quasi-steady situation. Coarse breakup of the thinned jet core was no relevant effect in the present calculations, neither with the Miles' nor with the Kelvin-Helmholtz approach. It occured only after strong thinning of the jet core just at the leading edge. Taylor instabilities as relevant fragmentation mechnism at the leading edge can be excluded even for the experiments with thick diameters at JRC Ispra due to the small decelerations. In the present calculation even an acceleration of the motion of the leading edge is obtained in an initial phase according to Fig. 7.

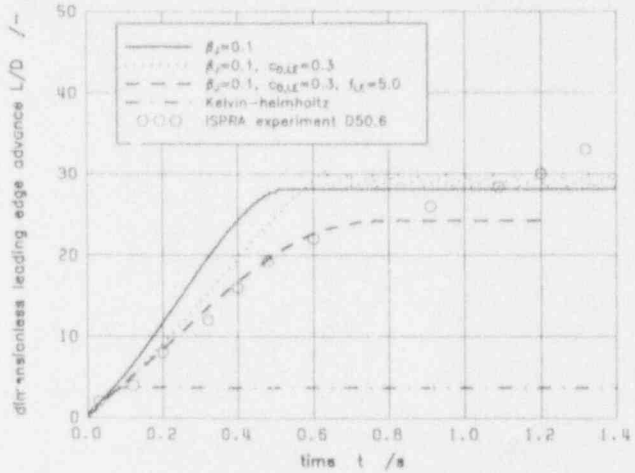

Fig. 7: Comparison of leading edge advance with different modelling approaches for JRC Ispra experiment D 50.6 (experimental conditions: Woods metal/water temperatures: 373 K/298 K, initial jet diameter 50 mm, initial jet velocity 2 m/s)

C. Final Coherent Jet Length

In Fig. 8a) experimental results on the dimensionless final coherent jet length from test series at IKE, ANL and JRC Ispra are drawn versus the ambient Weber number together with some results from calculations with the present model. A large experimental scatter can be seen which does not allow to identify a tendency with the Weber number. The same is true with the representation versus the jet velocity in Fig. 8b). A relevant range of L/D ~ 20-50 can be concluded and lies somewhat below the values given in /7/ for jets in gases. On the other hand, the correlation of Taylor (see e.g./7/) gives a constant L/D ratio of 5 times the square root of the density ratio between jet and ambient medium. Compared to this relation the experimental data in Fig. 8 lie between a factor of 1 to 3 higher than predicted by Taylor, while the gas data in /7/ lie a factor of 3 to 6 higher than Taylor's prediction.

Considering atomization as breakup regime the missing tendency of the scattered data could be roughly taken as supporting the (uncertain) assumption of constant L/D in this regime. The theoretical results for the IKE experiments however show a slight decrease of L/D with increasing Weber number. A thickness effect cannot be identified from the available data.

For further evaluation it must again be considered that the experiments with lower velocities may rather be in a transition range of jet breakup in spite of the relatively high Weber numbers due to increased diameters in the experiments of ANL and JRC Ispra. On the other hand, the results with the melt jets in water demonstrate that lower breakup regimes as observed with gas as surrounding medium are restricted to a very small low-velocity range.

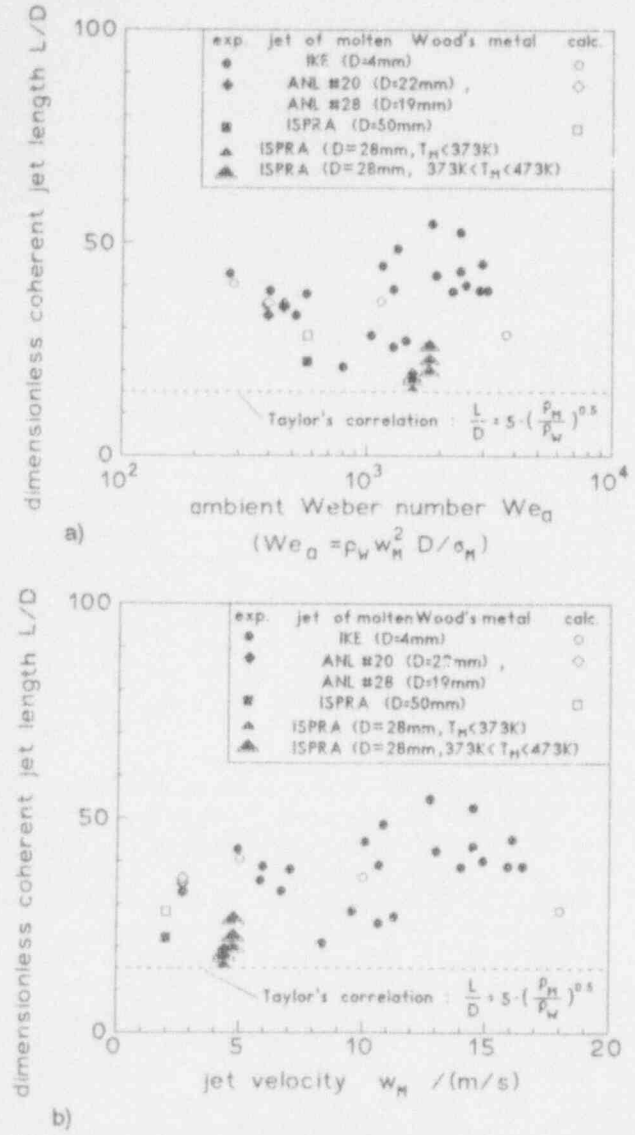

Fig. 8: Summary of experimental and theoretical values for the final coherent jet length
a) drawn versus Weber number
b) drawn versus jet velocity

D. Model Variation at Leading Edge

As discussed above, the results shown in Figs. 5 - 8 indicate a rather good applicability of the present model for the IKE case with 16 m/s, obviously in the atomization regime, but less good applicability for the ANL and JRC Ispra cases with uncertainties on fully developed atomization regime. As a further reason for the discrepancies in the latter cases a dependence of β_J with the jet velocity and diameter may be assumed. Higher β_J values, i.e. stronger fragmentation, for smaller velocities would be required to better explain the data. Further analyses of the influences on β_J are required for clarifying this point.

Here, a check concerning another effect has been done, which is related to the observations of a vortex ball reported in /6/. Although no specific modeling of this vortex ball has been performed in the present model, the development of enlargements at the leading edge must in principle be included in the present description of jet dynamics. The only effect to be added for this is an increased drag at the leading edge which is due to form drag. Here, a parametric approach for checking the effects in principle has been chosen. An increased drag coefficient of $c_{DLE} \approx 0.3$ has been chosen at the leading edge along the jet column, over a distance of the size of the jet diameter, assuming that the influence of form drag may extend over a region determined by the jet diameter. In addition, the calculated stripping rate has in this region been increased by a factor f_{LE} in order to take into account the effect of strong mass efflux due to layer stripping, in principle, which is modeled in /13/.

Results with these additional measures at the leading edge are given in Figs. 5-7 for the IKE, ANL and JRC Ispra cases considered. As can be seen, a better agreement with the experimental results of ANL and JRC Ispra concerning the penetration dynamics is already obtained by increasing the drag coefficient. This alone however does not alter the higher value of final jet length. Together with an assumed increase of the stripping rate at the leading edge (here a factor of $f_{LE} = 5$ was applied tentatively), improvements result for both experiments, but especially for the JRC Ispra case, whereas some worsening results for the IKE experiment.

Fig. 9a) shows the transient development of the jet contour for the JRC Ispra experiment with a jet diameter of 5 cm and 2 m/s entry velocity, applying the formulation with increased drag and stripping at the leading edge. A lateral enlargement develops at first and disappears again until establishment of a steady state, which agrees in principle with the experimental behavior reported in /6/. As an interesting effect, this description does not lead to an as significant lateral enlargement for the IKE experiments with jet diameter of 4 mm and 16 m/s entry velocity (Fig. 9b)). For a more detailed analysis a more detailed description of the leading edge appears therefore as worthwhile, e.g. according to the approach in /13/.

E. Calculation of β_J

For checking the parametrically chosen β_J-value in a first step, calculations have been performed under variation of values of effective roughness, which may be related to the geometrical roughness due to initial disturbances as indicated in Chapter IV. Furthermore, the distance x from the leading edge characterizing the effect of boundary layer growth of relative flow in Eq. (4.21) is varied over a large range. According to Fig. 10 the calculated β_J-values lie for practically the whole large range of roughnesses and distances as well as jet velocities between 0.1 and 0.6 or, excluding the smallest distance from the leading edge, between 0.1 and 0.3, i.e. in the range considered above. The values of β_J in Fig. 10 are determined for the wavelength of maximum growth and the assumed conditions. More detailed investigations and coupled calculations will be done in future.

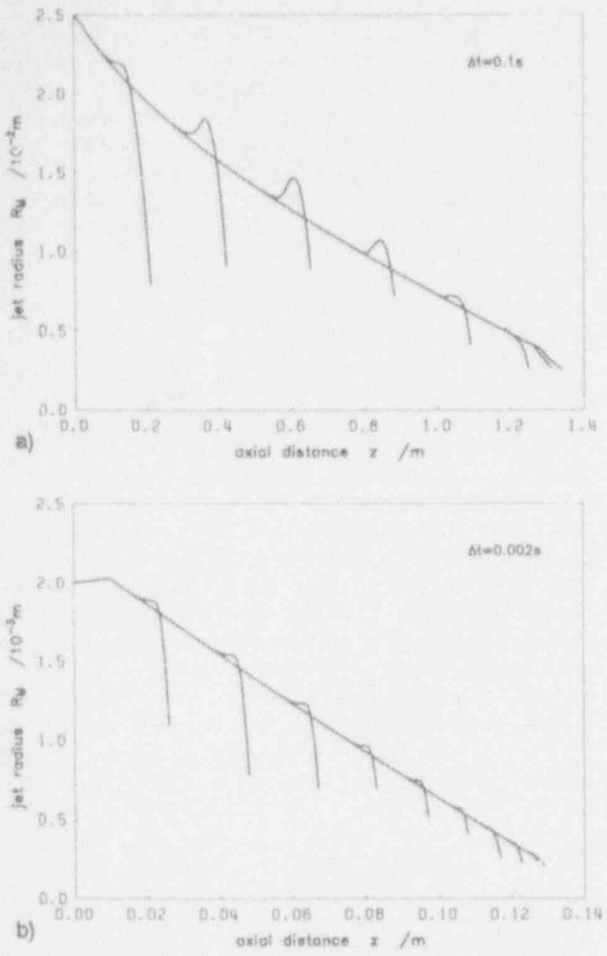

Fig. 9: Transient development of jet contour (Woods metal into water) calculated with modified leading edge formulation
a) for JRC-Ispra experiment D 50.6 with inital jet diameter 50 mm and initial jet velocity 2 m/s
b) for IKE experiment KL 10.40 with inital diameter 4 mm and initial jet velocity 16 m/s

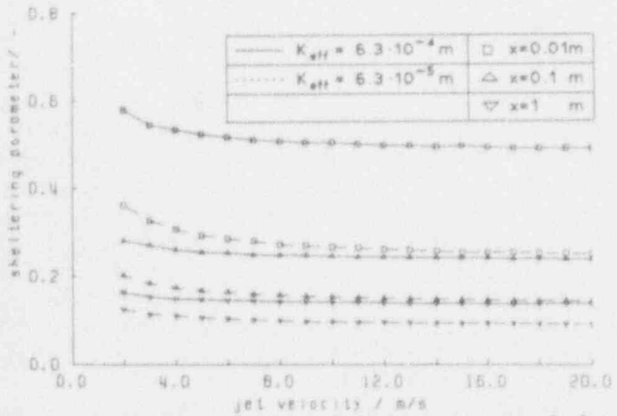

Fig.10: Calculated values of sheltering parameter β_J for different jet velocities, roughness heights and axial locations within the boundary layer

F. Further Results

More details on the jet behavior can finally be regarded in Figs. 11-13 for the experimental cases considered above. The results are from the calculations with β_J = 0.1, without special formulation at the leading edge. For steady state conditions reached, spatial developments with the distance z from water entry are given on the contour of the jet, the melt velocity in the jet, the fragment radius and the accumulated rate of stripped mass. The latter is related to the rate of melt inflow at the water entry and thus gives the grade of fragmented mass under steady state conditions. Deceleration of the melt occurs along the whole jet length for the IKE experiment, whereas it only sets in after a phase of acceleration in the other experiments. Practically total stripping is reached in all cases until the leading edge.

The calculated fragment sizes are rather small for all the experiments, as compared to those determined experimentally. From the IKE experiment with 16 m/s entry velocity a mean fragment diameter of ~ 500 µm has been determined by sieving. Values given for the ANL tests # 20 and # 28 are 3 - 5 mm /6/ and for the JRC Ispra tests 4 - 6 mm /22/, /23/. Corresponding values from the calculations (Figs. 11 - 13) are ~ 40-120 µm (IKE) and ~ 0,2-0,6 mm (ANL, JRC Ispra). The fragments obtained from the Kelvin-Helmholtz formulation are even smaller.

Further inspection shows that the much too small fragments from theory are not mainly due to the stripping description. They are already determined essentially by the dominant wavelength, i.e. by the instability description. Fragment diameters in the size range of about half this wavelength result, with the above stripping description applied in the approach based on Miles. Further investigations must be done however concerning more coarse parts of fragmentation especially at the leading edge and effects due to vortex ball formation. On the other hand, it must be noted that significant coalescence of fragments may occur in the dense sprays. The importance of coalescence effects is confirmed by the appearance of the fragments gained from the IKE experiments. These are in many cases obviously looking like agglomerations of smaller particles and as well often show the impact of small yet solidified drops into larger particles. Dependences on the temperature combinations have been noted in /6/ and /21/. Thus, also more distinct experimental determination is required.

VI. CALCULATIONS FOR CORIUM EXPERIMENTS

Experiments with corium jets in water performed at ANL /12/ have been chosen here for first calculations with the present model including film boiling. Uncertainties in determining L/D as revealed in Fig. 8 for the Wood's metal experiments can be expected to be even more severe in the corium experiments, indicating the need for additional work. In the CCM series presented in /12/ only six tests under different conditions are given. Thus reproducibility remains in any case an open question. Three of them are considered to be problematic in /12/ concerning L/D - evaluation because of the relatively small melt volume, i.e. small mass length. Two remain

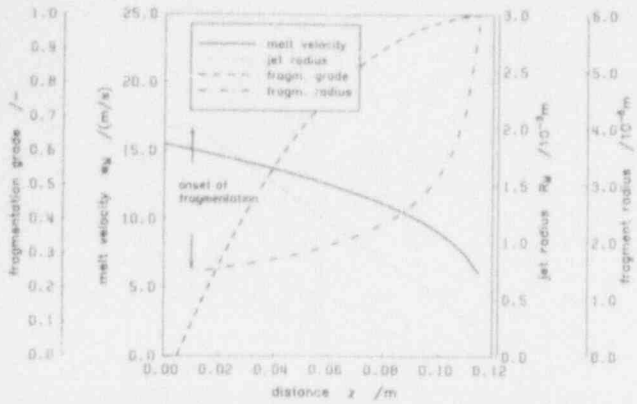

Fig.11: Calculated steady state spatial distributions of jet radius and melt velocity as well as fragment size and fragmentation grade for IKE experiment KL10.40

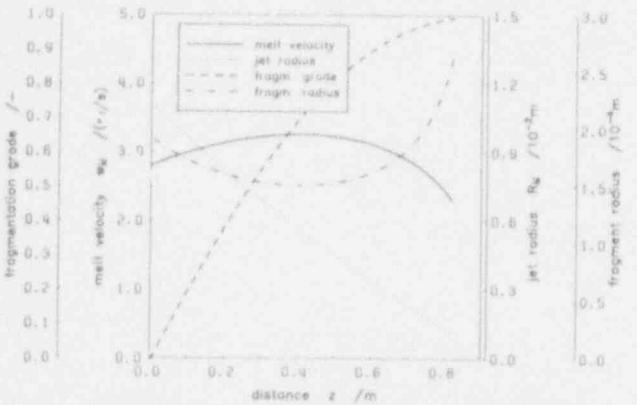

Fig.12: Calculated steady state spatial distributions of jet radius and melt velocity as well as fragment size and fragmentation grade for ANL-experiment # 2 from /6/

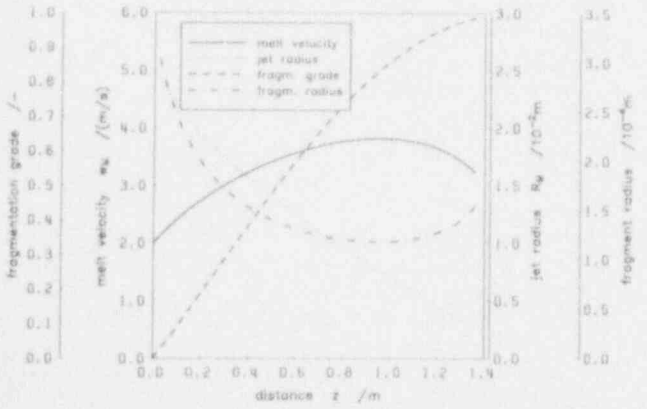

Fig.13: Calculated steady state spatial distributions of jet radius and melt velocity as well as fragment size

for analysis by means of our present model, presuming saturated water. The uncertainty ranges for L/D given in /12/ yield up to ≈ 100%, for CCM-2 only L/D > 25 is given, i.e. L >50 cm with D = 2 cm. No clear breakup length could be derived in this test from the thermocouple data. L > 50 cm means that the coherent core practically reaches the bottom of the vessel, in this test for L = 63 cm.

For test CCM-3 with similar conditions, a jet diameter of 2.54 cm and an entry velocity of 8.15 m/s (as compared to 5.3 m/s in test CCM-2), a probable value of L/D = 18 is given, however a range up to 36 indicated. This yields L = 46 cm - 91 cm. With the latter value the bottom of the vessel would again have nearly been reached (water depth of 1.1 m). The relatively restricted mass length as compared to CCM-2 conditions must be remarked additionally which is surpassed for L/D = 36. With larger melt masses an even longer jet may thus be expected. In test CCM-3, most of the thermocouples at the vessel bottom registered only mild temperature increases /12/ thus indicating no coherent jet impact at the bottom.

Thus, breakup of the jet core before reaching the bottom of the vessel appears not to be sure from these experimental results, although L/D = 10 - 19 is concluded in /12/ as range of jet breakup lengths in the CCM tests. Results from the correlations of Epstein and Fauske as well as Saito et al are given in /12/ with L/D = 116 (CCM-2) and 139 (CCM-3) as well as L/D = 72 (CCM-2) and L/D = 98 (CCM-3), supporting this view. From a calculation of Wang et al /13/ with an initial jet diameter of D = 2.54 cm and an entry velocity of 3 m/s an L/D - value of 23 results assuming no voidage in the water (40 with calculated voidage). This yields L = 58 cm. With the higher initial jet velocity in CCM-3 a higher L/D is expected.

Questions remain to what extent the jet has broken up in small particles, i.e. what mass has been stripped or broken off in the region of the leading edge, and what particle sizes occur. This is not clear from the experiments, at least if a coherent core should still exists when the jet reaches the bottom. From the model result in /13/ complete mass stripping may be concluded until L = 58 cm (for CMM-3 the higher initial velocity must however be taken into account).

On the extent of fragmentation only some indications are given in /12/ from the experiments. No extensive breakup is concluded for CCM-2. This is partly concluded from the sintered debris showing limited corium quench during the jet fall. As possible reasons for the small breakup and quench, Wang et al /12/ state however the increased voidage due to multi-jet formation in CCM-2 and the more shallow pool. For CCM-3 a fragment mass distribution with ≈ 70-80% of mass smaller than 10 mm is given as well as a mass median debris size of ≈ 4 mm. The distribution given for CMM-2 is not considered as representative due to neglection of large reagglomerated masses. For CCM-3 approximately 8% of mass have a size (diameter) smaller than 0.3 mm and 20% smaller than 1 mm. As a general theoretical result Wang et al /13/ mention a large portion of particles $\leq$ 1 mm in diameter.

For a first calculation the conditions of CCM-3 are chosen. Fig. 14 shows the transient jet penetration calculated with the Miles and the Kelvin-Helmholtz formulations. While with

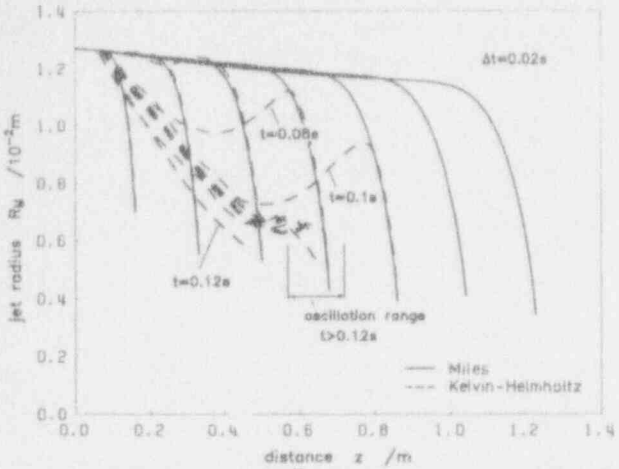

Fig.14: Transient development of jet contour calculated with the IKE model for the corium experiment CCM-3 from /12/: Comparison of results with the Miles and Kelvin-Helmholtz instability descriptions

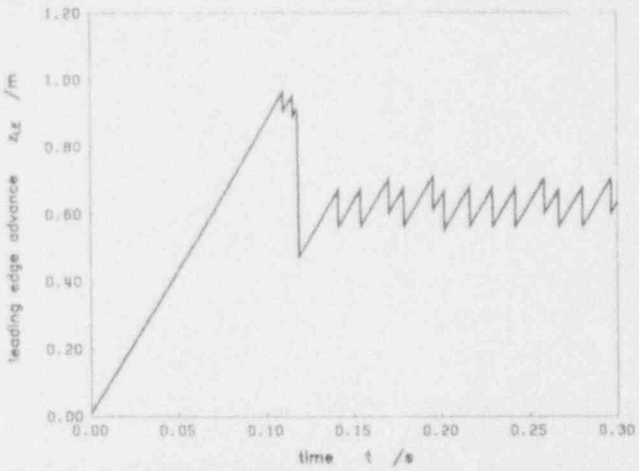

Fig.15: Leading edge advance from the calculation on CCM-3 /12/ with Kelvin-Helmholtz description

the Miles formulation a coherent jet core still exists after reaching the bottom of the vessel (water depth 1.1 m), a quasi-steady state is reached with the Kelvin-Helmholtz formulation for L ≈ 0.6 m (L/D = 24). The calculation with the latter formulation yields a slightly longer jet than the calculation in /13/ for a zero void fraction in the water. A significantly longer jet has been expected due to the higher entry velocity of the jet.

An oscillatory behavior around a quasi-steady coherent jet length can be observed in Fig. 14 for the Kelvin-Helmholtz case. In the first overshoot which is visible in Fig. 15 from the penetration curve the bottom of the vessel is practically also reached by a coherent core. The main body of fluctuations in jet length cannot be attributed to numerical effects, but results from physical effects, at least in the present model. With the low steam velocity at the leading edge only small fragmentation by stripping occurs in this region. Stripping then increases during the transient jet penetration in the upper regions with increasing steam production and thus steam velocities. By this, a thinner jet region above the leading edge is produced which can give rise to coarse break-off of the lower jet part. Indeed, this happens by support of the relatively large wavelengths resulting in this case from the Kelvin-Helmholtz formulation. By the break-off of the lower jet part according to the (still rough) present modeling the coherent jet length falls back to a length of approximately 45 cm. It increases again due to continued jet penetration and coarse break-off occurs again at the leading edge. But now, since continued penetration starts already from a thinned region the break-off happens already after much shorter distances thus leading to the smaller subsequent fluctuations around the length of L ≈ 0.6 m.

The outlined behavior may mainly be doubted with regard to three points. Firstly, taking special fragmentation effects at the leading edge into account as discussed already in Chapters II and III, a different behavior during the transient jet penetration phase may result, since the above first overshoot is essentially determined by the fragmentation extent at the leading edge. Secondly, the coarse jet breakup is at present only described in a rough manner, comparing the perturbation wavelengths (or more exactly the amplitudes of inception of stripping) with the local jet diameter. Thirdly, concerning the real behavior, the mass restriction must be taken into account, probably not allowing the establishment of the above quasi-steady state. Nevertheless, in view of the special uncertainties of the transient behavior, this quasi-steady state is here taken for further considerations. In this state specific leading edge effects should not any longer be important and stripping at the jet columns should dominate, as already argued by Spencer et al in /6/ for the Wood's metal cases.

More details on the quasi-steady state can be seen in Fig. 16, giving the jet and steam / water interface contours as well as the local distributions of steam velocities and stripped fragment sizes. Furthermore, the spatial increase of stripped mass part is given. This yields ≈ 65% of the mass inflow under steady state conditions. While the mass-averaged fragment size of 3.3 mm in diameter lies rather well in the experimental range indicated in /12/, it must be questioned whether such large particles can be really obtained in the atomization regime, i.e. in the stripping mode, only by comparing with the initial jet diameter of 2.54 cm. The model assumptions are also questioned by this (see Chapter IV). Furthermore, the experimental mass part of 20% with fragments < 1 mm is not obtained here, which can however be attributed to some extent to the special formulation of fragment size, with $\lambda/2$ for the Kelvin-Helmholtz approach in our model and $\lambda/2\pi$ according to /13/. Nevertheless, the above questioning remains in view of the large wavelengths.

With the Miles description taking $\beta_y = 0.1$, as adapted to the Wood's metal experiments, no steady state was obtained until the bottom of the vessel (Fig. 14). Thus, for more detailed inspection the state just before reaching the bottom has been chosen in Fig. 17. Again, the local distributions of the most important quantities are shown. A much smaller amount of fragmentation of approximately 11% is reached

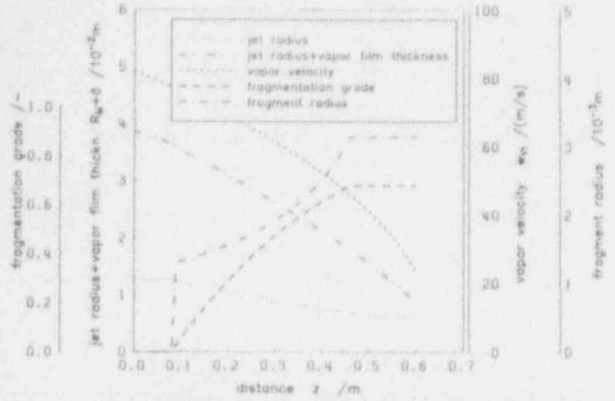

Fig. 16: Calculated spatial distributions of jet radius, vapor film thickness, steam (vapor) velocity, fragment radius and fragmentation grade for the Corium experiment CCM-3 from /12/: Quasi-steady state based on Kelvin-Helmholtz description

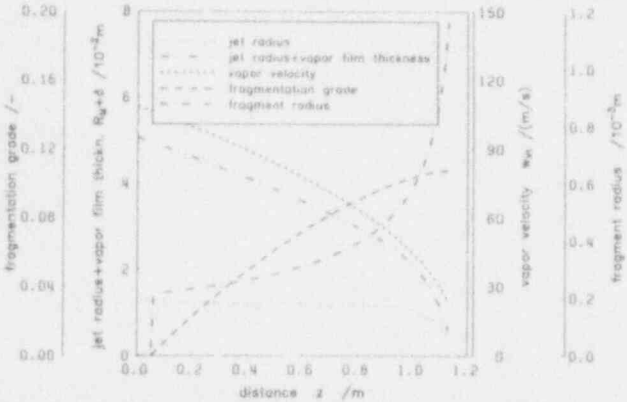

Fig.17: Calculated spatial distributions of jet radius, vapor film thickness, steam (vapor) velocity, fragment radius and fragmentation grade for the Corium experiment CCM-3 from /12/: Results based on Miles' description for a distance comparable with the depth of the experimental water pool

here, 10% with fragment sizes < 1 mm in diameter and a mean diameter of 0.7 mm. Thus, in this case, the fragment sizes based on Miles' approach (here from the more detailed stripping description outlined in Chapter IV) are much smaller than those from the Kelvin-Helmholtz approach. This is in contrast to the Wood's metal cases considered above where the relation is inverse. Such a change in the relation between the fragment sizes from the different descriptions (which occurs also for the wavelengths of maximum growing waves) has already been obtained in /17/ for fragmentation of melt jets in gas streams by variation of the gas velocity.

Extrapolating the conclusions on the different approaches from the Wood's metal experiments would mean to favor the results based on Miles' approach also for the corium case. Of course, such an extrapolation can at present only be done tentatively. A larger body of experimental data and comparisons with model calculations over a wide range of conditions would be necessary to draw firm conclusions. From the comparison with the experimental results of the CCM tests, here especially CCM-3, no conclusive result is obtained.

The result based on the Kelvin-Helmholtz formulation seems to be supported especially by the fragment sizes. A decision based on the L/D-values appears not to be possible in view of the above discussion. Concerning the fragment sizes, the result based on Miles description approximates the experimental debris smaller than 1 mm in diameter (mass part 20% from experiment, 10% between 0.4 mm and 1 mm, 10% from theory for the latter range). The question remains whether larger fragments between 1 mm and 10 mm for which a mass part of ~ 50% is given in /12/ can be attributed to additional coarser breakup or stripping processes in the range of the leading edge, not included in the model at present, or to some impact and splashing fragmentation effects when the coherent core hits the bottom wall of the vessel. According to the Kelvin-Helmholtz calculation 65% of mass should be between 2 and 7 mm as compared to the above mentioned 50% from experiment between 1 and 10 mm. Of course, this depends also on the choice of the stripping criterion itself. Since a quasi-steady state has been reached with the Kelvin-Helmholtz calculation, the remaining 35% of mass inflow break off at the leading edge within the oscillations, due to the coarse breakup criterion. Fragment sizes have not been considered for this mass part.

VII. CONCLUSIONS

The main conclusions which can be drawn from the present analysis are:

1. Experiments with jets of molten Wood's metal at low temperatures in water, excluding boiling, are essentially explained by stripping of shear flow induced waves at the columns, i.e. by breakup in the atomization regime. Contributions from coarse breakup mechanisms cannot be excluded completely, especially for the experiments with lower jet velocities. For larger jet diameters such effects should be restricted to regions where the jet has already strongly thinned.

2. This result was based on application of Miles' formulation of instability. The Kelvin-Helmholtz approach yielded much too rapid fragmentation.

3. Parametric calculations indicate that a detailed description of the vortex ball effect at the leading edge may be important for reaching better quantitative agreement with experimental results.

4. The calculated fragment sizes from both the Miles and the Kelvin-Helmholtz approaches are too small as compared with the experimentally determined ones. The uncertainties are however large and coalescence in the dense sprays must be considered.

5. If, by exclusion of the Kelvin-Helmholtz approach based on the analysis of the Wood's metal experiments, calcu-

lations for the case of corium jets into water are performed on the basis of Miles' approach, much longer coherent jets with relatively small fragmentation result.

6. From calculations performed with both approaches for the test CCM-3 from /12/ no final conclusions on the respective validity in the film boiling case can be drawn. This is due to uncertainties in the experimental results as well as in the present incomplete modeling.

7. Further work to check different approaches by comparisons of the models and with experiments is required. These comparisons must be done step by step, distinguishing between main aspects and single effects.

ACKNOWLEDGMENTS

This work was sponsored partly by the Bundesministerium für Forschung und Technologie, FRG, and the Deutsche Forschungsgemeinschaft (DFG), FRG. The authors, however, are responsible for its scientific content. The authors would like to express special thanks to the group at the JRC Ispra and especially to Dr. H. Hohmann and H. Schins for valuable informations and discussions.

REFERENCES

/1/ W.H. Amarasooriya and T.G. Theofanous, "Premixing of Steam Explosion: A Three-Fluid Model, 25th National Heat Transfer Conf., Houston, Texas, July 24-27, 1988, ANS-Proc., HTC-3, 191-200

/2/ D.F. Fletcher and A. Thyagaraja, "A Mathematical Model of Premixing", National Heat Transfer Conf., Houston, Texas, July 24-27, 1988, ANS-Proc., HTC-3, 184-190

/3/ M.F. Young, "IFCI: An Integrated Code for Calculation of all Phases of Fuel-Coolant Interactions", NUREG/CR-5084, SAND87-1048, 1987

/4/ N.I. Kolev, "IVA3: A Transient 3D Three-Phase, Three-Component Flow Analyzer", Int. Topical Mtg. on Safety of Thermal Reactors, Portland, USA, July 21-24, 1991, ANS-Proc.

/5/ D.F. Fletcher, "A Comparison of the Coarse Mixing Predictions Obtained from the CHYMES and PM-ALPHA models", Nucl. Engng. and Des. 135, 3 (1992) 419-425

/6/ B.W. Spencer, J.D. Gabor and J.C. Cassulo, "Effect of Boiling Regime on Melt Stream Breakup in Water", Particulate Phenomena and Multiphase Transport, Vol. 3, Ed. T.N. Veziroglu, Hemisphere Publishing Co., 1987

/7/ T. Ginsberg, "Liquid Jet Breakup Characterization with Application to Melt-Water Mixing", Nat. Heat Transfer Conf., Denver, Co., USA, August 1985, ANS Proc.

/8/ M.J. McCarthy and N.A. Molloy, "Review of Stability of Liquid Jets and the Influence of Nozzle Design", The Chemical Engineering Journal 7 (1974) 1-20

/9/ M. Epstein and H.K. Fauske, "Steam Film Instability and the Mixing of Core-Melt Jets and Water", National Heat Transfer Conf., Denver, Co, August 1985, ANS-Proc., 277-284

/10/ M. Saito, K. Sato and S. Imahori, "Experimental Study on Penetration Behavior of Water Jet into Freon-11 and Liquid Nitrogen", National Heat Transfer Conf., Houston, TX, July 24-27, 1988, ANS-Proc., HTC3, 173-183

/11/ B.W. Marshall, D.F. Beck and M. Berman, "Mixing of Isothermal and Boiling Molten- Core Jets with Water: The Initial Conditions for Energetic FCIs", International ENS/ANS Conf. on Thermal Reactor Safety, Avignon, France, Oct. 2-7, 1988, Proc., 117-127

/12/ S.K. Wang, C.A. Blomquist, B.W. Spencer and L.M. McUmber (ANL), J.P. Schneider (Univ. of Illinois), "Experimental Study of the Fragmentation and Quench Behavior of Corium Melts in Water", 25th National Heat Transfer Conference, Houston, Texas, July 24-2, 1988, ANS Proc., HTC-3, 120-135

/13/ S.K. Wang, C.A. Blomquist and B.W. Spencer, "Modelling of Thermal and Hydrodynamic Aspects of Molten Jet/Water Interaction", 26th National Heat Transfer Conference, Philadelphia, PA, August 6-10, 1989, ANS Proc., Vol. 4, 225-232

/14/ J.P. Schneider, M. Marciniak and G.J. Barclay, "Breakup of Metal Jets Penetrating a Volatile Liquid", Fifth International Topical Meeting on Reactor Thermal Hydraulics (NURETH-5), Salt Lake City, UT, Sept. 21-24, 1992, ANS Proc., Vol.II, 437-449

/15/ J.J. Sienicki, S.K. Wang and B.W. Spencer, "Analysis of Melt Arrival Conditions on the Lower Head in U.S. LWR Configurations", Fifth Int. Topical Mtg. on Reactor Thermal Hydraulics, NURETH-5, Salt Lake City, UT, USA, September 21-24, 1992, ANS Proc., Vol. 2, 450-460

/16/ C.C. Chu and M.L. Corradini, "One-Dimensional Transient Fluid Model for Fuel-Coolant Interaction Analysis", Nucl. Sci. and Eng. 101 (1989) 48-71

/17/ M. Bürger, E. v. Berg, S.H. Cho and A. Schatz, "Analysis of Fragmentation Processes in Gas and Water Atomization Plants for Process Optimization Purposes, Part II: Modelling of Growth and Stripping of Capillary Waves in Parallel Shear Flows - the Basic Fragmentation Mechanism", Powder Metallurgy International 1 (1992) 32-38

/18/ M. Bürger, C. Carachalios, D.S. Kim and H. Unger, "Theoretical Investigations of the Fragmentation of Drops of Melt with Respect to the Description of Thermal Detonations (Vapor Explosions) and their Application in the Code FRADEMO", Commission of the European Communities, Nuclear Science and Technology, Report EUR

10660 EN, 1986

/19/ Y.A. Ewing, "Wind Waves: A Review of Research During the Last Twenty-Five Years", Geophys. J. R. Astr. Soc. 74 (1983) 313-329

/20/ A. Benuzzi, P. Fasoli Stella, H. Hohmann and D. Magallon, "Progress of the FARO Programme. Results of the First Melt Quenching Test", CSARP Meeting, Washington DC, USA, May 4-8, 1992

/21/ S.H. Cho, E. v. Berg, M. Bürger and A. Schatz: "Experimental Investigations with Respect to the Modelling of Fragmentation in Parallel Shear Flows of Liquids", Sprays and Aerosols Conference, Guildford, UK, Sept.30-Oct. 2, 1991, Proc., 165-169

/22/ H. Schins and H. Hohmann (JRC Ispra), M. Bürger, E. v.Berg and S. H. Cho (IKE), "Breakup of Melt Jets in a Water Pool as a Key Process for Analysis of Lower PRV-Head Failure During Core Melt Accidents in LWR", Jahrestagung Kerntechnik '92, Karlsruhe, FRG, May 5-7, 1992

/23/ H. Hohmann and H. Schins: private communication

/24/ H. Schlichting, "Boundary-Layer Theory", McGraw-Hill Book Company, New York, 7th ed., 1979

/25/ S.H. Han and S.G. Bankoff, "Film Boiling from a Vertical Jet of Fuel Entering a Water Pool", Nucl. Eng. and Des. 75 (1982) 81-86

NOMENCLATURE

Symbols

A	flow cross section
c_D	drag coefficient
c_i	growth factor, from imaginary part of complex wave velocity
c_r	wave velocity, real part of complex wave velocity
D	diameter
f	factor on stripping rate
g	constant of gravity
h	latent heat of evaporation
k	wave number
K_{eff}	effective roughness height
L	length of jet
$\dot{m}_v$	evaporation mass rate per surface area
$\dot{M}$	stripped mass per jet length interval and time
$\hat{p}$	amplitude of complex perturbation pressure
R	jet radius
Re	Reynolds number
t	time
T	temperature
We_a	ambient Weber number, $We_a = \rho_K \cdot w_{rel}^2 \; D / \sigma$
w	velocity
w^*	shear stress velocity
x	coordinate along jet axis (moving jet system Fig.2b)
y	coordinate perpendicular to the jet axis
y_{eff}	geometrical parameter contained in shear flow velocity profile
z	coordinate along jet axis (laboratory system, Fig. 2a)
α_r	radiation heat transfer coefficient
α_J	coefficient in perturbation pressure amplitude
β_J	"sheltering parameter" (coefficient in perturbation pressure amplitude)
δ	thickness of vapor film
ε	emissivity
$\hat{\eta}$	wave amplitude
γ	density ratio ρ_K/ρ_M
κ	v. Karman's turbulence constant
λ	wavelength
μ	dynamic viscosity
υ	kinematic viscosity
ρ	density
σ	surface tension
σ_B	Stephan-Boltzmann-constant
τ	shear stress

Subscripts

c	critical layer
eff	effective value
K	fluid surrounding the jet
l	laminar
LE	leading edge
M	melt
m	maximum, dominant
rel	relative
S	saturation
t	turbulent
tr	transition
V	vapor
W	water
o	initial state
∞	infinity

Superscripts

$\bar{}$	mean value

VALIDATION OF CHYMES: SIMULANT STUDIES

R W Hall
Nuclear Electric plc
Berkeley Technology Centre
Berkeley, Glos., GL13 9PB
UK

D F Fletcher
AEA Safety & Reliability
Culham Laboratory
Abingdon, Oxon., OX14 3DB
UK

ABSTRACT

The CFD code CHYMES models the initial mixing between core material and water in the lower plenum of a PWR. This paper reviews experiments to validate the code being carried out by Nuclear Electric and Oxford University. These experiments use isothermal and hot simulant fluids and particles in a thin-tank geometry to aid flow visualisation. Comparison with CHYMES calculations (made at Culham Laboratory) shows that the code underpredicts the spreading in these experiments. It is believed that turbulent flow fields are assisting spreading, and that the accumulation of vapour in the wakes of hot droplets may be increasing the coupling between the phases.

I. INTRODUCTION

The CFD code CHYMES (Thyagaraja & Fletcher, 1988; Fletcher & Thyagaraja, 1991) models the initial mixing between molten core material and water in the lower plenum of a PWR. It is being used to help assess the probability of a damaging steam explosion following a gross core-meltdown, and hence aid quantification of a Containment Event Tree for a recent probabilistic safety study (Turland et al., 1993). As part of the validation and independent assessment of the code experimental and theoretical work is being conducted at Berkeley Technology Centre (formerly BNL); and the University of Oxford. The experimental studies are progressively working from simple isothermal systems, where the principal flow phenomena are better understood, towards hot simulant melts producing high rates of vapour generation; the programme is thus complementary to the Winfrith MIXA validation tests which use prototypic materials (Fletcher & Denham, 1993). A further feature of the experimental work has been the use of thin slab-sided ('2-d') transparent tanks, to aid the viewing of the various phases. Some confirmatory work in cylindrical ('3-d') geometries has also been performed.

II. REVIEW OF ISOTHERMAL EXPERIMENTS

II.A. Early BNL Work with Small Particles

Ms Lyell et al. (1990) investigated the behaviour of swarms of small glass and steel particles falling through water in a thin slab-sided transparent tank (1m high by 0.5m wide). The gap width of the tank was chosen to be only 10 to 20 percent greater than the ball diameter, except for the smallest particles studied (100 micron) for which a gap of 6mm was chosen. The principal instrumentation was CCTV recording with strobe illumination (GenRad type 1539), giving 50 pictures per second (pps) with 10-microsecond resolution. The smaller particles were introduced into the tank as a slurry from a nozzle, typically 1 to 2cm in diameter. However, the largest particles (6mm) were introduced in a more controlled fashion, (dropping in rows of 9 from a sliding tray), to minimise the effects of early collisions between balls.

Lyell et al. characterised their measurements in terms of the ratio of the slip velocity of single particles to the observed rate of fall of a swarm. They found that the behaviour of the swarms of the smallest size of balls studied (100 micron) followed that expected of a miscible fluid without surface tension (Fig 1a). A large head vortex (or 'starting plume') formed at the leading edge of the injected flow, and the probable similarity to the structure of a line-thermal (Fig. 1b) was noted; the spreading of the following plume (due presumably to the turbulence induced in the entrained flow) was also significant. Conversely 6mm steel balls, whose density and size were expected to be similar to those of UO_2 particles in the reactor case, showed only a very small rate of spread and no distinct head was formed. However, the balls in the packet were quite spread-out along the line-of-flight, and this would tend to reduce the rate of spread (Gilbertson et al. 1990). Finally,

glass beads in the millimetre size range, whose slip and fall rates were estimated to be comparable, showed intermediate behaviour, but with a distinct head (Fig 2), and discernable spread of the main plume.

II.B. Oxford University - Work with Small Particles

This work is being performed for NE by Dr Kenning and Mr Gilbertson of Oxford University Department of Engineering Science, and features both isothermal and heated-particle tests. The isothermal experiments performed to date represent a significant extension of the preliminary work of Lyell et al. A description of the apparatus and results from the experiments are given in more detail by Gilbertson et al. (1992). In brief a belt-mechanism has been developed for injecting steel or aluminium balls (6mm diameter) into a '2-d' tank (1m x 0.5m x 8mm nominal). Up to 10 rows can be injected, at velocities up to 2m/s. Observation is by high-speed (200pps) video recording. Typical results for steel balls (Fig 3) show a large and distinct 'starting plume', but there is very little spread of the following plume. For aluminium balls the spreading of the head is accentuated, presumably due to the lower density, and there is some evidence of a developing sinuous instability in the following plume.

II.C. BNL Work with Mercury/Water Systems

Gilbertson et al. (1990) studied the isothermal pours of mercury into water in a 2-d configuration. The tank (1m high by 0.5m with a gap of 3mm) contained about 1500ml of water and 20ml of mercury, and could be set at various angles to the vertical. In most of the observations a funnel was used to collect and direct the flow of mercury (typical results Fig 4 - tank inclined at 45 degrees); the exit orifice could be varied in width between 5mm and 20mm. A number of observations were also performed with the funnel absent, so that the breakup of a circular drop (the '2-d' analogue of an accelerating spherical particle) could be studied. Strobe-illuminated CCTV at 50pps was used to record the events.

Gilbertson et al. found that breakup lengths for jets and drops appeared consistent with 3-d data and that after breakup had occurred the dispersed mercury behaved in a qualitatively similar fashion to a collection of discrete solid particles - for instance a dispersed 'starting plume' formed which was of larger lateral spread than the following plume. The spread of the following plume was consistent with its being due to the turbulence field set up in the water phase by the shear between the entrained and stagnant liquid, when appropriate allowance was made for the 'crossing-trajectories' effect (the effect, discussed by Lumley (1978), reduces the turbulent transverse diffusion rate of a dense particle by the ratio of the local velocity of the carrier fluid to the total velocity of the particle).

The initial speed of fall and rate of spread of the unfragmented mercury was also considered and shown to be as expected:- the spreading mechanism for the lens-shaped head which forms initially is similar to that in the dispersed case, (ie due to the flow diversion at the stagnation point between the pool fluid and injected/entrained flow). However, the drag on the front lens is due to flow separation whilst in the dispersed case it is expected (by analogy with the single-fluid plume case, see Briggs, 1975) to be due to entrainment into the fluid mixture.

II.D. Comparison with CHYMES - results & discussion

The scoping analysis of the isothermal data conducted by Gilbertson et al. (1992) suggested that the behaviour of both the mercury-water and dispersed particle flows could be understood qualitatively using elements of classical plume theory. Separate studies (Fletcher, McCaughey & Hall, 1993) have shown that CHYMES, with laminar viscous terms added, is capable of giving good agreement with other 'state-of-the-art' single-phase codes when calculating single-phase transient plumes in the non-turbulent regime; however, it is not optimised for turbulent two-fluid jet problems presented by the mercury-water data. The Oxford and BNL experiments with pre-dispersed particles are preferable in this regard. Gilbertson et al (1992) made detailed comparison of the Oxford isothermal data with CHYMES calculations and found that an adequate fit could be found if an enhanced drag coefficent of about 2 were used (see Fig 5). This fourfold increase over the single-particle value was at the upper end of the range attributable to co-operative phenomena. The authors considered that the effect could instead be occurring because the induced water flow, dragged with the balls, was turbulent; the induced flow would thus be spread wider, and would travel slower, than calculated by CHYMES.

The small-scale glass-particle ('ballotini') data taken by Lyell et al, have also been compared with CHYMES calculations. Both single-particle and enhanced drag values have been used. Although there is qualitative agreement (see Fig 6), it is clear that there are still significant quantitative differences in the penetration velocity, and in the extent of spread of the main plume and the 'starting plume'. Separate studies by Fletcher have shown that the degree of sideways spreading of the starting plume is quite sensitive to the noding chosen, with a coarse noding showing little spreading. This is probably because several (~5) nodes are needed across the jet diameter to properly resolve the stagnation point at the leading edge. The discrepancy in predicted penetration rate is presumably because

the code does not allow for the widening and slowing of the flow in the main plume due to entrainment; the full dynamic head of the flow thus impinges at the front stagnation point, enhancing penetration.

III. EXPERIMENTS WITH HOT SIMULANT MATERIALS

III.A. BNL Single-Nozzle Tests

The first series of molten-tin/water tests (Hall & Brown, 1992) used a geometry similar to that of the isothermal mercury/water tests. Tin from an electrically heated furnace flowed through a single nozzle into a narrow-width tank; typical tank dimensions were 1m by 0.5m by 4.5mm, with a nozzle width of 15mm by 4.5mm, although some measurements in a smaller tank (0.3m by 0.3m by 6mm) were also made. Water was circulated via an external heater and was also heated within the tank. Water temperatures, measured by thermocouples at four points in the tank, typically varied from the mean by 1C. Tests were also performed in a cylindrical geometry; typical tank dimensions were 300mm diameter by 1m high, with a single nozzle of 14mm diameter. Water temperatures in the range 70 to 99C and tin temperatures in the range 450 to 800C were explored.

A typical sequence from the strobe-lit video recordings in Fig. 7a shows a pour of 100ml of tin at 700C into the larger (1m high) tank, containing water at 94C. (The water is dyed with fluorescein to aid discrimination of the steam void. Fig 7b shows a comparable experiment in which the water was undyed). Note the two extension pieces on the nozzle, which were fitted to minimise drawdown of air from the free surface during the initial transient.

Detailed measurements were made of the rate of fall and rate of spread of the dispersed flow (both 'head' and 'plume' regions, in so far as these could be distinguished) - see Fig 8 for typical results. The following were the key conclusions:-

Qualitatively the results were similar to the mercury/water work, but with the additional vapour phase collecting preferentially in the wake of the tin droplets, which in general took up a lenticular form.

Breakup lengths for the tin-jets were estimated from the closest point of breakup to the nozzle. Typical values (non-dimensionalised using the usual Taylor definition) of about 3.5 were found, compared with about 5 in the isothermal work; it was suggested that this reduction could be due to disturbance by boiling-bubbles near the entry region of the jet, promoting earlier breakup.

Triggering of an fci occurred in many events, and appeared most likely on first contact of melt with surfaces. The data did not appear to support a model, advocated by some workers, in which the probability of triggering is an independent event for each melt droplet.

The initial flows showed the qualitative features of single phase plumes, but the angles subtended at the nozzle ('spreading angles') by the starting-plume ('head') and by the main plume were in general more similar than in the isothermal work, and indeed the head was in some cases smaller. The spreading angles of the 'main plume' and 'starting plume' were both estimated to be about 15 degrees, compared with the value of 10+/-2.5 degrees derived for the main plume in the isothermal pours, and about 3 times this for the 'starting plume'. In the 3-d pours the head was in general less marked in wide cylinders than in narrow ones, suggesting that interaction with the 'return current' (the upflow of water displaced by the falling metal, entrained water and vapour) can be a major cause of broadening. (The effect of the return current on spreading and penetration rates, also appears to be visible in the latter stages of tests in the large '2-d' tank.)

The vapour was estimated to have three possible effects. Firstly it would increase the effective volumetric flow of material in the plume and thus increase the return current in the tank. Secondly, the integrated vapour source within the mixing region would drive a flow of water away from the axis of the plume which would tend to carry the metal droplets with it. Without detailed code comparison these two effects would appear similar in producing an enhanced rate of spread. However, neither effect could be positively identified in the tests. It was calculated that the radial flow driven by the vapour flux could, in the absence of condensation sinks, drive a radial spread comparable with the isothermal spreading mechanisms identified in the mercury/water tests.

Thirdly, the presence of void was expected to decrease the mean fall/penetration velocity. Considerable variability was found in the penetration rate of the front, with values ranging from 0.8 to 2m/s, and in rate of widening (expressed as a ratio of head width to depth of penetration). (Fig. 8 shows three typical results, for a water temperature of 96C; tin temperatures were 600C, 700C & 710C respectively). Faster penetration rate appeared to be weakly correlated with broader spreading angles. The average fall velocity in the 'large' tank (1m x 0.5m x 4.5mm) was similar to that in the isothermal tests (1.4m/s versus 1.5m/s), showing that any slowing of the water phase in the plume by the steam void was small. However, a series of measurements in a smaller tank (0.3m x 0.3m x 6mm), in which the penetration rate remains more constant during a run, gave a smaller mean velocity (1.1m/s).

Fletcher et al (1993) made calculations of the penetration rate and rate of widening for single-phase 'starting-plumes' and found that these were sensitive to the boundary conditions at inlet. This sensitivity, which was attributed to the variation in effective initial separation of the vortex pair set up at the leading edge of the plume, could in part explain the variation of penetration and widening rates observed experimentally. However, on this model, faster penetrating plumes would be narrower, whereas a weak correlation (+0.17) in the opposite sense is observed in the 'large tank' data.

III.B. Multi-Nozzle Tests

III.B.1. Experiment & Results

The single-nozzle tests are a useful set for comparison with the isothermal mercury/water studies. However, they are not ideal for direct comparison with CHYMES which has been optimised to deal with a predispersed droplet field. A better approximation to a predispersed field is achieved in the latest completed series of experiments (Hall & Brown, in prep.), in which the tin issued from 5 parallel nozzles (7mm wide, 14mm separation) into a 1m square slab-sided tank, of 4.5mm nominal gap. Typically, 100ml of tin at 800C have been poured into water at up to 99C. In the last few runs particular care was taken to achieve conditions near saturation in the tank, and temperatures in excess of 99C were recorded on all five thermocouple in the water. Momentum diffusers within the tin-nozzle ensured approximately equal flow from each jet.

Video frames from a typical experiment (run 11, 795C tin, 99.5C water) are shown in Fig. 9. An electronically-shuttered camera was used, (Sony type XC711P, 1/10,000th sec. time resolution), because the tank area was too great to be adequately lit by the strobes available. (In these experiments it was necessary to use a subsidiary support for the tank at half height to reduce the bowing due to hydrostatic head - the marks on the glass, also visible in Fig. 9, show contours of equal tank width.)

It can be seen that the breakup length of the tin jets is small compared with the tank height, so that the flow may be taken as predispersed for code comparison purposes. (Detailed videos, taken of the flow in the nozzle region, will allow the initial breakup and dispersion to be studied in detail.)

Results for penetration and spreading rates for the leading edge material are shown in Figure 10, for the last three runs. These again show significant variability, but it is clear that the spreading rate is much higher than achieved in the earlier tests. The penetration rate is typically under 1m/s. From the videos, there is little difference between the envelope traced out by the leading particles and that followed by subsequent material (contrast the behaviour of isothermal flows), with no strong differentiation between 'starting plume' and 'main plume'. At the edges of the plume individual particles of metal can typically be followed for several frames before losing their identity through splitting or coalescence. Those at the leading edge are again lenticular with vapour in their wake and appear to undergo a slow 'rocking' motion as they fall, similar to that described for bubble sizes in the mm range by Clift et al (1978). (By contrast, drops in the MIXA tests appear to be spherical (Denham, private communication), rather than flattened - it may be significant that in the tin/water tests the tin drops enter at low velocity and accelerate, so that drop deformation and breakup occurs progressively as the droplets fall, whilst in the MIXA tests the reverse is true, and most breakup will occur near the water surface.) Droplets some distance behind the front undergo a more complex motion and splitting and recoalescence occur frequently. The complexity of these motions is greatest in the void-rich central regions of the flow where some particles are swept upwards for a time.

III.B.2. CHYMES Calculations

Fig 11a shows a CHYMES comparison calculation performed by Dr Fletcher, using standard drag laws. A comparison calculation in which vapour generation was suppressed shows almost identical predictions for the melt phase (ie no substantial effect from vapour generation is predicted). The calculated sideways deviation is much less marked than that observed, and the penetration rate is too rapid. (The calculation is for a slightly smaller tank, 1m by 0.5m, than used, but this would be expected to increase the predicted spread.) Calculations made for an enhanced drag coefficient (C_d=2, a fivefold increase on the default value) show a slightly reduced pentration rate and enhanced rate of spread, but it is clear that the calculated flow still differs markedly from that observed.

III.C. Iron-water tests - Preliminary Results.

In an attempt to bridge the temperature range between conventional simulants and prototypic materials, tests are under way in which typically 3.5kg of iron at 2000C, produced by the thermite reaction, is released into a cylindrical tank of water (1m high by 300mm diameter). Stills from a preliminary experiment (95C water temperature) are shown in Fig.12. The iron was introduced via a momentum diffuser and a droplet spreader, comprising a 4 by 4 array of 10mm diameter holes on 20mm centres. The flow is in consequence rather dilute. However, the rate of penetration in the two tests performed to date is significantly lower (0.9m/s) than that in the equivalent tin tests (typically 1.5m/s), which may be due to the strong influence of the void. (Detailed void fraction measurements are not practicable in this geometry; however, the void

generation and accumulation behind the thermite drops can be clearly seen in the videos.) In addition there appears to be some hold-up of the main body of the melt (a phenomenon observed in the early MIXA tests, Denham et al.,1992).

IV. DISCUSSION

The BTC/Oxford experiments show a clear evolution from turbulence controlled dispersion (eg Lyell's isothermal work with smallest size of beads) to unequivocally vapour-controlled phenomena (late stages of multi-nozzle pours). It is to be expected that CHYMES will underpredict the former effect, since its standard version has neither viscous nor Reynolds' stress terms, although these could probably be added fairly straightforwardly for these simple problems.

The lack of a turbulence model in the code should not affect two key results from the reactor-scale calculations, namely the demonstration of the presence of substantial void in the melt immediately prior to any explosion and guidance on fall rates. It might affect calculation of detailed mixture ratios. However, even here it is possible that turbulence may be a significantly less important phenomenon for very hot melts - the turbulence field is generated in regions of velocity or density difference and convected with the mass flux, which is proportionally much lower through a melt front of prototypic materials than it is through a region of falling isothermal particles. The addition of a turbulence field would however facilitate the validation of the code against small-scale experiments or against experiments using simulants whose melting point is significantly below prototypic.

There is also the possibility, suggested both by our own latest work and some of the Winfrith MIXA tests (Denham et al., 1992, Fletcher & Denham, 1993), that CHYMES' drag laws presently underestimate the coupling between hot particles and their vapour. Similar evidence for tight coupling between the phases was shown in the Winfrith aluminium/water THERMIR tests (Fry & Robinson, 1979), where the incoming jet of molten metal was observed to undergo, at all stages of the pour, a rapid sideways spread as it entered the water. The preferential association of vapour with the region behind a lenticular hot drop has been a feature of our hot experiments on all scales, and appears to lead to a composite entity whose effective mass is low. An apparently similar phenomenon ('the inverse Leidenfrost effect') around very hot debris particles of laser-melted metals was reported by R S Hall et al. (1969). Again, these may be mainly small-scale phenomena, since in large scale prototypic events high vapour velocities may be expected to overcome surface tension forces and homogenise the void distribution.

V. CONCLUDING REMARKS

The series of experiments using simulant materials in flat tank geometries conducted at BTC and Oxford have allowed the detailed motion of the phases to be studied in more detail than is possible in the MIXA tests. These tests have shown that CHYMES tends to underpredict sideways-spreading rates and overpredict penetration rates. Two physical phenomena, not modelled in the code, may be responsible for this. These are the probable role of turbulent flow fields in assisting spreading and the possible role of the vapour which is observed to accumulate in the wake of a hot drop in increasing the role of inter-phase drag forces. A proper understanding of these mechanisms is probably required only if codes are to be used for predicting detailed fuel/coolant/steam ratios in explosion regions, but other key predictions of the codes, such as fall time and gross void distribution, are probably less sensitive.

VI. ACKNOWLEDGEMENT

This paper is published by permission of Nuclear Electric plc.

VII. REFERENCES

Briggs G A (1975) 'Plume Rise Predictions', USNOAA Report ATDL 75/15

Clift R, Grace J R & Weber M E (1978), 'Bubbles, Drops & Particles', Academic Press

Denham M K, Tyler A P & Fletcher D F (1992), ANS Proc. 5th Int. Topical Mtg. on Reactor Thermal Hydraulics (NURETH-5), pp1667-1675

Fletcher D F & Denham M K (1993), CSNI Specialist Meeting on FCI, Santa Barbara, January 1993

Fletcher D F, McCaughey M & Hall R W (1993), 'Numerical Simulation of a Laminar Jet Flow', submitted to Applied Math. Modelling

Fletcher D F & Thyagaraja A (1991), Prog. Nucl. Energy, 26, pp31-61

Fry C J & Robinson C H (1979), Proceedings of 4th CSNI Specialist Meeting on FCI, CSNI Report no. 37, vol 2, pp329-362

Gilbertson M, Hall C M, Hall R W, Hill K S (1990), Nuclear Electric Internal Memo. (TD/STB/MEM/0119)

Gilbertson M A, Fletcher D F, Hall R W & Kenning D B R (1992), 'Isothermal Coarse Mixing: Experimental & CFD Modelling', presented to UK National Heat Transfer Conf. Sept. 1992

Hall R S, Board S J, Clare A J, Duffey R B, Playle T S & Poole D H (1969), Nature, 224, pp266-267

Hall R W & Brown G E (1992), Nuclear Electric Internal Memo (TD/NS/MEM/0397)

Hall R W & Brown G E (1993), Nuclear Electric Internal Memo - in preparation.

Lumley J L (1978), Art. 7 of 'Turbulence', ed. Bradshaw P, Springer-Verlag

Lyell Ms F, Hall R W, Hill K S (1990), Nuclear Electric Internal Memo. (TD/STB/MEM/0129)

Thyagaraja A & Fletcher D F (1988), Computers & Fluids, 16, pp59-80

Turland B D, Fletcher D F, Hodges K I & Attwood G J (1993), CSNI Specialist Meeting on FCI, Santa Barbara, January 1993

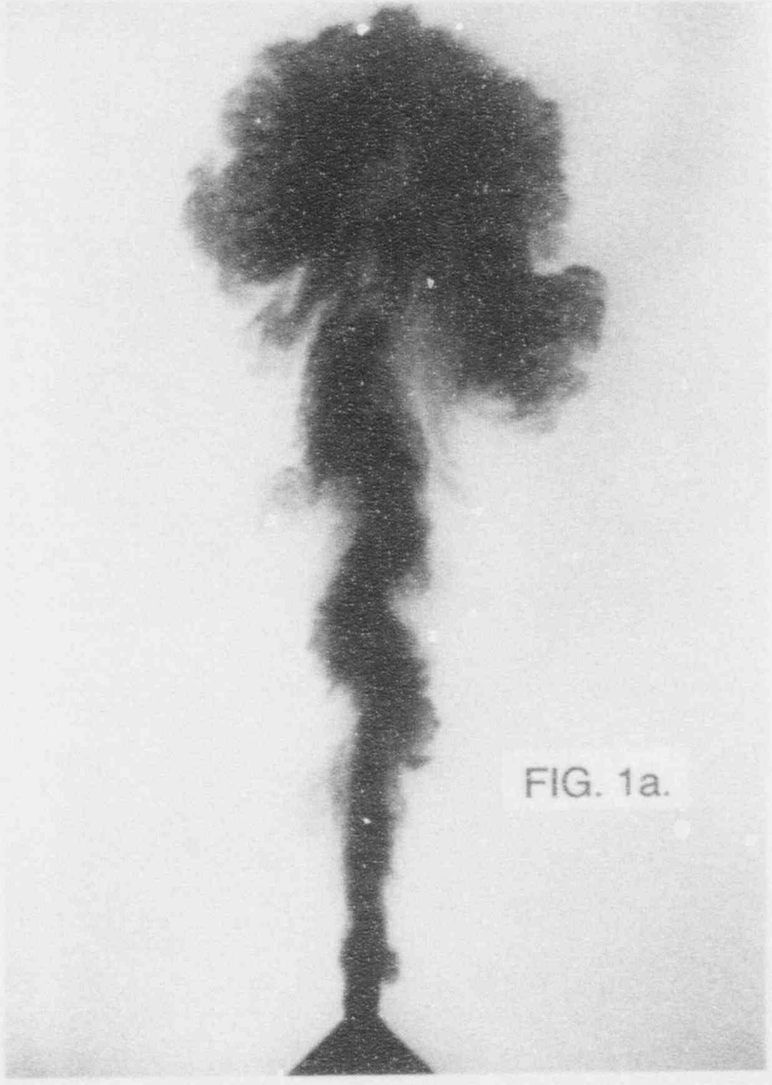

FIG. 1a.

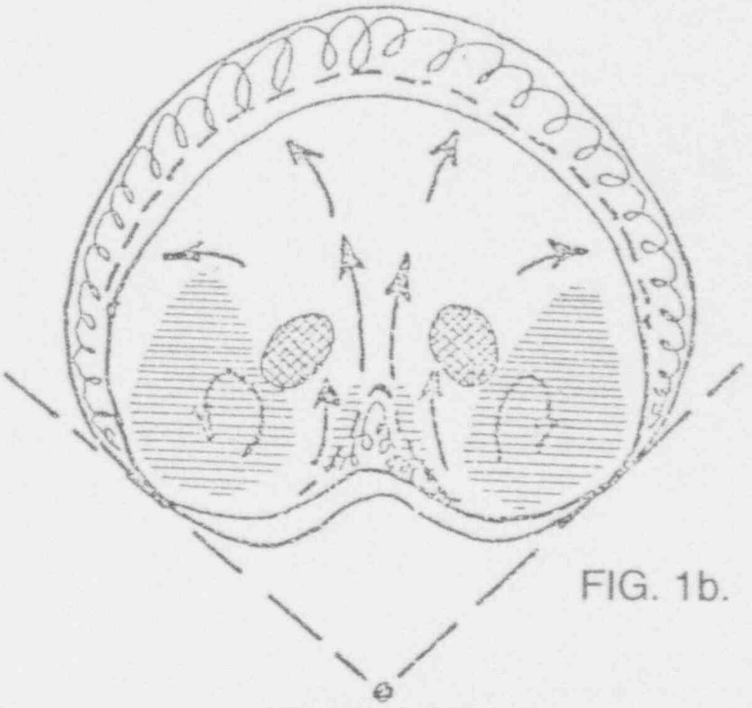

FIG. 1b.

Virtual Origin

Structure of a line thermal. Solid lines show thermal shape at two successive times. Dashed line shows advance of thermal boundary due to mean motion. Remainder of advance assumed due to turbulent entrainment, shown by curls. Arrows show streamlines of mean motion relative to center of widest part of the thermal. Horizontal hatching indicates high vorticity regions. Cross hatching indicates concentration maximums.

FIG. 1. FLOW OF a) 0.1mm GLASS BALLS AND b) LINE THERMAL (BRIGGS 1975)

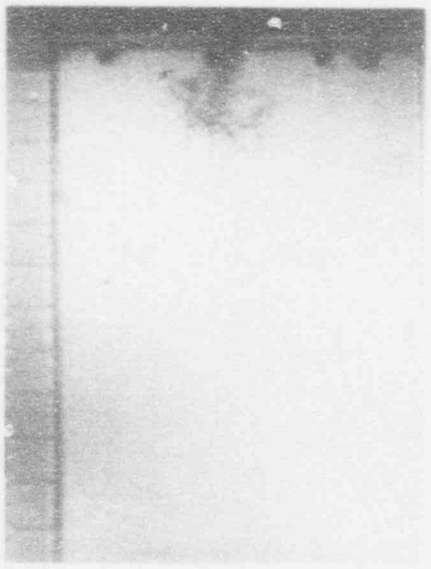

a 0.2s

b 0.4s

c 0.6s

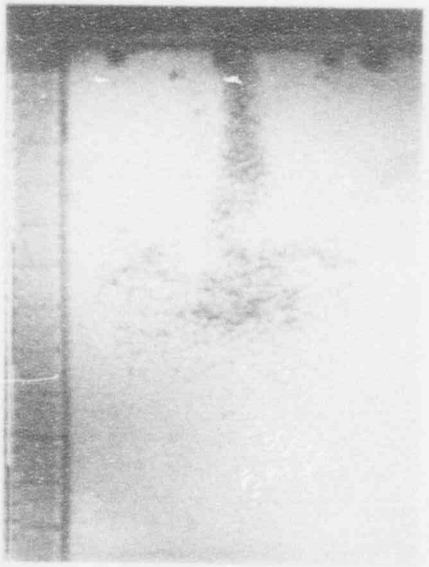

d 0.8s

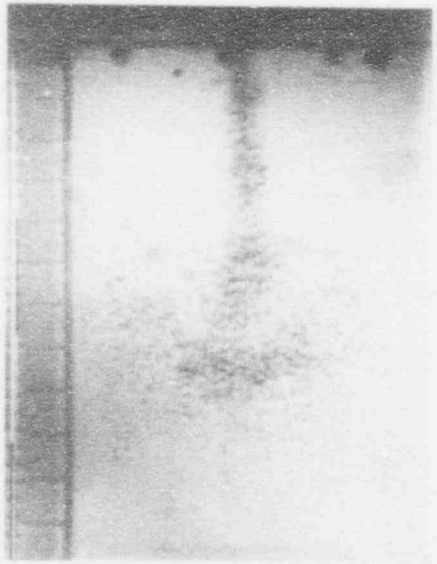

e 1.0s

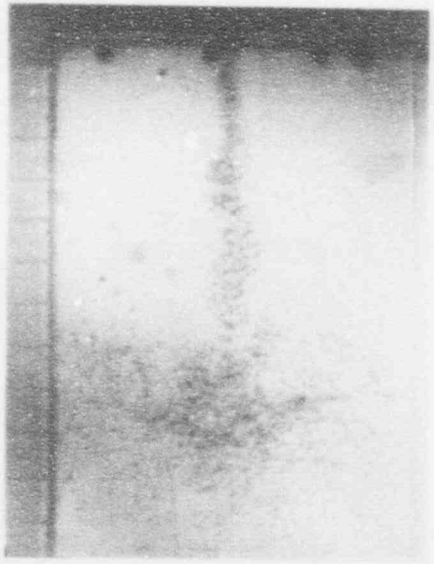

f 1.2s

FIG. 2. RESULTS OBTAINED WITH 1.2mm GLASS BALLS

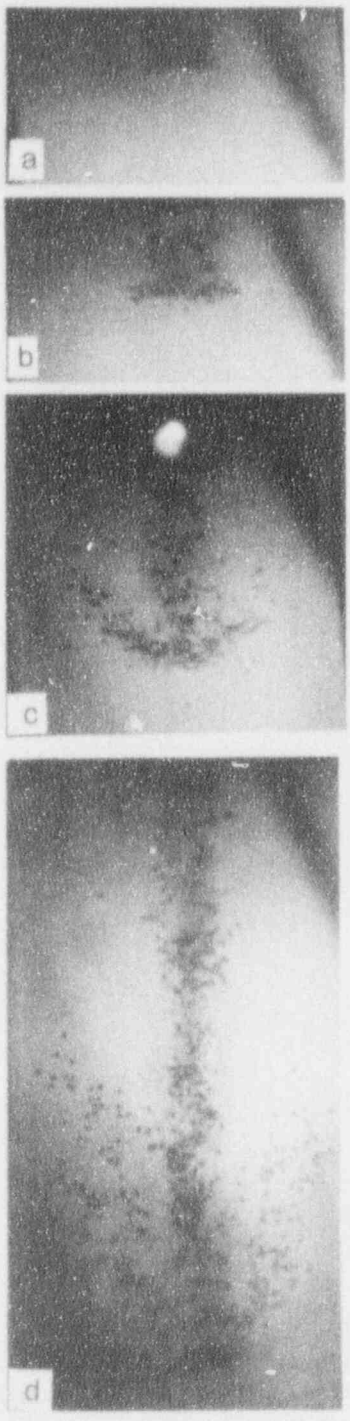

Stainless Steel
Entry Velocity 1.7m/s
Time (a) 0.06s (b) 0.13s
(c) 0.39s (d) 0.78s

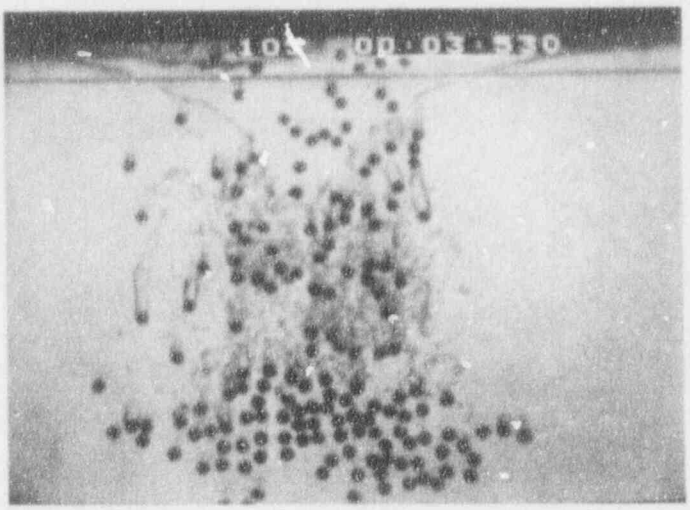

Stainless Steel
Entry Velocity 1.7m/s
Time 0.16s

Stainless Steel
Entry Velocity 1.9m/s
Time 0.80s

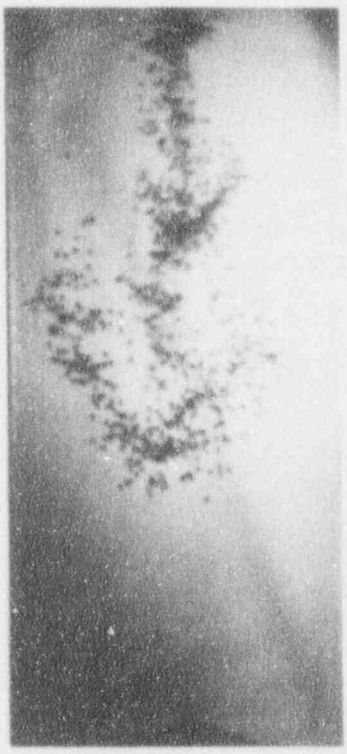

Aluminium
Entry Velocity 1.7m/s
Time 1.12s

FIG. 3. OXFORD BALL-BEARING EXPERIMENTS
TYPICAL RESULTS (GILBERTSON ET AL. 1992)

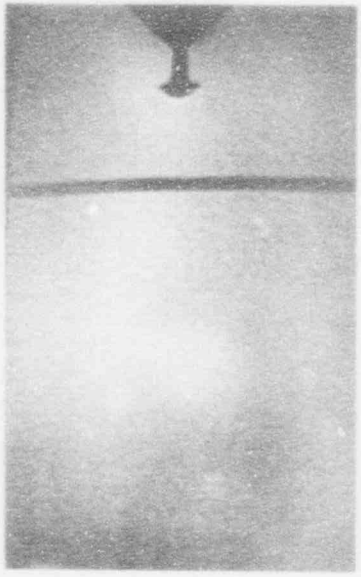

a 0.2s

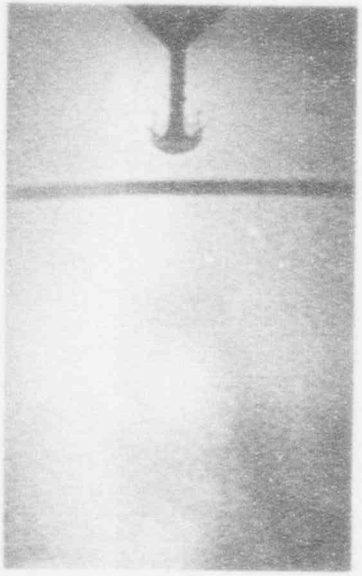

b 0.3s

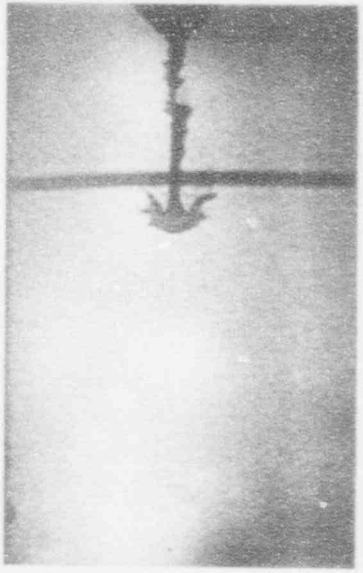

c 0.4s

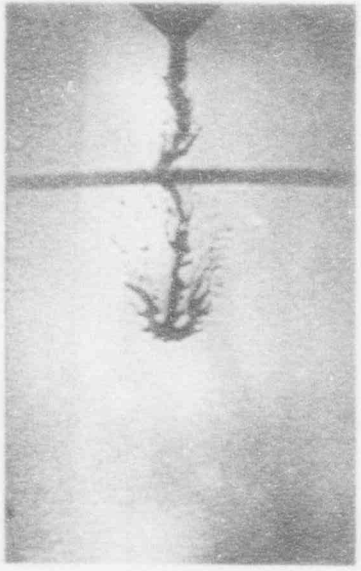

d 0.5s

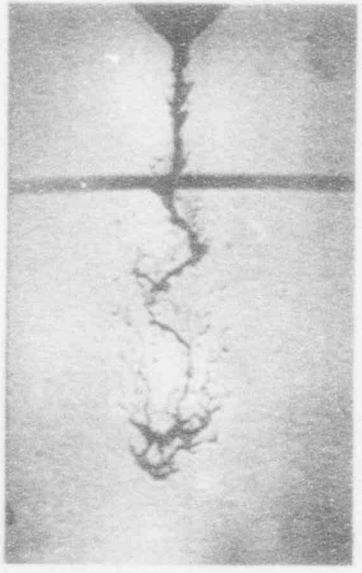

e 0.6s

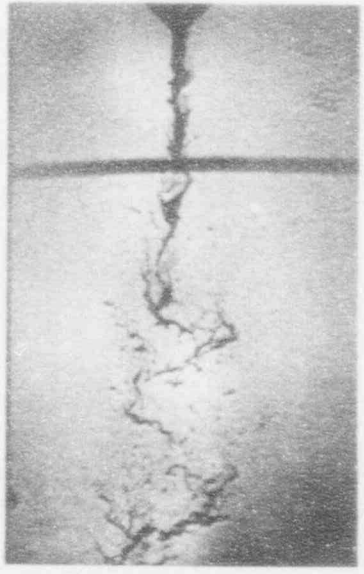

f 0.7s

FIG. 4. BREAKUP OF 20mm MERCURY JET IN WATER

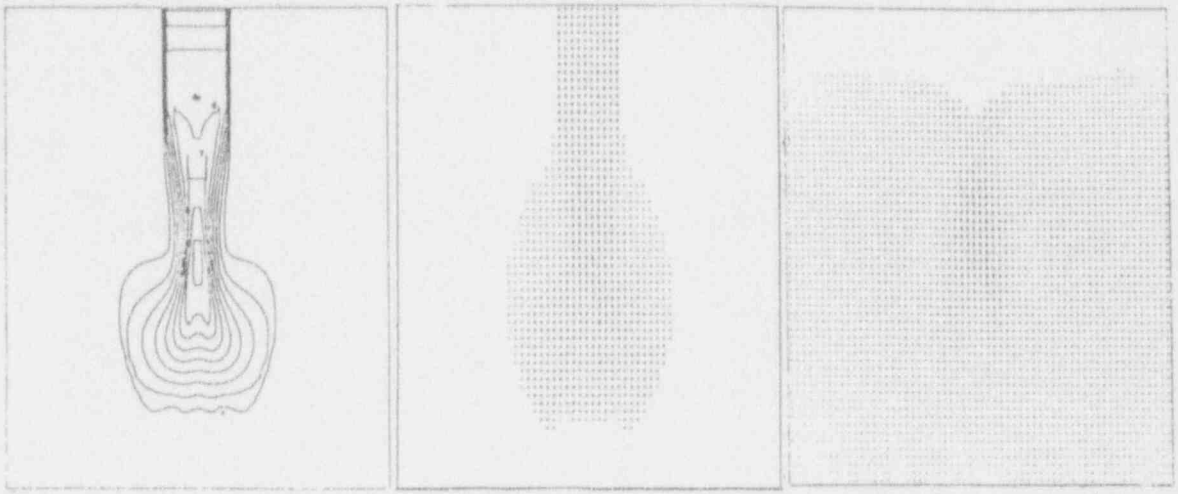

(a) C_{ij} eqn(6), α solid (b) solid velocity (c) water velocity

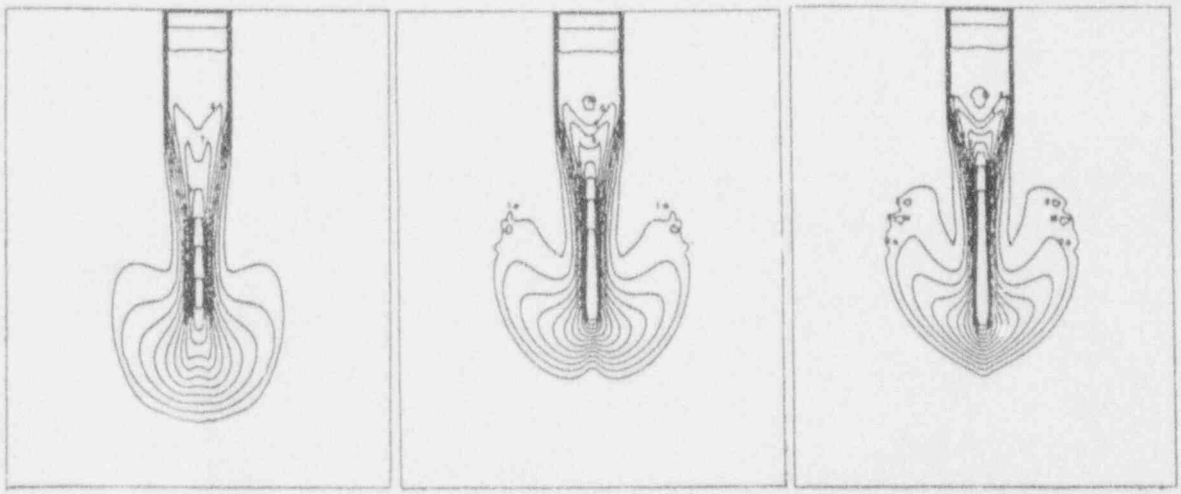

(d) C_{ij} 1.0, α solid (e) C_{ij} 2.0, α solid (f) C_{ij} 3.0, α solid

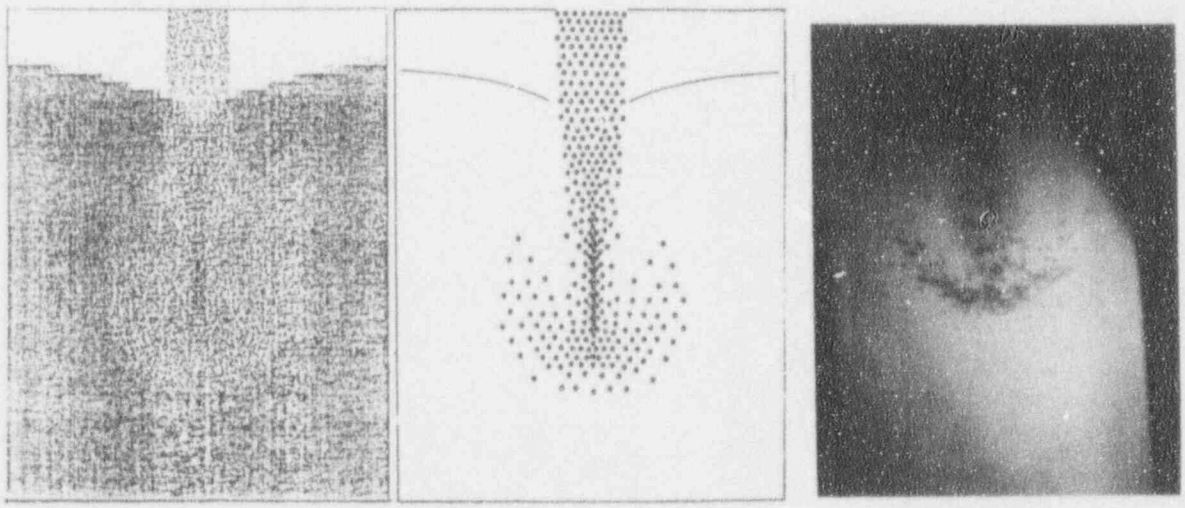

(g) C_{ij} 2.0, α solid shaded grid cells (h) C_{ij} 2.0, α solid scaled dots (j) experiment

FIG. 5. CHYMES CALCULATIONS FOR OXFORD EXPERIMENTS - VOLUME FRACTION OF BALLS AFTER 0.4s (GILBERTSON ET AL. 1992)

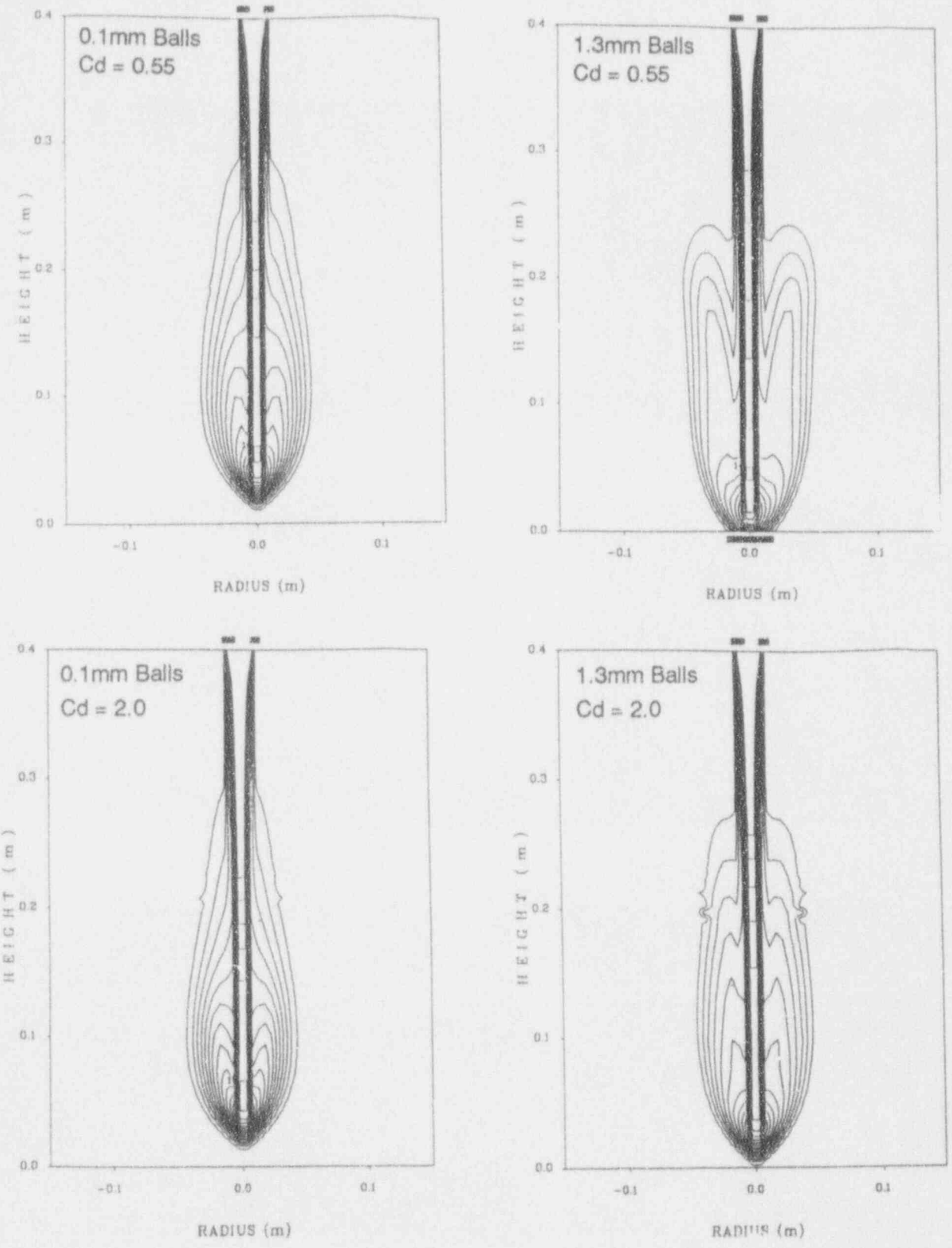

FIG. 6. CHYMES CALCULATIONS FOR GLASS BALLS EXPERIMENTS - VOLUME FRACTION OF BALLS AFTER 0.6 SECONDS

a 0.1s

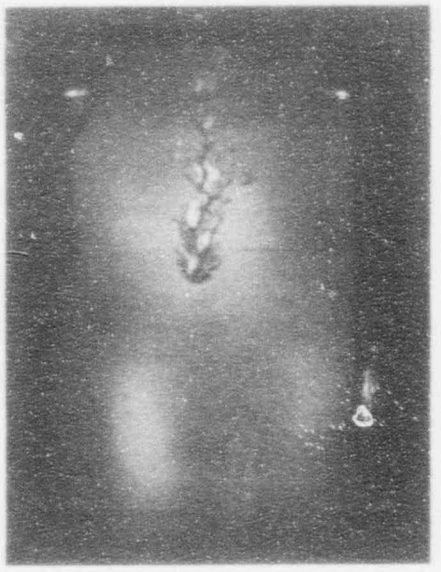

b 0.2s

c 0.3s

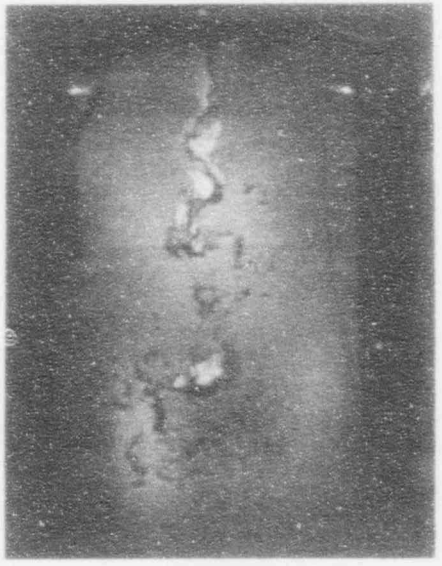

d 0.4s

e 0.5s

f 0.6s

FIG. 7a. SINGLE NOZZLE POUR (710°C TIN INTO 94°C WATER)

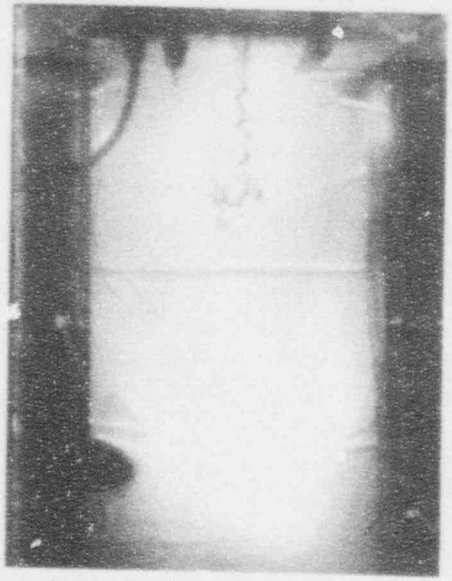

a 0.2s

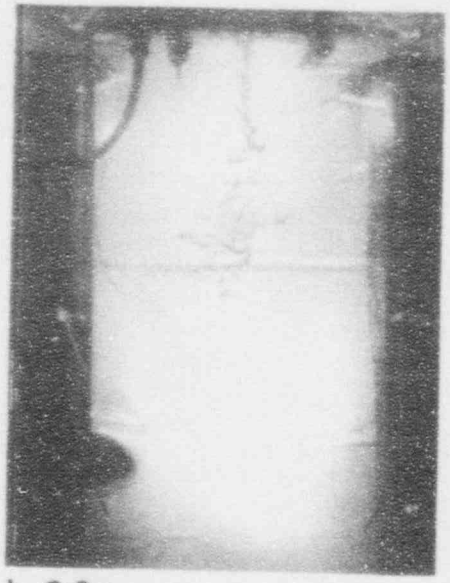

b 0.3s

c 0.4s

d 0.5s

e 0.6s

f 0.7s

FIG. 7b. SINGLE NOZZLE POUR (710°C TIN INTO 96°C WATER)

Run 10.

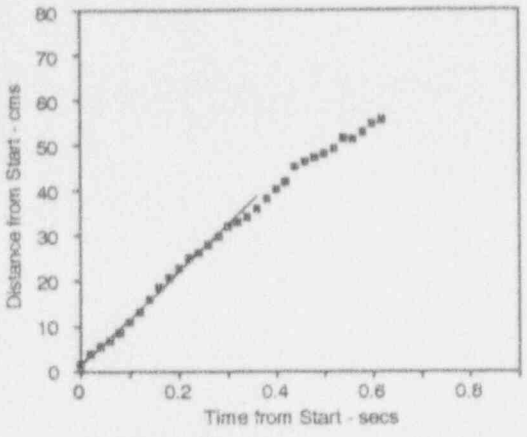

a) Rate of Fall

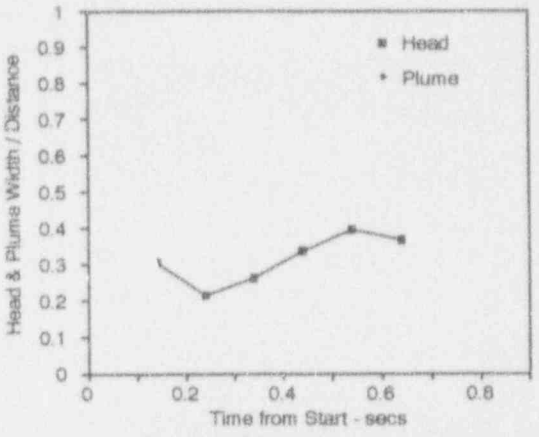

b) Angles of Dispersed Head & Plume

Run 11.

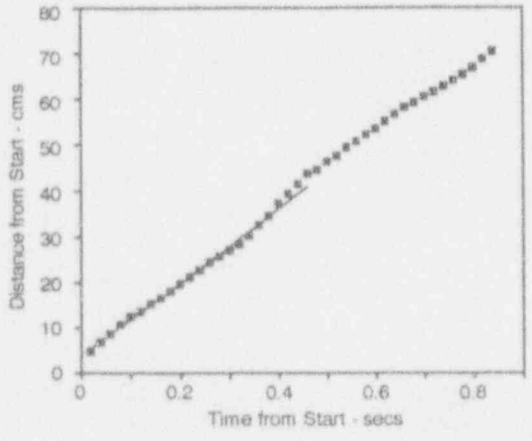

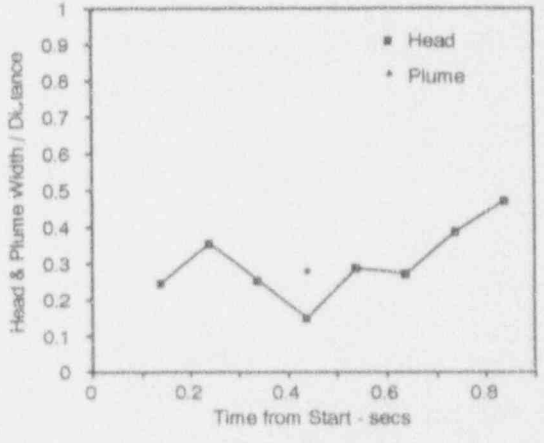

Run 12.

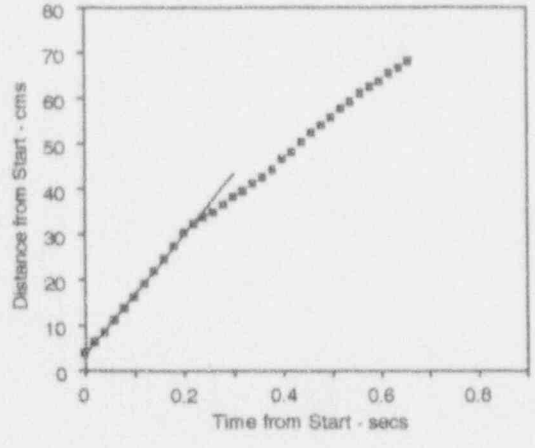

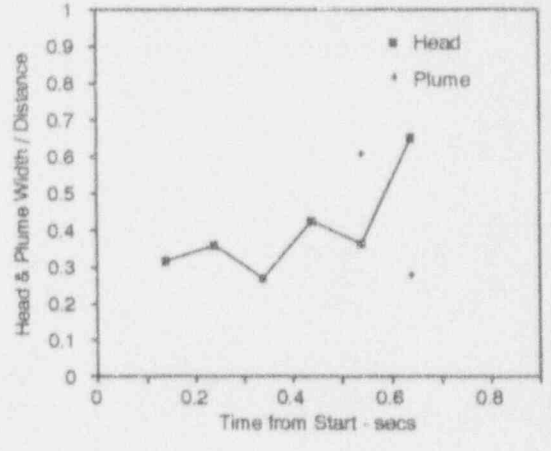

FIG. 8. SINGLE NOZZLE EXPERIMENTS (TIN INTO WATER) PENETRATION AND SPREAD RATES

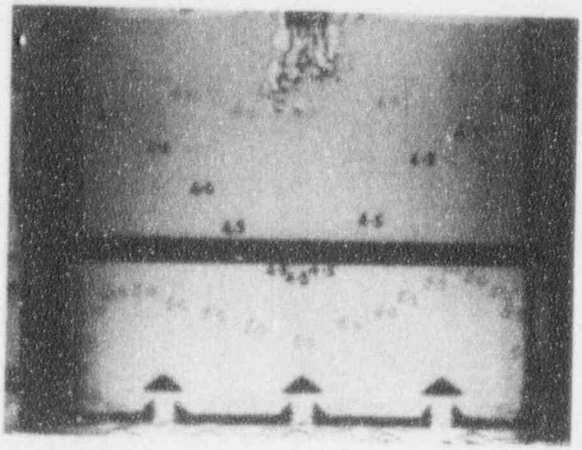

a 0.2s

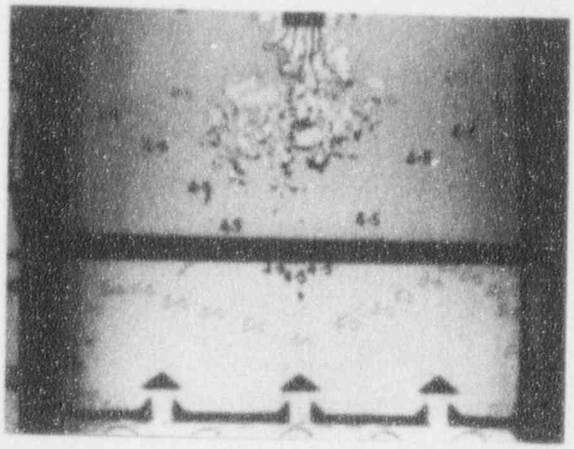

b 0.4s

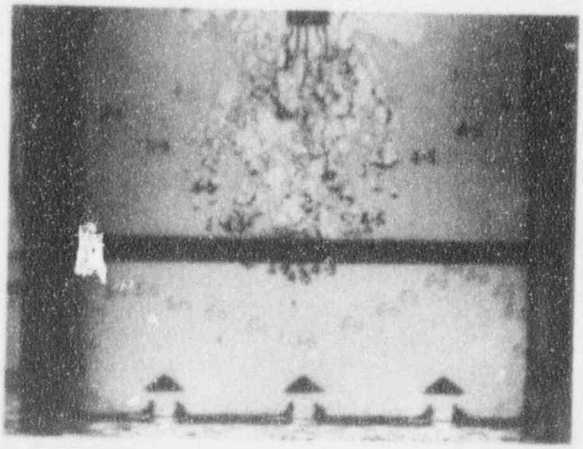

c 0.6s

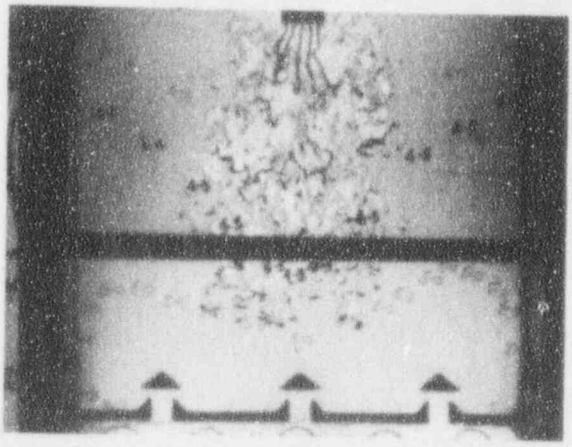

d 0.8s

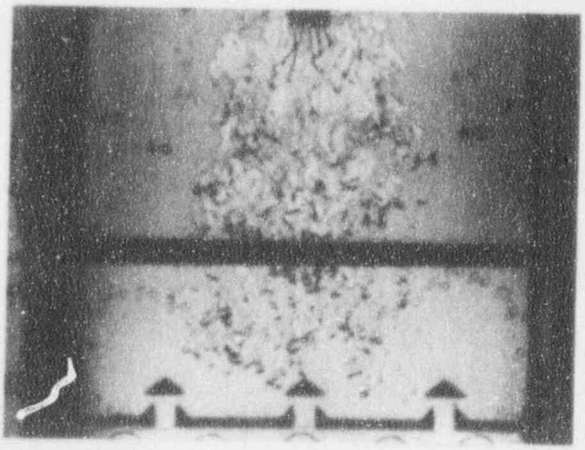

e 1.0s

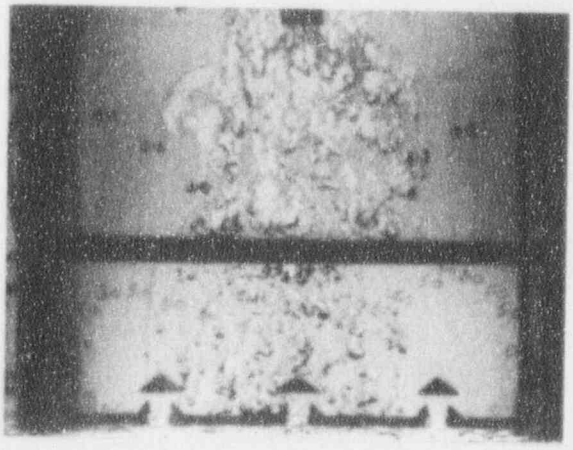

f 1.2s

FIG. 9. SELECTED FRAMES FROM MULTI-NOZZLE EXPERIMENT

Run 9.

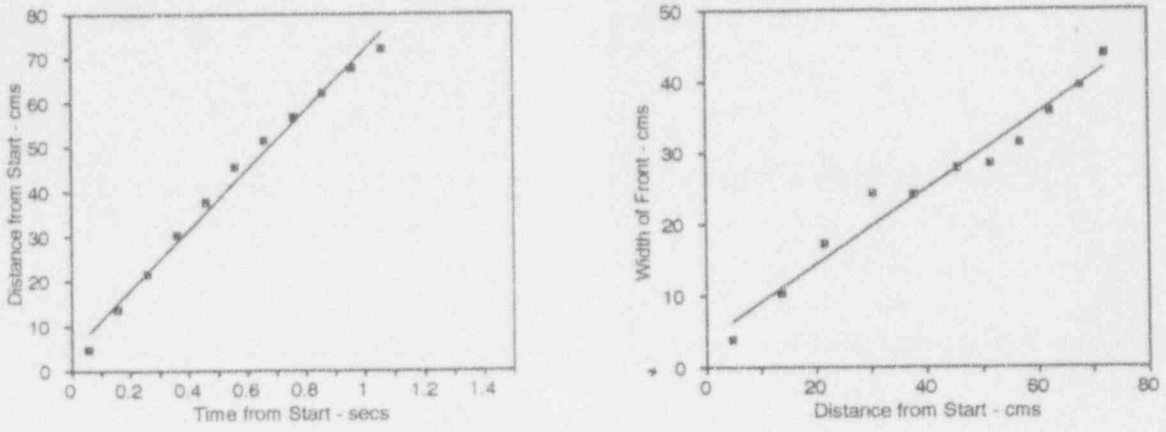

Run 10.

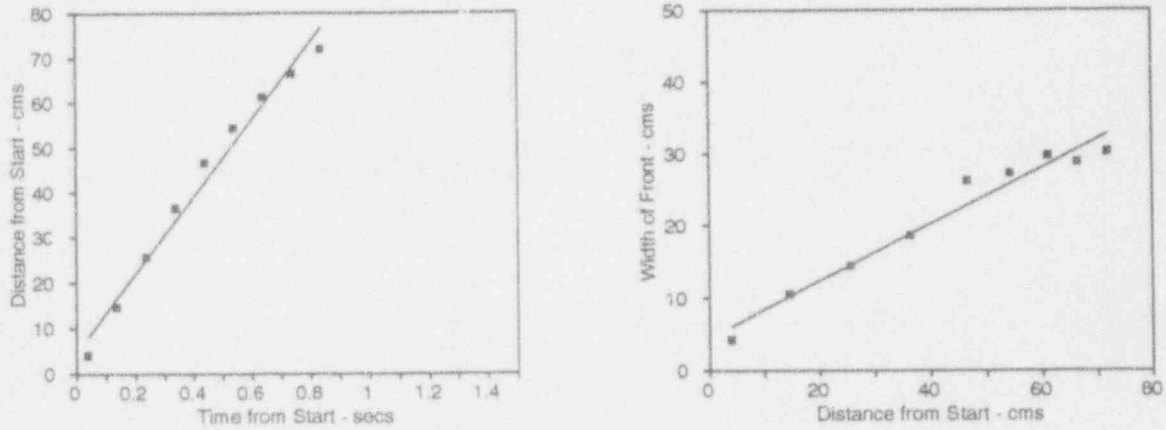

Run 11.

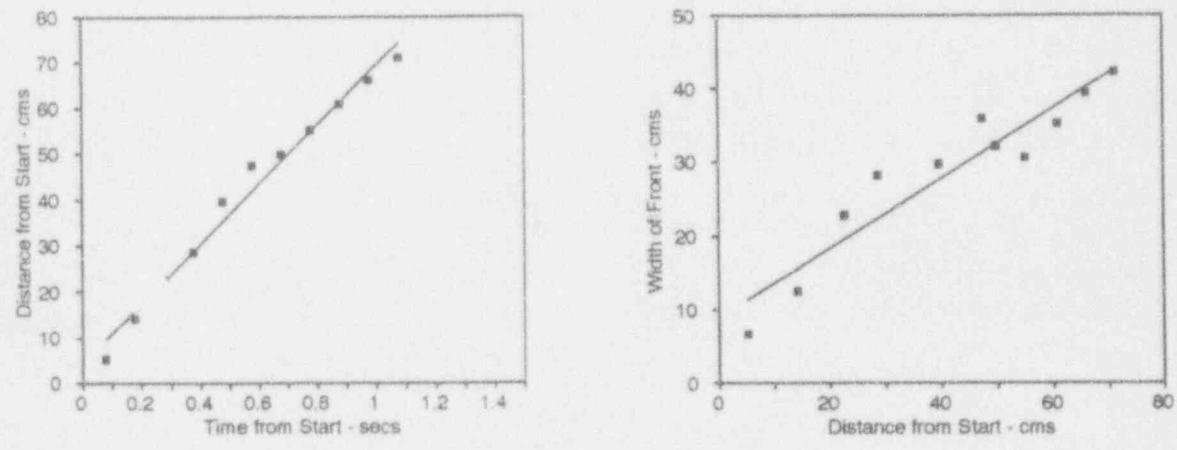

FIG. 10. MULTI-NOZZLE EXPERIMENTS (TIN INTO WATER) PENETRATION AND SPREAD RATES

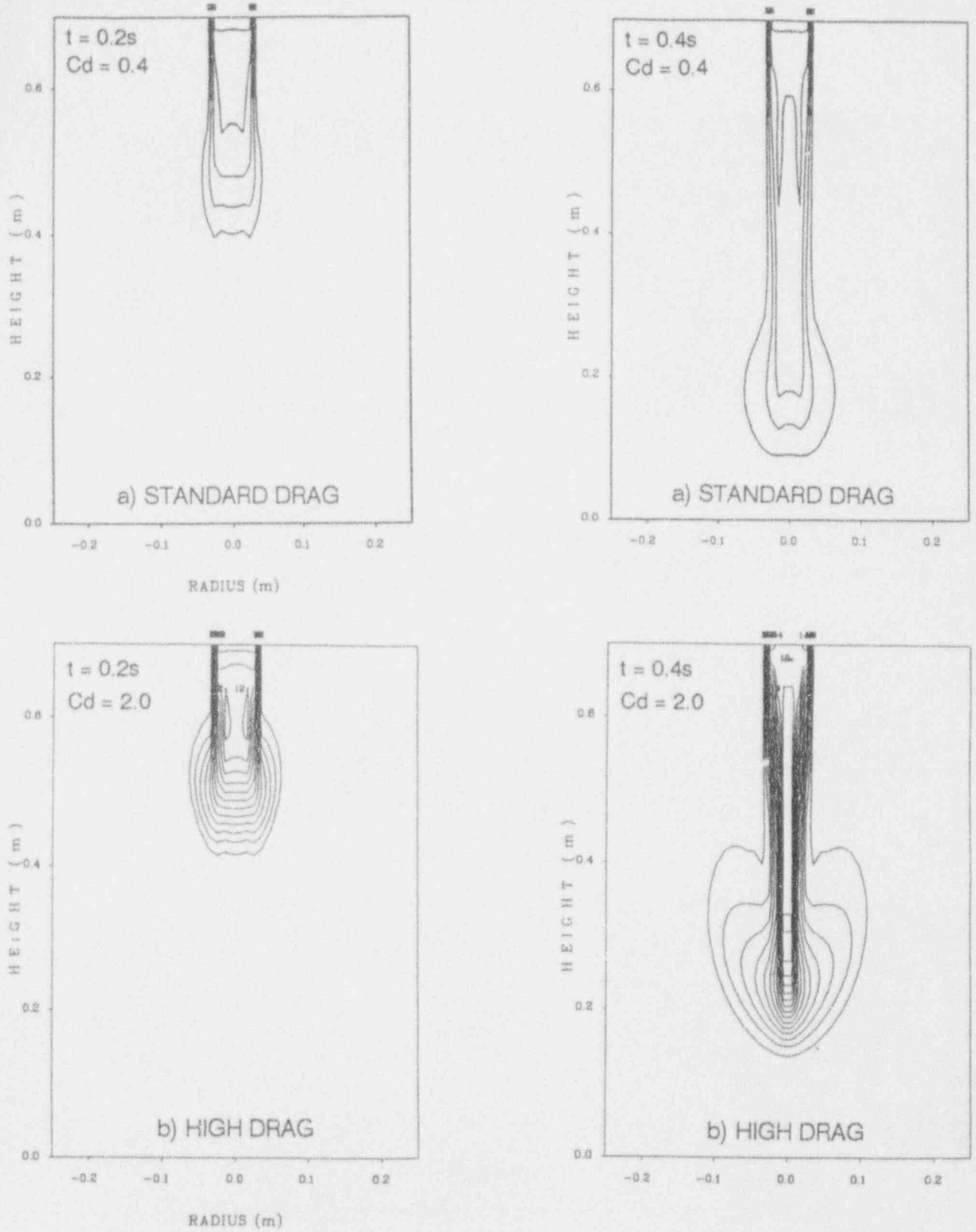

FIG. 11. CHYMES CALCULATIONS FOR MULTI-NOZZLE EXPERIMENTS - VOLUME FRACTION OF MELT AT 0.2 AND 0.4 SECONDS

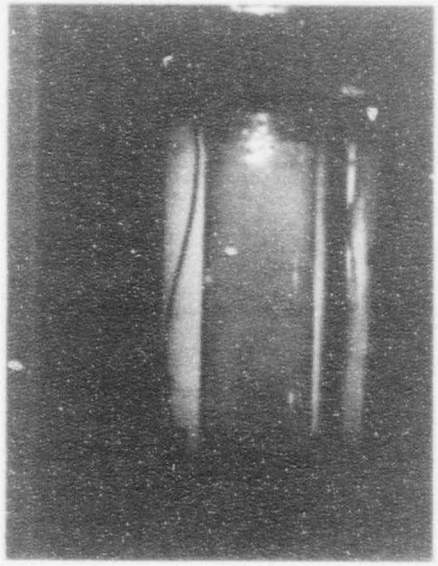

a 0.1s

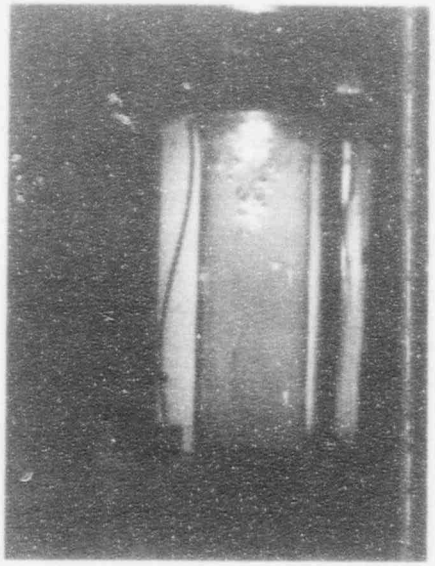

b 0.3s

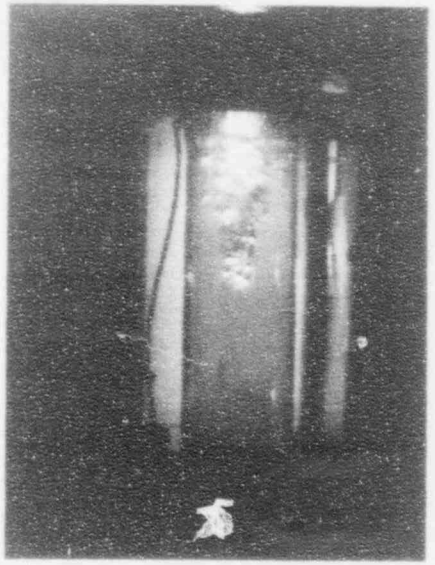

c 0.5s

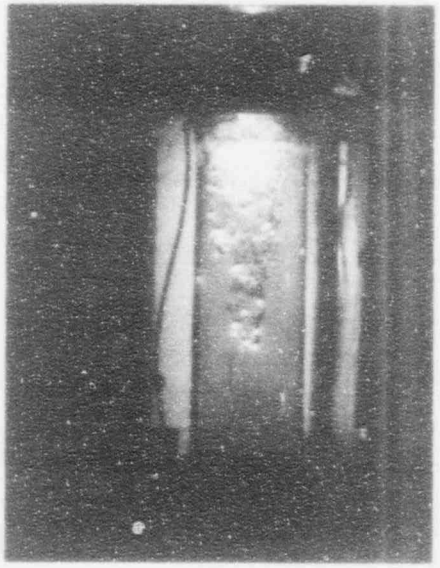

d 0.7s

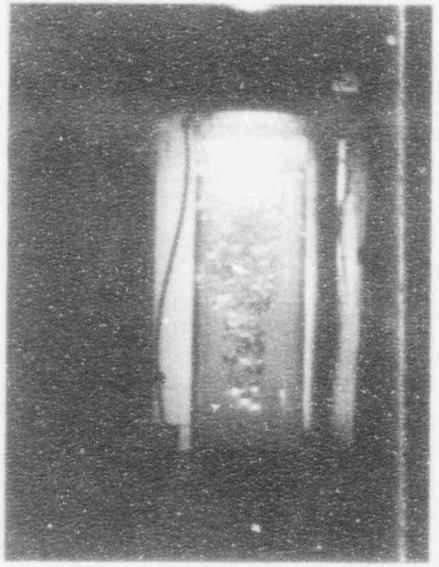

e 0.9s

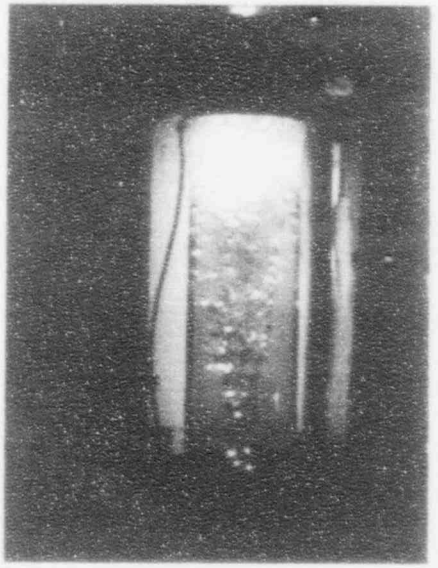

f 1.1s

FIG. 12. PRELIMINARY IRON THERMITE POURS

VALIDATION OF THE CHYMES MIXING MODEL

D.F. Fletcher
SRD, AEA Technology,
Culham Laboratory, Oxon., OX14 3DB, UK.
Tel. (44) 235-521840 — Fax (44) 235-464143

M.K. Denham
AEA Reactor Services,
Winfrith Technology Centre, Dorchester,
Dorset, DT2 8DH, UK. Tel. (44) 305-251888

ABSTRACT

This paper contains a discussion of the work being performed in the UK to validate the CHYMES coarse mixing model. Attention is focussed on the MIXA experiments performed at Winfrith Technology Centre in which 3 kg of molten fuel simulant were released into water. The validation of CHYMES against one of these experiments (MIXA06) is discussed in detail. It is concluded that CHYMES can reproduce some features of the experiment (such as the existence of steam chimney around the mixture and the steam production rate within a factor of two) but it does not predict the observed mixture development (the radial spreading and the deceleration of the first melt arriving at the surface) well. Additional model development and experimental analysis underway to resolve these differences is discussed.

I. INTRODUCTION

Over the last ten years a number of models of the coarse mixing stage of a steam explosion have been developed and used. Amongst these the most well-known are: CHYMES (Fletcher and Thyagaraja, 1991a) IFCI (Young, 1991), IVA3 (Kolev, 1991), PM-ALPHA (Amarasooriya and Theofanous, 1991), TEXAS (Chu and Corradini, 1989) and TRIO MC (Berthoud and Valette, 1993). In most cases the aim has been to use the model to place limits on the mass of melt that is 'mixed' for the given pour configuration. In order to use such models to place 'limits to mixing' it is necessary to postulate mixture configurations which will not support a propagation wave or to show that the yield obtained from a multi-volume thermodynamic model will be insufficient to damage the reactor. To formulate such models a large number of simplifications must be made, with the aim being to retain the essential physics. The key physical process which prevents intimate mixing, and therefore needs to be modelled, is considered to be the high volumetric steam generation rate as melt and water mix. The steam expels water from the mixture, leaving it water lean.

In the UK a probabilistic study of steam explosion-induced containment failure has recently been completed (Turland et al., 1993). It was judged that the models of mixing and propagation were not sufficiently well developed to produce deterministic limits to mixing. Instead results from simulations of the initial coarse mixing stage were used:

1. To determine the range of times at which melt first contacts the base of the vessel in sufficient quantities for base triggering to occur;

2. To generate mixture distributions to quantify the effect of steam-induced removal of water from the mixture on the ideal thermodynamic yield;

3. To support a physical picture in which the explosion is not tamped by a coherent slug of water.

A model, called CHYMES, was developed for these purposes in the UK (Fletcher and Thyagaraja, 1991a). The model is transient, two-dimensional and considers three components, namely melt droplets, water and steam, each of which are assumed to have their own velocity field. The usual multiphase flow equations are used to formulate the model, together with the assumption of incompressible flow and the restriction to the case of saturated water and steam. An equation is solved for the melt enthalpy, together with transport equations for the melt and water lengthscales. Constitutive relations are used to model heat transfer, interphase drag and fragmentation of the melt and water.

The remainder of the paper is concerned with validation of the CHYMES model and is organised as follows: Section II gives a brief description of the validation philosophy being used. Section III gives a description of the main series of validation experiments and Section IV contains the analysis of a particular experiment. Some general remarks on the validation exercise are presented in Section V and the conclusions are given in Section VI.

II. VALIDATION PHILOSOPHY

The task of validation (or showing that the models are fit-for-purpose) is a complex one because the models are based on a gross simplification of the real situation and the experimental conditions are necessarily far removed from severe accident conditions. For example, the models do not allow for the complex behaviour of a real core melt relocation event or for the role of the structures contained within the lower head. Also the experiments are necessarily at a much smaller scale than the reactor, involving kilogramme quantities of melt rather than tonne quantities.

The models require complex numerical schemes and contain uncertain physics. Thus verification, to check that the model has been correctly coded, and validation, to ensure that the model is an adequate representation of reality, are required before great reliance can be placed on the predictions. Verification is a relatively straightforward task, and CHYMES has been subjected to rigorous testing and comparison with other models.

The numerical scheme must be qualitatively consistent, in that it should be designed with the physics of the problem in mind (Thyagaraja and Fletcher, 1988). It is also important to check that the code performs well against the limited number of analytic solutions which are available, and if it does not the algorithm must be improved. An example of this type of checking is given in a recent study of a particle front falling in a vacuum (Fletcher and Thyagaraja, 1991b). The basic numerical scheme in CHYMES has been validated against the commercial codes FLAT and FLOW3D for the calculation of a laminar jet flow (Fletcher et al., 1992). All three codes were found to give very similar results for the jet penetration and spreading rates. In addition, results from CHYMES have been compared with a PM-ALPHA calculation of mixing in the lower head of reactor (Fletcher, 1992). This comparison showed that the two different models predicted very similar melt behaviour but very different coolant dynamics. This was due to differences in the chosen boiling and drag models.

It is the purpose of validation to allow the 'best' constitutive models to be identified. A validation exercise is currently underway against a number of different experimental series. The main series of validation experiments, which use prototypic materials, is described in the next section. Experiments are also being performed at Oxford University in which cold and hot ball-bearings are dropped into a narrow tank of water (Gilbertson et al., 1992). The data from these experiments are being used to examine the interfacial drag modelling in CHYMES. In addition, low temperature simulant experiments are being performed by Hall and co-workers at Berkeley Nuclear Laboratories (Hall, 1993).

It should be noted that the validation of coarse mixing models is a topic currently being pursued in many countries. In France the BILLEAU test using un-heated and heated shot are being performed to validate the TRIO MC code (Berthoud and Valette, 1993). Theofanous and coworkers have performed experiments (called MAGICO) in which heated shot is released into a tank which represents the lower head of a reactor (Angelini et al., 1992). These experiments are novel in that they are the first in which local measurements of the void fraction within the mixture have been made. Encouraging agreement between the experimental data and calculations using the PM-ALPHA code have been reported. In addition, the FARO tests being performed at the European Joint Research Centre ISPRA should provide data at a larger scale and for prototypic materials.

III. DESCRIPTION OF THE MIXA TESTS

A series of medium-scale mixing experiments, called the MIXA experiments, has been performed at Winfrith Technology Centre. The experimental arrangement has been described elsewhere (Denham et al., 1992) and will only be summarised here. The experiments involved the release of ~3 kg of molten fuel simulant (81% uranium dioxide and 19% molybdenum metal at a temperature of 3600 K) into a pool of water. A novel droplet former was used which ensured that the melt entered the water as a stream of droplets with a diameter of approximately 6 mm. 'Skirts' of varying lengths were attached beneath the droplet former to control the radial spreading of the stream of melt droplets. The mixing vessel was of square section with a side of 0.37 m and a pool depth of 0.6 m was used. The initial pressure was 0.1 MPa in all of the experiments and the water was initially saturated in all but one of them. The mixtures formed were relatively weak, having a melt fraction of typically 1%. The mixing process was recorded using cine photography with intense backlighting. The vessel was left open to the atmosphere via a vent line which contained a flowmeter to measure the steam produced as the melt entered the water.

The above experiments were specifically designed and performed to assist with the task of CHYMES validation. Therefore the experimental conditions were chosen to meet the validation requirements. Thus, these are the first experiments in which a stream of droplets of prototypic material have been injected into water. In addition, the experimental configuration was such that the assumptions of incompressible flow and saturated water were considered to be valid. One of the experiments was performed with the water initially subcooled by 20 K to provide a means of benchmarking the effect of subcooling.

Even with these experimental features, analysis of the data was not straightforward. After some experimentation, a well-defined two-dimensional inflow of melt was generated, but even then, the rapid steam generation and

level swell which occurred when the melt entered the water obscured the movie, so that the initial inflow rate could only be observed for a fraction of the inflow period. The movies gave very clear pictures of the mixing process, and features such as melt holdup and the existence of an extensive steam void in the mixing zone were observed. No steam explosions occurred.

There were five successful experiments in the series. Tests 01, 04 and 06 used increasing lengths of 'skirt' around the droplet former and resulted in a range of melt pours from one-dimensional initially (i.e. a pour of melt droplets over most of the vessel width) in 01 to a central pour (i.e. a pour over a small region in the centre of the vessel) in 06 (Denham et al., 1992). Experment 05 was similar to 06 except that the water was initially subcooled by 20 K in 05. Experiment 07 was similar to 06 except that a modified droplet former was used which resulted in larger droplets (10–30 mm instead of 6 mm).

An analysis of the MIXA01 experiment, in which the melt pour was initially one-dimensional, has already been published by Denham et al., (1992). In this paper an analysis of the MIXA06 experiment, in which the melt pour was two-dimensional, is presented.

IV. SIMULATIONS FOR THE MIXA06 TEST

A. Description of the MIXA06 Experiment

The main features of the MIXA06 experiment are now described. This experiment produced a central pour of 3 kg of melt in the form of ~6 mm diameter droplets. When the droplets were released from the melt generator they were initially contained within a 0.48 m long cylindrical 'skirt' and this produced a jet of particles ~120 mm in diameter. The data from the movies indicated that the melt left the charge container with a small pressure gradient driving the flow, since the melt droplets arrived at the water surface with a velocity of ~5 $m\,s^{-1}$ (which compares with 4.4 $m\,s^{-1}$ from a gravity pour). The velocity decreased gradually to 3.5 $m\,s^{-1}$ over a period of 0.2 s. The melt pour lasted for a total time of 1.5 s.

The pressure in the vessel remained close to its initial value. The peak pressure rise measured was 0.031 MPa, which would have induced a subcooling of 7 K. The measured pressure in the gas space in the vessel is shown in Figure 1. It is tentatively assumed that this degree of subcooling will not be significant in the comparison. (If it is important it should result in CHYMES over-predicting the steaming rate.) The thermocouples located in the vapour space recorded the saturation temperature throughout the transient.

The data available for CHYMES validation from this experiment comprise high quality cine records, the transient steam flow rate, quantities of material swept out of the vessel, and the particle size distribution of the quenched debris. It is important to note that all of the above are global comparisons. More detailed information on, for example, melt droplet velocities and trajectories is recorded on the films but has not yet been extracted. An original intention of the experiments was to make local measurements of the melt volume fraction (via X-ray cinematography) and to measure local void fractions (via conductance probes). However, the X-ray diagnostics had to be abandoned because of the cost of obtaining a sufficiently powerful source and the conductance probes failed to work correctly because of changes in the electrical properties of the water when the melt entered the water.

B. Data Used for the Assessment

The transient steam production rate can be compared with the code output. The data show that the steaming rate increased steadily from zero to a peak of ~1.0 $m^3 s^{-1}$ over a period of 0.7 s, and then fell away over a period of several seconds.

On entering the water the droplets penetrated a distance of ~100 mm with a velocity of 5 $m\,s^{-1}$, before slowing to a velocity of 0.8 $m\,s^{-1}$. There was no lateral spreading of the melt as it entered the water pool. The first melt took 0.69 s to travel from the water surface to the vessel base. The melt was observed to spread progressively as it penetrated the water pool, with the mixture being column shaped with the widest part near the original water surface. When the first melt reached the vessel base, melt had spread across almost the entire width of the vessel. The boundaries of the mixture envelope, as traced from the high speed movie, are shown in Figure 2.

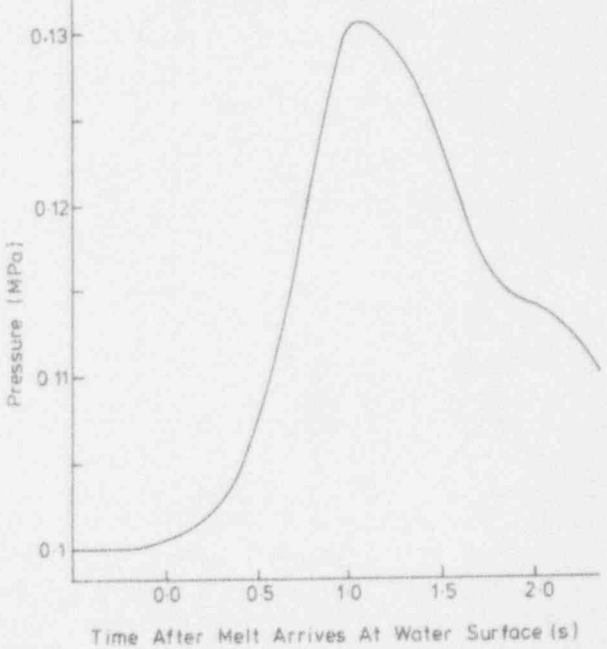

Figure 1. The measured pressure in the gas space for experiment MIXA06.

Melt was observed to be levitated by the steam flow. Melt droplets appeared to be suspended by the steam flow and to move sideways towards the vessel walls. At 0.18 s after the melt entered the water there was ~0.1 m of level swell. At 0.6 s after melt/water contact the level swell had reached the bottom of the 'skirt' at a height of 0.49 m above the initial water surface. At 0.8 s melt reached the level of the 'skirt'. After melt reached the base of the vessel, melt was observed to be levitated in the central region of the mixture and to flow downwards in the peripheral region. After 1.2 s the level swell had filled the vessel. The mixture contained a highly voided core or 'steam chimney'.

An insignificant amount of melt was swept out of the vessel, via the vent pipe. The mass of water lost during the experiment was 3.3 kg. Integration of the measured steam flow rate shows that approximately 0.5 kg of steam would have escaped from the system as mixing took place. Thus the mass of liquid lost via sweep-out was less than 2.8 kg, since some water would have been lost by evaporation during the heat-up stage.

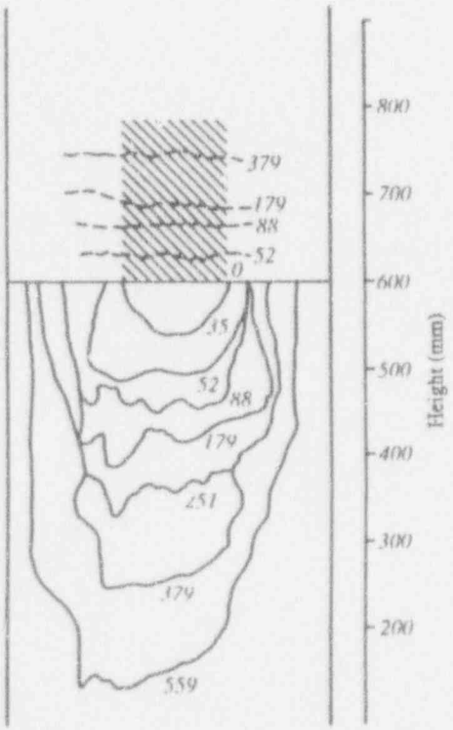

Figure 2. The development of the mixture region and level swell of the pool as measured from the high speed movie. The position of the melt front is shown via a solid line and the top of the level swell is shown via a dashed line. Numbers are times (in ms) from first melt arrival at the water. The width of the incoming stream of melt droplets is marked by a hatched region.

The frozen melt was recovered at the end of the experiment. It was in the form of irregular globules and sieving showed that 20% (by mass) of the debris was less than 2 mm in diameter, 45% was between 2–5 mm and 90% was smaller than 8 mm.

C. Specification of Calculations

The calculations were performed assuming that the square-section vessel could be replaced with a circular-section vessel with the same flow area. This gave a vessel diameter of 0.42 m. A total vessel height of 1.5 m was used, with 0.6 m consisting of a water pool and 0.9 m being the steam filled region below the melt generator. The vessel was assumed to have a lid of radius 0.195 m, which left an annular gap of width 0.015 m at the outside of the vessel as an exit region. A constant pressure boundary condition was employed at this exit.

The experimental data on melt flow consist of estimated mass fluxes for a central (0.12 m × 0.12 m) region, together with the melt velocity and estimated droplet size, all at the water surface. The experimenters obtained the above quantities by tracking the path of droplets on the cine records to obtain the velocity and counting the number of droplets passing a plane. Symmetry about the centre line was assumed and the droplet flux was integrated in time to obtain a value for the total number of droplets injected. The mass of a single droplet was then determined by dividing the total number of droplets by the mass of melt injected. The experimenters *assumed* that during the period for which the droplet flux could not be observed the flux remained constant at the last observed value. It is clear that this procedure is necessarily approximate by the nature of the assumptions (e.g. that the droplet size distribution remains constant) and because the flux of droplets could not be observed for a significant fraction of the pour duration. A calculation in which the melt flow rate was assumed to decay linearly with time (based on an analysis of the rate of melt flow from the charge container) after the period for which data were available gave very similar results, showing that this assumption is not particularly important.

The mass flux data measured at the surface were used to calculate a velocity and volume fraction at the inlet by assuming that the flux at the surface was equal to that at the inlet, and that the velocity at the inlet was that which would give the measured value at the water surface for melt falling under gravity. For part of the pour this assumption could not be made because of the effect of the steam drag on the melt and instead the initial velocity was determined at the inlet from that which would occur due to the hydrostatic pressure of the melt in the droplet former.

The melt enthalpy equation was solved to allow for the cooling of the melt as it transferred heat to the wa-

ter. Heat transfer from the melt was assumed to be by a combination of radiation and film boiling (Fletcher and Thyagaraja, 1991a). An initial melt temperature of 3600 K was used, together with a melt emissivity of 0.84. It was assumed that 60% of the emitted radiation was absorbed by the water and produced steam, the remainder being reabsorbed by the melt. (The reabsorption of radiation by the melt is a standard feature of the model which is likely to be applicable in the reactor situation but is unlikely to be correct in these experiments. However, it is not believed that its effect is significant.) A melt density of 8,400 kg/m^3 was used. For all calculations an initial melt droplet size of 6 mm was specified, since this value is consistent with the observed size from cine data. Melt fragmentation was calculated using the standard fragmentation model coded in CHYMES which is based on that used in IFCI (Young, 1991).

The calculations were performed using a finite difference grid with 15 cells in the radial direction and 30 cells in the vertical direction. (Using 50 cells in the vertical direction did not change the results significantly.) A time step of 2×10^{-5} s was used.

The following calculations were performed in order to examine the performance of CHYMES:

Base Case This calculation used the dispersed phase drag laws coded in CHYMES. In these drag laws the melt is always assumed to be the dispersed phase and the water-steam drag is calculated assuming that the water is the dispersed phase (Fletcher and Thyagaraja, 1991a). The standard water droplet fragmentation model, which is based on the melt fragmentation model, was switched on. All drag coefficients were set to 0.4 and an initial water length-scale of 30 mm was used. (A calculation in which the initial water length-scale was set to 10 mm gave very similar results.)

Regime Map This calculation used the flow regime map drag laws of Amarasooriya and Theofanous (1991). (Note that this is expected to give a different result to PM-ALPHA because of other differences in the modelling (Fletcher, 1992).)

High Drag This calculation was a repeat of the base case but with all of the drag coefficients set to 2.0. It was performed because analysis of the isothermal experiments performed at Oxford showed that this value reproduced the observed melt spreading (Gilbertson et al., 1992).

D. Results

1. Melt Droplet Location. In the base case calculation the melt stream entered the water and progressed to the bottom with very little lateral spreading. Figure 3 shows the melt volume fraction contours at times of 0.4, 0.6, 0.8 and 1.0 s. At 0.8 s melt started to be held-up near the water surface and by 1 s there was significant melt hold-up in the top third of the water pool. The calculational results show that this feature gradually developed, with some melt falling away towards the base of the vessel and other melt being pushed sideways. Some melt was levitated above the initial level of the water pool, a feature which was observed in the experiment.

The calculated melt penetration rate is further illustrated in Figure 4 which gives a plot of the development of the melt volume fraction on the axis of the vessel. It shows that melt first reached the vessel base after 0.4 s travel through the water pool. This figure is approximately 0.18 s earlier than was observed in the experiment. Thus the melt arrival time is predicted to within 36%. Over the last two-thirds of the water pool the melt front fell at a speed of approximately 0.9 m s^{-1} in the calculation compared with an observed speed of 0.8 m s^{-1} in the experiment. Thus it is the initial hold-up of the melt which is poorly predicted with the later behaviour (as far as melt front penetration is concerned) being reproduced well.

The results from the simulation in which the drag laws of Amarasooriya and Theofanous were used confirmed the picture observed in earlier calculations (Denham et al., 1992). The melt hold-up was very significant with melt collecting on the surface of the water pool and then falling down the walls of the vessel. Very little melt reached the base of the vessel in the 1.5 s of the calculation. Figure 5 shows the calculated melt volume fractions at times of 1.0 and 1.5 s and shows that these results are very different from those observed experimentally.

The case with the drag coefficients increased to 2.0 showed different behaviour again. Initially the melt penetrated into the water pool more slowly and spread slightly more. However, at later times the melt was held up near the water surface and spread across the top of the pool. Whilst this spreading was observed in the experiment it occurred throughout the mixture region, not only at the top of the pool. Melt then fell away from this layer towards the vessel base. Figure 6 shows the melt volume fraction at times of 0.8 and 1.3 s and illustrates these features.

It is clear from the above discussion that none of the calculations predicts the quantitative behaviour observed in the experiment. The base case calculation gave too rapid penetration of the melt and virtually no spreading. The increased drag coefficient calculation improved the fall speed but did not cure the spreading problem, with melt being held at the surface. The calculation using the drag laws of Amarasooriya and Theofanous gave far more levitation than was observed in the experiment.

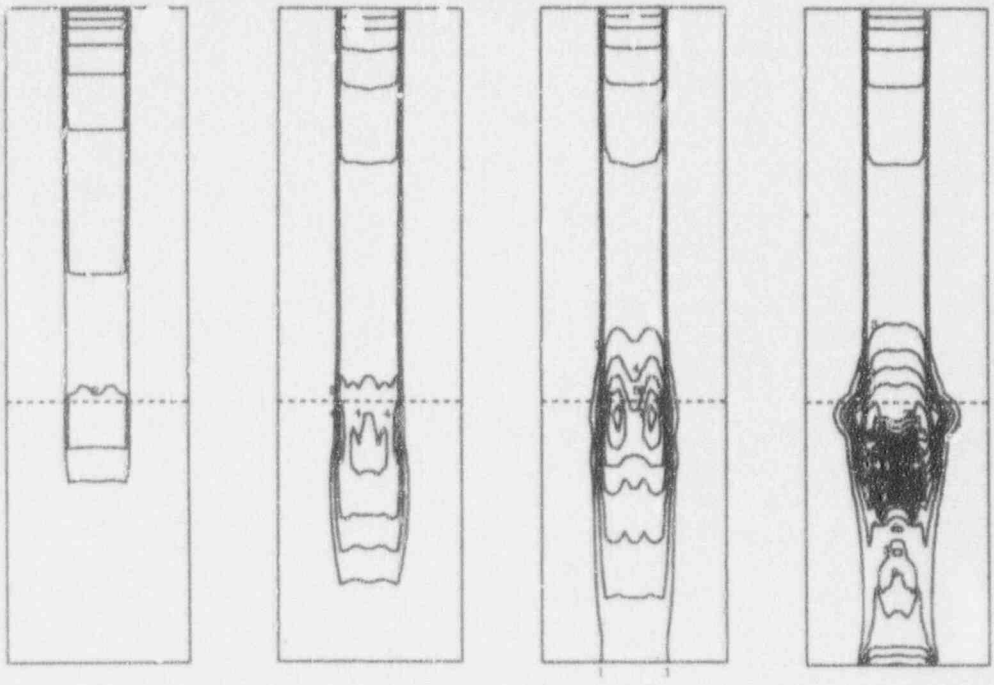

(a) Time = 0.4 s (b) Time = 0.6 s (c) Time = 0.8 s (d) Time = 1.0 s

Figure 3: The predicted melt volume fraction field for the base case. The dashed line marks the original water surface. (Contour level 1 corresponds to a volume fraction of 0.002, and the contour interval is 0.002.)

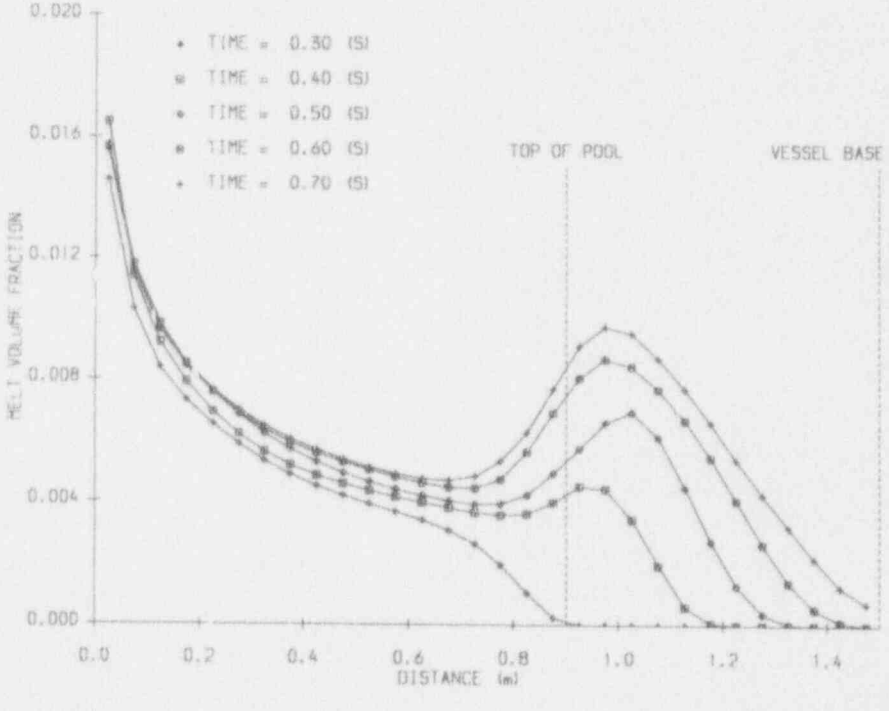

Figure 4: The calculated melt volume fraction on the vessel axis for the base case.

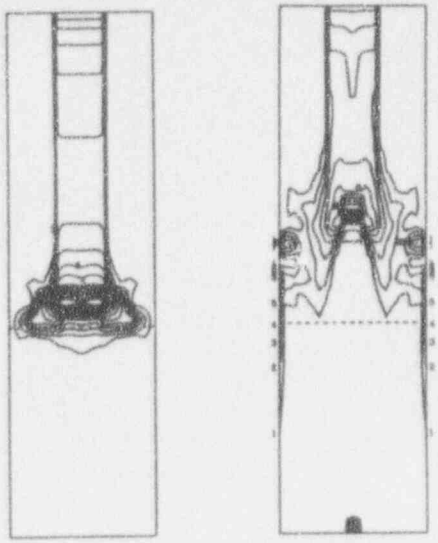

(a) Time = 1.0 s (b) Time = 1.5 s

Figure 5. The predicted melt volume fraction field for the regime map drag laws. (Contour level 1 corresponds to a volume fraction of 0.002, and the contour interval is 0.002.)

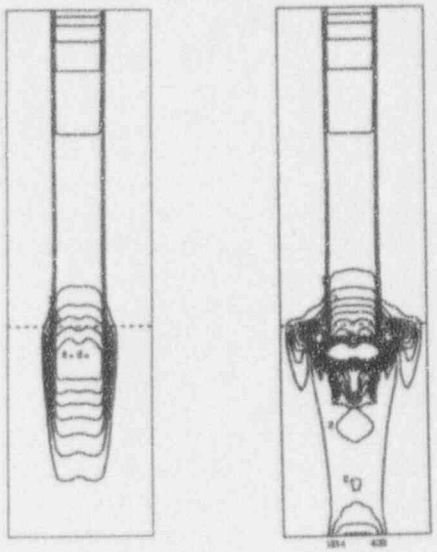

(a) Time = 0.8 s (b) Time = 1.3 s

Figure 6. The predicted melt volume fraction field for the high drag calculation. (Contour level 1 corresponds to a volume fraction of 0.002, and the contour interval is 0.002.)

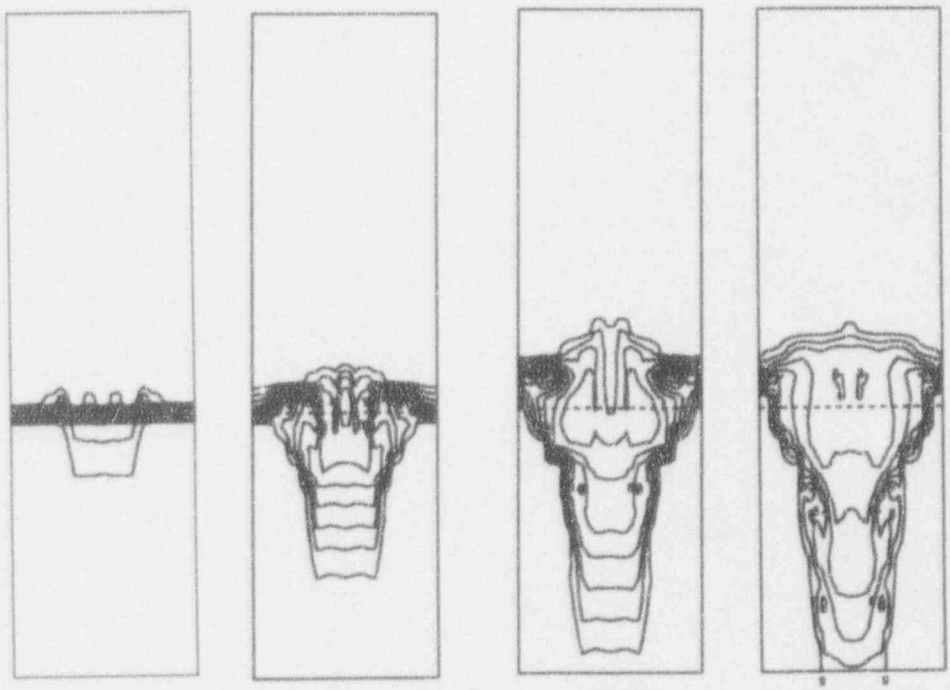

(a) Time = 0.4 s (b) Time = 0.6 s (c) Time = 0.8 s (d) Time = 1.0 s

Figure 7: The development of the level swell in the base case calculation. (Contour level 1 corresponds to a water volume fraction of 0.1, and the contour interval is 0.1.)

2. Level Swell. Comparison of the calculated level swell with the experimental data is difficult because the water volume fraction in the region of level swell is not known. In the calculations the 10% water fraction contour was taken to represent the pool surface. The calculated level swell for the base case is shown in Figure 7 and shows that the amount of level swell is relatively small. The figures also show that steam production is limited to a rather narrow cylindrical region in the centre of the vessel. It appears that the level swell is being under-predicted significantly in the calculation. However, it may be that a 'mist' is formed in the experiment which is not being reproduced in the calculation.

3. Sweep-Out. In the base case calculation 2 g of melt and 1 g of water were swept-out of the vessel. These values varied by no more than a factor of two between the different runs. The melt sweep-out is consistent with the experimental data and the water sweep-out is too low. This is either because the predicted level swell was too low or because the water droplet size is too large and therefore the amount of water carried out of the exit by the steam flow was too small.

4. Steam Generation Rate. Figure 8 shows a comparison of the calculated steam flow rates with the experimental data. In all cases the initial rate of steam production is too low and steam production continues for too long. This is almost certainly coupled with the failure of the code to predict the melt dynamics correctly.

The calculation using high drag coefficients predicts the lowest steaming rate. This is because the melt fragmentation rate was considerably reduced in this calculation (see below). In addition, the drag laws proposed by Amarasooriya and Theofanous also lead to a reduced steaming rate, as was observed in calculations for the earlier experiments (Denham et al., 1992).

It is worth noting that there was significant steam generation before the melt contacted the water in the experiment. Simple estimates suggest that this steam production can be explained by convective and radiative heat transfer from the droplets to the steam as they fell towards the water pool. This additional source of steam flow is not modelled in CHYMES and could have contributed to the discrepancy between the calculations and the experiment.

The current simulations appear rather disappointing but it is worth noting that even with a rather poor prediction of the melt dynamics the steam flow rate is calculated to within a factor of two during the first ~0.5 s of mixing, although the shape of the transient flow curve is not reproduced. The induced subcooling observed in the experiment would have led to a reduced steaming rate at late times, a feature which is not modelled in the current version of CHYMES.

5. Melt Droplet Size. The transient mass averaged melt droplet size is shown in Figure 9. The figure shows that in all but one case CHYMES predicts that the average droplet size falls slowly after melt contacts the water to a value of about 3 mm, which is consistent with the experimental data. The exception is the high drag case, in which low slip velocities between the species result and fragmentation is inhibited. This reduced fragmentation explains the reduced steaming rate observed in this calculation (see above). In all cases the calculated standard deviation of the melt diameter was in the range 1–2 mm. This is somewhat less than that observed in the experiments, where debris in the size range 0.1–10 mm was observed. This is easily explained by the fact that the current fragmentation model cannot reproduce the thermal fragmentation observed in the experiments. (The presence of 'blow-holes' in the debris suggested that

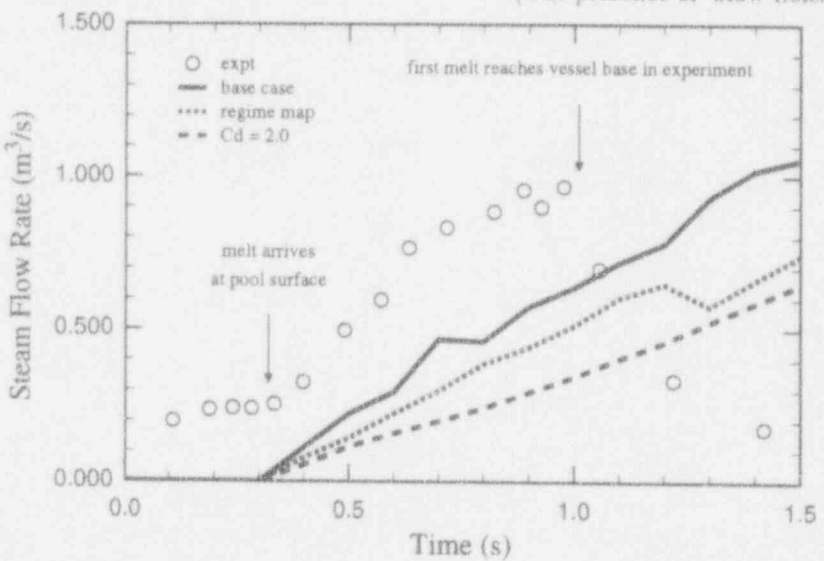

Figure 8: The transient steaming rate: a comparison of the calculated values with the experimental data.

water had been trapped in the melt droplets and had caused some fragmentation.)

V. CURRENT STATUS OF MODEL VALIDATION

The validation exercise carried out using data from the MIXA experiments has led to the following conclusions:

- CHYMES predicts the mixing behaviour when the flow is one-dimensional reasonably well (Denham et al., 1992). For two-dimensional pours the code under-predicts the melt spreading rate significantly. In the calculations the first melt arriving at the surface falls to the base of the vessel with virtually no spreading; subsequent spreading occurs because of steam levitation of the remaining melt rather than via progressive radial mixing.
- In the modelling of the isothermal experiments the spreading was increased in the simulations by increasing the melt-water drag, with a drag coefficient of 2.0 giving the best agreement with the experiment (Gilbertson et al., 1992) but this did not give a significant change in the calculation for the MIXA06 experiment.
- The initial slowing of the melt front observed in the experiments is not reproduced by CHYMES but the melt front speed through the lower half of the mixing vessel is better predicted.
- In general the steam production rate is calculated to rise too slowly and to persist for too long. It is believed that this is a consequence of the failure to reproduce the observed melt dynamics. However, the calculated steam flow rate was generally within a factor of two of the measured values during mixing.
- The fragmentation model produces final particle sizes consistent with those observed in the experiment.
- The validation exercise showed that the dispersed phase flow drag laws reproduce the experimentally observed behaviour better than the regime map proposed by Amarasooriya and Theofanous (1991). Use of the latter laws led to excessive levitation of the melt.

VI. CONCLUSIONS

This paper contains a summary of the work performed to date on the validation of the CHYMES coarse mixing model. The MIXA series of experiments in which ~3 kg of uranium dioxide/molybdenum melt at 3600 K was released into a pool of water as a stream of droplets have been described. Particular attention has been paid to the analysis of one of these experiments (MIXA06) in which a central pour of droplets was achieved. CHYMES can reproduce some features of the experiment (such as the existence of steam chimney and the steam production rate within a factor of two) but it does not predict the observed mixture development (the radial spreading and the deceleration of the first melt arriving at the surface) well. Work is currently underway to examine the role of key constitutive relations and to identify possible additional physics which may be required to interpret these experiments. In addition, further analysis of the high speed movies is planned to make better estimates of the droplet size and velocity, and to trace the motion of individual droplets within the mixture.

The experiments have confirmed all of the global features of coarse mixing used in the UK study and have provided much insight into the key aspects of code vali-

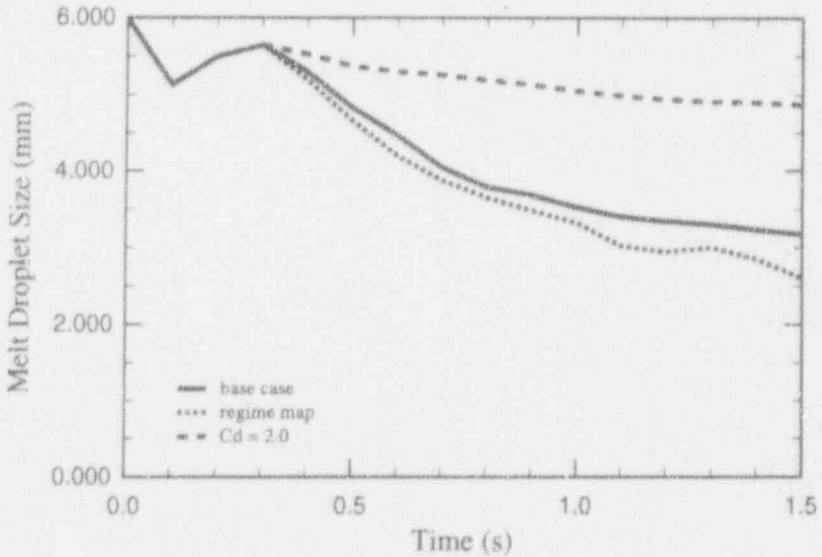

Figure 9: The mass averaged droplet size as a function of time.

dation. However, more work remains to be done before a validated code which can predict local mixture characteristics has been produced. Thus it is currently our view that whilst CHYMES is very valuable for providing a picture of the mixing process and the global conditions in the water pool prior to an explosion, it has not been sufficiently well validated to be used in a 'limits to mixing' role.

ACKNOWLEDGEMENTS

The MIXA experiments were funded by Nuclear Electric plc. Their permission to publish this paper is gratefully acknowledged. The authors thank A.P. Tyler and B.D. Turland for their contributions to the project.

REFERENCES

Amarasooriya, W.H. and Theofanous T.G., (1991) *Premixing of steam explosions: a three-fluid model.* Nucl. Engng. Des., **126**, 23–39.

Angelini, S., Takara, E., Yuen, W. and Theofanous T.G., (1992) *Multiphase transients in the premixing of steam explosions.* ANS Proc 5th Int. Topical Mtg. on Reactor Thermal Hydraulics (NURETH–5), 21–24 September, 1992, Salt Lake City, USA., 471–478.

Berthoud, G. and Valette M., (1993) *Calculations of the premixing phase of an* FCI *with the* TRIO MC *code.* Paper to be presented at the CSNI Specialist Meeting on Molten Fuel Coolant Interactions, Santa Barbara, 5–8 January, 1993.

Chu, C.C. and Corradini, M.L., (1989) *One-dimensional transient fluid model for fuel/coolant interaction analysis.* Nucl. Sci. Engng., **101**, 48–71.

Denham, M.K., Tyler, A.P. and Fletcher, D.F., (1992) *Experiments on the mixing of molten uranium dioxide with water and initial comparison with* CHYMES *code calculations.* ANS Proc 5th Int. Topical Mtg. on Reactor Thermal Hydraulics (NURETH–5), 21–24 September, 1992, Salt Lake City, USA., 1667–1675.

Fletcher, D.F., (1992) *A comparison of the coarse mixing predictions obtained from the* CHYMES *and* PM-ALPHA *models.* Nucl. Engng. Des., **135**, 419–425.

Fletcher, D.F., M°Caughey, M. and Hall, R.W., (1992) *Numerical simulation of a laminar jet flow: A comparison of three* CFD *models.* Submitted to Applied Mathematical Modelling.

Fletcher, D.F. and Thyagaraja A., (1991a) *The* CHYMES *coarse mixing model.* Prog. Nucl. Energy, **26**, 31–61.

Fletcher, D.F. and Thyagaraja, A., (1991b) *A finite difference error arising from the use of a staggered grid.* Appl. Math. Modelling, **15**, 496–498.

Gilbertson, M.A., Fletcher, D.F., Hall, R.W. and Kenning, D.B.R., (1992) *Isothermal coarse mixing: experimental and* CFD *modelling.* Paper presented at 3rd UK National Heat Transfer Conference, Birmingham, UK, 16–18 September, 1992, IChemE Symp. Series, **129**, 547–556.

Hall, R.W., (1993) *Validation of* CHYMES*: a review of work by Nuclear Electric.* Paper to be presented at the CSNI Specialist Meeting on Molten Fuel Coolant Interactions, Santa Barbara, 5–8 January, 1993.

Kolev, N.I., (1991) *A three-field model of transient 3D multiphase, three-component flow for the computer code* IVA3. Kernforschungszentrum Karlsruhe Reports KfK 4948, KfK 4949 and KfK 4950.

Thyagaraja, A. and Fletcher, D.F., (1989) *Buoyancy-driven, transient, two-dimensional thermo-hydrodynamics of a melt-water-steam mixture.* Comput. Fluids, **16**, 59–80.

Turland, B.D., Fletcher, D.F., Hodges, K.I. and Attwood G.J., (1993) *Quantification of the probability of containment failure caused by an in-vessel steam explosion for the Sizewell B PWR.* Paper to be presented at the CSNI Specialist Meeting on Molten Fuel Coolant Interactions, Santa Barbara, 5–8 January, 1993.

Young, M.F., (1991) *Application of the integrated fuel-coolant interaction code to* FITS*-type pouring mode experiments.* Prog. Astronaut. and Aeronaut., **134**, 356–386.

PREMIXING-RELATED BEHAVIOR OF STEAM EXPLOSIONS

S. Angelini,[a] W.W. Yuen[a] and T.G. Theofanous
Center for Risk Studies and Safety, Department of Chemical and Nuclear Engineering
University of California, Santa Barbara, CA 93106
Telephone (805) 893-4900 — Fax (805) 893-4927

ABSTRACT

Three recently published premixing experiments, the MAGICO, MIXA, and FARO, are discussed comparatively, and two of them, the MAGICO and FARO, are analyzed with the help of the computer code PM-ALPHA. The results of these analyses are shown to provide quantitative interpretations of the data , and to suggest conditions/measurements in further experiments to enhance the insights thus obtained. Also, a quantitative radiography technique is described and applied to MAGICO for the measurement of chordal-averaged void fractions in the mixing zone. The results are in excellent agreement with PM-ALPHA predictions, thus confirming the previously reported good comparisons with the local (point) measurements of FLUTE.

I. INTRODUCTION

Premixing is the multiphase transient obtained during the pouring of a high temperature melt in a liquid coolant; given an appropriate trigger, this transient can be transformed into an explosion (commonly referred to as a "steam explosion"[b]). An explosion can be triggered at any time by an externally supplied pressure pulse, or it can occur spontaneously as a result of a local thermal interaction if pertinent conditions for such are obtained during the premixing. In any case, the premixing transient provides the initial conditions for the explosion (or so-called "escalation" and "propagation" phases) and as such it provides the basis for assessing "what constitutes an adequate trigger," and the "magnitude of the energetics obtained from a resulting explosion." In general, these initial conditions can be characterized by the space–time variations of the volume fractions of the three constituents (melt, water, and steam); however, of particular significance is the so-called "water depletion" phenomenon.

The water depletion phenomenon refers to the formation of a high void (steam) fraction region in the major central portion of large-scale melt pours in water. This "steam bubble" is due to the high heat transfer rates and associated steaming that "drive" the water out while at the same time it is being vaporized. This means that large quantities of melt cannot coexist with large quantities of water in a coarsely mixed configuration, i.e., in a condition that is conducive to an efficient thermal interaction. On the one hand, such largely voided premixtures are not easily susceptible to triggering, and on the other hand, even assuming that an explosion can develop, it would be very inefficient. This allows for putting bounding limits on interacting masses from arbitrarily large pours, and thus it has served as a central element of the argument against the α-mode containment failure in the past (Theofanous et al., 1987; Steam Explosions Review Group, 1985). This is important because then, and this remains true now, late-phase, core-melt progression uncertainties do not allow a rigorous argument to be made against massive molten corium dumps into the lower plenum.

The water depletion phenomenon was first conjectured by Henry and Fauske (1981), and Bankoff and Han (1984) made an attempt to compute it. A first actual quantification was offered by Abolfadl and Theofanous (1987), using a two-fluid model, and this was further refined by a three-fluid formulation and the PM-ALPHA code (Amarasooriya and Theofanous, 1991). An independent but similar three-fluid formulation also has been pursued under the CHYMES code development effort in the UK (Fletcher and Thyagaraja, 1991), and the first comparisons with the above-mentioned PM-ALPHA results have just been published (Fletcher, 1992). Except for not accounting for subcooling, these CHYMES results can be interpreted to be supportive to PM-ALPHA and the predicted water depletion phenomenon (Theofanous et al., 1993). The first experimental verification of this phenomenon was made in the MAGICO experiment a little more than one year ago (Theofanous et al., 1991), and a detailed presentation of the first two series of experiments together with PM-ALPHA predictions was given in the recent NURETH-5 meeting (Angelini et al., 1992). The initial data from another premixing experiment, the MIXA, tied to the CHYMES verification effort, were also presented in the same meeting (Denham et al., 1992), and the first data from the FARO experiment at the CRC, Ispra have just become available (Magallon, et al., 1992; Magallon and Hohmann, 1993). Clearly, the major

[a] Also with the Department of Mechanical and Environmental Engineering

[b] Such explosions can occur with a variety of "hot"/"cold" liquid pairs, but without loss of generality we will speak here of a "melt" and "water."

new developments in this area will occur as these and subsequent data are studied and interpreted with the help of these codes. The main purpose of this paper is to discuss these experiments from such a standpoint and to take some initial, illustrative, steps in this direction.

II. OVERVIEW OF THE PREMIXING EXPERIMENTS

As noted above, there are three premixing experiments that are currently active (a fourth one is planned in Grenoble, France). Of these, the MAGICO and MIXA are specifically designed for this purpose. The stated scope of FARO is not specific to premixing; however, it provides an interesting complement from this standpoint, also, to the MAGICO and MIXA experiments. Indeed, viewed as a group, these three experiments provide a nice sequence from the well-defined conditions of MAGICO (fixed particle sizes), to MIXA (prefragmented melt pours into more-or-less regular streams, and apparent capability to observe particle sizes in flight), to the rather poorly defined melt conditions entering the water and no possibility of direct observation of the ensuing interaction in FARO. Except perhaps for the relatively small (compared to reactor) quantities of melt, the FARO is quite prototypic, and very valuable for this reason, to its main purpose: to determine the extent of quenching possible in the lower plenum at high pressures, and the extent, if any, of thermal attack on the lower head. As usual, gaining in prototypicality creates loss of definition, both in initial/boundary conditions, as well as in observations/measurements that characterize the interaction, and this loss is quite detrimental in achieving the basic understanding necessary for analyses to be useful in predicting the behavior in reactor accidents. On the other hand, one would be amiss expecting to securely bridge the gap between the well-defined experiments and the reactor without the actual experience of dealing with the less well-defined but more prototypical tests. We believe that it is very fortunate that these three independently-developed programs are so congruent to the overall purpose.

The major aspect of this view is that MAGICO is suitable for the unambiguous testing of the three-fluid formulation, especially of the phase-change and momentum interaction parts, while the MIXA and FARO can provide important perspectives on the extent and rate of melt breakup under two different melt-entry conditions. All tests involve the pouring of a hot mass (in liquid or solid particle form) into a liquid pool, but in addition to the above, there are other interesting differences well-suited to the overall task of understanding premixing in all its major aspects. A brief account of these other aspects is given below.

Regarding measurements, the MAGICO is focused on local steam volume fractions, as this is the key variable characterizing a premixture from the explosivity/energetics point of view (Theofanous et al., 1993; Yuen and Theofanous, 1993). This is a very difficult measurement, but it became possible using FLUTE (Angelini et al., 1992) and X rays (later in this paper). In MIXA, on the other hand, an integral measure of the thermal interaction is obtained by measuring the steam flow rates during the transient and observing the overall level swell in the interaction vessel. In both these experiments, the interaction progresses essentially at atmospheric pressure (i.e., there is no feedback from steaming). The same approach of measuring the steam generation rate is also intended for FARO; however, the two tests reported so far were performed with a closed interaction vessel which, as explained later in this paper, provides analysis-testing opportunities not previously anticipated nor available so far from the other two tests. Briefly, with a closed vessel, the thermal interaction leads to pressurization and an interesting boiling feedback due to the induced rise in saturation temperature. In these tests, this feedback was further accentuated by radiation heat transfer to the steam in the cover gas space. In addition, FARO is run at high pressures (~5 MPa), which provides opportunities (but also complications) for testing integral predictions in that constitutive laws are not as well known at elevated pressures (i.e., film boiling from spheres in subcooled water and high pressures). Regarding other measurements in both MAGICO and MIXA, the interactions have been observed visually (by high-speed photography), which makes possible melt-front and two-phase zone tracing, and perhaps even particle size measurements in MIXA (the extent to which this can provide the full information needed is yet to be determined). In FARO, no such data are possible, but some rough idea of melt-front advancement and level swell seems to be possible to extract from thermocouple signals.

Regarding melt temperature and delivery conditions, there are some interesting differences to be noted. In MIXA, the melt is heated up to ~3600 K. At such high temperatures, the optical depth of the emitted radiation in water increases rapidly so that non-local deposition of radiant energy becomes very important. For realistic simulations, one must treat the mixing zone as an absorbing-emitting medium taking into account spatial variations in melt and liquid volume fractions, and one must even include, in the scale of MIXA, the surrounding liquid zone, if any, and the container boundaries. For the FARO test (melt at 2650 °C) and the reactor case, on the other hand, such effects are negligible. We are currently modifying PM-ALPHA for this specialized heat transfer regime of MIXA, and for this reason, no comparisons are available at this time. Turning to melt delivery, in MIXA the pour is prefragmented (by passing it over a grid made of graphite bars) and characterized (length scales, velocities, and volume fraction) from high-speed movies; in FARO, the melt is allowed to pour by gravity through a 10-cm nozzle and to contact water after a fall of ~2 m through the cover gas (steam and argon) space. Melt delivery times are estimated, presumably by thermocouple data, but at this stage, it is not clear how this is done, nor what are the uncertainties involved.

III. OVERVIEW AND ORGANIZATION OF THIS PAPER

As noted already, the main purpose of this paper is to study the results from the MAGICO and FARO experiments with the help of PM-ALPHA. There is also an experimental component in addressing the local void fractions in MAGICO by an X-ray diagnostic technique, as an independent check on the FLUTE data reported earlier. To preserve some cohesiveness of presentation, this independent, experimental component is relegated to the appendix.

In the discussion of the experiments, we assume that the reader is already familiar with the original papers on them, i.e., Angelini et al. (1992) for MAGICO, and Magallon and Hohmann (1993) for FARO. Our presentation begins, in each case, with the aspects relevant to the simulations and how they were effected, and in the main part focuses on the comparisons and related interpretations. For completeness, we also provide a recently-implemented numerically advantageous treatment of phase-change in PM-ALPHA. [The complete formulation is also included, for convenience, in the appendix.] Starting from this introductory PM-ALPHA topic, the presentation proceeds from MAGICO to FARO.

IV. THE PM-ALPHA CODE

In the original formulation, the rate of phase change (J) was calculated such as to maintain the liquid phase saturated at the local pressure. This was accomplished by specifying ($J > 0$ for vaporization)

$$J = \frac{\rho_g'}{\tau_e} \left\{ \left(\frac{p_s}{p} \right)^{1/\gamma} - 1 \right\} , \qquad (1)$$

where γ is the usual specific heat ratio, p_s is the saturation pressure of liquid temperature, and p is the actual local pressure. The parameter τ_e is a relaxation time for thermodynamic equilibrium, and this model could couple very nicely with the iteration process given the correct amount of phase change accounting, implicitly, for pressure changes. We found it convenient to choose this relaxation time equal to the time step, but the results are not sensitive at least up to 5 times as large. With this model PM-ALPHA could accommodate a subcooled liquid, but numerically in a somewhat cumbersome way. On the other hand, the above formulation has occasionally caused criticism because of its heuristic nature. To eliminate this nuisance and at the same time achieve an explicit treatment of phase change, as a rate process, i.e., reflecting non-negligible amounts of superheat as well as subcooling, we replace Eq. (1) with:

$$J = \frac{1}{h_g - h_\ell} \left[R_g (T_g - T_s) + R_\ell (T_\ell - T_s) \right] . \qquad (2)$$

When the liquid and vapor are at their thermodynamically stable states (i.e., saturated or subcooled liquid, saturated or superheated vapor), the transfer coefficients (R_g and R_ℓ) are evaluated based on a set of constitutive laws that are consistent with the flow regime approach used previously. When the two phases are predicted to be in thermodynamically unstable states (i.e., superheated liquid and subcooled vapor), R_ℓ and R_g are adjusted upward to recover thermodynamic equilibrium. Sample calculations carried out with Eq. (2) and this approach are in excellent agreement with the previous results [i.e., based on Eq. (1)]. For convenience, the complete model after this modification is given in Appendix A.

V. CONSIDERATION OF THE MAGICO EXPERIMENT

A. Simulation Aspects

The basic concept of the experiment is illustrated in Figure 1. Tens-of-kilograms quantities of mm-sized steel balls are heated to a uniform temperature (up to 1000 °C), then transferred to an intermediate container equipped with a dumping mechanism, and within a few seconds are released into a pool of saturated (atmospheric pressure) water. The pool cross section is rectangular, 40.5 cm on the side. The major experimental parameters are pool depth (15, 25 and 50 cm), particle size (1.5 and 2.4 mm), particle temperature (600 to 1000 °C), pour diameter (12 and 20 cm), and particle entry velocity (corresponding to free fall from 5, 15, and 25 cm, with an initial velocity of 0.72 m/s). The initial velocity was obtained from high-speed movies and found to be independent of particle size or the particle depth in the intermediate container. From this and the measured total mass pour rate, the particle volume fraction at the outlet of the intermediate container could also be obtained as 1.87 and 2.5% for the 2.4 and 1.5 mm particles, respectively. Temperature losses in the intermediate container were minor, and the actual temperature of the particulate just before being released was reported.

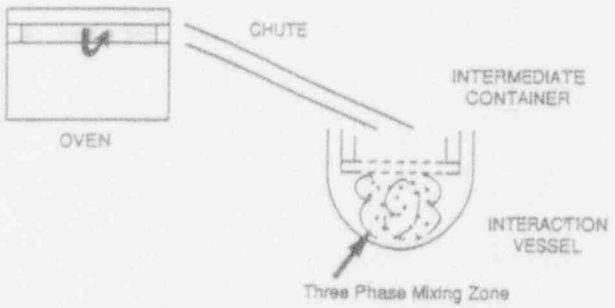

Figure 1. Schematic of the MAGICO experiment.

Thus, for any particular experiment, all conditions necessary for the simulation are exactly specified, and only one minor approximation and one minor non-ideality need to be mentioned. The approximation involves representing the rectangular cross section of the pool by a circular one of diameter equal to the side of the rectangular tank. The pour area is also circular, and this allows the simulations to be performed in axissymmetric cylindrical geometry. The non-ideality involves the presence of a few cold balls in the front of the falling particle cloud. These are the balls that fill the holes in the 6-mm-thick plate of the dumping mechanism; they are cold because of heat losses to the plate, and they fall in a "formation" with a considerably larger particle volume fraction than the rest of the cloud (this was confirmed experimentally). Certainly, these balls cannot influence the interaction itself, but one needs to be aware of them for some timing details and especially for interpreting the very initial FLUTE signal as previously discussed (Angelini et al., 1992).

The actual flow field employed in PM-ALPHA is illustrated in Figure 2. All geometric features and inlet conditions are specified for each experiment, as discussed above,

except for the vent openings. Since in the experiment the pool top was completely open to the atmosphere, the only requirement is that these vent openings are chosen of large enough area to avoid any pressurization in the vapor space. Cell sizes are 2.0 cm in the radial direction and 2.5 cm in the axial direction, which gives 10 radial cells and 12-26 axial cells, depending on tank depth and free-fall region. Node size studies showed that this is adequate.

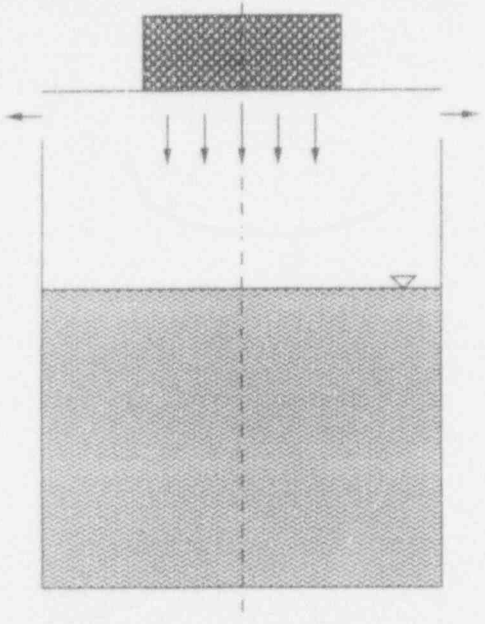

Figure 2. Illustration of the flow field utilized in PM-ALPHA for the interpretation of the MAGICO experiment.

The experimental data consist of mixing-zone-average void fractions obtained from high-speed movies (from the level rise around the mixing zone), and local void-fraction transients using a new instrument, the FLUTE. Both of these quantities can be easily obtained from the results of the PM-ALPHA computations for comparison with the data, and such comparisons have been reported previously (Angelini et al., 1992; Theofanous et al., 1992) with very good agreement. Also, chordal-average steam volume fractions can be obtained for comparisons with the projection-type information obtained from X-ray radiography, as described in Appendix B. These comparisons are also very good. As a next step in this study of MAGICO, we examine some of the more detailed features of the interactions as revealed in the computations and relate them, when possible, to the structure of the mixing zone as seen by direct visualization.

B. The Detailed Structure of Interactions in MAGICO

The premixing transient is a vastly complicated process, which besides the primary quantity of interest, the space-time evolution of the void fraction, has a number of other interesting features. These features relate to the detailed motions and associated interactions, and they are significant in creating the conditions within which the void fraction patterns develop. We study these motions here in terms of the calculated steam and water volume flux patterns for the conditions of MAGICO runs #702 (25-cm pool, 2.4-mm balls, 800 °C) and #905 (50-cm pool, 1.5-mm balls, 800 °C). These runs were chosen for the purpose of explaining the prediction of a "reversal of water volume flux" phenomenon, which we believe relates to, and explains, an experimentally-found sudden increase in steam generation rate under certain conditions during the premixing transient. More specifically, we believe that reversal of water flux causes a strong counter-current melt-water contact and an associated rapid increase in steam generation rates; accordingly, the resulting phenomenon is termed Energetic Transfer of Heat in a Counter-Current Ambient (ETHICCA).

The reversal of water volume flux is illustrated in Figures 3 and 4 for runs #702 and #905, respectively. [In these figures, spatial maps are given for only one-half of the flow field—symmetry.] In the initial stages, we can see that the generated steam moves upward and out of the mixing region, while the water is being pushed down and to the sides. This creates a counterclockwise motion in the liquid around the mixing zone. As time goes on, the behavior of the steam remains basically the same, except for being lifted from farther down the pool in a pattern that follows the particle cloud front penetrating the pool. However, the water volume flux undergoes two major changes, one at 0.2 and the other at 0.6 seconds. At 0.2 s in the interaction, water is seen to begin to move upward within the mixing zone, apparently being "lifted" by the steam flow. The mixing region is therefore becoming depleted of liquid for three reasons: vaporization, water being pushed down and to the sides by the particles, and water being lifted by the steam. The implied internal stagnation region is clearly visible in Figures 3b and 4b. The other change occurs around 0.6 s, when the water around the mixing zone reverses sense of "rotation" (note that these are all irrotational motions) and begins to flow into the mixing zone! At about the same time with this flow reversal, the high-speed movies show a relatively violent breakup of the pool surface, as if by a suddenly increased steam generation rate; this is the ETHICCA connection mentioned above. Quantitatively, this sudden change in steaming rate is illustrated in Figures 5a and 5b, and in detail is seen to depend on particle size and pool depth, and we expect on particle temperature also. However, we believe that the most important parameter affecting ETHICCA is the pour-to-pool diameter ratio, and in the limit to where this ratio is 1, ETHICCA should vanish; preliminary calculations confirm this expectation. The particular mechanism, in elementary terms, is due to the buildup of gravitational head between the inside (voiding) of the mixing zone and the outside water (hence, absolute value of water pool depth is also important), and is another manifestation of the decisively non-one-dimensional nature of premixing transients.

Apart from the water volume flux evolution, the ETHICCA can be tracked from the evolution of the steam volume fraction in time. This is shown in Figures 6 and 7 for runs #702 and #905, respectively. These figures are given in two forms, a synoptic one in 6i,j and 7i,j for visualizing the whole transient, and a quantitative one in 6a-h

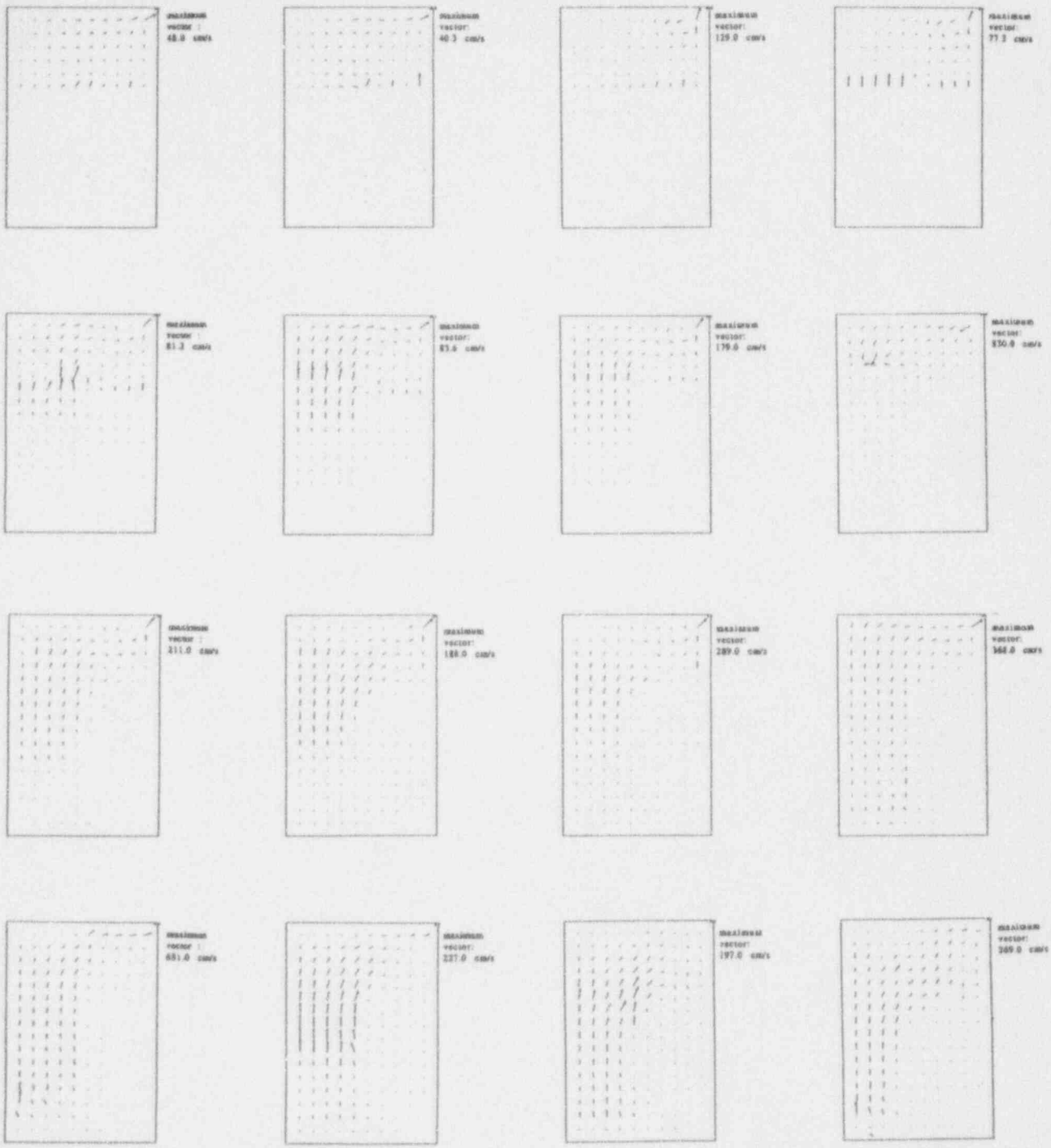

Figure 3a. Evolution of steam volume flux in numerical simulation of Run #702. Upper two rows, times (from impact of balls on the water) are .004 s, .054 s, .104 s, .154 s, .204 s, 254 s, .304 s, .354 s; lower two rows, times (from impact of balls on the water) are .404 s, .454 s, .504 s, .554 s, .604 s, .654 s, .704 s, .754 s.

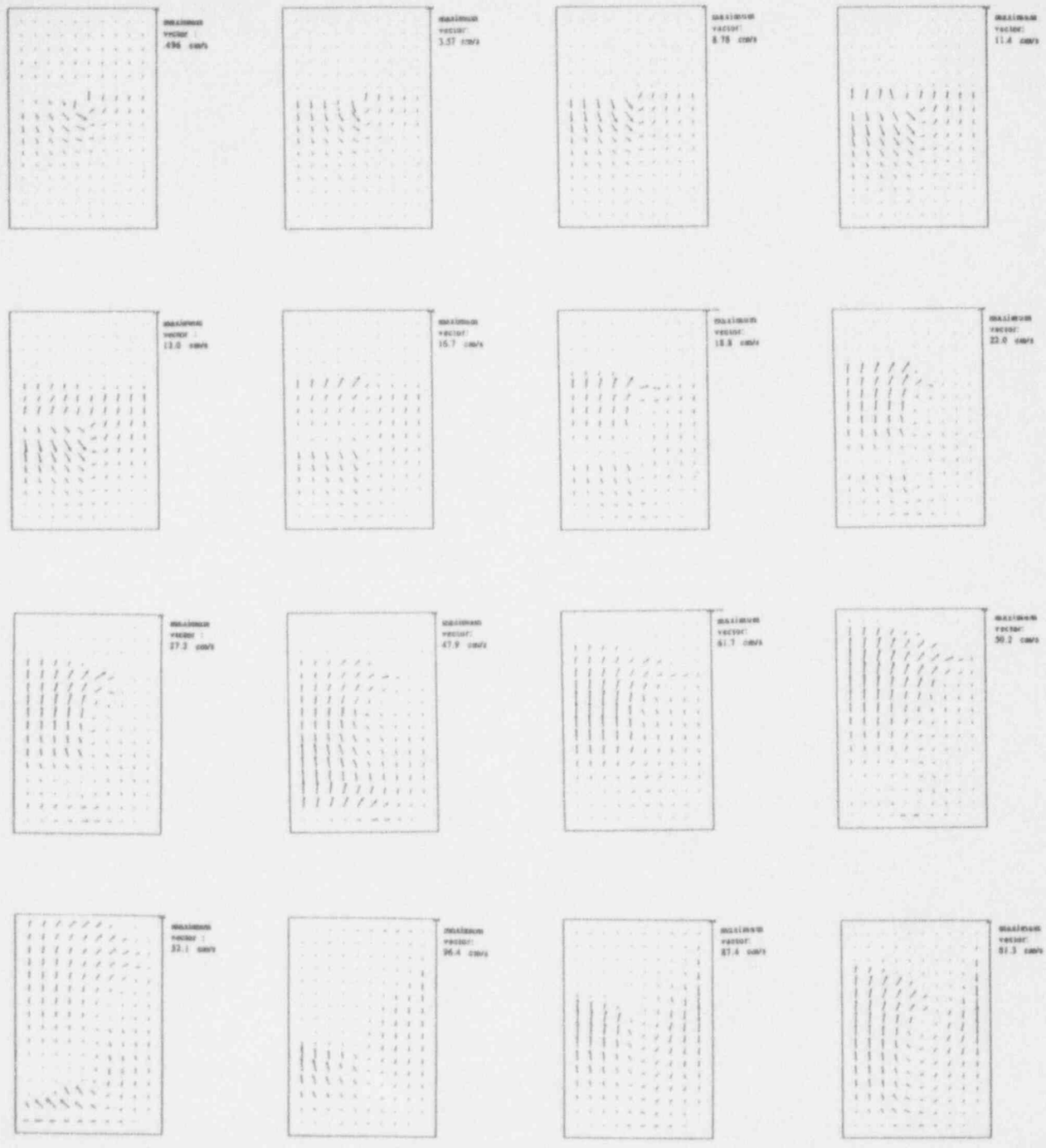

Figure 3b. Evolution of water volume flux in numerical simulation of Run #702. Upper two rows, times (from impact of balls on the water) are .004 s, .054 s, .104 s, .154 s, .204 s, .254 s, .304 s, .354 s; lower two rows, times (from impact of balls on the water) are .404 s .454 s, .504 s, .554 s, .604 s, .654 s, .704 s, .754 s.

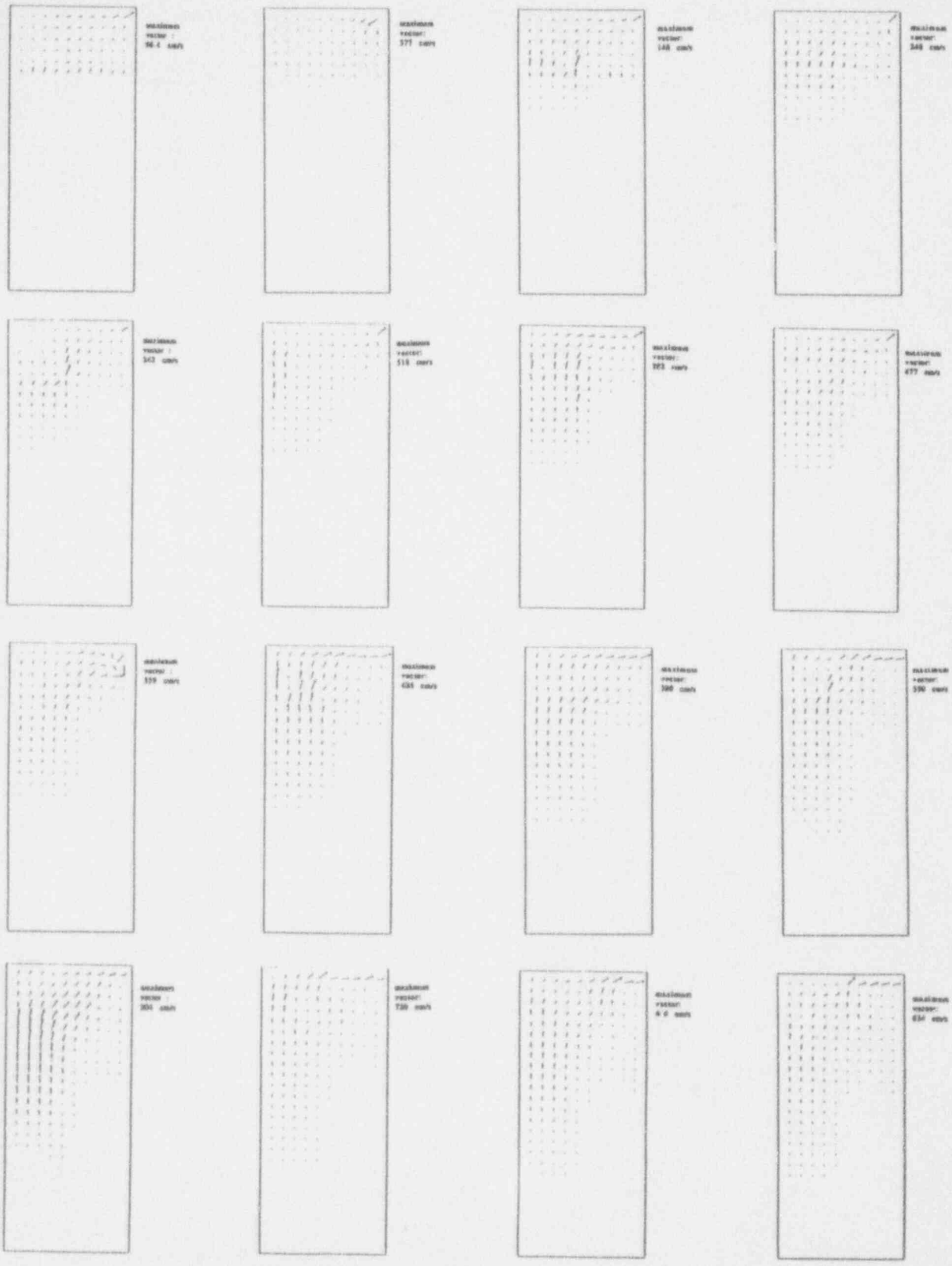

Figure 4a. Evolution of steam volume flux in numerical simulation of Run #905. Upper two rows, times (from impact of balls on the water) are .004 s, .054 s, .104 s, .154 s, .204 s, .254 s, .304 s, .354 s; lower two rows, times (from impact of balls on the water) are .404 s, .454 s, .504 s, .554 s, .604 s, .654 s, .704 s, .754 s.

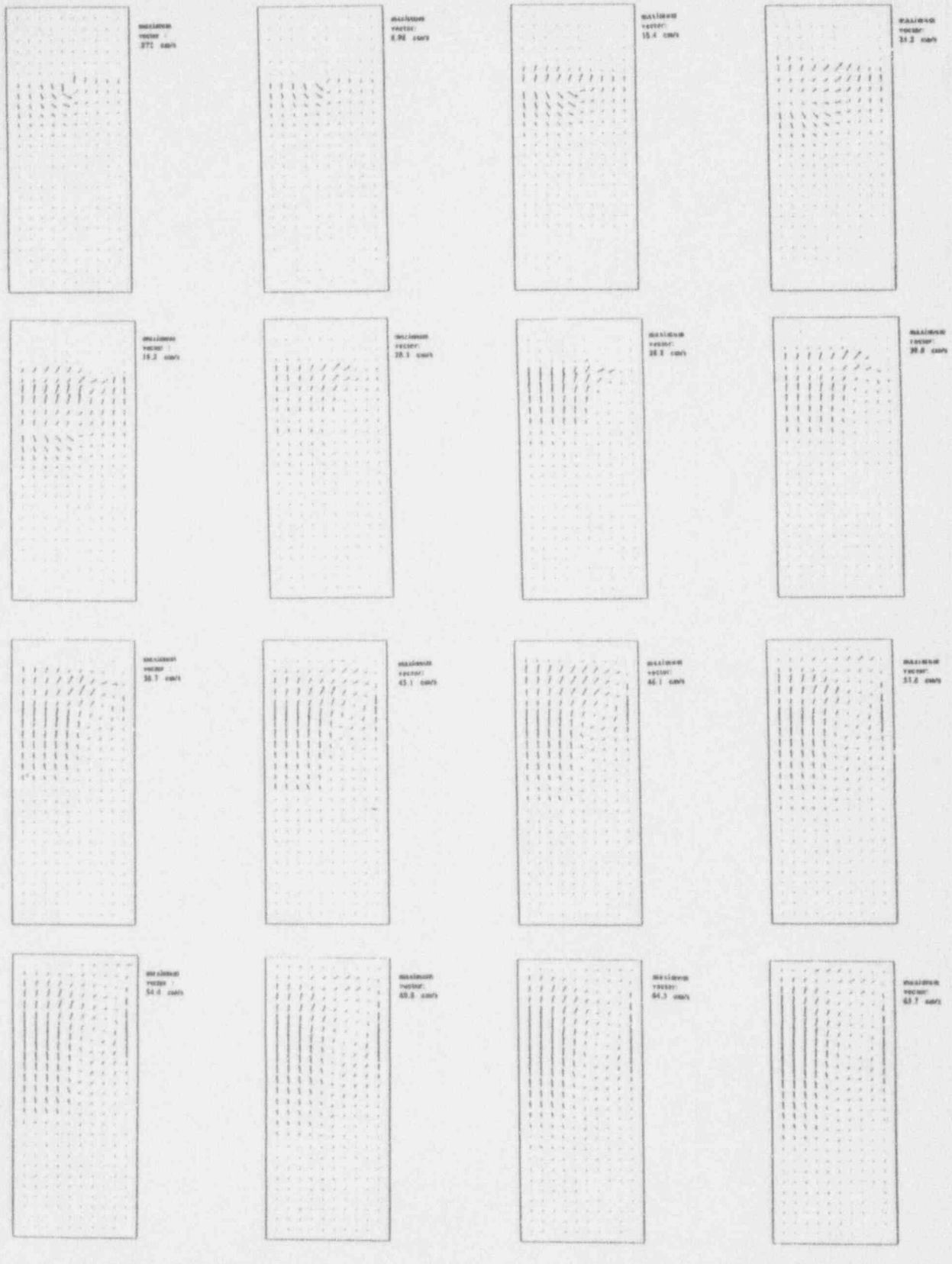

Figure 4b. Evolution of water volume flux in numerical simulation of Run #905. Upper two rows, times (from impact of balls on the water) are .004 s, .054 s, .104 s, .154 s, .204 s, .254 s, .304 s, .354 s; lower two rows, times (from impact of balls on the water) are .404 s, .454 s, .504 s, .554 s, .604 s, .654 s, .704 s, .754 s.

and 7a-h with the void fraction contours labelled. From these figures, we can visualize the growth of the mixing zone and the breakup associated with ETHICCA. In addition, they may be seen to be remarkably similar (in shapes) to sample snapshots taken during actual runs and collected in Figures 8 and 9. In particular, notice the agreement in the violent breakup of the pool surfaces seen to occur at around 0.4 s in run #905.

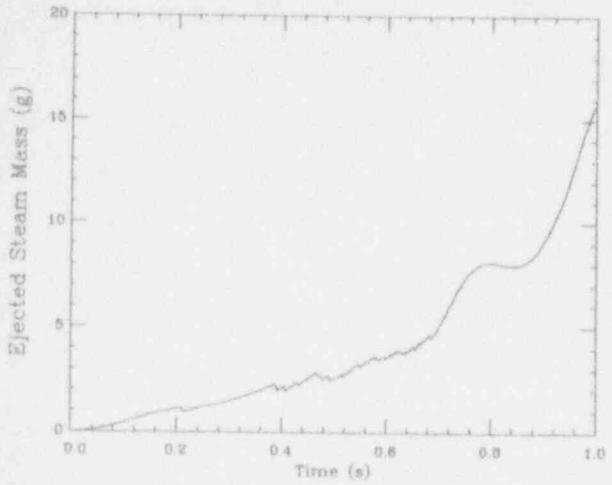

Figure 5a. Mass of steam ejected through venting cell in numerical simulation of run #702.

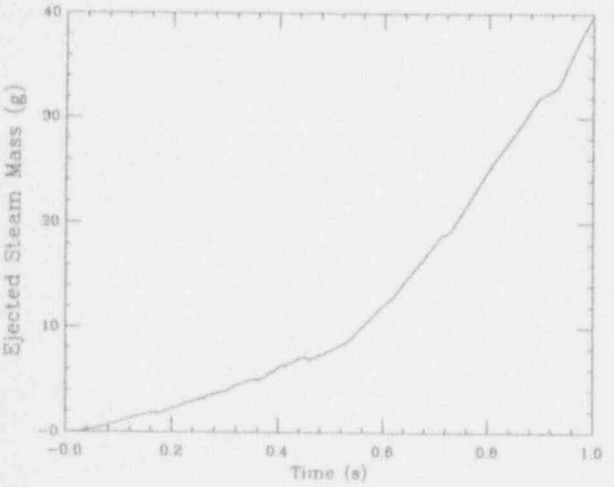

Figure 5b. Mass of steam ejected through venting cell in numerical simulation of run #905.

To conclude, it would appear interesting now to carry out more focused investigations suggested by these results; specifically by measuring velocity profiles in the water surrounding the interaction zone, and by visualizing the internal (void fraction) shapes within the zone itself (see Appendix B). Both are well within the technology currently available for MAGICO, and such studies are planned for the near future. Incidentally, we also plan experiments with aluminum oxide particles (different density than the steel ones used till now) of much higher temperatures. Finally, in a companion experimental/analytical program, we are studying film boiling from spheres in steam-water two-phase flows including conditions of elevated pressures (Liu et al., 1992).

VI. CONSIDERATION OF THE FARO EXPERIMENT

This experiment involves the pouring, under gravity, of tens-of-kilograms quantities of UO_2/ZrO_2 melts at high temperatures (~2700 °C) into deep water pools (~1 m) at high pressure (~5 MPa). The interaction is contained in a closed cylindrical vessel ~3 m in length and 0.47 or 0.71 m in diameter for the Scoping Test (ST) and the Quenching Test 2 (QT2), respectively. The initial pool temperature is well-characterized, and the water depth is given as 0.87 and 1 m for the ST and QT2, respectively. Thus, the flow field can be simply represented for simulations with PM-ALPHA, as illustrated in Figure 10. The length of the gas space was slightly reduced to preserve the total test vessel volume (accounting for the melt catcher volume in it) to the values of 0.64 and 1.3 m^3 given for the ST and QT2 conditions, respectively. This whole flow field was discretized, uniformly, into 5 radial and 60 axial cells (Δr = 4.7 cm, Δz = 6.1 cm). Cylindrical symmetry was assumed.

The only aspects of the simulations that require some elaboration are concerned with melt delivery, with certain transient behavior prior to the melt reaching the water pool surface, and with melt breakup in the interaction. The discussion of these aspects is limited here to the case of the Scoping Test, as only this test could be analyzed in the short time available since the release of these data (Magallon et al., 1992). However, the treatment is expected to be similar to the QT2 simulations that will follow in the near future.

The melt delivery time is given as 0.28 s, for a total release of 18 kg of melt. Using this release rate and the melt-exit nozzle diameter (10 cm), we find an inlet melt velocity of 1.07 m/s. Under free-fall, the melt front is found to have traveled 0.67 m by the time the tail-end of the pour is entering the gas space; the melt front at this time, 0.28 s after initiation of the pour, is still 1.15 m above the water pool surface. Based on this, the calculation is initialized at 0.28 s with the experimentally measured value of the pressure in the gas space (~5.1 MPa) and the fuel distributed along the indicated column in Figure 10 with volume fractions and velocities in each cell obtained by accelerating the respective "parcel" under gravity, with the quoted initial velocity, so as to arrive at the respective location at the appropriately available travel time ($0 \leq t \leq 0.28$ s). Note that the innermost cell diameter is very nearly equal to that of the melt-exit nozzle; thus, all melt is taken to be contained within it.

The other aspect of the simulation that requires some elaboration is the treatment of melt-to-gas radiation heat transfer. This is peculiar to a closed system, with large cover-gas space, at high pressure, as is the case here, and its importance has already been noted by Magallon et al. (1992). An *a priori* treatment of this aspect would only be possible if the extent of melt breakup, and its emissivity, were known, which of course, is not the case. However, our

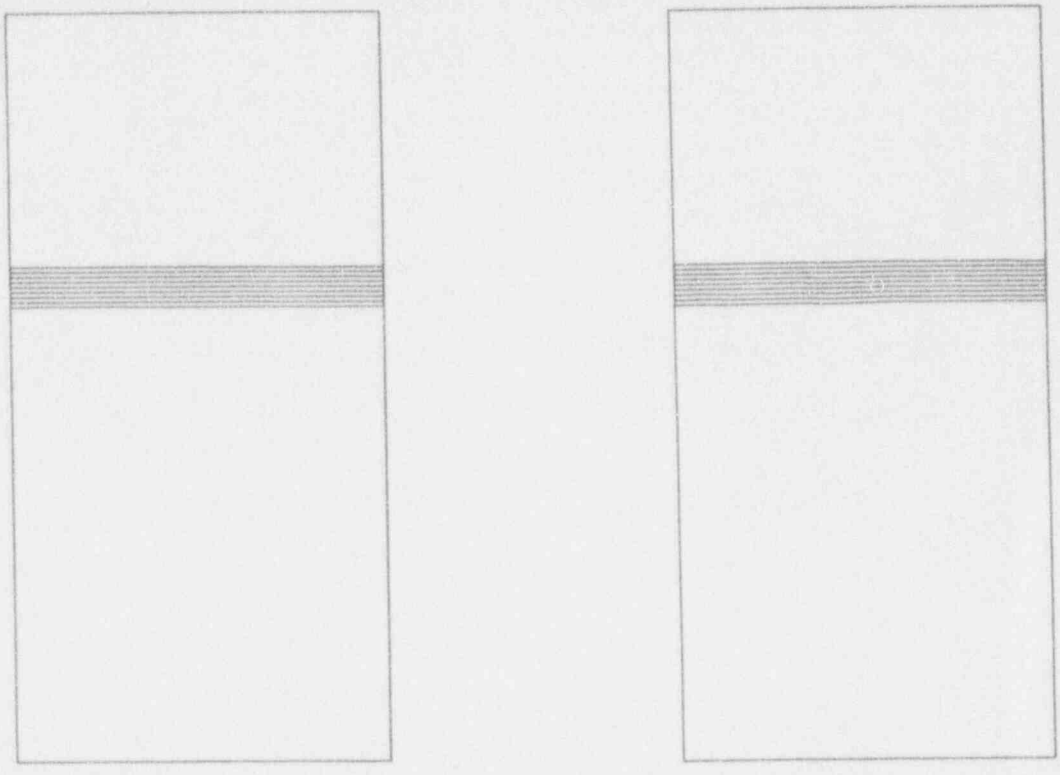

Figure 6a. Evolution of steam volume fraction in numerical simulation of Run #702. Times (from impact of balls on the water) are .004 s, .054 s.

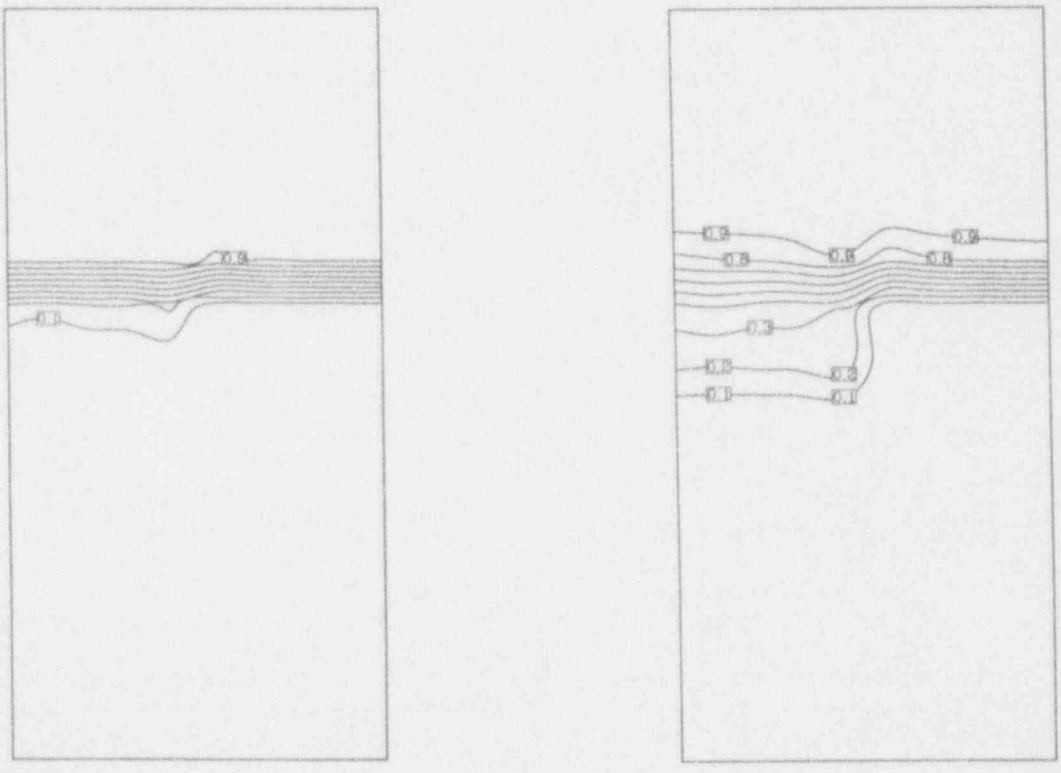

Figure 6b. Evolution of steam volume fraction in numerical simulation of Run #702. Times (from impact of balls on the water) are .104 s, .154 s.

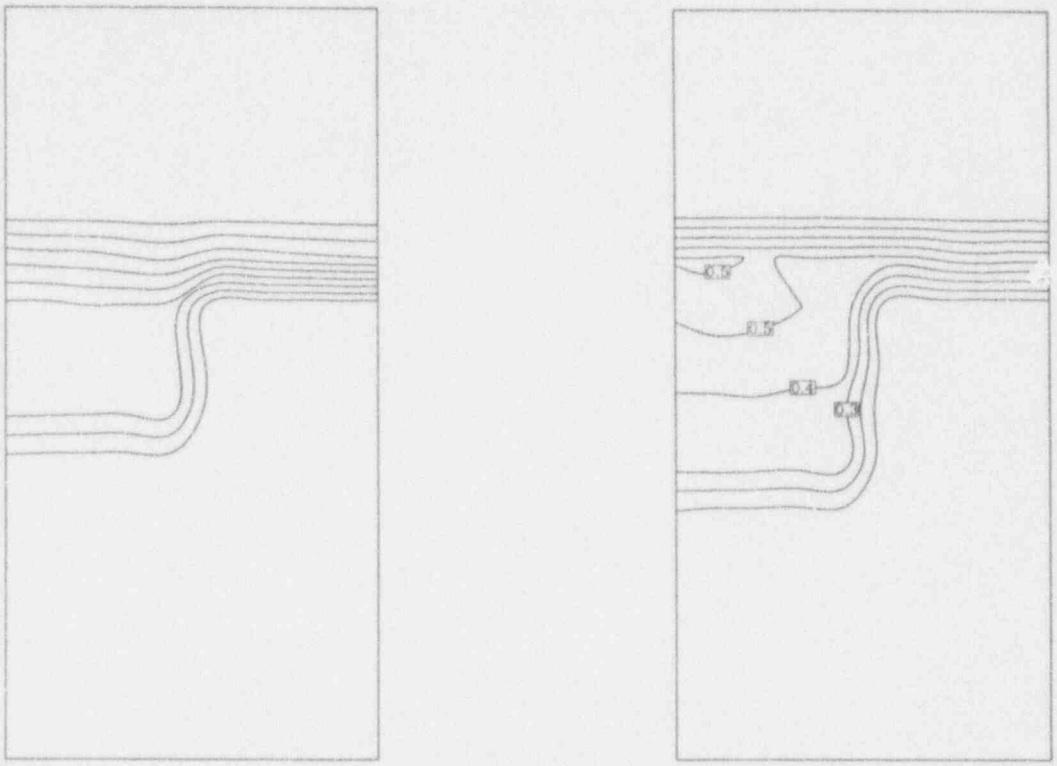

Figure 6c. Evolution of steam volume fraction in numerical simulation of Run #702. Times (from impact of balls on the water) are .204 s, .254 s.

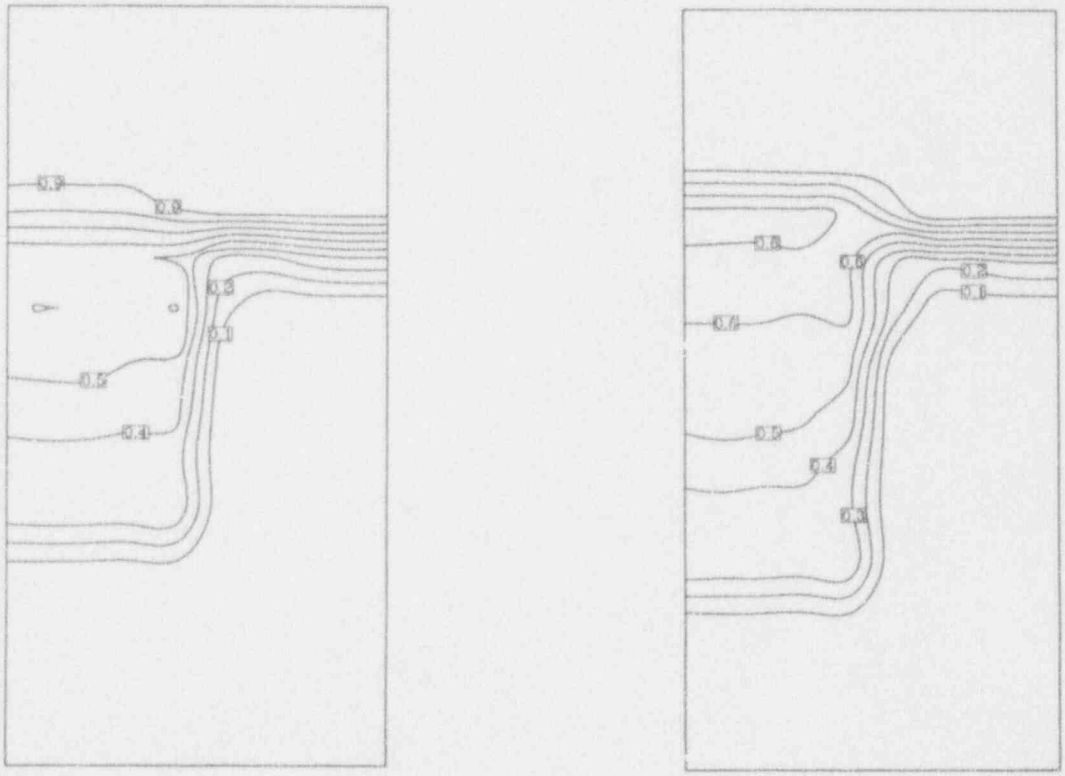

Figure 6d. Evolution of steam volume fraction in numerical simulation of Run #702. Times (from impact of balls on the water) are .304 s, .354 s.

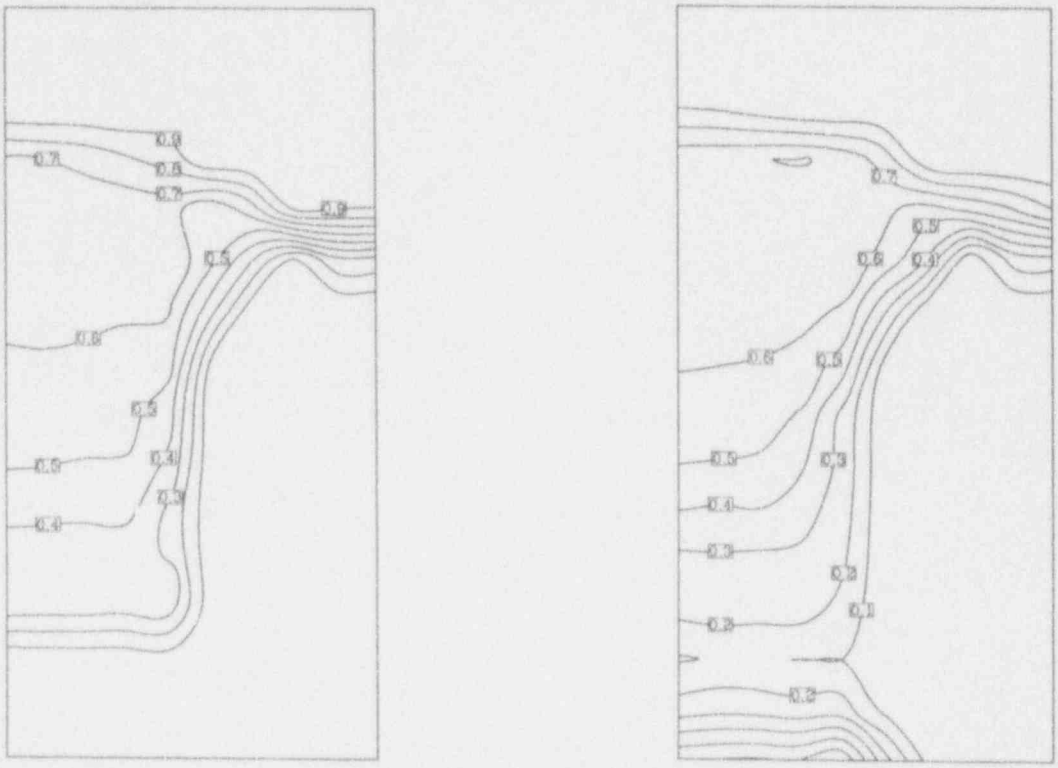

Figure 6e. Evolution of steam volume fraction in numerical simulation of Run #702. Times (from impact of balls on the water) are .404 s, .454 s.

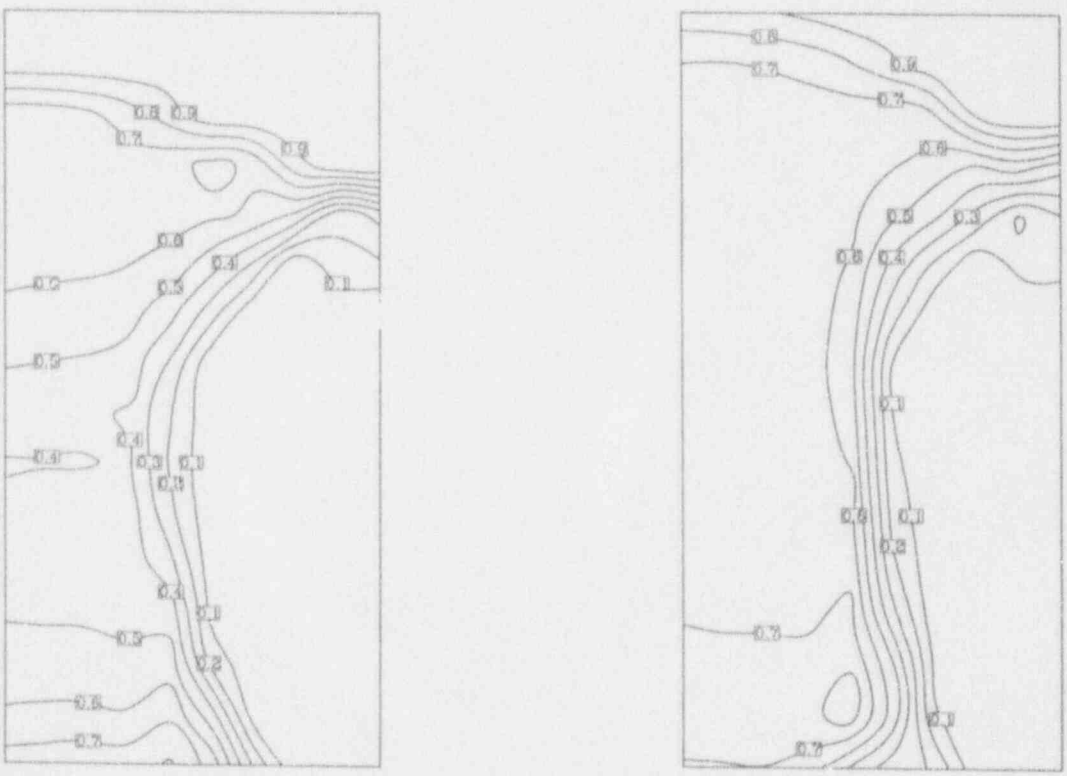

Figure 6f. Evolution of steam volume fraction in numerical simulation of Run #702. Times (from impact of balls on the water) are .504 s, .554 s.

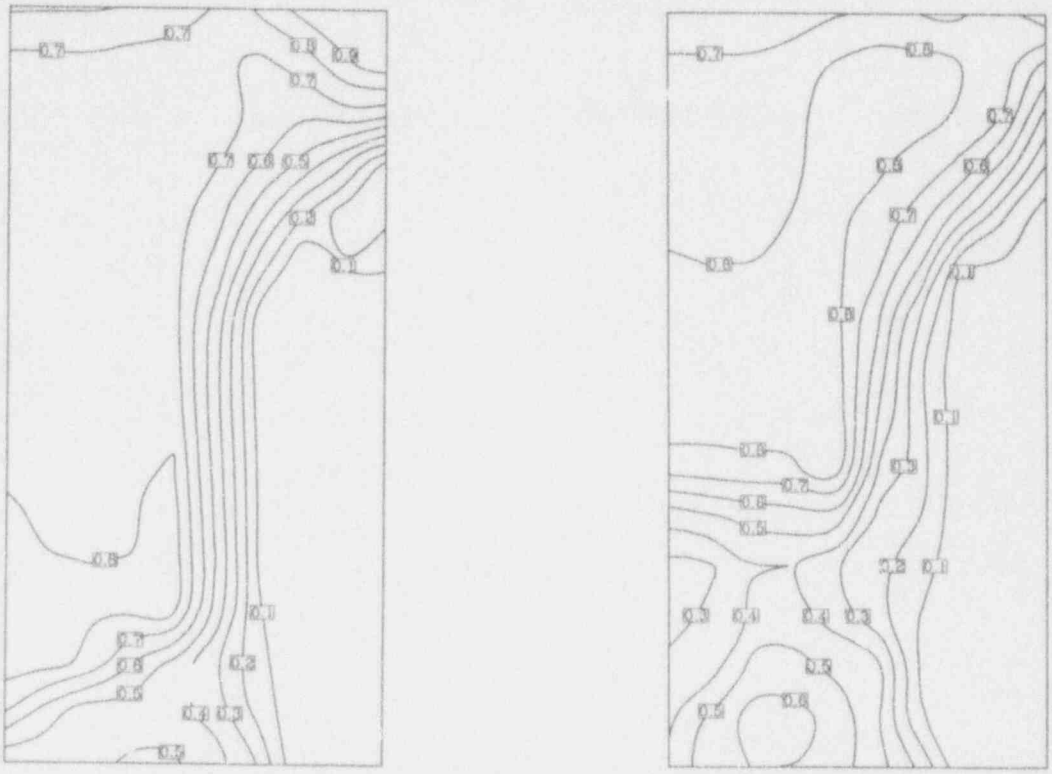

Figure 6g. Evolution of steam volume fraction in numerical simulation of Run #702. Times (from impact of balls on the water) are .604 s, .654 s.

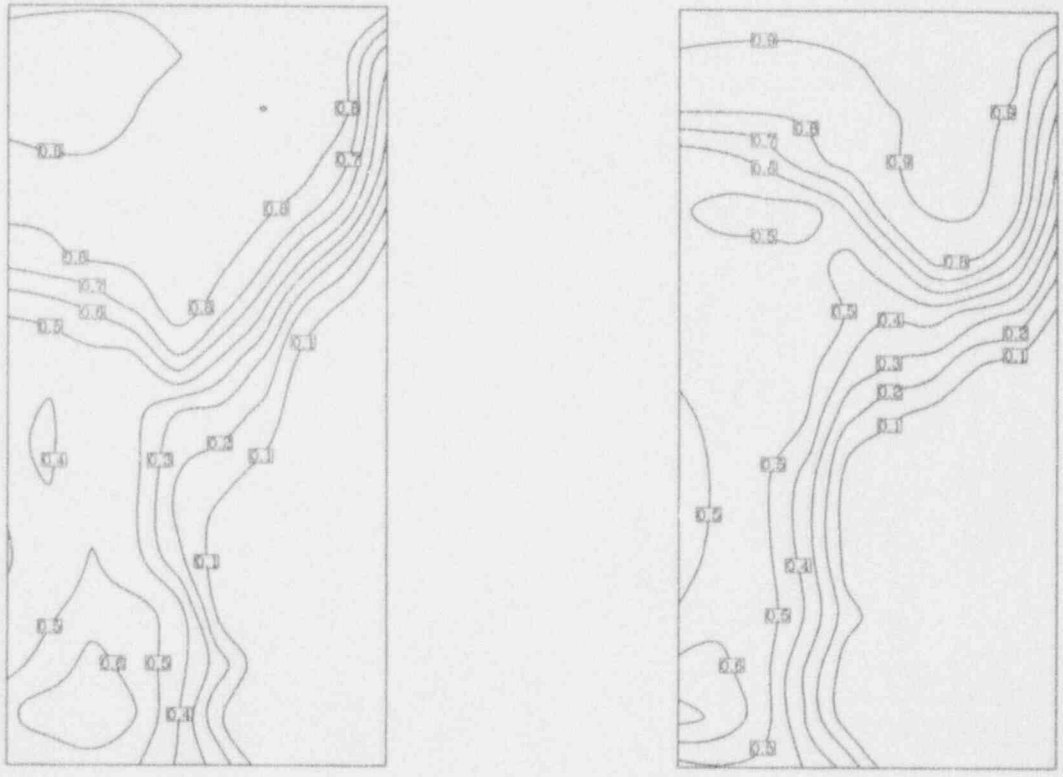

Figure 6h. Evolution of steam volume fraction in numerical simulation of Run #702. Times (from impact of balls on the water) are .704 s, .754 s.

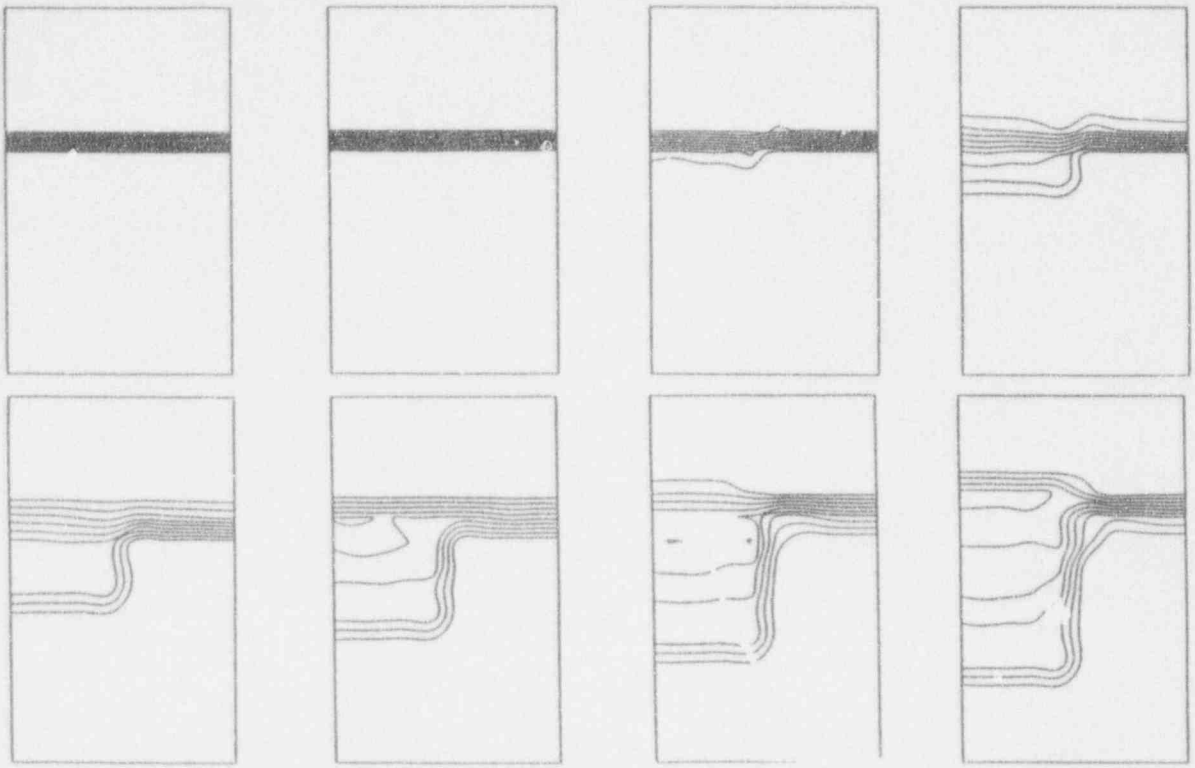

Figure 6i. Evolution of steam volume fraction in numerical simulation of Run #702. Times (from impact of balls on the water) are .004 s, .054 s, .104 s, .154 s, .204 s, .254 s, .304 s, .354 s.

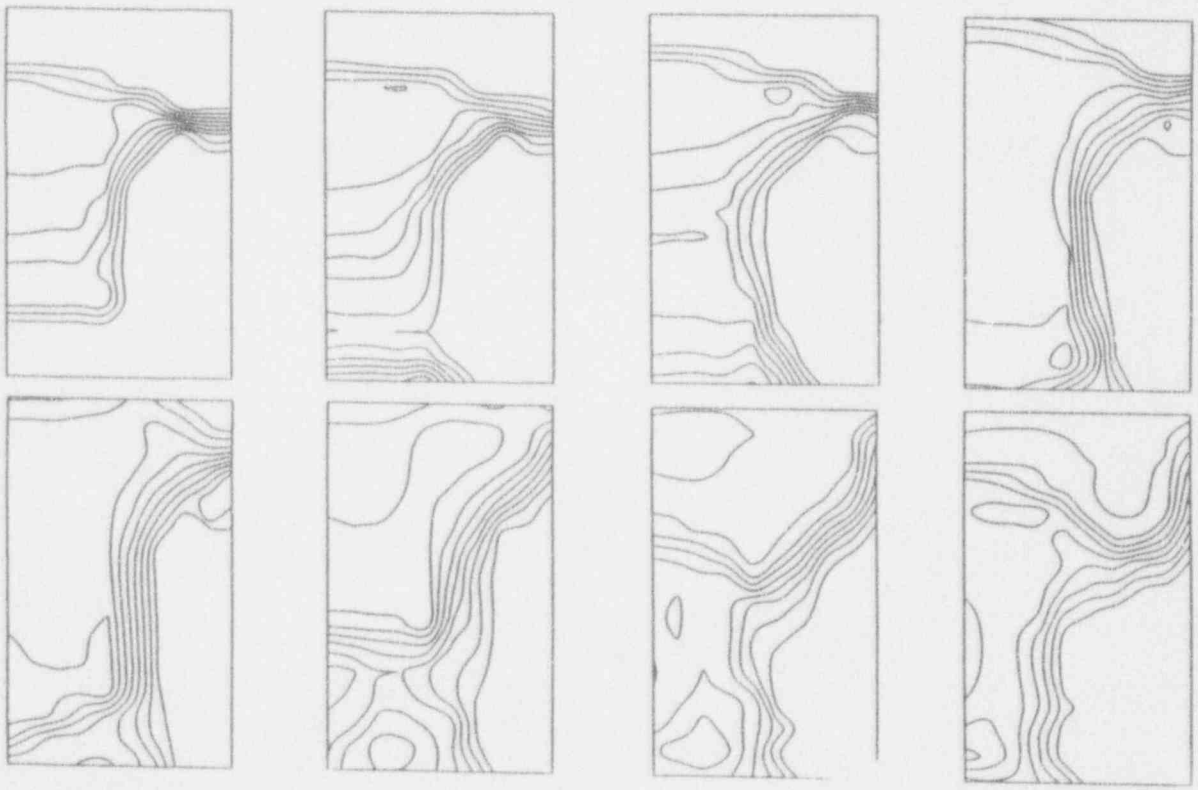

Figure 6j. Evolution of steam volume fraction in numerical simulation of Run #702 Times (from impact of balls on the water) are .404 s, .454 s, .504 s, .554 s, .604 s, .654 s, .704 s, .754 s.

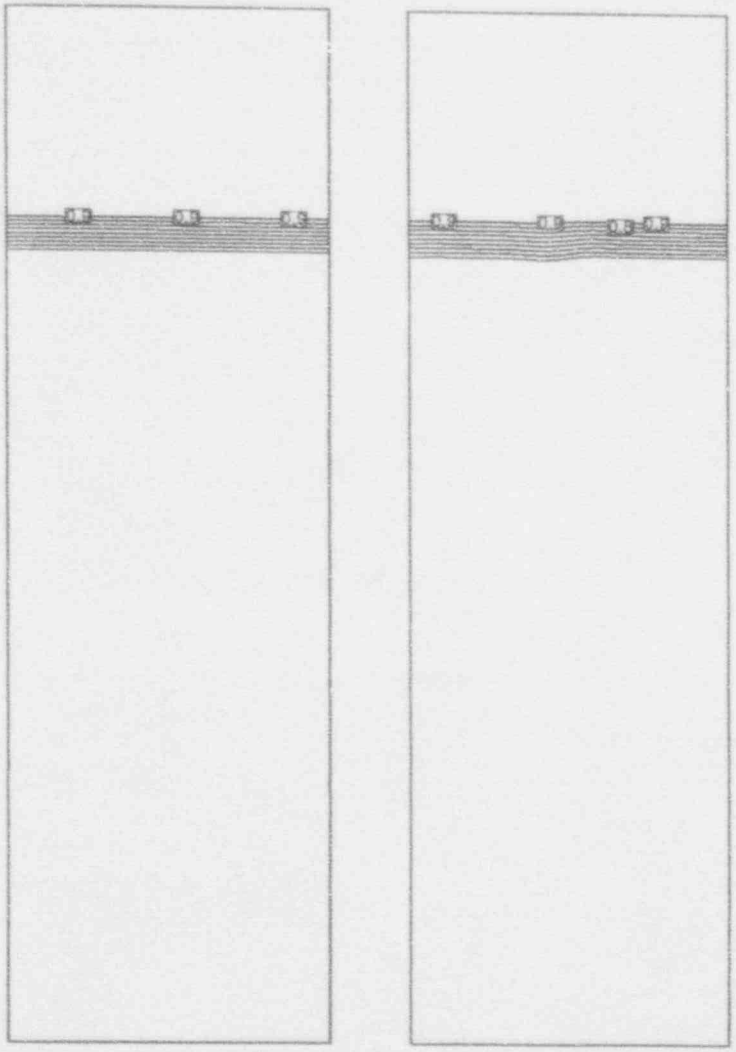

Figure 7a. Evolution of steam volume fraction in numerical simulation of Run #905. Times (from impact of balls on the water) are .004 s, .054 s.

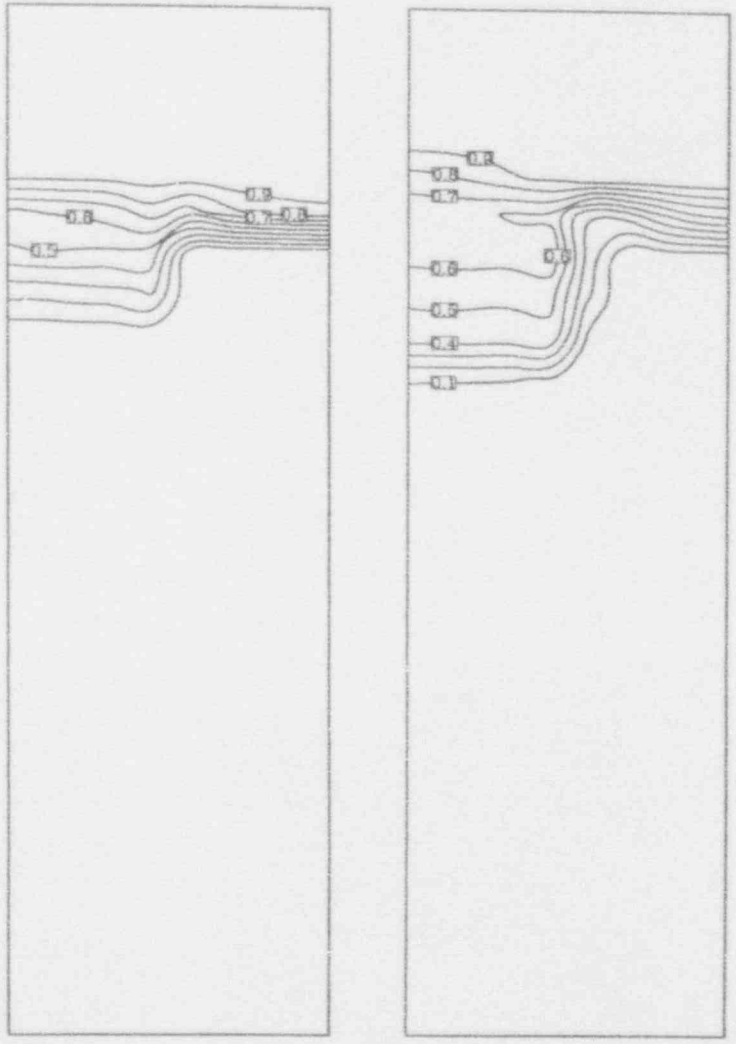

Figure 7b. Evolution of steam volume fraction in numerical simulation of Run #905. Times (from impact of balls on the water) are .104 s, .154 s.

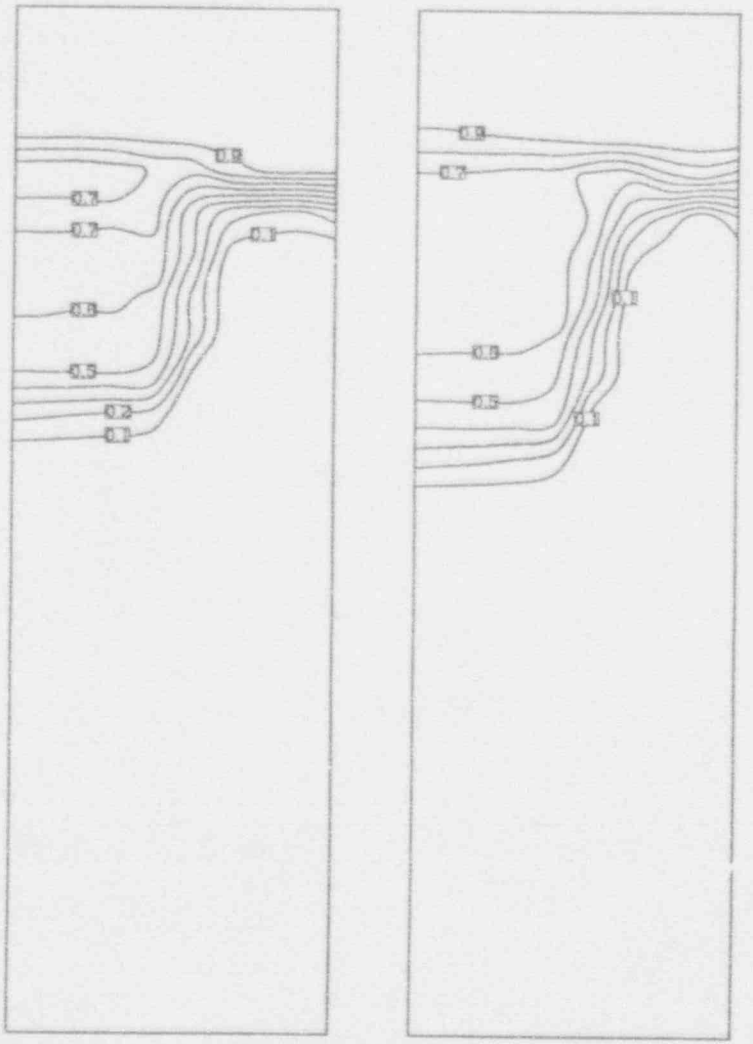

Figure 7c. Evolution of steam volume fraction in numerical simulation of Run #905. Times (from impact of balls on the water) are .204 s, .254 s.

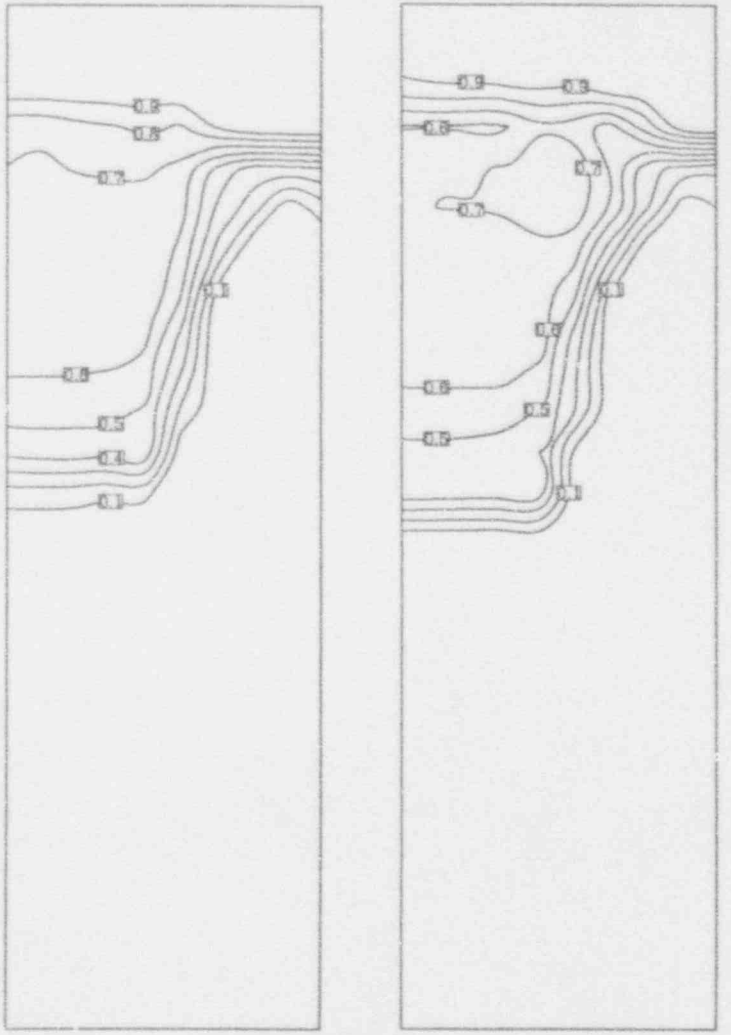

Figure 7d. Evolution of steam volume fraction in numerical simulation of Run #905. Times (from impact of balls on the water) are .304 s, .354 s.

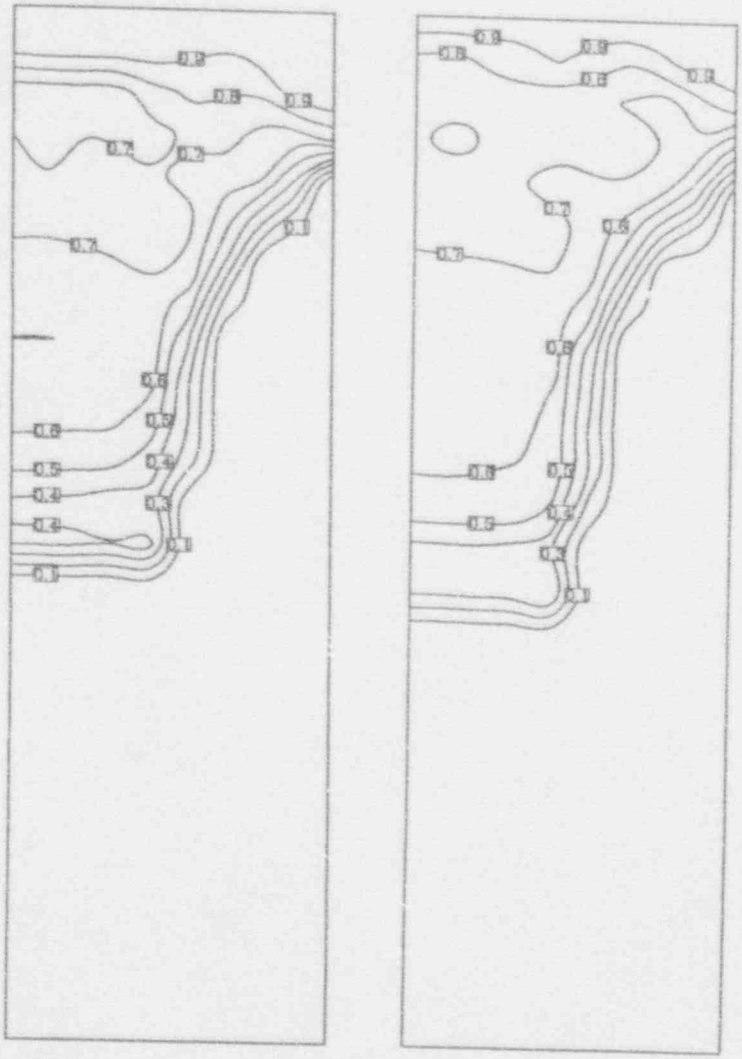

Figure 7e. Evolution of steam volume fraction in numerical simulation of Run #905. Times (from impact of balls on the water) are .404 s, .454 s.

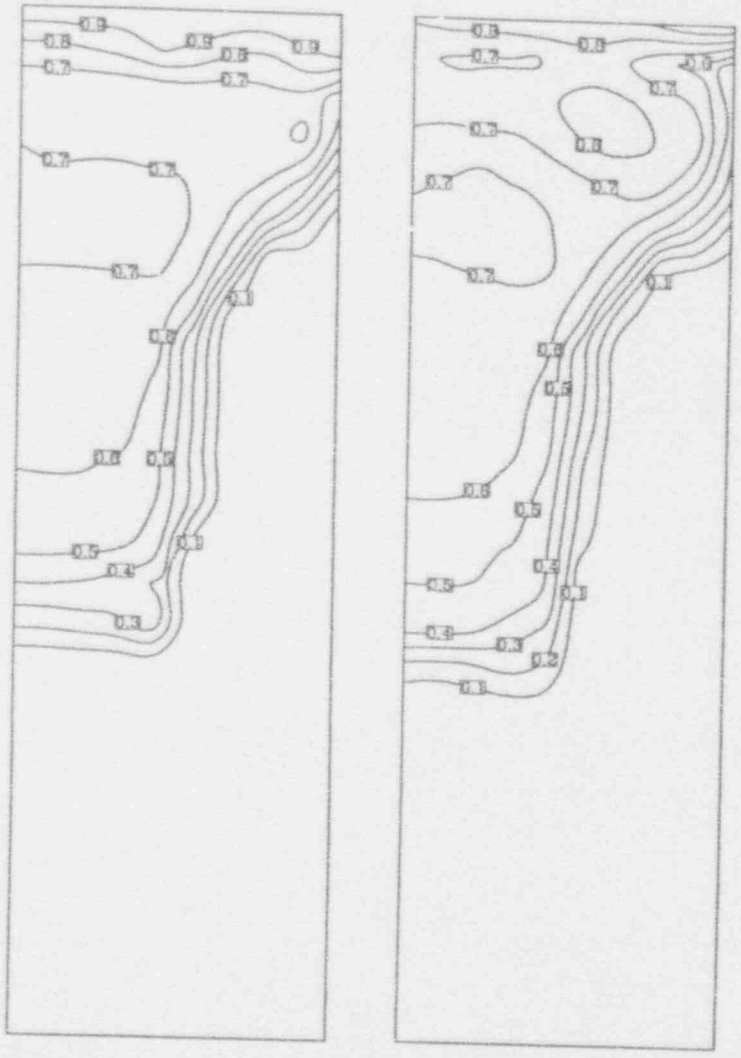

Figure 7f. Evolution of steam volume fraction in numerical simulation of Run #905. Times (from impact of balls on the water) are .504 s, .554 s.

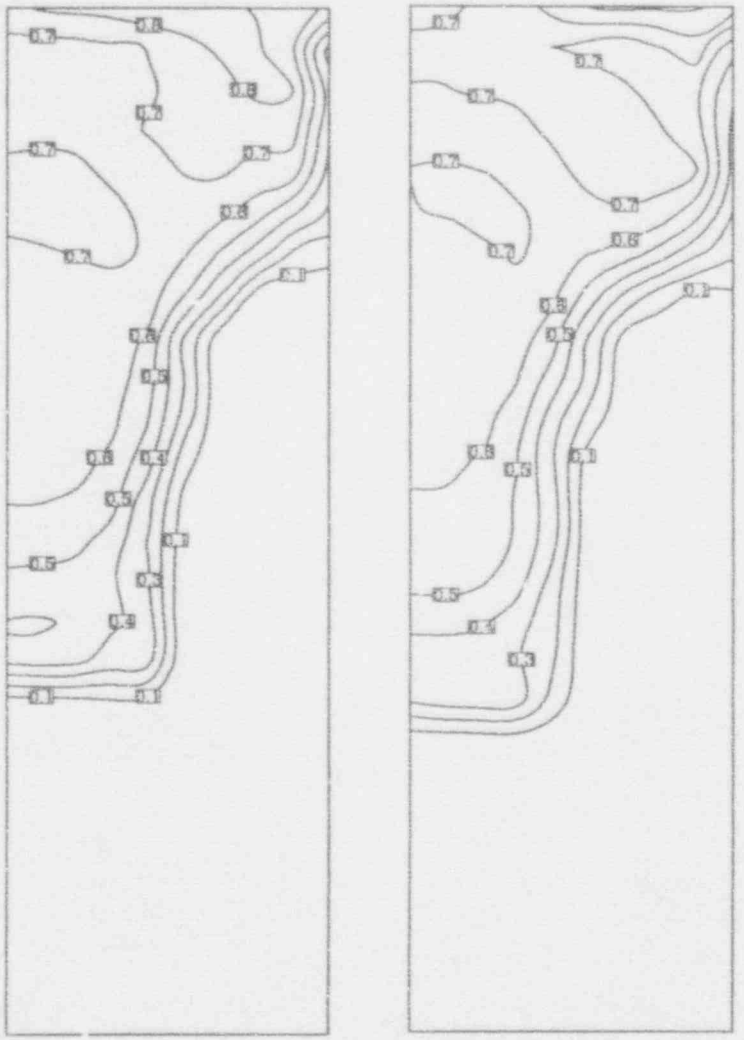

Figure 7g. Evolution of steam volume fraction in numerical simulation of Run #905. Times (from impact of balls on the water) are .604 s, .654 s.

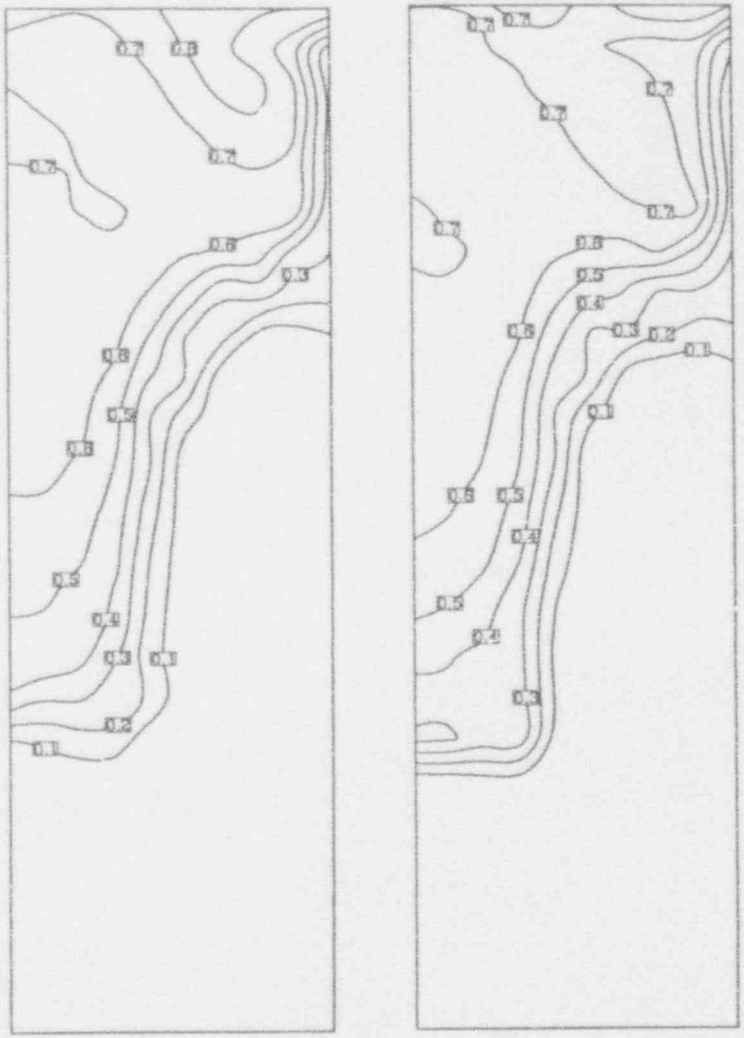

Figure 7h. Evolution of steam volume fraction in numerical simulation of Run #905. Times (from impact of balls on the water) are .704 s, .754 s.

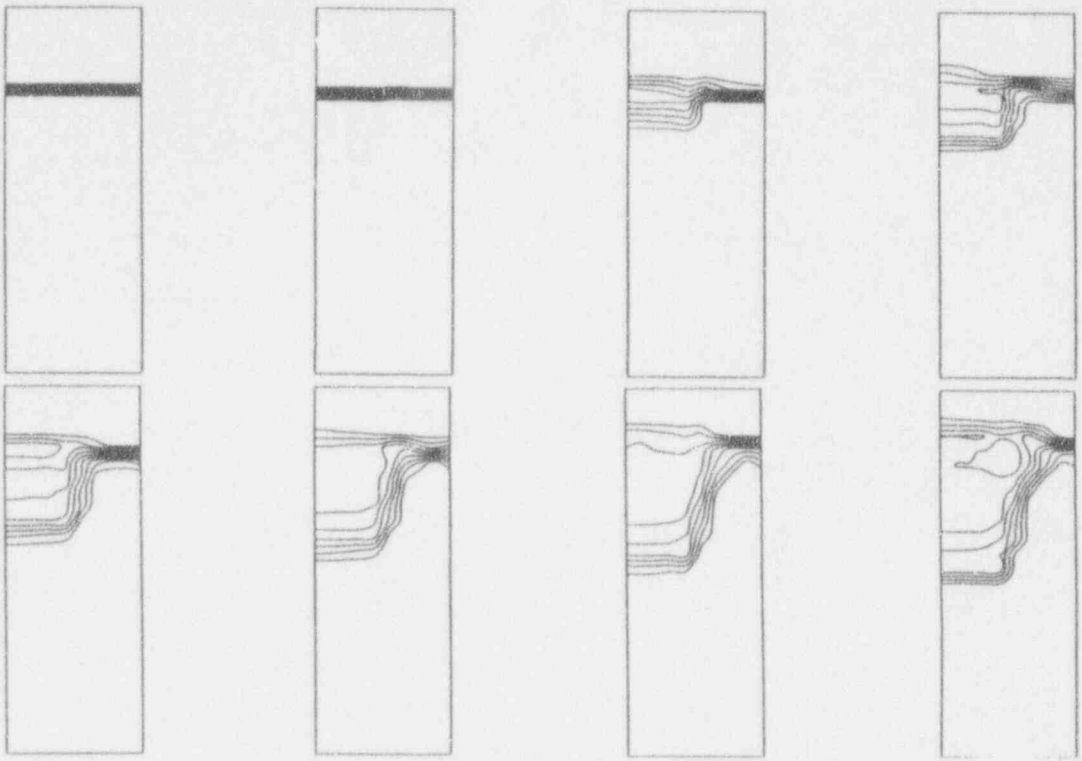

Figure 7i. Evolution of steam volume fraction in numerical simulation of Run #905. Times (from impact of balls on the water) are .004 s, .054 s, .104 s, .154 s, .204 s, .254 s, .304 s, .354 s.

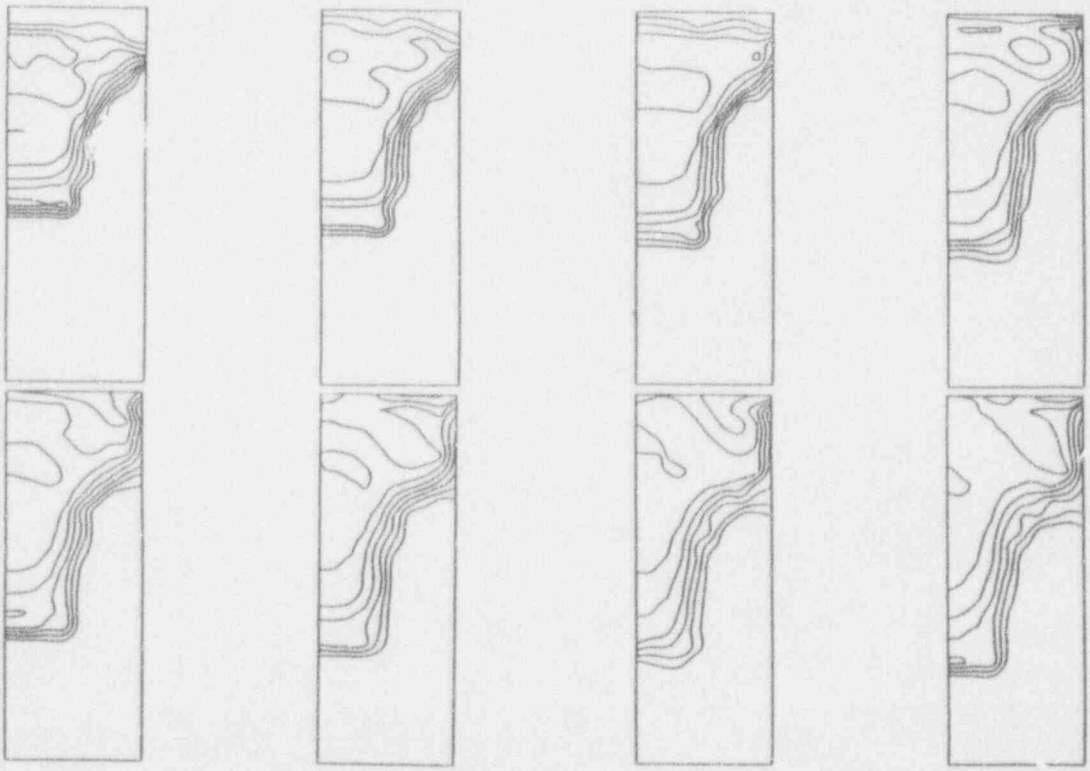

Figure 7j. Evolution of steam volume fraction in numerical simulation of Run #905. Times (from impact of balls on the water) are .404 s, .454 s, .504 s, .554 s, .604 s, .654 s, .704 s, .754 s.

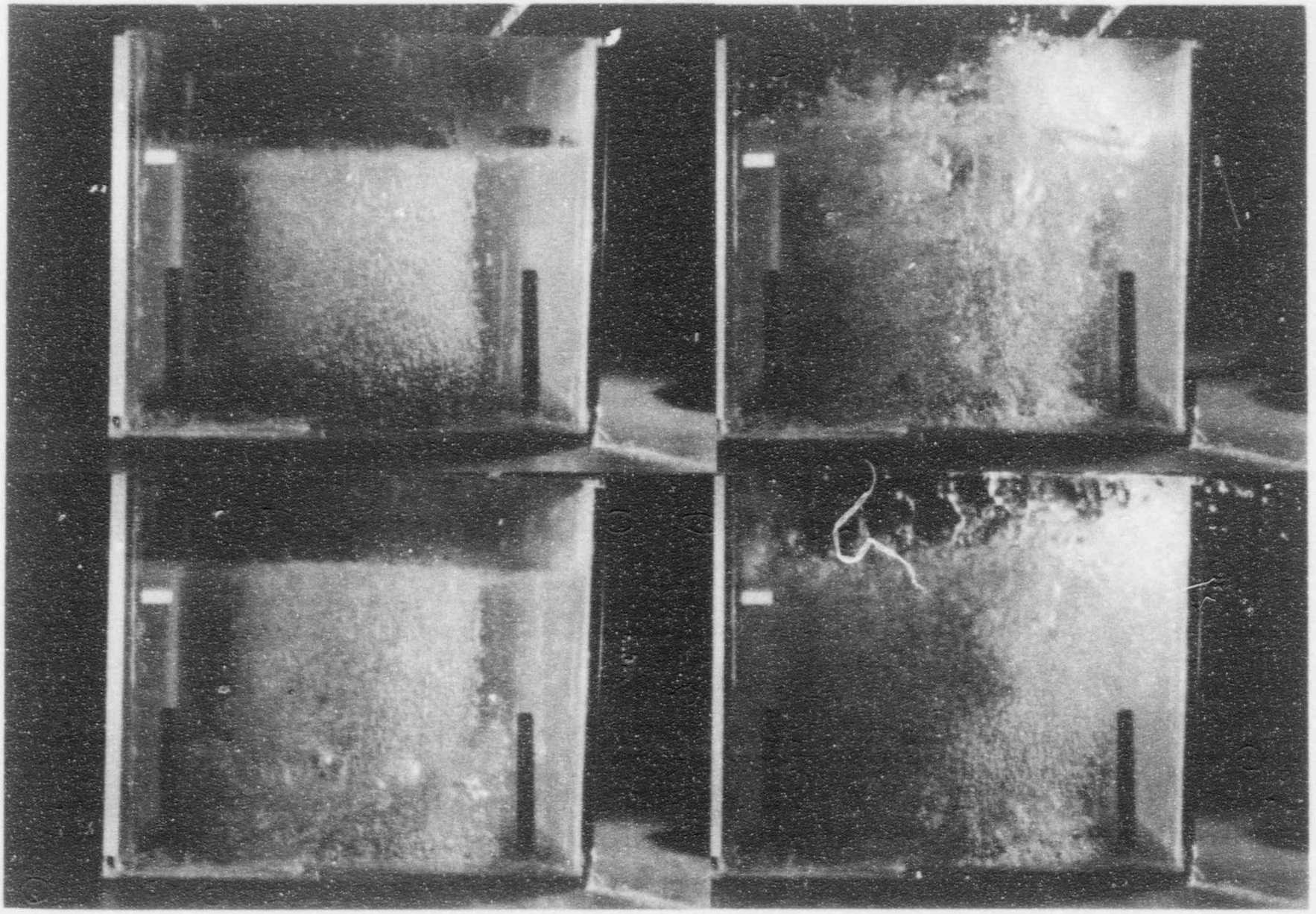

Figure 8. Snapshots of Run #205 (identical to Run #702). Times (from impact of balls on the water) are .27 s and .57 s.

Figure 8 (Continued). Snapshots of Run #205 (identical to Run #702). Times (from impact of balls on the water) are .87 s and 1.17 s.

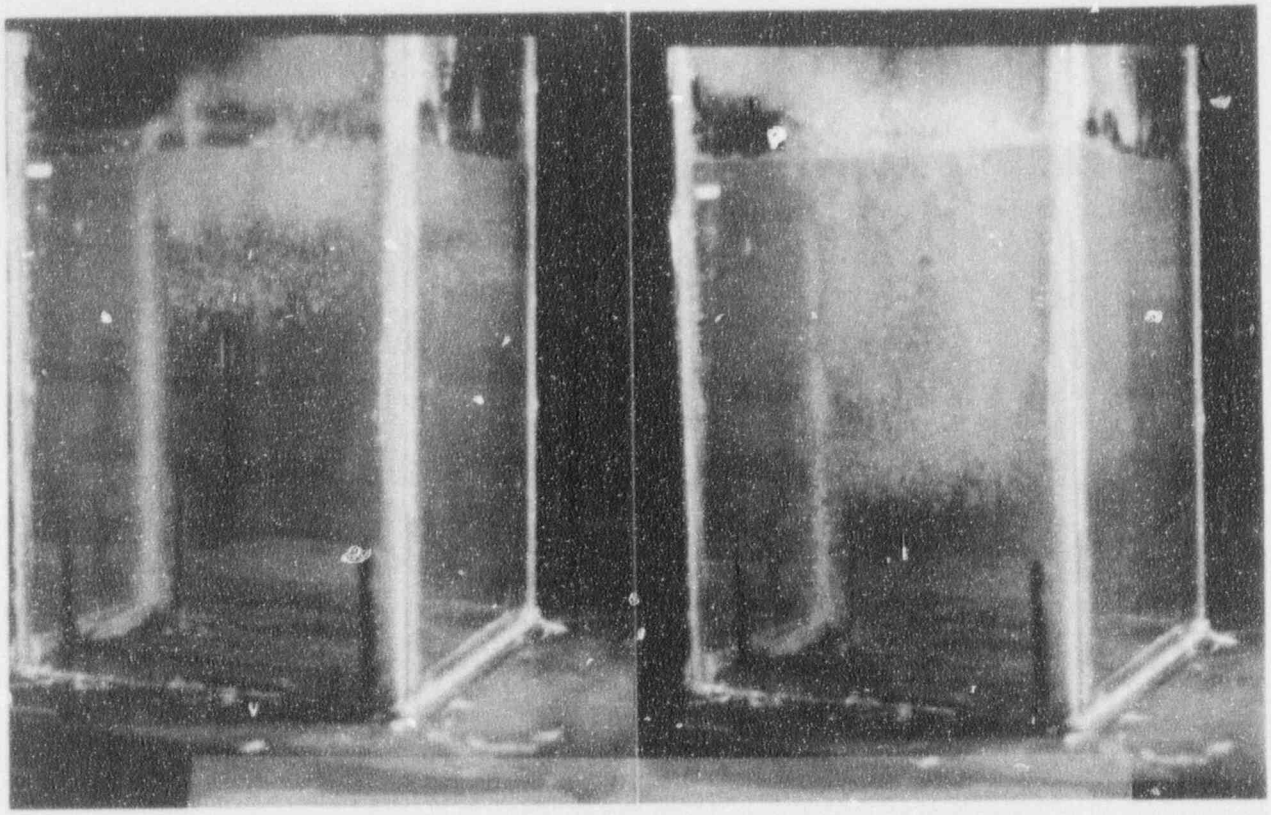

Figure 9. Snapshots of Run #905. Times (from impact of balls on the water) are .1 s and .4 s.

Figure 9 (Continued). Snapshots of Run #905. Times (from impact of balls on the water) are .7 s and 1.0 s.

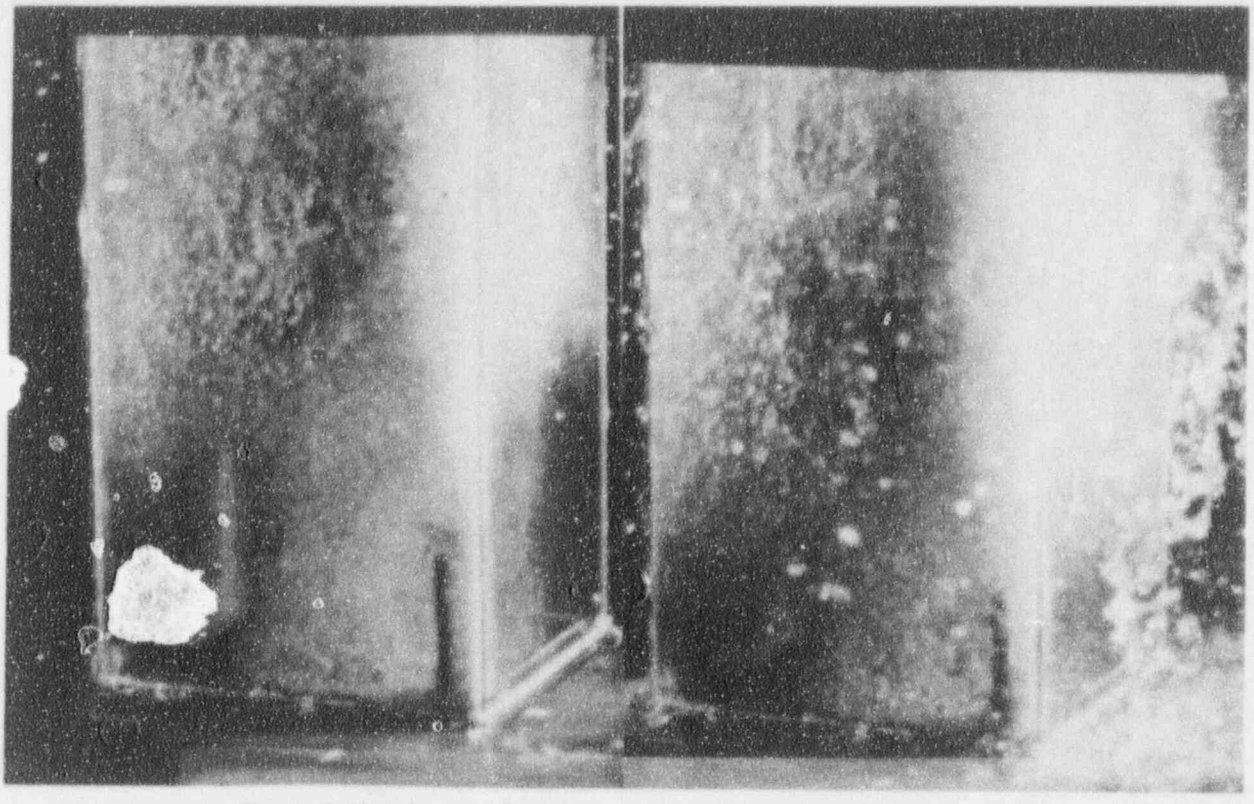

Figure 9 (Continued). Snapshots of Run #905. Times (from impact of balls on the water) are 1.3 s and 1.6 s.

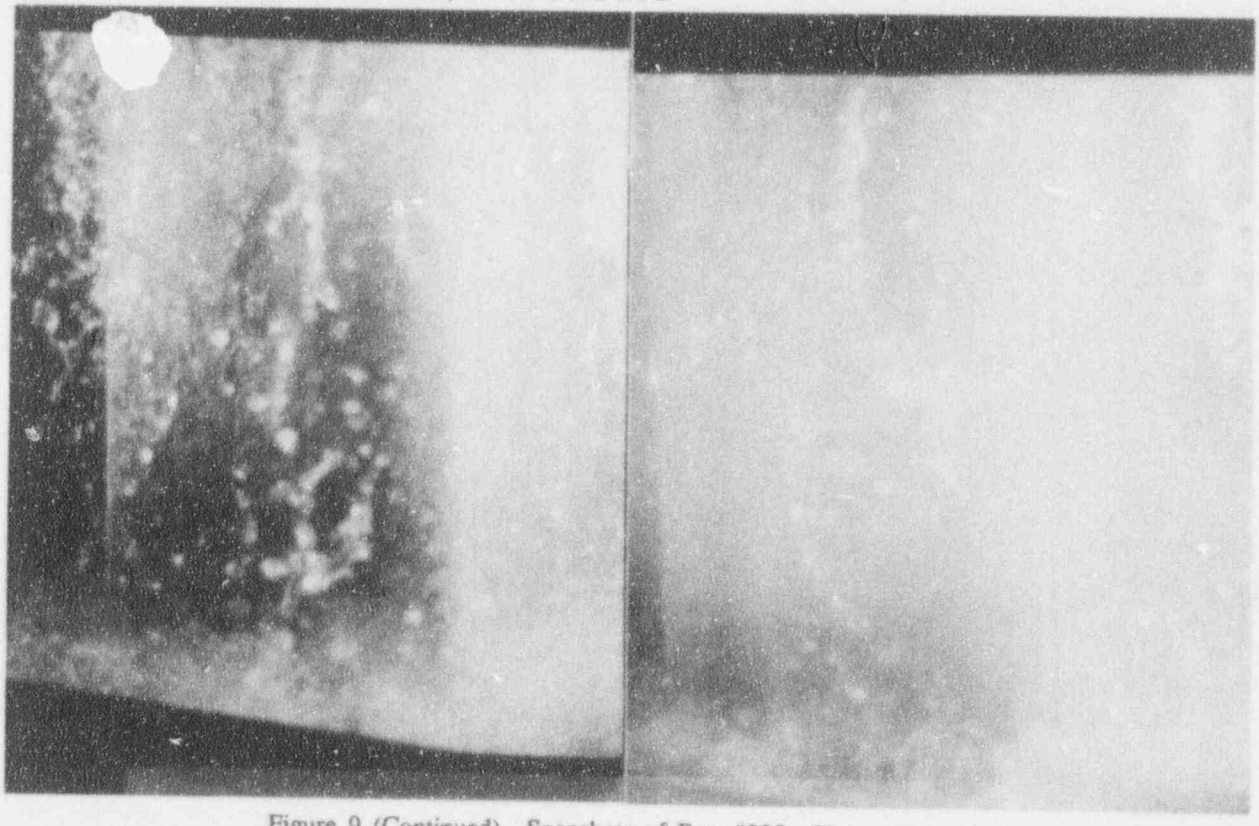

Figure 9 (Continued). Snapshots of Run #905. Times (from impact of balls on the water) are 1.9 s and 2.8 s.

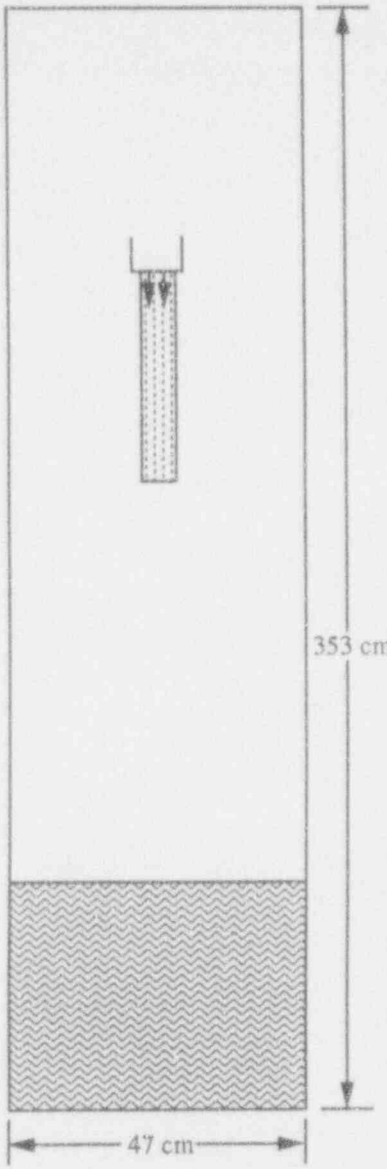

Figure 10. Illustration of the flow field utilized in PM-ALPHA for the interpretation of the FARO experiment.

interest in these tests is primarily on the melt-coolant interactions, and the melt-to-gas heat transfer is relevant only in providing the proper boundary conditions (subcooling induced due to pressurization) for this interaction. Our approach, therefore, is to sort out the melt-to-gas heat transfer from the early portion of the pressurization transient (prior to melt contacting the water) in such a way that it can be consistently "merged" with the fuel-coolant interaction portion. This is done by finding from the early pressurization rate an effective value of the product of "melt interfacial area density" times the melt emissivity (i.e., $6E_f/d_f$) and using it to estimate radiative power for all subsequent times, however, accounting for the reduction in total area as the melt "column" becomes submerged in the water pool. In actual numbers, at ~0.3 s, the pressurization rate of the gas (0.83 MPa/s) implies a uniformly applied heatup rate of 4.01 MW and a $6E_f/d_f$ value of 3.6 cm^{-1}. The latter is obtained from

$$\frac{6}{d_f} E_f \sigma T^4 \frac{m_f}{\rho_f} = \dot{Q}$$

where m_f/ρ_f is the total fuel volume, and $\dot{Q}$ is the total rate of radiative heating of the gas. Using an emissivity of 0.7, the above yields a melt particle size of 1.2 cm, which is certainly a reasonable degree of breakup of the ensuing melt jet under the conditions of this experiment (crusts were observed within the nozzle as well as in the melt catcher).

Finally, regarding further melt breakup within the interaction zone, by consideration of Weber number criteria, and with a melt-entry (the pool) velocity of 4 m/s, we estimate an initial breakup to mm-size particles. However, as the liquid pool is penetrated and set in downward motion (see earlier discussion on MAGICO) by the high velocity "swarm" of particles, the relative velocities decrease, and the continuous phase density decreases, which would tend to moderate this extensive initial breakup. For the calculation reported here, we chose a value of 0.5 cm. It happened that this first choice gave a good (compared to the experiment) timing for traversing the 0.87 m depth of the pool and also a good agreement with the interaction features of the calculation (pressurization). The fragmented debris found in the melt catcher was reported to have a mean particle size of 4.5 mm; however, from the photographs and the discussion, it appears that this fragmented debris represents only a relatively small fraction of the total melt; much of it collected as a "conglomerate in contact with the bottom plate. This part was certainly still molten when it contacted the plate" (Magallon et al., 1992). Thus, the chosen size of 0.5 cm may not be unreasonable, and as seen below, the degree of quenching obtained in the calculation with such a particle size appears to be consistent with a large fraction of the mass arriving in still molten form at the catcher.

As a final point in this discussion, we need to mention that we do not agree with the discussion in the quick-look report (Wider et al., 1992) about the role of Argon gas (used initially as a cover gas) and about the transient phenomena associated with the small expansion of the gas volume due to the opening of valve SO2. First of all, the Argon atom is considerably heavier than the steam molecule, and there is no way for it to stratify under the conditions of the experiment as claimed. Second, starting from 0.4 MPa pressure at 80 °C, as stated, the Argon partial pressure at 265 °C should be ~0.7 MPa, and with the partial pressure of steam (at 265 °C) should add up to 5.77 MPa, which is significantly higher than the measured value of 5.33 MPa. This is not surprising given the method and power of heating and likely heat losses. Third, after opening the valve, the system pressure decay was arrested at ~5.07 MPa by water flashing to steam, as it should; however, because of the Argon gas pressure, the pressure could not increase significantly above this value by flashing, as claimed in the quick-look report. [Free surface vaporization could provide some additional steam; however, it would be too slow to make a difference at the time frame (< 1 s) of interest.] We

conclude that the pressurization above 5.07 MPa is solely due to radiative heating, and steaming, of course, after melt-water contact. That is, the situation is quite straightforward, and the method of simulation described above is quite appropriate.

The results of the calculations are discussed next. Starting from the "bottom-line" results in Figures 11 and 12, we see the comparisons with the data on the pressurization transient and the pressurization rate, respectively. The agreement is remarkably good. In Figure 13, we see the water subcooling (at a position away from the interaction zone) building up rapidly as a result of the pressurization, a feedback quite important to the phase change processes within the mixing zone. The temperature rises quickly to saturation as the fuel penetrates deeper into the pool. The pressurization mechanism, initially due to radiative heating of the gas space, gradually reverts to the supply of superheated steam from the interaction zone. This can be seen from Figure 14 showing the "sinking" history of the melt in the water pool, Figure 15 showing the change in radiative heating of a typical volume element in the gas space as a result of this "sinking" of the melt, and Figure 16 showing the temperature transient of a typical cell in the gas space. This temperature transient is very consistent with that measured experimentally. In Figure 17, we see the buildup of fuel volume fractions at the bottom cell; the timing is in excellent agreement with the data. The level swell reported for this experiment is 13 cm, which is also in remarkable agreement with the calculated value of 12 cm. Finally, a sampling of the evolution of calculated fuel and volume fraction distributions at different times during the transient are shown in Figures 18 and 19, respectively. Because of the large aspect ratio of the full facility, the distributions below the initial water level are only shown in these figures.

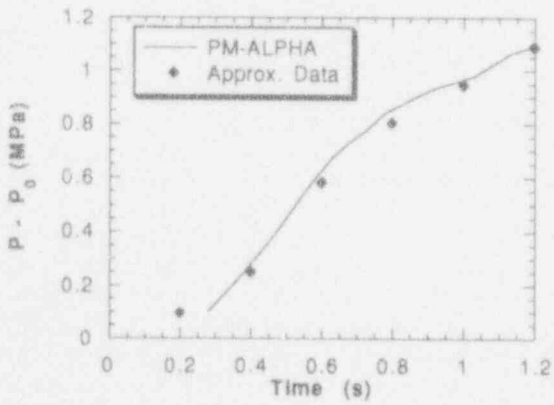

Figure 11. Comparison of calculated pressure history with the FARO data from the Scoping Test.

To conclude, these are very promising comparisons for a first calculation, and they indicate rich possibilities for further more detailed calculations and interpretations. In particular, we hope to examine the role of different degrees of breakup during the interaction with water, and hence to be able to backup more conclusively what actually took place in the experiment. This type of information would be most helpful in carrying out premixing calculations for reactor conditions.

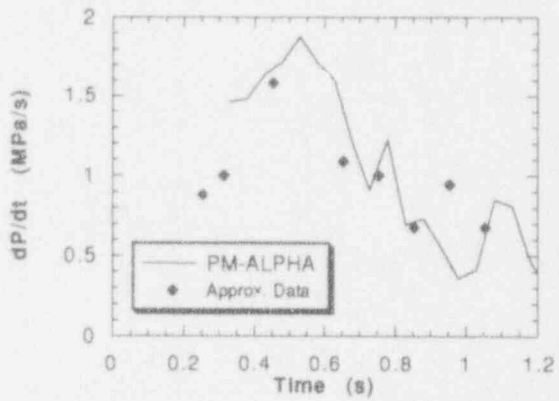

Figure 12. Comparison of calculated pressurization rate with the FARO data from the Scoping Test.

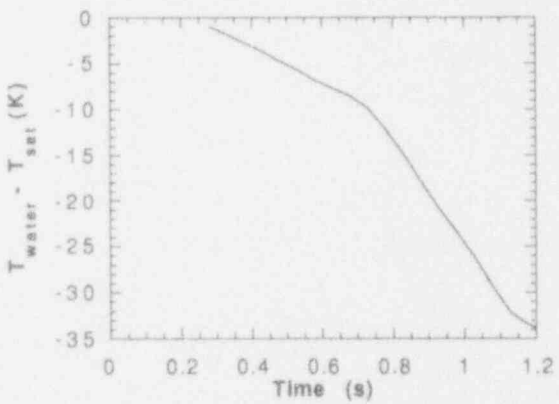

Figure 13. Calculated buildup of water subcooling, as a result of the pressurization transient, at locations away from the mixing zone.

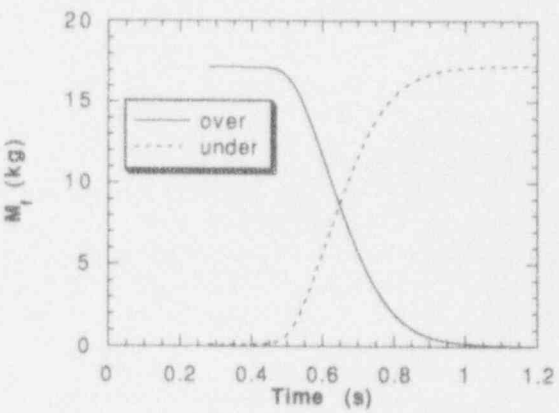

Figure 14. The calculated "sinking" of the fuel "column" into the water pool.

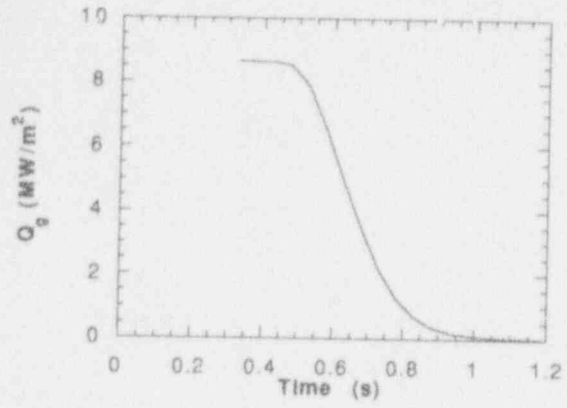

Figure 15. Illustration of the diminishing of the radiative heat source to a typical cell in the gas space, as a consequence of the melt sinking, per Figure 14.

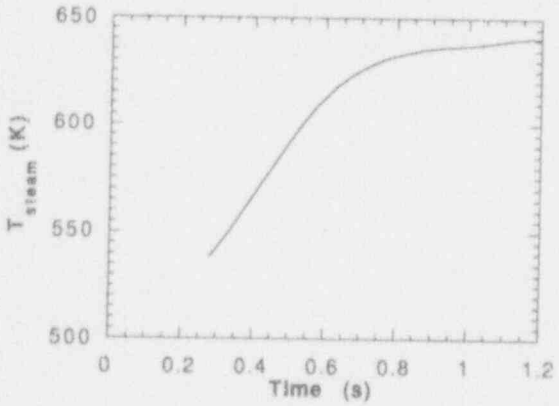

Figure 16. Calculated temperature rise in a typical cell in the gas space away from the water surface.

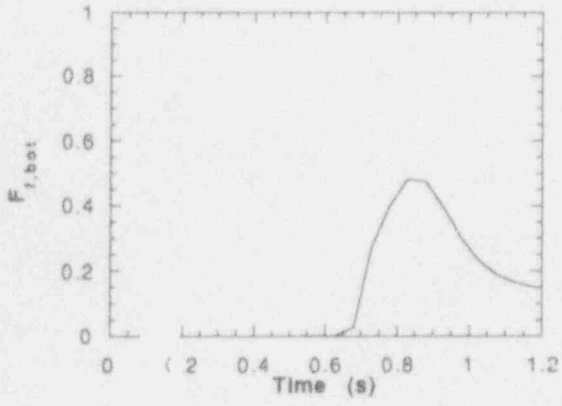

Figure 17. Calculated arrival rate of melt into the melt catcher.

VII. CONCLUSIONS

The water depletion phenomenon in premixing transients has been simulated in MAGICO, measured by FLUTE and by quantitative X-ray radiography, and predicted by PM-ALPHA. Moreover, PM-ALPHA seems to also predict some key multidimensional internal features of the flow field and thermal interaction regimes that appear to be consistent with what is observed in MAGICO. These latter results suggest additional experimental work in MAGICO for further insights into the detailed phenomena. By design, MAGICO allows no free parameters in analytical model predictions and is well-suited for unambiguous testing of the three-fluid and phase-change aspects of the formulation. At the other extreme, the FARO experiment with prototypic high temperature materials, high pressures, and unknown melt particulation during the transient provides some interesting challenges to analytical interpretations. We show, by means of comparison with the results of the Scoping Test, that PM-ALPHA can be fruitfully applied in a rather straightforward manner. Perhaps more importantly, these interpretations offer significant new insights on the effect of subcooling, as a feedback mechanism in closed (or constrained) systems, on the extent of vapor production and resulting voiding pattern. Future work will carry further these results to understanding the breakup and associated thermal interaction behavior.

ACKNOWLEDGMENTS

This work was supported by the U.S. Nuclear Regulatory Commission under Contract Number 04-89-084.

REFERENCES

1. Abolfadl, M.A. and T.G. Theofanous (1987) "An Assessment of Steam-Explosion-Induced Containment Failure. Part II: Premixing Limits," *Nuclear Science and Engineering* **97**, 282.

2. Amarasooriya, W.H. and T.G. Theofanous (1991) "Premixing of Steam Explosions: A Three-Fluid Model," *Nuclear Engineering and Design* **126**, 23-39.

3. Angelini, S., E. Takara, W.W. Yuen and T.G. Theofanous (1992) "Multiphase Transients in the Premixing of Steam Explosions," Proceedings NURETH-5, Salt Lake City, UT, September 21-24, 1992, Vol. II, 471–478.

4. Bankoff, S.G. and S.H. Han (1984) "An Unsteady One-Dimensional Two-Fluid Model for Fuel-Coolant Mixing in an LWR Meltdown Accident," presented at U.S.-Japan Seminar on Two-Phase Dynamics, Lake Placid, New York, July 29-August 3, 1984.

5. Denham, M.K., A.P. Tyler and D.F. Fletcher (1992) "Experiments on the Mixing of Molten Uranium Dioxide with Water and Initial Comparisons with CHYMES Code Calculations," Proceedings, NURETH-5, Salt Lake City, UT, September 21-24, 1992.

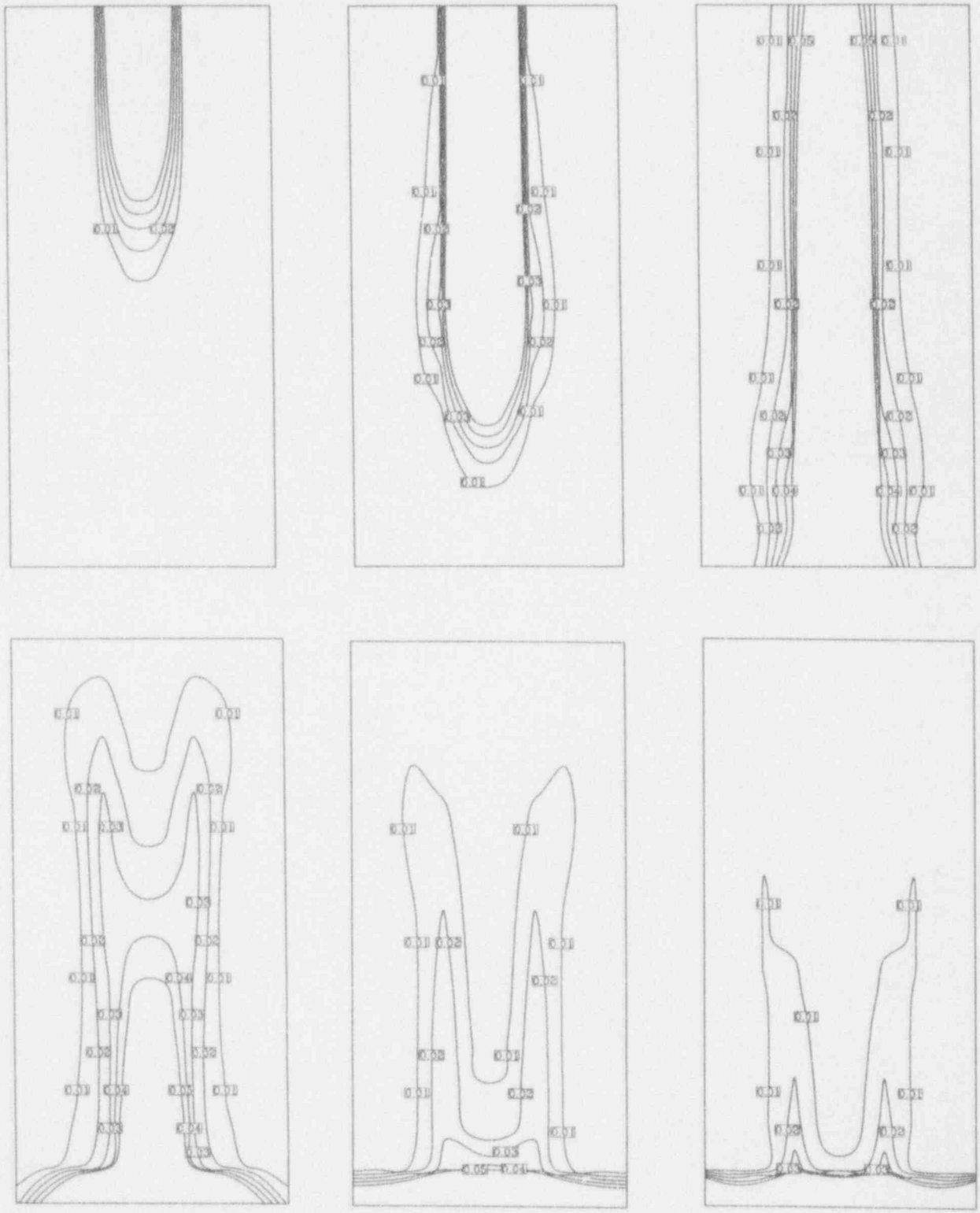

Figure 18. Melt Volume fraction distributions at selected times in the simulation of the FARO Scoping Test. Times (from the initial melt release) are 0.53 s, 0.63 s, 0.73 s, 0.83 s, 0.93 s and 1.03 s for plots reading from left to right and top to bottom. The width of the plot is 47 cm, and the height is 97.6 cm, corresponding to the volume of the test vessel below the initial water level.

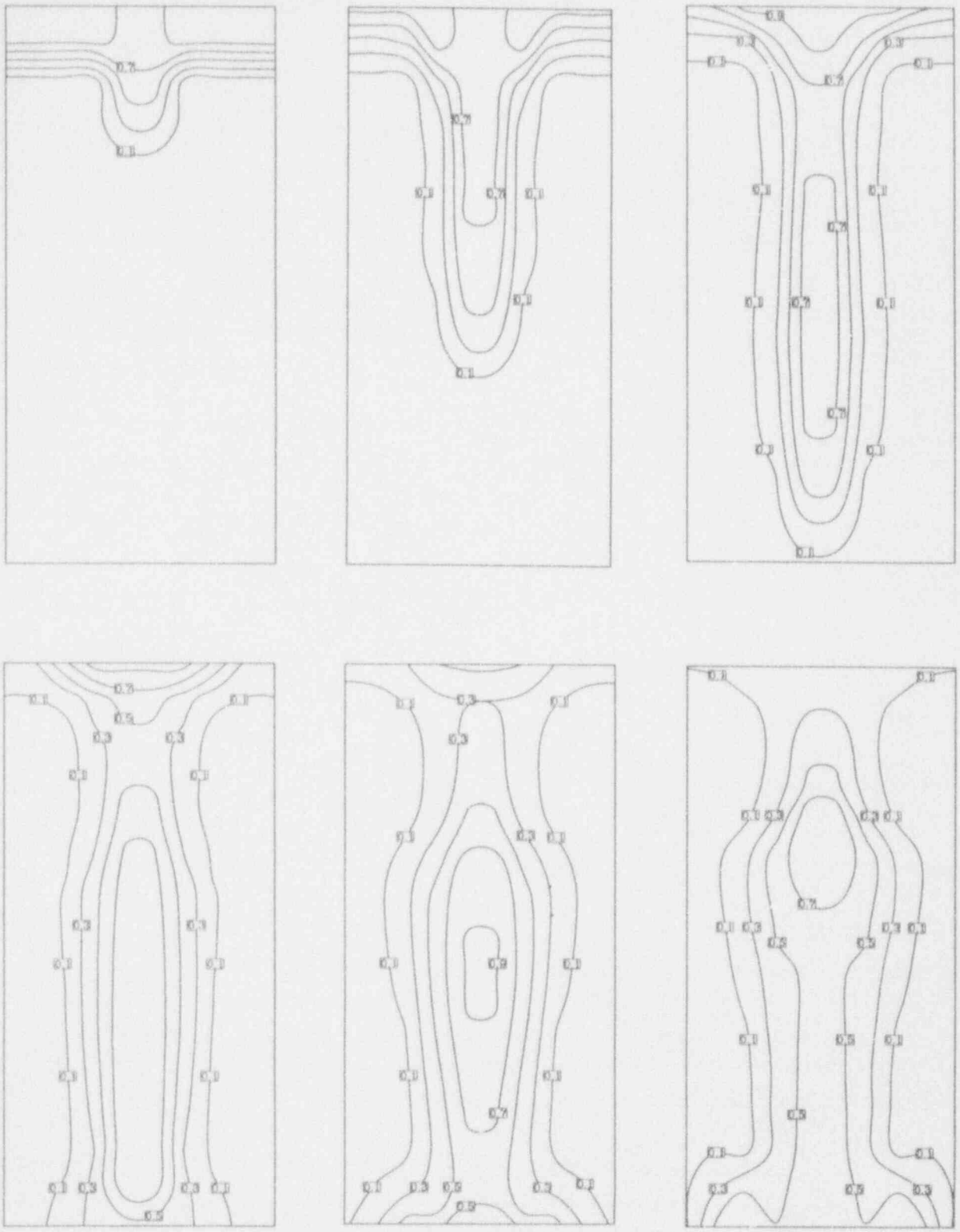

Figure 19. Steam volume fraction distributions at selected times in the simulation of the FARO Scoping Test (see Figure 18 caption for identification of time step and physical dimensions).

6. Fletcher, D.F. (1992) "A Comparison of Coarse Mixing Predictions Obtained from the CHYMES and PM-ALPHA Models," Technical Note, *Nuclear Engineering and Design*, **135**, 419-425.

7. Fletcher, D.F. and A. Thyagaraja (1991) "The CHYMES Coarse Mixing Model," *Progress in Nuclear Energy*, **26** No. 1, 31-61.

8. Henry, R.E. and H. K. Fauske (1981) "Required Initial Conditions for Energetic Steam Explosions," *Fuel-Coolant Interactions, HTD-V19*, American Society of Mechanical Engineers.

9. Liu, C., T.G. Theofanous and W. Yuen (1992) "Film Boiling from Spheres in Single- and Two-Phase Flow," ANS Proceedings1992 National Heat Transfer Conference, San Diego, CA, Aug. 9-12, 1992, Vol. 6, 211–218.

10. Magallon, D. et al. (1992) "FARO LWR Programme, Scoping Test Data Report." Technical Note No I.92.135, Institute for Safety Technology.

11. Magallon, D. and H. Hohmann (1993) "High Pressure Corium Melt Quenching Tests in FARO," CSNI Specialists Meeting on Fuel-Coolant Interactions, Santa Barbara, CA, January 5-8, 1993.

12. Steam Explosion Review Group (1985) "A Review of Current Understanding of the Potential for Containment Failure Arising from In-Vessel Steam Explosions," NUREG-1116, U.S. Nuclear Regulatory Commission.

13. Theofanous, T.G., B. Najafi and E. Rumble (1987) "An Assessment of Steam-Explosion-Induced Containment Failure. Part I: Probabilistic Aspects," *Nuclear Science and Engineering*, **97**, 259-281.

14. Theofanous, T.G., S. Angelini, R. Buckles and W.W. Yuen (1991) "On the Prediction of Steam Explosions Energetics," Proceedings, 19th Water Reactor Safety Information Meeting, October 24, 1991.

15. Theofanous, T.G., W.W. Yuen, S. Angelini, X. Chen, W.H. Amarasooriya, S. Medhekar and H. Yan (1992) "Steam Explosions: Fundamentals and Energetic Behavior," to be published as NUREG/CR-5960 by the U.S. Nuclear Regulatory Commission.

16. Theofanous, T.G., W.W. Yuen and B.W. Sheron (1993) "The Probability of Alpha-Mode Containment Failure Updated," CSNI Specialists Meeting on Fuel-Coolant Interactions, Santa Barbara, CA, January 5-8, 1993.

17. Wider, H.U., et al. (1992) "The FARO/LWR Experimental Programme," JRC Technical Note No. I.92.139.

18. Yuen, W.W. and T.G. Theofanous (1993) "The Fundamental Mechanisms and Structure of Thermal Detonations," CSNI Specialists Meeting on Fuel-Coolant Interactions, Santa Barbara, CA, January 5-8, 1993.

APPENDIX A: FORMULATION OF THE PM-ALPHA MODEL

I. CONSERVATION EQUATIONS

There are three separate phases: namely, coolant vapor, coolant liquid, and fuel (melt) drops. They will be referred to as gas, liquid, and fuel, respectively. Each phase is represented by one flow field with its own local concentration and temperature. Thus, we have three continuity equations, three momentum equations, and three energy equations. In the usual manner, the fields are allowed to exchange energy and momentum with each other, but only the steam and water fields are allowed to exchange mass. With the definition of the macroscopic density of phase i,

$$\rho_i' = \theta_i \rho_i \qquad \text{for} \quad i = g,\ \ell,\ \text{and}\ f, \tag{A.1}$$

and the compatibility condition,

$$\theta_g + \theta_\ell + \theta_f = 1, \tag{A.2}$$

these equations can be interpreted rather directly (Ishii, 1975).

• Continuity Equations.

Gas:

$$\frac{\partial \rho_g'}{\partial t} + \nabla \cdot (\rho_g' \mathbf{u}_g) = J \tag{A.3}$$

Liquid:

$$\frac{\partial \rho_\ell'}{\partial t} + \nabla \cdot (\rho_\ell' \mathbf{u}_\ell) = -J \tag{A.4}$$

Fuel:

$$\frac{\partial \rho_f'}{\partial t} + \nabla \cdot (\rho_f' \mathbf{u}_f) = 0 \tag{A.5}$$

• Momentum Equations.

Gas:

$$\frac{\partial}{\partial t}(\rho_g' \mathbf{u}_g) + \nabla \cdot (\rho_g' \mathbf{u}_g \mathbf{u}_g) = -\theta_g \nabla p - F_{g\ell}(\mathbf{u}_g - \mathbf{u}_\ell) - F_{gf}(\mathbf{u}_g - \mathbf{u}_f) + J(H[J]\mathbf{u}_\ell + H[-J]\mathbf{u}_g) + \rho_g' \mathbf{g} \tag{A.6}$$

Liquid:

$$\frac{\partial}{\partial t}(\rho_\ell' \mathbf{u}_\ell) + \nabla \cdot (\rho_\ell' \mathbf{u}_\ell \mathbf{u}_\ell) = -\theta_\ell \nabla p + F_{g\ell}(\mathbf{u}_g - \mathbf{u}_\ell) - F_{\ell f}(\mathbf{u}_\ell - \mathbf{u}_f) - J(H[J]\mathbf{u}_\ell + H[-J]\mathbf{u}_g) + \rho_\ell' \mathbf{g} \tag{A.7}$$

Fuel:

$$\frac{\partial}{\partial t}(\rho_f' \mathbf{u}_f) + \nabla \cdot (\rho_f' \mathbf{u}_f \mathbf{u}_f) = -\theta_f \nabla p + F_{gf}(\mathbf{u}_g - \mathbf{u}_f) + F_{\ell f}(\mathbf{u}_\ell - \mathbf{u}_f) + \rho_f' \mathbf{g} \tag{A.8}$$

• Energy Equations.

Gas:

$$\frac{\partial}{\partial t}(\rho_g' I_g) + \nabla \cdot (\rho_g' I_g \mathbf{u}_g) = -p\left[\frac{\partial \theta_g}{\partial t} + \nabla \cdot (\theta_g \mathbf{u}_g)\right]$$
$$+ J(H[J]h_\ell + H[-J]h_g) - R_{gs}(T_g - T_s) + \dot{Q}_{fg} \quad (A.9)$$

Liquid:

$$\frac{\partial}{\partial t}(\rho_\ell' I_\ell) + \nabla \cdot (\rho_\ell' I_\ell \mathbf{u}_\ell) = -p\left[\frac{\partial \theta_\ell}{\partial t} + \nabla \cdot (\theta_\ell \mathbf{u}_\ell)\right]$$
$$- J(H[J]h_\ell + H[-J]h_g) - R_{\ell s}(T_\ell - T_s) + \dot{Q}_{f\ell} \quad (A.10)$$

Fuel:

$$\frac{\partial}{\partial t}(\rho_f' I_f) + \nabla \cdot (\rho_f' I_f \mathbf{u}_f) = -\dot{Q}_{fg} - \dot{Q}_{f\ell} \quad (A.11)$$

In the above equations $H[J]$ is the Heavyside step function that becomes unity for positive values of the argument and zero otherwise, and J is given by

$$J = \frac{1}{h_g - h_\ell}\left[R_{gs}(T_g - T_s) + R_{\ell s}(T_\ell - T_s)\right]$$

It should be pointed out that diffusive transport **within** each field (shear stresses and conduction) has been ignored in the above formulation. Indeed, resolution of the shear layers would impose quite more extensive demands on the computation in both nodalization and the physics of turbulence processes responsible for such transport. Although this is certainly an area for further improvement, we doubt that it will materially change the results for the particular process quantified here.

II. THE EXCHANGE LAWS

The interfacial exchanges of mass, momentum and energy are clearly regime dependent, and uncertainties remain even for two-phase flows. For now, our approach aims to incorporate first-order physics that account for the major flow and heat transfer regimes as identified by simple criteria of fuel volume fraction, θ_f, and gas void fraction, α, i.e., $\alpha = \theta_g/(\theta_g + \theta_\ell)$. The flow regimes are shown in Figure A.1. For $\theta_f < 0.3$ we consider the fuel particles immersed in a two-phase gas-liquid flow, whose own flow regimes are defined by the value of the void fraction: $\alpha \leq 0.3$ (Bubbly), $0.3 < \alpha < 0.7$ (Churn-Turbulent), and $\alpha \geq 0.7$ (Droplet). For $\theta_f \geq 0.3$, as the fuel particles are densely packed, we considered a flow of gas and liquid through a porous bed of fuel particles.

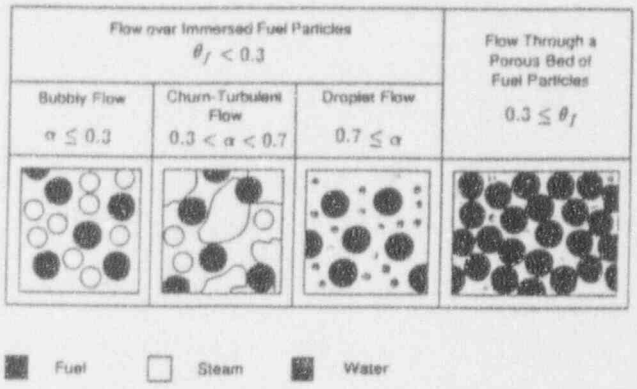

Figure A.1. Schematic diagram of flow regimes considered in characterizing interface transfers.

We use the exchange laws available for two-phase systems after making suitable modifications to account for, as a first approximation, the effect of a third phase. In calculating interfacial momentum exchange, one needs to know the projected area concentration of the dispersed phase. Also, in calculating interfacial heat exchange, one needs to know the interfacial area concentration. In a two-phase system, these area concentrations can be estimated from the length scale and the volume fraction of the dispersed phase. However, the presence of a third phase reduces the area concentration as the third phase must also share the same area. Therefore, we modify the area concentration, by a factor, ϕ_{ij}; ϕ_{ij} representing the effect of the phase k on the area concentration of phase i for its interaction with phase j. This is calculated from the respective volume fractions as

$$\phi_{ij} = \frac{\theta_j}{\theta_j + \theta_k}. \quad (A.12)$$

Note that with this definition ϕ_{ij} lies between 0 and 1.

II.A Interfacial Momentum Coupling

The interfacial momentum coupling is primarily due to drag. For the bubbly flow regime ($\alpha < 0.3$) we have also included the added mass effect as given by Wallis (1969)

$$F_a = \frac{\theta_g}{3 - \theta_g}\rho_\ell \frac{1}{|\,\mathbf{u}_g - \mathbf{u}_\ell\,|}\,\left|\,\frac{\partial}{\partial t}(\mathbf{u}_g - \mathbf{u}_\ell)\,\right| \quad (A.13)$$

For $\theta_f < 0.3$ the drag force is based on Ishii and Zuber (1979). Specifically,

$$F_{ij} = \frac{3}{4}\theta_i \phi_{ij} \rho_j \frac{C_{Dij}}{\ell_i}\,|\,\mathbf{u}_i - \mathbf{u}_j\,| \quad (A.14)$$

where suffices i and j refer to dispersed and continuous phases, respectively. The drag coefficient for churn flow ($0.3 < \alpha < 0.7$) is defined by:

$$i = g,\ j = \ell,\ C_{Dij} = \frac{8}{3}(1-\alpha)^2 \text{ and } \ell_i = 4\left\{\frac{g\Delta\rho}{\gamma}\right\}^{-1/2} \quad (A.15)$$

For dispersed flow we have:

$$C_{Dij} = \frac{2}{3}\ell_i \left\{\frac{g\Delta\rho}{\gamma}\right\}^{1/2} \left\{\frac{1+17.67(f(\alpha_i))^{6/7}}{18.67 f(\alpha_i)}\right\}^2 \quad (A.16)$$

where

$$i = g, \quad j = \ell, \quad \alpha \le 0.3 \qquad f(\alpha_i) = (1-\alpha)^{1.5} \quad (A.17)$$

$$i = \ell, \quad j = g, \quad \alpha > 0.7 \qquad f(\alpha_i) = \alpha^3 \quad (A.18)$$

$$i = f, \quad j = g, \ell, \quad f(\alpha_i) = (1-\theta_f)^{1.5} \quad (A.19)$$

and ℓ_i is obtained from

$$\frac{\rho_j \mid \mathbf{u}_\ell - \mathbf{u}_g \mid^2 \ell_i}{\gamma} = \mathrm{We}_{cr} \begin{cases} 8 & \text{for } i = g \\ 12 & \text{for } i = \ell \end{cases} \quad (A.20)$$

For the "dense fuel regime" ($\theta_f > 0.3$) we use laminar and turbulent permeabilities (Sissom and Pitts, 1972).

$$F_{if} = F^{\ell}_{if} + F^{t}_{if} \qquad i = g, \ell \quad (A.21)$$

where

$$F^{\ell}_{if} = \begin{cases} 150 \frac{\theta_i \theta_f^2}{(1-\theta_f)^3} \frac{\mu_i}{\ell_f^2} & \text{for } \mathrm{Re}'_i < 1000 \\ 0 & \text{for } \mathrm{Re}'_i \ge 1000 \end{cases} \quad (A.22)$$

and

$$F^{t}_{if} = \begin{cases} 1.75 \frac{\theta_i \theta_f}{(1-\theta_f)^3} \frac{\rho'_i \mid \mathbf{u}_i - \mathbf{u}_f \mid}{\ell_f} & \text{for } \mathrm{Re}'_i > 10 \\ 0 & \text{for } \mathrm{Re}'_i \le 10, \end{cases} \quad (A.23)$$

$$\mathrm{Re}'_i = \theta_f \frac{\rho'_i \ell_f \mid \mathbf{u}_i - \mathbf{u}_f \mid}{\mu_i} \quad (A.24)$$

It is noted, however, that this regime is of very limited relevance to computations of practical interest.

II.B Interfacial Heat Transfer and Phase Change

The distinction of the fuel-to-coolant heat transfer mechanisms is made again on the basis of the flow regimes. The key distinction is whether or not there is sufficient water in the coolant phase to completely engulf the fuel particles, thus a gas void fraction criterion is used.

For $\alpha < 0.7$, heat transfer to liquid is estimated by superposition of radiation and film boiling heat fluxes. That is,

$$\dot{Q}_{f\ell} = n_f (h_r + h_c) \pi \ell_f^2 \phi_{f\ell} (T_f - T_\ell) \quad (A.25)$$

where

$$n_f = \frac{6\theta_f}{\pi \ell_f^3}, \qquad h_r = \sigma E_f \frac{T_f^4 - T_\ell^4}{T_f - T_\ell} \quad (A.26, A.27)$$

and (Witte, 1968; Liu et al., 1992)

$$h_c = 2.98 \left\{ \frac{\rho_g k_g [h_{fg} + 0.68 c_{pg}(T_f - T_\ell)]}{\ell_f (T_f - T_\ell)} \mid \mathbf{u}_f - \mathbf{u}_\ell \mid \right\}^{\frac{1}{2}} \quad (A.28)$$

The emissivity value $E_f = 0.7$ is selected for the calculations of typical interest. Heat transfer from fuel to gas in this regime need not be accounted for separately.

For $\alpha > 0.7$, we assume a vapor-continuous regime in which heat is transferred to liquid drops by irradiation and to the gas by convection. The gas is allowed to superheat and convect heat to the liquid drops which boil at saturation. Thus:

$$\dot{Q}_{f\ell} = \min(n_\ell \pi \ell_\ell^2, n_f \pi \ell_f^2)\, \sigma E_f E_\ell (T_f^4 - T_\ell^4) \quad (A.29)$$

and

$$\dot{Q}_{fg} = n_f \phi_{fg} \pi \ell_f^2 h'_c (T_f - T_g) \quad (A.30)$$

where $n_\ell = 6\theta_\ell / \pi \ell_\ell^3$ and h'_c is given by Bird et al. (1960):

for $\theta_f < 0.3$

$$h'_c = \frac{k_g}{\ell_f} \left\{ 2 + 0.6 \mathrm{Re}_g^{1/2} \mathrm{Pr}_g^{1/3} \right\} \quad (A.31)$$

where

$$\mathrm{Re}_g = \frac{\rho_g \mid \mathbf{u}_g - \mathbf{u}_f \mid \ell_f}{\mu_g} \quad (A.32)$$

and for $\theta_f \ge 0.3$

$$h'_c = 0.91 c_{pf} \rho'_g \mid \mathbf{u}_g - \mathbf{u}_f \mid \mathrm{Re}_g^{''-0.51} \mathrm{Pr}_g^{-2/3} \text{ for } \mathrm{Re}''_g \le 50 \quad (A.33)$$

$$h'_c = 0.61 c_{pf} \rho'_g \mid \mathbf{u}_g - \mathbf{u}_f \mid \mathrm{Re}_g^{''-0.41} \mathrm{Pr}_g^{-2/3} \text{ for } \mathrm{Re}''_g > 50 \quad (A.34)$$

where

$$\mathrm{Re}''_g = \frac{\rho'_g \ell_f \mid \mathbf{u}_g - \mathbf{u}_f \mid}{6\theta_f \mu_g} \quad (A.35)$$

The factor E_ℓ in Eq. (29) was introduced to empirically degrade the radiation heat transfer to liquid by the portion that could not be absorbed. For reactor calculations we typically use $E_\ell = 0.3$ to conservatively bias the predictions.

Similarly, for vapor-to-liquid heat transfer we have:

For $\alpha < 0.7$, with vapor as the dispersed phase

$$R_{\ell s} = c_\ell n \phi_{g\ell} \pi \ell_g^2 \frac{k_\ell}{g_g} \left\{ 2 + 0.6\ \mathrm{Re}^{1/2} \mathrm{Pr}_\ell^{1/3} \right\} \quad (A.36)$$

$$R_{gs} = 2 n_g \phi_{g\ell} \pi \ell_g^2 \frac{k_g}{\ell_g}$$

while for $\alpha > 0.7$, with liquid (drops) as the dispersed phase

$$R_{gs} = n_\ell \phi_{\ell g} \pi \ell_\ell^2 \frac{k_g}{\ell_\ell} \left\{ 2 + 0.6\ \mathrm{Re}^{1/2} \mathrm{Pr}_g^{1/3} \right\} \quad (A.37)$$

$$R_{\ell s} = 2 c_\ell \eta_\ell \phi_{\ell g} \pi \ell_\ell^2 \frac{k_\ell}{\ell_\ell}$$

In the above the coefficient c_ℓ was introduced as a way to control the liquid superheat in cases where these simplified formulations for heat transfer coefficients are not deemed adequate.

NOMENCLATURE

C_D	drag coefficient
c_ℓ	control coefficient
c_p	specific heat at constant pressure
E_f	emissivity of fuel particles
E_ℓ	absorptivity of water droplets
F	factor for interficial momentum exchange
g	acceleration of gravity
H	Heaviside step function
h	heat transfer coefficient; specific enthalpy
h_{fg}	enthalpy of evaporation
I	specific internal energy
J	phase change rate per unit volume
k	thermal conductivity
ℓ	length scale
n	number of particles (or drops) per unit volume
Pr	Prandtl number
p	pressure
$\dot{Q}$	rate of heat transfer per unit volume
R	heat transfer coefficient between the phase (liquid or vapor) and interface
Re	Reynolds number
T	temperature
t	time
u	velocity vector
We_{cr}	critical Weber number for bubble/drop breakup

Greek

α	void fraction of vapor (per unit volume of coolant)
γ	surface tension between vapor and liquid; specific heat ratio
θ	volume fraction (per unit volume of total mixture)
μ	viscosity
ρ	microscopic density
ρ'	macroscopic density
σ	Stefan–Boltzmann coefficient
ϕ_{ij}	area concentration factor, defined in eq. (A.12)

Subscripts

a	added-mass effect
c	convection
f	fuel
g	gas (steam)
ℓ	liquid (water)
r	radiation
s	saturation

Superscripts

ℓ	laminar flow
t	turbulent flow

REFERENCES

1. Bird, R.B., W.E. Stewart and E.N. Lightfoot (1960) *Transport Phenomena*, Wiley, New York.
2. Liu, C., T.G. Theofanous and W. Yuen (1992) "Film Boiling from Spheres in Single- and Two-Phase Flow," 1992 National Heat Transfer Conference, San Diego, August 9–12, 1992.
3. Ishii, M. (1975) "Thermo-Fluid Dynamic Theory of Two-Phase Flow," Eyrolles.
4. Ishii, M. and N. Zuber (1979) "Drag Coefficient and Relative Velocity in Bubbly, Droplet or Particulate Flows," *AIChE J.* **5**, 843.
5. Sissom, L.E. and D.R. Pitts (1972) *Elements of Transport Phenomena*, McGraw-Hill, New York.
6. Wallis, G.B. (1969) *One-dimensional Two-phase Flow*, McGraw-Hill, Inc., New York.
7. Witte, L.C. (1968) *Ind. Eng. Chem. Fundamentals* **7**, 517.

APPENDIX B: INDEPENDENT VERIFICATION OF THE FLUTE MEASUREMENTS

The reason for creating the FLUTE is that our efforts in using absorbing radiation to image the whole mixing zone during the design phase of MAGICO did not yield promising results. The working concept in this effort was to make use of two different γ- and X-ray energies and the differences in attenuation between the water and the material of the balls so as to simultaneously measure both. Although in principle this approach is fine, in practice, it results in a stiff system of equations that yield large error amplification in the solution, and thus it was abandoned.

We returned to it recently after the completion of the first phase of the experimental program in MAGICO that made use of FLUTE. The reapproach appeared hopeful, basically because actual experience with MAGICO indicated that the particle volume fractions in the mixing zone are in the 2 to 3% range, thus creating the possibility of "seeing" through limited (sporadic) areas of this zone without ball interference. Numerical experiments attempting to recreate realization of the particle cloud and the optical paths through it revealed that this was indeed the case. These experiments also provided guidance on how to optimize the orientation of the X-ray shot and the source-to-object distance, taking advantage of the hole pattern in the dumper plate.

In actual implementation, we used a flash of "soft" X rays timed at the desired instant within the premixing transient in MAGICO. The image is recorded on a 13- x 18-cm film positioned to cover the region of interest in the mixing zone. By changing the timing of the flash and the film position, we can map out a premixing transient in any temporal and spatial detail desired—this is possible because of the excellent reproducibility of the MAGICO runs, as already demonstrated by the FLUTE measurements and the high-speed movies. We have limited our goal here to the independent check of the FLUTE results, and only a few runs are adequate for this purpose. In the process of developing the quantitative aspects of this technique, we have made quite a few runs that successively appeared more and more promising. A great deal of the success depends on

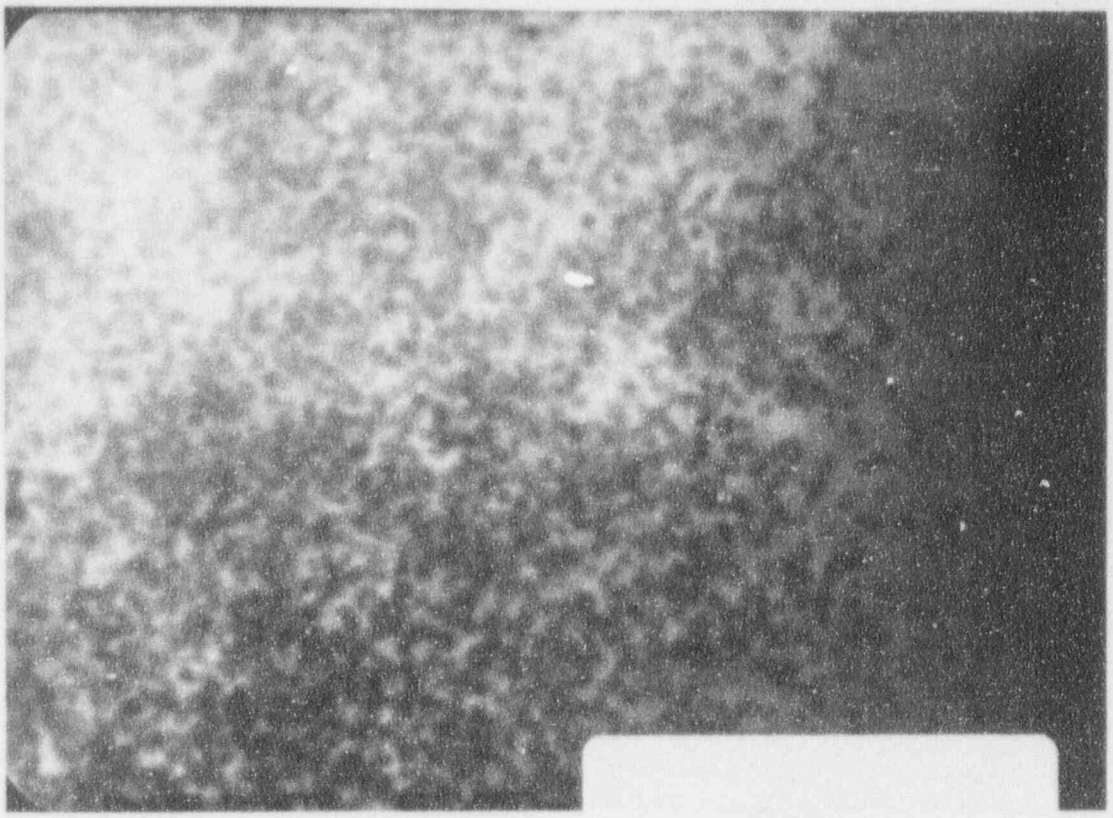

Figure B.1. Print of the X-ray film taken in Run #1005.

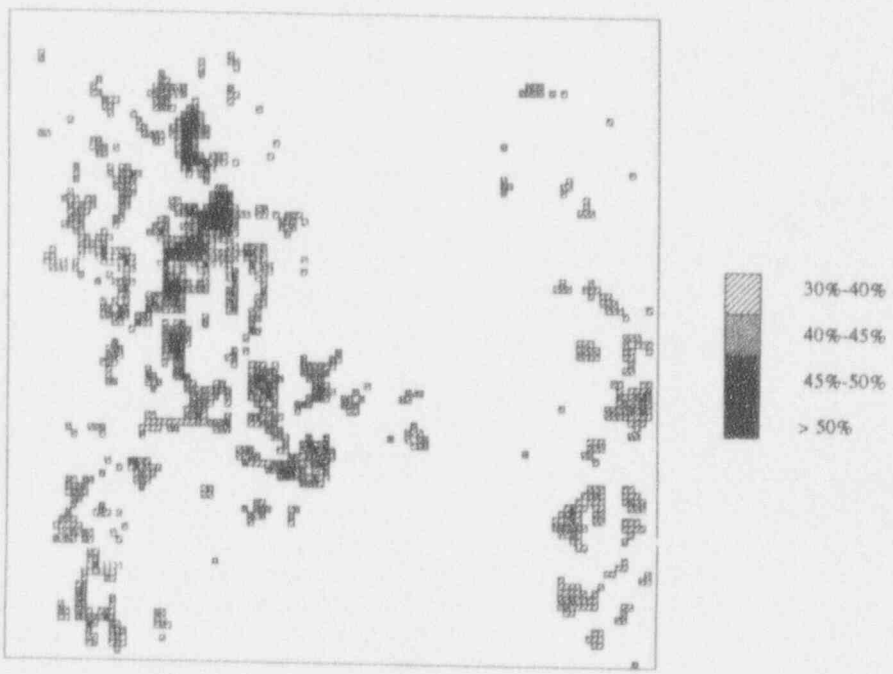

Figure B.2. Void fraction distribution obtained from X-ray analysis of run #1005. The region covered is $-1.5 < r < 5.5$ cm and $19 < z < 25$ cm.

establishing adequate safeguards and procedures to ensure that the image obtained can be directly related to a calibration image obtained with a stepwise variation of void in the optical path. Besides, we confirmed that the effect of X-ray scattering from the steel balls (they are not present, clearly, in the calibration shot) is negligible. At this time, the technique is well-developed, and we have one run in the MAGICO series (the 1000-series) to discuss here. Rather than carry out the many special FLUTE runs needed to cover the information on the X rays, our approach is to use PM-ALPHA as the means of comparison; the PM-ALPHA interpretations are the ultimate purpose in any case.

This MAGICO test, #1005, was run with the 2.4-mm steel balls at 600 °C poured into a 25-cm-deep pool of saturated water from a height of 21 cm. The X-ray shot was timed at 0.52 s after initiation of the pour, which corresponds to just about when the particle front hits the pool bottom. The X-ray image obtained is shown in Figure B.1. It is noteworthy that individual balls are recognizable, even when they partly overlap, and we believe with a pattern recognition technique, we will have, from such shots, the particle number densities as well. Also in this figure, small areas where balls are completely absent are clearly distinguishable, and it is in these areas that with the application of the water/void calibration curve we can obtain the chordal-average void fractions.

The "reading" and analysis of these films was done on 6- x 6-cm film segments in order to obtain the high resolution required—this gave a pixel size of 0.12 mm. These readings were analyzed in groups of 20 pixels. For each such group, an average value of void (and hence of void fraction) was obtained by using the calibration curve and a criterion excluding readings indicating the presence of spheres. Moreover, to ensure that readings too close to the sphere boundaries were excluded, we used as an additional criterion that the fraction of unaffected readings within a group was above some value—otherwise, the space associated with the particular group of (20) pixels was taken to be interfered by the presence of steel. The data analysis was repeated with f values of this fraction set to 25, 50, and 75%, with very consistent results, indicating absence of the boundary-type influence being addressed by this operation.

The results from film segments covering the region $19 < z < 25$ cm (i.e., a 6-cm slice of the pool top; z is measured from the pool bottom) over two radial segments, $-1.5 < r < 5.5$) cm and $5.5 < r < 11.5$ cm presented here. Spatial void fraction maps (using the 50% criteria discussed above) are shown in Figures B.2 and B.3 for the above two radial regions, respectively. The plank spaces in these maps indicate regions at ball interference. Immediately, we can notice that these results indicate void fractions in the general range measured by FLUTE (Angelini et al., 1992). In a more detailed examination, we have plotted these results against PM-ALPHA predictions for four different radial computational cells (at $r = 1$, 3, 5, and 7 cm) at three axial positions ($z = 18.75$, 21.25, and 23.75 cm), as shown in Figures B.4. In these figures, the PM-ALPHA results were obtained by an appropriate chordal-average equivalent to projecting the cylindrically-symmetric void fraction distribution, as effected by the X ray on the film. The X-ray results were obtained from the spatial maps by averaging all measured values within the cell being considered. The agreement is quite remarkable in all cases. It is also interesting to note that the "water flux reversal" phenomenon discussed in Section 4 is quite evident in Figure B.4d; the insurge of water causes a precipitous drop of void fraction at the outer edges of the mixing zone. The X ray happened to be taken just prior to this time, but it is clear now how to best time the X-ray shot in the next run.

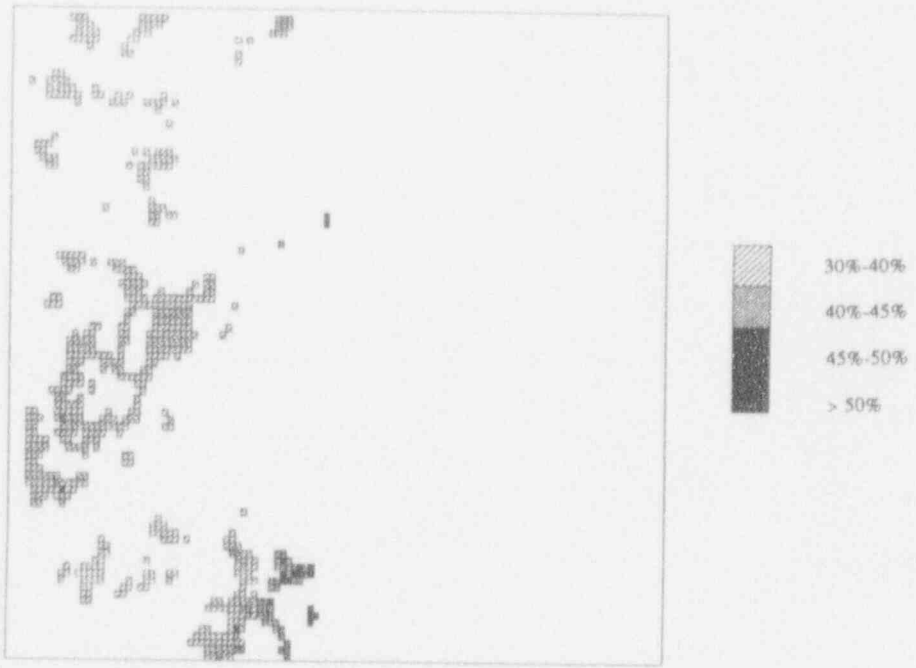

Figure B.3. Void fraction distribution obtained from X-ray analysis of run #1005. The region covered is $5.5 < r < 11.5$ cm and $19 < z < 25$ cm.

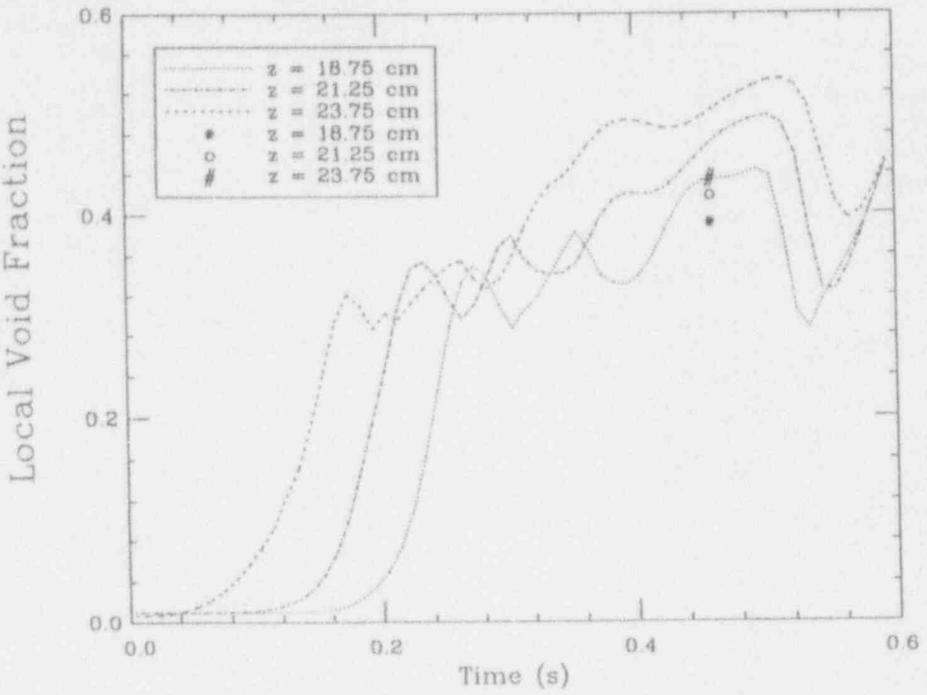

Figure B.4a. Comparison between prediction and X-ray measurement for run #1005 for cell centered at $r = 1$ cm and three different heights.

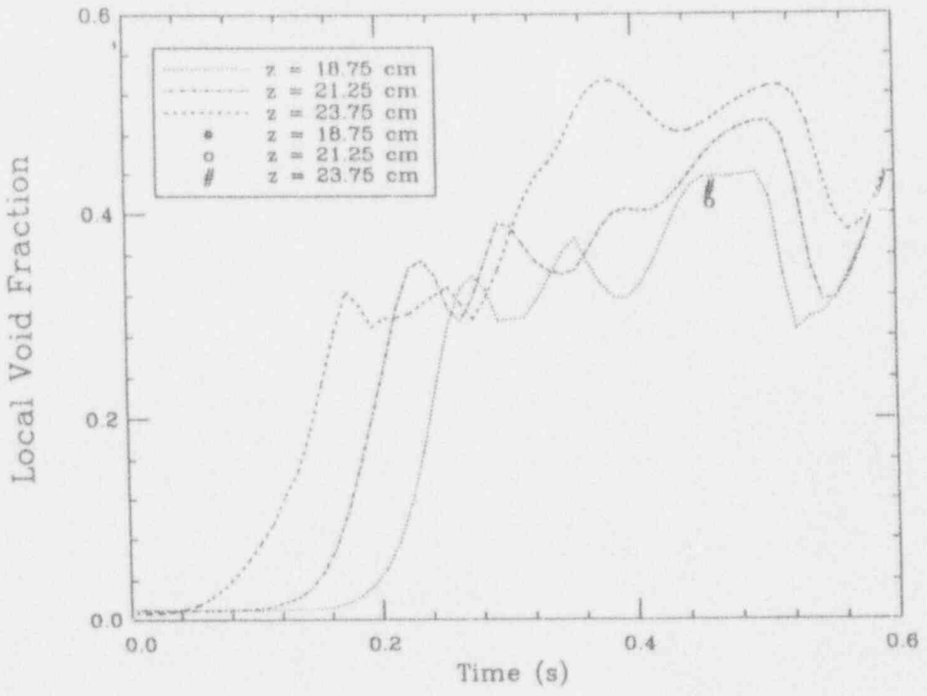

Figure B.4b. Comparison between prediction and X-ray measurement for run #1005 for cell centered at $r = 3$ cm and three different heights.

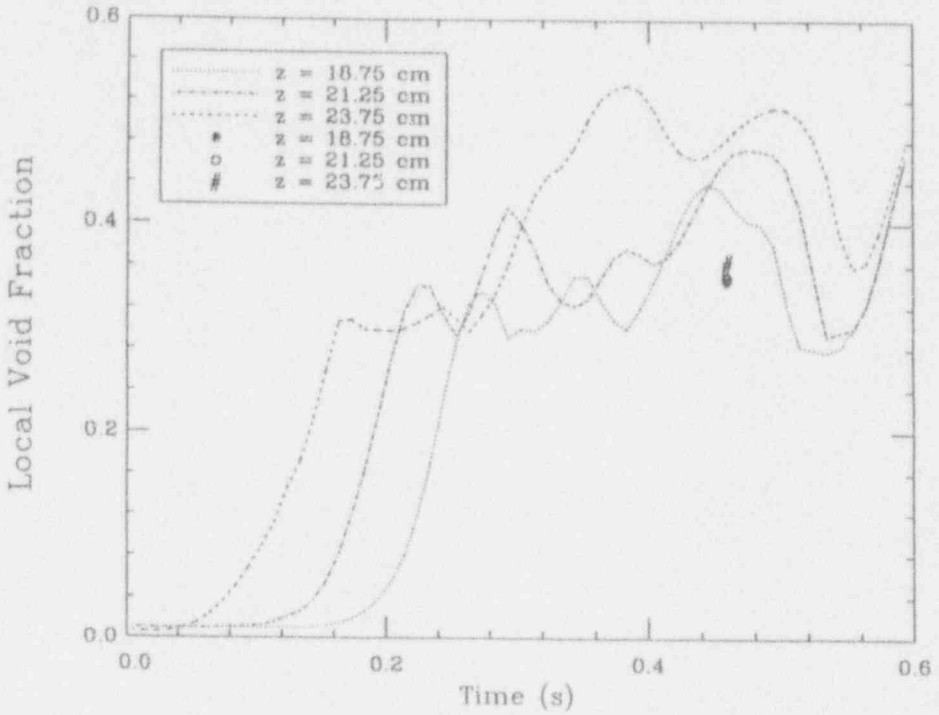

Figure B.4c. Comparison between prediction and X-ray measurement for run #1005 for cell centered at $r = 5$ cm and three different heights.

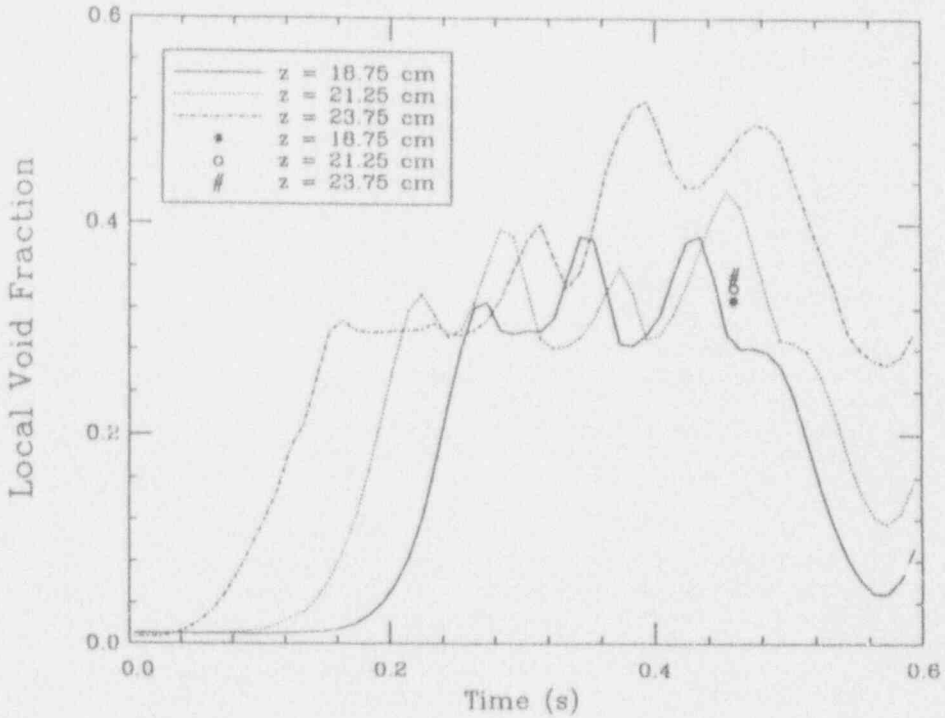

Figure B.4d. Comparison between prediction and X-ray measurement for run #1005 for cell centered at $r = 7$ cm and three different heights.

A THERMODYNAMIC MODEL FOR ALUMINUM-WATER INTERACTIONS

S. McCahan
Dept. of Mechanical Engineering
University of Toronto
5 King's College Rd
Toronto ON M5S 1A4
(416) 978-0490

J.E. Shepherd
Dept. of Mechanical Engineering
Rensselaer Polytechnic Institute
Troy NY 12180
(518) 276-6192

ABSTRACT

The thermodynamic aspects of the explosive interaction between aluminum and water are modeled computationally. The general model used in this investigation is an extension of the one used in previous work, (McCahan & Shepherd, 1991, Shepherd et al., 1990). The flow is considered steady and one-dimensional and the reaction wave is captured in a control volume. The metal oxidation reaction is taken into account and the Rankine-Hugoniot relation is solved in conjunction with suitable equations of state for each component. A variety of upstream conditions were investigated to examine the effect on the solution curve, and more specifically the effect on the Chapman-Jouguet solution. The initial temperature of the aluminum, the initial vapor quality of the water and the amount of excess water were varied. Changing the initial temperature of the aluminum has very little effect, however, changing amount of water and the vapor quality significantly effect the CJ solution.

I. INTRODUCTION

Although the problem of metal-water interactions has been studied for some time much of the work to date has focused on non-reacting systems. The interaction of aluminum and water is a reactive process which is highly exothermic. This type of interaction is relevant to the aluminum industry as well as the nuclear industry. In case of a loss of coolant accident (LOCA) in a nuclear reactor the core and cladding material, which may contain aluminum, may melt and interact with fluid either present in or introduced into the containment. The chemical reaction which occurs in conjunction with an aluminum-water interaction is an important aspect of this problem and this reaction must be considered in the modeling of these processes.

A number of transient and steady-state simulations of non-reacting thermal detonation waves have been carried out (see review by Corradini et al., 1988). However, the peak pressures and wave speeds predicted by these models often significantly exceed the values available from experimental observation. One model which is commonly used is the thermal detonation model proposed by Board and Hall (1975). This model uses the Rankine-Hugoniot relation to construct a result analogous to the solution for a chemical detonation. The present work builds upon this model by including the metal oxidation process and by considering both the subsonic and supersonic solution branches. Furthermore, realistic equations of state for theconstituent components are employed and particular attention is given to developing a realistic and consistent thermodynamic construction to be used in conjunction with the Rankine-Hugoniot relation.

In the present study the reaction wave is assumed to be at steady-state and the flow is considered one-dimensional. The triggering process and initial transient behavior are not considered. This model, therefore, represents a limiting behavior for these types of waves. The wave structure is enclosed in a control volume and the upstream fluid mixture is fully specified. The upstream and downstream regions are assumed to consist of homogeneous fluid mixtures. The thermodynamic end-state is then achieved by an adiabatic oxidation of the aluminum. The results from these calculations form a solution curve which represents the possible downstream thermodynamic states and wave velocities that may be attained. This model does not uniquely determine a downstream solution. Additional information is required in order to predict a single unique solution. However, the results presented here indicate the range of possible wave propagation behavior. Also, it is found that the thermodynamics of the reaction process contribute significantly the solution.

II. MODEL FORMULATION

The model used in the present work is an extension of the model outlined previously in McCahan and Shepherd (1991) and Shepherd et al. (1990). In the case of aluminum and water the wave front is treated as reactive. This model is illustrated in Figure 1. The reaction wave is captured in an inviscid, adiabatic control volume. The control volume is held stationary and the reactants, consisting of aluminum and water, enter the control volume from the upstream region. The products, consisting of aluminum oxide, hydrogen and water, leave the control volume at a high temperature downstream of the reaction wave. The flow is considered one-dimensional and steady. Upstream from the wave is a region containing hot, molten blobs of aluminum in a cooler water bath. The aluminum is surrounded by a blanket of water vapor due to the film boiling process. This vapor blanket allows the aluminum and water system to remain in thermal non-equilibrium for a limited time. The aluminum and water are considered to

be in mechanical equilibrium. In every case studied the initial, upstream pressure is taken to be 1 atm and the water is saturated. Three upstream, state 1, parameters are varied in this study; the quantity of water in the initial mixture,the initial vapor fraction of the water, and the initial temperature of the aluminum.

The region downstream of the wave, state 2, contains an equilibrium mixture of aluminum oxide, hydrogen and water. The reaction which results in these products can be expressed;

$$2Al + 3H_2O + XH_2O \rightarrow Al_2O_3 + 3H_2 + XH_2O$$

where X is the quantity of excess water specified for each case studied. This is a parametric study which assumes that the metal is completely oxidized in the reaction. Also, it is assumed that both the upstream and downstream mixtures are homogenous. The conservation relations for mass, momentum and energy and the second law of thermodynamics can be applied to the reaction wave control volume. The resulting expressions consist of jump conditions,

$$[\rho w] = 0 \tag{1}$$

$$\left[P + \rho w^2\right] = 0 \tag{2}$$

$$\left[h + \tfrac{1}{2} w^2\right] = 0 \tag{3}$$

$$[s] \geq 0 \tag{4}$$

where ρ is density, w is velocity, P is pressure, h is the specific enthalpy, s is the specific entropy, and the square brackets indicate a jump across the discontinuity, i.e. $[s] = s_2 - s_1$. This set of expressions is analogous to the set of jump conditions used in shock theory. The first three jump equations can be combined to form the familiar Rankine-Hugoniot relation,

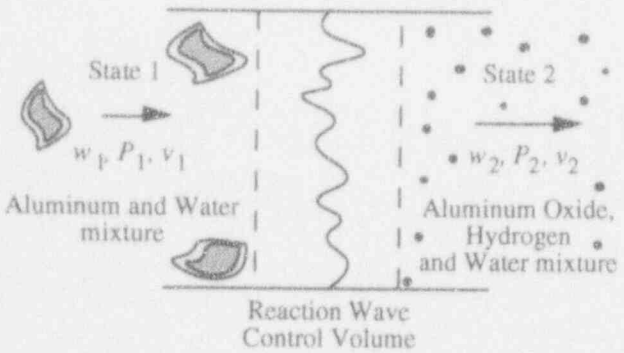

Figure 1. Schematic of the reaction wave model. The control volume captures the structure of the reaction wave. State 1 consists of hot, molten blobs of aluminum surrounded by water vapor in a liquid water medium. State 2 consists of dispersed aluminum oxide fragments in a hydrogen and water mixture.

$$h_2 - h_1 = \tfrac{1}{2}(P_2 - P_1)(v_2 + v_1) \tag{5}$$

where v is the specific volume. Given a specified state 1 this relation can be solved for the corresponding possible state 2 conditions. The only additional information needed for this solution are the appropriate equations of state for each component.

The equations of state chosen for this study are carefully selected to provide appropriate substance descriptions. The Keenan and Keyes equation of state is used to describe the water at state 1 (Reynolds, 1979) and the $\beta - \kappa$ constant equation of state is used for the aluminum, where β refers to the expansivity and κ to the isothermal compressibility of the substance. The $\beta - \kappa$ constant equation of state can be written;

$$v = v_o \exp\left[\beta(T - T_o) - \kappa(P - P_o)\right] \tag{6}$$

where the subscript o refers to a reference state and T is temperature. The $\beta - \kappa$ constant equation of state is also used for the aluminum oxide at state 2. The expansivity for solid aluminum oxide is $\beta = 5.0\times10^{-6}$ 1/K (Raznjevic, 1976) and for solid aluminum $\beta = 23.5\times10^{-6}$ 1/K (Smithell's, 1983). Values for the compressibility of aluminum and aluminum oxide are not readily available so a numerical method was developed (McCahan, 1992) to derive the values for κ from shock Hugoniot data (March, 1980). The compressibility for solid aluminum and aluminum oxide are estimated to be $\kappa = 1.0\times10^{-11}$ 1/Pa and $\kappa = 2.8\times10^{-12}$ 1/Pa respectively. Data for liquid aluminum and aluminum oxide are not available so the values for the solid materials are used for the liquid states as well. The constant $\beta - \kappa$ equation of state allows the inclusion of the metal and metal oxide compressibility in the calculation.

The TIGER correlation (Cowperthwaite and Zwisler, 1974) for the ideal gas specific heat is used to complete the substance descriptions. The reference states for the aluminum and aluminum oxide are shown in Table 1. The reference pressure is 1 atm and the reference temperature is 298.15 K. It is assumed that the aluminum is in a liquid state above 933.5 K, the melting temperature of aluminum at 1 atm. Similarly, when the temperature of the final mixture is above 2323. K, the aluminum oxide it is assumed to be liquid. The heat of fusion and other solid/liquid property changes are also shown in Table 1.

Expressions for the enthalpy and entropy change for a constant $\beta - \kappa$ material are as follows;

$$h - h_o = \int_{T_o}^{T} \left(c_p^{ig}\right)_{P_o} dT \tag{7}$$

$$+ \frac{v_o}{\kappa}\left\{1 - \exp\left[\kappa P_o\right]\right\}\left\{(\beta T - 1)\exp\left[\beta(T - T_o)\right]\right.$$

$$\left. -(\beta T_o - 1)\right\} + \frac{v(\beta T - 1)}{\kappa}\left\{1 - \exp\left[\kappa(P - P_o)\right]\right\}$$

Table 1. Data for the references states and fusion properties of aluminum and aluminum oxide.

	v_o[c] (m³/kg)	h_o[a] (J/kg)	s_o[a] (J/kg-K)	v_{sl}[b] (m³/kg)	h_{sl}[a] (J/kg)	s_{sl}[a] (J/kg-K)
Al	3.7037e-4	0.0e0	1047.22	2.4e-5	3.9667e5	424.93
Al_2O_3	2.519e-4	-1.6297e7	525.49	4.37e-7	8.5784e5	369.28

[a]JANNAF Thermochemical Tables (1985).

[b]calculated from TIGER (see Cowperthwaite and Zwisler, 1974), and the $\beta - \kappa$ constant equation of state

[c]Incropera and DeWitt (1985).

Table 2. Formation data and potential parameters for hydrogen and water.

	h_f^o[a] (J/mol)	s_f^o[a] (J/mol-K)	v_o[b] (m³/mol)	α[c]	r_m[c] (Å)	ϵ/k_B[c] (K)
H_2	0.0	130.57	2.4466e-2	13.5	3.34	37
H_2O	-241799.	227.09	2.4785	13.5	3.37	136

[a]JANNAF Thermochemical Tables (1985), and the adjustment to water values from Reynolds (1988).

[b]volume for H_2 from the ideal gas equation, and for H_2O from Reynolds (1988).

[c]Chirat and Pittion-Rossillon (1981).

and

$$s - s_o = \int_{T_o}^{T} \left(\frac{c_p^{ig}}{T} \right)_{P_o} dT \tag{8}$$

$$+ \frac{\beta}{\kappa} \left\{ v\left(1 - \exp[\kappa P]\right) - v_o\left(1 - \exp[\kappa P_o]\right) \right\}$$

where c_p^{ig} is the ideal gas specific heat. These expressions can be derived from fundamental thermodynamic property relationships and the constant $\beta - \kappa$ assumption. Equations (6), (7) and (8) complete the set of relations necessary to describe the aluminum at state 1 and aluminum oxide at state 2 .

For the hydrogen and water at state 2 the Byers Brown (1987) equation of state is used. This equation of state is a pressure explicit expression formulated for high density, high temperature fluid states. The Byers Brown equation provides an expression for the residual Helmholtz free energy a^r, the compressibility Z, and residual internal energy u^r. The residual enthalpy can be expressed simply as a function of the residual internal energy and compressibility;

$$h^r = u^r + RT(Z-1) \tag{9}$$

where R is the universal gas constant and

$$h = h^r + h^{ig}(T, v) \tag{10}$$

i.e. the residual, denoted by the superscript r, represents the difference between the actual property and the ideal gas value compared at the same temperature and volume. Similarly the residual entropy can be expressed as;

$$s^r = \frac{u^r - a^r}{T} \tag{11}$$

The complete formulas for entropy and enthalpy are expressed as a sum of the residual, ideal gas, and standard state values. That is;

$$s = s^r + \Delta s^{ig} + s_f^o \tag{12}$$

and similarly for enthalpy, where

$$\Delta s^{ig} = \int_{T_o}^{T} \left(\frac{c_p^{ig}}{T} \right) dT - R \ln\left(\frac{P^{ig}}{P_o^{ig}} \right) \tag{13}$$

and

$$\Delta h^{ig} = \int_{T_o}^{T} c_p^{ig} dT \tag{14}$$

and $P^{ig} = RT/v$. The Byers Brown equation of state is applied to the hydrogen and water as a single fluid mixture at state 2.

Because the hydrogen and water are combined in a single fluid model for use with the Byers Brown equation of state, all the parameters and quantities necessary to evaluate the properties at state 2 must be averaged. To accomplish this, the formation quantities, h_f^o and s_f^o, and the ideal gas specific heats are evaluated as averaged values for the mixture. The individual heats of formation, h_{fi}^o, entropies of formation, s_{fi}^o, and ideal gas volumes at 298.15 K are shown in Table 2. The values for water take into account the entropy and enthalpy change from standard

state to an approximate ideal gas state at 298.15 K. The mixture values are found by summing the individual properties multiplied with their respective mol fractions, i.e.

$$h_f^o = \sum x_i h_{fi}^o \tag{15}$$

where x_i is the mol fraction of species i. Values for s_f^o, v_o, and c_p^{ig} are evaluated similarly. The ideal gas volume at 298.15 K, v_o, is used to calculate P_o^{ig} for the entropy expression.

The Byers Brown equation of state requires three substance parameters. These parameters are; the Buckingham exponential index, α, the potential well depth energy, ε, and the potential minimum, r_m. The individual values for these parameters for hydrogen and water are shown in Table 2, where k_B is the Boltzmann constant. The mixing rules for these parameters are given in Chirat and Pittion-Rossillon (1981) and Byers Brown (1987). The Byers Brown equation allows a wide range of states to be accurately calculated. This completes the set of property equations necessary to evaluate the state of the initial aluminum and water mixture and the final hot mixture of aluminum oxide, hydrogen and water.

III. SOLUTION METHOD

The method for solving the Rankine-Hugoniot relation in conjunction with these equations of state is similar to the method used for tin and water mixtures in McCahan and Shepherd (1991). However, the chemical reaction which occurs in this case changes the iteration process. The properties for the water at state 1 are found by using the subroutines from Reynolds (1979). The properties of the aluminum are computed using the $\beta - \kappa$ constant equation of state, as described above, given P_1=1.01325 bar and a specified value for the initial temperature of the aluminum. The complete enthalpy at state 1 is calculated as follows;

$$H_1 = 2h_{Al} + (3+X)\left[y_v h_v + (1-y_v)h_l\right] \tag{16}$$

where h_{Al}, h_v, and h_l are the enthalpies of the aluminum, saturated water vapor and saturated liquid water respectively. X is the coefficient for extra water, and y_v is the vapor fraction chosen for the water. The complete entropy and volume for state 1 are calculated in a similar manner.

Once the initial state is fully defined, the downstream temperature is specified and a solution for state 2 is found. To find this solution a search range for the density of the downstream hydrogen and water mixture is chosen. This density along with the state 2 temperature are used with the Byers Brown equation of state to evaluate the pressure at state 2 and the other hydrogen and water mixture properties. The state 2 pressure and temperature are used with the $\beta - \kappa$ constant equation of state to find the properties of the aluminum oxide. The aluminum oxide and the hydrogen and water mixture enthalpies are combined;

$$H_2 = h_{Al_2O_3} + (3+X)h_{H_2/H_2O} \tag{17}$$

to produce a value for the complete enthalpy at state 2. The downstream entropy and volume are calculated similarly. This value for H_2 is compared to the value found from the Rankine-Hugoniot relation;

$$H_2 \stackrel{?}{=} H_1 + \tfrac{1}{2}(P_2 - P_1)(V_1 + V_2) \tag{18}$$

where V is the complete volume which is calculated in a manner analogous to the evaluation of the complete enthalpy. The root solver uses this comparison to find the Hugoniot solution for the given downstream temperature. This solution method is applied to a range of downstream temperatures to produce a complete Hugoniot curve.

The melting of the aluminum oxide at 2323. K is handled as a constant temperature process. That is, when the downstream temperature is 2323. K, the program holds this temperature constant and gradually adds in a percentage of the enthalpy, entropy and volume changes associated with the phase change. So, the oxide melting is considered a smooth, constant temperature process and solutions are calculated at intervals through the phase change.

IV. RESULTS

An example of a complete solution curve is shown in Figure 2. The curve is divided into three parts; a subsonic branch, a supersonic branch and a non-physical region. The subsonic and supersonic branches each have a Chapman-Jouguet (CJ) point. The Chapman-Jouguet point represents a local minimum in the wave speed and entropy

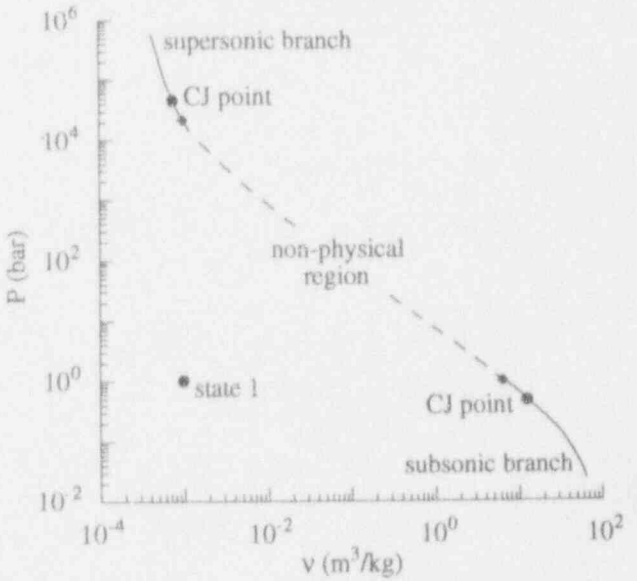

Figure 2. A complete Hugoniot solution for an aluminum-water interaction. At state 1 the aluminum is at 1000. K, X= 5, and y_v=0.0001. The supersonic and subsonic Chapman-Jouguet points are noted.

production on the supersonic branch and a local maximum in the wave speed and entropy production on the subsonic branch. At state 1 the aluminum is at 1000. K, the coefficient for extra water, X, is 5 and the vapor mass (or mol) fraction of the water, y_v, is 0.0001. This set of conditions is used as a basis of comparison for varying the three parameters; initial aluminum temperature, amount of excess water and initial vapor fraction of the water. Figure 2 shows that the pressures exhibited by the subsonic and supersonic solutions are very different. Because of the disparity in the pressures the supersonic and subsonic data have been graphed separately for the other data sets. For the Hugoniot solution illustrated in Figure 2 the CJ points have wave velocities of 0.065 m/s and 4410. m/s on the subsonic and supersonic branches respectively. The high wave speeds exhibited by the supersonic solutions are a result of the low compressibility of the constituent components at very high pressures and densities.

Figure 3 demonstrates the effect of varying the initial temperature of the aluminum. The case where $T_{1Al} = 2500$ is compared to the baseline solution, for which $T_{1Al} = 1000$. K. It is apparent from Figure 3 that changing the initial temperature of the aluminum has very little effect on the solution. Presumably, the change in the energy contribution made by changing the temperature of the aluminum is overwhelmed by the energy contribution of the reaction.

Given the importance of the chemical reaction in this problem one would expect that changing the composition of the mixture would have a larger effect on the solution than the aluminum temperature. This is illustrated in Figure 4. While varying X does not change the supersonic branch very much, it does effect the subsonic branch considerably. At low pressures the additional water, which has a high heat capacity, will tend to 'soak up' the available energy. This causes the solution to be shifted toward a lower temperature and, in turn, a lower volume. However, if X is decreased the solution will shift toward higher temperatures. In fact, at $X = 0.0$ the supersonic branch of the Hugoniot is no longer within the temperature range of the equation of state.

Changing the vapor fraction in the initial mixture has the opposite effect. The subsonic solution remains virtually the same while the supersonic branch is strongly effected. This is demonstrated in Figure 5. The shift in the supersonic branch seems to be caused by the change in the volume at state 1. As the initial volume is moved to a larger value the constant volume supersonic solution is also, necessarily, moved. Because a larger portion of the water is already vaporized, the rest of the supersonic solution will be shifted to a larger volume. This is similar to the case where the composition of the mixture is changed. The solution will tend toward the water adiabat as the amount of water, and therefore its influence on the solution, is increased. Similarly, when the water adiabat is changed by increasing the initial volume, the supersonic solution will be altered.

The low pressure limit of the subsonic branch in each case shown is determined by the applicable temperature range for the Byers Brown equation of state. If the complete subsonic branch could be calculated the low pressure limit would be determined by the restriction imposed by the second law shown in equation (4). Therefore, the subsonic branches that are illustrated are not, theoretically, complete. However, in all the cases shown a substantial portion of the subsonic solution branch can be computed, and in each case a subsonic CJ point is found. The subsonic CJ point is not assigned any special significance in our interpretation of the results. The CJ

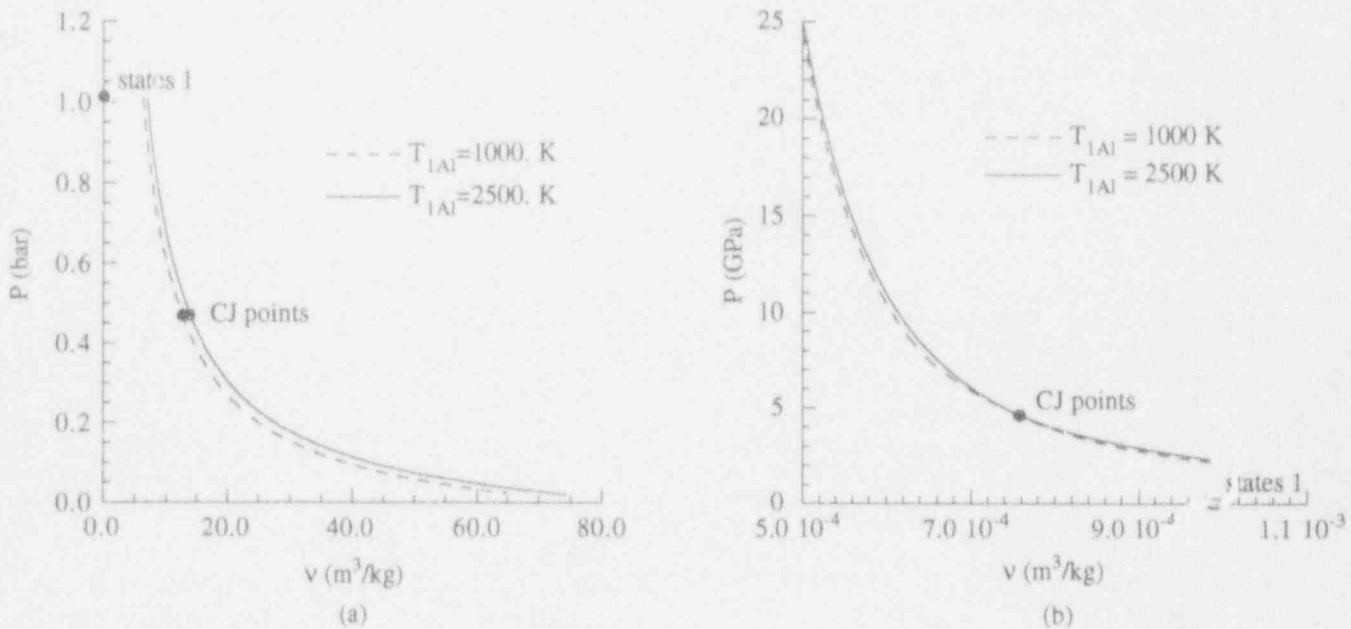

Figure 3. A comparison of two subsonic (a) and supersonic (b) Hugoniot solutions with different initial aluminum temperatures, 1000. K and 2500. K. At state 1 for both cases $X = 5$, and y_v=0.0001. The Chapman-Jouguet points are noted.

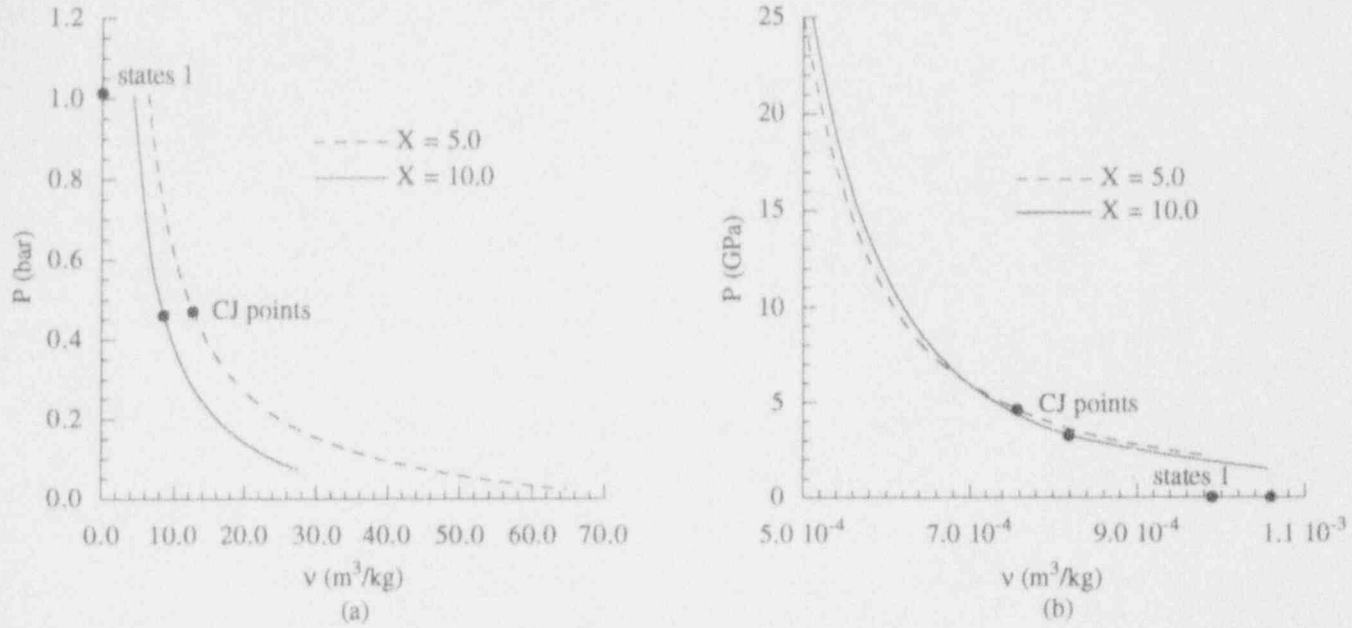

Figure 4. A comparison of two subsonic (a) and supersonic (b) Hugoniot solutions with different coefficients for extra water, $X = 5$ and $X = 10$. At state 1 for both cases the aluminum is initially at 1000. K and y_v=0.0001. The Chapman-Jouguet points are noted.

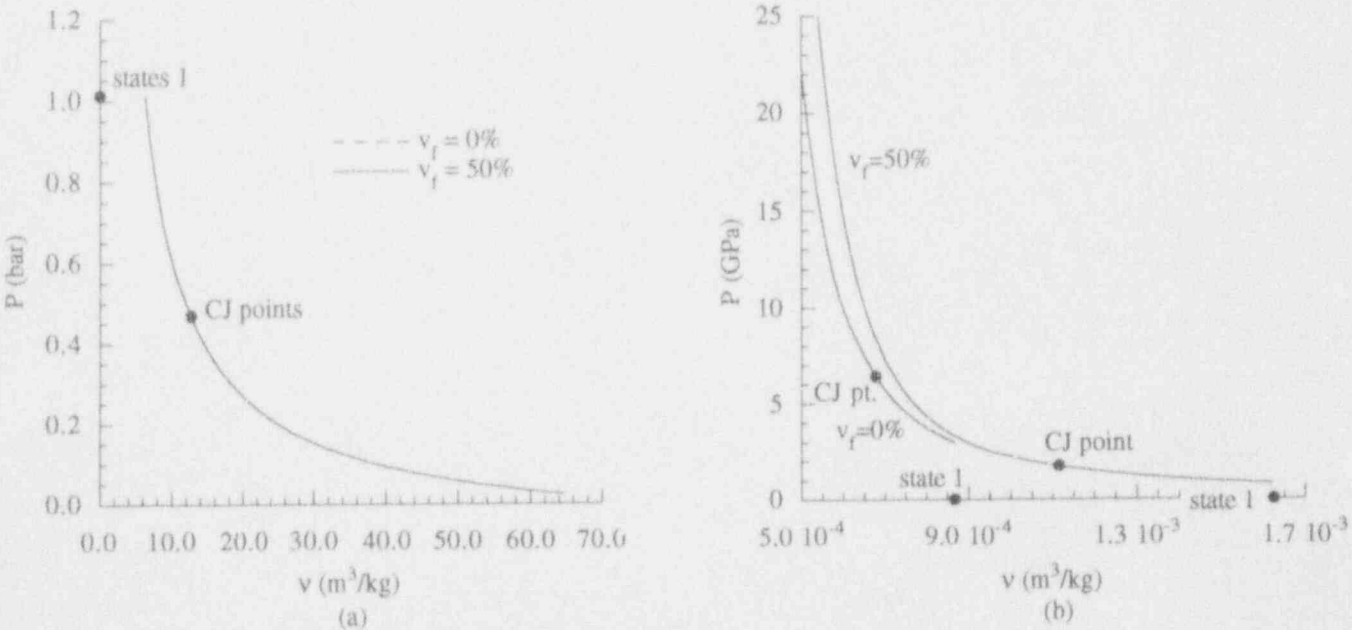

Figure 5. A comparison of two subsonic (a) and supersonic (b) Hugoniot solutions with different initial vapor qualities, y_v=0.0 and y_v=0.0006233, which correspond to v_f = 0% and v_f = 50% respectively. Where v_f is the volume fraction of the water that is vapor. At state 1 for both cases the aluminum is initially at 1000. K and $X = 5$. The Chapman-Jouguet points are noted.

solutions are used as points of comparison in this study since they provide a convenient characterization of the Hugoniot for a given set of parameters.

V. CONCLUSIONS

Destructive metal-water interactions are a hazard in a number of industries. To date, the computational investigation of rapid evaporation phenomena, particularly in fuel-coolant mixtures, has focused on supersonic solutions for non-reacting mixtures. We suggest that the entire Hugoniot solution should be considered and that the chemical reaction plays an important role in the process. The subsonic solution may characterize an important propagation mode for these types of waves.

We have developed a model to describe one-dimensional, steady state wave behavior. This model is used in conjunction with realistic thermodynamics to describe wave behavior in an aluminum-water mixture. The downstream equilibrium state is achieved by an adiabatic oxidation of the metal. The solution curves computed cover both the subsonic and supersonic solution branches. It is found that the thermodynamics of both the components as well as the oxidation reaction play a key role in the solution of these problems. An inconsistent or unrealistic thermodynamic construction will produce a very different solution, so it is essential to use equations of state that are as realistic as possible.

It is interesting to compare the results computed here with the results found for a non-reacting metal-water mixture. The solutions presented in McCahan and Shepherd (1991) for tin-water mixtures are based on the same model as is used in the present work, however, the tin-water mixture is assumed to be inert. In the four main cases studied for tin-water the supersonic CJ points fall at significantly lower pressures, 12. to 407. MPa, compared to the aluminum-water supersonic CJ point pressures computed here. Also, the wave velocities at the supersonic CJ points are significantly lower, 151. to 1290. m/s for the tin-water system, versus, 3010. to 5060. m/s for the aluminum-water system. The subsonic CJ solutions for both systems fall at similar pressures. However, the aluminum-water subsonic solutions fall at a much larger volume and temperature so the resulting wave speeds tend to be lower than those computed for the tin-water solutions. These results indicate that the reaction thermodynamics included in the aluminum-water system contribute significantly to the solution.

Unfortunately, the experimental data available on the downstream thermodynamic states of aluminum-water reaction waves are quite limited. Furthermore, no one-dimensional metal-water waves have been produced in the laboratory. However, investigations of the destructive force of these interactions can be found in the literature. One such study was performed by Hess and Brondyke (1969). While the force of the explosions created during their study was substantial (using 3.5 lbs of aluminum the sides of their containment were thrown 400 ft), it is unclear that the pressures produced reached the gigapascal range predicted by our model for a supersonic wave. Also, the medium necessary for the propagation of a supersonic wave, i.e. a continuous volume of finely dispersed metal in water contained in a highly confined environment, would be difficult to achieve in an experimental setting. It would seem more likely that the destructive force observed is due to the influence of the boundary conditions and other factors combined with a wave that is subsonic in nature.

The aluminum-water solutions presented here suggest a limiting behavior for these types of wave fronts. The triggering mechanism which initiates the wave and the transient process following initiation are not taken into account. We assume that the wave has already reached a steady state. Furthermore, this model can not, by itself, predict a unique downstream state and wave velocity. The solution provides a range of possible final states represented by a Hugoniot curve. A single solution can not be determined because the number of unknown variables exceeds the number of equations in the system by one. To uniquely define a downstream solution another equation must be added or any one of the variables, except wave velocity, must be specified. Choosing a wave velocity is not adequate because the wave velocity is not single valued along the solution curve. Matching the downstream pressure to some exhaust condition would seem to be a useful choice for simple one-dimensional problems with subsonic wave behavior. However, if the propagation mode is supersonic then it is not clear that choosing a downstream pressure is relevant to experimental conditions. Also, if any additional variables are added to the problem, such as slip between the phases, then the question of how to uniquely determine a solution is made even more difficult.

There are a number of conditions which are probably important for determining a unique solution including; the initial conditions, the boundary conditions, the wave structure and the downstream flow structure. Although all of the solutions calculated using the Rankine-Hugoniot relation satisfy the thermodynamic constraints on the system, it is the structure of the wave, and the other flow parameters, that will determine the unique wave behavior. For metal-water mixtures the fragmentation of the metal is probably the dominant mechanism which characterizes the wave structure. Thus, the fragmentation mechanism will contribute in a large part to the determination of a unique solution. The wave structure for fuel-coolant interactions has not been fully resolved. The strength of the triggering event which initiates the wave will also contribute to the nature of propagation process, as will the boundary conditions. Also, the wave front may be significantly effected by the structure of the downstream flow. These issues remain unresolved.

Finally, while we believe the subsonic behavior is the predominant propagation mode, it is possible that in an accident where the trigger is strong, and the geometry is complex, supersonic wave phenomena may occur. However, it is unclear whether such a wave could be sustained, given that propagation of a thermal detonation would require a large region of finely mixed fuel and coolant present in a confined space. More likely, the initiation of a thermal explosion in a confined geometry would lead to the formation of a precursor shockwave, which would run out ahead of the phase transition wave. The resulting over-pressures and apparent wave speeds from this configuration may be large enough to cause the substantial destruction experienced in these types of accidents.

ACKNOWLEDGEMENT

This research was partially supported by subcontract 525706 from Lawrence Livermore National Laboratories. The contract manager was Dr. William Tao of the HET group. We thank Lloyd Nelson of Sandia National Laboratories, Albuquerque, NM for useful discussions.

REFERENCES

Board, S.J., Hall, R.W. and Hall, R.S. (1975) "Detonation of Fuel Coolant Explosions," *Nature*, Vol. 254, pp. 319-321.

Board, S.J., and Hall, R.W. (1974) "Propagation of Thermal Explosions. 2 - Theoretical Model," CEGB Report RD/B/N 3249.

Byers Brown, W. (1987) "Analytical Representation of the Excess Thermodynamic Equation of State for Classical Fluid Mixtures of Molecules Interacting with α-Exponential-Six Pair Potentials up to High Densities," *J. Chem. Phys.*, Vol. 87, pp. 566-577.

Chirat, R. and Pittion-Rossillon, G. (1981) "A New Equation of State for Detonation Products," *J. Chem. Phys.*, Vol. 74, pp. 4634-42.

Corradini, M.L., Kim, B.J. and Oh, M.D. (1988) "Vapor Explosions in Light Water Reactors: A Review of Theory and Modeling," *Prog. in Nuc. Engr.*, Vol. 22, no. 1, pp. 1-117.

Cowperthwaite, M. and Zwisler, W.H. (1974) Vol. IV, TIGER User's Guide, SRI publication Z106.

Hall, R.W. and Board, S.J. (1979) "The Propagation of Large Scale Thermal Explosions," *Int. J. Heat Mass Trans.*, Vol. 22, pp. 1083-1093.

Hess, P.D. and Brondyke, K.J. (1969) "Molten Aluminum-Water Explosions, and Their Prevention," *Metal Prog.*, Vol. 95, no. 4, pp. 93-100.

Incropera, F.P. and DeWitt, D.P. (1985) Fundamentals of Heat and Mass Transfer, John Wiley & Sons, Inc., New York.

JANNAF Thermochemical Tables, 3rd Edition (1985) *J. Phys. and Chem. Ref. Data*, Vol. 14, suppl. 1.

March, S.P. (Ed.) (1980) LASL Shock Hugoniot Data, University of California Press, Berkeley.

McCahan, S. Thermodynamic Applications: Rapid Evaporation and Reacting Flow, PhD Thesis, Dept. of Mech. Engr., RPI, Troy, NY, 1992.

McCahan, S. and Shepherd, J.E. (1991) "Models of Rapid Evaporation in Nonequilibrium Mixtures of Tin and Water," in publication, 13th ICDERS, held in Nagoya, Japan, July 28-Aug. 2, 1991.

Raznjevic, K. (1976) Handbook of Thermodynamic Tables and Charts, Hemisphere Publishing Corp.

Reynolds, W.C. (1979) Thermodynamic Properties in SI, Dept. of Mech. Engr. Stanford Univ.

Shepherd, J.E., McCahan, S. and Cho, J.H. (1990) "Evaporation Wave Model for Superheated Liquids," Adiabatic Waves in Liquid-Vapor Systems, Eds. G.E.A. Meier and P.A. Thompson, Springer-Verlag, pp. 3-12.

Smithell's Metals Reference Book, (1983) Butterworth and Co. Ltd., Boston.

ON THE REQUIREMENTS FOR ENERGETIC MOLTEN ALUMINUM-WATER CHEMICAL REACTION

Hans K. Fauske and Michael Epstein
Fauske & Associates, Inc.
16W070 West 83rd Street
Burr Ridge, Illinois 60521
(708) 323-8750

ABSTRACT

An explanation is provided for the large difference in noted chemical oxidation between the SL-1 accident (1-2% oxidation) and recent aluminum-water pour type experiments (20-30% oxidation). A simple model of the steam explosion reaction zone is developed and shows that the presence of significant voids in the premixture prior to the explosive event is required in order to produce significant oxidation potential on an explosive time scale. Such voids would be largely absent in unprotected accident scenarios similar to the SL-1 accident.

I. INTRODUCTION

Several experimental studies of aluminum-water steam explosions have reported the probable contribution of aluminum-water chemical reactions (Hess and Brondyke, 1969, Lemmon, 1980, Rightly and Beck, 1992). Indeed Rightly and Beck observed very powerful steam explosions and estimated the extent of oxidation to be as high as 20-30%. In all of these experiments the aluminum and water components were initially separated and brought together via a pouring mode of contact (i.e., aluminum into water). In contrast, when masses of molten aluminum and water are initially premixed the release of chemical energy appears to be insignificant. In 1962, SL-1, a small experimental nuclear reactor at the Idaho test site was destroyed when the main control rod was rapidly removed during shutdown maintenance. The reactor core consisted of parallel, aluminum clad, Al-U alloy plates separated by water coolant channels. A millisecond nuclear power excursion melted and partially vaporized the U-Al alloy which penetrated the cladding and contacted the intervening layers of water producing a strong steam explosion. An extensive post accident analysis of the Sl-1 debris, however, indicated that metal oxidation was minimal and limited to 1-2% (SL-1 Project, 1962).

It is noteworthy that the millisecond nuclear power burst associated with the SL-1 accident resulted in little or no void formation prior to the aluminum-water explosive interaction, whereas in the pouring mode of contact, used, for example, by Rightly and Beck (1992), substantial steam voids have time to form in the premixture configuration prior to the explosion event. In this paper we suggest that the presence of significant voids in the premixture is a necessary condition for the release of chemical energy on an aluminum/water explosive time scale. This suggestion is based on the crucial assumption that the length of the reaction zone behind the shock front is of the order of a few centimeters and is approximately independent of the properties of the premixture configuration and oxidation kinetics.

II. PHYSICAL MODEL AND EQUATIONS

We begin our analysis of an aluminum/water steam explosion in progress by considering a steadily propagating steam explosion wave (shock or detonation, see Board et al., 1975) which is supported by the rapid thermal energy transfer from the hot aluminum fragments to the water in the wake of the shock. In order to describe the shock motion through the two-phase premixture configuration in the simplest possible way, we ignore the presence of the aluminum melt and assume that there is negligible heat and mass transfer between the water and steam phases ("frozen" flow model). This may not be exactly the case during an energetic steam explosion, but, hopefully, the frozen flow model will yield the correct dependence of the fluid velocity behind the shock on the steam phase void fraction. Also we assume that (i) the vapor and liquid move with the same velocity (homogeneous flow), (ii) the vapor is an ideal gas, and (iii) the compressibility of the liquid can be ignored.

With the assumptions given in the foregoing and the application of mass, momentum and energy conservation equations across the shock it can be shown that the shock velocity, u_s, is given by

$$u_s \approx \frac{a_{g,o}}{\alpha_o}\left(\chi_o \frac{P_\infty}{P_o}\right)^{1/2} \qquad (1)$$

and that the velocity in the wake of the shock, u_∞, is

$$u_\infty \approx a_{g,o}\left(x_o \frac{P_\infty}{P_o}\right)^{1/2} \qquad (2)$$

The velocities u_s and u_∞ are in the laboratory frame of reference. In writing Eqs. (1) and (2) we have ignored the presence of the metal (aluminum) component of the premixture configuration. In view of the discussion of the underlying assumptions which follows later on it is worth noting that the above equations are correct to within a factor of the square root of the heat capacity ratio for shocks which collapse the void in their wakes. In the above equations $a_{g,o}$ is the sound speed in the steam component of the undisturbed premixture (in front of the shock), P_∞ is the pressure behind the shock, α_o, P_o and x_o are the steam void fraction, pressure and steam mass fraction (quality) in the premixture. The latter quantity is given by the expression

$$x_o \approx \frac{\rho_{g,o}\alpha_o}{\rho_\ell(1 - \alpha_o)} \qquad (3)$$

where $\rho_{g,o}$ is the steam density in front of the shock and ρ_ℓ is the density of the liquid (water). Equations (1), (2), and (3) are reasonable approximations to the complete solution of the governing frozen-flow shock equations for $\alpha_o > 0$ and $P_\infty/P_o > 5$. The ratio of the mixture velocity behind the shock to the shock speed is, from Eqs. (1) and (2),

$$\frac{u_\infty}{u_s} \approx \alpha_o \qquad (4)$$

In accord with the detonation theory of thermal explosions, the velocity discontinuity across the shock front accelerates the aluminum and water components of the premixture configuration at rates dependent on their densities, thereby causing a velocity differential between the aluminum and water in the wake of the shock. If this velocity differential is sufficiently large one of several well known instabilities may lead to the fragmentation of the premixture-size aluminum drops. The first is the Rayleigh-Taylor instability that occurs because the aluminum-water interface on the upstream side of the aluminum drop is accelerated from the lighter fluid (water) towards the heavier fluid (aluminum). In this case, "fingers" of the two fluids interpenetrate each other. The second instability, the Kelvin-Helmholtz instability, occurs on account of a differential shearing motion between the two fluids. In this case, waves are caused to grow to the point of breaking in a manner similar to water waves driven by the wind, but without gravity to hold the waves "down". A third mechanism is the so-called boundary layer stripping mechanism proposed by Taylor (1963a). The melt in the viscous boundary layer beneath the surface of the drop flows to the equator of the drop where it breaks away from the surface. Finally, a still more complicated phenomenon may occur in which the fragmentation of the drop is a result of the action of the steam film that surrounds the drop. In this so-called thermal fragmentation mechanism melt breakup has been postulated to occur as a result of water jet contact or penetration of the melt following steam film collapse (see, e.g., Buchanan, 1974; Ochiai and Bankoff, 1976) or as a result of rapid erosion of the melt by steam flow within the steam film (Ciccarelli and Frost, 1992).

Regardless of the mechanism of aluminum fragmentation in water, experimental work with other material pairs suggests that the time constant t_B for the significant breakup of the aluminum drops in the wake of the shock can be approximated by

$$t_B \approx \frac{cd}{u_\infty}\left(\frac{\rho_{Al}}{\rho_\ell}\right)^{1/2} \qquad (5)$$

where d is the premixture dimension of molten aluminum. The constant of proportionality c in Eq. (5) has been determined by measurement to range from 1 to 5 (Theofanous et al., 1979; Reinecke and Waldman, 1970; Simpkins and Bales, 1972; Baines and Buttery, 1979; Kim et al., 1983; Ciccarelli and Frost, 1992). Here we select the average value c = 2. In a future paper we plan to show that this empirically determined range of values for c can be rationalized on the basis of non-linear Rayleigh-Taylor and Kelvin-Helmholtz instabilities (Epstein and Fauske, 1992a).

In a propagating explosion the reaction zone is defined as the distance behind the shock over which energy transfer occurs. Strong explosion waves can only occur in regions of coarse intermixing which are large compared with the reaction length. Since the dimensions of the initial mixing zone in the Rightly and Beck test and in the SL-1 incident were of the order of 0.5 m, it is reasonable to presume that during the recorded explosions energy transfer was complete in a distance of only a few centimeters behind the shock. In particular, we will assume that if strong aluminum/water thermal explosions occur over a certain range of premixture configuration conditions, then the thicknesses (or lengths) of the corresponding reaction zones are roughly equal (within a factor of, say, two) and known and, therefore, approximately independent of premixture conditions and chemistry. If we denote L_{ex} as the known explosion length, the characteristic explosion time t_{ex} becomes

$$t_{ex} = \frac{L_{ex}}{u_s - u_\infty}, \qquad (6)$$

assuming that the melt accelerates up to the flow velocity u_∞ in a time that is short compared with the explosion time. Had we assumed that the melt drops remain stationary as the reaction zone passes then $t_{ex} = L_{ex}/u_s$. The actual situation lies between these limiting cases. It should be noted that the results presented below would not differ by much if t_{ex} values corresponding to $u_\infty = 0$ in Equation (6)

were used. It follows from Eqs. (4) - (6), that the fraction f_B of molten aluminum that experiences breakup is

$$f_B = \frac{t_{ex}}{t_B} = \frac{\alpha_o L_{ex}}{c(1 - \alpha_o)d}\left(\frac{\rho_\ell}{\rho_{Al}}\right)^{1/2} \quad ;$$

$$f_B \le 1.0 \tag{7}$$

The mean diameter d_p of aluminum fragments (microspheres) produced by the breakup process in the reaction zone is estimated using the Weber-number criterion with a Weber number coefficient of 10:

$$d_p = \frac{10\sigma}{\rho_\ell u_\infty^2} \tag{8}$$

where σ is the surface tension of molten aluminum ($\sigma = 0.9$ kg s^{-2}). Unfortunately, no measurements have been reported to date of the fineness of the fragments produced by drop breakup in shock-induced liquid flow. Laboratory studies of drop breakup in shock-induced gas flows (Hanson et al., 1963; Gelfand et al., 1972; and Hass, 1964) indicate that the Weber number best correlates the characteristic size of the fragmented drop material. A discussion of the expected accuracy of the Weber number criterion for the aluminum/water application is given in the next section.

We will assume that oxidation of the aluminum microspheres is controlled by oxygen or aluminum species diffusion through a growing molten oxide layer beneath the surface. The formation of the very protective solid oxide phase that ordinarily prevents aluminum oxidation is assumed to be delayed, as postulated by Epstein and Fauske (1992b). Note that we are assuming an early transition from an external gas-phase diffusion-limited rate to an internal diffusion-limited rate of reaction. If x is the instantaneous radial location of the oxide/metal interface (oxidation front) measured from the center of a representative aluminum microsphere, the microsphere oxidation fraction f_{ox} is

$$f_{ox} = 1 - \left(\frac{2x}{d_p}\right)^3 \tag{9}$$

It is assumed that the aluminum oxidation process in steam is approximately parabolic. Thus while the microsphere resides in the reaction zone its oxide layer grows to a thickness of roughly $(Dt_{ex})^{1/2}$, where D is the Fick binary diffusion coefficient for an oxygen or aluminum species in molten Al_2O_3. In general, diffusion coefficients vary exponentially with temperature, but for liquids the activation energy and argument of the exponent are small and the temperature effect is usually slight. As a result, virtually all non-polymeric liquids have remarkably similar diffusion coefficients, regardless of the temperature or chemical composition. Based on known values for other binary systems the value $D = 10^{-9}$ m^2 s^{-1} appears to be a reasonable choice (Jost, 1960).

Since

$$x + (Dt_{ex})^{1/2} = d_p/2 \tag{10}$$

Eq. (9) becomes

$$f_{ox} = 1 - \left[1 - \frac{2(Dt_{ex})^{1/2}}{d_p}\right]^3 \quad ;$$

$$f_{ox} \le 1.0 \tag{11}$$

The overall oxidation fraction F_{ox} of the total aluminum mass in the premixture configuration is

$$F_{ox} = f_B f_{ox} \tag{12}$$

or, equivalently, from Eqs. (4), (6), (7), and (11),

$$F_{ox} = \frac{\alpha_o L_{ex}}{c(1 - \alpha_o)d}\left(\frac{\rho_\ell}{\rho_{Al}}\right)^{1/2} \cdot \left\{1 - \left[1 - \frac{2}{d_p}\left(\frac{D\,L_{ex}}{u_s(1 - \alpha_o)}\right)^{1/2}\right]^3\right\} \tag{13}$$

III. RESULTS

The overall oxidation fraction F_{ox}, as predicted with Eq. (13), is plotted in Fig. 1 as a function of the steam-void fraction α_o in the premixture configuration. The curves in this figure were obtained by assuming a shock-to-ambient pressure ratio $P_\infty/P_o = 100$, with $P_o = 10^5$ Pa. This pressure ratio is chosen on the basis that a spontaneously triggered explosion resulting from homogeneous nucleation of superheated water at ~ 310°C would result in a shock pressure corresponding to half the critical pressure of water.[a] The physical properties and remaining fixed parameter used in the construction of Fig. 1 are $\rho_{Al} = 2.37 \times 10^3$ kg m^{-3}, $\rho_\ell = 10^3$ kg m^{-3}, $\rho_{g,o} = 0.58$ kg m^{-3}, $a_{2o} = 473.0$ m s^{-1}, $\sigma = 0.9$ kg s^{-2}, $D = 10^{-9}$ m^2 s^{-1}, and $c = 2.0$ (see discussion following Eq. 5).

The two shaded areas in Fig. 1 represent two families of curves, each area bounded above by the curve for a reaction zone length $L_{ex} = 0.04$ m and bounded below by the curve for $L_{ex} = 0.02$ m. Based on the previous discussion of the magnitude of L_{ex}, it is our feeling that the actual reaction length falls between these values. The upper shaded region in Fig. 1 represents results obtained with a premixture configuration aluminum-dimension $d = 2 \times 10^{-3}$ m

---

[a] The homogeneous superheat limit of 310°C has never been attained in the laboratory. Apfel (1972) and Blander et al. (1971) superheated water to 280°C. Thus a practical shock-to-ambient pressure ratio is $P_\infty/P_o = 66$.

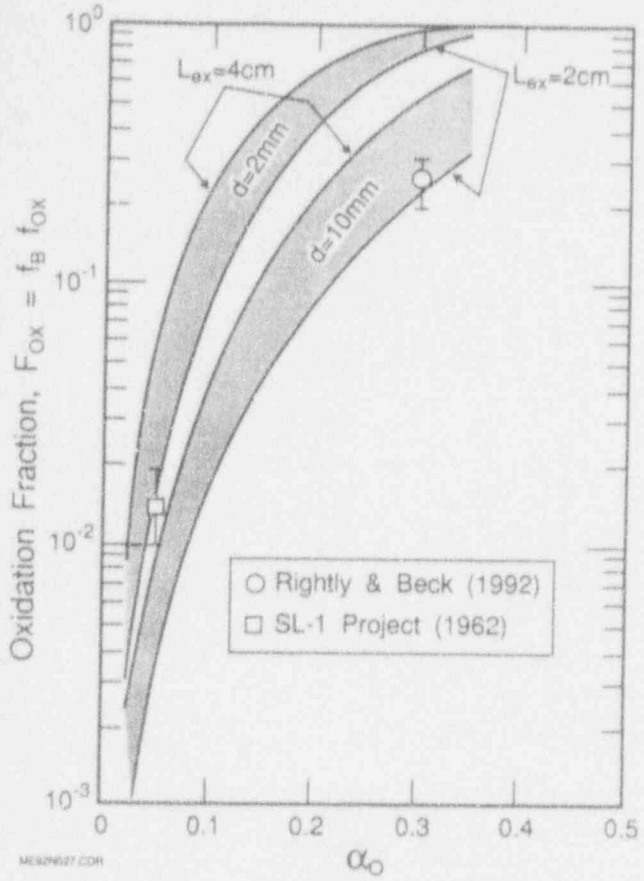

Fig. 1 Illustration of the overall oxidation potential as a function of the steam void fraction in the premixture prior to an explosion event; premixture aluminum-drop size and length of explosion zone as parameters.

(2 mm), which was approximately the thickness of the Al-U alloy plates within the SL-1 reactor core. The lower shaded region was obtained by setting d = 0.01 m, which is of the order of the capillary size for aluminum and is believed to be appropriate for the "pour" mode of contact employed in the Rightly-Beck (1992) experiments.

The curves in Fig. 1 indicate that the overall oxidation potential is rather sensitive to the magnitude of the initial voids present in the aluminum/water premixture configuration. This predicted behavior is a consequence of the fact that at low void fractions the steam explosion wave propagates at a high velocity u_s relative to the velocity u_p of the mixture in its wake. This combination of u_p and u_s leads to large aluminum fragment sizes d_p and short explosion times t_{ex} and, as a result, the explosion shock "outruns" the oxidation process. As the void fraction is increased u_s decreases and u_∞ increases which in turn causes a reduction in d_p and an increase in t_{ex}, thereby allowing more time for significant chemical energy release.

The reported final extent of reaction for the SL-1 incident and for the recent experiments of Rightly and Beck (1992) are plotted in Fig. 1. It is clear from the figure that our present theoretical approach is capable of accounting for the lack of aluminum oxidation when little or no initial voids are present, as was the case during the SL-1 accident, and the substantial oxidation believed to have taken place after pouring molten aluminum into water and producing a premixture zone of approximately 30% void fraction (Rightly and Beck, 1992). We note that the absence of significant oxidation during the SL-1 incident is not inconsistent with the observation of a relatively strong fuel-coolant thermal interaction, considering the initial fuel dimension of about 2×10^{-3} m and the large thermal diffusivity of molten aluminum of 6×10^{-5} m^2 s^{-1} as compared with the oxygen (or aluminum) species diffusion coefficient of about 10^{-9} m^2 s^{-1}. It appears from Fig. 1 that the best agreement between the two data points and the theory is obtained with L_{ex} = 0.02 m. Interestingly enough, Debora et al. (1959) have shown that the reaction length is about 0.02 m in two phase chemical detonations where the fuel is in droplet form in a gaseous oxidizing atmosphere.

IV. DISCUSSION AND CONCLUSIONS

Before we summarize the reactor safety implications of the present work, it is prudent to consider the extent to which the viscosity of the aluminum may affect the fineness of the metal cloud behind the vapor explosion shock and to add some additional remarks concerning our assumption of a reaction zone of fixed dimension.

Our two-phase shock calculations reveal shock induced velocities as high as u_∞ = 84 m s^{-1}. The Weber number formulation, Eq. (8), results in corresponding predicted aluminum drop fragments as small as $d_p \approx 1.0$ μm. It is well known that the influence of viscosity on the size of the stable drop fragment increases in importance as d_p is made smaller. If indeed the Weber number determines the mean size of the drop fragments that comprise the micromist in the wake of the shock, then the final stage of the aluminum drop disintegration process must be controlled by the Kelvin-Helmholtz (or capillary wave) mechanism. The most general capillary-wave analysis of present interest is where both phases (water and aluminum) have comparable density and viscosity. Unfortunately, solution of the stability equations for this case is extremely complex. A special case treated by Taylor (1963) is that of an inviscid gas passing over a viscous liquid. At first glance his solution may not seem relevant to the aluminum drop/water case. However, our experience with this class of stability problems indicates that the solution for the dense viscous phases does not differ in a significant way from that where only one of the phases has density and viscosity, as long as the density difference between the phases is more than about a factor of

two. Using the results of Taylor's analysis, we find that the Weber number We_μ in the presence of viscosity, when normalized by the Weber number for inviscid material pairs, as given above by Eq. (8), is strictly a function of a modified capillary number; that is

$$\frac{We_\mu}{We} = f\left\{\left(\frac{\rho_\ell}{\rho_{Al}}\right)^{1/2} \frac{\mu u_\infty}{\sigma}\right\} \qquad (14)$$

where in our application μ is the viscosity of the aluminum and the modified capillary number appears as the argument of the function. The actual functional relationship between the Weber number ratio and the capillary number follows immediately from Taylor's numerical results. Suffice it to say that the ratio does not rise significantly above unity until the capillary number exceeds approximately unity. Thus viscosity exerts little influence on the numerical value of the Weber number as long as the following criterion is obeyed:

$$\left(\frac{\rho_\ell}{\rho_{Al}}\right)^{1/2} \frac{\mu u_\infty}{\sigma} \lesssim 1.0 \qquad (15)$$

For the water-aluminum application we find, with $\mu \approx 2.5 \times 10^{-3}$ kg m^{-1} s^{-1} for molten aluminum, that the shock-induced velocity of the surrounding water must exceed $u_\infty \approx 560$ m s^{-1} before viscous limitations to the fineness of the molten metal fragments behind the shock become apparent. Such a high shock-induced velocity is not predicted for the aluminum-water system. Thus it is permissible to use Eq. (8) to predict the size of the aluminum microdrops in the wake of the explosion shock.

The correctness of the oxidation versus void fraction trends displayed in Fig. 1 relies heavily on the validity of the assumption that the length of the reaction zone is roughly independent of the premixture configuration conditions and the combustion process in the wake of the shock. With regard to the void fraction in the premixture configuration, photographs of single hot melt drops in a shock-induced flow reveal that the shock wave initiates collapse of the thick vapor film that surrounds the drop (see, e.g. Ciccarelli and Frost, 1992). Indeed, if the sequence of events behind the shock during the propagation of a coherent interaction is steam collapse, aluminum fragmentation, energy release and the production of high-pressure vapor, one would anticipate that the length of the reaction zone does not depend on how the steam (void) is distributed ahead of the shock. Unfortunately, without a detailed knowledge of the structure of the reaction zone, it is difficult to prove that L_{ex} is also independent of the characteristic size of the molten metal in the pre-mixture (ahead of the shock) or of the combustion process behind the shock. All we can say at this stage is that the conclusions drawn from Fig. 1 would not change in an important way if we assigned L_{ex} values for the SL-1 incident (1962) and the pour tests (Rightly and Beck, 1992) that differ somewhat from each other (e.g., $L_{ex} \simeq 4$ cm for SL-1 and $L_{ex} \simeq 2$ cm for the pour tests, or vice versa).

A hypothetical unprotected accident in a heavy water production reactor (or research reactor) sets the stage for the principal mode of aluminum/water contact of concern. The rapid power excursion and subsequent fuel melting, with the coolant and moderator largely in place, results in a premixture configuration similar to that of the SL-1 accident. According to the theory presented here, due to the absence of significant voids for this type of contact mode, a large-scale interaction of molten aluminum alloy fuel and water in the reactor core would be largely thermal in nature with chemical oxidation contributing very little to the explosion. With regard to hypothetical protected accident scenarios where the "pour" mode of contact becomes relevant, an energetic chemical explosion may be possible, but would be limited to about 1% of the total fuel mass considering the limiting fuel pour rate of about 100 kg s^{-1} (based upon 1% decay heat and satisfying the fuel heat of fusion).

V. REFERENCES

Apfel, R. E., 1972, "Water Superheated to 279.5°C at Atmospheric Pressure", Nature Phys. Sci. 238, 67-71.

Baines, M. and Buttery, N. E., 1979, "Differential Velocity Fragmentation in Liquid-Liquid System", Berkeley Nuclear Labs, RD/B/N 4643.

Blander, M., Hengstenberg, D. and Katz, J. L., 1971, Bubble Nucleation in n-Pentane, n-Hexane, n-Pentane + Hexadecane Mixtures, and Water", J. Phys. Chem. 75, 3613-3619.

Board, S. J., Hall, R. W., and Hall, R. S., 1975, "Detonation of Fuel Coolant Explosions", Nature, 254, 319-321.

Buchanan, D. J., 1974, "A Model for Fuel-Coolant Interactions", J. Phys. D., App. Phys., 7, 1441-1457.

Ciccarelli, G. and Frost, D. L., 1992, "Fragmentation Mechanisms Based on Single Drop Experiments Using Flash X-Ray Photography", Proc. 5th Int'l Topical Meeting on Reactor Thermal Hydraulics", September, Salt Lake City, UT, 615-626.

Dabora, E. K., Ragland, K. W., Nicholls, J. A., 1969, "Drop-Size Effects in Spray Detonations", 12th Int'l Symposium on Combustion, Pittsburgh, 19-26.

Epstein, M. and Fauske, H. K., 1992a, "Time Scales Relative to the Breakup of Drops in Gases and Liquids", to be submitted for publication.

Epstein, M. and Fauske, H. K., 1992b, "A Crystallization Theory of Underwater Aluminum Ignition", Proc. 5th Int'l Topical Meeting on Reactor Thermal Hydraulics, September, Salt Lake City, UT, Vol. II, 637-645.

Gelfand, B. E., Gubin, S. A., Kogarko, S. M., and Komar, S. P., 1973, "Breakup of Liquid Drops in a Flow Behind Shock Waves with a Triangular Gas-Velocity Profile", Translated from Izvestiya Akademii Nauk SSSR, Mekhanika Zhidkosti i Gaza, No. 5, September-October, 54-60 (1975 Plenum Publishing Corp., New York).

Hanson, A. R., Domich, E. G., and Adams, H. S., 1963, "Shock Tube Investigation of the Breakup of Drops by Air Blasts", Physics of Fluids, 6, 1071-1080.

Hass, F. G., 1964, "Stability of Droplets Suddenly Exposed to a High-Velocity Gas Stream", Journal American Institute of Chemical Engineers, 10, 920-924.

Hess, P. D. and Brondyke, K. J., 1969, "Causes of Molten Aluminum-Water Explosions and Their Prevention", Metal Progress, 95, 93-100.

Jost, W., 1960, Diffusion in Solids, Liquids, Gases, Academic Press, New York.

Kim, D. S., Burger, M., Frohlich, G., and Unger, H., 1983, "Experimental Investigation of Hydrodynamic Fragmentation of Gallium Drops in Water Flows", Proceedings Int. Meeting on Light Water Reactor Severe Accident Evaluation, Cambridge, MA, Vol. 1, 6.4-1 (August 28-September 1).

Lemmon, A. W., Jr., 1980, "Explosions of Molten Aluminum and Water", Light Metals, Metallurgical Society of AIME, Warrendale, PA, 817-836.

Ochiai, M. and Bankoff, S. G., 1976, "Liquid-Liquid Contact in Vapor Explosions", Proc. Int. Conf. on Fast Reactor Safety, Am. Nucl. Soc., Chicago, IL.

Reinecke, W. G. and Waldman, G. D., 1970, "Investigation of Water Drop Disintegration in a Region Behind Strong Shock Waves", Proc. Third Int. Conf. on Rain Erosion and Related Phenomena, Hampshire, UK, 629.

Rightly, M. J. and Beck, D. F., 1992, "NPR/FCI EXO-FITS Experiment Series Report", Sandia National Lab Report SAND91-1544, Revision 1, Draft for Review, May.

Simpkins, P. G. and Bales, E. L., 1972, "Water-Drop Response to Sudden Accelerations", Journal of Fluid Mechanics, 55, 629-639.

SL-1 Project, 1962, "Final Report of SL-1 Recovery Operations", TM62-7-704, IDO-19311, July.

Taylor, G. I., 1963a, "The Shape and Acceleration of a Drop in a High Speed Air Stream", in The Scientific Papers of Sir Geoffrey Ingram Taylor, Vol. III, ed. G. K. Batchelor, Cambridge University Press, 457-464.

Taylor, G. I., 1963b, "Generation of Ripples by Wind Blowing Over a Viscous Fluid", in The Scientific Papers of Sir Geoffrey Ingram Taylor, Vol. II, ed. G. K. Batchelor, Cambridge University Press, 244-254.

Theofanous, T. G., Saito, M., and Efthimiadis, T., 1979, "The Role of Hydrodynamic Fragmentation in Fuel Coolant Interactions", Fourth CSNI Specialist Mtg. on Fuel-Coolant Interactions in Nuclear Reactor Safety, Bournemouth, England, CSNI Report No. 37, Vol. 1, 112, Paper #FC14/P5, April 2-5.

PROPAGATION OF VAPOR EXPLOSION IN A STRATIFIED GEOMETRY

EXPERIMENTS WITH LIQUID NITROGEN AND WATER

J. Sainson* - M. Gabillard* - T. Williams**

* Gaz de France - DETN - SEC
BP 1140, 44024 NANTES Cedex 01, FRANCE

** Gas Research Institute
8600 West Bryn Mawr Avenue, CHICAGO, ILLINOIS 60631, USA.

ABSTRACT

An experimental investigation relative to Liquid Nitrogen/water interaction at large laboratory scale isdescribed in this paper. The self-sustained propagation of a triggered vapor explosion for this liquid pair was never attained in an initially well-stratified geometry. The interaction was always limited to the triggered zone which varied as a function of the different parameters of the experiment (trigger characteristics, Liquid Nitrogen layer thickness). However, experiments suggested that an increase of the initial wavyness of the liquid Nitrogen/water interface prior to triggering, was a sufficient condition to sustain the vapor explosion all along the ring.

INTRODUCTION

Many experiments have shown that under special conditions when a cryogenic liquid is spilled onto a relatively hot liquid such as water, a rapid heat transfer occurs which can yield a large amount of energy. Such explosive events could happen if sufficiently large quantities of liquefied natural gas (LNG) are spilled onto a body of water such as the sea either in the case of the rupture of a loading arm or in the case of a spill from an LNG carrier. The kind of vapor explosion studied here is quite similar, even though it is of lesser intensity than those produced in fuel/coolant interactions.

To assess the potential hazards induced by LNG/water explosions, Gaz de France and the Gas Research Institute, in cooperation with other Gas companies, are involved in studies for a better understanding of LNG/water interactions. Since 1981, many tests involving continuous or instantaneous LNG spills on seawater were performed at large scale in order to simulate an industrial release scenario. To go further in the fundamental understanding of LNG/water explosions for future predictive numerical models, theoretical studies and laboratory scale experiments (Sainson et al. 1990) have been conducted.

Current state of the art supports the assumption that a vapor explosion is only possible if a mixing of water and cryogenic liquid occurs, thus causing the thermal energy from the water to be effectively transferred to the LNG. Actually, two extreme situations are met in industrial configurations :

- the cryogenic liquid (lighter liquid) is in a boiling state over the water (the warmer liquid). This situation is often called " stratified geometry". In this case, it is necessary to find out whether or not a premixing mechanism is required to produce a propagation of the vapor explosion in a stratified medium.

- the two liquids are premixed. In this case the knowledge of constitutive relations between the initial mixing ratio and others crucial parameters such as the energy yield or the propagation speed is of prime interest.

In order to investigate these situations, an experimental programme on vapor explosion at a large laboratory scale (2.5 m long) has been carried out involving water and pure liquid nitrogen, abbreviated LN2 subsequently. The first step of this study is to investigate stratified geometries. Such experiments with LN2 have already been conducted (Bang & Corradini 1991) at different smaller laboratory scales (up to 50 cm), where interactions were detected with wave speeds ranging from 100m/s to 250 m/s, but with no real propagation at larger scale. Very few other experimental studies in this geometry were conducted in the past with different liquid pairs (Board & Hall 1975, Green et al. 1983, Frohlich 1984, Anderson et al. 1988, Frost & Cicarelli 1991). Brayer & Berthoud 1992 made a review of all these experimental works, concluding that the propagation and intensity of the interaction seem to be closely linked to the ability of the pressure wave to destabilize the vapor film depending on the nature of the liquid pair, the degree of confinement and premixing.

A specific outdoor facility was built in order to perform high energy release experiments and to insure reproducible and reliable measurements. Preliminary tests were carried out with water alone in order to qualify the triggering device and the different kind of measurements. Then several visualizations were achieved to characterize the LN2-Water interface or to see the effect of the trigger on the water surface. Finally, stratified geometry tests were performed to provide pressure measurements and video records, looking for stationary propagation.

The results of this work will have repercussions on future studies in premixed medium whose characteristics are presented at the end of the paper, and for future numerical models.

I. TEST RIG

An out-door test rig has been built in order to measure the stability of a pressure shock - artificially generated by a conventional detonator - propagating through a stratified mixture of water and LN2. Some other devices will be set-up in the future in order to study the propagation in a calibrated premixed medium.

Since strong vapor explosions have been observed in the past, the test rig is located about 120 meters from the measurement area. It consists of two independent sections. The first one is a channel section (figure 1) where the explosions take place and the second section comprises the LN2 unloading system (figure 2).

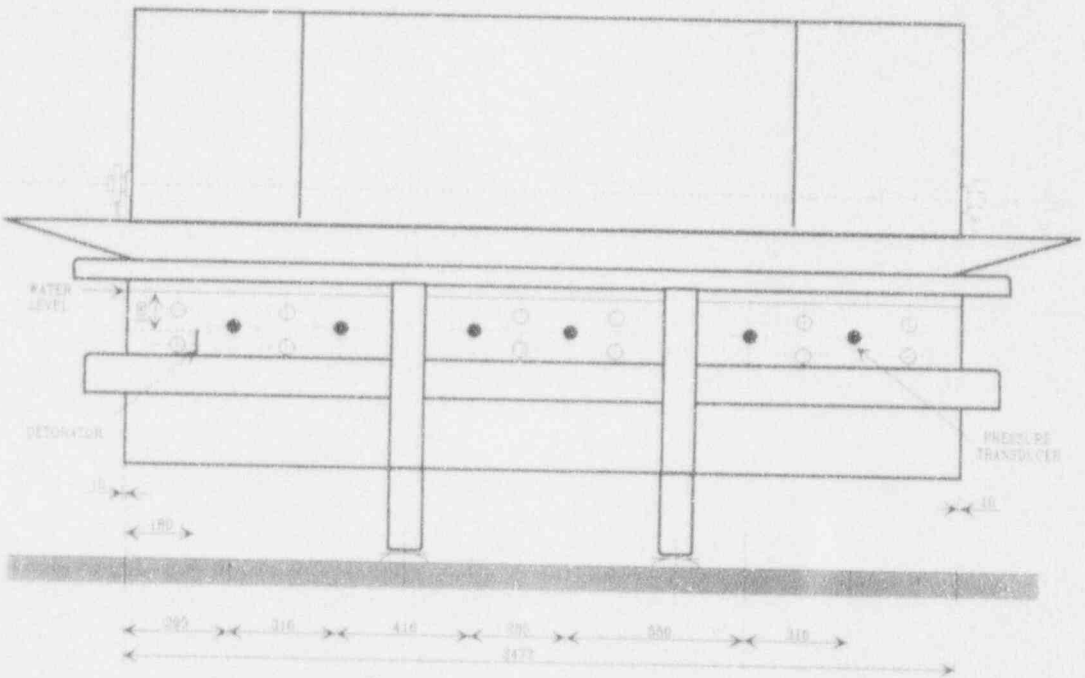

Figure 1 : Rig : General view

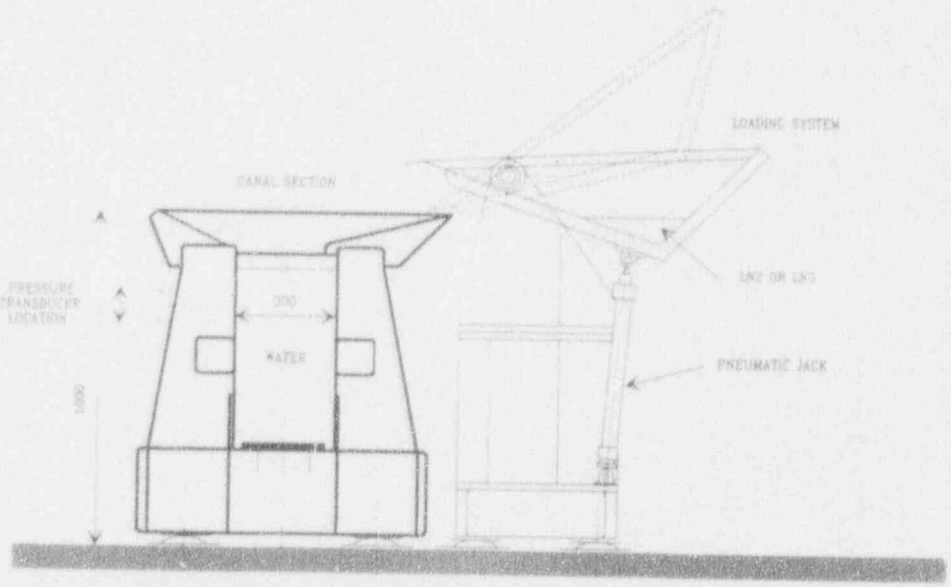

Figure 2 : Rig : Lateral View

The inner dimensions of the channel section are 2500 mm long, 300 mm wide and 600 mm deep. The channel consists of 304L stainless steel, supported by external stiffeners and a base plate in the same material. The channel and its accessories are placed over a concrete slab and secured with anchoring braces. A "tray" (sloped panel with a low incline) is welded to the upper part of the large wall located at the unloading end, so that the cold liquid can be discharged smoothly. The tray is 400 mm wide. Various apertures (3 horizontal ramps with 6 threaded internal boss holes, positioned at various heights) are provided along a side wall of the channel in order to mount sensors. The mounting system is designed so that sensors are placed parallel to the water surface and for the majority of the tests, about 50 mm below the water surface. The channel is drained through nozzles following each test.

The unloading system is also built with 304L stainless steel, with a 120° triangular base and a pivot joint articulation. The rotational movement is provided by two pneumatic jacks connected to a hydraulic system. Their positions are adjustable in order to select the optimum discharge time. The unloading system has an internal insulation consisting of polyurethane covered with a wood plate and a fine stainless steel sheet. The system is designed to contain a maximum of 75 liters of cryogenic liquid.

The initiation of vapor explosions is produced by instantaneous electric detonators (Nr. 8 detonators) with an explosive charge of about 1 g. of pentrite (3.64 kJ equivalent energy). One test was performed with a smaller charge (about 70 mg). The triggering support, fixed to the channel structure, is installed at one end. Two detonator supports were used during the tests. The first support (figure 3a) is composed of a tube fitted with two "jacks" which allow the tightening on the internal walls of the rig. An 8 mm tube, welded in the middle of the support allows to insert the detonator basis. The second support (figure 3b) is similar to the first one, except that the detonator is located inside a 150 mm long cylinder, closed at the bottom, with an internal diameter of 10 mm in order to direct the pressure wave toward the water interface and to limit the premixing area. The detonator is triggered by a conventional electric system.

The dynamic pressure sensors (6 along the rig) are piezoelectric sensors (500 KHz) with a built-in electronic system connected to a 6 way power supply. The transducers are linked to an analog multi-track magnetic tape recorder (100 KHz) connected at its output to a digital oscilloscope which processes the signal. Hard-copy output are printed out on a plotter. A synchronized triggering signal is generated from the magnetic recorder. The LN2 depth is measured inside the insulated spillage with marks that indicate the pure LN2 initial depth which would be obtained in the rig. Usually, experiments were performed with LN2 depths between 30 mm and 70 mm. Because of the good insulation of the spillage system, the LN2 level didn't vary notably during the necessary time to evacuate the test rig area prior to triggering the test.

Test procedure : first, a predetermined depth of water (usually 440 mm) at a known initial temperature is released into the channel and a known volume of LN2 is set up in the unloading system.

After triggering the pressure measurement acquisition system, the pneumatic jacks are activated in order to release the cold liquid, first onto the flap (to reduce to flow rate) and then over the water. As soon as the release is completed, an electric signal is generated in order to trigger the detonator. A time delay can be adjusted (between 0 and 5 seconds) between the end of the spillage and the triggering instant to assure stratification. The test is completed as soon as the cold liquid has finished evaporating.

II. PRELIMINARY TESTS

Preliminary tests were carried out in order to characterize the trigger. Some visualization tests were also performed to characterize the water-LN2 interface during and after the spillage and to select the right initial water temperature for inhibiting ice formation.

Prior to performing tests involving LN2, preliminary tests were carried out to characterize the trigger with the two different supports, to measure the range of the triggering device and the reproducibility of the signal in the absence of any cold liquid and to estimate the trigger effects on the water interface.

Figures 4a (non shielded detonator) and 4b (shielded detonator) show typical pressure measurements recorded by the 6 pressure transducers when the detonator explodes without any LN2. The detonator and the pressure sensors coordinates relative to a reference are given on the figures. Usually, the detonator is located about 100 mm below the water level, about 200 mm lengthwise from the end of the rig and in the center relative to the width. The time delay between each first maximum pressure peak of each signal is in good agreement with the necessary time for a pressure wave to propagate through water (1500 m/s). The pressure peak width (100 - 150 μs) is due to reflections by the wall and vibrations of the structure. The difference in the pressure peak shows a 1/d2 dependence on pressure attenuation for transducers located beyond 300 mm from the detonator. The total time scale for the shock wave to completely cross the channel lengthwise which is given by the detonator pressure measurements and includes the reflections and vibrations is about 2 ms. This characteristic time scale is very low with respect to the vapor explosion development time scale (see below). We noted also a good reproducibility of the trigger both in terms of the propagation velocity of the waves and in terms of the pressure signal amplitude.

A visualization of the detonator explosion was carried out by video recordings close to the channel water interface. The video-films showed that the non shielded detonator (support Nr. 1) produces a water spray affecting 50 to 100 cm of the length of the rig during a period of about 100 ms (2-4 frames). During this time, the rest of the surface remains planar, the larger water waves being developed at a larger time scale. With the shielded detonator (support Nr. 2), about 30 to 50 cm of the length of the rig is affected by the explosion.

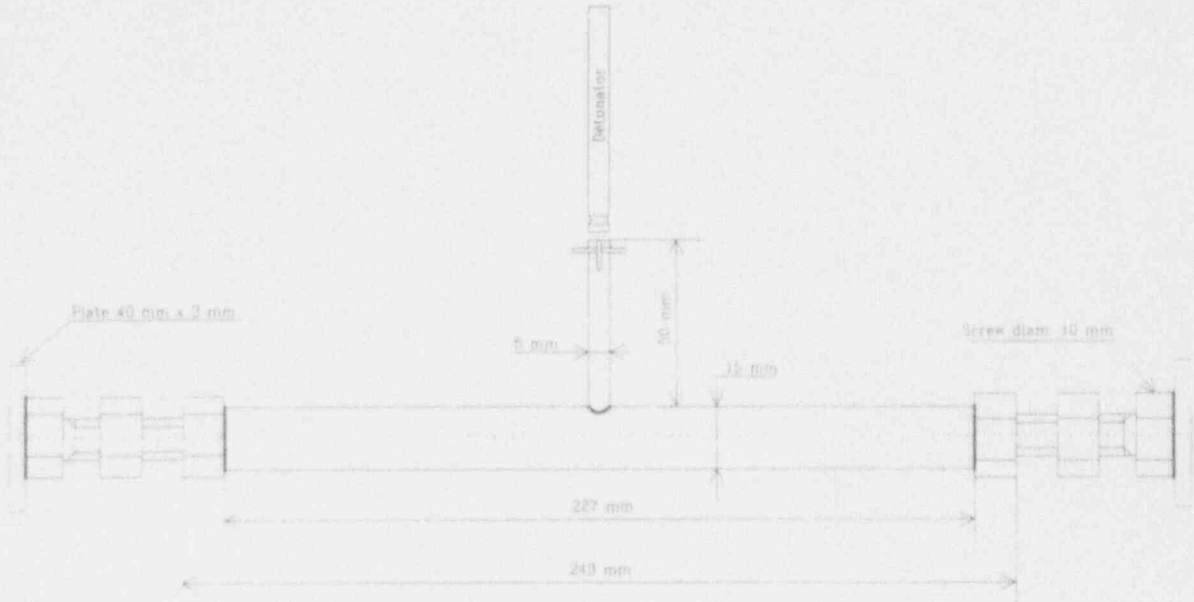

Figure 3.a : Detonator support N° 1

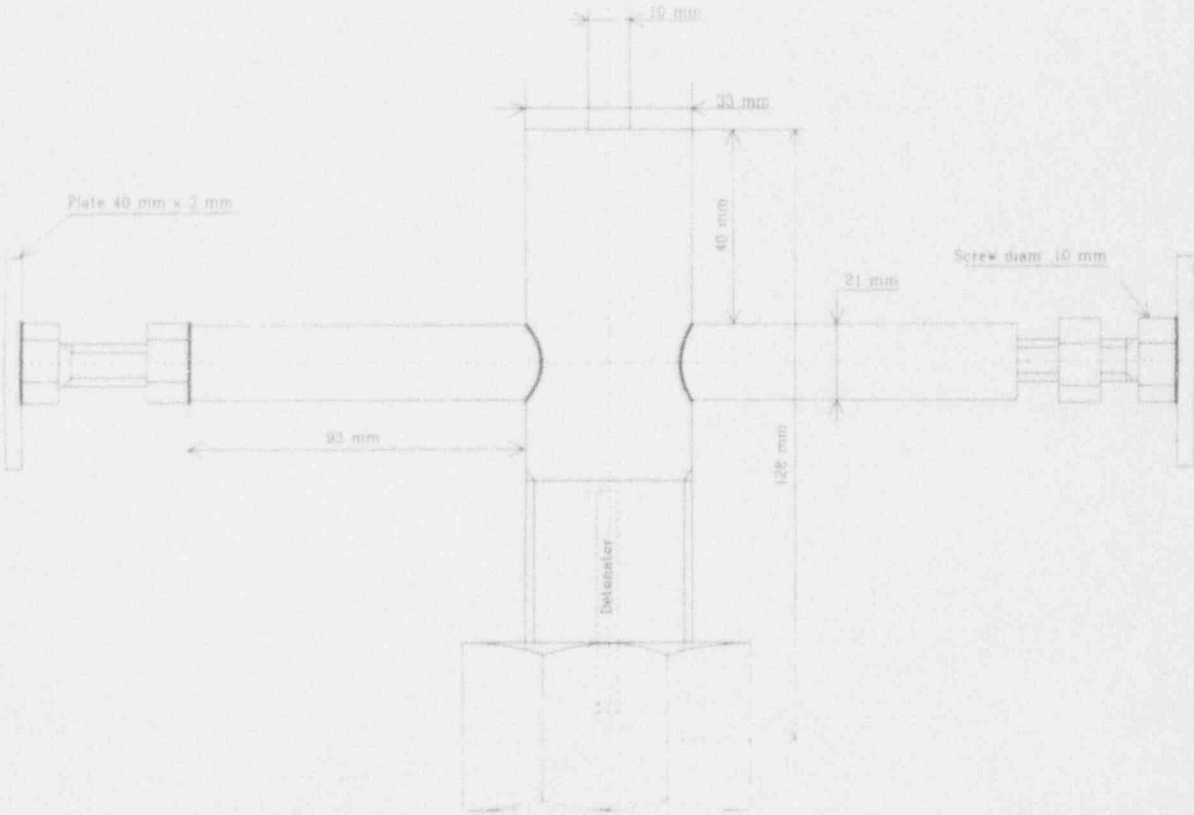

Figure 3.b : Detonator support N° 2

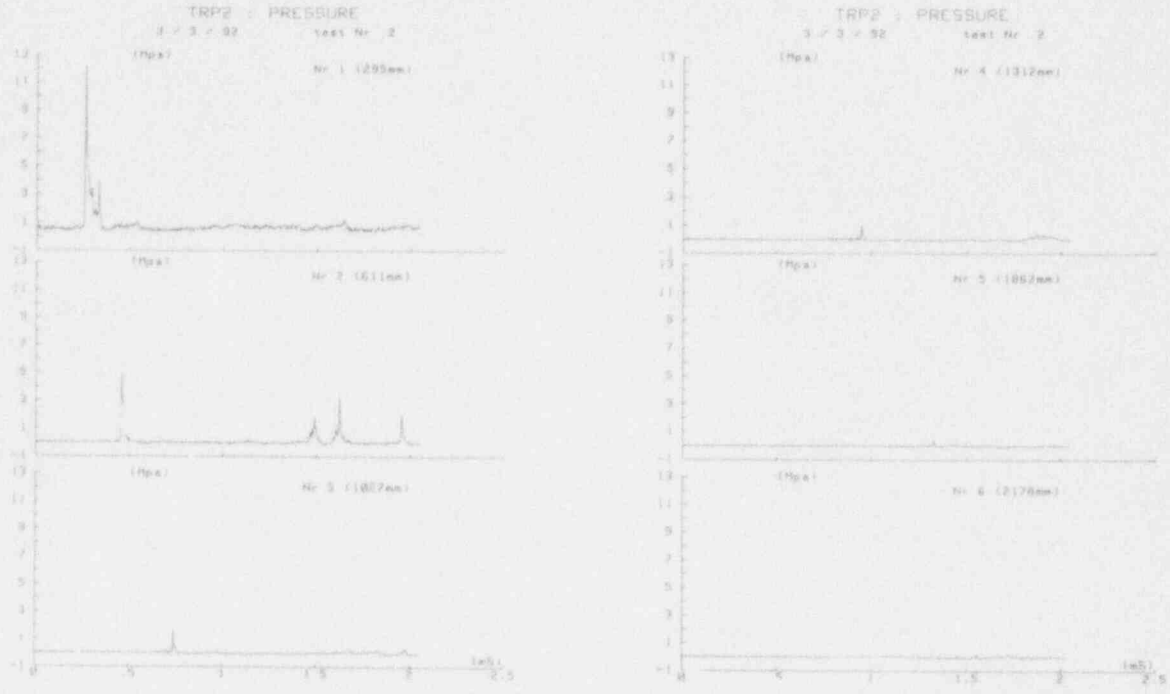

Figure 4.a : Non shielded detonator in water

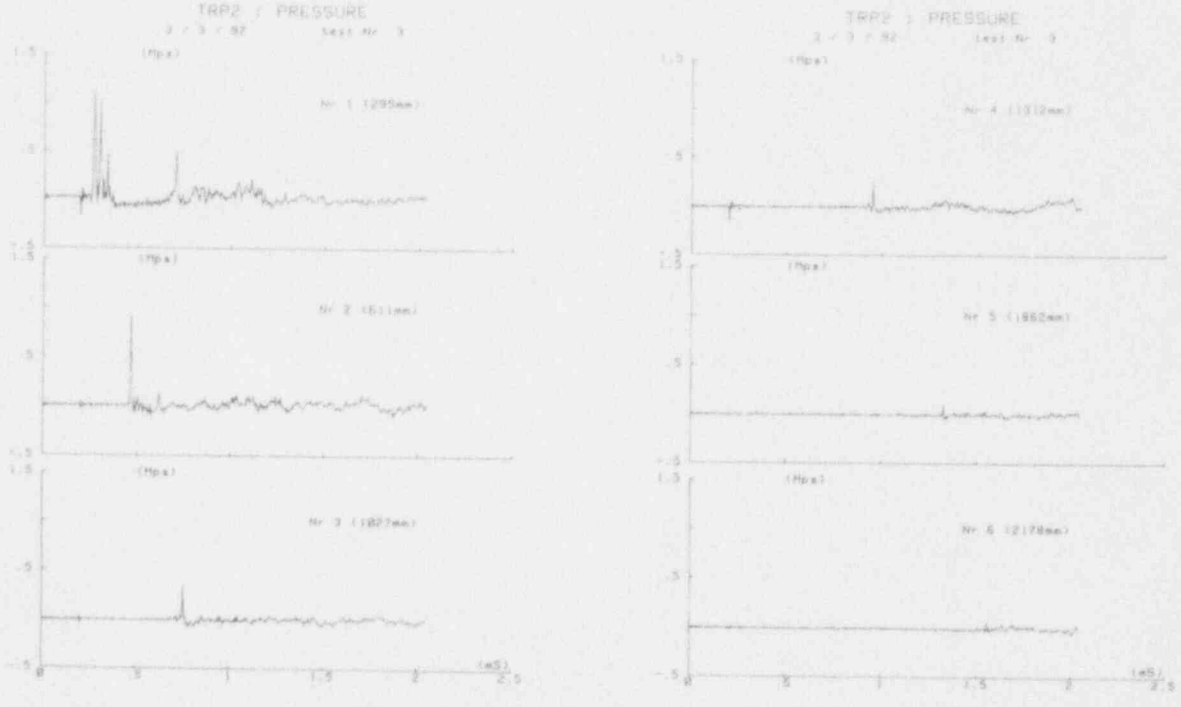

Figure 4.b : Shielded detonator in water

Other visualization tests were performed in order to observe the effect of the LN2 spillage on the water. For this purpose, the rig and spreading system were slightly modified in order to set up a video camera inside the test rig (figure 5). A plexiglas window separated the test rig into two isolated chambers, one for the videocamera and accessories (665 mm long about 1/3 of the rig) and the other for the tests (rest of the rig). The videocamera chamber was isolated at the top to prevent any LN2 splashing during a test. A light, placed behind the videocamera signals the end of the spillage which induces the immediate trigger initiation if a 0 s time delay is requested, time delay. The plexiglas window was marked at cm. intervals in order to measure the deviation during the spillage relative to the water level and to estimate the LN2 depth as soon as the stratified geometry was established. An insulated dividing wall was placed in the spreading system, facing the plexiglas window so as to limit the LN2 volume and to reproduce the same spillage conditions as obtained in a real test. The videos showed that the spillage takes about 3 s. During the 2 s. after the end of the LN2 spillage (delay characterized by the light turning on), for a water temperature above 18°C and an initial LN2 depth of 60 mm, the water-LN2 interface was very wavy and agitated. The evaporation rate is probably very important during the spillage due to a large exchange surface area, as showed by the rapid changing in depth of the mixture. It was noticed that the interface between the two liquid was the most agitated just when the light was turned on (photo 1). However it is impossible at this stage to evaluate the premixing rate. After the 2 s.period which follows the end of the spillage, the interface was calmer (photo 2), and the LN2 boiled on top of the water due to the density difference. Moreover, the LN2-water interface remained slightly agitated up to the end of the test because of the coupled effects of boiling and density gap. Finally, a detailed analysis of the video tapes showed that the stratified geometry was attainable beyond 2 s. after the end of the spillage. For this water temperature and above, no ice was observed for all the test, except near the wall, and only at the end of the experiment. It was possible to observe, during the experiment, the establishment of convection in the water which allows hot water to be maintained at the interface. For water temperatures below 18°C, ice formed rapidly after the end of the spillage. The whole surface is covered 5 - 10 s after the end of the spillage. When a stratified geometry was established, the 2 phase liquid-vapor nitrogen depth was about 60 - 75 mm or 30 mm depending of the initial liquid depth (60 mm and 30 mm respectively). However, it was impossible to estimate a void fraction because of the evaporation during the spillage. The boiling was film boiling regime, characterized by the bubbles diameter (about 1 cm) and the critical Rayleigh-Taylor wavelength (about 2 cm.).

Photo 1 : view of LN2/water interface at the end of spillage (0s. time delay)

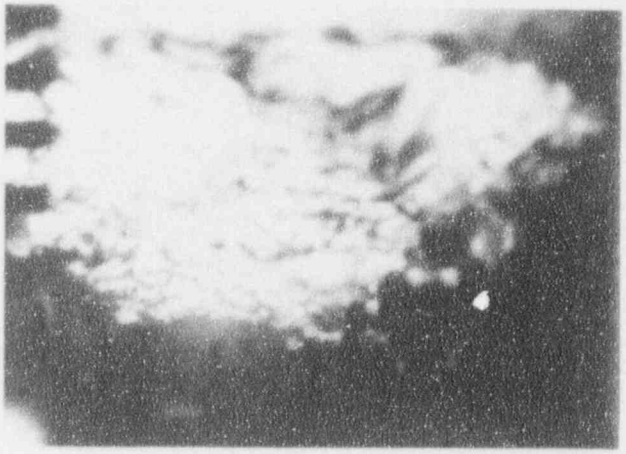

Photo 2 : view of LN2/water interface 2s. after the end of spillage

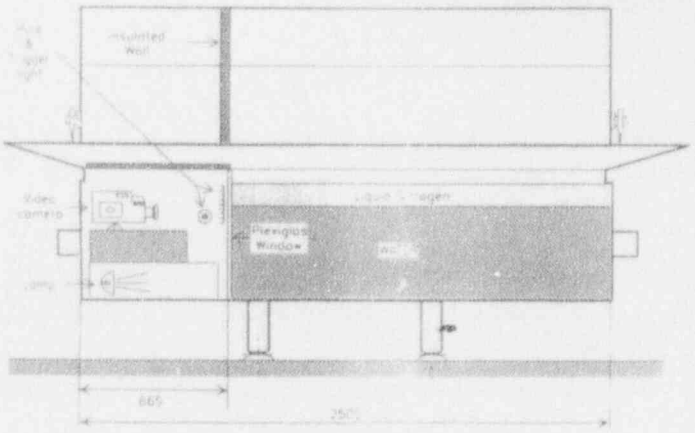

Figure 5 : General view of the test rig for vizualisations

III. TRIGGERED LN2/WATER EXPERIMENTS

The prelirminary results have allowed the establishment of the parameter ranges. The time delay is actually the main parameter, because depending on its value, the experimental medium can be considered either as slightly premixed or as well stratified.

In fact, the early triggered experiments were performed with a zero time delay, without controlling the state of the interface. For these tests, violent vapor explosions with propagation occurred, and these can be qualified as reference explosions for the whole experimental campaign. It is for this reason that one of these experiments is described below . Then, the tests in a stratified geometry are compared to this reference as a function of the different parameters defined above. Major experimental conditions for each described tests are summarized in table 1.

III.a. Reference Test (Slightly Premixed Geometry)

The characteristics of this trial were the following : the time delay was zero ; the trigger was a detonator of type 8 in the shielded configuration ; the LN2 layer was 60 mm high and the water temperature about 15°C. The water depth was 440 mm and the pressure transducers were 50 mm below the initial presumed interface.

At this time, the only way to quantify the level of premixing is via the video recordings obtained during the preliminary tests.

These operating conditions generated a violent interaction. The maximum peak pressure (50 bars) was recorded approximately in the middle of the channel on the pressure transducer 4 (figure 6). The observed wave is quasi-stationnary with a propagation speed between 225 and 240 m/s (mean value 235 m/s). The overpressure peak is about 15 to 20 cm wide and the rise time is about 1 ms. The pressure data show the presence at the end of the channel of a reflected wave whose intensity decreases very quickly, probably due to a small quantity of material (LN2/water) remaining in the rig. These results justify the scale of the experimental rig and constitute the reference data for comparison to the other trials. This kind of test with a zero time delay is quite reproducible as several additional trials have shown.

III.b. Triggered Tests in a Stratified Geometry

A total of 18 trials were conducted in a stratified geometry. The time delay for these tests was equal to or greater than 2 s. The parameters were the following : the characteristics of the trigger (type and shield) and the LN2 layer thickness. The water temperature was kept between 20°C and 30°C. The water layer depth was the same as in the reference test to allow comparisons of pressure recordings.

Figure 7 illustrates the pressure recordings for a trial with the stronger trigger (Type 8 and not shielded), which is more efficient for mixing and with 60 mm of LN2 above water. A small explosion can be seen closed to the detonator. The maximum pressure peak is about ten times lower than the one of the reference test. The explosion is concentrated in the area influenced by the trigger, but does not propagate at all along the rig.

The conclusion that no propagation could occur in such a LN2/water stratified geometry is confirmed by the 18 trials. The intensity and width of the explosion seems to depend only on the initial dimension and the degree of mixing of the triggered zone. The initial dimension is function of the type of detonator and the shield around it : for a shielded detonator (figure 8) and for a weaker one (figure 9), pressure peaks are nonexistent 100 cm away from the trigger. The degree of mixing is function of the LN2 depth above water ; figure 10 shows pressure traces for a test with 30 mm of LN2 ; the explosion can be detected only by the first three transducers. If the time delay is increased to 5 seconds, the results are similar (figure 11) due to the initial state which is the same, as confirmed by visualizations.

Table 1 : Major experimental conditions

	Trial #	Shielded Trigger	Trigger Type	LN2 depht	Time Delay	Figure #
Preliminary tests						
	03/03/92 - Nr 1	No	8	-----	-----	4.a
	03/03/92 - Nr 2	Yes	8	-----	-----	4.b
Slightly premixed geometry						
Reference test	03/03/92 - Nr 3	Yes	8	60 mm	0 s.	6
Stratified geometry						
	19/06/92 - Nr 1	No	8	60 mm	3 s.	7
	19/06/92 - Nr 3	No	8	60 mm	5 s.	8
	25/06/92 - Nr 2	Yes	8	60 mm	3 s.	9
	22/07/92 - Nr 1	No	70 mg Pentrite	60 mm	3 s.	10
	19/06/92 - Nr 2	No	8	30 mm	3 s.	11

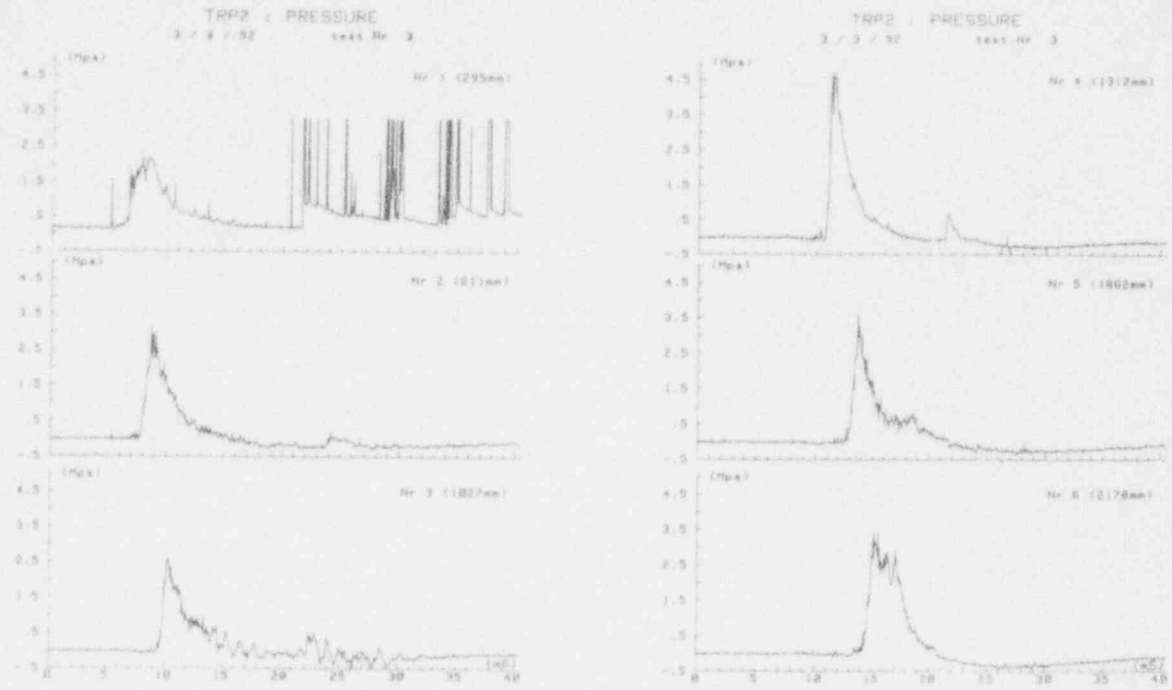

Figure 6 : Reference test in a slightly premixed geometry
Shielded type 8 detonator
Time delay : 0 seconds
LN2 layer depth : 60 mm

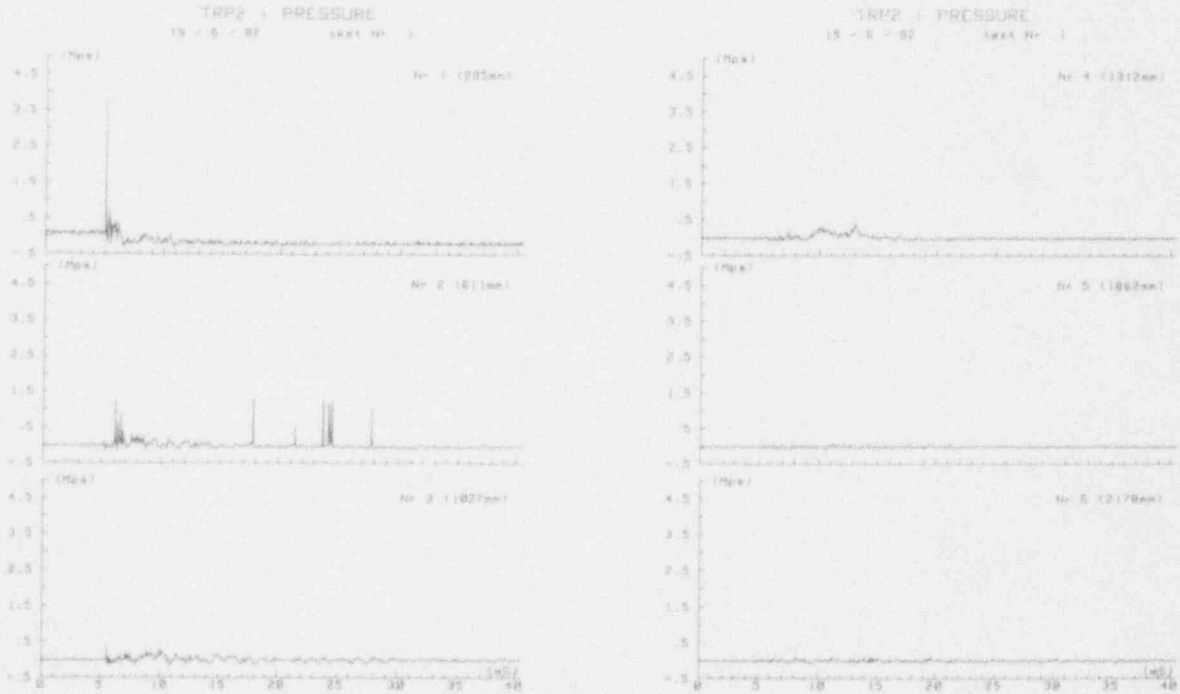

Figure 7 : Reference test in a stratified geometry
Non shielded type 8 detonator
Time delay : 3 seconds
LN2 layer depth : 60 mm

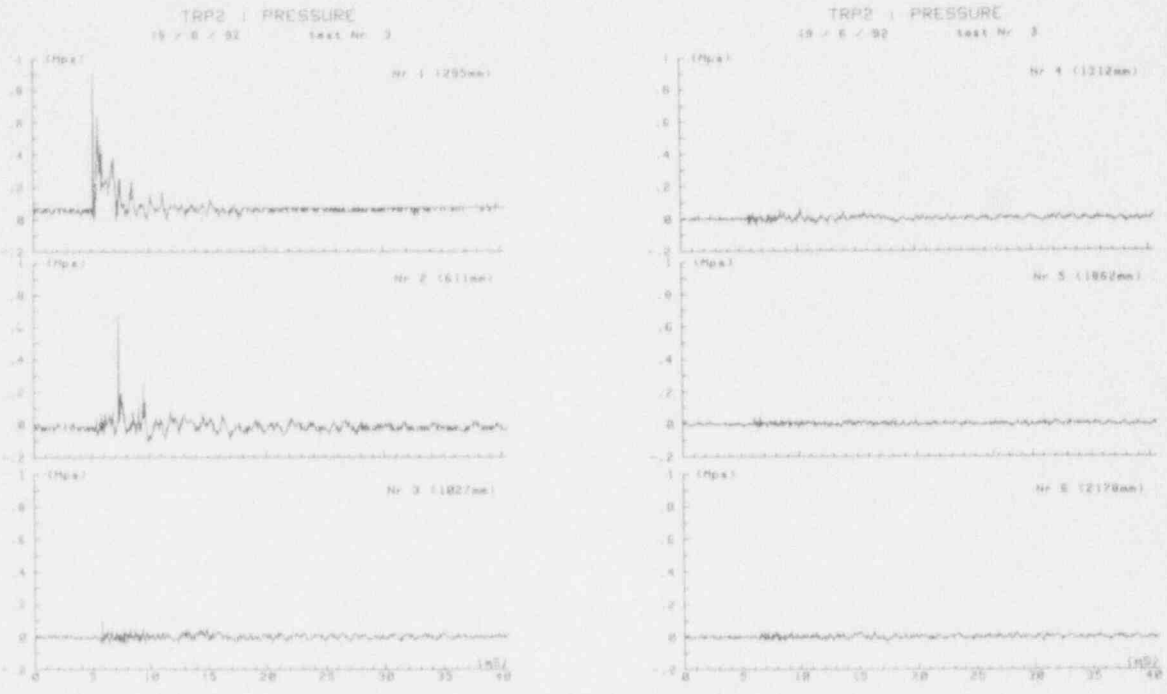

Figure 8 : Influence of the time delay
Non shielded type 8 detonator
Time delay : 5 seconds
LN2 layer depth : 60 mm

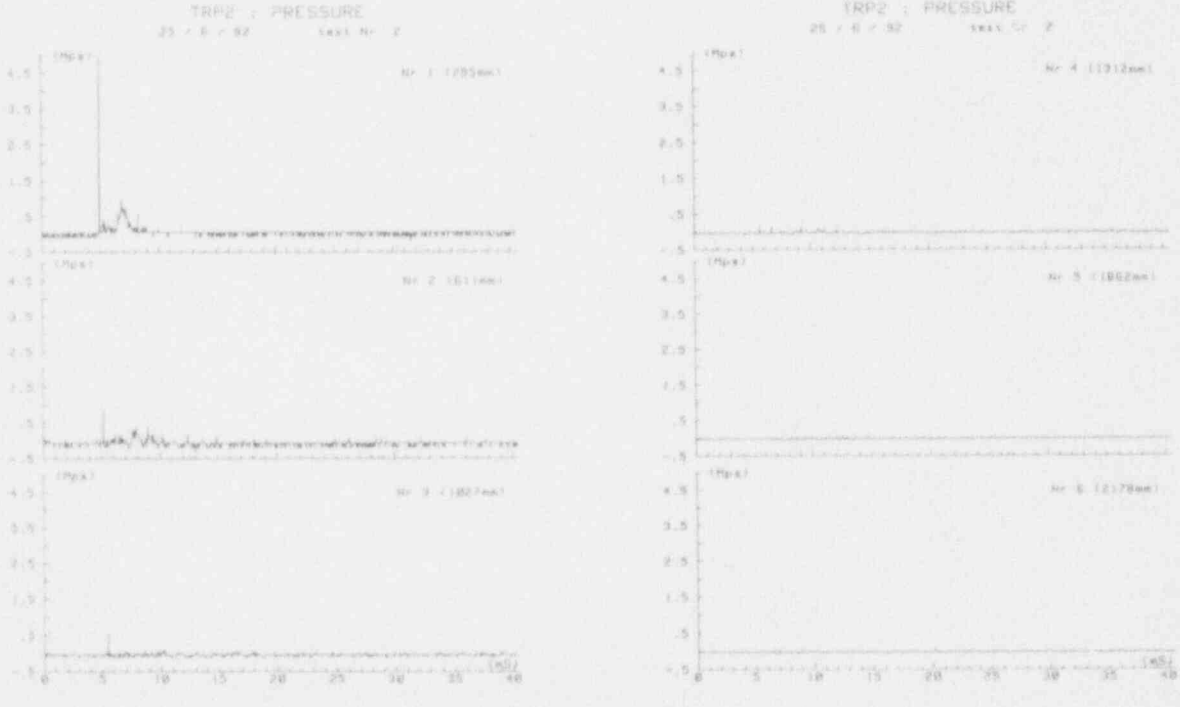

Figure 9 : Influence of the shield around the detonator
Shielded type 8 detonator
Time delay : 3 seconds
LN2 layer depth : 60 mm

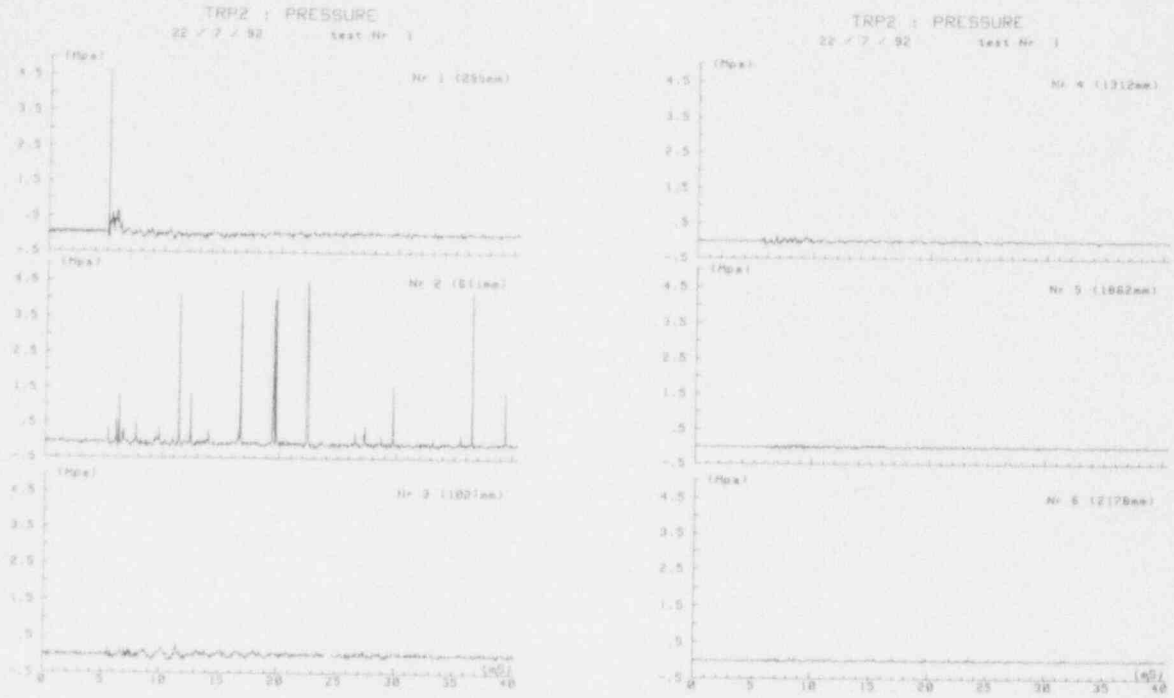

Figure 10 : Influence of the strength of the trigger
Non shielded 70 mg Pentrite detonator
Time delay : 3 seconds
LN2 layer depth : 60 mm

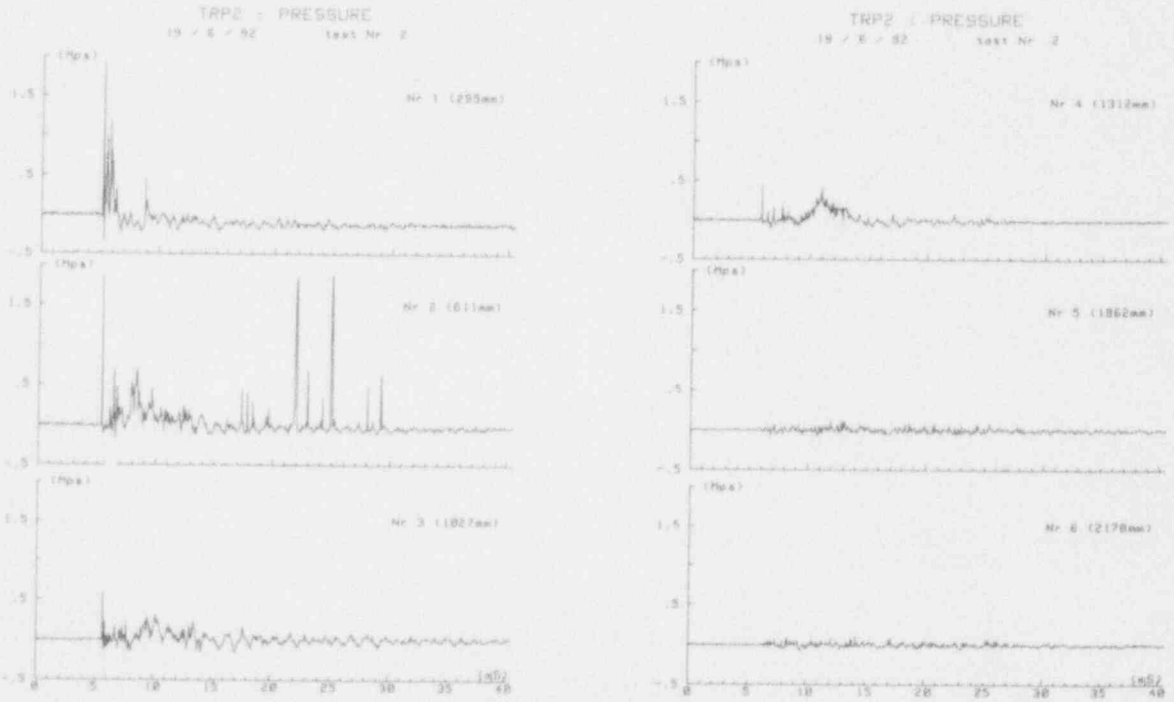

Figure 11 : Influence of the height of LN2
Non shielded type 8 detonator
Time delay : 3 seconds
LN2 layer depth : 30 mm

All the remarks seem to lead to the same conclusion : the trigger has two coupled effects, first of all to create a premixed medium close to the ignition point, second of all to collapse the vapor blanket and thus initiate the vapor explosion. However, LN2-water explosion propagation seems to "die" outside of the triggered zone if the two initial layers are well stratified.

IV. CONCLUSION AND FURTHER EXPERIMENTS

The first part of an experimental investigation concerning LN2/water interaction has been achieved. The objective of this study was to determine the potential for vapor explosion propagation of such a liquid pair in an initially stratified geometry. Propagation never occured in such a configuration. The vapor explosion was always limited to the triggered zone (initial mixed medium) which varied as a function of the different parameters of the experiment (external trigger, LN2 layer thickness).

If the ignition of the trigger is not delayed after the end of the spillage of LN2 onto water, the wavyness of the interface becomes much more important and seems to be a sufficient condition to sustain the vapor explosion along the whole rig. Thus, in the second part of this research program, we will try to calibrate and quantify the degree of premixing necessary to sustain a vapor explosion, in order to link it to the energy yield, to the pressure peak and to the propagation speed ; one of the final aims is to complete the constitutive relations for predictive numerical models.

ACKNOWLEDGEMENTS

All of the experimental results presented in this paper are part of an agreement between Gaz de France (France) and the Gas Research Institute (USA) and are integrated into the more general framework of an international collaboration with Statoil (Norway) and other international gas companies.

REFERENCES

ANDERSON R., ARMSTRONG D., CHO D., KRAS A. (1988), "Experimental and analytical study of vapor explosions in stratified geometries", ANS Proc.of Nat. Heat Transfer Conference, Houston, pp. 236-243.

BANG K. H., CORRADINI M. L. (1991), " Vapor explosions in a stratified geometry ", Nuclear Science and Engineering, 108, pp.88-108.

BOARD S. J., HALL R. W. (1975), " Thermal explosions at molten tin/water interfaces ", Moving Boundary Problems in Heat Flow and diffusion, Oxford University Press, pp. 259-269.

BRAYER C., BERTHOUD G. (1992), CEA Internal Report.

CICCARELLI G., FROST D. L., ZARAFONITIS C. (1991), " Dynamics of explosive interactions between molten tin and water in stratified geometry ", Progress in Astronautics and Aeronautics, 134, Washington DC.

FROHLICH G. (1984), "Similarities and differences between stratification experiments and entrapment experiments", ASME, Paper N° 84-HT-19

GREEN G.A. et al. (1983), "Some observations on simulated molten debris-coolant layer dynamics", Proceedings Int. Meeting on LWR severe accident evaluation,Vol. 2, Cambridge

SAINSON J., Baradel C., Roulleau M., Leblond J., Hakim V.(1990), "Rapid phase transitions of cryogenic liquid boiling on water surface", Proceedings Eurotherm seminar 14, May 15-17, Louvain, Belgium.

EFFECT OF BOUNDARY CONDITIONS ON THE PROPAGATION OF A VAPOR EXPLOSION IN STRATIFIED MOLTEN TIN/WATER SYSTEMS

David L. Frost and Barbara Bruckert
McGill University,
Department of Mechanical Engineering,
817 Sherbrooke St. W., Montreal,
Quebec, Canada H3A 2K6
Phone (514) 398-6279 Fax (514) 398-7365

Gaby Ciccarelli
Brookhaven National Laboratory,
Nuclear Energy Dept., Building 130,
Upton, N.Y., USA 11973
Phone (516) 282-3906
Fax (516) 282-3957

ABSTRACT

The propagation of a vapor explosion in a stratified molten tin-water system has been investigated experimentally in three different configurations: (i) linear propagation in a narrow channel open at the top, (ii) propagation in a narrow channel with vertical confinement, and (iii) radial propagation in a cylindrical tank. In each case an interaction is initiated by an exploding wire trigger, and self-sustained spatial propagation of the interaction is observed to occur with an average propagation speed of 40–50 m/s. A minimum degree of inertial confinement provided by the water above the tin is required to sustain a propagating interaction. In the narrow channel experiments, the effective mixing depth for the interaction is ≤ 2 mm. The thermodynamic efficiency of the first interaction, or the ratio of the conversion ratio to the maximum thermodynamic conversion ratio, is about 1% and is not strongly dependent on the boundary conditions. A comparison between the energetics of single molten tin drop interactions and interactions in the stratified systems suggests that similar dynamic processes occur during the first interaction cycle in each case. In both cases, the first interaction is an efficient method for mixing the tin and water and is often a precursor to a second, more violent interaction.

I. INTRODUCTION

Direct contact between a hot liquid (e.g., molten metal) and a volatile cold liquid (or coolant) may result in an energetic vapor explosion. The explosion is due to rapid heat transfer from the hot liquid to the cold liquid and subsequent phase transition of the coolant. The rate of heat transfer is enhanced by fine fragmentation of the hot liquid during the interaction, increasing the surface area available for heat transfer. The expansion of the high-pressure vapor that is generated can produce strong loads on surrounding structures. Accidental vapor explosions have occurred in a variety of industries (e.g., see the summary by Reid, 1983) and are a concern in the nuclear industry regarding a hypothetical loss-of-coolant scenario in which molten fuel comes into contact with a coolant. A recent paper by Corradini et al. (1988) gives a comprehensive review of past experiments and modelling efforts regarding vapor explosions in light water reactors.

When hot and cold liquids are mixed together, several different geometrical arrangements are possible. In a common accident scenario, a hot liquid is poured into a cold liquid (or vice-versa), and the hot liquid breaks up into fragments which are dispersed in the coolant to form a *coarse mixture* undergoing stable film boiling. Alternatively, the hot and cold liquids may form two *stratified* layers, again separated by a stable vapor film. The majority of past experimental and modelling efforts have been directed towards the coarse mixture geometry, in part because it was commonly believed that the lack of premixing in a stratified geometry precluded the possibility of a strong energetic interaction. However, the possibility of violent vapor explosions in initially stratified systems has been demonstrated conclusively by tests at Sandia National Laboratory (Berman, 1986) with spills of water onto a pool of molten metal, and in large-scale spills of liquefied natural gas onto water carried out by Lawrence Livermore Laboratory (Koopmann et al., 1981). In the large-scale tests, there will of course be some mixing of the fluids during the initial contact phase. In this case, the degree of stratification of the system will depend on the contact mode, the delay time following the initial contact of the fluids as well as the stability of the subsequent film boiling process.

Colgate and Sigurgeirsson (1973) were the first to postulate the existence of a stratified vapor explosion during molten lava-water interactions, although they carried out no experimental or detailed theoretical calculations. The plausibility of a self-sustained propagating interaction in a stratified geometry was investigated numerically by Harlow and Ruppel (1981). They showed that pressure-driven collapse of the vapor film separating the liquid layers can be sustained by the subsequent mixing of the liquids and rapid boiling of the volatile liquid. Propagating interactions have been observed in exploratory laboratory-scale experiments with a vertically stratified water/refrigerant-22 system by Anderson et al. (1988) An extensive series of tests has been carried out by Bang and Corradini (1988, 1991) with water/liquid nitrogen and water/refrigerant-12 systems. They observed energetic propagating interactions

(with the water/refrigerant system being more energetic) with propagation speeds ranging from 40 to 250 m/s. They measured the work release and estimated the depth of intermixing of the fluids to be ≤ 1 cm, although in this case, the collection of post-test debris is not possible because the solidified hot liquid (i.e., ice) melts following the interaction at ambient temperature. From these values they calculated the conversion ratio of thermal to mechanical work (for the water/refrigerant-12 system) to be 1.2% corresponding to a thermal efficiency (i.e., relative to the Hicks & Menzies work yield) of ≤ 6.5%. The thermal efficiency for the water/liquid nitrogen system was smaller by an order of magnitude. The mechanical work release data showed considerable scatter which may be attributed to ice formation at the interface and to variations in the shape and motion of the vapor film at the time of triggering of the interaction. The work output increased with water depth up to a certain depth, above which the work yield remained constant. They also reported that multiple propagating interactions occurred in some cases.

Experimental work on propagating interactions in stratified *molten metal*/water systems is quite limited. Board and Hall (1974) were the first to study molten tin/water interactions in two stratified geometry experiments. In the first, they poured 200 g of tin at 750°C into a shallow V-shaped trough immersed in an open water tank with a water depth of at least 10 cm. Both spontaneous and triggered interactions were observed and in both cases consisted of a series of localized bubble growth and collapse interactions along the tin surface. They speculated that the discontinuous propagation was the result of the relatively open geometry of the tin layer, giving only weak coupling between adjacent areas of tin. In a second experimental arrangement, they poured 200 g of tin at 700°C into a narrow channel (20 cm long, 3 cm wide, 15 cm high). In a single triggered experiment, after some delay, they observed a continuous propagating interaction with an velocity (estimated from the film record) of about 50 m/s that generated a peak pressure in the water of about 0.17 MPa. Board et al. (1975) also noted that the passage of the first interaction in a stratified system may not cool all the metal and leave behind a coarsely mixed region through which a second, more efficient, explosion may propagate.

More recently, Anderson et al. (1988) carried out a series of tests to study stratified tin/water interactions. They poured about 10 kg of molten tin into a trough (1 m long, 5 cm wide and 9 cm deep) to form a layer of tin 3 cm deep. Hot water was then poured on top and the interaction was initiated at one end. They found that their system was rather insensitive to an external trigger and spontaneous explosions frequently occurred. However, in four trials interactions were observed to propagate at low speed (17 to 26 m/s) with low pressures. In a fifth trial, the interaction propagated much faster and destroyed the apparatus, possibly due to the chemical reaction of a powdered aluminum-tin compound present in the system.

The present experiments were carried out to investigate the influence of boundary conditions on the propagation of explosive molten tin/water interactions in a stratified geometry. Three different systems are considered, with different degrees of inertial confinement of the tin. The characteristics of the propagating interactions were observed with high-speed photography and pressure records and post-test debris analysis were used to estimate the work yield and effective intermixing depth during the interactions. A comparison with single drop tests illustrates the influence of scale on the explosive interaction. More details of the results for the unconfined narrow channel experiments have been presented earlier (Ciccarelli et al., 1991).

II. EXPERIMENTAL RESULTS

Molten tin/water interactions were studied in three different configurations: (i) linear propagation in a narrow channel open at the top, (ii) propagation in a narrow channel with vertical confinement, and (iii) radial propagation in a cylindrical tank. In each case, molten tin is heated to 700–800°C and poured into the water and the interaction is initiated by an exploding wire trigger. The experimental results will be described separately for each configuration, followed by a discussion of the common features of the interactions.

A. Narrow Channel (Open at Top) Experiment

1. Experimental Apparatus. The first set of experiments was carried out in a narrow channel (1.3 cm wide, 13 cm high, 40 cm long) submerged in a main water tank, as shown schematically in Fig. 1. The channel was constructed of an aluminum frame with either Lexan or glass windows. The base was constructed of Lexan to minimize the heat transfer from the molten metal. The tin was placed into a slotted graphite cylinder which was mounted within a semicylindrical ceramic oven for heating. The oven assembly was positioned above the water tank and the tin was discharged into the tank below by rotating the cylinder. After the tin formed a stable layer along the base of the channel (approximately 1 s after the tin reached the channel base), the interaction was initiated. The propagating interaction was triggered by discharge of a high-

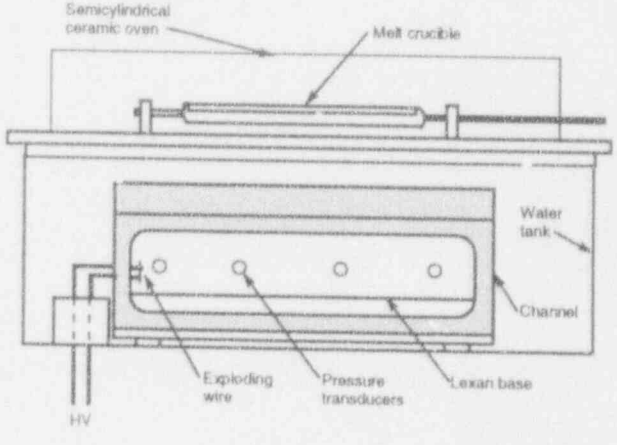

Figure 1. Schematic of experimental apparatus.

voltage capacitor (4 μF charged to 4 kV) through a thin copper wire mounted within the channel at one end, 3 cm above the channel base. The end of the channel that contained the exploding wire was closed with a metal plate, whereas the other end was open.

The pressure-time history of the interaction was recorded using four piezoelectric pressure transducers (PCB model 113A24, 5 mV/psi, 1 μs risetime) flush mounted on the back face of the channel. The transducers were mounted in watertight Delrin plugs and spaced 10.2 cm apart along the length of the channel, 2.2 cm above the channel base. The pressure traces were recorded with a PC-based data acquisition system, recording at 1 MHz. The propagation of the interaction was visualized with either a Hycam 16-mm high-speed camera at up to 5,000 frames/s, or a Cordin Dynafax rotating drum camera at speeds of up to 16,000 frames/s. Several 1000 W flood lamps were used for lighting with the Hycam camera. To provide a light source of sufficient intensity and duration (about 20 ms) for the Cordin camera, four zirconium-filled flashbulbs (Sylvania FP-26) were mounted in reflectors and fired simultaneously by an output pulse from the camera. When the high-voltage capacitor was discharged, the associated electrical noise generated a spike on the pressure trace. The simultaneous flash that was generated by the exploding wire was recorded by the high-speed camera, allowing the film record to be synchronized with the pressure traces.

Figure 2 shows a typical example of the pressure traces recorded from the trigger system alone. The first spike is due to the electrical noise generated by the capacitor discharge. The initial blast wave generated decays

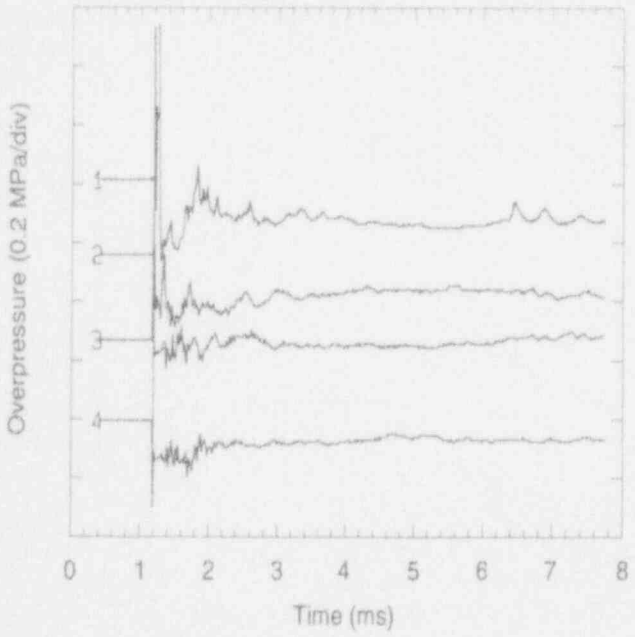

Figure 2. Pressure traces recorded from trigger system alone.

rapidly with distance. The growth of the steam bubble generated by the exploding wire induces a pressure field in the surrounding water that is recorded by the first transducer. This pressure pulse has a peak pressure of about 0.2 MPa with a duration of about 1 ms.

2. Characteristics of Propagating Interaction. In each trial, 400±10 g of tin were heated to 700±50°C and dropped into water heated to between 67 and 71°C, forming a layer about 1.1 cm thick at the base of the channel. In each case the height of the water layer above the channel base was 12.7 cm. The stable vapor film separating the tin and water was nonuniform in shape. During film boiling, steam accumulated forming domes that pinched off forming bubbles (ranging in size from several millimeters to a centimeter) that rose to the surface. The interaction was triggered at one end of the channel, and the subsequent interaction propagated in a self-sustained manner along the tin layer surface. For the range of water temperatures used, propagating interactions were consistently observed. In a few trials, interactions spontaneously initiated at one end of the channel. The characteristics of the subsequent propagating interaction were the same as for the triggered interactions indicating that the triggering system provides only a local disturbance and does not significantly influence the subsequent propagating interaction. Increasing the water temperature increased the thickness and stability of the vapor film separating the layers, making it more difficult to trigger a propagating interaction. However, no systematic influence of water temperature on the propagating interaction was observed.

The general features of the propagating interaction are illustrated in Fig. 3, reproduced from the high-speed Hycam film record of one of the trials. The time between successive frames shown in the figure is 400 μs. The molten tin layer above the channel base is visible near the bottom of each of the photographs, and one of the pressure transducers flush mounted in the back of the channel in a cylindrical plug is visible at the left. The horizontal wire near the center of each photograph is the transducer signal cable, located *behind* the channel. After the interaction is initiated at the left end of the channel, the high pressure generated by the rapid production of vapor induces a pressure field in the surrounding water (as well as an associated hydrodynamic flow field) which causes the adjacent film to collapse. In this way, the interaction propagates along the surface of the tin with an average speed of about 40 m/s. The wake region behind the leading edge of the propagating interaction region contains a complex three-phase mixture of vapor, water droplets and molten and solidified tin fragments. The explosion wake has an overall shape of a wedge (with an angle of about 10°), formed by the interface between the expanding high-pressure vapor and overlying water and the base of the channel. During the interaction, the water above the tin layer is accelerated vertically by the high pressure within the reaction zone and ejected from the tank. A small amount of water is often trapped beneath the tin layer as it settles to the base of the channel. Boiling of this water generates a cavity under the tin layer, lofting the tin layer at periodic intervals (an example of this can be

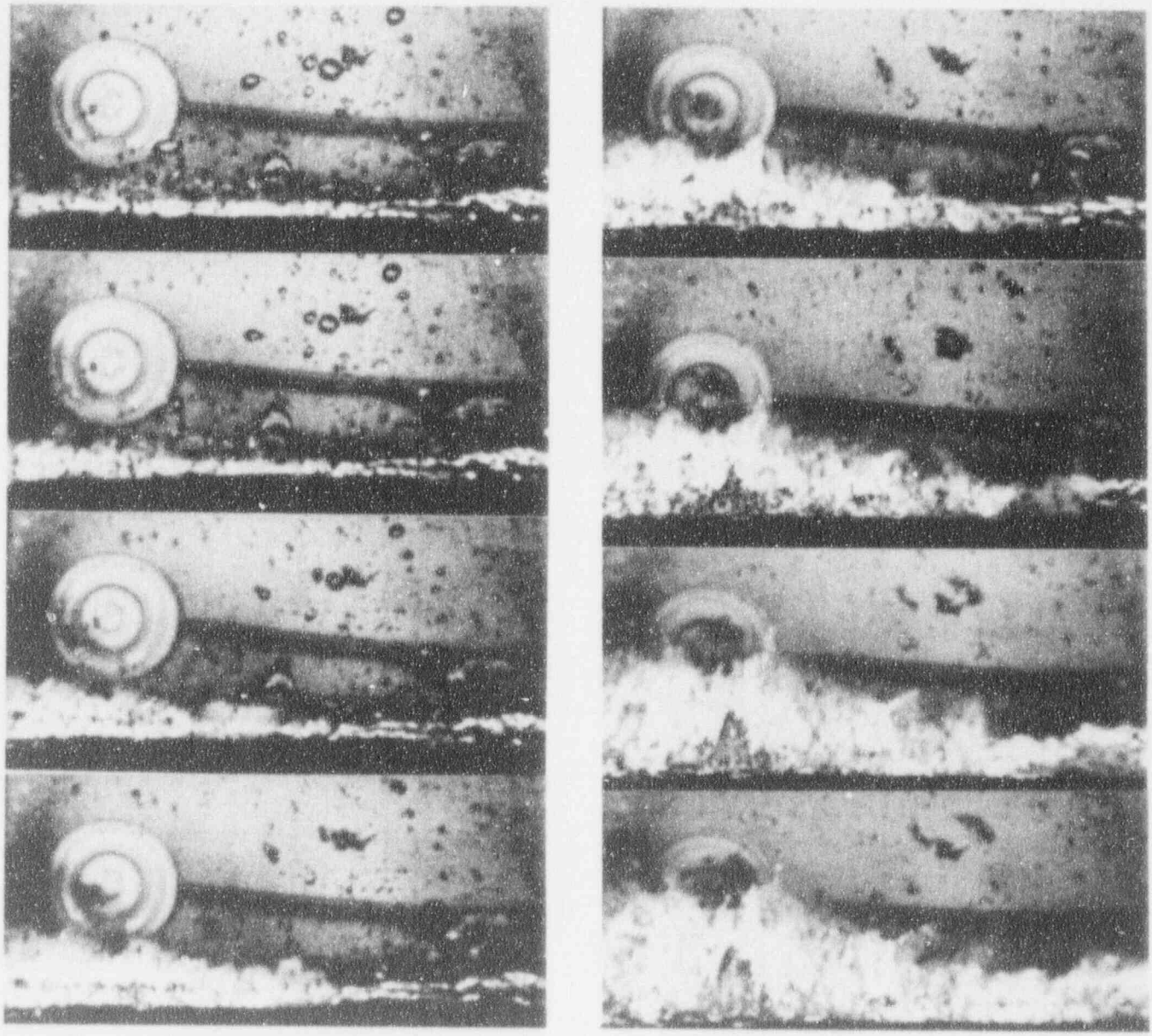

Figure 3. Single frames from Hycam film record illustrating self-sustained propagation of interaction in stratified tin-water system. Time between frames is 400 μs. Outer diameter of transducer pulg, visible at left is 2.54 cm.

seen in the last four frames of Fig. 3, just under the transducer plug).

Figure 4 shows a typical example of the transient pressure field recorded about 1 cm above the tin layer during a propagating interaction. The rise time of the pressure pulses is usually about 1 ms or less. Taking a value of 1 ms for the rise time, together with the average velocity of 40 m/s (the propagation speed of the pressure front, as inferred from the pressure signals, corresponds to the same value as observed from the film record) implies that the pressure rises in the water to a maximum value over a horizontal distance of less than 4 cm. The pressure rise in the water above the interaction zone can be inferred from the film record by observing the collapse of the bubbles in the water above the interaction zone (e.g., note the collapse of the bubbles near the center of the first four frames of Fig. 3).

From Fig. 3 it is difficult to discern the structure inside the reaction zone, particularly near the leading edge. This region appears blurred as a consequence of the rapid expansion of the interaction zone generated following local film collapse and the relatively long exposure time (about 100 μs) of each frame of the Hycam film. To obtain better resolution of the wake region, the interaction was filmed using the Cordin camera at speeds up to 16,000 frames/s. At this speed, the corresponding exposure time of each frame was about 3 μs, effectively freezing the motion. The spatial growth of the interaction region is illustrated in Fig. 5, which shows single frames (254 μs between frames)

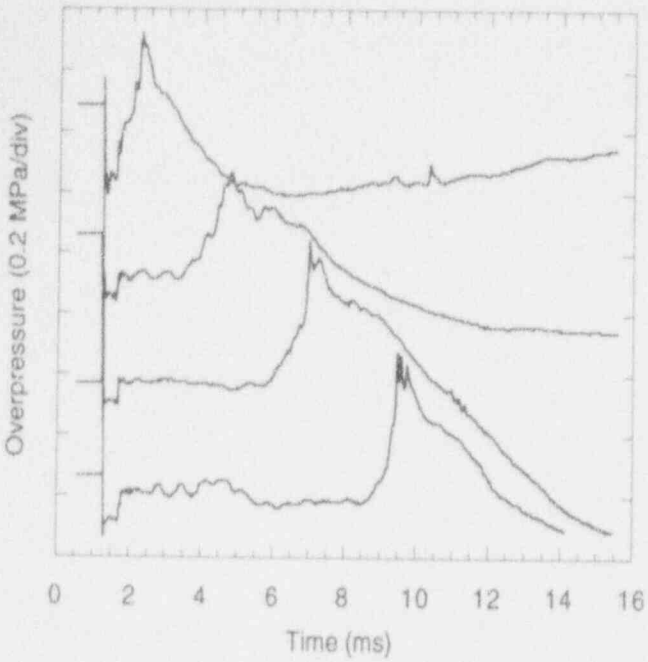

Figure 4. Pressure recorded 2.2 cm above channel base (about 1 cm above tin layer) during propagating interaction. Space between transducers is 10.2 cm.

taken from a high-speed film. In the region shortly after the vapor film collapses (i.e., the left portion of the tin layer in frames 1 and 2), only fine-scale disturbances are evident on the surface of the tin layer. As the vapor region expands, a substantial amount of tin is lofted within the wedge-shaped interaction region. High-pressure vapor that is generated at the leading edge of the interaction zone moves away rapidly from the explosion front. The relative motion between this turbulent vapor flow and the molten tin filaments lofted within the interaction zone leads to direct hydrodynamic fragmentation of the tin. The significant amount of fragmentation that occurs away from the leading edge of the explosion is illustrated in Fig. 6, which shows single frames (194 μs between frames) from a high-speed film of another trial. Note the filament of molten tin (indicated by an arrow in the sixth frame) that is lofted, distorted and finally shattered by the flow within the interaction region. Occasionally secondary interactions are evident from the pressure records as well as the high-speed films when water contacts a molten tin fragment within the interaction zone. In this case the secondary interaction causes the tin fragment to shatter and a spray of fine water droplets and vapor is generated (which appears as a fast-moving white cloud in the high-speed films) which moves away at speeds that can exceed 100 m/s.

During each trial, the tin is fragmented into debris with a range of sizes. A small fraction of the tin is finely fragmented shortly after film collapse near the leading edge of the propagating interaction. Other tin is lofted within the interaction region and is fragmented by the relative vapor flow. However, a large portion of the lofted molten tin

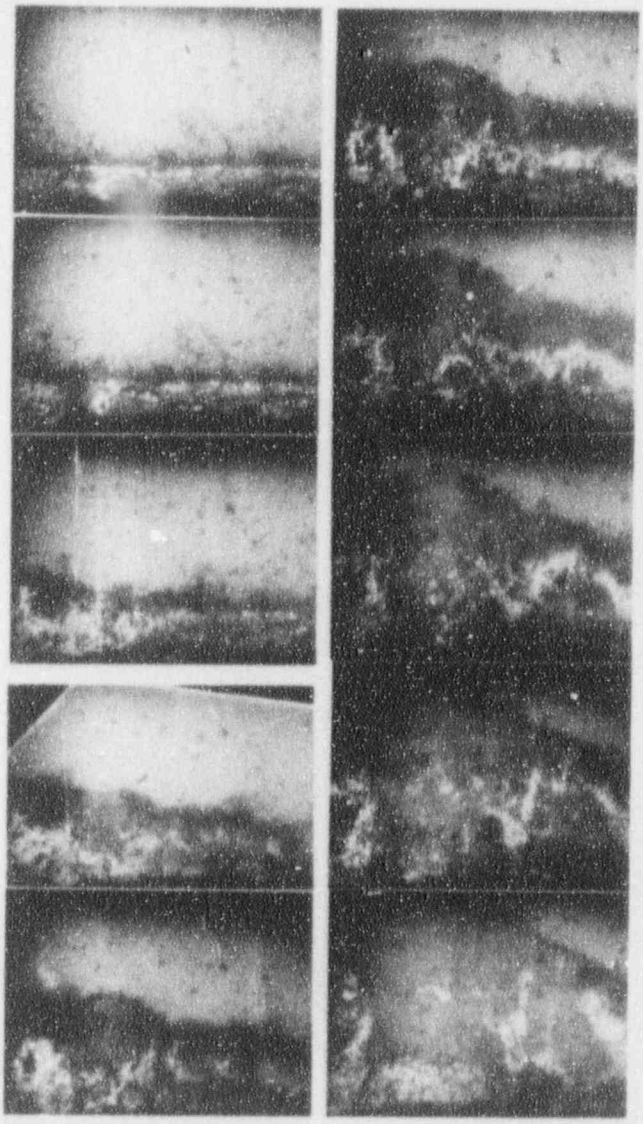

Figure 5. Single frames from Cordin film record of propagating interaction. Time between frames is 254 μs.

does not interact explosively with the water and settles to the base of the channel after explosion propagation and solidifies. After each trial the debris was collected and sieved to determine the size distribution. An arbitrary cutoff size of 1 mm was used to characterize the amount of tin that participates energetically in the interaction. In three trials, over 95% of the initial tin mass was recovered and sieved. Based on these trials, the fraction of the total initial mass that was fragmented to sizes less than 1 mm was 17±4%. With an initial mass of 400 g, this corresponds to an effective mixing depth of about 2 mm.

3. Effect of Water Layer Height. A series of trials was carried out to study the effect of inertial confinement on the propagation behavior. The degree of confinement was varied by changing the height of the water layer above the molten tin layer. Each of the 25 trials in which

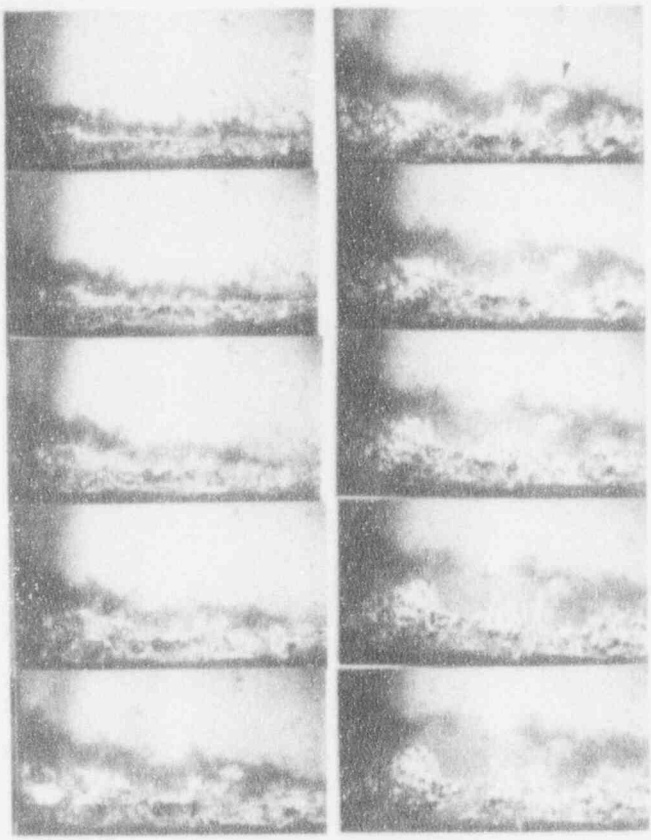

Figure 6. Single frames from Cordin film record of propagating interaction. Time between frames is 194μs. Note fragmentation of lofted tin fragment (indicated by arrow).

the distance from the free surface of the water to the base of the channel was 12.7 cm resulted in a self-sustained propagation of the interaction for the length of the channel. However, in 7 trials in which the water height was 5.1 cm, a propagating interaction was *never* observed. Figure 7 shows a series of photographs taken from one such trial. Note that the time between each photograph is 1.665 ms. The exploding wire is located out of view, about 5 cm to the left of the left edge of each photograph. The dark horizontal line near the middle of each photograph corresponds to the water level in the tank outside of the channel. The disturbance created by the exploding wire causes some disruption of the tin layer as well as the free surface of the water. Note that the free surface of the water breaks up due to Rayleigh-Taylor instability as a result of the acceleration of the water by the pressure generated by the exploding wire. Figure 8 shows the pressure recorded during one such trial. The first transducer, located about 5 cm from the exploding wire, records a pressure pulse that shows the combined effects of the disturbance from the trigger as well as the pressure generated by a local interaction. However, the interaction fails to propagate along the layer and, as a result, the pressure generated decays rapidly with distance from the electrodes (see Fig. 8).

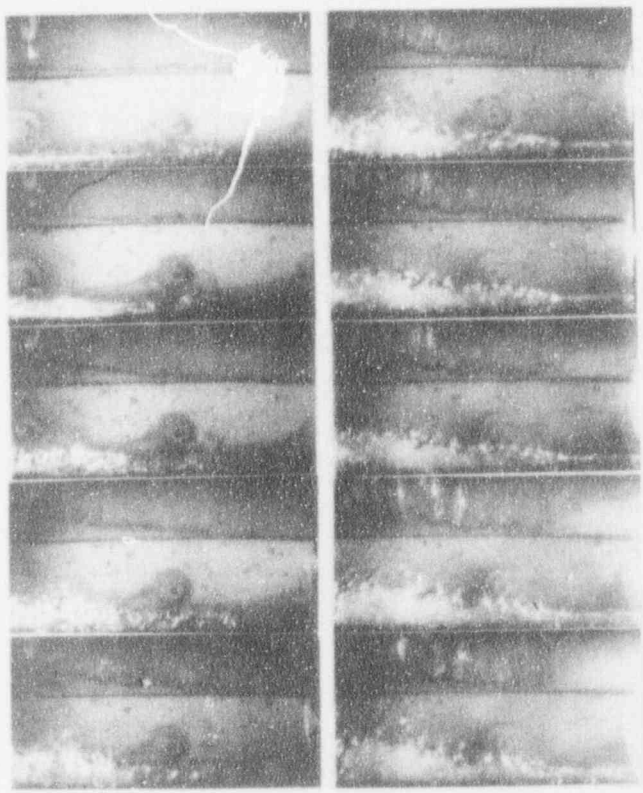

Figure 7. Failure of explosion propagation for water height of 5.1 cm (1.665 ms between frames). Free water surface is visible near centrer of each photograph.

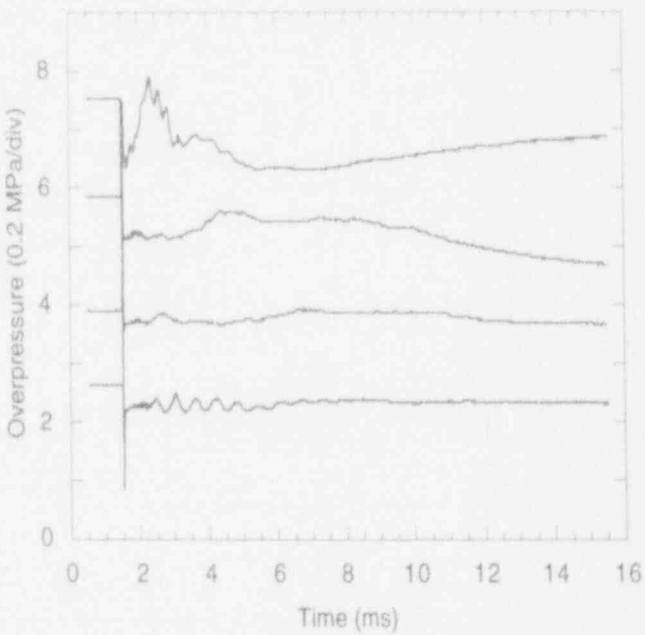

Figure 8. Pressure recorded for water height of 5.1 cm illustrating failure of propagation.

At an intermediate water height of about 7.6 cm, a transitional behavior occurs. In the majority of the trials with this water height, the trigger failed to initiate a propagating interaction, similar to the behavior observed with a water height of 5 cm. However, in several of the trials, after the decay of the initial disturbance, a secondary interaction initiated spontaneously and propagated. Figure 9 shows the pressure recorded during one of these trials, illustrating the decay and reinitiation of the interaction. The propagation speeds for the secondary propagating interactions in the two trials were 63 and 73 m/s, which are considerably faster than the average propagation speed of about 40 m/s observed in other trials. The initial decaying disturbance apparently causes sufficient mixing of the tin and water so that the propagation speed of the secondary disturbance is augmented. Single frames from the high-speed film corresponding to the pressure traces shown in Fig. 9 are shown in Fig. 10. The transducer visible in the center of the initial photographs in Fig. 10 corresponds to the third pressure trace from the top in Fig. 9. The violent interaction that occurs near the center of the photographs in Fig. 10 corresponds to the large pressure pulse recorded by the third transducer.

B. Narrow Channel Experiment with Vertical Confinement

1. Experimental Apparatus. To investigate the effect of vertical confinement on the explosion propagation, a second channel was constructed with similar dimensions as the first (45.7 cm long, 1.5 cm wide, 13.9 cm high). However, in this case, a slot running the length of the frame near the top accommodated a spring-loaded sliding gate. *After* the tin entered the channel and *before* the interaction

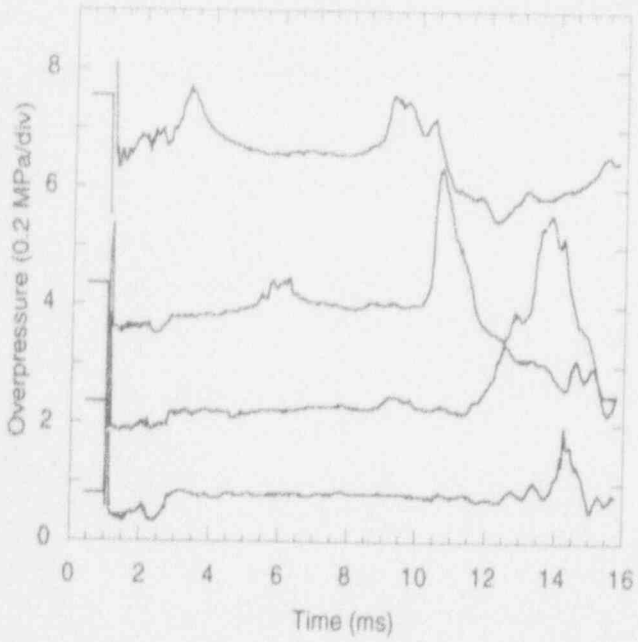

Figure 9. Pressure recorded for water height of 7.6 cm illustrating decay and reinitiation of propagating interaction.

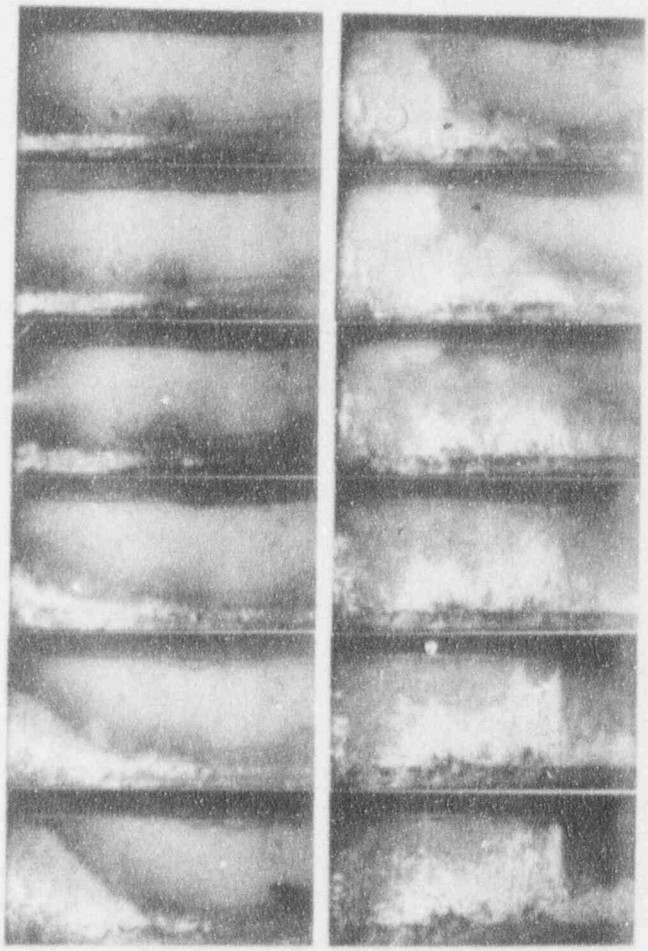

Figure 10. Decay and reinitiation of propagating interaction for water height of 7.6 cm (308 μs between frames) corresponding to pressure traces shown in Figure 9.

was triggered, the gate was closed, preventing any vertical expansion of the water in the channel. The interaction was initiated at the closed end of the channel by an exploding wire discharge system. The opposite end of the channel was sealed with thin aluminum foil, which would break shortly after the start of the interaction, allowing the water to vent out the end of the channel.

2. Results. In each trial 400 g of tin were heated to 750°C and dropped into water heated to between 75 and 80°C. In each of the four trials carried out, a self-sustained propagation of the interaction occurred in a similar manner as for the earlier experiments in the open-topped channel. The propagating interaction again generated a wedge-shaped interaction region (with a wedge angle between 8 and 10°) moving at a velocity of about 50 m/s, as compared with an average of 40 m/s for the earlier trials. Figures 11 and 12 show a comparison of the peak pressure and impulse measured for the trials with and without vertical confinement, respectively, plotted as a function of average propagation velocity for the first interaction. Although the additional inertial confinement increases the propagation

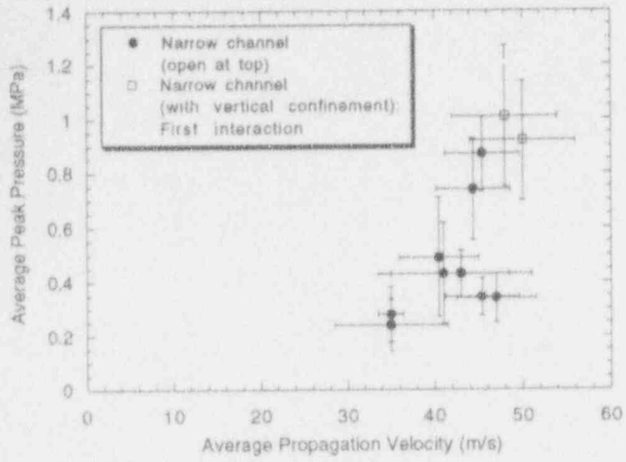

Figure 11. Comparison of the effect of vertical confinement on the average peak pressure vs average propagating velocity.

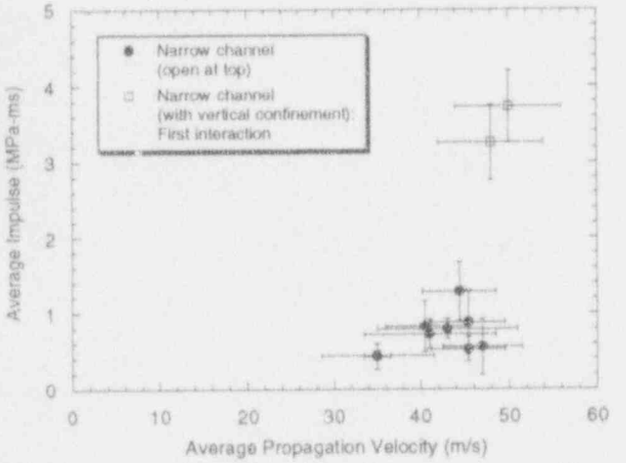

Figure 12. Effect of vertical confinement on the average impulse and average propagation velocity.

velocity only a small amount, the duration, or impulse of the pressure pulses is considerably augmented. A significant effect of adding vertical confinement was that in *each* of the trials a second, more violent interaction occurred from 10 to 40 ms after the first interaction. Figure 13 shows the pressure history from one of the trials, illustrating the multiple interactions. Since the first interaction generated a well-mixed mixture of molten tin, water, and steam, the propagation velocity, peak pressures and pulse durations for the second interaction are all substantially increased. In particular, the propagation velocities, peak pressures and impulses for the second interactions ranged from 100–125 m/s, 1–3 MPa, and 7–12 MPa-ms, respectively.

The distribution of sizes of the fragmented tin after an interaction was determined by sieving the debris. Figure 14 shows the debris size distribution for the vertically confined

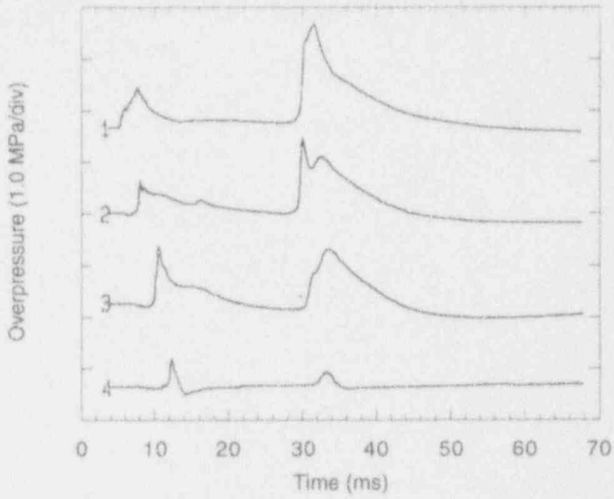

Figure 13. Pressure recorded during propagating explosion in vertically confined narrow channel. Note second, more violent interaction that occurs after first interaction.

channel in comparison with the distribution for the trials in the narrow unconfined channel. For the vertically confined channel, the occurrence of a second interaction results in considerably finer debris. The fraction of the tin that was fragmented to particle sizes less than 1 mm was 34% as compared to 17% for the unconfined channel.

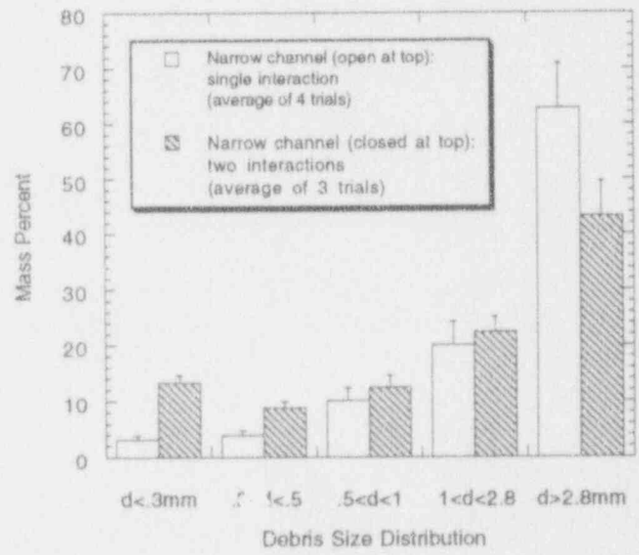

Figure 14. Effect of vertical confinement on debris size distribution for explosion propagation in narrow channel.

C. Cylindrical Tank Experiment

1. Experimental Apparatus. To determine the role of confinement on the propagating interaction, experi-

ments were carried out in a cylindrical geometry in which the propagation occurs in a radial manner. In this arrangement, in the absence of confining walls, the interaction region is effectively *self*-confined. A schematic of the apparatus is shown in Fig. 15. Due to the large quantities of molten tin involved, the experiment was carried out inside a 1 m diameter steel tank. The apparatus consists of a Lexan cylinder (27.3 cm dia) with a Teflon base, filled with water with a temperature ranging between 73 and 75°C to a depth of between 9 and 11 cm. In each trial, about 4 kg of tin were heated in a graphite crucible inside a ceramic oven to 800°C and discharged through a Teflon tube into the cylinder to form a layer of molten tin about 1 cm deep. The interaction was initiated several seconds after the formation of the tin layer in the center of the tank by the discharge of a HV capacitor (0.2 μF charged to 17.5 kV) through a thin copper wire mounted about 3.3 cm above the tin layer. Six pressure transducers were flush-mounted in Delrin plugs (located about 3.7 cm above the tin layer), mounted vertically within copper cylinders, 3.8 cm apart. The interaction was filmed through a window at the top of the tank with the Hycam camera operating at 2,000 frames/s.

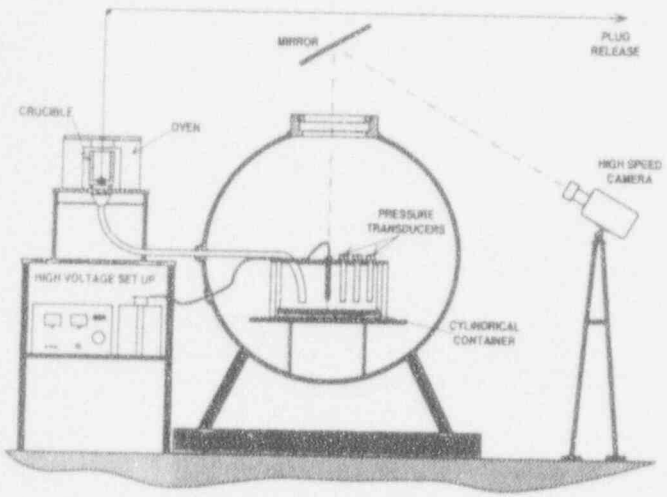

Figure 15. Schematic of experimental facility for experiments in cylindrical geomtry.

2. Results. The stability of the vapor film and the relatively unconfined geometry made it more difficult to trigger the interaction in comparison with the narrow channel experiments. After firing of the trigger system, the interaction initiated near the center of the tank after a short delay, typically between 0 and 30 ms. Occasionally the trigger failed to initiate an interaction and an energetic interaction occurred spontaneously after a delay of more than 30 s. Of the eight trials in which an interaction was initiated by the trigger, one-half resulted in a single propagating interaction whereas in the other half a second interaction also occurred. Figure 16 shows the pressure field recorded during a single propagating interaction. Although the interaction propagates in a radial manner, in this case the interaction intensity is somewhat asymmetric, with higher peak pressures (ranging from .15 to .3 MPa) recorded on one side of the cylinder. Variations in vapor film thickness and water depth (due to waves generated by the discharge of the trigger system) may cause the propagation velocity to have a nonradial component. Consequently, the propagating front may not be necessarily perpendicular to the pressure transducers, hence the propagation velocity inferred from the pressure traces may overestimate the propagation speed. Although the visibility of the propagating front is poor in the top view obtained, from the film records and pressure traces, the propagation velocity is estimated to fall between 30 and 60 m/s.

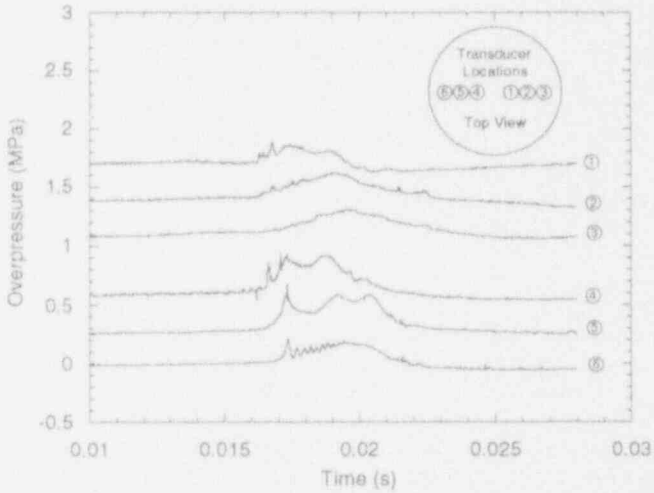

Figure 16. Pressure recorded during single propagating interaction in cylindrical tank.

After a single interaction, the majority of the tin (about 65%) settles to the base of the cylinder and solidifies into a disc. If two interactions occur during a trial, virtually all the tin is fragmented and few large tin fragments are recovered. Figure 17 shows a comparison of the debris size distribution for trials in which a single interaction occurred as well as for trials with multiple interactions. For the trials with a single interaction, about 6% of the tin was fragmented to particle sizes less than 1 mm, in contrast with a corresponding value of 19% for trials with multiple interactions.

III. DISCUSSION

A. Propagation Mechanism

The characteristic features of the propagating interaction are exhibited by the high-speed film and pressure records, although the details of the complex phenomena that occur near the leading edge of the interaction are still poorly understood. The relatively long rise time (~ 1 ms) and slow propagation velocity (40-50 m/s for the channel experiments) indicate that the propagating interaction is not coupled to the initial triggering shock wave that travels at about 1500 m/s within the water. After the interaction is

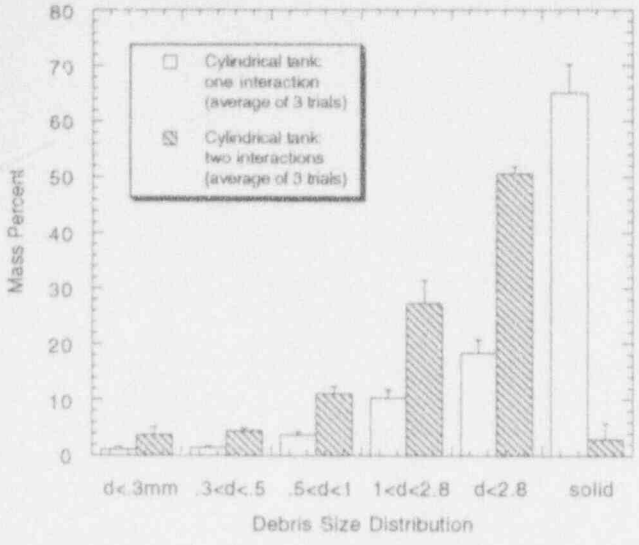

Figure 17. Debris size distribution for trials with a single interaction as well as for trials with two interactions in cylindrical geometry.

initiated, the high pressure produced within the interaction zone generates a pressure distribution (and associated flowfield) within the surrounding water, causing the adjacent vapor film to collapse and leading to spatial propagation of the disturbance. In the narrow channel geometry, the propagation of the explosion generates a wedge-shaped interaction region, which effectively displaces the water above the molten tin layer. If we consider a frame of reference moving with the front, then the hydrodynamic flow (and associated pressure field in the water) created by the interaction can be modeled reasonably well with a simple incompressible potential flow model for flow over a wedge.

In particular, Fig. 18 shows a schematic of a potential flow model for the flow of water above the explosion zone in a frame of reference moving with the interaction zone. Far from the interaction, the incoming flow is assumed to be uniform. The presence of the explosion zone begins to influence the flow at some distance ahead of the interaction zone (denoted R^* in Fig. 18), and the streamlines begin to be deflected vertically. The model cannot be expressed in closed form since an appropriate value of R^* must be determined from experiments. In the region near the interaction zone (i.e., for $R < R^*$), the flow of water is approximated by flow over a solid wedge (with a wedge angle of about 10°). The pressure distribution within the flow over the wedge can be obtained from the potential flow solution for flow within a sector (with a sector angle of about 170°). The complex potential for flow within a sector is of the following form (Curry, 1974):

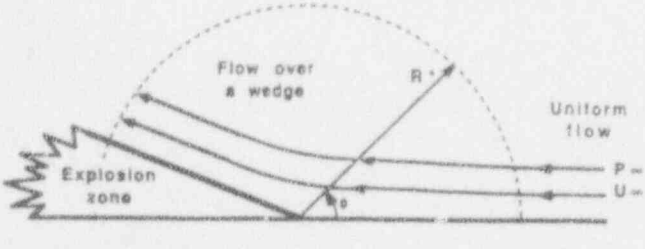

Figure 18. Schematic of potential flow model for flow of water above explosion zone.

$$F(z) = -Uz^n \tag{1}$$

where π/n is the sector angle. The corresponding velocity potential is given by

$$\phi = -UR^n \cos n\theta \tag{2}$$

This yields the following velocity components in the radial and tangential directions:

$$u_r = -nUR^{n-1} \cos n\theta$$
$$u_\theta = nUR^{n-1} \sin n\theta \tag{3}$$

The preceding solution for potential flow within a sector yields unbounded velocity far from the vertex of the sector. However, we will consider only the portion of the solution for $R < R^*$, i.e., near the vertex of the wedge. For $R > R^*$, the flow is assumed to be uniform. Setting the velocity equal to the freestream velocity, U_∞, at $R = R^*$ in Eq. (3) gives

$$U = \frac{U_\infty}{n(R^*)^{n-1}} \tag{4}$$

Using the steady-state Bernoulli equation and setting $P = P_\infty$ when $R = R^*$ where P_∞ is the ambient pressure, the pressure distribution is given by

$$p - p_\infty = \frac{\rho U_\infty^2}{2}\left[1 - \left(\frac{R}{R^*}\right)^{2(n-1)}\right] \tag{5}$$

From the preceding equation, we can see that the maximum increase in pressure occurs at the wedge vertex ($R = 0$) and is zero at $R = R^*$. From experiments, we can obtain R^* by the product of the pressure rise time and the propagation velocity. A typical pressure rise time of 1 ms and propagation velocity of 40 m/s yields an R^* of 4 cm.

If we express R in terms of cartesian coordinates x,y (i.e., $R^2 = x^2 + y^2$), then from Eq. 5 we can find the pressure distribution as a function of horizontal distance x for a given vertical position y above the tin layer. Or with the assumption of steady flow, the corresponding pressure-time history can be determined. In particular, taking a characteristic propagation velocity of $U_\infty = 40$ m/s with a wedge angle of 10°, overpressure traces for various vertical positions can be determined from Eq. 5 and are shown in Fig. 19. The predicted peak pressure is sensitive to the vertical position above the tin layer and ranges from a little over 0.1 MPa for $y = 1$ cm to 0.8 MPa for $y = 0$ (i.e., along the stagnation streamline).

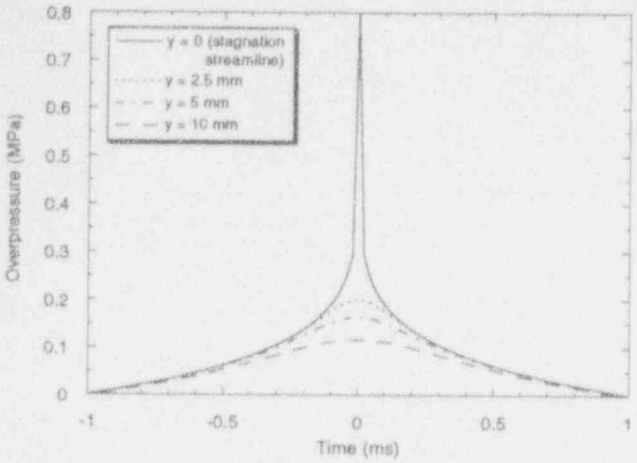

Figure 19. Pressure variation with time from potential flow model at various vertical locations y above vertex of wedge.

The experimental pressure profiles were recorded at a nominal position of about 1 cm above the tin layer. The overall shape of the predicted pressure rise is similar to the recorded pressure records (e.g., see Fig. 4) suggesting that the potential flow model is a reasonable approximation to the overall features of the flow outside of the interaction region. The predicted peak pressure at a position y = 1 cm is less than the experimental values (which range from 0.2 to 0.9 MPa from Fig. 11). However, the potential flow model assumes that the vertex of the explosion wedge is a point, whereas in reality it has a finite extent. In addition, the potential flow model assumes that there is no flow across the wedge boundary, which neglects the volume of water that participates in the interaction region and is converted to vapor. The sensitivity of the predicted peak pressure and pulse half-width to vertical position is consistent with experimental results. In particular, in several trials, three transducers were mounted vertically, at three different positions above the tin layer. As the distance from the tin layer increased, the peak pressures recorded decreased and the half-width of the pressure pulses increased, consistent with the model predictions (i.e., Fig. 19).

The pressure traces recorded experimentally (see Fig. 4) are usually not symmetric about the peak with the pressure rise occurring more rapidly (or over a shorter horizontal distance) than the pressure decay. A comparison of the pressure records with the high-speed film record indicates that the peak pressure is recorded in the water just above the explosion zone. As the interaction region moves across the transducer face the pressure falls. Most of the pressure traces exhibit a "shoulder" or plateau region where the pressure falls more slowly inside the explosion region. It is possible that in this complex multiphase region compressible effects may play a role in limiting the rate of pressure decay. Earlier investigators (e.g., Board et al., 1975) have noted that the low speed of sound within the explosion zone may limit the rate at which material leaves the front and hence the rate of expansion.

The propagation speed of the interaction is limited by the time for film collapse as well as the time required for the thermal energy contained in the tin to be transferred to the water and the subsequent vapor production. When the vapor film collapses and the water contacts the surface of the molten tin, only a thin surface layer of tin participates in rapid heat transfer to the water on the time scale of the rise time of the pressure (i.e., ~ 1 ms). Shortly after film collapse, the surface of the tin appears rough with fine tin filaments projecting from the tin layer surface. The high-speed flow of vapor away from the leading edge of the interaction region lofts tin within the wedge-shaped interaction region. The relative velocity between the lofted molten tin filaments and the vapor leads to considerable direct fragmentation of the tin within the interaction zone. At later times, the majority of the remaining molten tin is lofted vertically, partly due to the boiling of water drops trapped underneath the tin layer.

B. Effect of Geometry on Interaction Energetics

The degree of confinement of the explosion zone influences the rate of decay of the pressure generated during the interaction. Decreasing the inertial confinement of the tin (e.g., by lowering the height of water above the tin), leads to a reduction in the duration of the pressure pulse generated (and hence the impulse). Below a critical water height, the impulse generated is not sufficient to sustain film collapse and propagation fails. Increasing the inertial confinement (e.g., by preventing vertical expansion of the water) increases the explosion impulse but does not significantly increase the propagation velocity. The mixing and rapid heat transfer processes, that occur after film collapse near the leading edge of the interaction and sustain the propagation, are not strongly dependent on the degree of confinement. The characteristic length scale that governs the turbulent tin-water mixing following film collapse is the initial film thickness, a parameter that does not vary significantly between the different experimental configurations considered.

To investigate the effect of geometry on the explosion yield (i.e., the amount of thermal energy converted to mechanical energy during the interaction), an estimate of the ratio of the yield to the initial tin surface area has been made and is summarized in Table 1 below. The mechanical energy yield can be determined by directly estimating the velocity of the water accelerated by the interaction, or indirectly from the mechanical impulse imparted to the water for the cases where the water is free to move vertically during the interaction. In particular, by assuming one-dimensional flow and applying Newton's first law to the slug of water, the velocity can be related to the impulse as follows:

$$V = \frac{\int F dt}{m} = \frac{A\int P dt}{m} = \frac{AI}{m} \qquad (6)$$

where A is the surface area of the slug of water across which the pressure acts, m the accelerated mass, and I the pressure impulse, $\int P dt$. The kinetic energy can then be

written as

$$KE = \frac{1}{2} mV^2 = \frac{1}{2} \frac{(Af)^2}{m} \qquad (7)$$

Table 1. Effect of Geometry on Interaction Energetics

Geometry	Yield/Surface Area for Single Interaction (J/cm^2)	Effective Tin Mixing Depth for Single Interaction (mm)*	Yield/Surface Area for Multiple Interactions (J/cm^2)	Effective Tin Mixing Depth for Multiple Interactions (mm)*
Single Drop† (0.5 g)	0.55	–	2.33	2.6
Narrow Channel (open at top)	0.31‡	2.0	–	–
Narrow Channel (closed at top)	–	–	–	2.8
Cylindrical Tank	0.21§	0.6	–	1.8

*definition of mixing depth corresponds to the fraction of the mass of tin fragmented to particle sizes less than 1 mm

†calculations for single drop explosions described in earlier work (Ciccarelli, 1992)

‡estimated from the kinetic energy imparted to the water slug above the tin layer (Ciccarelli et al., 1991)

§estimated by integrating the pressure profiles recorded (see Fig. 16) and using Eq. (7) below

From Table 1, the yield/area for a single interaction varies by less than a factor of about three between the explosion of a single 0.5 g drop and a stratified cylindrical layer containing about 4 kg of molten tin. The difference in the initial tin surface area for these two configurations is almost three orders of magnitude. This suggests that the rate of the dynamical processes that occur immediately following film collapse (i.e., tin/water mixing, rapid heat transfer and vaporization) for the single drop are similar to those that occur locally following the initial film collapse in the stratified system. In fact, the fine tin filaments that are visible (using X-ray photography) protruding from the tin surface during the first interaction in single drop experiments (Ciccarelli, 1992) are reminiscent of the initial disturbances visible on the tin layer surface following film collapse in the stratified geometry experiments, suggesting that similar mechanisms play a role in each case.

Table 1 also shows an estimate of the effective depth of the tin that participates energetically in the interaction (obtained from Figs. 14 and 17). Here the mixing depth is defined arbitrarily as the effective thickness of the tin that is fragmented to particle sizes less than 1 mm. Due to the extensive fragmentation observed in the interaction region away from the leading edge of the front (e.g., see Figs. 5 and 6) the mixing depth as defined will be larger than the *actual* depth of the tin layer that interacts energetically shortly after film collapse at the leading edge of the interaction zone. The fraction of tin that is finely fragmented during a single interaction is larger for the narrow channel than for the cylindrical geometry, perhaps due to the higher vapor velocities that occur within the interaction region in the narrow channel due to the larger degree of confinement. Although the effective mixing depth for the narrow channel is about three times larger than for the cylindrical geometry, the yield/area is only about 50% larger. This suggests that in the narrow channel experiments, a larger proportion of the tin is finely fragmented by relative flow in the wake region where the fragments lose their heat slowly and do not significantly contribute to the yield of the interaction. The yield and mixing depth can be used to estimate the conversion ratio, or the ratio of the mechanical energy yield to the initial thermal energy (including the latent heat of solidification) of the tin that participates in the interaction. Using the values from Table 1, conversion ratios of 0.11% and 0.26% are obtained for the narrow channel with an open top and the cylindrical tank, respectively. To find an effective *thermodynamic efficiency* for the interactions, we can divide the above results by the maximum conversion ratio, as calculated using the standard Hicks and Menzies thermodynamic path (Bang and Corradini, 1991). In particular, if we consider constant volume heat transfer followed by adiabatic expansion of the mixture to atmospheric pressure, for an equal volume mixture of molten tin at 700°C and water, the conversion ratio is 19%. Therefore the thermodynamic efficiencies for the interactions in the narrow channel and cylindrical tank are 0.61% and 1.4%, respectively. Of the two estimates, the narrow channel results are probably more reliable, given that the conversion ratio is based on a direct measurement of the mechanical yield (as opposed to an estimate from the integrated pressure field).

Perhaps the most significant effect of increasing the confinement of a stratified system is that multiple interactions are much more likely to occur, significantly increasing the degree of fragmentation of the tin and the overall yield of the explosive interaction. Table 1 indicates for cylindrical geometry, that the second interaction increases the fraction of tin that is finely fragmented by a factor of about three. The first interaction can be considered a precursor event which efficiently produces a coarse molten tin/water/steam mixture prior to the second interaction which produces the majority of the mechanical energy release.

IV. CONCLUSIONS

The propagation of a vapor explosion in a stratified molten tin-water system has been investigated experimentally in three different configurations: (i) linear propagation in a narrow channel open at the top, (ii) propagation in a narrow channel with vertical confinement, and (iii) radial propagation in a cylindrical tank. In each case, a quantity

of tin was heated to 700–800°C and poured into hot water to form a layer of tin about 1 cm deep. In each configuration, self-sustained propagation of an energetic interaction was observed. Interactions were triggered by underwater spark discharge, which locally collapsed the vapor film, leading to liquid-liquid contact and rapid heat transfer. After the interaction was initiated, the high pressure generated by the rapid production of vapor produced a pressure field (and associated flowfield) within the surrounding water which caused the adjacent film to collapse, sustaining the propagation.

In the narrow channel experiments, the interaction propagated with an average velocity of about 40 m/s producing a wedge-shaped (wedge angle: 10°) interaction region. The velocity was limited by the time for film collapse as well as the time required for the thermal energy contained in the tin to be transferred to the water and the subsequent vapor production. For self-sustained propagation, the duration of the pressure pulse (or impulse) generated near the leading edge of the front must be sufficient to sustain film collapse. The rate of decay of the pressure was determined by the degree of inertial confinement provided by the water layer above the tin. Below a critical water height (in this case about 5 cm), propagation of the interaction always failed. Increasing the confinement of the tin by restricting the vertical expansion of the system increased the impulse by a factor of 3–4 but increased the propagation velocity only slightly to 50 m/s.

Radially propagating interactions were also observed in a stratified system in a cylindrical tank. The energetics of the interaction were not significantly altered by the change in geometry: the yield/surface area for a single interaction was about 30% lower than the corresponding value for the narrow channel experiments. However, considerably less tin was finely fragmented within the interaction region. A comparison between the energetics of single molten tin drop interactions and interactions in a stratified geometry suggested that similar dynamic processes occurred during the first interaction cycle in each case. Increasing the inertial confinement of the stratified systems increased the probability of the occurrence of a second interaction. In highly constrained stratified systems, the first interaction represents an efficient method for producing a well-mixed tin/water/steam mixture which can then support the propagation of a second, more energetic interaction. This is analogous to single drop experiments in which the collapse of the first bubble generated leads to a violent second interaction that releases the majority of the thermal energy of the drop.

Additional experiments are required to investigate the transferability of the present results to larger scale reactor conditions. For example, in a hypothetical loss of coolant scenario for a reactor, melting of the fuel rods may lead to the formation of a submerged pool of high-temperature molten fuel. The vapor film thickness and stability of the film will both be a function of the melt and coolant temperatures. The characteristic mixing length following film collapse may also be a function of the film thickness. However, there is no reason to conclude, a priori, that self-sustained propagation of an energetic interaction is precluded for stratified high-temperature melt-coolant systems at larger scale.

ACKNOWLEDGMENTS

The authors would like to thank Ryan Katofsky, Eric Proietti, Lawrence Ko, and Karim Sahyoun for assistance in carrying out the experiments, as well as Profs. J. H. S. Lee and J. E. Shepherd for stimulating discussions. The authors would also like to thank one of the reviewers for the useful comments. Financial support was provided by the Natural Sciences and Engineering Research Council of Canada and Sandia National Laboratories.

REFERENCES

1. Anderson R., Armstrong D., Cho D., and Kras, A. (1988) "Experimental and Analytical Study of Vapor Explosions in Stratified Geometries," *ANS Proceedings of the 1988 National Heat Transfer Conference*, **3**, 236-243.

2. Bang K. H. and Corradini M. L. (1988) "Stratified Vapor Explosion Experiments," *ANS Proceedings of the 1988 National Heat Transfer Conference*, **3**, 228-235.

3. Bang K. H. and Corradini M. L. (1991) "Vapor Explosions in a Stratified Geometry," *Nucl. Sci. and Eng.*, **108**, 88-108.

4. Berman M. (1986) "Light Water Reactor Safety Research Program Semiannual Report," Oct. 1983-March 1984, Sandia National Labs. Rept. SAND85-2500.

5. Board S. J. and Hall R. W. (1974) "Propagation of Thermal Explosions: 1—Tin/Water Experiments," CFRSWP/PP(74)11, CEGB Rept. RD/B/N2850, Central Electricity Generating Board, Berkeley Nuclear Laboratories, Berkeley, Gloucestershire, UK.

6. Board, S. J., Hall, R. W. and Hall, R. S. (1975) "Detonation of Fuel Coolant Explosions," Nature, **254**, 319-321.

7. Ciccarelli G., Frost D. L. and Zarafonitis C. (1991) "Dynamics of Explosive Interactions Between Molten Tin and Water in Stratified Geometry," *Prog. in Astronautics and Aeronautics*, **134**, AIAA, Washington, 307-325.

8. Ciccarelli G. (1992) "Investigation of Vapor Explosions with Single Molten Metal Drops in Water using Flash X-Ray," *Ph. D. Thesis*, McGill University, Mech. Eng. Dept., Montreal, Quebec, Canada.

9. Colgate S. A. and Sigurgeirsson T. (1973) "Dynamic Mixing of Water and Lava," *Nature*, **244**, 552-555.

10. Corradini M. L., Kim B. J., and Oh M. D. (1988) "Vapor Explosions in Light Water Reactors: a Review of Theory and Modeling," *Prog. Nucl. Energy*, **22**(1), 1-117.

11. Curry, I. G. (1974) *Fundamental Mechanics of Fluids*, McGraw-Hill, Montreal, Canada.

12. Harlow F. H. and Ruppel H. M. (1981) "Propagation of a Liquid-Liquid Explosion," Los Alamos National Lab., Rept. LA 8971 MS.

13. Koopmann R. P., et al. (1981) "Description and Analysis of BURRO Series 40-m^3 LNG Spill Experiments," Lawrence Livermore Lab., Rept. UCRL-53186.

14. Reid R. C. (1983) "Rapid Phase Transitions from Liquid to Vapor," *Advanced Chemical Engineering*, **12**, 105-208.

EXTERNALLY TRIGGERED STEAM EXPLOSION EXPERIMENTS: AMPLIFICATION OR PROPAGATION?

Robert E. Henry
Fauske & Associates, Inc.
16W070 West 83rd Street
Burr Ridge, Illinois 60521
(708) 323-8750

ABSTRACT

A vapor explosion is the rapid exchange of energy between a hot and cold liquid caused by, and resulting in, the propagation of shock waves through the liquid-vapor mixture. Many vapor explosion experiments have been performed using an external trigger to initiate the event. In general, the assessment of the explosive behavior has been to report the pressure history resulting from the "explosive interaction". However, with the mutual dispersion of high temperature liquid within the colder temperature host liquid, the pre-mixed configuration represents substantial stored energy. With the imposition of an external trigger to fragment and rapidly mix the debris, some of this stored energy could be released without causing propagation of the event. This paper discusses the difference between amplification of a trigger pulse due to the release of stored energy and propagation of the explosion within the premixed zone. Also, a criterion for deciding if propagation has occurred is provided. It is recommended that if the experiments do not satisfy this criterion, propagation of the event should not be concluded and the results should not be considered as a large scale explosion. Rather such data should be considered as a characterization of what could occur within an explosion if an explosion (shock wave) could be initiated.

I. INTRODUCTION

Vapor explosions can occur when two liquids, at greatly different temperatures come into intimate contact. Prior to the actual explosion, these liquids intermix as illustrated in Figure 1. This stage has been termed the coarse mixing, or coarse pre-fragmentation stage. Once this liquid-liquid state has been established, the mixture could potentially support a thermal detonation wave as described by Board, et al. (1975), Figure 2, assuming all the necessary conditions for explosive vapor formation are met. Numerous experimental studies have been performed to investigate the nature of vapor explosions (Henry and Fauske, 1979; Avedisian, 1982; Board, et al., 1974) the propagation in a thermal detonation, and these

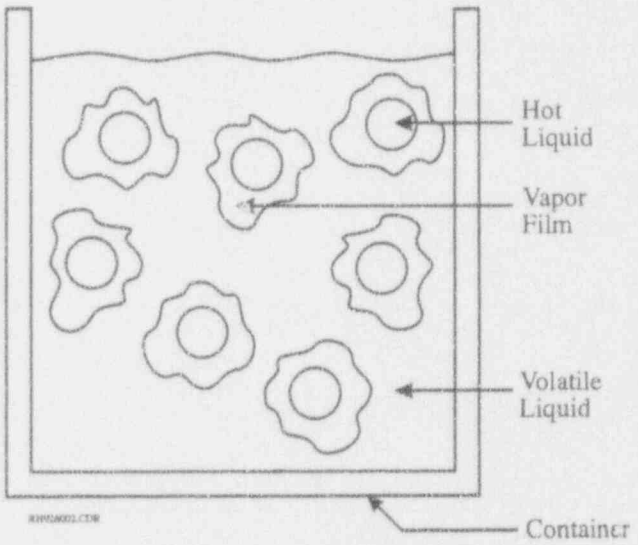

Fig. 1 Coarse pre-fragmentation.

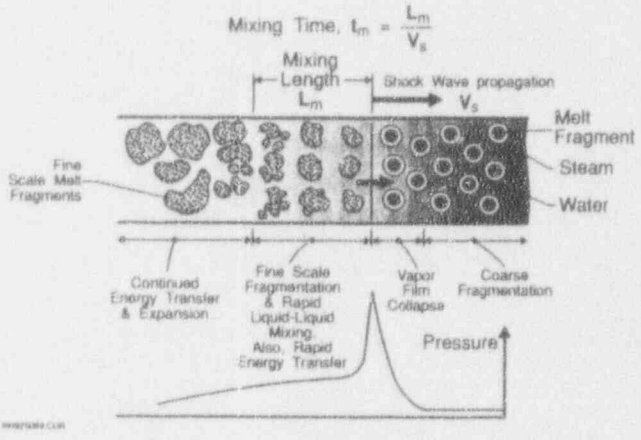

Fig. 2 Coarse fragmentation and rapid liquid-liquid mixing flow regimes postulated for the thermal detonation and parametric models.

can be separated into two categories, i.e. those using an external trigger and those which do not. Here we will focus on those investigations which used an external trigger.

The concept of a thermal detonation is that a shock wave moves through a coarsely mixed configuration and (1) forces liquid-liquid contact, (2) fragments the two liquids to increase the surface area for heat transfer, and (3) rapidly mixes the liquids to promote the energy transfer. These processes are illustrated in Figure 2. One means of initiating the shock wave is through an external trigger such as a blasting cap, an exploding wire or the rupture of a small, high pressure gas volume.

Once the coarse premixing has occurred, there is substantial stored energy in the high temperature melt, which could be released if one or more of the high temperature globules, or particles, could be rapidly subdivided and intermixed with the colder working fluid. An external trigger provides such a stimulus. Therefore, if the energy delivered by the trigger fragments and rapidly mixes a portion of the high temperature fluid such that the thermal energy is released from essentially only this part of the fluid, then the process is one of amplification, not propagation. Let us first review the considerations for rapid mixing and then the implications with respect to some experimental results.

II. RAPID LIQUID-LIQUID MIXING

When considering the rapid intermixing of hot and cold liquids which are initially in a separate state, the energy requirements for the fine scale mixing must be considered. Such an evaluation was presented in Cho, et al. (1976) for the material being mixed by a strong shock wave. This is illustrated in Figure 2, which is the conceptual foundation for both the thermal detonation model, Corradini (1982), and the parametric models such as that presented in Caldarola and Kousouvelis (1974). The basic mixing configuration is shown in Figure 3 and illustrates a linear mixing in the direction of the shock wave brought about by the density

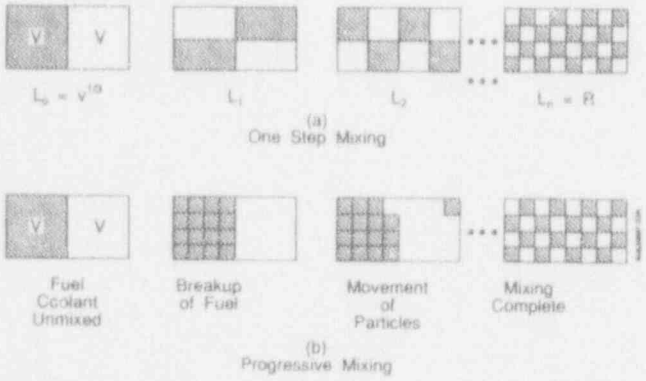

Fig. 3 Assumed configurations for mixing energy models.

differences between the hot and cold liquids. In this assessment, the energy requirements to overcome the frictional dissipation were found to be substantial for rapid intermixing.

The evaluation of frictional dissipation was based upon two different types of intermixing processes. The first assumes that the total intermixing occurred in a "one-step" manner as illustrated in Figure 3a, and the other formulation assumed a progressive mixing pattern as illustrated in Figure 3b. The frictional dissipation for such a mixing process is expressed by

$$\text{Frictional Dissipation} = N\, C_D\, \pi\, R^2 \left(\frac{1}{2}\, \rho_f\, U_m^2\right) L_m \qquad (1)$$

where N equals a number of fuel particles, R is the final radius of the fuel particle, U_m equals the mixing velocity, L_m is the mixing distance, ρ_f represents the water density, and C_D is the drag coefficient. The mixing energy is generally dominated by the frictional dissipation term, especially if rapid intermixing is postulated as was done in the Reactor Safety Study (1975). While the term is designated as frictional dissipation, it is principally characterizing the form drag. If the mixing velocity is assumed to be equal to the mixing length divided by the mixing time (t_m) and the mixing length in the direction of the shock wave is approximated by the cube root of the volume to be mixed, ($L_m \sim V^{1/3}$) the one step mixing energy is then given by

$$(E_m)\ \text{One-Step} = 3/8\ C_D\, \frac{\rho_f\, V^2}{t_m^2\, R} \qquad (2)$$

where ρ_f is the density of the fluid receiving the finely particulated material and C_D is the drag coefficient. As discussed in Cho, et al (1976), the mixing energy depends upon the breakup mode during the intermixing of the hot and cold materials. The "one-step" mechanism requires the maximum energy and the actual energy requirements could be considerably less if the intermixing process occurs in a progressive fashion involving a number of steps. If this is assumed to occur in a finite number of steps, the expression for the energy required in progressive mixing is given by

$$E_n = V\, \frac{3}{8}\, C_D\, \rho_f\, \frac{L_o^2}{t_m^2} \left(\frac{1 - \gamma^n}{1 - \gamma}\right)^2 \frac{n}{\gamma} \qquad (3)$$

where n is the number of steps in the mixing process, L_o is the mixing distance, and γ is the reduction factor of fuel particle size in each step. This energy expression exhibits a minimum when

$$n = \frac{1}{1.74}\, \ln\left(\frac{L_o}{R}\right) \qquad (4)$$

and if this number of steps is considered, the progressive mixing formulation is then given as

$$\left(E_m\right)_{min} = 1.81\ C_D\ \rho_f\ V\left(\frac{V^{2/3}}{t_m^{\,2}}\right) \cdot \left(1 - \frac{R^2}{V^{2/3}}\right)\ \ln\left(\frac{V^{1/3}}{R}\right) \qquad (5)$$

where the mixing length has again been assumed to be equal to the cube root of the mixing volume.

In addition to the models for dissipative forces in rapid liquid-liquid mixing, a model was presented for the kinetic energy required to move the materials the specified distance to achieve the dispersed configuration shown as the end state in Figure 2. The kinetic energy of the melt is given by

$$K.E. = \frac{1}{2}\ \rho_F\ V\ U_m^{\,2} = \frac{1}{2}\ \rho_f\ V\left(\frac{L_m^{\,2}}{t_m}\right) \qquad (6)$$

Considering the mixing length in the direction of the shock wave to again be approximated by $L_m \approx (V)^{1/3}$, the kinetic energy for mixing can be expressed as

$$K.E. = \frac{1}{2}\ \frac{\rho_F\ V^{5/3}}{t_m^{\,2}} \qquad (7)$$

Comparing the kinetic energy model with the progressive mixing model, the major difference is the drag coefficient in the progressive mixing formulation. A derivation of this drag coefficient in dense dispersions is given in IDCOR (1983) and results in the predictions shown in Figure 4. As illustrated, for an equal volume dense dispersion, $\epsilon \sim 0.5$, the effective drag coefficient is about 20; the large value being due to the torturous path of the fluid passing through the dense particle array. This drag coefficient is used here to analyze the response to external triggers.

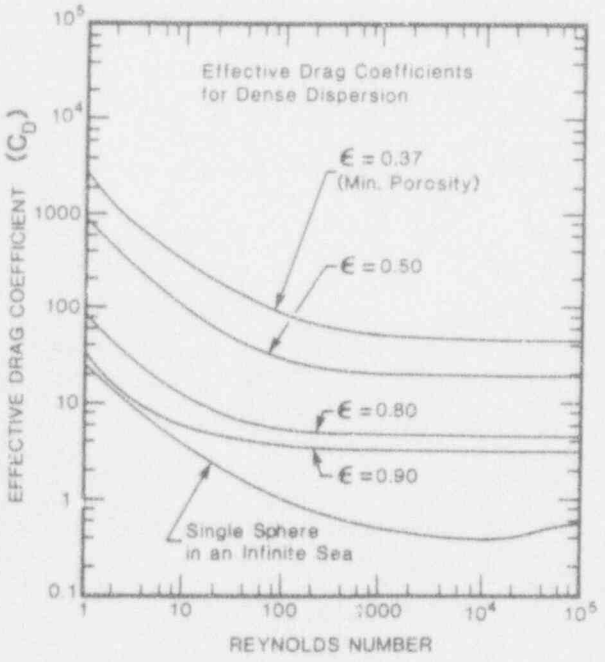

Fig. 4 Effective drag coefficient for dense dispersions.

With this value of the drag coefficient and the other coefficients, the progressive mixing energies are about two orders of magnitude greater than the kinetic energy mixing value which represents the minimum energy level required to achieve the final state.

For analyses such as those conducted in WASH-1400 (Reactor Safety Study, 1975), the rapid intermixing of hot and cold materials conceptually produces thermal energy transfer which is realized as rapid vaporization of the water resulting in expansion and mechanical work. Estimates of such work from large scale steam explosion experiments is a small fraction of the thermal energy transfer from the melt, typically less than 1% (Buxton and Benedick, 1979). However, the amount of thermal energy extracted from the melt is a useful reference against which to compare the energy required for mixing these materials on a rapid time scale. This thermal energy cannot be transferred faster than it can be conducted to the surface of the hot material. The rate of thermal penetration into the hot material can be estimated by approximating the error function solution as

$$x = 2\left(\alpha_F\ t_m\right)^{1/2} \qquad (8)$$

where x is the thermal penetration distance, and α_F is the thermal diffusivity of the molten core material. For oxidic core material with a thermal diffusivity of about 10^{-7} m²/sec, a time scale of 1 millisecond would result in a thermal penetration of approximately 20 microns. Consequently, if all the energy is assumed to be transferred within this interval, a particle radius of 60 microns (120 μm dia.) would be necessary since the equivalent thermal length for a spherical particle is approximately 1/3 of the radius. This is a typical final particle size used for the fine particulation assessments for large scale experimental results. For the sample calculations in this paper, we will assume a final fragment size of 100 μm even though many of the experiments used metals which have larger thermal diffusivities and could achieve the necessary energy transfer with larger particle sizes.

III. CRITERIA FOR PROPAGATION

External triggers are very useful for ensuring that an event can be initiated, particularly when high speed photography is being used. Typically the external trigger is characterized as representing the early phase of the explosion such that the interactions caused by the shock wave from the trigger are like those occurring as the wave propagates through the mixture. This is reasonable when investigating individual interactions. However, one must be careful when applying this to the global system

and forming conclusions of whether a propagating event was observed and particularly whether a propagating event could occur in the absence of a trigger. For many applications, such as nuclear reactor safety, this latter point is a key issue.

As an example let us consider coarsely mixed particles of a high temperature material with a radius of 1 cm and specific enthalpy change of 2.0×10^6 J/kg if they are quenched in water. This represents a reasonable size for a coarsely mixed condition and a reasonable stored energy for many of the experiments which have been done. If the particles have a density of 7000 kg/m^3, each would have a mass of 0.029 kg and a thermal energy transferred of 5.8×10^4 J when quenched. We will use the one-step mixing model as a conservative (overestimate) of the energy necessary to rapidly mix the two fluids. It is important to note at this point that if the two materials can be mixed more easily than the one step approach, the following arguments become even more crucial. In the following evaluation, complete mixing of the particle is assumed, fully realizing that mixing 10% of 10 particles requires one-tenth of the energy to completely mix a single particle. Assuming a final particle size of 10^{-4} m (100 μm), a mixing time of 1 msec and a water density of 1000 kg/m^3, the energy required to rapidly mix each particle is about 1300 J/particle. This is 45 times less than the thermal energy released and therefore satisfies the criterion for propagation. However, if an external trigger with an energy release of 10 kJ is used, the trigger could rapidly mix 7.7 particles with a subsequent thermal energy transfer of 4.7×10^5 J. Approximately one-third of the energy transferred can be realized as work. Therefore, the work done by such an event is about 1.5×10^5 (150 kJ). From this hypothetical example, a 10 kJ external trigger could cause sufficient rapid mixing to cause an event demonstrating the work of 150 kJ. Therefore, this event may only reflect an amplification (15 times) of the external trigger and not a propagating event. Hence, the fundamental question: Is this representative of propagation in an explosive interaction or merely amplification of the trigger? Without addressing this, the investigator has not established the applicability to a large scale system.

This amplification has an analogy in nuclear fission, i.e. a subcritical mass with a neutron source. When the mass is subcritical, there are more neutrons created than are released by the source but the reaction reaches an asymptote. If the source is removed, the neutron production will decrease because the nuclear reaction is not self-sustaining.

The above example for an external trigger only illustrates the extent of the amplification that could occur. Of course, it is unrealistic to assume that all of the work done by the trigger would be realized as intimately mixed materials. Conversely, with such a large potential amplification factor, it is also unrealistic to only compare the work done by the explosion to the work done by the trigger to conclude whether a propagating event has occurred.

To address this, the following criteria are recommended.

1. If the work done by the explosion is less than, or comparable to, the trigger, it should be concluded that a propagating event did not occur.

2. If the work done is comparable to that which could be accomplished by the external trigger (considering the amplification factor) a propagating event may have occurred.

3. If the explosive work greatly exceeds (order of magnitude greater) that which could have resulted from the external trigger (with amplification), then a propagating event did occur.

IV. COMPARISON WITH EXPERIMENTS

It is not the intent of this paper to compare the above criteria with an extensive data base. Rather, the criteria are compared with a few experiments to illustrate the use of the criteria.

Higgins (1955 and 1956) was one of the first who used external triggers to induce interactions between molten metals and water. The metals used were:

- pure zirconium,
- Zircaloy 2,
- uranium,
- uranium-molybdenum alloy,
- pure aluminum,
- 95% aluminum-5% lithium alloy,
- pure magnesium,
- pure nickel, and
- 321 stainless steel.

With a total of 39 tests, 21 were performed with an external trigger (a No. 6 blasting cap with an available energy of 2.2 kJ) and 18 were conducted without a trigger. No explosions occurred unless an external trigger was used regardless of the metal tested. For those tests which did exhibit explosive interactions, the only observation was the fragmented character of the metal after the test, i.e. there was no estimate of the energy released. However, for these tests the external trigger is three orders of magnitude greater than the energy required for one step mixing (IDCOR, 1983). Thus, it is not surprising that considerable particulation and energy release occurred. In fact, one should not conclude that this represents a propagating event.

Buxton and Benedick (1979) carried out large scale steam explosion experiments in which 3-13 kg of molten iron thermite was poured into a water filled vessel at one atmosphere. An explosive detonator (0.64 g of high explosives) was used to trigger an explosive interaction. Assuming the detonator was PETN or the equivalent, the reaction products are all gaseous and the work delivered to coarsely mixed liquids can be approximated by the heat of reaction, i.e. ~ 5800 J/g for PETN or 3.7 kJ for these tests. If we use a value of 1.3 kJ/particle for fine scale mixing as calculated in Section 3, three particles could be mixed by this trigger. The specific enthalpy change for quenching thermite is about 2.9 MJ/kg and the average density is about 4000 kg/m^3. Therefore, the rapid mixing and quenching of three coarsely mixed droplets would result in the transfer of 146 kJ and an effective work of 59 kJ (1/3 of the thermal energy transferred). Table 1 shows the results of the experiments with external triggers, the interesting result being that the measured work done by the explosion in every test is comparable to, but less than, that which could be generated with rapid mixing induced by the external trigger. Here again, one cannot conclude that a propagating event occurred.

Another test series was performed by Buxton, Benedick and Corradini (1980) in which a thermite mixture was used to simulate the mixture of metals and oxides that could be anticipated during a core melt accident. Specifically the mixture was UO_2, ZrO_2, Fe, Cr and Ni. In one of these experiments, an external trigger of 0.64 g of PETN was used, while in the other, an explosive cord containing 6 g PETN was the trigger. Table 2 summarizes the results of these tests and it is interesting that the work done was increased by a factor of 10 when the strength of the trigger was increased by an order of magnitude. This observation would tend to indicate that a propagating event did not occur in these experiments. The smaller trigger would mix 2.8 droplets as characterized in Section 3 and the larger trigger could mix 23 particles 1 cm in diameter. It is assumed that the specific enthalpy change for this melt is 2 MJ/kg and that the density is 7000 kg/m^3. The energy transferred for the small trigger is 162 kJ or an explosive work of 54 kJ. For the larger trigger the energy transferred is 1.3 MJ and a work of 445 kJ. Comparing this to the measured values showed the calculated results to be an order of magnitude greater than the measured values, i.e. the measured work is comparable to the work delivered by the trigger. Once again, we cannot conclude that this is a propagating event, i.e. this may only be an amplification of the trigger event due to the stored energy in the coarsely mixed system.

Mitchell, Corradini and Tarbell (1981) reported results for two iron thermite-water tests at an elevated pressure (1 MPa), one without an external trigger (FITS-4A) and one with 0.6 g of PETN (3.8 kJ) external trigger (FITS-5A). Only the test with an external trigger demonstrated explosive behavior. If we once again consider the coarse and fine scale fragmentation discussed in Section 3, the work from the trigger could mix three particles causing an energy transfer of about 146 kJ or a work due to steam formation and expansion of 49 kJ. Table 3 summarizes the results reported for the FITS-5A test and as illustrated, the experimental values are 3-6 times the calculated quantities. This is an example where a propagating event may have occurred.

This example illustrates the uncertainties that need to be addressed when making such comparisons. Firstly, the coarse mixing and final sizes of the molten material influence the calculated results substantially. Secondly, all of the trigger energy is not focused on individual drops and much of the energy could be consumed in merely accelerating the water. Conversely, it takes less energy to mix 10% of 30 droplets than to mix 100% of three droplets. Lastly, if energy is released due to heat transfer in the mixture, this could cause additional mixing and energy transfer which is amplified but not self-sustaining.

In another small scale experiment Nelson and Duda performed single drop (~ 1.4 mm dia.) experiments with molten Fe_3O_4 using an external trigger with a work delivered of about 14 J.

Table 1

SANDIA THERMITE EXPERIMENT
SAND/79-1399, NUREG/CR-0947
COARSE FRAGMENTATION AND MIXING ANALYSIS
SINGLE STEP, EQUAL VOLUME MIXING

Quantity	Run Number 27	29	30	35	38	41
Melt mass, kgm	4.2	3.4	3.2	12.0	13.0	9.4
Detonator Available Energy, kJ	3.7	3.7	3.7	3.7	3.7	3.7
Reported Efficiency, %	0.42	0.47	0.36	0.20	0.19	0.26
Measured Work, kJ	23.9	21.6	15.6	32.5	33.4	33.0

Table 2

SANDIA CORIUM EXPERIMENTS
COARSE FRAGMENTATION AND MIXING
SINGLE STEP, EQUAL VOLUME MIXING

Quantity	Run Number 57	59
Corium Mass, kg	13.6	19.4
Detonator Available Energy, kJ	3.7	30
Reported Efficiency, %	<< 0.01	0.05
Measured Work, kJ	2.5	36

Table 3

FITS-5A IRON THERMITE-WATER TEST
COARSE FRAGMENTATION AND MIXING
SINGLE STEP, EQUAL VOLUME MIXING

Quantity	Value
Melt Mass, kg	5.38
Detonator Available Energy, kJ	3.8
Reported Efficiency, %	1-2
Measured Work, kJ	156-312

The estimated work resulting from the interactions was approximately 1-6 J. Hence, inthese experiments, one could not conclude that the results characterize a propagating condition.

V. CONCLUSIONS

Experiments using external triggers are useful to determine the behavior if a shock wave is imposed on a coarsely mixed liquid-liquid system. However, unless analyses of the experiment show that the resulting energy released is far in excess of that which could result if the trigger pulse rapidly mixed the two liquids, then it has not demonstrated that the system is self-sustaining, i.e. a propagating system. Rapid mixing was evaluated as a one step process in this paper as a conservatism, not a prerequisite. If one postulates that mixing can occur in a more efficient manner, then the analysis of the trigger pulse becomes more crucial. All of these lead to the conclusion that much weaker triggers should be used, or perhaps none at all, when determining if an explosive interaction can be initiated on a large scale.

To address experiments with an external trigger, the following criteria are recommended.

1. If the work done by the explosion is less than, or comparable to, the trigger, it should be concluded that a propagating event did not occur.

2. If the work done is comparable to that which could be accomplished by the external trigger (considering the amplification factor) a propagating event may have occurred.

3. If the explosive work greatly exceeds (order of magnitude greater) that which could have resulted from the external trigger (with amplification), then a propagating event did occur.

If the analyses of the experimental results indicate a non-propagating, or marginally propagating system, then the externally triggered studies should be combined with studies using no external triggers and the same fluids to determine if an explosive interaction can be initiated. At the very least, weak external triggers should be used to determine the role of the trigger.

VI. REFERENCES

Avedisian, C. T., 1982, "Effect of Pressure on Bubble Growth within Liquid Droplets at the Superheat Limit", ASME Journal of Heat Transfer, Vol. 104, pp. 750-757.

Board, S. J., Hall, R. W. and Brown, G. E., 1974, "The Rate of Spontaneous Nucleation in Thermal Explosions: Freon/Water Experiments", RD/BIN-3007.

Board, S. J., et al., 1975, "Detonation of Fuel-Coolant Explosions, Nature, 254, p. 319.

Buxton, L. D. and Benedick, W. B., 1979, "Steam Explosion Efficiency Studies", NUREG/CR-0947, SAND79-1399.

Buxton, L. D., Benedick, W. B. and Corradini, M. L., 1980, "Steam Explosion Efficiency Studies: Part II-Corium Experiments", NUREG/CR-1746, SAND/80-1324, Sandia National Laboratory.

Caldarola, L. and Kousouvelis, G., 1974, "A Theoretical Model with Variable Masses for Molten Fuel-Sodium Thermal Interactions", Proc. of the Fast Reactor Safety Mtg., Beverly Hills, CA, CONF-740401-P2, p. 969.

Cho, D. H., et al., 1976, "Some Aspects of Mixing in a Large-Mass, Energetic Fuel-Coolant Interactions", Proc. of the International Mtg. of Fast Reactor Safety and Related Physics, CONF-761001, Vol. 4, Chicago, IL, pp. 1852-1861.

Corradini, M. L., 1982, "A Proposed Model for Fuel-Coolant Mixing During a Core-Melt Accident", Paper presented at the ANS/ENS Mtg. on Thermal Reactor Safety, Chicago, IL.

Henry, R. E. and Fauske, H. K., 1979, "Nucleation Processes in Large Scale Vapor Explosions", Trans. ASME, Jr. of Heat Transfer, Vol. 101, pp. 280-287.

Higgins, H. M., 1955, "A Study of the Reactor of Metals and Water", AECD-3664, Aerojet General Corporation, Azusa, California.

Higgins, H. M., 1956, "The Reaction of Molten Uranium and Zirconium Allows with Water", Aerojet Report No. 2914-2, Metallurgy & Ceramics, Aerojet-General Corporation, Azusa, California.

IDCOR, 1983, "Final Report of Key Phenomenological Models for Assessing Explosive Steam Generation Rates", IDCOR Technical Report 14.1.

Mitchell, D. E., Corradini, M. L. and Tarbell, W. W., 1981, "Intermediate Scale Steam Explosion Phenomena: j Experiments and Analysis", Sandia National Laboratory, SAND/81-0124, NUREG/CR-2145.

Nelson, L. A. and Duda, P. M., 1981, "Steam Explosion Experiments with Single Drops of Iron Oxide Melted with a CO_2 Laser", Sandia National Laboratory, SAND/81-1346, NUREG/CR-2295.

Reactor Safety Study, 1975, WASH-1400, NUREG/75-0114.

PROPAGATION INVESTIGATIONS USING THE CULDESAC MODEL

D.F. Fletcher
SRD, AEA Technology,
Culham Laboratory, Oxon., OX14 3DB, UK.
Telephone (44) 235-521840 — Fax (44) 235-464143

ABSTRACT

This paper contains a description of the CULDESAC propagation model, which has been developed at Culham Laboratory, and a summary of results from a number of computational studies. The conservation equations which make up the model are described, together with the fragmentation and heat transfer models used to close it. Example results are then presented which illustrate the importance of solution parameters, the heat transfer and fragmentation models, and geometrical considerations on the calculated propagation behaviour. The difficulties in comparing model predictions with the available experimental data are then discussed. Finally, a summary of what are believed to be the important issues in propagation modelling is presented.

I. INTRODUCTION

Propagation is the crucial stage in a large-scale steam explosion. Without a *coherent* propagation through a large region of mixture containing many tonnes of melt it is highly unlikely that a steam explosion could fail a reactor vessel. It is widely believed that the conditions following coarse mixing of a large mass of melt are such that propagation cannot occur through most of the mixture. Thus the study of propagation is important in building a complete picture of the steam explosion process.

There is little doubt that propagation can occur in small-scale (involving ~10 kg) quantities of melt as evidenced by the explosions observed in the FITS (Mitchell et al., 1981) and SUW (Bird, 1984) experimental series. Cine-photography shows that such explosions are caused when a wave propagates through the mixture; the position of the wave being marked by the transition from hot to quenched fuel. However, the means of propagation of this wave and the detailed physics controlling the propagation process remain elusive. This is not surprising. It is hard to study the initial mixing stage, which may last for ~500 ms, in which a complex three phase dispersion of melt, liquid water and steam develops (Fletcher and Denham, 1993). The propagation stage then takes just a few milliseconds, during which time the mixture is converted into a region containing tiny quenched melt fragments and fluid at a supercritical pressure and temperature.

A variety of experiments have been performed to determine the microscopic physical processes occurring during fragmentation (droplet fragmentation and rapid heat transfer are two examples) and to observe the global propagation behaviour (Corradini et al., 1988; Corradini, 1991). In addition, a large number of models have been developed to study this process. Most of these owe their existence to the analogy between steam explosions and chemical detonations postulated by Board, Hall and Hall (1975). These models have been reviewed in detail by Fletcher and Anderson (1990). Since that review was written considerable additional work has been performed by Theofanous and co-workers at the University of Santa Barbara (Medhekar et al., 1989, 1991; Yuen et al., 1992) and Fletcher at Culham Laboratory. It is a presentation of the latter work which forms the main content of this paper.

The paper is organised in the following way: Section II contains a description of the CULDESAC model and the constitutive physics currently used in it. Section III contains a presentation of some of the calculations performed using the model. This presentation includes a discussion of the important numerical solution parameters, as well as the physics parameters. Section IV contains a discussion of experimental validation, and Section V contains the conclusions.

II. DESCRIPTION OF THE MODEL

The CULDESAC model has been developed over the last five years and is presented in a series of publications (Fletcher and Thyagaraja, 1989a, 1991; Fletcher, 1991a, b,c). The reader is referred to these papers for a detailed description of the model, as only a summary will be given here. The physical picture on which the model is based is given in Figure 1. The model is transient and one dimensional, although this may be planar, cylindrical,

spherical or any user-specified slowly varying shape. The mixture is assumed to consist of melt droplets, water and steam. Behind the pressure front the droplets are fragmented and the water is heated by energy transfer from the fragments.

The model assumes that this configuration can be represented using three different components, namely melt droplets, melt fragments and water. In order to restrict the number of constitutive relations required to close the model, the simplifying assumption that steam and water are always in mechanical and thermal equilibrium is made. This assumption is justified once supercritical temperatures and pressures occur and provides a first approximation for subcritical conditions. Each species is assumed to have its own velocity field. Two different fragmentation models are available in the code: one models boundary layer stripping and the other represents a mode in which there is a delay between the shock passing a droplet and fragmentation being initiated. Heat is transferred from the fragments to *all* of the water at a finite rate. Thus no allowance is made for local thermal disequilibrium, around the fragments, in the water phase or within the fragments themselves.

This problem has been formulated mathematically using the usual multiphase flow equations. The simplifying assumption that the melt and fragments are incompressible is made, so that $\rho_f = \rho_m = \text{constant}$.

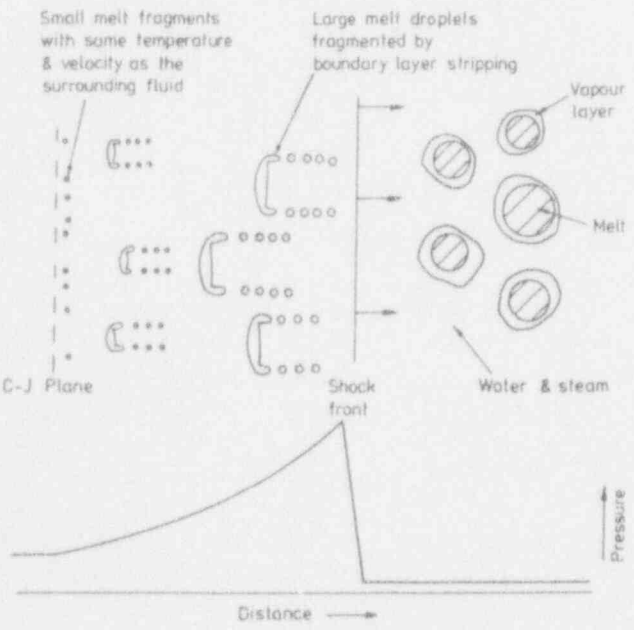

Figure 1. The physical picture underlying the model. In this picture it is assumed that fragmentation is caused by a boundary layer stripping mechanism.

A. Conservation Equations

Conservation of mass applied to the water, melt and fragments gives

$$\frac{\partial}{\partial t}(\alpha_w \rho_w) + \frac{1}{A}\frac{\partial}{\partial x}(A\alpha_w \rho_w V_w) = 0, \tag{1}$$

$$\frac{\partial}{\partial t}(\alpha_m \rho_m) + \frac{1}{A}\frac{\partial}{\partial x}(A\alpha_m \rho_m V_m) = -\Gamma_f \tag{2}$$

and

$$\frac{\partial}{\partial t}(\alpha_f \rho_m) + \frac{1}{A}\frac{\partial}{\partial x}(A\alpha_f \rho_m V_f) = \Gamma_f. \tag{3}$$

In equations (2) and (3) Γ_f is the mass exchange rate between the droplet and fragment species due to fragmentation and is specified later.

Conservation of momentum for the water, melt and fragments gives

$$\begin{aligned}\frac{\partial}{\partial t}(\alpha_w \rho_w V_w) + \frac{1}{A}\frac{\partial}{\partial x}(A\alpha_w \rho_w V_w^2) = \\ -\alpha_w \frac{\partial p}{\partial x} + \frac{\partial}{\partial x}\left(\alpha_w \mu_a \frac{1}{A}\frac{\partial}{\partial x}(AV_w)\right) \\ + K_{mw}(V_m - V_w) + K_{fw}(V_f - V_w),\end{aligned} \tag{4}$$

$$\begin{aligned}\frac{\partial}{\partial t}(\alpha_m \rho_m V_m) + \frac{1}{A}\frac{\partial}{\partial x}(A\alpha_m \rho_m V_m^2) = \\ -\alpha_m \frac{\partial p}{\partial x} + K_{mw}(V_w - V_m) - \Gamma_f V_m\end{aligned} \tag{5}$$

and

$$\begin{aligned}\frac{\partial}{\partial t}(\alpha_f \rho_m V_f) + \frac{1}{A}\frac{\partial}{\partial x}(A\alpha_f \rho_m V_f^2) = \\ -\alpha_f \frac{\partial p}{\partial x} + K_{fw}(V_w - V_f) + \Gamma_f V_m.\end{aligned} \tag{6}$$

The terms on the RHS of equations (4), (5) and (6) represent the effect of the pressure gradient force, drag between the various species, and momentum transfer from the large droplets to the fragments due to fragmentation. The fragments are assumed to be moving with the melt droplet velocity at the instant they are formed.

Conservation of energy (based on the stagnation form of the equations to improve the shock capturing) for the water, melt and fragments gives

$$\begin{aligned}\frac{\partial}{\partial t}(\alpha_w \rho_w e_{sw}) + \frac{1}{A}\frac{\partial}{\partial x}\left(A\alpha_w V_w\left(\rho_w h_{sw} - \mu_a \frac{\partial V_w}{\partial x}\right)\right) \\ = -p\frac{\partial \alpha_w}{\partial t} + R_{mw}(T_m - T_w) + R_{fw}(T_f - T_w) \\ + V_w K_{mw}(V_m - V_w) + K_{mw}(V_w - V_m)^2 \\ + V_w K_{fw}(V_f - V_w) + K_{fw}(V_w - V_f)^2,\end{aligned} \tag{7}$$

$$\frac{\partial}{\partial t}(\alpha_m \rho_m e_{sm}) + \frac{1}{A}\frac{\partial}{\partial x}(A\alpha_m \rho_m V_m h_{sm})$$
$$= -p\frac{\partial \alpha_m}{\partial t} + R_{mw}(T_w - T_m)$$
$$+V_m K_{mw}(V_w - V_m) - \Gamma_f h_{sm} \quad (8)$$

and

$$\frac{\partial}{\partial t}(\alpha_f \rho_m e_{sf}) + \frac{1}{A}\frac{\partial}{\partial x}(A\alpha_f \rho_m V_f h_{sf}) = -p\frac{\partial \alpha_f}{\partial t}$$
$$+R_{fw}(T_w - T_f) + V_f K_{fw}(V_w - V_f) + \Gamma_f h_{sm}. \quad (9)$$

In the above equations the terms involving R_{mw} etc. represent thermal equilibration and the terms containing K_{mw} etc. are the drag work. All of the irreversible drag work has been added to the water equation.

It is assumed that the melt is composed of spherical droplets, so that the droplet diameter satisfies the following equation:

$$\frac{\partial}{\partial t}(\alpha_m \rho_m L_m) + \frac{1}{A}\frac{\partial}{\partial x}(A\alpha_m \rho_m V_m L_m) = -\Gamma_f L_m - \Gamma_{\text{frag}}. \quad (10)$$

In the above equation the term involving Γ_f arises as a consequence of writing the transport equation in conservation form and the term $-\Gamma_{\text{frag}}$ models the chosen fragmentation process.

In addition to the above equations there is the constraint that

$$\alpha_m + \alpha_f + \alpha_w = 1. \quad (11)$$

B. Constitutive Relations

In this section a brief summary of the constitutive relations for drag, heat transfer and fragmentation employed in the model is given. Full details are available elsewhere (Fletcher, 1991a).

1. Momentum Exchange. The drag between the melt droplets and the water phase was modelled using the usual drag law representation and a drag coefficient $c_{d,mw} = 2.5$. This value is higher than the usual value of 0.4 to account for the increased drag when droplets are fragmenting (Pilch and Erdman, 1987). Similarly, the drag between the melt fragments and the water was calculated using $c_{d,fw} = 0.4$.

2. Heat Transfer. The heat transfer mechanisms between the melt and water are very complex and depend on the time-history of each particle. The only experimental data available are rather crude and consists of time-averaged heat transfer coefficients for the duration of the fragmentation process (Fletcher and Anderson, 1990). Thus at present only crude models of this process can be formulated. In the present version of CULDESAC it is possible to specify either constant heat transfer coefficients for the fragments and droplets or to make the fragment to water heat transfer rate a function of the local water density. This is achieved by using the following simple formula (Fletcher, 1991b)

$$h_{fw} = h_{\text{steam}} + (h_{\text{liquid}} - h_{\text{steam}})\frac{(\rho_w - \rho_{\text{steam}})}{(\rho_{\text{liquid}} - \rho_{\text{steam}})} \quad (12)$$

where ρ_w is the water density, and h_{steam} and h_{liquid} are appropriate heat transfer rates to steam and liquid water respectively. The end point densities were given values of $\rho_{\text{liquid}} = 1000\ \text{kg m}^{-3}$ and $\rho_{\text{steam}} = 0.6\ \text{kg m}^{-3}$. Values of $h_{\text{steam}} = 10^3\ \text{Wm}^{-2}\text{K}^{-1}$ and $h_{\text{liquid}} = 10^5\ \text{Wm}^{-2}\text{K}^{-1}$ are currently used. The model allows for the increase in heat transfer from the large droplets once the vapour film collapses.

3. Fragmentation. Two different models of fragmentation are available in the CULDESAC code. These are based on hydrodynamic and thermal fragmentation, respectively (see Fletcher and Anderson, (1990) for a detailed discussion of both modes of fragmentation). In the real world, it is expected that a combination of the two processes would take place, with possibly thermal fragmentation dominating during the early stage of an interaction, and with hydrodynamic fragmentation dominating when the amplitude of the pressure wave has become significant (Ciccarelli and Frost, 1991).

The first is the boundary layer stripping model proposed by Carachalios et al., (1983) which gives the following stripping rate from a single fragment

$$\frac{\mathrm{d}m}{\mathrm{d}t} = c_{\text{frag}}|V_m - V_w|\pi L_m^2\sqrt{\rho_m \rho_c} \quad (13)$$

where the empirical constant c_{frag} takes a value of approximately 1/6. This stripping rate gives

$$\Gamma_f = \alpha_m c'_{\text{frag}}|V_m - V_w|\sqrt{\rho_c \rho_m}/L_m \quad (14)$$

where all of the constant terms are combined to give $c'_{\text{frag}} \sim 1$.

The length-scale of the droplets is changed by the mass loss due to boundary layer stripping. For spherical drops it is easily shown that the mass loss rate given in equation (14) implies a length-scale source term of

$$\Gamma_{\text{frag}} = \frac{1}{3}\Gamma_f L_m. \quad (15)$$

A simple cut-off has been added to ensure that breakup only occurs for Weber numbers above a critical value ($\text{We}_{\text{crit}} \approx 12$).

The fragment size is not determined by the fragmentation models currently employed and was specified by reference to experimental data, with a typical value of 100 μm being used.

The second model is very empirical and has been developed to simulate the processes which occur in ther-

mal fragmentation. A study of the available data suggests that the key feature of thermal fragmentation which must be reproduced is that, following vapour film collapse, there is a delay before fragmentation takes place. This was represented by setting

$$\Gamma_{frag} = \alpha_m \rho_m H(t^* - t_{lag})/\tau_{frag} \qquad (16)$$

where $H(...)$ is the Heaviside function, t_{lag} is a lag time, and τ_{frag} is a fragmentation timescale. The quantity t^* is a 'time clock' which is initially set to zero in each cell, and is started once the pressure in that cell exceeds the trigger pressure, i.e. when $p > p_{trig}$. Thus no fragmentation takes place until a time t_{lag} has elapsed since the vapour film collapsed. Once this time is exceeded, the droplets fragment at a rate determined by the parameter τ_{frag}. The motion of the droplets was accounted for by solving the following transport equation for the elapsed time (t^*)

$$\frac{\partial}{\partial t}(\alpha_m \rho_m t^*) + \frac{1}{A}\frac{\partial}{\partial x}(A \alpha_m \rho_m V_m t^*) = -\Gamma_f t^* + \alpha_m \rho_m H(p - p_{trig}). \qquad (17)$$

The mass production rate of fragments, Γ_f, was determined using equation (15). This assumption has the effect of treating the thermal fragmentation process as one in which droplets are removed from the outside of the droplet as in boundary layer stripping.

It should be noted that the above treatment of the thermal fragmentation process, where the time delay and fragmentation rate are fixed, is used to perform scoping calculations only. In reality these parameters would be a function of the local pressure, coolant void fraction etc. However, this representation provides a first approximation which can be used to investigate propagation modes and can be improved as knowledge of the fragmentation process improves. Studies like those being performed at McGill University (Ciccarelli and Frost, 1991, 1992) and at the University of Santa Barbara (Yuen et al., 1992) should be very helpful in determining a correlation applicable to a wide range of system conditions.

C. Equations of State

The melt equation of state is very simple. The melt is assumed to be incompressible so that $\rho_m = \rho_f =$ constant, and to have a simple caloric equation of state so that $E_m = c_{vm} T_m$ and $E_f = c_{vm} T_f$. The latent heat is accounted for by use of an 'effective' value for c_p.

The EOS for water is more complicated and there are virtually no thermodynamic data available in a suitable form on the properties of water at high temperatures and pressures. In this study an approximate EOS, based on the Grüneisen approximation, has been used. The equation of state is fully described in Fletcher and Thyagaraja (1989a) and has been shown to agree well with steam table data in the region where they can be compared (Fletcher and Thyagaraja, 1991).

D. Artificial Viscosity

The equations are solved using a semi-implicit finite difference method which captures shock fronts (Fletcher and Thyagaraja, 1989b). An artificial viscosity term is included in the water species momentum equation in order to remove numerical instabilities at the shock front. The artificial viscosity, μ_a, is assumed to be of the following form (von Neumann and Richtmyer, 1950):

$$\mu_a = \rho_w (b_0 \Delta x)^2 \left| \frac{\partial V_w}{\partial x} \right| \quad \text{if } \frac{\partial V_w}{\partial x} < 0,$$
$$= 0 \quad \text{otherwise.} \qquad (18)$$

This form for μ_a has the property that viscosity is only added in regions of flow compression, thus it does not smear out expansion fans and it is only added where there are large velocity gradients, i.e. at the shock front itself. Numerical experiments show that the coefficient b_0 should be in the range 5–15 (Fletcher, 1991a).

E. Boundary and Initial Conditions

The above equations are solved in a solution domain which represents an initial stationary mixture contained in a closed vessel. Thus the only boundary condition needed is to set the velocities to zero at the vessel walls. Initially, the volume fractions, void fraction, velocity and particle size distribution are specified. To simulate triggering a fraction of the melt is fragmented in a small region of the solution domain. This causes a high heat transfer rate in these cells, the pressure rises locally and a propagating wave may subsequently develop.

III. PRESENTATION OF RESULTS

This section contains a presentation of results obtained from the model. The emphasis here is to draw attention to key phenomena; full details of the calculations are given in the supporting references. Typically the calculations are for a mixture containing a 10% volume fraction of 5 mm melt droplets at a temperature of 3400 K with saturated water at 0.1 MPa and a void fraction of 70%. These conditions are appropriate to the SUW experiments (Bird, 1984). Unless otherwise stated all of the calculations are for a planar geometry.

A. Numerical Aspects of the Problem

Experience shows that the calculation of multiphase propagation waves is not straight-forward. A key issue appears to be that of capturing the shock wave using a practical grid size. If the grid size is too large, the prop-

agation speed is controlled by the grid size rather than the physical processes (Thyagaraja and Fletcher, 1989; Fletcher, 1991c). Figure 2 shows the effect of grid refinement for an example propagation calculation. It is clear that the pressure profile is very poorly calculated in the coarse grid case, and that the initial shock front has been completely lost.

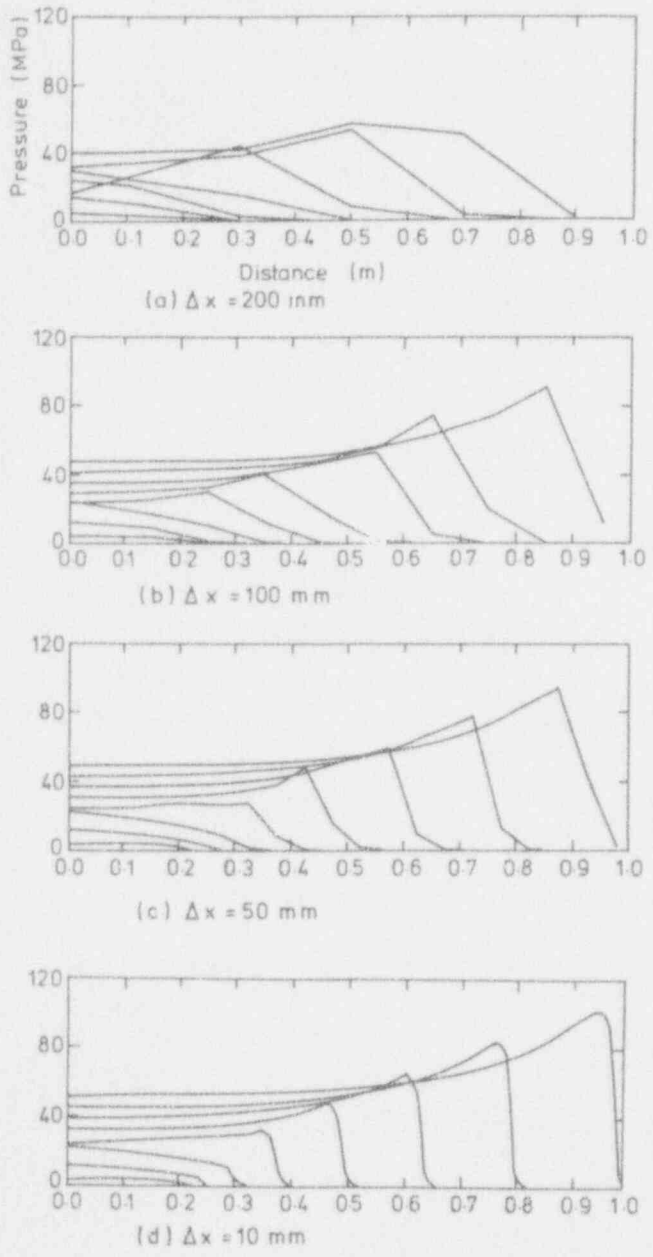

Figure 2. The effect of grid size on the calculated propagation behaviour. These calculations used the density-dependent heat transfer rate and an initial void fraction of 0.9. (Pressure profiles are shown every 0.5 ms.) Taken from Fletcher, (1991c).

The amount of artificial viscosity used in the calculation is a very important solution parameter (Fletcher, 1991a). It is worth noting here that without artificial viscosity unphysical high frequency pressure spikes were calculated and that these lead to severe numerical instabilities. The effect of introducing artificial viscosity is illustrated in Figure 3. In addition a low Mach number instability was identified in this investigation and was cured by changing the scheme from being explicit to semi-implicit (Thyagaraja and Fletcher, 1991).

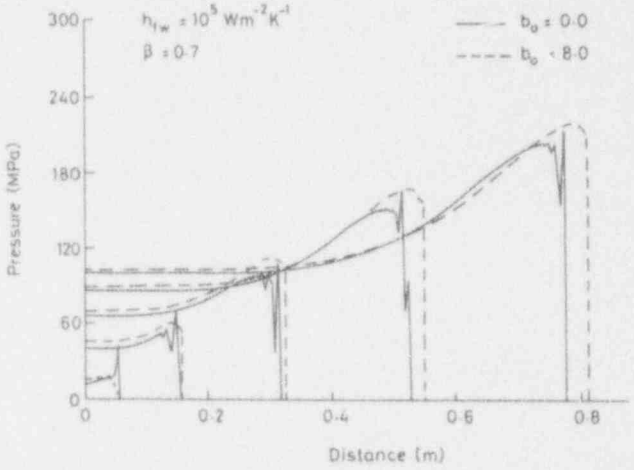

Figure 3. A comparison of the development of the pressure profile for simulations with and without artificial viscosity. The grid size is 5 mm. Taken from Fletcher, (1991c).

B. The Effect of Mixture Conditions

A wide range of calculations have been performed using the model to investigate the propagation behaviour for a high temperature melt mixed with water. It is clear from the calculations performed that the initial mixture configuration, i.e. melt volume fraction, void fraction and the initial melt droplet size are all important variables. In general increasing the melt fraction leads to an increase in the pressure and propagation speed whereas increasing the droplet size leads to a decrease in the peak pressure and an increase in the escalation length (Fletcher, 1991b). Increasing the initial droplet size from 5 mm to 20 mm resulted in a halving of the pressure behind the front and a decrease in the fraction of melt fragmented from 96% to 68% (Table 1 of Fletcher, 1991b).

Changing the void fraction *for a fixed fragment to coolant heat transfer rate* leads to the prediction of a wide variety of pressure profile shapes and propagation speeds as illustrated in Figure 4. The pressure profile shape changes because of the differences in the local water temperature and in the location of the fragments. (In high void fraction calculations the motion of the fragments is

significant and assists with the compression at the shock front (Fletcher, 1991a).) Depending on the spatial distribution of heat input to the water behind the front, the pressure traces may exhibit a von Neumann spike or appear almost flat. If the front velocity is plotted against the void fraction the resulting curve is very similar in shape to that obtained for pressure waves in air-water mixtures (Fletcher, 1991a).

Finally, it is worth noting that no real mixture is homogeneous and that mixture inhomogeneities have been shown to have a significant effect on the generated pressures (Fletcher, 1991b). Simulations for a wave propagating from one region of mixture to another show that the redevelopment behaviour of the wave is very sensitive to the void fraction in the intervening zone. If the void fraction is low, a pressure wave passes through the region with modest attenuation whereas if the region consists largely of steam the fragments pass through the steam zone and restart the propagation via a 'hammer-like' pressure. This behaviour is illustrated in Figure 5.

If the mixture inhomogeneities are significant the peak pressure can be reduced considerably, and the propagation wave may never develop fully. Figure 6 shows the calculated pressure escalation for a very inhomogeneous mixture and should be compared with Figure 8(b) which shows the escalation for a similar mixture without the voided regions present. The reduction in the peak pressure and the increased escalation time is evident.

C. The Effect of the Heat Transfer Model

The calculated propagation behaviour is obviously sensitive to the chosen heat transfer rate. Changing the heat transfer coefficient from the fragments to the coolant from 10^5 W m^{-2}K^{-1} to 10^6 W m^{-2}K^{-1} was shown to change the escalation behaviour and the presure distribution considerably. This is illustrated in Figure 7.

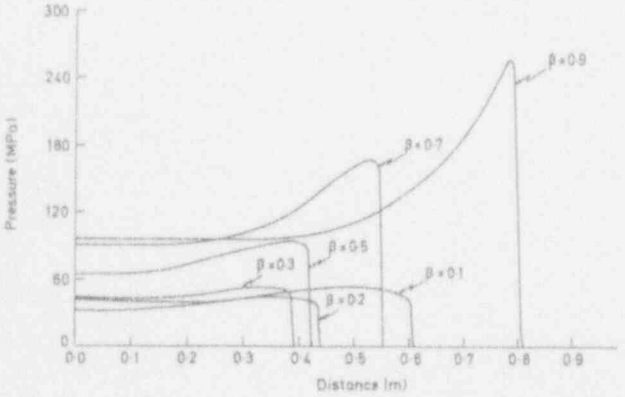

Figure 4. The effect of the initial void fraction (β) on the shape of the calculated pressure profile for a fixed fragment to water heat transfer coefficient. All the plots are shown at the same time after triggering. Taken from Fletcher, (1991a).

If the heat transfer coefficient is made to depend on the local water density (see equation 12) then propagation pressures and velocities are reduced at the high void fraction limit. The effect of using the density-dependent heat transfer coefficient is illustrated in Figure 8. It is clear that allowing for the poor heat transfer in highly voided regions is important, and that the effect of voiding is to increase the escalation length and reduce the calculated pressures. However, at present, there are insufficient data to quantify this variation precisely. A simple limit, such as assuming that the heat transfer is cut-off when the void fraction exceeds, say, 70% (on the grounds that the water is now in dispersed form) is too simplistic and would give a limit to propagation which does not require the use of a model.

D. The Effect of Geometry

The assumed geometry has a significant effect on the propagation behaviour, and in particular on the escalation behaviour. A repeat of the calculation shown in Figure 8(b) for a spherically symmetric geometry rather

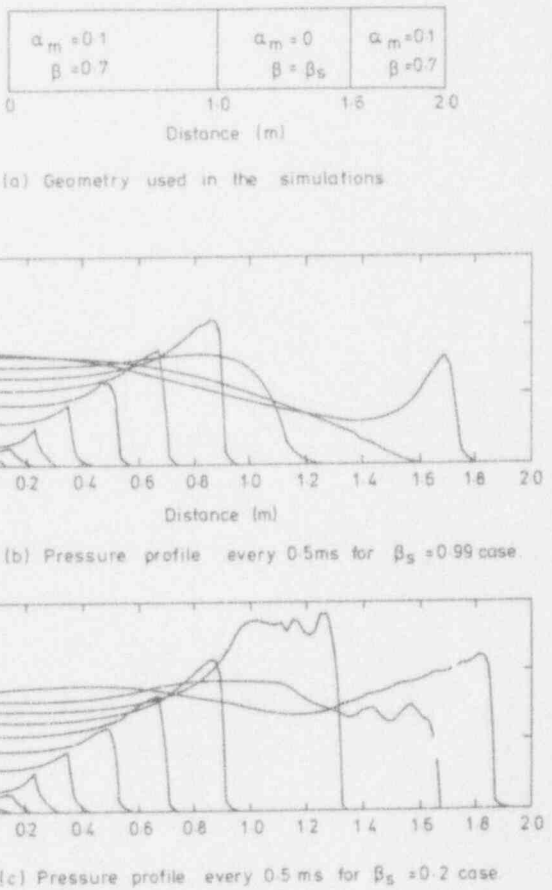

Figure 5. The effect of the composition of the buffer zone between two regions of mixture on the restarting behaviour of the propagation wave. (Pressure profiles are shown every 0.5 ms. Taken from Fletcher, (1991c).

than a planar one is shown in Figure 9. It is clear that in this case the development of the wave is much slower and that peak pressures are reduced.

A propagation could be started very easily in a planar geometry. In a spherical geometry, it was found that if the boundary layer stripping fragmentation model was used a propagating wave developed for very small triggers (10% of the melt fragmented in the centre 20 mm). However, if the thermal fragmentation model was used the critical value of t_{lag} for propagation to occur in a spherical geometry was relatively short ~0.2 ms. This illustrates the importance of knowing the trigger strength accurately if data from small-scale experiments (in which a steady-state propagation wave has not developed) are to be used to benchmark such models.

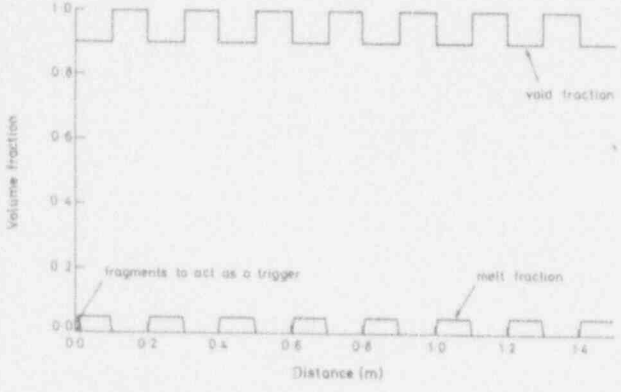

(a) Mixture configuration used in the simulation.

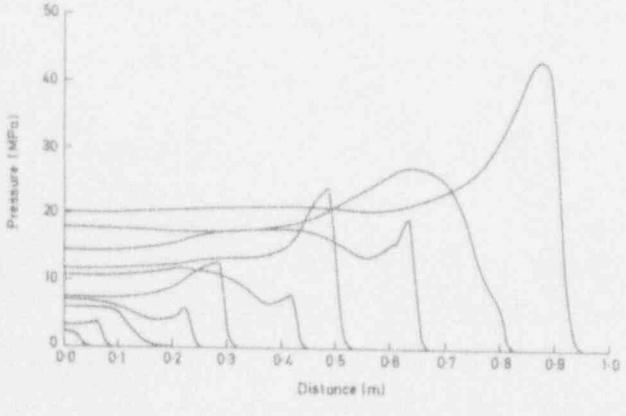

(b) Pressure profiles.

Figure 6. Development of the pressure profile for an inhomogeneous initial mixture and a density-dependent heat transfer coefficient. (Pressure profiles are shown every 0.5 ms.)

E. Deflagration Modes of Propagation

Over recent years a number of workers have suggested that a spectrum of propagation modes, ranging from deflagrations to detonations, can occur. A detailed review of these ideas is given in (Fletcher, 1992). CULDESAC has been used to investigate this question using the two different fragmentation models available in the code. The thermal fragmentation model has been used to perform calculations in which there is a significant delay between the shock wave passing a droplet and it fragmenting. These calculations showed that a deflagration-like mode could be *calculated*. In the calculations an explosion was triggered by assuming that 90% of the melt was fragmented instantaneously in the first 20 mm of the tube. A comparison of the development of the pressure front for the two different cases is given in Figure 10, which shows the difference between the two modes. In the thermal fragmentation case the lag-time (t_{lag}) was 2 ms and $\tau_{frag} = 10^{-4}$ s.

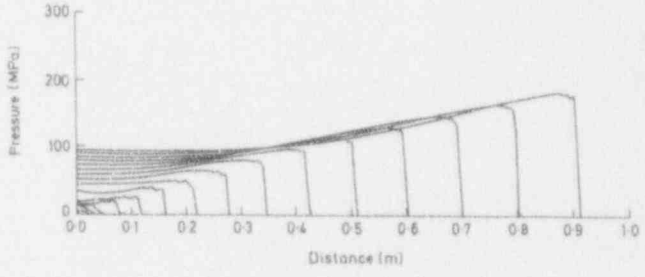

(a) Using a constant heat transfer coefficient of 10^5 W m^{-2} K^{-1}.

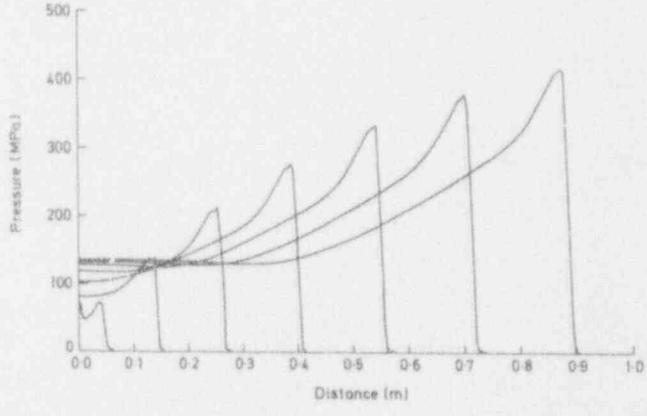

(b) Using a constant heat transfer coefficient of 10^6 W m^{-2} K^{-1}.

Figure 7. The effect of the heat transfer coefficient on the development of a propagating wave. (Pressure profiles are shown every 0.2 ms.) Taken from Fletcher, (1991a).

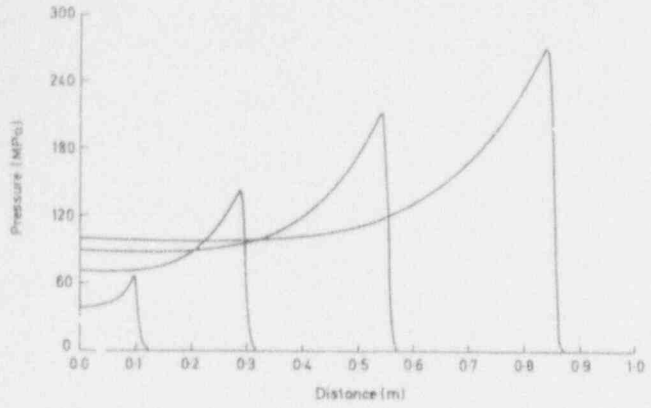

(a) Using a constant heat transfer coefficient of 10^5 W m^{-2} K^{-1}.

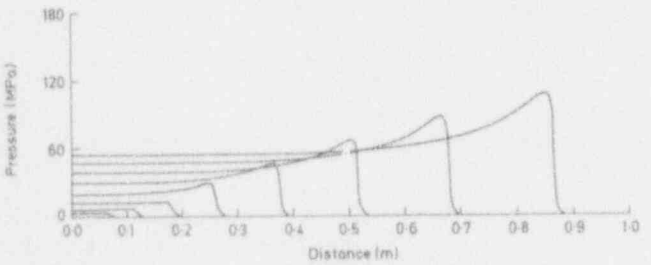

(b) Using the density-dependent heat transfer coefficient given in equation (12).

Figure 8. The effect of assuming a density-dependent heat transfer coefficient for the case of an initial void fraction of 0.9. (Pressure profiles are shown every 0.5 ms.) Taken from Fletcher, (1991b).

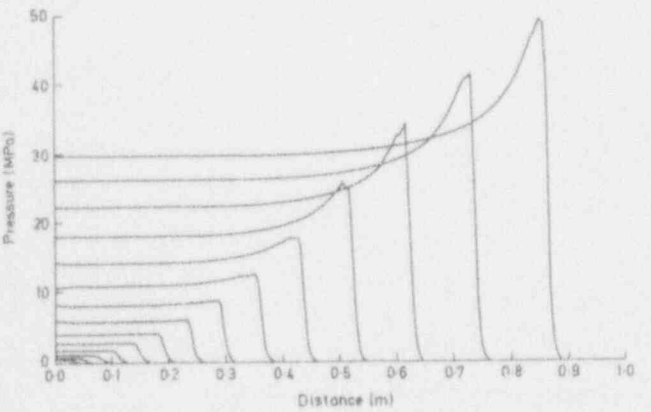

Figure 9. The effect of the geometry on the development of a propagating wave. (Pressure profiles are shown every 0.5 ms.) Taken from Fletcher, (1991b).

Figure 11 shows volume fraction plots for the hydrodynamic fragmentation and thermal fragmentation cases at a time of 3 ms after triggering. It is clear from this Figure that very different behaviour is predicted for the two different cases, with the melt fraction being increased ahead of the plane of fragmentation in the case using the thermal fragmentation model. The velocity distributions at the same time are shown in Figure 12. In the hydrodynamic fragmentation case the fluids are following the shock wave, except near the right hand wall where flow reversal is required to satisfy the boundary condition. In the thermal fragmentation case the flow is reversed at the fragmentation front, and the fluids stream away from the shock wave. This difference in behaviour is characteristic of the difference between detonations and deflagrations.

The difference is further illustrated in Figure 13 which shows a pressure-time plot for a hypothetical transducer located in the mixture. The two different modes are shown to give rise to very distinctive pressure traces. Comparison with the available data suggests that it is the detonation-like mode which is observed, as experimental traces do not show a rise some way behind the initial shock front. These calculations show the value of modelling in attempting to distinguish between different hypotheses.

IV. DISCUSSION

There are relatively few experimental data available for model validation. To date the best instrumented tests are the tin-water experiments of Baines (1984). However, both the analysis of Baines and use of the current model show that thermal disequilibrium effects in the water are important in this situation (Fletcher, 1991b). Thus results from such experiments cannot be compared with calculations obtained from the current model. It is worth noting that Theofanous and co-workers have come to the same conclusion in a recent paper (Yuen et al., 1992). In order to reproduce a propagating wave for an experiment performed in the KROTOS facility in which a propagating wave was observed, they modified their code so that the energy from 2.5% of the fragments was used directly to produce vapour. The authors recognised the approximate nature of this assumption and the need for further work in this area.

The CULDESAC model described in this paper is very idealised compared with reality and contains a number of assumptions which make comparison with experiment difficult, e.g. the assumptions of one-dimensional flow, thermal equilibrium in the water phase, an initial state in which the melt is in the form of a dispersion of steam blanketed droplets in a pool of liquid water and the absence of any melt in a stratified geometry. In addition, the high degree of constraint inherent in a one-dimensional model will lead to an over-estimation of the pressures that

can be obtained in any real three-dimensional situation, where much of the explosion energy will not be available to drive the propagating wave. Thus there may be little point in generating experimental conditions which could be used to validate this model, when they would be very different from those which could be obtained in the reactor safety application. For example, if propagation calculations are to be used to estimate the pressures on the lower head of a reactor vessel the results must be realistic not conservative, because use of conservative pressures would lead to lower head failure being predicted erroneously.

However, if it is required to produce data which can be used to validate the present model then the following conditions/diagnostics are required:

- A highly constrained one-dimensional geometry.
- A knowledge of the initial premixture state, including the void fraction, melt fraction, melt particle size and spatial variations within the mixture.
- A sufficiently high melt fraction that the assumption that the fragments transfer their heat to all of the water is approximately valid.
- A trigger with well-defined characteristics, i.e. the trigger strength and duration.
- Experimental data which comprises reliable pressure traces (although these are often difficult to interpret because of wall reflection effects) and high speed photographic records.

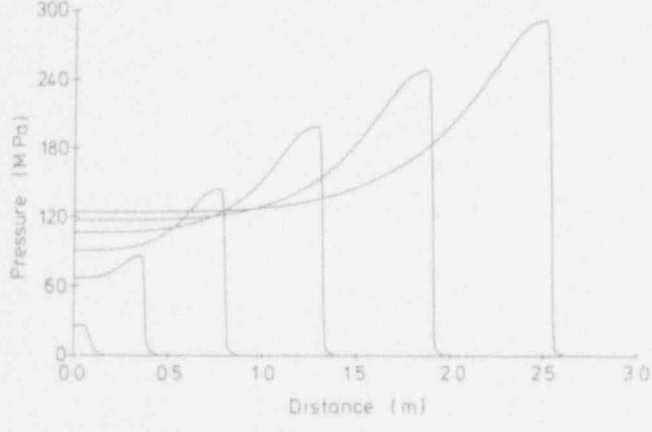

(a) Hydrodynamic fragmentation.

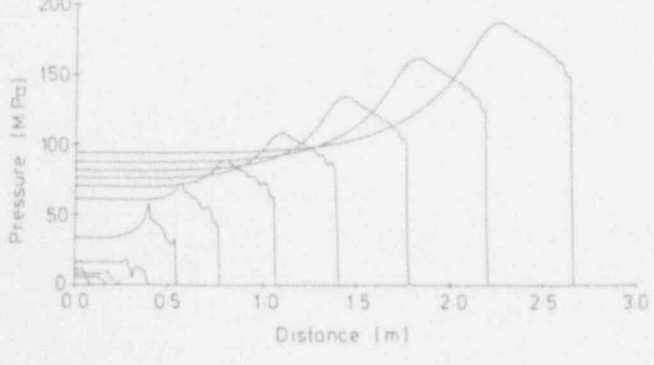

(b) Thermal fragmentation.

Figure 10. The effect of the fragmentation mode on the transient development of the pressure profile. (Pressure profiles are shown every 0.5 ms.) Taken from Fletcher, (1992).

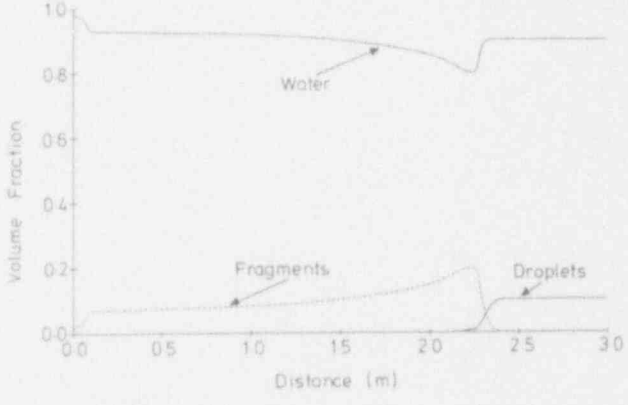

(a) Hydrodynamic fragmentation.

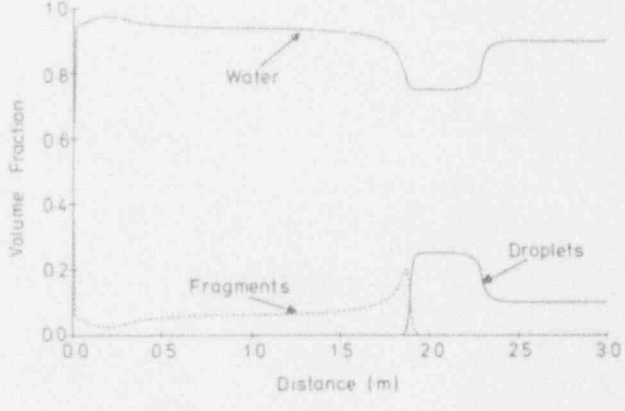

(b) Thermal fragmentation.

Figure 11. The effect of the fragmentation mode on the calculated volume fraction distributions. Taken from Fletcher, (1992).

V. CONCLUSION

This paper contains a description of the CULDESAC propagation model and a summary of some of the key issues associated with the modelling of propagation. These results may be summarised as follows:

- Care is needed to ensure that suitable choices are made for the numerical solution parameters, particularly the grid size.
- The model predictions are very sensitive to the assumed heat transfer rate, especially if the heat transfer model takes the flow-regime into account. If high heat transfer coefficients are assumed the model predicts the rapid development of very high pressure propagation waves. The use of lower heat transfer coefficients, particularly the model which is density-dependent, leads to calculated pressures much closer to those observed in experiments.
- The predicted behaviour is sensitive to the initial melt droplet size and the fragment size but this dependence is not as significant as that on the heat transfer rate.
- Geometrical considerations are important. Calculations show that a propagating wave escalates more slowly in a spherical geometry than in a planar geometry and is more difficult to trigger in the former case.
- Mixture inhomogeneities reduce the peak pressures and lead to complicated transient pressure profiles.
- Using a suitable model for thermal fragmentation CULDESAC can predict a deflagration-like mode of propagation. However, it is noted that such propagations lead to presure-time transients which are different from those observed experimentally.
- Detailed experimental data are needed for model validation but the task of specifying the type of experiments required is difficult because of the gross simplifications made in the modelling.

The investigations performed using the CULDESAC model has highlighted the following areas where more work would be useful:

- Improved modelling of fragment to water heat transfer, based on *relevant* experimental data is probably the highest priority.
- The development of a framework to allow for non-homogeneous heating of the cold fluid would be useful for experimental analysis, especially for the tin-water system.
- A composite fragmentation model which covers both hydrodynamic and thermal fragmentation is required to study escalation behaviour.
- Calculations in two dimensions are required to examine the effect of mixture inhomogeneity in these circumstances. (Some two dimensional calculations have been performed for the reactor application by Theofanous and co-workers using their model (Medhekar et al., 1989). However, additional work is required to determine acceptable grid sizes and trigger sizes before this approach can be used with confidence.)
- The development of a model that allows the liquid water and steam to have separate velocity and temperature fields during the escalation stage would be useful. This task would require the specification of flow regime dependent constitutive relations for interfacial drag, heat transfer and phase change modelling.

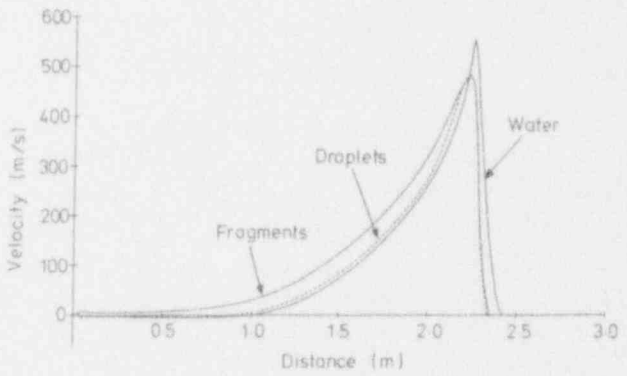

(a) Hydrodynamic fragmentation.

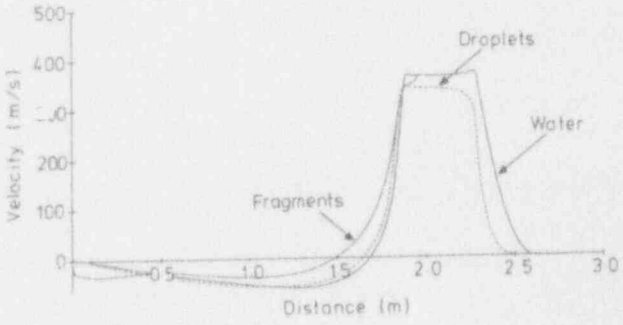

(b) Thermal fragmentation.

Figure 12. The effect of the fragmentation mode on the calculated velocity distributions. Taken from Fletcher, (1992).

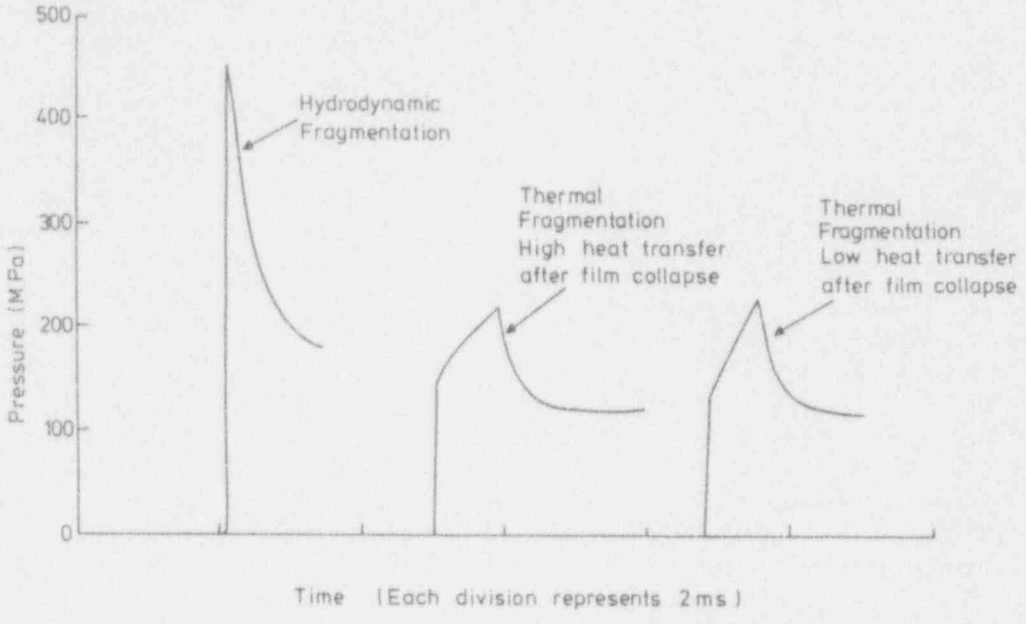

Figure 13. The effect of the fragmentation mode on the calculated pressure-time curve as observed by a pressure transducer. Taken from Fletcher, (1992).

- A better understanding of triggering is needed, to enable a better prescription of the initiating event and to determine whether triggering can occur in highly voided mixtures.

It is clear that much more could be done to improve the modelling of propagation. However, this work needs to be led by new data from well-designed propagation experiments.

ACKNOWLEDGEMENTS

This model developed as part of the GNSR programme funded by the Department of Energy. The numerical scheme used in this model was developed in cooperation with Dr. A. Thyagaraja of AEA Fusion. The author is grateful to Dr. R.P. Anderson for numerous stimulating discussions on this topic and Dr. B.D. Turland for helpful comments on a draft of this paper.

NOMENCLATURE

A	area factor
c_d	drag coefficient
c_{frag}	constant in the hydrodynamic fragmentation model
c_v	specific heat at constant volume
e_s	stagnation energy
h	heat transfer coefficient
h_s	stagnation enthalpy
K	momentum exchange function
L	length-scale
m	mass stripped from a single droplet
p	pressure
p_{trig}	vapour film-collapse pressure
R	energy exchange function
T	temperature
t	time
t_{lag}	time delay before fragmentation
t^*	'time clock' variable used in the thermal fragmentation model
V	velocity
x	spatial coordinate

Greek Symbols

α	volume fraction
β	void fraction
ρ	density
μ_a	artificial viscosity
τ_{frag}	fragmentation timescale
Γ_f	mass exchange rate between melt droplets and fragments
Γ_{frag}	length-scale source term

Subscripts

e	effective fluid (water plus fragments)
f	fragments
m	melt droplets
w	water

REFERENCES

Baines, M., (1984) *Preliminary measurements of steam explosion work yields in a constrained system.* Inst. Chem. Eng. Symp. Series, **86**, 97–108.

Bird, M.J., (1984) *An experimental study of scaling in core melt/water interactions.* Paper presented at 22nd National Heat Transfer Conference, Niagara Falls, 5–8 August, 1984.

Board, S.J., Hall, R.W. and Hall, R.S., (1975) *Detonation of fuel coolant explosions.* Nature, **254**, 319–321.

Caracharios, C., Bürger, M. and Unger, H., (1983) *A transient two-phase model to describe thermal detonations based on hydrodynamic fragmentation.* Proc. Int. Meeting on LWR Severe Accident Evaluation, Cambridge, Massachusetts, 28 August–1 September, 1983.

Ciccarelli, G. and Frost, D.L., (1991) *The effect of fluid flow velocity on the fragmentation mechanism of a hot drop.* Paper presented at the 13th International Colloquium on Dynamics of Explosions and Reactive Systems, 28th July–2nd August, 1991, Nagoya, Japan.

Ciccarelli, G. and Frost, D.L., (1992) *Fragmentation mechanisms based on single drop experiments using flash X-ray photography.* ANS Proc 5th Int. Topical Mtg. on Reactor Thermal Hydraulics (NURETH–5), 21–24 September, 1992, Salt Lake City, USA., 615–626.

Corradini, M.L., (1991) *Vapor explosions: a review of experiments for accident analysis.* Nucl. Safety, **32**, 337–362.

Corradini, M.L., Kim, B.J. and Oh, M.D., (1988) *Vapour explosions in light water reactors: a review of theory and modelling.* Prog. Nucl. Energy, **22**, 1–117.

Fletcher, D.F., (1991a) *An improved mathematical model of melt/water detonations—I. Model formulation and example results.* Int. J Heat Mass Transfer, **34**, 2435–2448.

Fletcher, D.F., (1991b) *An improved mathematical model of melt/water detonations—II. A study of escalation.* Int. J Heat Mass Transfer, **34**, 2449–2459.

Fletcher, D.F., (1991c) *Developments of the* CULDESAC *physical explosion model.* Paper presented at the 13th International Colloquium on Dynamics of Explosions and Reactive Systems, 28th July–2nd August, 1991, Nagoya, Japan. (To appear in Progress in Astronautics and Aeronautics.)

Fletcher, D.F., (1992) *Vapour explosions: multiphase detonations or deflagrations?* To appear in Shock Waves.

Fletcher, D.F. and Anderson, R.P., (1990) *A review of pressure-induced propagation models of the vapour explosion process.* Prog. Nucl. Energy, **23**, 137–179.

Fletcher, D.F. and Denham, M.K., (1993) *Validation of the* CHYMES *coarse mixing model.* Paper to be presented at the CSNI Specialist meeting on Fuel-Coolant Interactions, Santa Barbara, USA, 5–8 January, 1993.

Fletcher, D.F. and Thyagaraja, A., (1989a) *A mathematical model of melt/water detonations.* Appl. Math. Modelling, **13**, 339–347.

Fletcher, D.F. and Thyagaraja, A., (1989b) *Some calculations of shocks and detonations for gas mixtures.* Comput. Fluids, **17**, 333–350.

Fletcher, D.F. and Thyagaraja, A., (1991) *Multiphase detonation modeling using the* CULDESAC *code.* Prog. Astronaut. Aeronaut., **134**, 387–407.

von Neumann, J. and Richtmyer, R.D., (1950) *A method for the numerical calculation of hydrodynamical shocks.* J. Appl. Phys., **21**, 232–237.

Medhekar, S., Abolfadl, M. and Theofanous, T.G., (1991) *Triggering and propagation of steam explosions.* Nucl. Engng. Des, **126**, 41–49.

Medhekar, S., Amarasooriya, W.H. and Theofanous, T.G., (1989) *Integrated analysis of steam explosions.* Proc 4th Int. Topical Mtg. on Reactor Thermal Hydraulics (NURETH–4), 10–13 October, 1989, Karlsruhre, FRG., 319–326.

Mitchell, D.E., Corradini, M.L. and Tarbell, W.W., (1981) *Intermediate scale steam explosion phenomena. experiments and analysis.* NUREG/CR–2145.

Pilch, M. and Erdman, C.A., (1987) *Use of breakup time data and velocity history data to predict the maximum size of stable fragments for acceleration-induced breakup of a liquid drop.* Int. J. Multiphase Flow, **13**, 741–757.

Thyagaraja, A. and Fletcher, D.F., (1989) *Numerical aspects of multiphase detonation modelling.* Procs. of 6th Int. Conf. on Numerical Methods in Laminar and Turbulent Flow, Swansea, 11–15 July, 1989, (eds. C. Taylor, P. Gresho, R.L. Sani and J. Haüser), **6**(2), 1753–1763, Pineridge, Swansea, UK.

Thyagaraja, A. and Fletcher, D.F., (1991) *Low Mach number instability of an explicit numerical scheme.* Appl. Math. Modelling, **15**, 40–45.

Yuen, W.W., Chen, X. and Theofanous, T.G., (1992) *On the fundamental microinteractions that support the propagation of steam explosions.* ANS Proc 5th Int. Topical Mtg. on Reactor Thermal Hydraulics (NURETH–5), 21–24 September, 1992, Salt Lake City, USA., 627–636.

FCI EXPERIMENTS IN THE ALUMINUMOXIDE/WATER SYSTEM

H. Hohmann, D. Magallon, H. Schins, A. Yerkess

Commission of the European Communities
Joint Research Centre
Safety Technology Institute
21020 Ispra (VA) - ITALY -

ABSTRACT

The KROTOS facility at JRC Ispra was recently used to study experimentally melt-coolant premixing and steam explosion phenomena in Al_2O_3 - water mixtures with 1,5 kg melt at 2300 - 2400°C. In the five tests performed the main parameter was the water subcooling, 10,40 and 80 K, respectively. In the nearly saturated system, steam explosions could be externally triggered, which resulted in high (supercritical) explosion pressures in the test tube: KROTOS 26,28. Without triggering, melt penetration in water and melt agglomeration on the bottom plate of the test tube could be observed, which gave rise to strong steaming during the melt cooling-down process: KROTOS 27. In the two tests KROTOS 29,30, performed with 80 K subcooled water, self-triggered steam explosions occurred with pressures of more than 100 MPa. Post-test analysis of the debris revealed that 85 % of the interacting fuel mass fragmented in particles of sizes smaller than 250 μ. An energy conversion ratio of 1.25 % was estimated from vessel pressurization data taking into account the energy content in the fuel mass which broke up to particle diameters of less than 250 μ. The test section was damaged in the test KROTOS 30.

I. INTRODUCTION

FCI research in the context of Severe Accidents in Nuclear Power Plants has been performed at JRC Ispra for many years. In the Ispra-Tank-Facility the quenching/explosion behaviour of melt/water mixtures has been extensively studied, especially the molten salt/water system. The research objectives were to study the influence of water subcooling and system pressure (up to 4 MPa) on the quenching, and on the initiation and suppression of steam explosions. From the tests performed a better understanding of processes which occur in coarsely premixed melt/water systems was gained (Hohmann et al., 1982; Burger et al., 1984).

Firstly, it was found that the pouring of the NaCl-melt into subcooled water at 0.1 MPa system pressure always led to spontaneously triggered steam explosions. Secondly, it was demonstrated that in nearly saturated water at elevated system pressures ($0.3<P<3$ MPa) stable mixtures in film boiling could be established for long time periods (seconds). The application of adequate external triggers to these systems could generate thermal explosions. However, a system pressure threshold existed above which these triggers were no more effective. These tests have been analysed with the steady state explosion model FRADEMO of the IKE-Stuttgart (Burger et al., 1986).

After, many experiments were conducted in the KROTOS facility at a 0.1 MPa system pressure with Sn/H_2O. By pouring the melt into nearly saturated water in a shock tube coarse mixing was obtained and thermal detonations of this mixture could be externally triggered. The results and analysis of the characteristic test KROTOS 21 using FRADEMO and IDEMO are given in references (Carachalios et al., 1983; Burger et al., 1991). This test was also analysed using the codes PM-ALPHA and ESPROSE (University of California, Santa Barbara) (Yuen et al., 1992) and using the code TEXAS III (University of Wisconsin, Madison) (Tang et al., 1993).

In support to the large scale tests FARO (Magallon et al., 1993), in which melts of real reactor material are quenched in saturated water at 5.0 MPa system pressure, the KROTOS facility was recently used for FCI-studies with Al_2O_3/water. Again the objective of these tests was to investigate premixing in subcooled and saturated water, and to study the energetics of triggered or spontaneous explosions. In this paper the experimental set-up and procedures are described, the ex-

perimental results for the five tests performed so far are reported and discussed.

II. DESCRIPTION OF THE KROTOS EXPERIMENTAL SET-UP

Fig.1 shows the general experimental set-up as is was used for the Al_2O_3 test series, consisting of a radiation furnace, the release tube and the test section below.

A. Furnace

The furnace consists of cylindrical tungsten or graphite heater elements inside which special crucibles containing the melt material are held in place by means of a pneumatically operated release hook. Eight concentric tungsten, molybdenum and steel radiation shields are radially placed around the heater, as well as an array of thermal screens on the bottom and top of the heater to reduce heat losses to the surroundings. A bell-shaped, water-cooled lid covers the furnace designed to withstand 0.25 MPa overpressure (Ar, He) or vacuum. The 3-phase electric power supply has a maximum voltage of 30 V and a maximum power of 130 kW.

Melt masses in the range of about 1 to 10 kg can be used. Maximum temperatures reached in the furnace are of the order of 3000°C. The melt temperature is controlled by an optical pyrometer measuring the wall temperature of the crucible.

B. Release procedure

Having reached the desired melt temperature, the crucible containing the melt is released from the furnace and drops by gravity through a 4 m long release tube of 95 mm inner diameter. Half-way down the tube, a rapid-acting slide valve separates the furnace from the test section below. During its fall, the crucible fractures a copper wire generating the zero time signal for the data acquisition. Finally the crucible impacts onto a retainer ring at the end of the tube where a conical shaped metallic puncher breaks the bottom of the crucible and penetrates into the melt (Fig.2a) The exit of the melt is delayed by some hundreds of ms by a disc placed beneath the puncher which has to be melted by the melt itself. In this way the melt is released by gravity through a funnel of high temperature refractory material which defines the melt jet diameter (30 mm). Simulant tests done under these conditions show only a disturbance of the jet leading edge but no perceptible breakup.

C. Test section

The test section consists of the pressure vessel and the test tube, both made of stainless steel. The pressure vessel is designed for 2.5 MPa at 220°C: it is a tubular vessel of 400 mm inner diameter, a height of 221 cm (volume: 0.290 m^3) with a flat bottom plate and flanged flat upper head plate. A number of feed-throughs exist in this vessel for auxiliary gas and water connections, and for instrumentation.

A test tube is fixed inside the pressure vessel: this is a strong tube of inner diameter 95 mm and thickness 18.5 mm. The tube contains water at variable heights up to about 125 cm (corresponding to a volume of ~ 9 l).

In some of the earlier experiments (salt/water and tin/water) spontaneous interactions occurred near the water surface, therefore additional means had to be introduced to allow better penetration of the melt into the water. One of these consisted in providing the test tube with a 2 mm thick plexiglass tube of 89 mm internal diameter (see Fig.1), thus avoiding direct contact between the melt and the wall.

At the upper part of the test tube, 20 holes (diameter 50 mm) allow for the vapour produced to be released into the pressure vessel volume. Surrounding the perforated section, a steel vessel of 205 mm inner diameter is mounted, filled with water as indicated in Fig.1.

The trigger device is attached at the lower end of the test tube and is described in (Schins et al., 1986). The gas chamber volume of 15 cm^3 can be pressurized up to 15 MPa (Argon). It is closed by a 0.1 mm thick steel membrane. After melt penetration down into the lower region of the test tube, the mechanical destruction of the membrane generates a pressure pulse which propagates vertically upwards through the mixture melt - water - steam.

D. Instrumentation

Pressures, temperatures and level swell are the main experimental quantities measured in the KROTOS test section during melt-coolant interactions.

1. Pressure. Up to fourteen piezoelectric pressure transducers of different types (KISTLER, MECLEC) and pressure ranges (up to 100 MPa) are used in the test tube to measure the pressure in the interaction zone and in the gas trigger (K- pressure transducers in Fig.1). The pressure increase in the

cover gas atmosphere can be detected at six positions in the pressure vessel by means of piezo-resistive pressure transducers (KELLER, MECLEC: C-pressure transducers in Fig.1). All pressure transducers have response frequencies of ≥ 5 kHz and the signals are normally recorded on transient recorders with sampling times of 20 μs.

The positions (in mm) of the K-pressure transducers with respect to the trigger membrane for KROTOS 26 to 28 and with respect to the bottom plate upper surface of the test tube for KROTOS 29-30 were:

KROTOS 26-28		KROTOS 29-30	
Membrane	0	BOTTOM PLATE	0
K 11 - K 1	190		150
K 10	290		-
K 12	-		350
K 2	390		350
K 20	490		-
K 13	590		550
K 3	590		550
K 30	690		-
K 4	790		750
K 15	990		-
K 5	990		950

2. Temperature. Several thermocouples (normally K-type) are used to control the temperatures of the water in the test tube, the position of the melt jet leading edge during its penetration into the water and to monitor the vessel atmosphere temperatures. In order to decrease the response times, thermocouples of 0.5 mm diameter are normally used. The thermocouples TC1 to TC7 are positioned on the axis of symmetry of the test tube.TC1 to TC5 are submerged in water at the same elevations as the pressure transducers K1 to K5. TC6 and TC7 are placed in the vapour space: TC6 slightly above the water free surface and TC7 directly below the nozzle.

3. Water level swell. In all the tests we tried to deduce the integral volumes of melt and vapour in the test tube during the premixing phase measuring the water "level swell" in the upper water container. This level change was measured using an inductive level-meter with a float as indicated in Fig. 2b. This level-meter was mounted in a tube on the outside of the upper water container. It has been assumed that the level increase was only due to pure liquid volume displacement from the test tube into this container. The signal of the level-meter, cannot indicate the level perturbations induced by melt impact but the level swell measurements are considered reliable for the rest of the melt penetration.

III. EXPERIMENTAL RESULTS

Up to now five experiments (KROTOS 26 to KROTOS 30) of the programme have been carried out. In all the tests about 1.5 kg of melt (density 2.6 g/cm3) at temperature 2300-2400°C was contained in a Mo crucible of diameter 84 mm. The initial water temperature was 90°C in KROTOS 27 and 28 , 60°C in KROTOS 26, and 20°C in KROTOS 29 and 30, respectively. The tests were performed at an initial system pressure of 0.1 MPa. The height of the water column in the test tube varied between 1.08 and 1.12 m. The nozzle exit (30mm diameter) for the melt release was situated 0.455 m above water free surface. Tin membranes of 7 and 2 mm thicknesses were used to obtain gravity release from the crucible. The position of the melt with respect to the puncher at the instant of its release into the nozzle is indicated in Fig. 2a. Some unsuccessful attempts were made in the tests to measure melt release rates from the nozzle exit. However we were able to evaluate melt release rates of the order of 1 kg/s from simulation experiments.

The description of the five tests performed is subdivided into two classes as "saturated water conditions" and "subcooled water conditions", respectively. Only the main results of all tests are presented. However, the KROTOS 28 test results are given and discussed in more details.

A. Experiments in "saturated water conditions"

1. KROTOS 27 - 10 K subcooled water. The objective of this test was to study quenching of 1.5 kg Al_2O_3 melt in nearly saturated water at 0.1 MPa system pressure in constant volume (0.3 m^3 pressure vessel volume) conditions. The external trigger system was not applied. In the course of the test 1 kg of Al_2O_3 melt at 2350°C entered into the test tube, which contained 7.2 kg water at temperature 90°C and height 112 cm. Furthermore, an additional water mass of about 3 kg was present in the upper water container where the levelmeter was placed.

No steam explosion occurred after melt/water mixing, but an important steaming for nearly 5 minutes together with a water level swell up to nearly 20 cm, and a small pressurization of the pressure vessel were measured. Post-test examination showed that most of the melt mass was collected on the test tube bottom plate as rubble including a large resolidified cake of 0.45 kg mass. About 0.3 kg of melt was found in the upper water container: it is not obvious whether this debris (60 w% above 12 mm size) comes from melt quenched in the container or was

swept out from the test tube during the vaporization phase.

2. KROTOS 28 - 10 K subcooled water. The objective of the test KROTOS 28 was the triggering of a steam explosion in a well established fuel/coolant mixture, using the "strong gas trigger system". 1.45 kg of Al_2O_3 melt at 2400°C was released into the tube filled with 7.2 kg of water at 87°C, up to a height of 112 cm.

After melt-through of the tin disc (brake) of 2 mm thickness and free fall of 0.45 m in the gas space the melt penetrated into the test tube water. As shown in Fig.3 a melt front progression velocity of 0.6 m/s in the water can be deduced from the thermocouple signals; the zero time corresponds to the instant of breaking the copper wire. The "gas trigger system" (volume: 15 cm^3, pressure: 85 bar) was activated by the melt front arrival at the TC2-thermocouple position; the trigger membrane being ruptured after an additional delay time of 0.2 s. At that instant the melt front position was at level K1 and from post-test analysis it was deduced that an Al_2O_3 mass of 1.22 kg (about 85% of the total mass) was present in the mixing zone. The level swell at the instant of triggering was 2 cm.

The steam explosion was triggered about 1.6 s after the first melt/water contact. Fig. 4 (zero time corresponds to 2.53 s after breaking the copper wire) shows the leading edges of the pressure pulses in the nine locations (K1 to K5) along the tube and the K0-pressure history. An escalation of the detonation can be seen in the sequence K1, K2, K3 and an average propagation velocity of 650 m/s is deduced from the curves.

To illustrate this further, pressure histories (duration 5 ms) measured at the locations K10, K2, K3 are shown in Fig. 5. Pressure rises were interrupted shortly afterwards, due to transducer (or cable) destruction. The pressures measured at locations K20, K3 indicate levels which were cut-off at 50 MPa. The explosion caused the blow-out of all pressure transducers (except K0) from the test tube wall. Besides the disruption of the thermocouples and pressure transducer cables, six K-pressure transducers did not survive their mechanical impact on the pressure vessel wall. Also the levelmeter was destroyed.

B. Experiments in "subcooled water conditions"

1. KROTOS 26 - 40 K subcooled water. The test KROTOS 26 was the first FCI experiment of the Al_2O_3 water test series and the objective was the triggering of a steam explosion at 0.1 MPa system pressure. From a mass of 1.4 kg Al_2O_3 at 2300°C melted in the furnace, less than 1 kg was drained from the Mo-crucible. The late and incomplete melt release from the crucible was caused by a bad crucible bottom rupture (thickness 0.3 mm instead of 0.2 mm as used in all further tests) and by the use of a too thick tin disc (7 mm; it was changed to 2 mm in further tests). The trigger pulse was fired 2 s after 0-time (rupture of the copper wire in the release tube; see above) but at that instant the melt front was at most above K4. Nevertheless a steam explosion did occur.

A comparison of the transient pressure signals at location K1 and K15 is shown in Fig. 6 and may help in understanding KROTOS 26. At the locations K1 up to K3 the trigger pulse propagation is clearly seen, followed by a strong "recoil" pressure starting from the test tube upper region and propagating downwards, with a speed of about 1500 m/s, which corresponds to the speed of sound in water. At location K15 the trigger pulse was no longer visible and the K15 pressure rise to a level of more than 25 MPa further indicates that a steam explosion was initiated in this region. As a consequence of the explosion the upper water container, the levelmeter and the internal plexiglass liner were destroyed.

2. KROTOS 29 - 80 K subcooled water. The objective of test KROTOS 29 was to investigate the quenching behaviour of an Al_2O_3 melt in highly subcooled water at 0.1 MPa system pressure. Triggering off a steam explosion was not intended, therefore the trigger system was not included. 1.5 kg molten Al_2O_3 at 2300°C was released into the test tube filled with water at 20°C up to a height of 100 cm (water mass: 7.65 kg). The total melt mass entered the water in about 2 s.

The melt leading edge had penetrated down to level K1 (15 cm above bottom plate), when a self-triggered steam explosion occurred at 2.95 s after breaking the copper wire. The melt-water mixing region was similar to KROTOS 28 and explosion pressures up to 100 MPa were measured (pressure range of detectors used in this test: 0-100 MPa). In the pressure vessel an additional pressurization of about 0.2 MPa with respect to the initial pressure was recorded.

3. KROTOS 30 - 80 K subcooled water. This test was a repetition of KROTOS 29. However, an attempt was made to avoid self-triggering of a steam explosion introducing some modifications in the test arrangement: firstly, the tin membrane below the crucible had been removed, in order to inhibit the ge-

neration of an explosion due to a possible tin/water interaction ahead of the Al_2O_3 melt jet. Secondly, the plexiglass liner on the test tube bottom plate and up to 40 cm in the tube lower part was reinstalled (not present in KROTOS 29). However these modifications were not sufficient to eliminate the spontaneous triggering.

1.5 kg molten Al_2O_3 at 2300°C was released into the test tube filled with water at 20°C up to a height of 108 cm (water mass: 7. 45 kg). The melt left the nozzle exit of 30 mm diameter (no tin disc!) with a much higher velocity than in tests KROTOS 26 to 29. The melt release rate and melt velocity from the nozzle could not be measured directly. A series of simulation experiments are being performed, using water, tin and Wood's metal and the nozzle melt release is filmed. For the KROTOS 30 test arrangement, an initial melt release velocity of the order of 25 m/s was deduced from these simulations. In KROTOS 30 all the melt entered the water. At 1.3 s, after breaking the trigger wire, when the melt was still above level K3 a very strong self-triggered explosion occurred. The transient pressure signals showed that the explosion propagated downwards from the top of the test tube and led to exceptionally high pressures in the lower test tube region where only water was present (see KROTOS 26). Pressures of 90 MPa were recorded at level K5 and more than 100 MPa at the lower levels. In the cover gas of the pressure vessel an additional pressure of 0.55 MPa with respect to the initial pressure was measured 30 ms after the explosion.

The four K-pressure transducers mounted in the lower part (pure water region) of the test tube were blown out from the wall and damaged by striking the outer pressure vessel, causing indentations in it (see Fig. 7,8). Due to the very strong water hammer the twelve bottom plate bolts (M 16) were plastically elongated up to 6 mm and the test tube diameter was distended by about 1%. All thermocouples and cables of pressure transducers were broken. As in KROTOS 26, 28 and 29 the upper water container and levelmeters were destroyed. Post-test analysis showed an extremely fine fragmentation of the melt, never found in our previous experiments (see the next section).

IV. DISCUSSION AND CONCLUSIONS

The generation of a stable coarse mixture was only possible in nearly saturated conditions (KROTOS 27,28), and in order to produce a steam explosion an external trigger was needed, as verified in test KROTOS 28. No noticeable difference in the melt penetration was found in neither nearly saturated nor subcooled water. Comparing the tests KROTOS 28 (10 K subcooled) and 29 (80 K subcooled) the melt leading edge velocities were similar (KROTOS 28: 0.6 m/s, KROTOS 29: 0.5 m/s).

On the basis of the present KROTOS test series and of our past work in the system Sn/H_2O (Burger et al., 1991), it is reasonable to think that transition to unstable film boiling when the coarse mixture contacted the structures, acted as a trigger in KROTOS 29. For KROTOS 30 it is thought that the enhanced fuel breakup induced by the higher velocity melt release into the water facilitated the spontaneous triggering of the explosion.

From penetration depth and level swell measurements a rough estimate of the mixture composition has been derived for KROTOS 28 to 30. Considering that the whole mass was present in the test tube at the time of the explosion and assuming that a 1-D homogeneous mixture existed, the global volume fractions of the melt (α_m), coolant (α_c) and vapour (α_v) are calculated as:

	α_m	α_c	α_v
KROTOS 28	0.08	0.88	0.04
KROTOS 29	0.07	0.89	0.04
KROTOS 30	0.18	0.59	0.23

It can been seen from the table that the calculated compositions of KROTOS 28 and 29 are similar and that the vapour fractions are low even though the subcooling are very different (10 and 80 K, respectively). One can understand the higher value of the vapour fraction in KROTOS 30 because there was a more intensive breakup of the melt, which led to higher vapour production.

In the tests KROTOS 28 to 30 supercritical steam explosions were encountered, detonation wave propagation velocities of 650-1000 m/s were measured in the melt/water mixture. In KROTOS 30 the explosion occurred in the upper part of the test tube. Consequently, the water in the lower region remained single-phase and the base plate was subjected to a strong water hammer. Taking into consideration the elongation of the bolts of about 6 mm (Fig. 9) and the distension of the test tube of about 1% it was estimated that the impact pressure must have been at least 150 MPa. The value of the impulse which depends on the duration of the pulse could not be calculated because the pressure gauges were destroyed early. Fig. 10 shows the particle size distributions for the tests KROTOS 27 to 30. It is clear that KROTOS 27, in which no steam explosion happened, gives a small percentage

(10%) of particles smaller than 6 mm. KROTOS 28 and 29 show nearly the same particle size distribution with a large percentage of small particles (about 60% smaller than 250 μ). The debris in KROTOS 30 was extremely fine (85 % below 250 μ and 70% below 100 μ). Sample images of a Scanning Electron Microscopic analysis are shown in Fig.11. During the experiments there was a pressurization of the pressure vessel. After an initial pressure peak caused by the rapid steaming which immediately followed the explosions, the pressure remains relatively constant for some time. In KROTOS 30, the additional pressure in the pressure vessel was 0.55 MPa, the largest one found in all tests. An estimate of the explosion work done by assuming an isentropic compression of the cover gas gives 1.3, 0.8 and 1.25%, respectively for KROTOS 28,29 and 30 (Farawila et al., 1990). This is only a lower bound estimate, and does not include mechanical work done in plastically deforming the various components in the pressure vessel. These conversion ratios are related to the interacting fuel mass which was fragmented in particle sizes less than 250 μ.

The Al_2O_3/water mixing test series gave interesting results, especially in view of the high pressures found in the explosions. The results can be used to verify FCI fragmentation models in thermodynamic codes, not only for the coarse mixing phase, but also for the thermal detonation phase. Only a limited quantity of data could be gathered. In particular, local fuel distribution and local void fraction measurements are not available and this has been critized in the past for KROTOS 21 (Fletcher et al., 1991). Nevertheless, much useful and new information has been made available and a continuing effort is being made to improve instrumentation in this high temperature, multi-phase, multi-component environment. Further KROTOS tests are envisaged using prototypic reactor melt materials, that is, mixtures of 80 w% UO_2-20 w% ZrO_2, with melt masses of up to 5 kg.

ACKNOWLEDGMENTS

This work was performed in collaboration with the US Nuclear Regulatory Commission in the framework of a Technical Exchange Agreement. The authors acknowledge the work and efforts of the whole KROTOS experimental team.

REFERENCES

BURGER M., D.S. KIM, W. SCHWALBE, H. UNGER, H. HOHMANN, H. SCHINS, Two-phase description of hydrodynamic fragmentation processes within thermal detonation waves, J.Heat Transfer 106 (1984) 728-734.

BURGER M., C. CARACHALIOS, D.S. KIM, H. UNGER, Theoretical investigations of the fragmentation of drops with respect to the description of thermal detonations (vapor explosions) and their application in the code FRADEMO, Commission of the European Communities, Nuclear Science and Technology, Report EUR 10660 EN (1986).

BURGER M., K. MULLER, M. BUCK, S.H.CHO, A.SCHATZ, H.SCHINS, R.ZEYEN, H. HOHMANN, Examination of thermal detonation codes and included fragmentation models by means of triggered propagation experiments, in a tin/water mixture, Nucl.Eng.Des. 131 (1991) 61-70.

CARACHALIOS C., M. BURGER, H.UNGER, A transient two-phase model to describe thermal detonations based on hydrodynamic fragmentation, Int. Mtg. on Light Water Reactor Severe Accident Evaluation, Cambridge, USA, Aug.28-Sept.1, 1983.

M. FARAWILA Y., S.I. ABDEL-KHALIK, On the calculation of steam explosion conversion ratios from experimental data, Nucl.Sci. Eng.104 (1990) 288-295.

FLETCHER D.F., An improved mathematical model of melt/water detonations - II. A study of escalation, Int.J. Heat Mass Transfer 34 (1991) 2449-2459.

MACALLON D., H. HOHMANN, High pressure corium melt quenching tests in FARO, to be presented at the CSNI Specialist's Meeting on Fuel-Coolant Interactions, Santa Barbara, CA, Jan.5-8, 1993.

HOHMANN H., H. KOTTOWSKI, H. SCHINS, R. E. HENRY, Experimental investigation of spontaneous and triggered vapour explosions in the molten salt/water system, Proc. of the Int. Mtg. on Thermal Reactor Safety, Chicago, NUREG/CP-0027, Vol.2 (1982), 962-971.

SCHINS H., Characterization of shock triggers used in thermal detonation experiments, Nucl. Eng. Des. 94 (1986) 983-98.

YUEN W.W., X.CHEN, T.G.THEOFANOUS, On the fundamental microinteractions that support the propagation of steam explosions, Proc. NURETH 5, Salt Lake City, UT (September 1992).

TANG J., M.L. CORRADINI, Modelling of a complete process of one-dimensional vapour explosions, to be presented at the CSNIS Specialist's Meeting on Fuel-Coolant Interactions, Santa Barbara, CA, Jan.5-8, 1993.

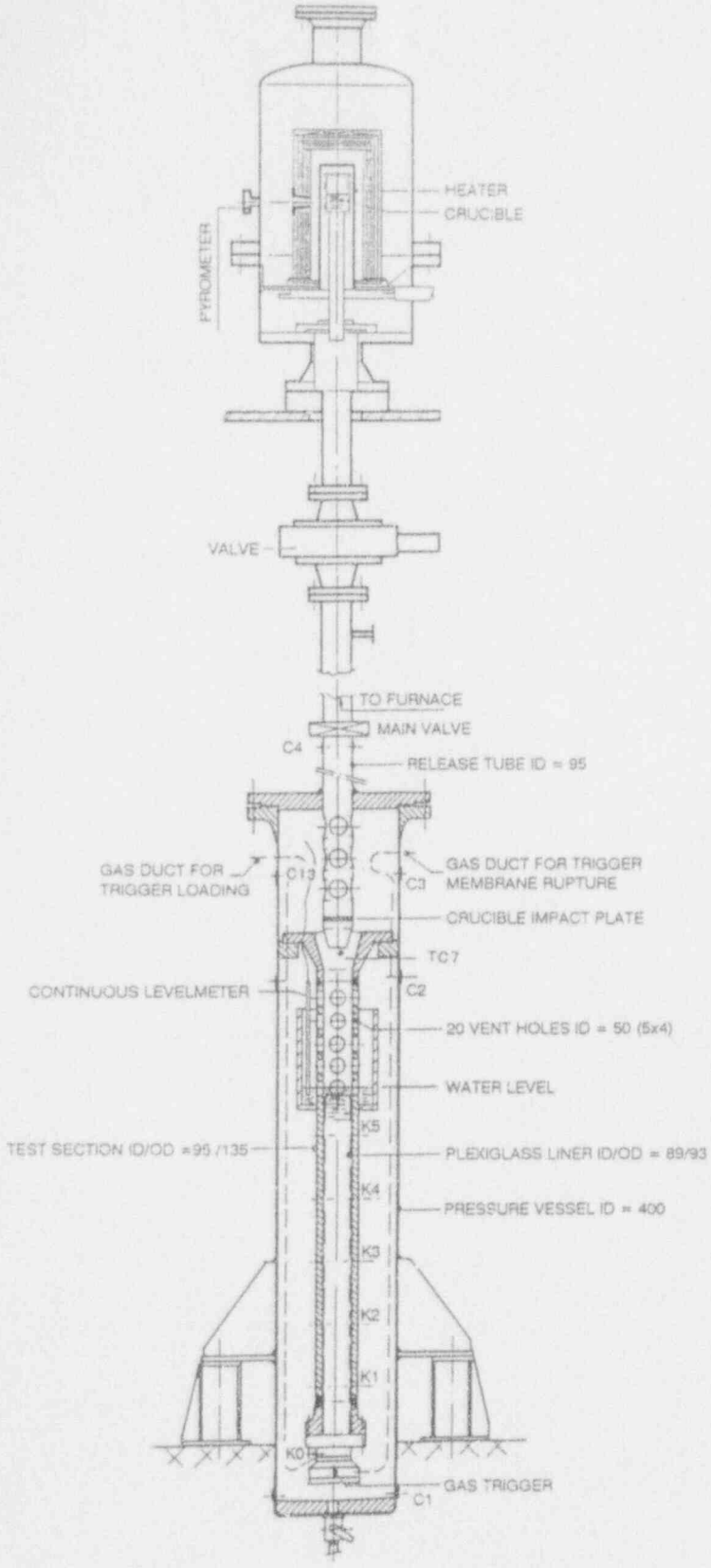

Figure 1. General lay-out of the KROTOS test facility.

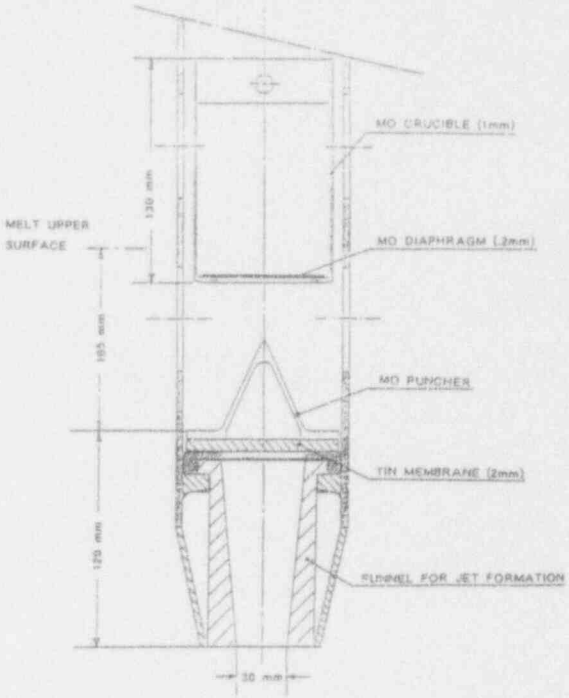

Figure 2a. Crucible with puncher for Al_2O_3-water tests.

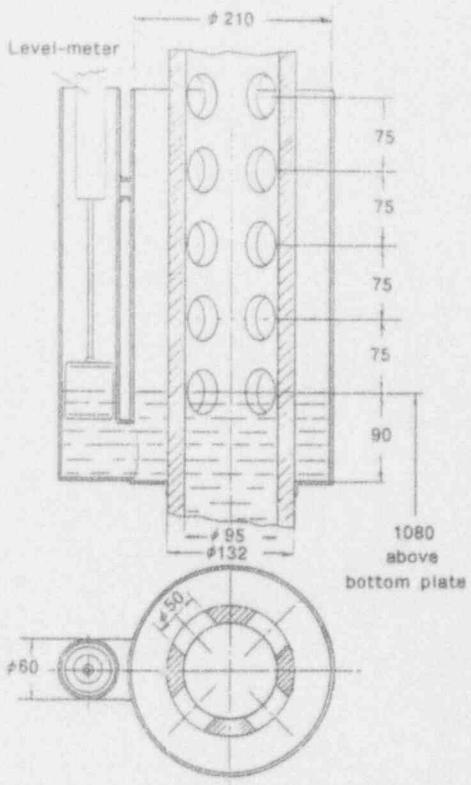

Figure 2b. Sketch of upper water container with level-meter.

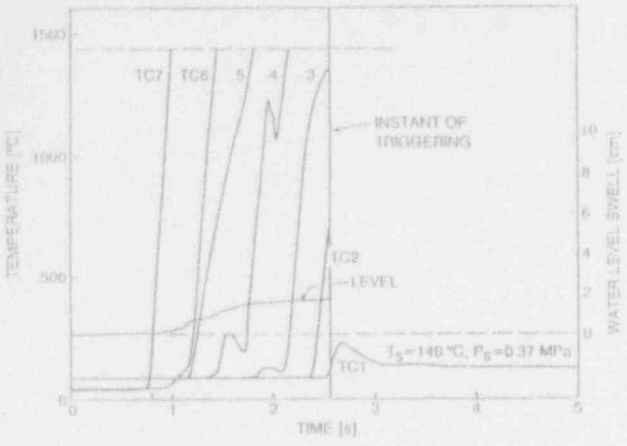

Figure 3. KROTOS 28: melt leading front advance.

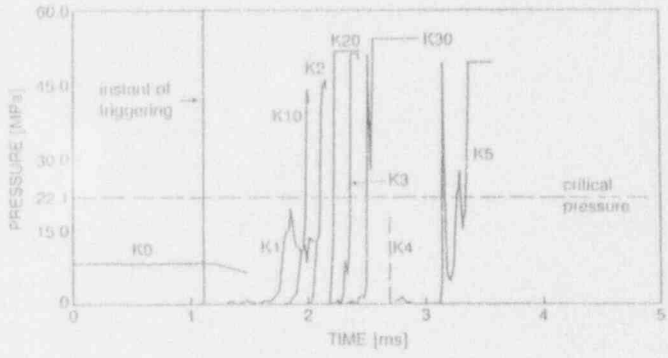

Figure 4. KROTOS 28: advance of shock wave in the test tube.

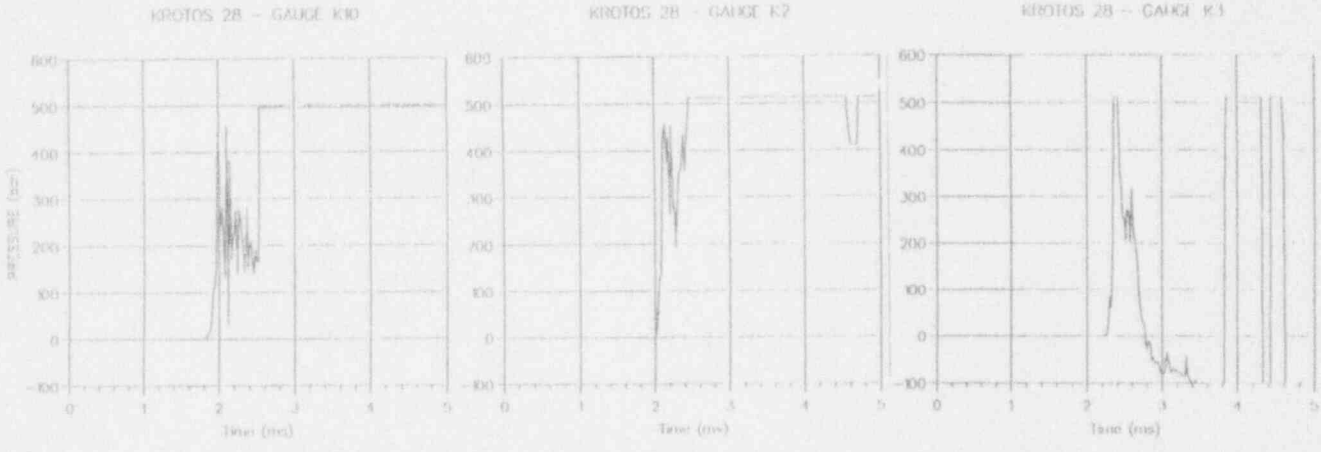

Figure 5. KROTOS 28: pressure histories at locations K10, K2, K3.

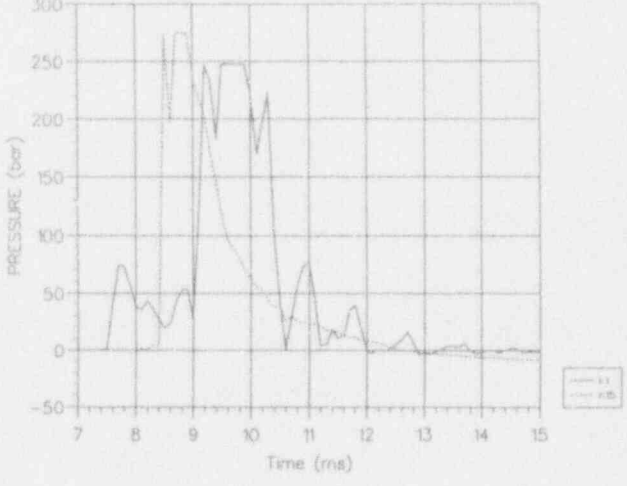

Figure 6. KROTOS 26: pressure histories at locations K1 and K15.

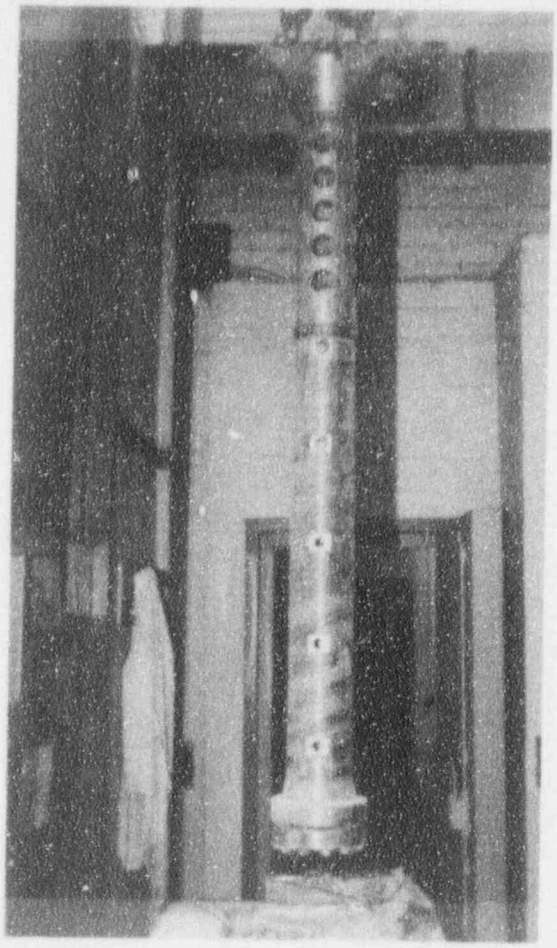

Figure 7. KROTOS 30: view of test tube.

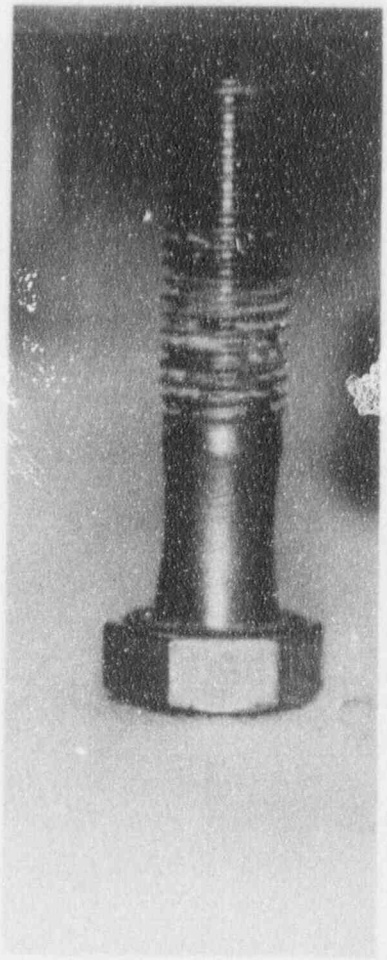

Figure 9. KROTOS 30: plastically deformed bolt (M 16) from bottom plate.

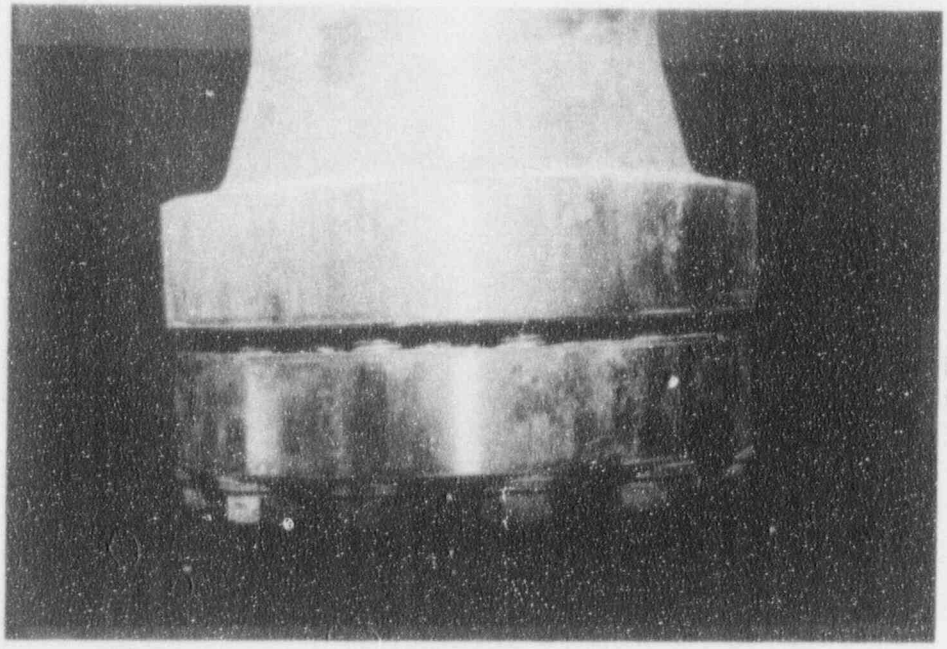

Figure 8. KROTOS 30:
view of test tube bottom plate.

THIS PAGE INTENTIONALLY

LEFT BLANK

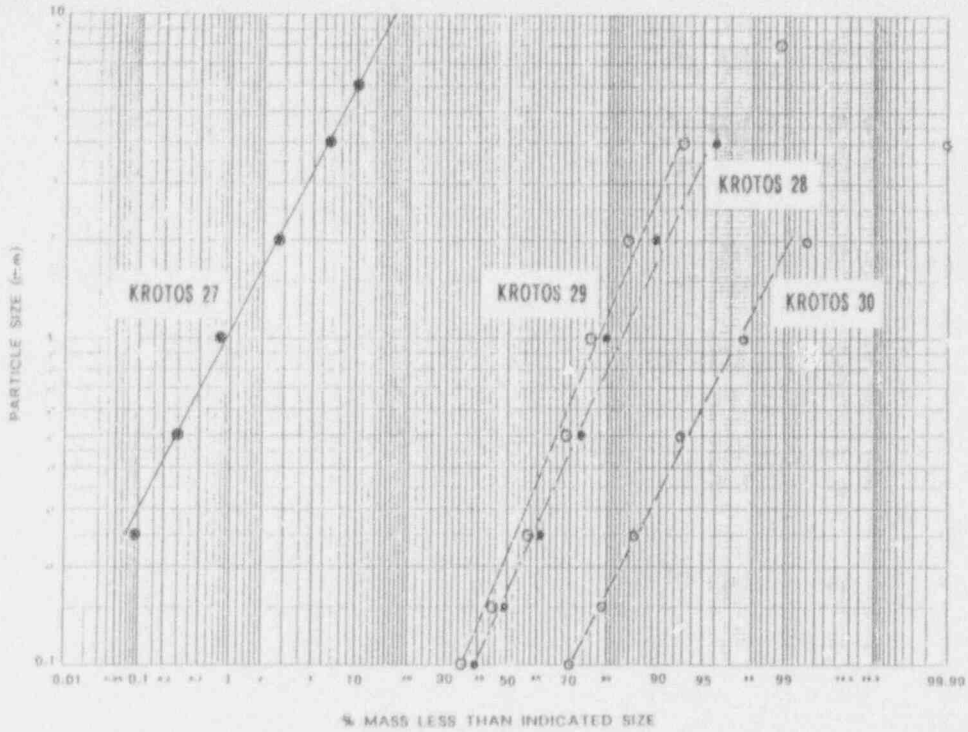

Figure 10. Particle size distributions.

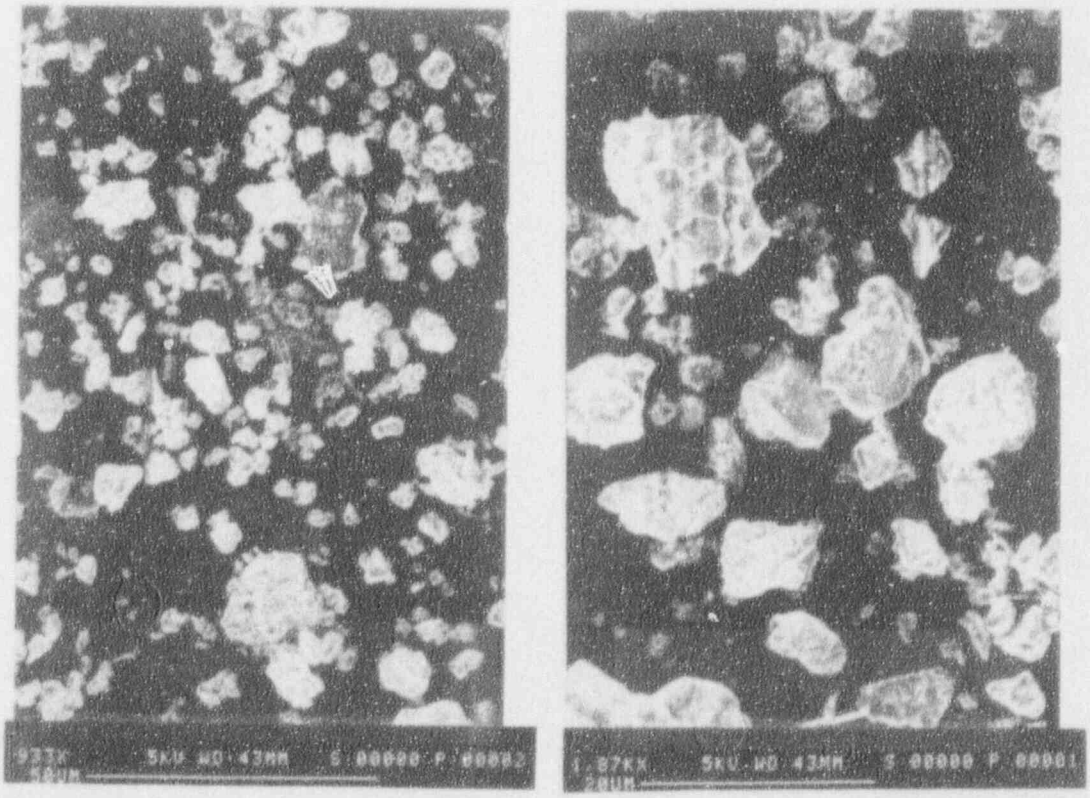

Figure 11. KROTOS 30: SEM images of the debris.

MODELLING OF THE COMPLETE PROCESS OF ONE-DIMENSIONAL VAPOR EXPLOSIONS

Jian Tang
Nuclear Engineering and Engineering Physics
University of Wisconsin-Madison
1500 Johnson Drive
Madison WI 53706
(608) 263-4447

Michael L. Corradini
Nuclear Engineering and Engineering Physics
University of Wisconsin-Madison
1500 Johnson Drive
Madison WI 53706
(608) 263-2196

ABSTRACT

Due to limited data and experimental scale limitations, simulation modelling is needed for better understanding of the vapor explosion. This paper presents a computer model, TEXAS-III capable of simulating the process of a one-dimensional vapor explosion. To develop such a model, an explosion fragmentation model for the propagation phase is essential. A semi-empirical fragmentation model based upon the mechanism of film collapse and coolant jet penetration was formulated and incorporated into the overall TEXAS model. This fragmentation model considers the fuel fragmentation rate as a function of the local pressure difference and the fuel interfacial surface area in film boiling with the coolant. This fragmentation model is combined with the TEXAS-II code, a hydrodynamics model for fuel-coolant mixing and fuel dynamic break-up due to relative velocity between the phases. This allows for a consistent mixing-explosion simulation. The model was used to analyze the experiment KROTOS-21 performed at JRC-Ispra and compared to the data. The simulation models the experiment starting from the fuel pouring into the coolant. The calculated pressure propagation speed and pressure profiles are compared with the liquid phase pressure data along with the fragmented debris and the gas phase pressure in the surrounding containment. In addition post-test blind calculations are presented for a recent aluminum-oxide/water test conducted at the JRC Ispra.

INTRODUCTION

In general a molten fuel-coolant interaction (FCI) is a physical event in which a hot liquid (fuel) fragments and transfers its internal energy to a colder more volatile liquid (coolant). The rate of energy transfer between the fuel and coolant determines if the FCI will become explosive in nature; i.e. a vapor-explosion. When the two liquids first contact, the coolant begins to vaporize at the fuel-coolant interface as a vapor film separated the two liquids. The system can remain in this metastable state for a period ranging from a fraction of a second to many seconds. During this time the fuel and coolant liquid intermix due to density and velocity differences as well as vapor production. One liquid (e.g., fuel) will breakup and disperse into the other (e.g., coolant, Figure 1). If the FCI progresses no further the fuel could quench in this metastable state as coolant vapor is produced by the fuel thermal energy; an example being the TMI melt relocation (Spencer, 1988).

If vapor film destabilization occurs by a triggering event, an energetic FCI, vapor explosion, may be produced. The film collapse seems to initiate rapid fuel fragmentation by closer liquid-liquid contact (e.g., Fauske, 1974; Nelson et al, 1981). This rapidly increases the fuel surface area, vaporizing more coolant liquid and increasing the local vapor pressure. This "explosive" vapor formation spatially propagates throughout the fuel-coolant mixture escalating the "explosion" as a larger macroscopic region becomes pressurized by the coolant vapor (Figure 2). Subsequently, a high pressure coolant vapor expands against the inertial constraint of the surroundings and the mixture. The vapor explosion process is now complete, transforming the fuel internal energy into the kinetic energy of the mixture and its surroundings.

In the past (e.g., Board et al., 1974a, b) the vapor explosion process has been conceptually subdivided into these four phases of (1) mixing, (2) triggering, (3) explosion propagation and (4) expansion. These phases can possibly occur in three geometrical arrangements (Figure 3), (a) fuel pouring into coolant, (b) coolant injected into fuel or (c) fuel and coolant as stratified layers. In most accident situations in current fission reactors one is concerned with the pouring mode of contact with consideration given to stratified geometries when water may reflood a region where a melt pool is present. In this work we restrict our analysis to this former contact mode, although the techniques described have been applied to a stratified geometry (Bang et al, 1990).

Our objective in this paper is to present a model, TEXAS-III, for the overall vapor explosion process; i.e., mixing, triggering, explosion/propagation and expansion. Previous work has presented the TEXAS model for fuel-coolant mixing (Chu et al, 1984, 1986, 1989), so this is only summarized here. The contribution here focuses on the modelling of the explosion escalation/propagation and expansion with a proposed thermal fragmentation model. First, we provide some background of past vapor explosions experiments and models. Next, we present the proposed model and finally, we discuss the application of this model to the JRC KROTOS-21 tin-water experiment with data comparisons and present post-test blind calculation for an alumina-water test.

BACKGROUND

The analysis of the vapor explosion has been a subject of interest over many years. One could classify models of the process into thermodynamic, parametric, mechanistic and empirical multi-dimensional expansion models. A relatively comprehensive review of such models is given by Corradini et al. (1988). If one examines past hypotheses and models (e.g., Board et al, 1974 a,b; Burger et al., 1989; Corradini, 1988; Fauske et al., 1974; Fletcher, 1984, 1990, 1991; Kim et al., 1988; Oh et al., 1987; Theofanous et al., 1988, 1989, 1991) it becomes clear that models for fuel fragmentation during the explosion propagation fall into two general categories; i.e., thermal fragmentation and hydrodynamic fragmentation. In the former, Fauske was first to propose that boiling processes (i.e., homogeneous nucleation) as the root cause of the explosion fragmentation process. In the latter Board et al first suggested hydrodynamic instabilities driven by relative velocity differences between the fuel and coolant liquid are important to the detonation concept of the explosion.

Building on these hypotheses mechanistic models were developed. Kim (1988) developed a detailed model for single drop tests (Nelson et al., 1981) based on thermal fragmentation due to vapor film collapse and liquid coolant jet impingement; this concept was also used by Oh (1987) for his parametric model of the large scale explosion. These models focused on the details of film collapse which would cause coolant entrapment below the fuel droplet surface; eventually causing the coolant to vaporize, expand and fragment the fuel quite rapidly. Kim and Oh both noted that this thermal fragmentation concept is needed for the explosion to escalate and progress from its initial triggering stage. Corradini (1988) noted this and proposed that the thermal and hydrodynamic mechanisms were not necessarily mutually exclusive. Rather, based on analysis it appeared that the thermal fragmentation model is needed for the initial explosion escalation and a transition would occur as the hydrodynamic fragmentation rate would increase at higher explosion pressures; i.e., this latter type of model would be valid at supercritical coolant pressures as Board originally estimated.

Subsequently other investigators (Burger et al., 1989; Theofanous et al., 1988, 1989, 1991; Fletcher, 1990, 1991) have advanced detailed models for hydrodynamic fragmentation. These models are based on a conceptual picture of an array of molten drops intermixed with the coolant and its vapor as the beginning state. For these models the explosion is initiated by assuming a portion of the initial fuel-coolant mixture becomes thermally equilibrated instantly; thus generating the initial pressure shock wave necessary to propagate through the remainder of the mixture. Subsequent propagation of the explosion is predicted based on the assumption of complete film collapse surrounding the fuel particles and hydrodynamic fuel fragmentation caused by fuel-coolant relative velocities; i.e., fuel droplet deformation, Rayleigh-Taylor instabilities and shear flow instabilities as well as boundary layer stripping. Recently, Theofanous et al (1992) compared this model to the KROTOS-21 experiment and empirically assumed 2% of the fragmented melt thermal energy went into vapor production to obtain reasonable agreement. Although these models have been applied to experimental analysis (Baines et al., 1984; Burger et al., 1989, Theofanous et al., 1989) it is felt the analysis of the escalation phase of the explosion is critical, and a hydrodynamic model may be lacking since it does not seem to be able to predict rapid fragmentation at these lower initial pressures. Our hypothesis is that this escalation phase is driven by thermal fragmentation given the prior mixing conditions and only the experimental or spontaneous trigger source.

TEXAS MODEL DESCRIPTION

To improve upon the groundwork laid by past investigators we have developed a thermal fragmentation explosion model which begins with a complete simulation of fuel-coolant mixing, triggering and the escalation/progagation and expansion phase of the FCI. The approach to the analysis is to be able to specify the initial and boundary conditions for fuel pouring into a coolant pool and then simulate the combined process from this point onward.

The first step to such a model is the description of the fuel-coolant mixing process, wherein fuel breaks apart due to relative velocities between the two liquids as the fuel falls through the liquid pool in film boiling. Past analyses (e.g., Bankoff 1984, Theofanous et al 1988) have considered the fuel particles to be of constant diameter as mixing occurs. The focus in these studies has been to characterize the multi-dimensional aspects of the mixing process in a large coolant pool, which is quite important to understand under certain circumstances. However, we feel Fletcher (1991) has correctly pointed out that for an experiment to be useful for analysis of the explosion process a one-dimensional geometry is required. Because our focus is an analysis of one-dimensional experiments we consider the dynamic fuel fragmentation to be the important physical process to model during the mixing process.

In an attempt to remove the restriction of a constant fuel diameter during mixing that is a simplifying assumption in simple analyses as well as multidimensional analyses, Chu et al. (1984, 1986, 1989) developed a technique to predict the dynamic fragmentation of the fuel due to relative velocities. This was incorporated into the transient multifluid, one-dimensional model that would allow one to consider the mixing between fuel and coolant and can account for dynamic fuel fragmentation. Chu et al., (1986) based this model on the TEXAS code (Young 1982), a fuel-coolant interaction model for LMFBR safety. Two Eulerian fields (coolant vapor and liquid) and one Lagrangian particle field (fuel) are employed in the model. The key constitutive relation is a fuel fragmentation model based on hydrodynamic instabilities (i.e., Rayleigh-Taylor). This constitutive model considers the fuel to be dynamically fragmented into a discrete number of particles from its initial entry diameter to smaller sizes. In the model shear forces by parallel velocity (e.g., Kelvin-Helmholtz instabilities and boundary layer stripping) are neglected because of their limited effect with a vapor film present (Fauske 1985). The model for fuel breakup as used in TEXAS was simplified from the detailed model (Chu 1984) to a linear time-independent form where

$$D_f^{n+1} = D_f^n \left(1 - C_0 \Delta T^+ We^{0.25}\right) \qquad (1)$$

where: n, n+ 1 designated the old and new timestep values

We is the fuel Weber number

ΔT^+ is a dimensionless timestep

$$We = \rho_c V_{rel}^2 D_f^n / \sigma_f \tag{2}$$

$$\Delta T^+ = \frac{V_{rel}(t^{n+1} - t^n)}{D^n_f} \left(\frac{\rho_c}{\rho_f}\right)^{1/2} \tag{3}$$

$$C_o = 0.108 - 0.0785 \left(\frac{\rho_c}{\rho_f}\right)^{1/2} \tag{4}$$

where V_{rel} is the relative velocity

D_{is} the fuel diameter

ρ is the density of fuel, f, and coolant, c

This TEXAS model, when applied to the breakup of a fuel jet in a coolant for steady-state conditions similar to those considered by Fauske (1985), also predicts the amount of fuel jet breakup and mixing is small. However, for the initial fuel jet entry the leading edge can mix with the coolant, and this is the condition of interest here.

Quite recently, Young (1987, 1989) has adopted the concept of dynamic mixing with separate dynamic mixing investigations by Pilch and developed a two-dimensional model for fuel-coolant mixing analysis, IFCI. This represents an advance in modelling of mixing prior to a vapor explosion because (1) it is two-dimensional, and (2) it employs a model for dynamic fuel fragmentation instead of a user-specified pre-fragmented size. The results published to date are quite preliminary, but the capabilities seem promising.

The major focus of our efforts with the TEXAS fuel mixing model is to predict the initial conditions prior to the vapor explosion triggering and escalation/propagation phase. This is felt to be most important as the leading edge of the jet passes through the coolant pool, breaks apart and mixes with the coolant. The important variables to identify prior to triggering are the vapor volume fraction axially within the coolant pool, the fuel volume fraction within the pool, the fuel temperature and its characteristic diameter following jet breakup. Each of these variables are calculated by the model as the transient mixing process progresses as a function of axial height. The energetic vapor explosion begins when the vapor film surrounding the fuel is destabilized by a pressure or temperature perturbation. These variables are directly used as initial conditions for the explosion calculation. In difference to past experimental analysis we do not parametrically alter these mixing values to predict the explosion propagation.

The fragmentation modelling during the explosion is critical in simulating the vapor explosion. Fuel may break up during all phases of an energetic fuel-coolant interaction, but the mechanism and magnitude of the driving force can vary significantly in the different phases, leading to different fragmentation rates. The fragmentation models known to us are not efficient enough in terms of their breakup rates to account for the rapid escalation and propagation of the explosion from initially subcritical coolant conditons. A strong trigger alone cannot assure the explosion propagation unless complete film collapse occurs and the mode of explosion propagation becomes similar to the Board-Hall detonation model under supercritical conditions (Corradini, 1988). Kim's analysis (1988) of Nelson's tests (1981) indicated that complete film collapse did not occur under conditions in which the trigger and resultant event produced pressures below 10 MPa. Our focus is on the initial explosion escalation/propagation following the trigger as the key phenomenon to be modelled. Our hypothesis is that a thermal fragmentation model is necessary for the escalation of the explosion, under the assumption that subcritical conditions are initially present following the trigger. The model we propose intends to delineate these conditions.

The proposed explosion fragmentation model is based on the same fragmentation concept proposed by Kim (1988) in the modelling of Nelson's original tests (1981) and later used in analysis of Kim's data (1989). However, because Kim's model requires detailed tracking of the coolant vapor-liquid interface we propose a rather ad-hoc model as the first approach to model this process. The conceptual picture of the mechanisms considers that Rayleigh-Taylor instabilities are induced on the coolant vapor-liquid interface during the vapor film collapse; the coolant jets formed penetrate the fuel and vaporize inside the fuel leading to rapid fragmentation of the fule surrounding these entrapped globules of liquid coolant (Figure 4). Given this conceptual picture, the fragmentation rate ought to be proportional to the original fuel droplet surface area and an average jet velocity. The model for the rate of fragmentation is given by:

$$\dot{m}_f = \rho_f 4\pi R_p^2 N_p V_{jet} F \tag{5}$$

where:

ρ_f is the fuel density;

R_p is the fuel particle radius ($2R_p = D_f(t)$) determined by the mixing process;

N_p is the number of fuel particles in one Lagrangian fuel particle group;

V_{jet} is the average coolant jet velocity;

F is a compensation factor for the fragmentation time.

Remember the TEXAS model treats the fuel in a Lagrangian manner tracking a discrete number of fuel particle masses. Knowing the total mass of all fuel particles in one of these Lagrangian particle groups, m_p, the fuel particle number N_p can be calculated by:

$$N_p = \frac{m_p}{\frac{4}{3}\pi R_p^3 \rho_f} \tag{6}$$

This model is a simplification of Kim's multidimensional treatment for a single droplet (1988) which indicated that the stages of vaporization of the entrapped coolant and the accompanying fuel fragmentation were much

faster than the stages of jet formation and penetration into the fuel.

Based on this concept the fragmentation process due to coolant entrapment consists of three stages; vapor film collapse, jet formation and jet penetration into the fuel with subsequent vaporization. The first two processes occur simultaneously and determine the velocity of the jet entering the fuel, V_{jet}. Based on Kim's analysis (1988) this velocity is proportional to the ratio of the instability amplitude to its wavelength, $\eta o/\lambda$, multiplied by the product of the initial acceleration, a, which generates the jet by Rayleigh-Taylor instability growth and its wavelength, λ; i.e.,

$$V_{jet} \sim (\eta o/\lambda)\,(a\lambda)^{1/2} \sim C\,(aR_p)^{1/2} \qquad (7)$$

where this wavelength is a fraction of the fuel particle radius, Rp. This constant, C, also includes the ratio of the initial amplitude of the instability to its wavelength; this is consistent with Kim's more detailed analysis (1988). From the Rayleigh equation for a spherical geometry, the acceleration term can be derived for the initial jetting behavior by

$$a = \left(\frac{(P - P_o)}{\rho_c R_p}\right) \qquad (8)$$

where:

P is the local pressure at any time near the fuel mass;

P_o is the initial ambient pressure.

Combining one obtains the approximate expression for the jet velocity as a function of the local variables in the fuel-coolant mixture

$$V_{jet} = C\left(\frac{P - P_o}{\rho_c}\right)^{1/2} \qquad (9)$$

Now this coolant jet impinges on the fuel surface and entraps coolant below the fuel interface (Figure 4). Such a process causes the coolant to rapidly vaporize due to local overheating and as it expands the surrounding fuel is fragmented and expelled outward into the surrounding coolant. This coolant vapor expansion is driven by the fragmented fuel which has small sizes compared to the parent droplet and could quench rapidly. In Kim's analysis (1988) of Nelson's single droplet tests this resulted in a cyclic behavior as the vapor initially produced by jet entrapment over expanded and the coolant interface again collapsed on the remaining unfragmented fuel and the process repeated itself until the fuel droplet was consumed. In the large scale fuel-coolant mixture this process would be substantially different. First, for this mechanism to cause explosion escalation and spatial propagation there is only a finite time available for this cyclic fragmentation. Second, because of the local pressurization due to the past fragmentation in the fuel-coolant mixture this cyclic process cannot continue indefinitely; but rather would only occur until the local vapor and liquid pressures in the region of the fragmented fuel equilibrate--therefore only a few cycles would occur as the pressure builds in the mixture. Kim's analysis of Nelson's tests (1988) indicated that as the ambient pressure increased the cyclic frequency of this film-collapse/jet-impingement process increased markedly in good agreement with Nelson's data. Thus, it seems clear that the characteristic time for this fragmentation rate decreases as the pressure derived from the explosion increases.

The factor F is introduced into the model as an empirical way to account for this characteristic time when this fragmentation mechanism is operative. Thus the factor F should decrease from 1 to 0 as this characteristic time is exceeded (Figure 5). Beyond this time the local pressures equilibrate and only the relative velocity between the fluids can continue to cause fuel fragmentation. It is recognized that this approach to the analysis is not complete, but semi-empirical and more detailed film-collapse studies are needed to identify the realistic range of these characteristic times. Substituting Eqs. (6) into Eq. (5) gives the combined expression for the fragmentation model:

$$\dot{m}_f = C m_p V_{jet} F/R_p \qquad (10)$$

The threshold pressure necessary to cause film boiling collapse is evaluated based on the theoretical work of Kim (1988) and the empirical results of Nelson (1981) and Kim (1989). These studies indicate that at ambient pressures (0.1 MPa) the threshold triggering pressure above the ambient pressure is in the range of 0.1 to 0.3 MPa. As the ambient pressure rises empirical evidence suggests that the threshold triggering pressure difference also rises (Nelson, 1981); however, no definitive values have been suggested from data, and we use a differential pressure value of 0.2 MPa in this work for these conditions.

The final point to discuss is the constant of proportionality, C. As mentioned previously it is less than one because it represents the ratio of the instability initial amplitude to its wavelength and the wavelength fraction of the fuel particle radius. Therefore, this is expected to be less than 0.01 based on the analysis of Nelson's single droplet data (Kim, 1988). In addition the conceptual picture of the fragmentation process is that the impact of the coolant jets on the fuel surface would occupy much less than the total surface area at any time during the event. Thus, C is expected to be much less than one for these two reasons; a value much less than 0.01 is expected to be in agreement with the assumptions of the fragmentation model.

Given this fragmentation rate one needs to now consider the energy transfer rate from the fuel fragments to the coolant. Remember the TEXAS model uses a multi-fluid formulation where the fuel is modelled as discrete material volumes of mass, m_p. Thus each parcel of mixed fuel mass, m_p (modelled as a discrete material volume) rapidly fragments into fine fragments forming a new material volume of fragmented fuel. The model thus removes mass from one parcel and transfers it to the other, where the fuel fragments are assumed to have a small diameters (20-40 microns based on Kim's analysis and Nelson's data). Based on such small sizes the fuel quickly quenches on a time scale much smaller than the propagation through the mixture. At these small diameters the continued existence of film boiling may be suspect and local heat transfer coefficients would be high (Fletcher, 1990). Thus for a spherical particle and

diffusivity limited heat transfer, the large fraction of its thermal energy is released in a time , t_H, of

$$t_H = 0.1 \frac{D^2_{frag}}{4a_t} \quad (11)$$

where D_{frag} is the fragment size and a_t is the thermal diffusivity of the fuel. For example for tin with a particle size of 10 microns this time is much less than a microsecond and less than 100 microseconds for 100 micron particles. The energy from these fuel fragments is then deposited at the coolant vapor-liquid interface of the original mixed fuel mass, m_p, as a heat flux over this fragmentation time. The amount of coolant vapor produced is determined by the normal interfacial model for energy exchange in TEXAS (Chu et al., 1989). In summary this vapor generation rate per particle is given by the difference of the heat flow into the interface, q_f, minus the heat transferred to the bulk coolant, q_c, divided by the enthalpy difference needed for vaporization;

$$\dot{m}_v = (q_f - q_c)/i_{fg} \quad (12)$$

where

$$q_f = \dot{m}_f (c_{pf} (T_f - T_c) + i_{fs}) \quad (13)$$

$$q_c = \pi D_f^2 h_c (T_{sat} - T_c) \quad (14)$$

The heat transfer coefficient into the bulk coolant, h_c, is determined by separate analyses (Chu, 1986, 1989) to be given by

$$h_c = \frac{k_c}{D_f} (2 + 1.12 \, Re_f^{.5} Pr_c^{.4}) \quad (15)$$

where the Reynolds number is based on the relative fuel to coolant liquid velocity for the initial mixing diameter, D_f, Pr_c is the liquid coolant Prandtl number, and k_c is the liquid thermal conductivity. This heat transfer coefficient is similar to steady state correlations for a sphere, except account is taken that the vapor film alters the no-slip boundary at the vapor-liquid interface increasing the heat transfer coefficient. With such a model the vapor produced raises the local pressure and thus feedback into the further fragmentation of the "parent" fuel parcels. Remaining transfer coefficients needed for the multiphase hydrodynamic calculation have been described in the work of Chu (1986, 1989).

The current model reflects the key features of a "chain reaction" required for the rapid escalation and propagation of the vapor explosions, i.e.:

- A pressure shock wave directly contributes to rapid fuel fragmentation;
- Fragmented fuel is quenched by the coolant and generates more vapor;
- The increased vapor raises the local pressure and sustains the shock wave propagation to neighboring fuel-coolant mixture regions.

The model has been incorporated into TEXAS and is used as the thermal fragmentation model for propagation of vapor explosions in the experimental analysis.

EXPERIMENTAL APPARATUS DESCRIPTION

To illustrate the behavior of the combined mixing/propagation model we wanted to choose a well-characterized benchmark experiment. Although there are many experimental data from past tests none are very well characterized to allow detailed analysis. In our efforts we have found a couple tests where most of the critical initial and boundary conditions are known or can be estimated. These involve one-dimensional tests with lower melting point fuels (e.g., tin) poured into water, i.e., Baines et al. (1984) and Hohman and Schins (1988). These are the same tests chosen by Theofanous et al. (1989, 1992) and Burger et al. (1989) for their respective analyses. Our reasons for this choice are (1) that the experiment is a highly constrained 1-D geometry that is much more tractable for analysis, and (2) that when the experiments resulted in vapor explosions one can more clearly identify the effect that the mixing has on the explosion escalation/propagation.

In this paper we focus on the JRC Ispra tests. Triggered vapor explosion experiments in a one-dimensional geometry were performed in the JRC-Ispra KROTOS facility using molten tin (7.5 kg) at 1275 to 1375 K pouring into water at 293 to 373 K. The breakup of the molten tin jet in water results in an axially distributed configuration of coarsely fragmented fuel in a cylindrical water column. Past experiments in KROTOS indicated that the molten tin spread across the coolant tube diameter during mixing. Corresponding to the initial conditions, the fuel fragments are surrounded by a stable vapor film. An interaction between the fuel and coolant is triggered by a gas trigger which generates a high pressure shock travelling from the bottom of the water column upwards through the premixed fuel-coolant region. More recently similar experiments have begun with molten aluminum oxide (1.5 kg at 2600K) poured into water under similar conditions.

The general experimental apparatus consists of a radiation furnace, a release tube and the test section underneath (Figure 6). Inside the heater, a steel container held in place by a pneumatically operated release hook, carries a crucible in which the molten materials are melted and heated. The temperature is controlled by an optical pyrometer measuring the side-wall temperature of the container. The container and crucible are released together and dropped by gravity through a 4m long release tube. The container impacts onto a retainer ring at the end of the tube where a strong metal grid cuts out the bottom of the crucible. The molten material pours onto a tin plate which melts in less than 300 ms. In this way, the molten material is released with no initial velocity towards the water surface, and the impact Weber number is considerably reduced preventing any initial fragmentation in the air. Its temperature is measured right at the exit of this braking system. The test section consists of two concentric tubes (Figure 6). Inside a tubular pressure vessel of an inner diameter of 400 mm, a height of 221 cm and a design pressure of 2.5 MPa, hangs the actual experimental tube with an inner diameter of 95 mm and an outer one of 135 mm. The experimental tube contains a water column of 1.1 m height and 7.4 liters volume.

A gas trigger is attached at the lower end of the experimental tube. This trigger device is described by Burger et al. (1989). The gas volume is 15 cm^3 at a pressure of 12 MPa and closed by a 0.1 mm steel membrane. After an allowed mixing time of about 2 seconds (i.e., ~1.05 seconds after water entry) the membrane is ruptured by a knife and transmits the pressure pulse upwards through the mixture of tin, water and steam.

Five piezo-electric pressure transducers with a range of 10 MPa are used in the test tube to monitor the dynamic pressures in the interaction zone. Their positions are shown in Figure 6. K0 is situated inside the gas trigger, while K1 to K5 are fixed at the test tube inner surface. Further, pressure transducers (C1 to C6) are preset to measure the pressure development in the cover gas of the outside containment vessel. All pressure transducers have response frequencies of ≥ 10 kHz and are recorded on a transient recorder with a sampling time of 20µs. Several thermocouples are applied to control the temperature of the melt (e.g., TC1 and TC2 in Figure 6) as well as the water temperature and detect the passage of the molten tin in the water and thus the premixing process.

Because of the instrumentation provided in the experiments the test section does not measure any parameters during the fuel-coolant mixing stage beyond the fuel mass entering the water pool, its temperature and time of entry; as well as coolant temperature and mass. Thus, the void fraction is not known nor the fragmented fuel diameter distribution of the molten tin prior to the trigger. This is a known deficiency in the tests (similarly in Baines tests, 1984) and makes the analysis not possible for validation of any specific models. Nevertheless, these tests are most appropriate for analysis of the vapor explosion process. The more recent KROTOS tests are now being instrumented to determine the average void fraction history in the water pool by level swell.

KROTOS TEST 21 RESULTS

KROTOS test 21 has been selected for analysis because of its relatively unambiguous results. In this test 7.5 kg of tin at 1370 K was released into water at 361 K. Pressure pulses detected by the pressure transducers K0 to K5, positioned at a distance of 20 cm demonstrate the upwards propagation of a pressure wave with a sharp leading edge (Figure 7). Rather similar pressure traces and levels, especially at K3 and K4, indicate the possible establishment of a quasi-steady propagation behavior. The wave velocity begins at approximately 270 m/s as an average value between K1 and K3, and stabilizes to 150 m/s between K3 and K4. This behavior was also noted in the tin experiments of Baines (1984) where the propagation speed decreased, and was attributed to a higher void fraction. While sharp pressure peaks occur at the leading edge of the wave, a large pressure plateau of approximately 2.0 to 4.0 MPa develops behind lasting more than 5 ms. The peak pressures vary with position from 6.5 MPa at K0, falling then to 5 MPa and rising again to 6.2 MPa at K4. Transducer K0 shows the pressure development inside the trigger gas volume with a sharp decrease from 12 MPa to nearly ambient pressure, indicating the shock-like relief, and after a slower expansion phase the relatively smooth pressure buildup due to inertially controlled recompression of the trigger gas. Because the pressure decreases so much at the last transducer K5, it was considered unreliable or to be located in a region containing a large amount of vapor.

In addition to the measurement of pressure within the coolant chamber, pressure transducers were placed in the outer containment vessel. These registered a sharp pressure rise to 0.25 MPa approximately 15 milliseconds after the trigger pulse. If all the steam produced in the explosion were used to cause this pressure rise it would correspond to a little less than 0.3 kg and this corresponds to quenching about 1kg of the tin mass.

Besides the transient pressure signals the outer containment vessel allowed the investigators to collect and analyze the solidified fuel debris. The post-test analysis of the tin debris showed that 6.5 kg could be assumed to have fallen into the water pool and participated in the mixing process. Only approximately 0.85 kg, i.e., 13% of this mass, however, fragmented to diameters below 250 µm and 1.2 kg or 18.6% below 500 µm. Part of the fragments may, however, have stuck together again, based on the agglomerated tin masses that were found as highly porous structures in the central region of the tube. This again may suggest uniform mixing over the cross-sectional area of the tube at any axial level, but non-uniform mixing axially along the tube.

TEXAS ANALYSIS RESULTS

To provide a complete set of initial and boundary conditions for the TEXAS simulation auxiliary calculations were needed. First, it was noted that the initial pour diameter would decrease from about 50 mm and the entrance velocity increases from initially zero due to the melt fall through the gas space above the water pool. Based on simple kinematics the entry diameter was estimated to be about 25 mm with a terminal velocity of about 2 m/s. Also because the pour ended at about the same time as the trigger was fired it was clear not all of the fuel mass entered the water. The fall time in air was about 0.25s so our estimate was that at least 0.5 kg of melt never entered the water; this corresponds well to the amount of observed post-test debris. These estimates also correlate well with thermocouple excursions. For the TEXAS model the water pool was nodalized into twelve Eulerian cells in the water pool and eight in the gas space of the vessel, and a reflective bottom boundary during mixing. The gas trigger volume at the time of the explosion was modelled during the propagation phase as an expanding high pressure gas Eulerian cell. The melt was partitioned into forty Lagrangian fuel parcels which entered the water pool uniformly throughout the pouring time.

The results of the mixing process are given in Figures 8 to 11. One should first note (Figure 8) the relatively quiescent pressure signature during mixing even at the bottom of the water chamber. Only when the first couple of fuel parcels enter the water pool does one note small pressure spikes of 0.1 - 0.2 bar. After this time the smaller pressure oscillations can be attributed to fuel parcels moving through the Eulerian cells as the vapor produced dampens the pressure amplitudes. We doubled the number of Eulerian cells in the water pool and the oscillations were

reduced in magnitude to much less than 0.1 bar while the frequency increased. All other results remained the same for the simulation. Figures 9 and 10 illustrate the development of the fuel-coolant mixture fuel and vapor volume fraction during the pouring time. One notes that with the uniform pouring rate from the crucible the mixture developed is approximately uniform within the coolant pool. The only non-uniformity occurs at the end of the mixing simulation when fuel has not yet reached the bottom of chamber and before it begins to accumulate (the axial profiles in Figures 9 and 10 designate x = 0 at the bottom of the water chamber). Thermocouples detected the presence of melt all along the channel in the test. The one discrepancy to note is that the simulation predicts fuel arrival a little sooner in time (< 0.2 sec.) than measured by the thermocouples. This probably overestimates the local void at the bottom of the chamber and would reduce the initial explosion pressure signal. The predicted vapor void fraction is relatively large (15-25%) because the subcooling is low (12°K) and decreases due to liquid heating. In the simulation the jet diameter for mixing begins at about 25 mm at the pool surface and by fragmentation decreases to below 8 mm near the pool base (Figure 11). The increase in fuel surface area and steam produced at the leading edge causes the vapor to accumulate at elevations above it providing an increasing void up the tube. The vapor superheat temperature above saturation has a characteristic rise at the leading edge of the fuel (~45°K) where the fuel-coolant local heat transfer is high and then levels off uniformly to slightly above saturation (~20°K).

In the explosion simulation, the trigger is simulated by the expansion of a high pressure volume of steam (12 MPa, 15 cc) less than one second after the fuel enters the water (i.e., 1.25 sec after pouring begins). Figures 13-16 present the simulation results for the constant value of 0.003. This is in the range of expected values. The characteristic time, τ, for fragmentation (Figure 5) was empirically taken to be 2 milliseconds: Figure 13 shows the dynamic pressure history for Eulerian cells at locations corresponding to the pressure transducers and Figures 14 - 16 the fragmented fuel mass, and the vapor temperature and volume fraction throughout the chamber at particular times during the propagation. The peak pressures (Figure 13) from the test are well predicted for the simulation and the predicted propagation velocity is a little slower throughout the propagation. The average propagation velocity from data was estimated to be about 165 m/s while the simulation has an average value of 150 m/s. In both the experiment and the simulation the propagation velocity was seen to decrease ; i.e., the test shows a velocity decrease from 250 m/s (K1 to K3 transducers) to 150 m/s (K3 - K5 transducers) while the simulation shows a similar decrease, 200 m/s down to 177 m/s. The reason for the decreased velocity is that all the smaller diameter fuel masses are near the chamber bottom, where more rapid fuel fragmentation would occur with faster propagation, and the void is initially larger at higher axial elevations in the tube.

The pressure history at K0 (Figure 13b) is located in the gas trigger cell and is in good agreement with the data. The delayed pressure rise at 9 msec, which seems to be due to the downward propagation of the explosion wave from above recompressing the gas, is also in good qualitative agreement; although somewhat lower in magnitude. The simulation treats the gas as steam allowing condensation in difference to a noncondensible gas and this probably reduces the peak pressure during recompression. The pressure history at K1 (Figure 13b) is located about 10 cm above the gas trigger and here some discrepancies are noted at early times. The early peak pressure (68 bar) has been interpreted by Hohman et al., (1988) to be from the trigger and the simulation does not exactly show this. Rather it shows a slightly higher first pressure from the trigger falling more slowly to explosion values as the explosion propagates. As noted in the mixing simulation (Figure 10) and again shown in Figure 14 the void at the bottom of the chamber at the time of the trigger is near 15% (Note the void of 100% at the very bottom, x = 0, is in the trigger cell of the high pressure steam). This is probably caused by a different vapor void distribution in the actual test; e.g., the fuel is predicted to be closer to the chamber bottom earlier in time compared to the actual test, where the molten tin is not detected at the chamber bottom. This void adds compliance to the pool at this point and dampens the trigger shock, slowing the initial propagation, thus delaying the subsequent explosion propagation upward in the channel by about 0.5 milliseconds. This time delay persists in all the subsequent pressure history plots although the pressure shape compared to data is quite good, and the peak pressures show a progressive increase in strength and decrease in the rise time. Again the later explosion pressurization at about 10 msec is predicted by the simulation. As stated previously the validity of the K5 pressure peak has been questioned in the past (Burger, 1989), although its timing is quite consistent with all the other data.

Figure 14 and 15 also indicate the propagation of the explosion wave through the mixture. The minimum in the void fraction profile is seen to propagate up the channel coincident with the peak in the vapor temperature. Both of these are indicative of the high pressure shock wave which compresses the steam in the fuel-coolant mixture as the local vapor temperature rises due to the compression and the local deposition of energy from fuel fragmentation and quenching. This local energy transfer causes steam generation, further pressurization and propagation up the channel.
Figure 16 also indicates that the predicted fragmented fuel mass that quenches in the water is about 0.2 kg; i.e., in reasonable agreement with that calculated from the test from the vessel overpressure and fragmented debris. More fuel mass would be fragmented from the melt dispersal into the containment chamber and aid in the vaporization and atmospheric heating.

A major uncertainty in the proposed thermal fragmentation model involves the constant of proportionality. A range of expected values was proposed to be less than 0.01 and the value used falls in this range, however, the exact value is not known and only continued sensitivity analysis and comparison to additional data will give us further insight. To demonstrate the sensitivity of our prediction to this value we performed a parametric calculation where this constant was doubled in magnitude (Figure 17). These pressure histories indicate the same qualitative trends as the past calculation (Figure 13), but also show the explosion to be propagating much faster (average propagation velocity of 300 m/s) and at higher pressures than the data indicates (a factor of two). Nevertheless, because of the fuel-coolant mixing results the early pressure history in K1 still does not show the trigger pulse at 1

millisecond; this is again due to the void caused by accumulated fuel. Thus the mixing conditions still determine the qualitative trends of the analysis.

A second uncertainty in the model is the tacit assumption that hydrodynamic fragmentation is too slow to solely account for the observed explosion escalation, and a thermal model must be the important contributor. Burger reached a similar conclusion in his analysis of vapor explosion experiments considering hydrodynamic fragmentation boundary layer stripping (1989). We demonstrate the basis of this assumption by simulating the trigger and observing if the explosion can propagate due solely to Rayleigh-Taylor hydrodynamic fragmentation by relative velocities. We use the fuel breakup model already employed in TEXAS for mixing (Equ 1-4, which considers Rayleigh-Taylor breakup). This volumetric breakup concept is recognized to be a good model for catastrophic breakup at high Weber numbers (Chu et al., 1984, 1986), but neglects the effects of boundary-layer stripping. This is known to be a deficiency in the current model and further analysis with this effect included is planned. However, the model should be expected to qualitatively show the proper trend if the explosion escalates solely due to hydrodynamic effects. As Figure 18 indicates the explosion dies away as the trigger propagates upward through the fuel-coolant mixture. The relative velocity generated by the trigger is not large enough to escalate the fragmentation into a vapor explosion. The vapor void dampens the shock pressure significantly and the fuel is not significantly fragmented (a few percent). Another mechanism must be operative to initially escalate the explosive event; i.e., a thermal mechanism.

TEXAS ANALYSIS OF KROTOS-26

Recently, a new KROTOS test series has begun in which molten aluminum-oxide is used as the fuel (about 1.5 kg at 2600K). This presents an interesting challenge to the model predictive capabilities since alumina at this temperature has an order of magnitude larger thermal energy than tin (0.3 to 4.5 MJ/kg). This should cause the explosion pressures to increase dramatically. For our semi-empirical model if the explosion pressure rises then the characteristic time for the cyclic film-collapse/jet penetration fuel fragmentation should decrease (based on Kim's work, 1988). In this simulation we assumed the proportionality constant remained the same as for KROTOS-21 (0.003) and the characteristic fragmentation time decreased from 2 msec to 0.5 msec. This decrease is inversely proportional to the pressure increase noted in the predictions.

The prediction for the fuel-coolant mixing phase in KROTOS-26 (the first alumina test) is given in Figures 19 and 20 for the fuel and vapor volume fraction. In this simulation the fuel is at a temperature of 2600 K and the coolant at 333 K for a total mixing time of about 0.65 seconds before the gas trigger is fired. These values are based on verbal information from JRC Ispra. As one can see the fuel does not fall very far into the water pool during this time and the associated void is small (<25%). Most of the water pool is intact below a depth of 30 cm of fuel penetration. One reason for this result is partially due to the fact that not much of the melt mass has fragmented to smaller sizes in this time; i.e., less than 10% of the mass with a mean size of about 10 mm. Secondly, the water pool has a higher subcooling when compared to KROTOS-21 (40 versus 12 K).

The explosion predictions (Figure 21) show very interesting behavior. First the trigger (80 bars) can be seen propagating upward to the fuel-coolant mixture at a velocity of about 1350 m/s; close the theoretical sound speed in water. Next, the explosion is triggered at a location between transducers K3 and K4 at the leading edge of the fuel-coolant mixture. The resultant explosion sends a shock wave back downward into the water below and upward through the remainder of the fuel-coolant mixture. The resultant explosion pressures escalate from 250 to 400 bars with a propagation speed of 450 meters/sec. A major reason for this more energetic event is that the fuel thermal energy is much larger. This prediction is a good indication of the TEXAS model capability to predict a super-critical vapor explosion with a fuel of large thermal energy content.

CURRENT OBSERVATIONS AND SUGGESTED FUTURE WORK

The study of vapor explosions must be properly posed to advance the fundamental state of knowledge as part of overall safety efforts. The analytical work presented in this paper is specifically focused on trying to develop an explosion model than can (1) describe fuel mixing more mechanistically to aid in predicting fuel mixing behavior, and to (2) use these mixing models with a proposed thermal fragmentation model to predict explosion pressure propagation, and the effect that mixing conditions have on the explosion in terms of explosion.

We reviewed the TEXAS model for the fuel-coolant mixing process and described our semi-empirical model for fuel fragmentation during an explosion; i.e., fuel breakup is augmented by a process of film-collapse/coolant-jet-impingement/coolant-liquid entrapment/fuel fragmentation. We chose one particular experiment, KROTOS-21, which was fairly characterized (except for mixture volume fractions) to compare to the model simulation. The results of the data-model comparison were encouraging, although the fuel-coolant mixing prediction at the bottom of the chamber may have more void than actually present which caused an initial time delay in the explosion pressure propagation. The propagation velocity and the secondary pressurization during the explosion in the channel were well predicted. Also there is good agreement with the quenched fuel debris mass. We demonstrated our uncertainty of the details of this semi-empirical model by sensitivity calculations; although more extensive sensitivity calculations are needed to indicate the range of characteristic fragmentation times and initial conditions needed for propagation. Also the analysis suggests that hydrodynamic fragmentation alone cannot account for the explosion propagation data.

Although this one test was successfully analyzed, this is not a validation of our model; it is only a first step. We actively seek other available data to compare to the model. The importance of such tests is to provide a means to observe the effect of mixing on the explosion energetics, and thereby validate the dynamic mixing models used. In addition, it is important to compare the mechanisms for fragmentation to see which may be dominant and why. Different initial conditions and explosion energetics may

indicate the importance of different fragmentation mechanisms. Because of this we also presented the results of blind post-test predictions for KROTOS-26, an experiment with alumimum-oxide as the fuel. The predictions indicate that this explosion exhibits super-critical pressures due to the large thermal energy of the fuel and high velocities. These questions may also have scaling implications for different initial conditions. In the future our focus will continue to be in this area where fundamental benchmark experiments are compared to the model.

REFERENCES

Baines, M. (1984) "Preliminary Measurements of Steam Explosions Work Yields in a Constrained System," Proceedings of the National Heat Transfer Conf., Leeds, UK.

Bang, K.Y., Corradini, M.L. (1990) "Stratified Vapor Explosions," Nuclear Science and Engr, V102.

Bankoff, S.G. and Han A. (August 1984b) "An Unsteady One-Dimensional Two-Fluid Model for Fuel Coolant Mixing in an LWR Meltdown Accident," U.S.-Japan Seminar on Two-Phase Dynamics, Lake Placid, New York.

Board, S.J., Farmer, C.L. and Pool, D.H. (1974a) Fragmentation in Thermal Explosions. Int. J. Heat Mass Transfer, Vol 17, pp 331-339.

Board, S.J. and Hall, R.W. (1974b) Propagation of Thermal Explosions, 2 - Theoretical Model, CEGB Report RD/B/N 3249.

Burger, M. et al., (October 1989) "Analysis of Thermal Detonation Experiments by Means of a Transient Multiphase Detonation Code," Proc of the Int'l Mtg. on Nuclear Reactor Thermal Hydraulics, Karlsruhe.

Chu, C.C. and Corradini, M.L. (November 1984) Hydrodynamic Fragmentation of Liquid Droplets. Trans Amer Nucl Soc, Vol 47, Washington D.C.

Chu, C.C. (May 1986) One-Dimensional Transient Fluid Model for Fuel-Coolant Interactions. PhD Thesis, University of Wisconsin, UWRSR-30.

Chu, C.C. and Corradini, M.L. (February 1986b) "One-Dimensional Transient Model for Fuel-Coolant Fragmentation and Mixing," ANS/ENS Int'l Thermal Reactor Safety, San Diego CA.

Chu, C.C. and Corradini, M.L. (January 1989) "A One-Dimensional Transient Fluid Model for Fuel-Coolant Interaction Analysis," Nuclear Science and Engr, Vol 101, No 1.

Corradini, M.L. et al., (December 1988) "A Critical Review of Vapor Explosion Modelling, Progress in Nuclear Energy,

Fauske, H.K. (1974) "Same Aspects of Liquid-Liquids Heat Transfer and Explosive Boiling," Proc of Fast Reactor Safety Mtg., 992-1005, Beverly Hills, CA, 2-4 April.

Fauske, H.K. and Epstein, M. (August 1985) Steam Film Instability and Mixing of Core Melt Jets and water. ANS Thermal Hydraulic Div Proc, ASME/AIChE National Heat Transfer Conference, Denver.

Fletcher, D.F. (May 1984) Modelling Transient Energy Release from Molten Fuel Coolant Interaction Debris. Winfrith, United Kingdom Atomic Energy Authority, AEEW-M2125.

Fletcher, D.F. (June 1984) "Modelling the Transient Pressurization During a Molten Fuel Coolant Interaction." Winfrith, United Kingdom Atomic Energy Authority, AEEW-M2126.

Fletcher, D.F. (1985) A Review of Coarse Mixing Models, UKAEA Culham Laboratory Report.

Fletcher, D.F. (August 1988) "A Mathematical Model of Premixing," ANS Proc. National Heat Transfer Conf., Houston

Fletcher, D.F., R.P. Anderson (1990), "A Review of Pressure-Induced Propagation Models of the Vapor Explosion Process," Prog Nuclr Energy, V23, No. 2, p 137.

Fletcher, D.F. (1991) "An Improved Mathematical Model of Melt/Water Detonations: Model Formulations and Example Results," Int'l Jul Heat Mass Transfer, V34, No. 10, p. 2475.

Hohmann, H. and Schins, P. (June 1988) Private Communication.

Kim, B.J. and Corradini, M.L. (January 1988) "Modelling of Small-Scale Single Droplet Fuel/Coolant Interactions," Nuclear Science and Engr., Vol 98, No 1.

Kim, H., Krueger J. and Corradini, M.L. (October 1989) "Single Droplet Vapor Explosions; Effect of Coolant Viscosity," Proc. of 4th Int'l Mtg. on Nuclear Reactor Thermal Hydraulics, Karlsruhe.

Nelson, L.S. and Duda, P.M. (September 1981) "Steam Explosion Experiments with Single Drops of Iron Oxide Melted with CO_2 Laser." SAND 81-1346, NUREG/CR-2295, Sandia National Laboratory.

Oh, M.D. and Corradini, M.L. (March 1987) "A Propagation/Expansion Model for Large Scale Vapor Explosions," Nuclear Science and Engr., Vol 95, No 3.

Tang, J. (1992) A Complete Model for the Vapor Explosion Process, PhD Thesis, University of Wisconsin, Madison WI.

Theofanous, T.G., et al., (August 1988a) "Premixing of Steam Explosions: A Three Fluid Model," ANS Proc of National Heat Transfer Conf., Houston.

Theofanous, T.G. et al., (August 1988b) "Triggering and Propagation of Steam Explosions," ANS Proc. of National Heat Transfer Conf., Houston.

Theofanous, T.G., et al., (October 1989) "Integrated Analysis of Steam Explosions," Proc of 4th Int'l Mtg on Nuclear Reactor Thermal Hydraulics, Karts, Huhe.

Theofanous, T.G., et al, (October 1991), "Triggering and Propagation of Steam Explosions," Nuclr. Engr. Design, V126, p 41.

Young, M.F. (July 1982) "The TEXAS Code for Fuel-Coolant Interaction Analysis." Proc ANS/ENS Fast Reactor Safety Conference, Lyon, France.

Young, M.F. (September 1987) "IFCI: An Integrated Code for Calculation of All Phases of Fuel-Coolant Interactions," NUREG/CR-4986, SAND 87-1048, Sandia National Laboratory.

Young, M.F. (April 1989), "IFCI: A Sample Calculation of Mixing and Explosion Propagation," Presentation at NRC CSARP Meeting, Idaho Falls, ID.

Figure 1

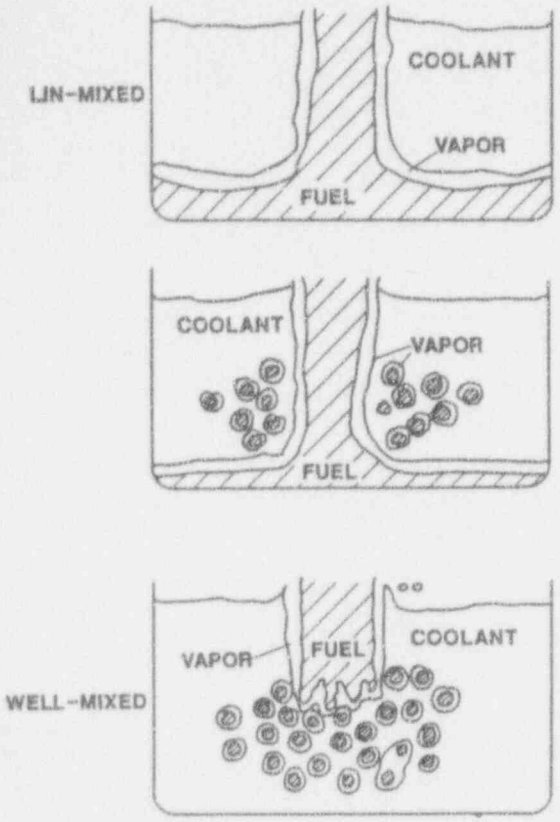

Figure 3

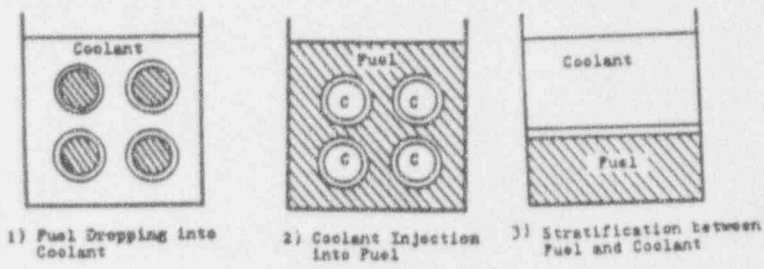

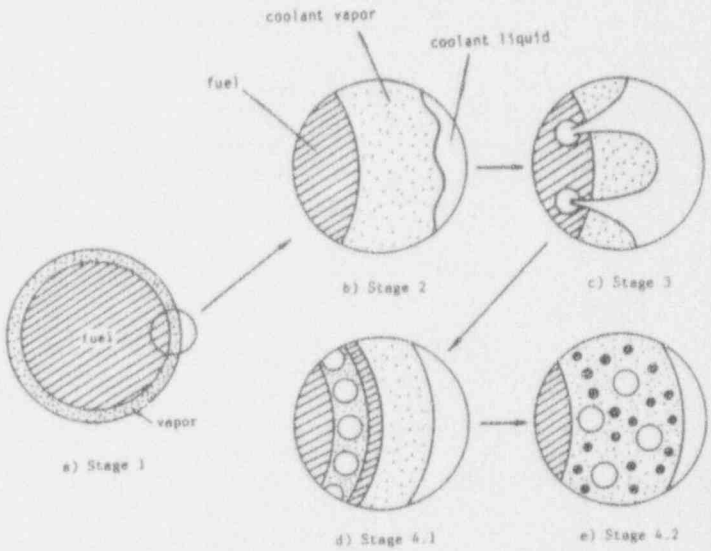

Figure 2

Figure 4. Conceptual Pictures of a Small-Scale Single-Droplet Fuel-Coolant Interaction.

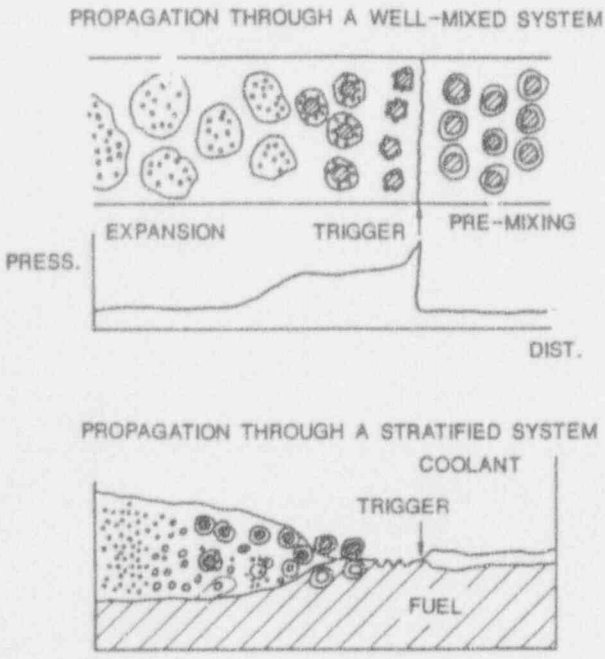

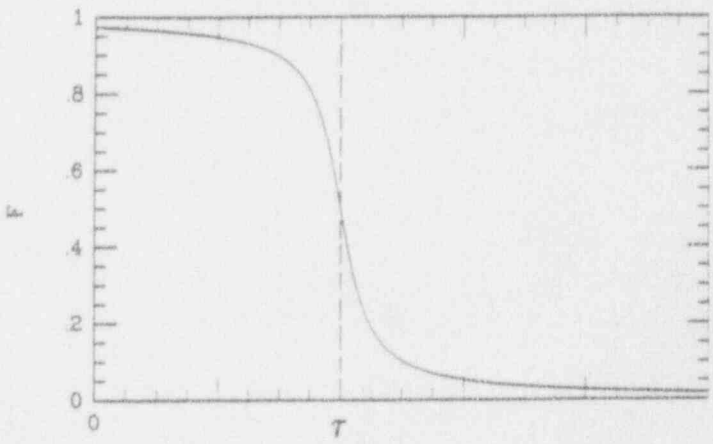

Figure 5. Factor F as Function of Characteristic Time τ

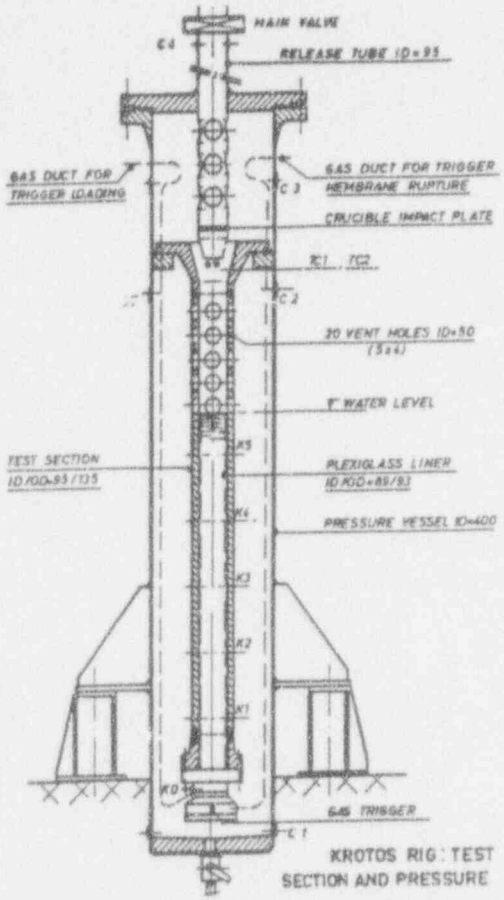

Figure 6

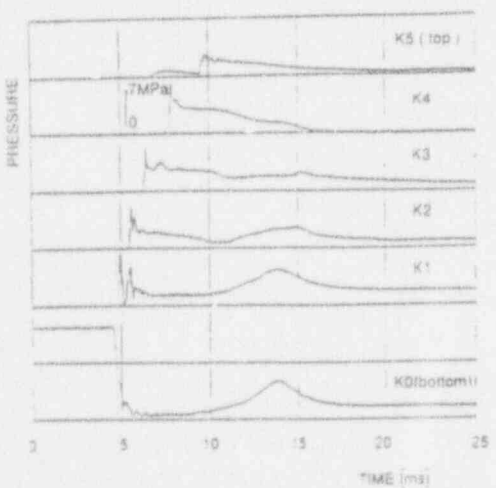

Fig. 7 - Pressure traces detected from the transducers K1 to K5 in test No. 21 (K0: pressure of the integer gas. K1 to K5: pressures measured by the detectors in the tube wall at distances of 20 cm).

Figure 8a

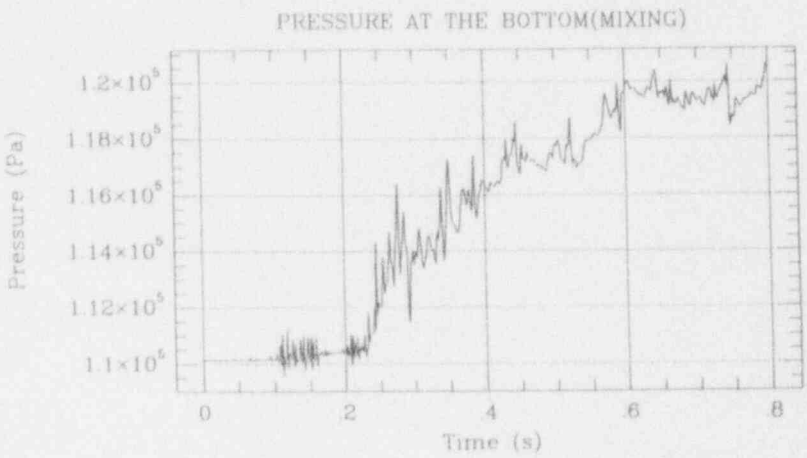

Figure 8b

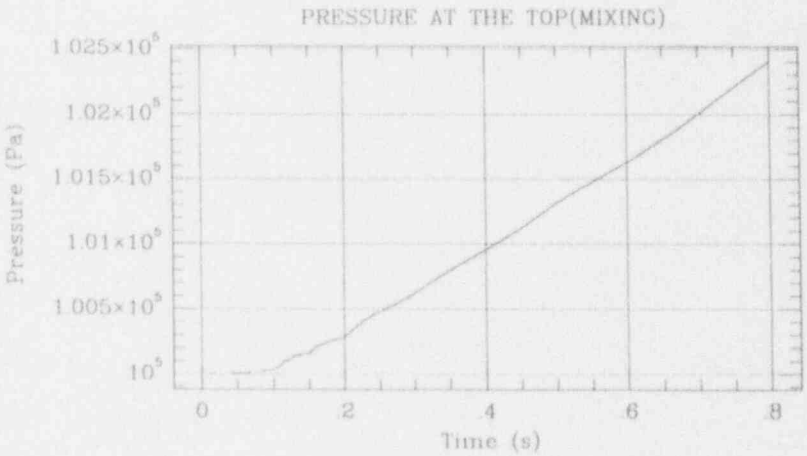

Fuel Volume Fraction During Mixing KROTOS-21

Figure 9

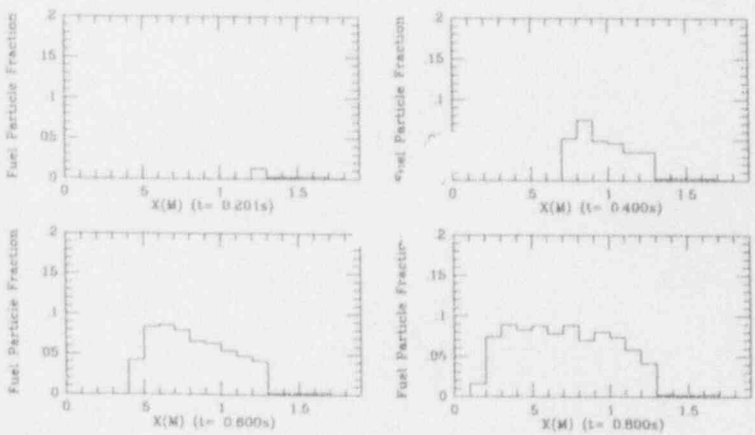

Figure 10

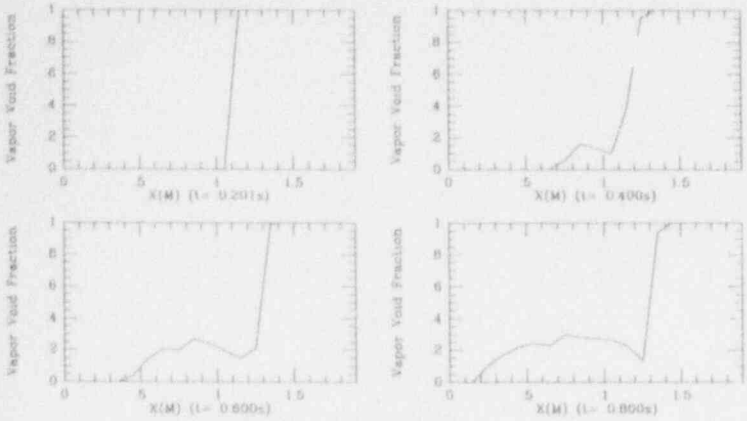

PREDICTED FUEL DIAMETER DURING MIXING

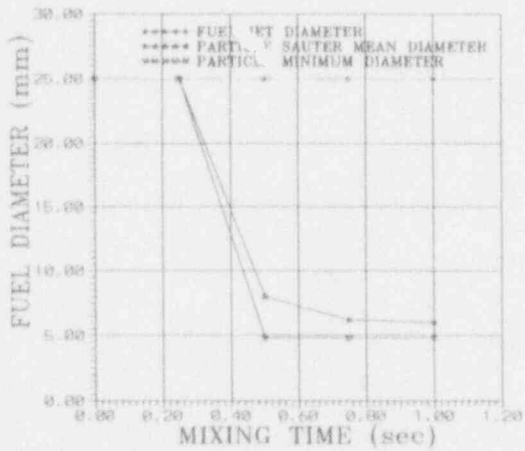

Fig. 12 PARTICLE DISTRIBUTION

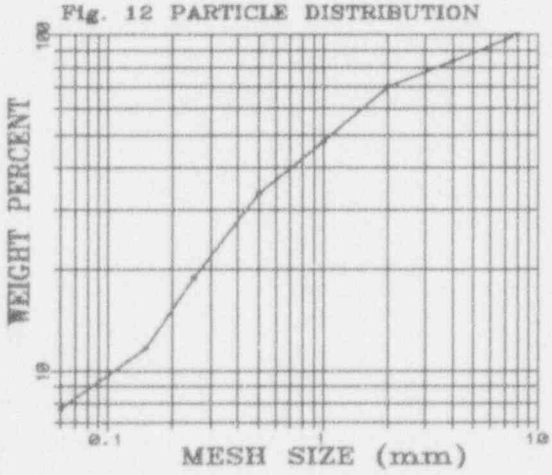

Figure 13 PRESSURE AT K0

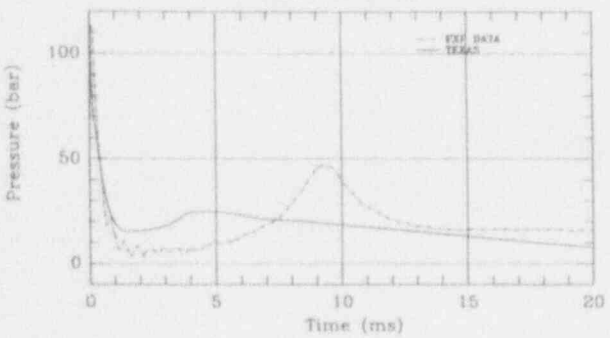

PRESSURE AT K1

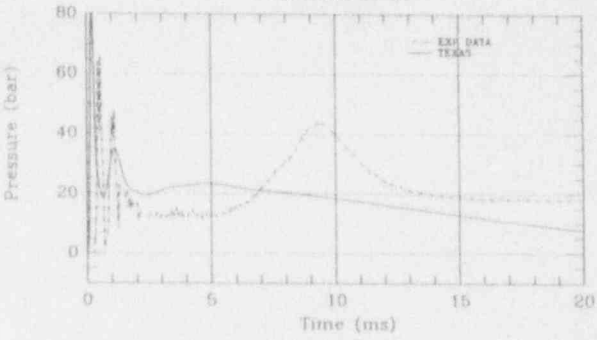

PRESSURE AT K2

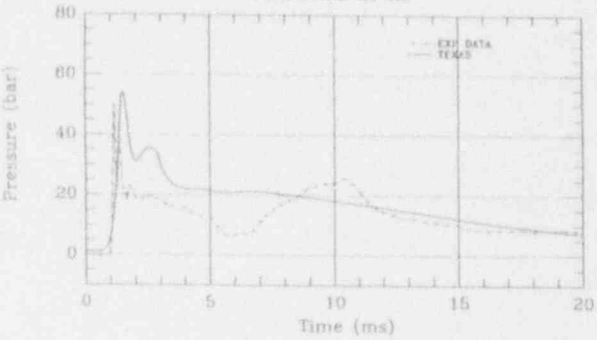

PRESSURE AT K3

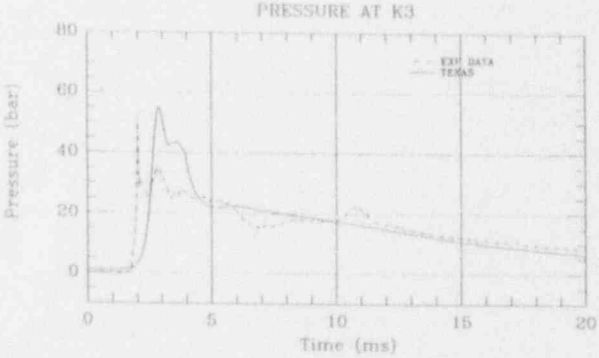

PRESSURE AT K4

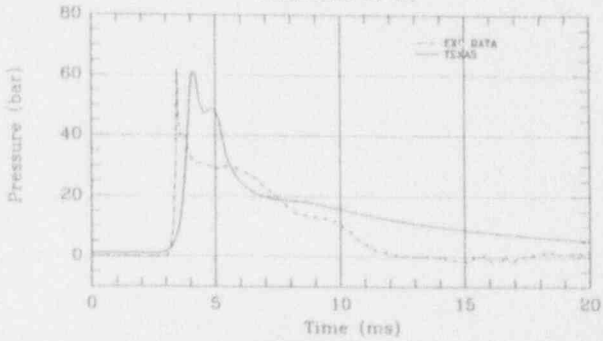

PRESSURE AT K5

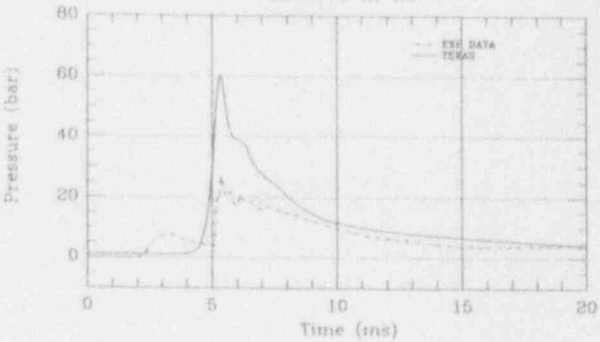

Figure 14

Void Fraction Profile at Selected Times During the Explosion

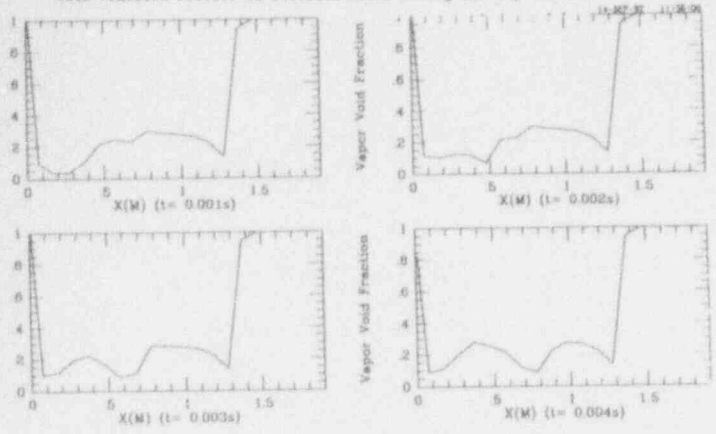

Figure 15

Vapor Temperature Profile at Selected Times During the Explosion

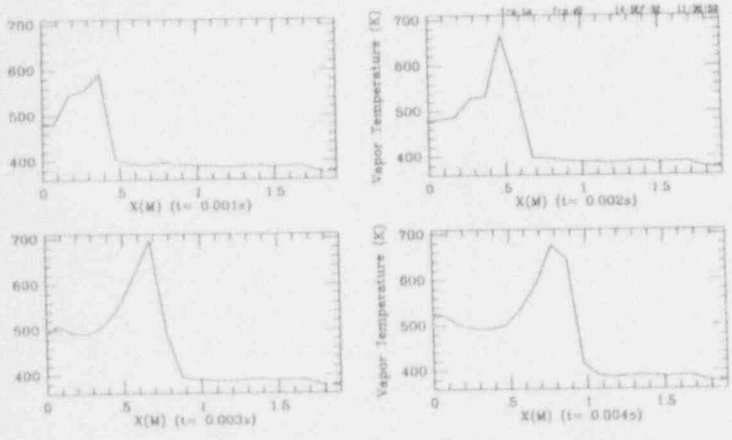

Figure 16

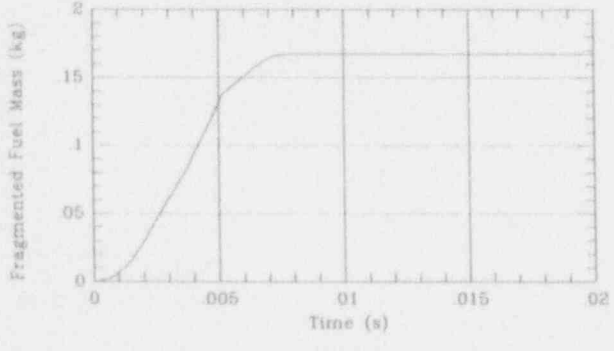

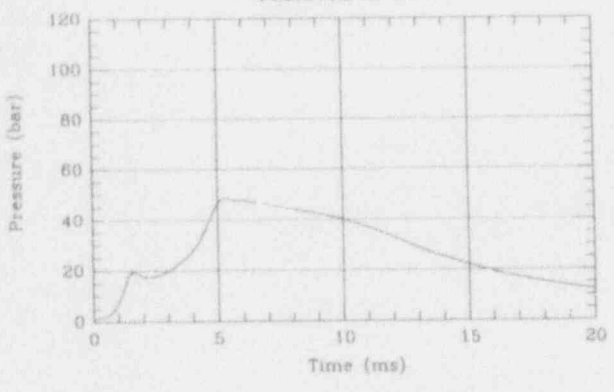

Figure 17c

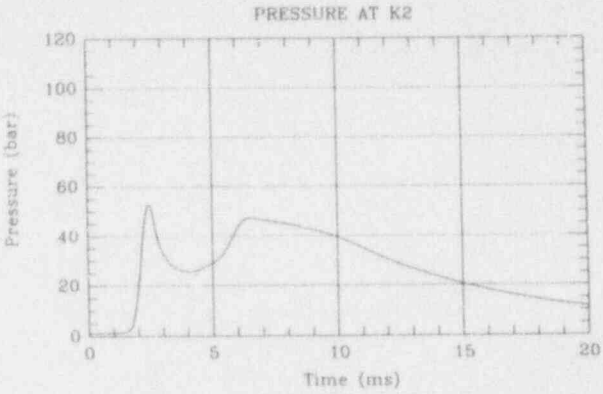

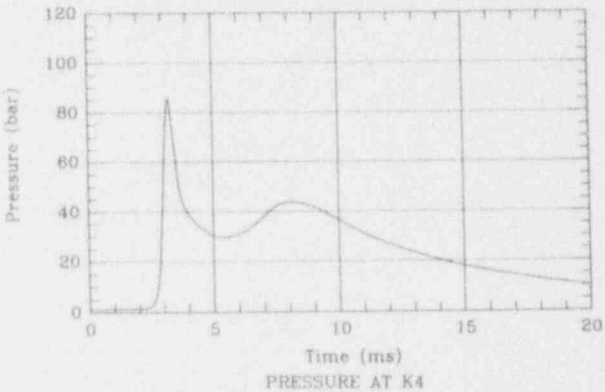

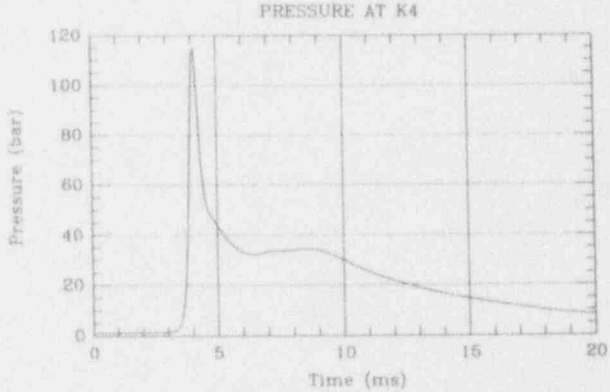

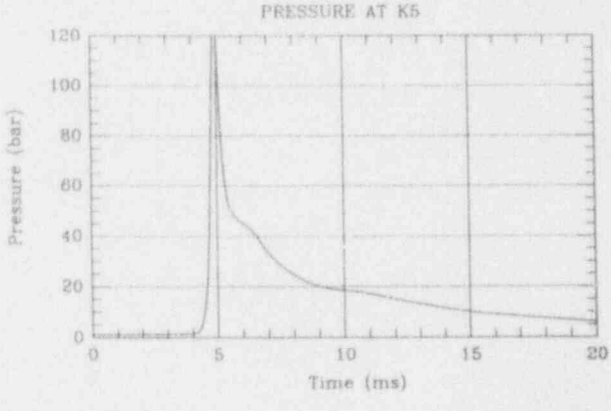

Sensitivity Calculation for KROTOS-21; No Thermal Fragmentation

Figure 18

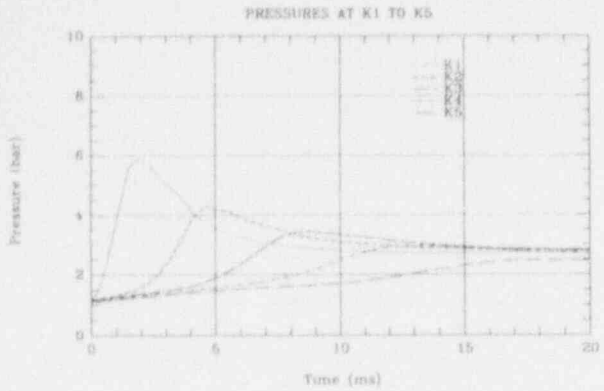

Figure 19

Fuel Volume Fraction During Mixing -- KROTOS-26

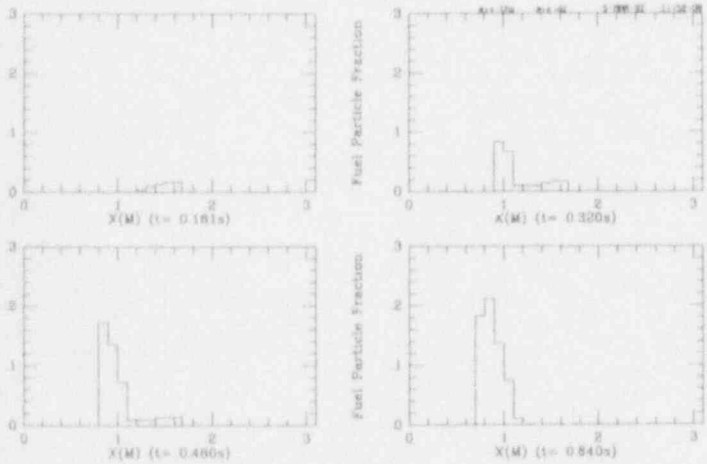

Figure 20

Vapor Void Fraction During Mixing -- KROTOS-26

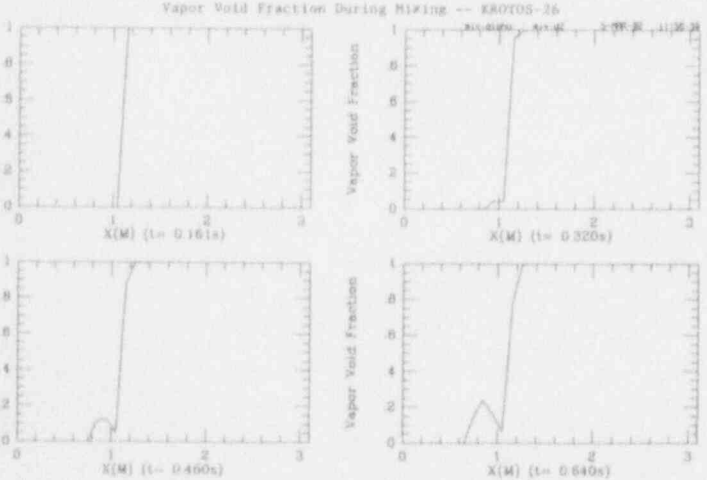

Figure 21a

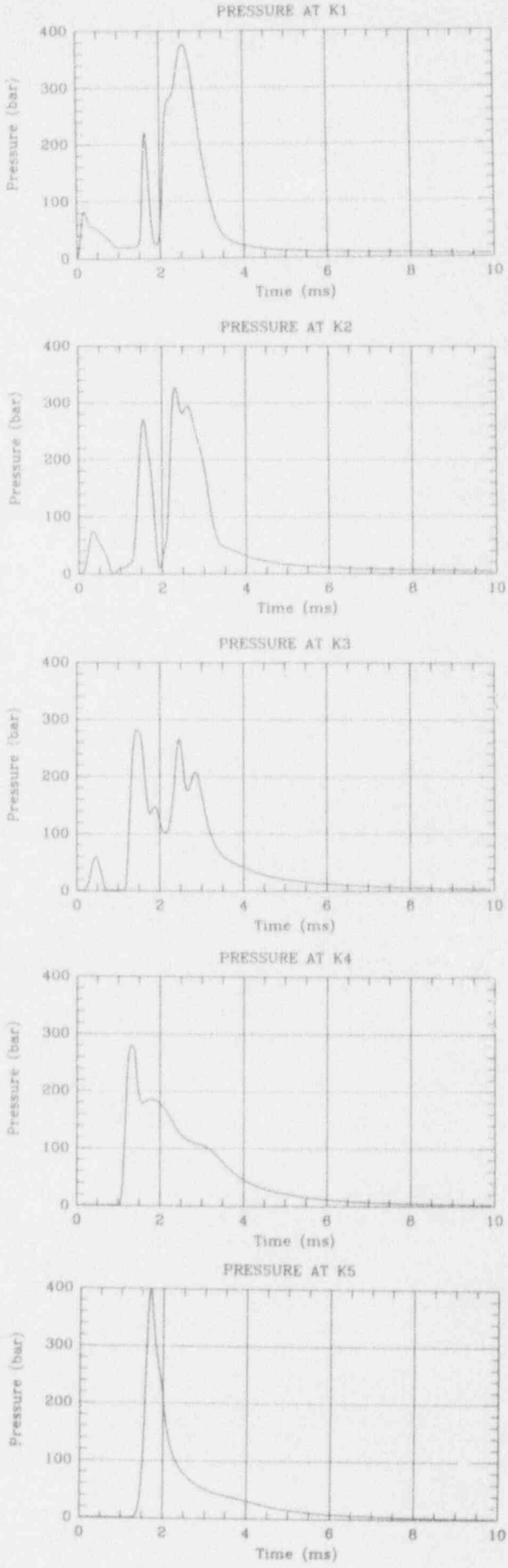

STEPWISE VERIFICATION OF THERMAL DETONATION MODELS:

EXAMINATION BY MEANS OF THE KROTOS EXPERIMENTS

M. Bürger, M. Buck, K. Müller, A. Schatz
Institut für Kernenergetik und Energiesysteme (IKE), University of Stuttgart,
Pfaffenwaldring 31, 7000 Stuttgart 80, Germany
Telephone ++49-711-685-2368 FAX ++49-711-685-2010

ABSTRACT

This paper picks up a verification line which has been started in an earlier publication with analyses on triggered thermal detonation experiments in the KROTOS facility. Improvements and extensions performed meanwhile in the thermal detonation code IDEMO as well as present results obtained with the improved code are described. New calculations on tin/H_2O experiments and a first calculation for experiments with an Al_2O_3/H_2O system are presented. The comparison of our computational results with calculations of other authors for the tin/H_2O experiments shows that the experimental results can in principle be reproduced by two different approaches, both introducing however rather extreme assumptions. From these observations it can be concluded, that further progress in code development and verification requires specific checks between different codes and working out of determining features such as the fragmentation process and non-equilibrium effects in water heating and steam production. Further, the calculations and comparisons lead to more specific requirements for experimental checks.

I. INTRODUCTION

State of Modelling. Steam explosions remain an important topic for LWR safety considerations, not only concerning violent events threatening the reactor pressure vessel (RPV) and the containment but also milder interactions between molten core material and water affecting the course of a severe accident. This broadening of interest is mainly due to the increased emphasis on accident management. Therefore, in this frame, tools are required for analyses of all relevant phenomena, ranging from milder to violent interactions and encompassing all phases of the explosion process, i.e.

- breakup of melt streams in water,
- premixing with the water under vapor film boiling,
- spontaneous triggering of interactions due to local film breakdown and/or entrapment interactions as well as triggering by external shocks,
- escalation and propagation of mild interactions or strong pressure waves, i.e. thermal detonations,
- expansion of the pressurized mixture delivering the resulting load to structures.

Such modelling has to a large extent been performed and promoted by Theofanous and coworkers, e.g. /1/ - /3/. Special features of their code development are the integration of premixing and propagation models in the PM-ALPHA & ESPROSE code system, both based on transient two-dimensional multiphase description. Not only thermal detonations with sharp shock fronts as in earlier versions of the 1D propagation code IDEMO of IKE (still applied in /4/) can be calculated, but also milder interactions with slower pressure development. Further advanced code developments on premixing and propagation have especially been done by Fletcher and Thyagaraja with the CHYMES premixing code /5/ and the 1D propagation code CULDESAC /6/ as well as by Young /7/ with the IFCI and Chu and Corradini /8/ with the TEXAS codes, mainly orientated at premixing and slow propagation (see /9/).

However, although for the key phases premixing and escalation/propagation several rather sophisticated codes are available, the problem of modelling vapor explosions appears to be far from being solved. On the one hand, the formulation of exchange terms in the multiphase descriptions remains incomplete and uncertain. This concerns heat transfer and drag forces as well as the partitioning of transfered heat between water and steam and also within the water. Fletcher demonstrated strong influences of these exchange formulations even for the premixing models /10/ and discussed the uncertainties in this respect for the propagation modelling /6/.

For both stages of a vapor explosion, most severe uncertainties exist on the fragmentation processes. The initial coarse fragmentation of melt jets impinging into the water pool and of resulting droplets falling down in the pool under vapor film boiling determine the premixing behavior. Rapid fine fragmentation either thermally-induced after vapor film collapse or due to relative velocities between the droplets and the coolant within fully developed detonation waves form the basis of the explosive behavior.

Necessity and Procedure of Stepwise Verification. On the other hand, experimental verification of the models remains to be done. Integral experiments will not be sufficient because of the existing uncertainties in the modelling of single processes and of their complex interactions. Thus, it is necessary to perform experiments which concentrate in an idealizing manner on single aspects and separate, specific processes. Since, nevertheless, also separated phenomena such as fragmentation remain itself complex, it is necessary to vary modelling approaches for searching possible explanations. Only by exhausting such approaches, by going to their limits, eventually up to the point of contradiction with experimental results and also by confrontation with alternative explanations, it may be possible to work out the real physical mechanism. Thus, verification of the modelling

cannot simply mean to check the difference between an experimental result and a certain modelling approach or even to fit the model to the experimental output. Verification must instead be a stepwise procedure in different ways:

1. Separate verification for single processes and aspects of modelling under idealizing and well-defined conditions, e.g. separate analysis of different stages of vapor explosions such as coarse premixing and escalation/propagation, separate analyses of drift of solid particles in water streams, of vapor film boiling and collapse at solid spheres, of shock wave interaction with assemblies of solid spheres, of fragmentation of single drops etc.

2. Examination in steps with increasing complexity, eg. single drops-drop assemblies, cold-hot, solid-liquid, single stages-integral process.

3. Stepwise working out of central mechanisms also from more integral experiments. This must be done based on some hypothetical modelling of single processes and their interactions. Different approaches of this type must be applied, varying elements of modelling. Decision on alternative approaches can be done by confrontation of their consequences with experimental results, especially with tendencies resulting from variation of experimental parameters.

Present Contribution. The present contribution picks up a verification line which has been started in /4/ with analyses on the KROTOS experiments at the JRC Ispra. These experiments are integral thermal detonation experiments with melt input from above in a test tube of approximately 1 m height and triggering from below by a gas trigger. Special features which yield relatively defined conditions and specific detection of phenomena are the defined gas trigger, the resulting unidirectional propagation of a pressure wave from below in the rather narrow tube, indicating the possibility to restrict to 1D analysis, and the detection of sucessive pressure pulses in the given direction of wave propagation. Due to the otherwise integral character mainly the third procedure had however to be chosen.

Calculations with the transient 1D multiphase thermal detonation code IDEMO have been performed, not mainly for showing - as sometimes misunderstood - that IDEMO just correctly describes the experiments. Instead, a main aim was to work out the uncertainties and deficits in presently available approaches. Furthermore, by variations of uncertain premixture conditions and especially of the fragmentation description it was intended to work out different possibilities of explaining in principle the experimental results. This should serve as a basis for further checks, possibly including more decisive approaches. Such more decisive modelling was e.g. demanded from the results in /4/ for the triggering process, the thermal fragmentation contribution and the part of water heated up including steam production. From the experiments or from coarse premixing models more defined coarse mixture data were desired.

For the present contribution these demands could only partly be fulfilled. But, significant extensions and improvements have meanwhile been performed in IDEMO, e.g. concerning the numerics, especially introduction of shock capturing, of variable cross-sections, several types of boundary conditions and specifically for KROTOS the improved modelling of the gas trigger. Thus, alone by this a further calculational approach to KROTOS seems to be justified. In addition, other authors have meanwhile performed calculations for KROTOS /11/, which gives rise to comparisons and discussions.

The main aims pursued in this paper are

- to check the state of interpretations of tin/H_2O experiments in KROTOS and the remaining uncertainties,
- to present specific verification of the new trigger formulation with IDEMO,
- to consider the influence of this and of other extensions in IDEMO on the analysis of KROTOS,
- to present a calculation for Al_2O_3/H_2O experiments in KROTOS /12/, which may introduce other aspects in the discussion of the fragmentation process, due to the stronger explosion potential.

IMPROVEMENTS AND EXTENSIONS IN IDEMO

Basic descriptions of the transient, one-dimensional thermal detonation code IDEMO can e.g. be found in /13/-/15/. Four flow phases, melt droplets, melt fragments, steam and water were included, however with the simplifying assumptions of mechanical equilibrium between steam, water and the fragments as well as thermal equilibrium between steam and water. The usual multiphase flow equations have been applied with all species at a common pressure. Melt and fragments are considered as incompressible. Heat transfer from the fragments to the coolant is uniformly attributed to the coolant phase composed in principle of water and steam, while the drag work is divided up between coolant and fragments, thus heating both. For the heat transfer from the fragments only a description with parametric heat transfer coefficient has been chosen. Usually a formulation for instantaneous thermal equilibration is applied based on the assumption of very small fragments.

More detailed descriptions have been developed for the drag forces between melt drops and coolant as well as for the fragmentation of the melt drops. A key role has been attributed to the corresponding constitutive relations because fragmentation can be considered as determining the whole process and drag determines the development of relative velocities between the drops and the coolant, which produce hydrodynamic fragmentation. For the formulation of the drag law a correlation for assemblies of spheres is used, weighted with a factor which contains the influence of the drop deformation with single drops (see e.g. /13/). The presence of fragments is considered in the drag law via a mean coolant density, thus taking into account an increase of inertia of the fluid surrounding the drops. The same is done in the fragmentation model.

Detailed models have been developed for the fragmentation process, mainly with respect to hydrodynamic fragmentation due to relative velocities. Especially, these are models on drop deformation and resulting breakup, on breakup by Taylor instabilities and on stripping of crests of shear-flow produced waves /16/. Wave stripping showed to be by far the most rapid mechanism. For saving time in the transient computations, a simplified correlation form for hydrodynamic fragmentation has been worked out by means of various calculations with the detailed fragmentation description integrated in the steady state version /13/.

Some deficits in the state of IDEMO concerning the analysis of KROTOS experiments have been mentioned in /4/. The state of revision and extension may be roughly characterized as follows.

In the earlier versions of IDEMO a shock fitting technique was applied. A sharp shock front was assumed as leading edge of a detonation wave and was treated as a boundary for the flow field inside the wave. An iterative procedure was necessary to solve the Hugoniot equations in order to couple the flow field inside the detonation wave to the coarse mixture ahead of the shock front. In contrast to his formulation, the application of a shock capturing technique in the numerical solution procedure is an important feature of most of the more recently published premixing and detonation models (e.g. /1/ - /3/ and /5/ - /9/). It allows in principle not only the calculation of thermal detonations but also of milder interactions which propagate more slowly through the mixture, thus not fulfilling the requirements of quasi-coherent events. Furthermore, the possible buildup of sharp shock fronts can in principle be calculated by this type of modelling. Also the modelling of interactions between a detonation wave and several types of boundary conditions as well as the extension to multiple dimensions can be carried out in a more straightforward way.

In view of the large spatial gradients that can appear in the modelling of thermal detonations, it is clear that for this task a very robust and elaborate numerical scheme is required. Thus, starting from the early numerics in IDEMO based on the MacCormack's method, a Total Variation Diminishing (TVD) scheme has been implemented, using a modified version of the method described in /17/. The basic feature in TVD methods is to append to the difference scheme a non-linear term which applies precisely the correct amount of artificial viscosity needed at each mesh point to prevent overshoots and undershoots. The advantage of this description over usual artificial viscosity methods is due to the automatic choice of artificial viscosity. Further details of the chosen numerical description will be given in a paper to be published later-on.

A key demand with respect to KROTOS was to model more adequately the gas trigger applied in the experiments. In detail, the triggering device is shown in Fig. 1, together with a test section which was applied in /18/ to characterize triggers. The gas chamber has a volume of 15 cm^3 and can be loaded to a desired pressure which after pressurization is blocked with a tightening screw. After a certain delay time, a piston is accelerated by a pneumatic drive destroying instantly a 0.1 mm thick steel membrane separating the pressurized gas and the water column, thus delivering the pressure pulse.

For modelling this pulse due to the expansion of the gas, the gas volume is treated as a separate region coupled to the mixture region via boundary conditions at the moving gas/mixture interface. These are especially equal pressures and velocities on both sides of the interface. For the gas region adiabatic behavior and instantaneous pressure equilibration, i.e. an unique pressure, is assumed. Numerically, an iterative procedure is necessary to fit the boundary conditions and to determine the boundary behavior. Furthermore, for getting an adequate trigger description, it turned out to be necessary to take into account the changing cross-section in the conical part of the triggering device as given in Fig. 1. Therefore, in the basic multiphase equations in IDEMO variable cross-sectional areas had to be included.

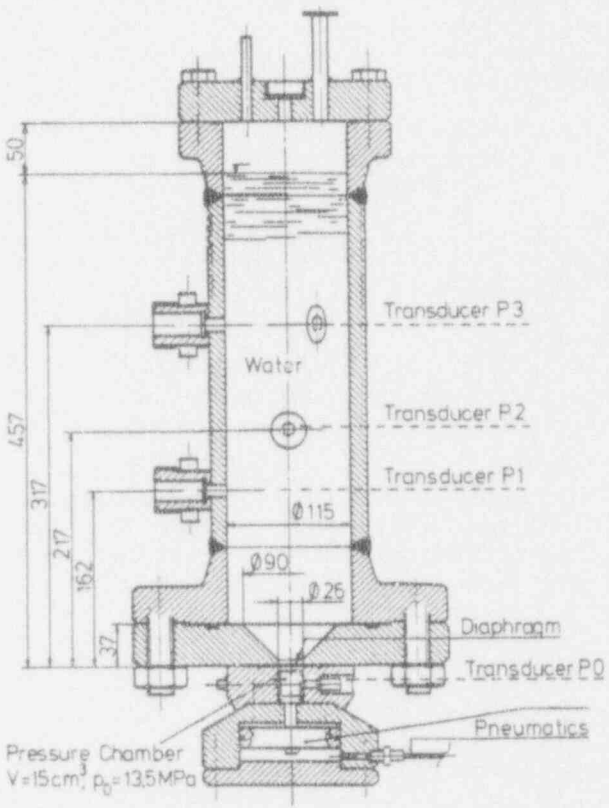

Figure 1. Sketch of KROTOS gas trigger together with the test section used in the trigger tests /18/.

A rough modelling of nonhomogeneous heating of coolant has already been implemented earlier /14/, dividing the liquid part up into volumes, one heated and the other remaining unaffected from heat transfer. The two volumes remain in mechanical equilibrium and especially have the same pressure. Steam production is presently only modeled under thermal (as well as mechanical) equilibrium conditions. In the present calculations on KROTOS no consideration on nonhomogeneous heating of water has been done. Furthermore, for heat transfer from the fragments the formulation with instantaneous thermal equilibration has been applied.

III. STATE OF ANALYSIS ON KROTOS EXPERIMENT

Since the experiment KROTOS-21 (see /4/ for a description of the experimental device and main results) appears to be the most interesting one in the series of tin/water experiments, all our analyses up to now are concerned with it. Main conclusions of the analyses in /4/ have been, that

- hydrodynamic fragmentation based on realistic models, especially the wave stripping model /15/, /16/, is not sufficient to explain the experimental results, at least without additional assumptions such as strongly nonuniform mixtures (axially as well as radially), nonhomogeneous water heating and strong influences from the triggering process,

- only by assuming an additional thermally motivated

fragmentation contribution a rough approach to the experimental pressure pulses could be reached, yielding rapidly a steady wave propagation comparable with the experimentally obtained pressure level, however with much too long waves, not fitting wave propagation and a too small final pressure level,

- the choice of a stronger trigger which supports the wave propagation from behind relaxes somewhat the necessity of an additional fragmentation contribution and together with axially varying mixture data yields a better explanation of the experimental results,

- a large discrepancy remains between the theoretically and experimentally obtained fine fragments of 70% vs. 20%, in spite of the strong uncertainties in experimental detection.

For the calculations with IDEMO in /4/ heat transfer has been attributed to the whole water content in the mixture. However some increased melt content has been assumed with the argument of concentration of melt in the middle of the tube. A strongly increased melt content in the middle has been assumed by Yuen, Chen and Theofanous /11/ (mass ratios of about 8 to 12 of melt to coolant). This has especially been done for simulating nonuniform heating of the water, which has also been considered as important for the analysis of KROTOS-21 in /4/. In addition to heat transfer only to the water in the mixture region, direct steam production under nonequilibrium conditions has been assumed in /11/. Such additional assumptions were necessary also with the hydrodynamic fragmentation description of the authors in /11/ to obtain a roughly sustained wave propagation. Only by dropping direct vaporization the propagation fizzles out according to /11/.

Thus, the results and conclusions in both analyses appear to be essentially consistent in that only such special assumptions as proposed in /4/ may allow hydrodynamic fragmentation as explanation for the experimental results. Using two radial nodes in /11/ gives an additional feature, however seems to make no essential point for the interpretation. Actually, as can be seen from the comparison of the pressure developments in the inner and outer radial nodes given in /11/, the pressure reduction is not very strong, considering the rather small and also somewhat erratic peaks from the inner nodes. These peaks seem to be caused by the rapid steaming events assumed in the analysis. The main bodies of the pressure curves of the inner nodes are however rather similar to those from the outer nodes. This indicates a rather strong coupling which is underlined by the simultaneous wave propagation. The question remains wether the coupling to the water in the outer node yields an effective pressure decrease in the inner node with the mixture, due to the compressibility of the water volume.

For a further comment on this, the statement in /11/ may be considered that calculations with 1D models even in apparently 1D-geometries force to mix the debris with too much water or by using less water content in the mixture lead to distortion (reduction) in the actual compressibility of the system. This is of course true, in principle. However, also in a 1-D model part of the water volume can be taken as unaffected from heat transfer, considering it as an additional flow phase. Assuming the same pressure in these water parts, i.e. instantaneous pressure equilibration, would mean to overestimate the pressure reduction in the heated water part. But, this reduction remains nevertheless small if the compressibility in the inner part is much higher than in the outer part, which is certainly the case already for small amounts of steam existing in the inner part.

Thus, this means that 1D approximations should be sufficient under the present conditions, also with assuming a concentration of the mixture in the middle of the tube. Improvements concerning coupling of the pressures can also be done in this approach by roughly taking into account the sideways expansion. Of course a real 2D description contains more possibilities of description. It appears however questionable whether only two radial nodes can be taken as a real 2D approach, actually calculating radial flow and pressure dynamics.

Thus, the main differences of the analyses and interpretations in /4/ and /11/ concern the actual coarse mixture configuration, the role of fragmentation, especially of hydrodynamic fragmentation, and the influence of nonhomogenous water heating with steam production. The quality of agreement of the calculations with the experimental results however appears to be comparable and therefore gives no support for one of the different interpretations. This can be seen from the comparison in Fig. 2.

IV. ANALYSIS WITH THE IMPROVED DETONATION CODE IDEMO

However, an uncertainty was noted in /4/ concerning the modelling of the trigger. In the final result of /4/, shown also in Fig. 2, a formulation based on a prescribed heat input into an initial volume was chosen which yielded an approximation to the experimental signal at K1. The resulting wave propagation was considered to be significantly influenced by the trigger, as an overdriven case. This may also be true for the calculation from /11/ in Fig. 2.

For getting a more definite result, starting with the simulation of the trigger itself as in /11/, the formulation for the gas trigger developed meanwhile and described above has been applied in a new calculation. Before, this formulation has been checked against experimental results from tests in which the KROTOS gas trigger was applied to a column of pure water in the test section sketched in Fig. 1. Results from calculations with IDEMO are shown in Fig. 3, with the distance taken from the diaphragm. Pressure wave propagation, development and reflection at the upper water level can be seen. A comparison with the experimental results is shown in Fig. 4 together with results from a calculation with the EURDYN (2D-Finite-Element) code performed at JRC Ispra /18/.

A rather good agreement is firstly obtained for the pressure development in the trigger gas. The experimental pressure signals at the subsequent pressure transducers in the water can be interpreted in view of Figs. 3 and 4 as follows.

After the destruction of the membrane the trigger produces a compression wave running upwards, leading to a fast increase of pressure. The peak pressure detected at the transducers is lower than the loading pressure of 13.5 MPa in the gas trigger, caused by distortion of the pressure wave in the conical part of the test section and the expansion of the trigger gas. This leads also to a first slower and somewhat fluctuating decrease of pressure, especially visible at transducer P1 next to the trigger. The initial pressure wave is reflected at the upper water level as a rarefaction wave running downward and extinguishing rapidly the increased pressure, leaving behind a region below saturation pressure and thus with steam production.

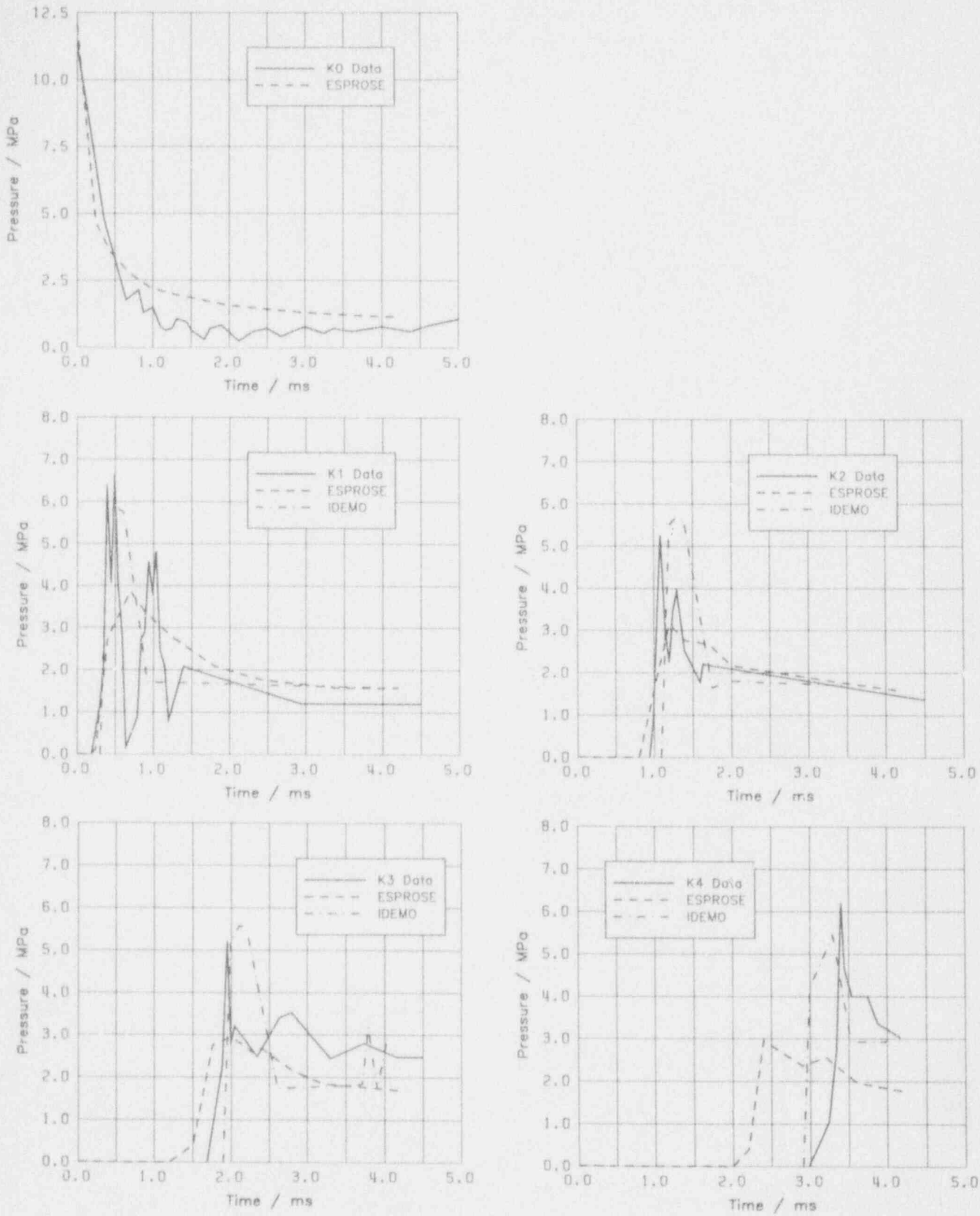

Figure 2. Comparison of the pressure traces detected in test KROTOS-21 with the results of calculations with IDEMO (taken from /4/) and ESPROSE (taken from /11/)

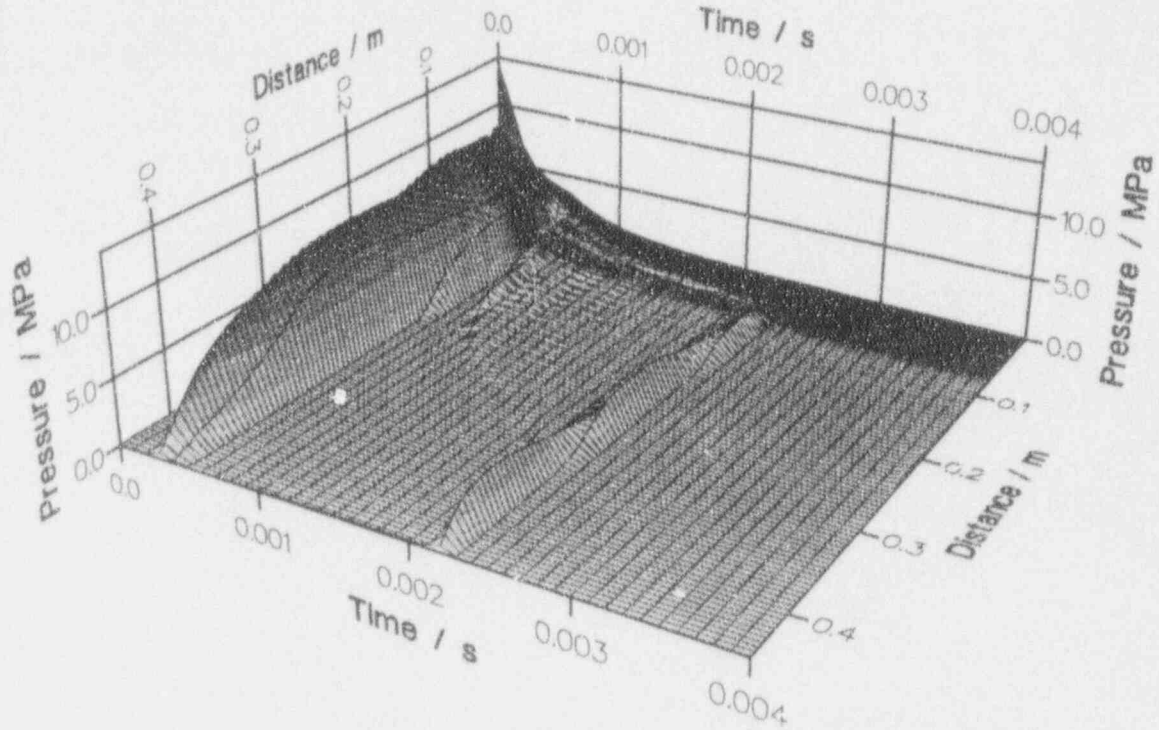

Figure 3. Calculated time development of the pressure versus distance from the diaphragm for tests with the KROTOS gas trigger applied to a column of pure water

Due to the different distances of the subsequent transducers from the two surfaces, the resulting first pressure peaks become narrower from transducers P1 to P3. Reflection of the rarefaction wave at the (upwards moving) lower gas boundary leads again to a compression wave directed upwards running into the region with steam, thus becoming slower and weaker due to the increased compressibility and collapsing steam, which produces some pressure fluctuations.

Meanwhile, a small compression wave has been started from the upper region of the water column caused by the gradient between the pressure in the cover gas and the previously established sub-pressure in the column. It collapses the steam in the upper region and collides with the upwards running compression wave yielding the significant and relatively strong pressure peak after somewhat less than 3 ms. This is mainly due to the decrease in compressibility produced by the compression wave from above. The resulting pressure increase propagates upwards as well as downwards. The strong decrease in time of this peak is again caused by the reflection of these waves as rarefaction waves after reaching the water levels.

This dynamic behavior is well reproduced and thus explained by the present calculation as can be seen in detail in Fig. 3 and for comparison with the measured pressure development in Fig. 4. In some aspects the results from IDEMO appear even to be in better agreement with experimental data than those from the EURDYN calculation, also included in Fig. 4. Especially, this concerns the shape of the first pressure pulse and the occurence of the second relatively wide pulse which does not exist in the EURDYN calculations. The time delay between this pulse and the experimental one may be explained by uncertainties in the modelling of steam production and collapse due to the interaction with the travelling waves. Nonequilibrium effects may also play a role in this respect, whereas the present steam model only considers equilibrium states. While IDEMO does not reproduce the sharp pressure peaks following the first pulse which are given better from EURDYN, the result for the impulse from IDEMO is in still better agreement with the experiment.

With the present gas trigger formulation, justified by the above comparison, a new calculation for KROTOS-21 has been performed. The volume fractions of the flow phases in the premixture have been chosen as included in Fig. 5 which shows the calculated time development of the pressure wave. As compared to the earlier IDEMO calculation an even more rapid thermal fragmentation has been assumed here, yielding the shorter pressure peaks, more similar to the experiment. The time development of fragmentation is shown in Fig. 6 for different locations. It contains the hydrodynamic fragmentation according to the correlation based on wave stripping /13/ as well as the thermal fragmentation contribution assumed additionally. For further information, the time development of the local distributions of important quantities are given in Figs. 7-10.

Furthermore, the shock capture formulation described above has been applied, however still assuming steam to be instantaneously in thermal equilibrium with the water. The representation as pressure traces at the transducer locations in Fig. 11 shows some improvements in comparison with the

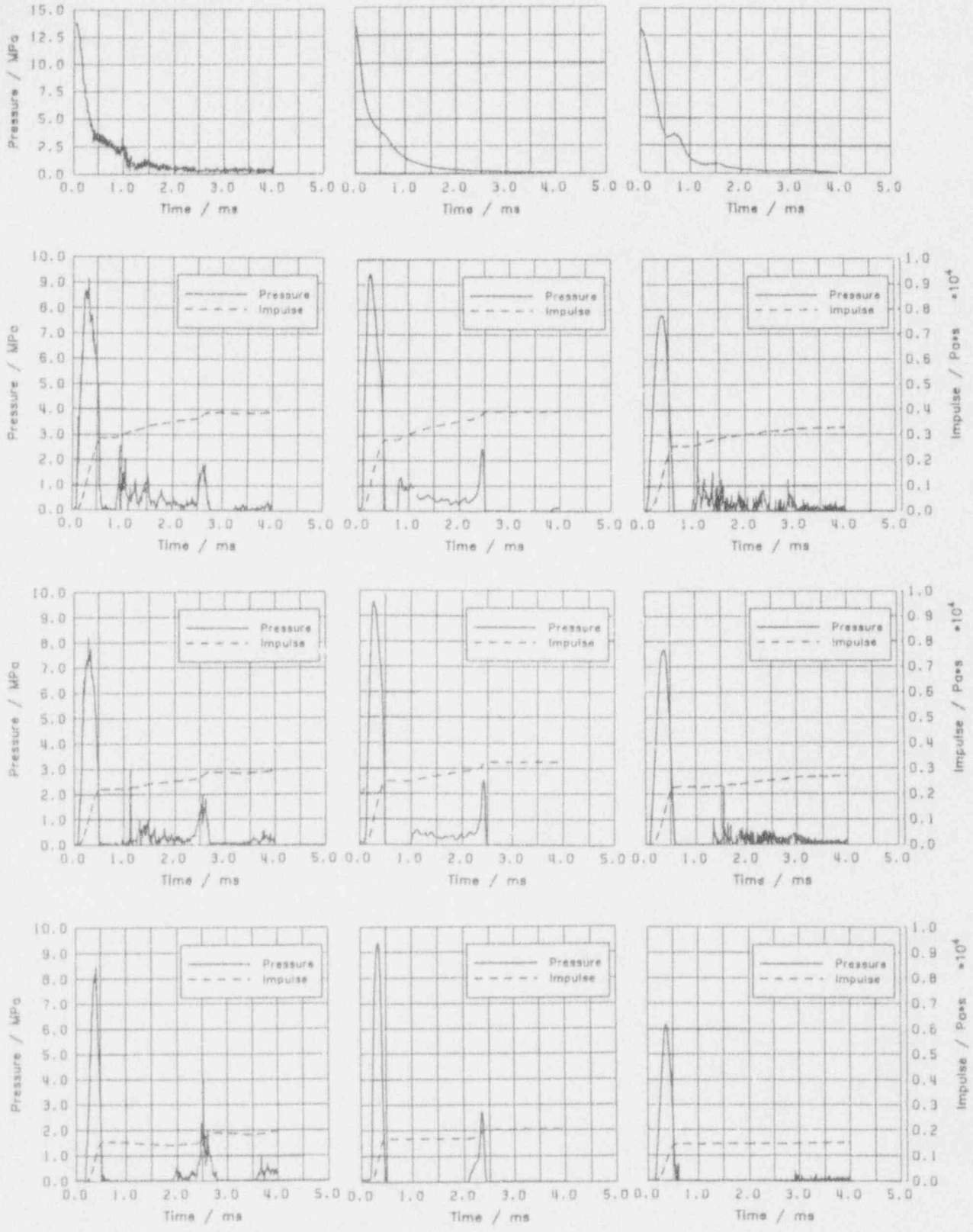

Figure 4. Comparison of the pressure and impuls ns from the trigger experiment detected at JRC Ispra (left column) with the results of IDEMO (middle) and EURDYN olumn). P0-P3 from top to bottom.

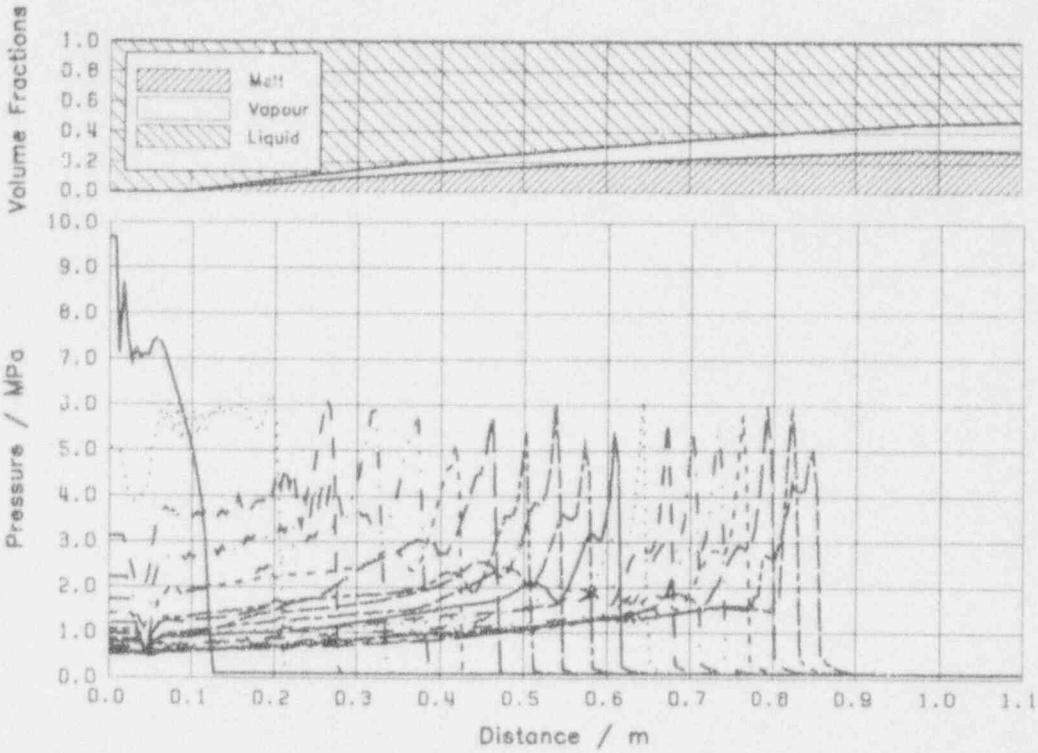

Figure 5. Time development (increment is 0.2 ms) of the pressure versus distance from the trigger diaphragm from the present calculation for test KROTOS-21 with included coarse mixture data.

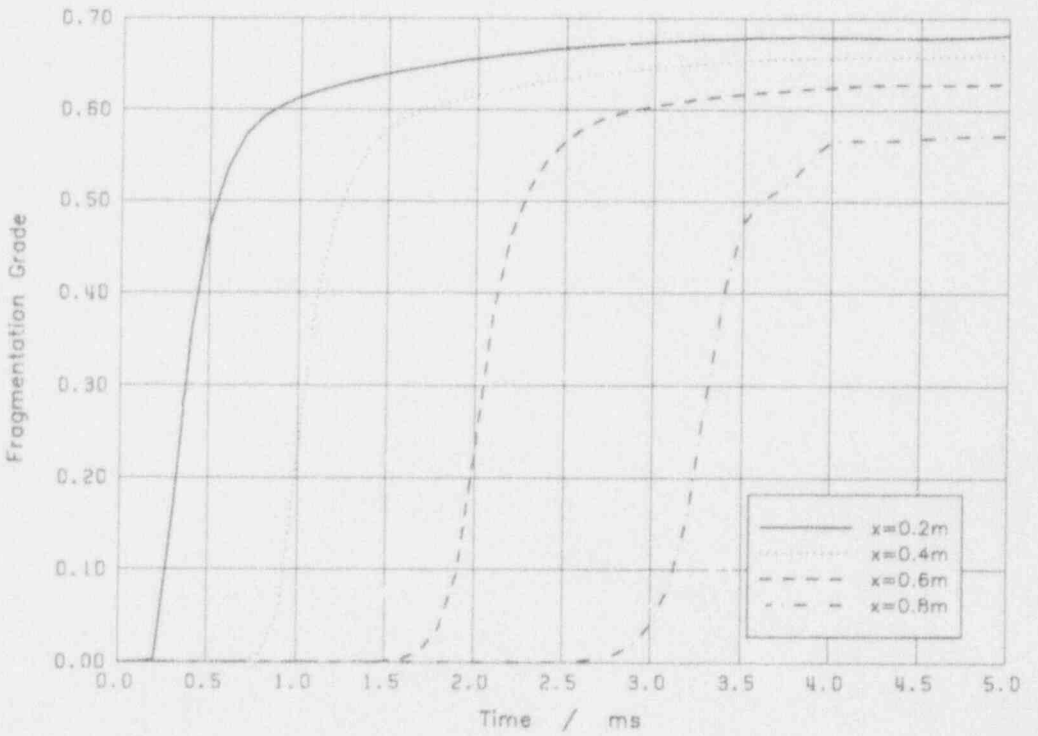

Figure 6. Time development of fragmentation (sum of hydrodynamic and additionally assumed thermal fragmentation) at different locations for the new calculation on KROTOS-21.

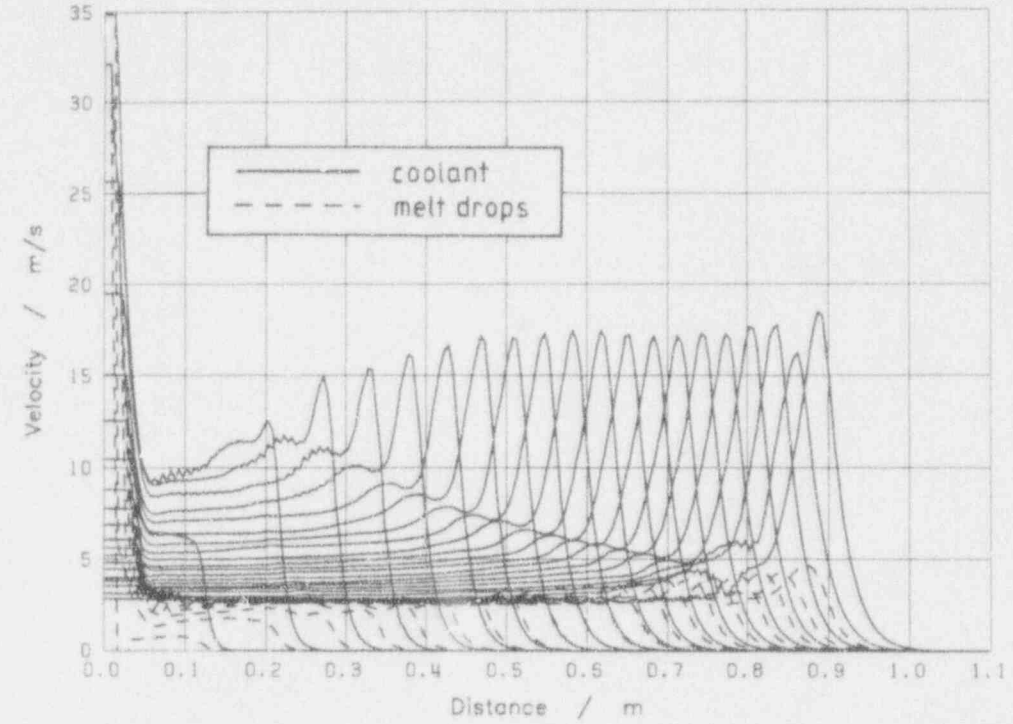

Figure 7. Time development (increment is 0.2 ms) of the local distributions of melt and water velocities in the test tube from new calculation on KROTOS-21.

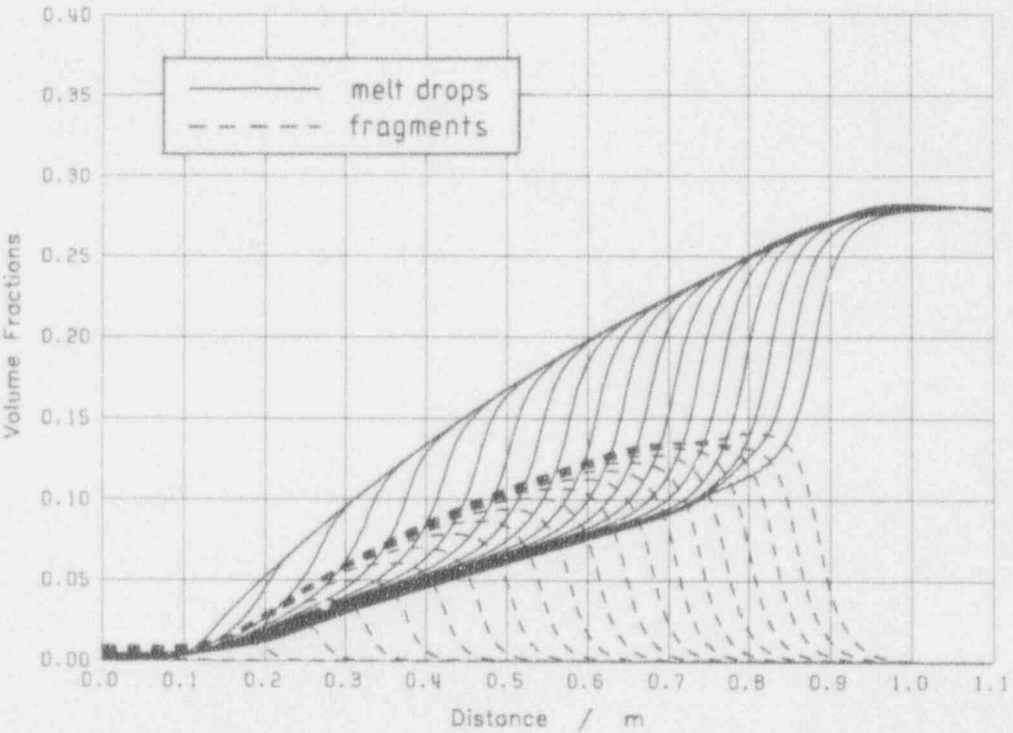

Figure 8. Time development (increment is 0.2 ms) of the local distributions of melt drops and fragments in the test tube from new calculation on KROTOS-21.

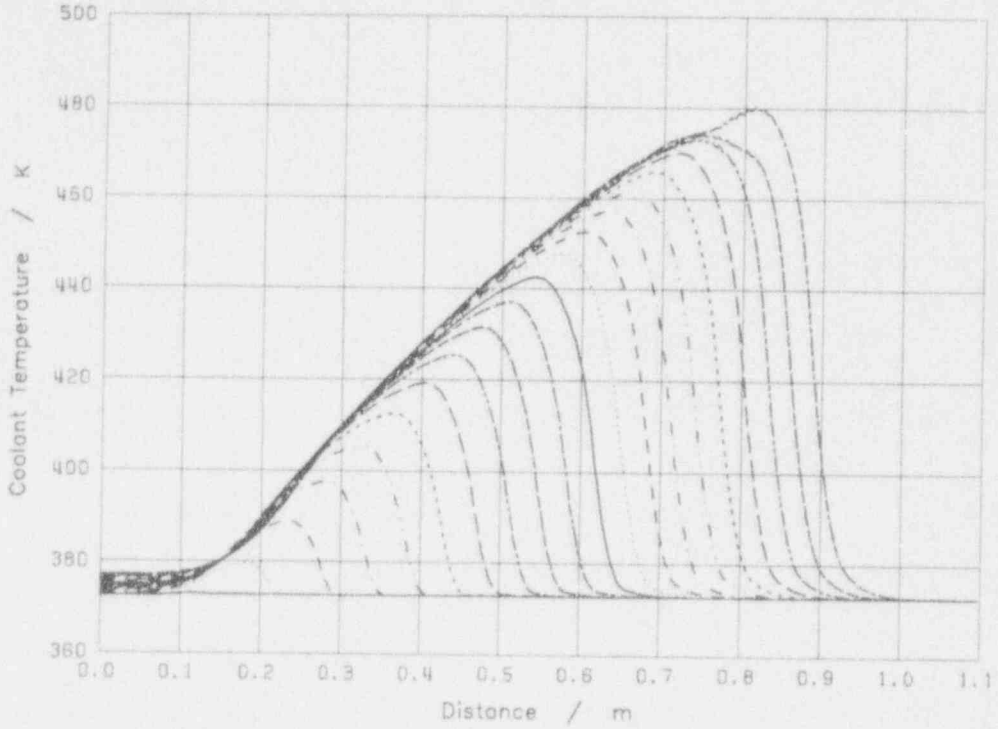

Figure 9. Time development (increment is 0.2 ms) of the local distribution of coolant temperature in the test tube from new calculation on KROTOS-21.

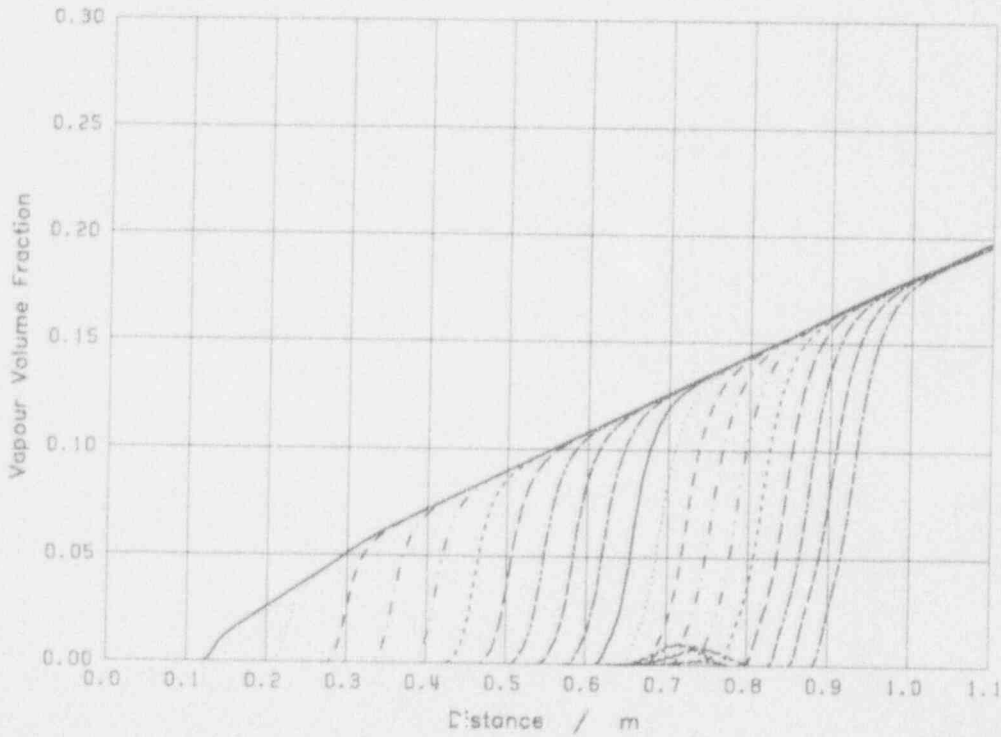

Figure 10. Time development (increment is 0.2 ms) of the local distribution of void fraction in the test tube from new calculation on KROTOS-21.

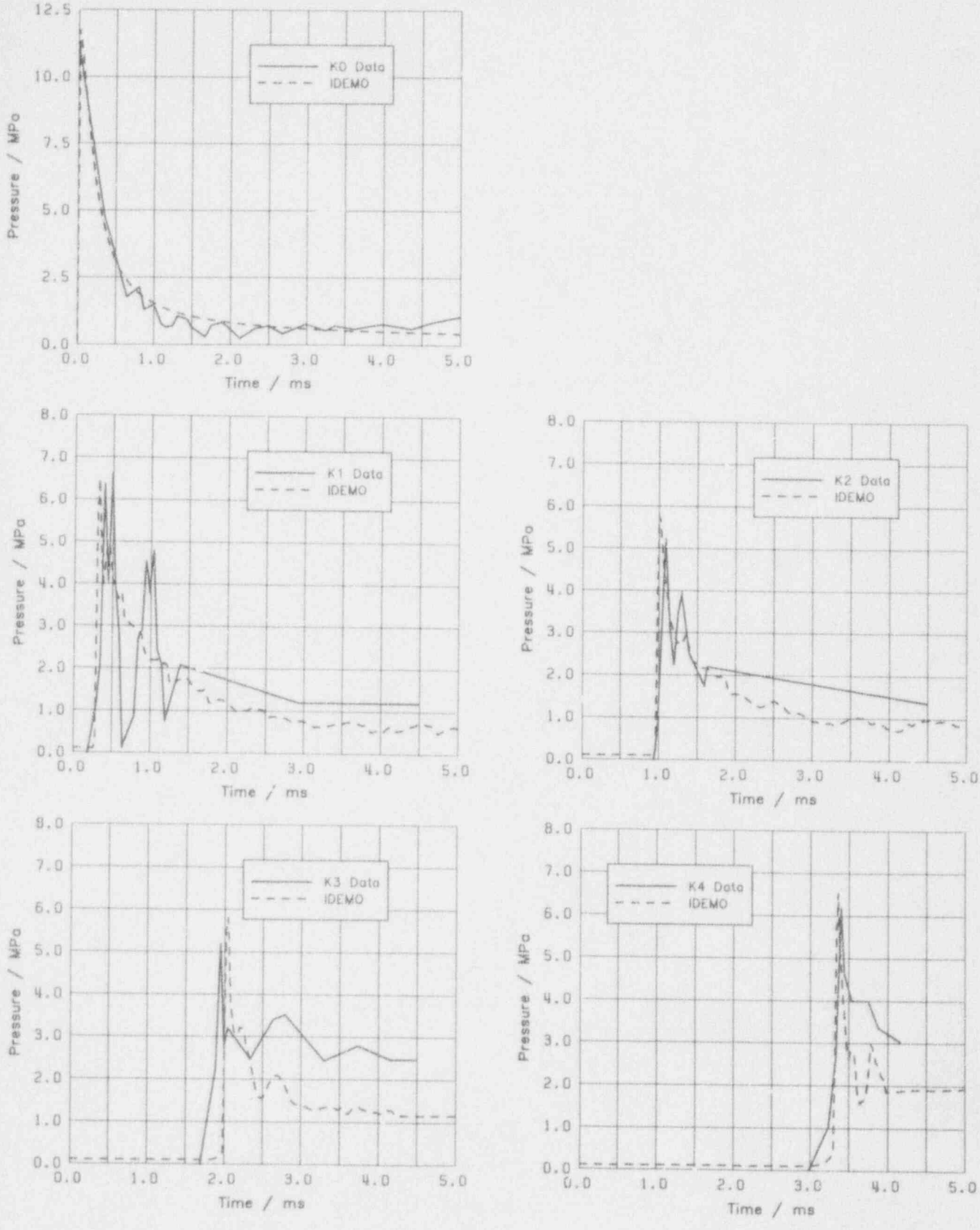

Figure 11. Comparison of the pressure traces detected in the test KROTOS-21 with the results of the present IDEMO calculation.

experimental data against the earlier IDEMO results. This concerns especially the shorter leading pressure peaks reproducing better the shape of the experimentally detected pressure traces and the arrival times of the shock wave at the locations of the subsequent pressure transducers, while for the final pressure level relatively low values have been obtained.

Altogether, the discrepancies between the different calculations and the experiment remain within a common range of uncertainties. Thus, the above statement is underlined. Taking into account the uncertainties in the experimental data, especially on the coarse premixture, the main problem appears not to lie in the remaining discrepancies but in the fact, that comparable results have been obtained using different approaches. On one hand, a strong concentration of melt in a center region of the test tube had to be assumed together with a prescribed fraction of the debris energy given directly to vapor production in order to interpret the experimental results on the basis of a hydrodynamic fragmentation law. On the other hand, with less strong assumptions on the premixture, an additionally assumed strong thermal fragmentation contribution had to be considered. Both calculations necessarily include assumptions on the axial variation of the premixture. Nevertheless, the calculations appear to support the interpretation of a significant trigger contribution in sustaining the wave (see /4/) since even with the extreme assumptions on the premixture or the fragmentation process no escalation is obtained.

V. DISCUSSION ON THE FRAGMENTATION FORMULATION

Further decision on the correct interpretation of KROTOS-21 can be reached by considering in more detail the fragmentation process, especially by introducing validated models in the detonation codes. Concerning hydrodynamic fragmentation processes a considerable amount of work has already been done in this direction in the frame of IDEMO development. Different hydrodynamic fragmentation models based on wave stripping due to shear flow instabilities ("wave stripping model"), on breakup by Taylor instabilities and on deformation breakup have been developed and integrated in IDEMO or in the corresponding steady state version. Comparison with various experimental results and between the models are considered to support the wave stripping mechanism and model (see e.g. /15/, /16/, /19/-/21/). From calculations with this model a correlation has been developed based on the typical features of the stripping process, i.e. proportionality of the instantaneous stripping rate to the surface of the drop and the relative velocity. Constants for different premixing conditions have been fixed due to comparisons between the application of this correlation and of the fragmentation model. The simplified correlation approach described in /13/, /15/ has been used in the present IDEMO calculation.

A more detailed discussion on the fragmentation descriptions must be done separately in future. Here, it seems to be sufficient for a first step to roughly compare the correlations for hydrodynamic fragmentation applied in /4/ and /11/. The correlation used in /11/ corresponds in principle to that used in the IDEMO calculations, with the only difference that the correlation in /11/ contains the dimensionless fragmentation time expressed by an instantaneous dependence on the Bond number (according to the idea of the Taylor instabilities mechanism) while this expression corresponds to a constant in the IDEMO correlation (expressing the idea of stripping process).

Fig. 12 shows a comparison between applications of these

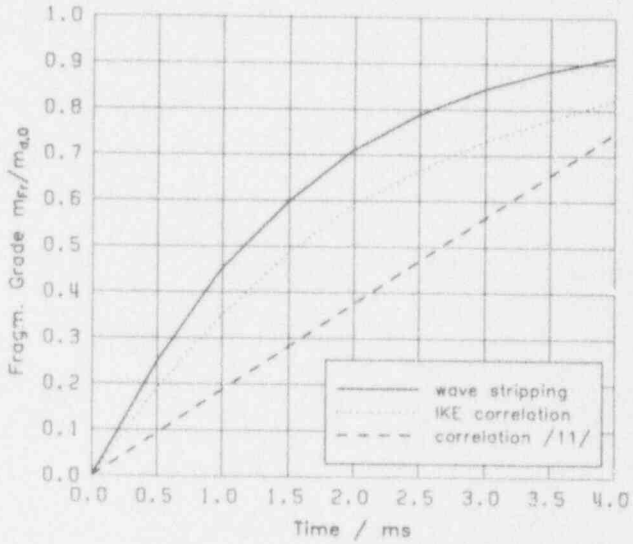

Figure 12. Comparison of results calculated with the IKE wave stripping model and the IDEMO correlation with the ESPROSE correlation for the mercury/water system of /4/.

descriptions for the mercury drop case given in Fig. 2 of /11/. In Fig. 1 of /11/ data points from single drop experiments are given which give support to the linear correlation line from /11/. The IKE description yields significantly stronger fragmentation in an initial phase, slowing down with decrease in drop size. The amount of fragmented mass after this is however roughly comparable. Further data and comparisons appear to be necessary for getting a firm basis. The much stronger fragmentation assumed for explanation of the KROTOS-21 experiments in IDEMO is shown in Fig. 13 (hydrodyn. + therm.). The comparison with the correlation for pure hydrodynamic fragmentation in the time range < 1 ms relevant to the detonation calculation (see Fig. 6) underlines the dominant contribution attributed to thermal fragmentation which had to be assumed. Again the hydrodynamic fragmentation correlation from /11/ gives a significantly weaker hydrodynamic fragmentation (with even stronger differences than for the mercury water system).

According to /11/, experiments with tin drops of 1273 K in 6.8 MPa shock waves yield a thermally driven fragmentation which is essentially complete by 1.5 ms. Dominance of thermal fragmentation under these conditions can be concluded from the much less fragmentation for a tin temperature of 633 K obtained with the same shock pressure /11/. This result could be taken as support for the assumed strong thermal fragmentation contribution in the IDEMO calculations (see Fig. 13). However, the results in /11/ appear not to be definitive. Especially informations on the grade of fragmentation within a certain time scale are needed. Further, the fragmenation assumed in the IDEMO calculations is still significantly stronger according to Fig. 13, yielding already 60% of fragmented mass after 0.5 ms.

Thus the conclusion remains that hydrodynamic fragmentation alone without additional strong assumptions, either on the coarse mixture and the steam production in /11/ or on the additional contribution of thermal fragmentation here and in /4/, cannot explain the experimental results obtained in KROTOS-21 with very similar conditions (shock pressure level of ~6 MPa, melt temperature of 1348 K) as in the single drop experiments of /11/.

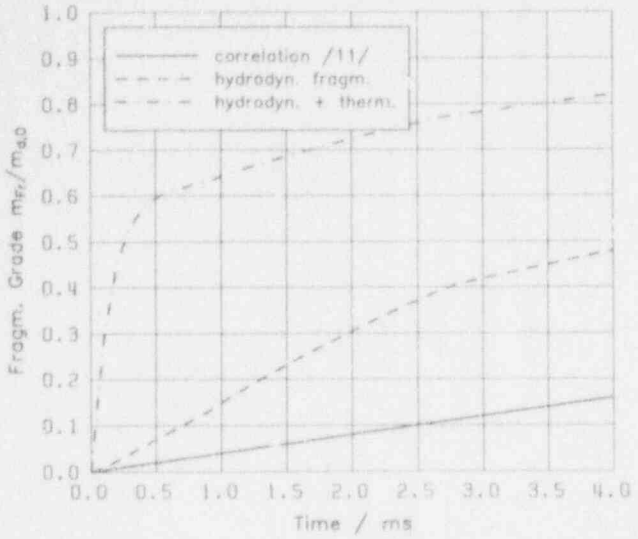

Figure 13. Fragmentation behavior of single tin drops in a 6.8 MPa shock wave from IDEMO and ESPROSE correlations.

Concerning the final grade of fine fragmentation, the present calculation as well as those in /4/ yield much too high grades of ~70 % of fragmented mass as compared to ~20 % in the experiment. On the other hand, from the calculation in /11/ only ~ 5 % result. In spite of the strong uncertainties in the experimental evaluation of fragmented mass, this may indicate in addition to the above results that an interpretation of the experiments between the extremes may be more adequate.

VI. CALCULATION ON AN Al_2O_3/WATER EXPERIMENT IN KROTOS

Some more insight may be gained from experiments with Al_2O_3 melt performed in KROTOS /12/. Due to the much higher melt temperature (2670 K) and melt enthalpy stronger resulting pressure waves and as stated in /4/ dominance of hydrodynamic fragmentation could be expected. Thus, the first point of interest was whether strong pressure escalations as observed in KROTOS-28 /12/ are obtained from calculations without extreme assumptions on the premixture from the present correlation of hydrodynamic fragmentation alone.

Indeed, the calculated pressure waves in Fig. 14 and the corresponding signals at the locations of the pressure transducers in Fig. 15 show a strong escalation. The premixture data used in the calculation are given in Table 1.

While a smaller value of the melt volume fraction of ~ 0.05 results from considering mixing of 1.5 kg of melt with all the water in the tube, higher fractions in the premixture are expected due to axial or radial concentrations. In the present calculation with a melt volume fraction of 0.1 no axial variation has been assumed. More detailed considerations and calculations will be done in future. Here, also an approximate trigger formulation has been used for a first calculation, not the extended one described above.

In Fig. 14, effects of a rarefaction wave from reflection at the upper water level can also be seen in the upper tube region. This corresponds to the beginning of an upwards expansion behavior of the mixture column under the assumption that the sideways tube walls hold, which was not the case in the KROTOS-28 experiment. For considering sideways expansion due to wall breaks a two-dimensional model is required, at least. The present calculation with reflection of a rarefaction wave demonstrates the improved abilities of the code after dropping the sharp shock front assumption and the shock fitting method and implementation of the shock capturing method.

Table 1. Mixture data used in the calculation for test KROTOS-28.

Melt	Al_2O_3
Coolant	H_2O
Pressure	0.1 MPa
Melt temperature	2673 K
Coolant temperature	373 K
Melt volume fraction	0.1
Vapor volume fraction	0.1
Melt drop radius	0.005 m

In spite of the restrictions mentioned above, the calculations reproduce essential features of the experimental results. In addition to the strong pressure increase up to pressures of more than 40 MPa, propagation velocities of up to > 600 m/s have been obtained from the calculations as well as from the experiment. While in the experiment practically all the melt was fragmented to an extremely fine grade, the calculated mass fraction of fine fragments is however only ~50 %. Thus, in refined calculations it may be checked whether even premixtures with assumed smaller melt fractions are sufficient for explaining the experimental results. The present result indicates finally that the present formulation of hydrodynamic fragmentation roughly explains the experimental results with Al_2O_3 without extreme assumptions on the premixture, whereas simulations of the tin experiments need such additional assumptions if based only on hydrodynamic fragmentation.

VII. CONCLUSIONS

The calculations performed up to now on the KROTOS experiments with thermal detonation codes show that the experimental results from the tin/water experiment of KROTOS-21 can in principle be reproduced with two extreme approaches. On one hand, a strong radial concentration of melt may be assumed in the center region of the tube as already proposed in /4/. With this approach performed in /11/ together with assumptions on direct steam production due to a part of transfered heat, hydrodynamic fragmentation becomes sufficient for explanation. On the other hand, with less extreme assumptions on the premixture and without taking into account nonhomogeneous heating of the water, a strong additional contribution of a thermal fragmentation had to be assumed in the present calculations and in those of /4/.

Thus, finally the question of interpretation of the experiments and of code verification leads to the questions of actual coarse mixture conditions, of nonhomogeneous heating and nonequilibrium vapor production as well as to the appropriate modelling of fragmentation. An approach between the extremes may be finally more adequate. Concerning fragmentation the

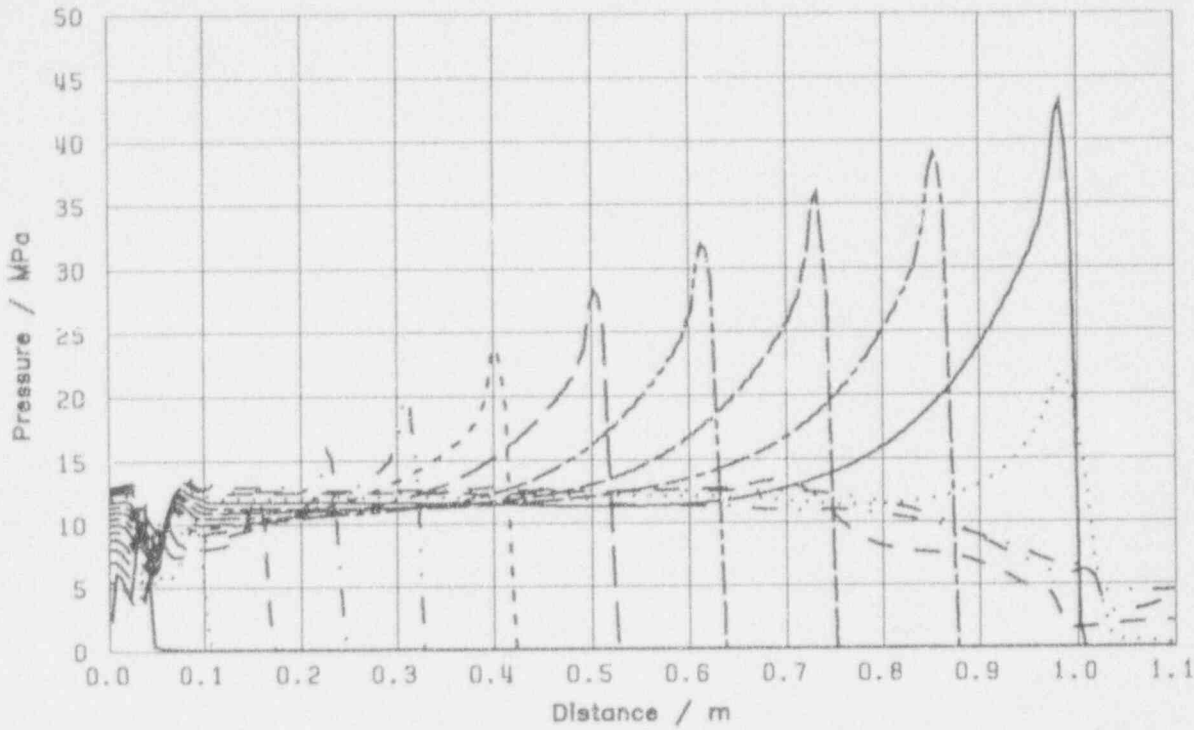

Figure 14. Time development (increment is 0.2 ms) of the pressure versus distance from the trigger diaphragm calculated for the Al_2O_3/H_2O experiment KROTOS-28.

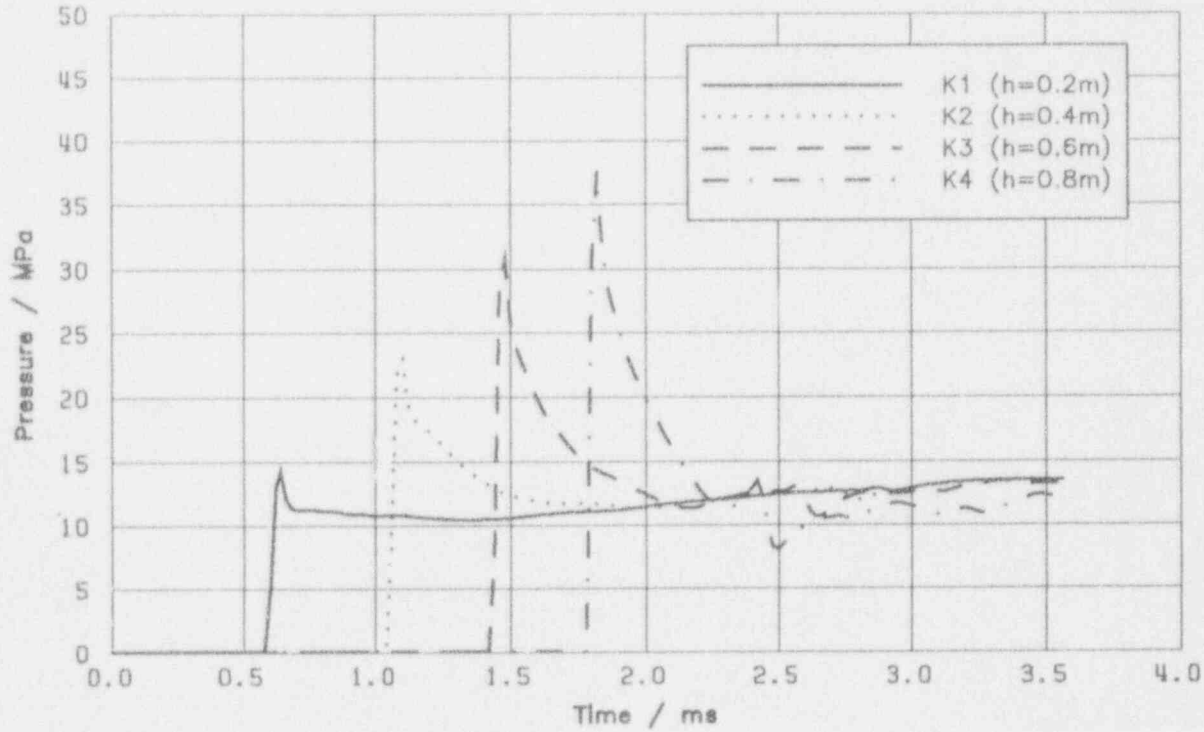

Figure 15. Calculated pressure traces at the transducer locations for the Al_2O_3 experiment KROTOS-28.

present calculations for KROTOS-28 with Al_2O_3 melt yield an additional feature since the stronger pressure development in this experiment appears to be explainable without extreme assumptions on premixture conditions by the present modelling of hydrodynamic fragmentation based on the wave stripping model.

Thus, in the opinion of the present authors progress seems to be attained and further to be attainable in the analysis of the KROTOS experiments and combined with this in code verification by the procedure of stepwise checking and by pointing different approaches, even in spite of experimental uncertainties, especially concerning the premixture data. Although it is justified to stress the limitations to this procedure with the present uncertainties in experimental conditions and measurements, the opinion expressed in /6/ that "there would seem to be little point in even attempting such a comparison" with the KROTOS experiments appears to be too strict.

Further work should, on one hand, be concentrated experimentally along the lines of more defined conditions and measurements, e.g. outlined in /6/. On the other hand, the theoretical work should be continued with specific checks between the different codes and approaches and especially with working out and pointing important features as the fragmentation process, nonhomogeneous water heating and steam production.

ACKNOWLEDGEMENTS

The models applied in this paper were developed partly in projects which were sponsored by the Bundesministerium für Forschung und Technologie, FRG, and the Joint Research Centre of the European Community in Ispra, Italy. The authors, however, are responsible for its scientific content. The authors would like to express their appreciations to the members of BETULLA group at the JRC in Ispra performing the experiments and especially to Dr. H. Hohmann and H. Schins for valuable informations and discussions. The Al_2O_3 experiments are sponsored by the US-NRC.

REFERENCES

1. T.G. Theofanous et al. "An Assessment of Steam Explosion Induced Containment Failure. Parts I-IV", Nuclear Science and Engineering 97 (1987) 259-326
2. S. Medhekar, W.H. Amarasooriya and T.G. Theofanous, "Integrated Analysis of Steam Explosions", Proc. 4th Int. Topical Meeting on Nuclear Reactor Thermal Hydraulics, Karlsruhe, F.R.G., October 10-13, 1989, 1 (1989) 319-326
3. T.G. Theofanous, W.W. Yuen, S. Angelini and X. Chen, "Physics of Steam Explosions", CSARP Meeting, Bethesda, Maryland, May 4-8, 1992
4. M. Bürger, K. Müller, M. Buck, S.H. Cho, A. Schatz (IKE), H. Schins, R. Zeyen, H. Hohmann (CEC - JRC Ispra), "Examination of Thermal Detonation Codes and Included Fragmentation Models by Means of Triggered Propagation Experiments in a Tin/Water Mixture", Nucl. Eng. Design 131 (1991) 61-70
5. D.F. Fletcher and A. Thyagaraja, "The CHYMES Coarse Mixing Model" Prog. Nucl. Energy 26 (1991) 31-61
6. D.F. Fletcher, "An Improved Mathematical Model of Melt/Water Detonations - Parts I, II", Int. J. Heat Mass Transfer 34 (1991) 2435-2459
7. M.F. Young, "IFCI: An Integrated Code for Calculation of all Phases of Fuel-Coolant Interactions", NUREG/CR-5084, SAND87-1048, 1987
8. C.C. Chu and M.L. Corradini, "One-Dimensional Transient Fluid Model for Fuel/Coolant Interaction Analysis", Nucl. Sc. Eng. 101 (1989) 48-71
9. D.F. Fletcher and R.P. Anderson, "A Review of Pressure-Induced Propagation Models of the Vapor Explosion Process", Prog. Nucl. Energy 23 (1990) 137-179
10. D.F. Fletcher, "A Comparison of Coarse Mixing Predictions Obtained from the CHYMES and PM-ALPHA Models", Nucl. Eng. Design 135 (1992) 419-425
11. W.W. Yuen, X. Chen and T.G. Theofanous, "On the Fundamental Microinteractions that Support the Propagation of Steam Explosions", Proc. Fifth Int. Topcial Meeting on Reactor Thermal Hydraulics, Salt Lake City, UT, USA, September 21-24, 1992, 2 (1992) 627-636
12. A. Benuzzi, P. Fasoli Stella, H. Hohmann and D. Magallon, "Progress of the FARO Programme. Results of the First Melt Quenching Test", CSARP Meeting, Washington, DC, USA, May 4-8, 1992
13. C. Carachalios, M. Bürger and H. Unger, "A Transient Two-Phase Model to Describe Thermal Detonations Based on Hydrodynamic Fragmentation", Int. Mtg. on Light-Water Reactor Severe Accident Evaluation, Cambridge, Mass., USA, August 28-September 1, 1983
14. M. Bürger, C. Carachalios, W. Schwalbe and H. Unger, "Beschreibung der Dampfexplosion mit Hilfe eines thermischen Detonationsmodells", Institut für Kernenergetik und Energiesysteme, Univ. Stuttgart, IKE 2TF-39 (1983)
15. M. Bürger et al. "Theoretische und experimentelle Untersuchungen zur Eingrenzung von Dampfexplosionen im Rahmen von Sicherheitsbetrachtungen bei Leichtwasserreaktoren", Institut für Kernenergetik und Energiesysteme, Univ. Stuttgart, IKE 2TF-27 (1987)
16. M. Bürger, C. Carachalios, D.S. Kim and H. Unger, "Theoretical investigations of the Fragmentation of Drops of Melt with Respect to the Description of Thermal Detonations /Vapor Explosions) and their Application in the Code FRADEMO", Commission of the European Communities, Nuclear Science and Technology, Report EUR 10660 EN (1986)
17. H. Nessyahu and E. Tadmor, "Non-oscillatory Central Differencing for Hyperbolic Conservation Laws", J. of Computational Physics 87 (1990) 408-463
18. H. Schins, K. Klein and G.P. Marzi, "Concept, Construction and Testing of Apparatus for the Detection and Quantitative Description of Thermal or Chemical Detonations with $E \leq 1$ KJ", CEC-JRC Ispra, Applied Mechanics Division, Technical Note No. 1.07.C1.84.51, April 1984
19. D.S. Kim, M. Bürger, G. Fröhlich and H. Unger, "Experimental Investigation of Hydrodynamic Fragmentation of Gallium Drops in Water Flows", Int. Mtg. on Light-Water Reactor Severe Accident Evaluation, Cambridge, Mass., USA, Aug. 28-Sept. 1, 1983
20. M. Bürger, D.S. Kim, W. Schwalbe and H. Unger (IKE), H. Hohmann and H. Schins (JRC Ispra), "Two-Phase Description of Hydrodynamic Fragmentation Processes within Thermal Detonation Waves", J. of Heat Transfer, Trans. of the ASME 106, (1984), 728
21. M. Bürger, C. Carachalios, D.S. Kim and H. Unger (IKE), H. Hohmann and H. Schins (JRC Ispra), "Description of Vapor Explosions by Thermal Detonation and Hydrodynamic Fragmentation Modeling", Int. Mtg. on Thermal Nuclear Reactor Safety, Karlsruhe, FRG, Sept. 1984

THE PREDICTION OF 2D THERMAL DETONATIONS AND RESULTING DAMAGE POTENTIAL

W.W. Yuen and T.G. Theofanous
Center for Risk Studies and Safety
Department of Chemical and Nuclear Engineering
University of California, Santa Barbara, CA 93106
Tel. (805) 893-4900 — Fax (805) 893-4927

ABSTRACT

The main purpose of this paper is to introduce a new concept for the processes responsible for the escalation and propagation of steam explosions. The concept recognizes that initially only a small quantity of coolant around each coarsely premixed melt mass "sees" the fragmenting debris coming off it, hence it is called the concept of "microinteractions." We also derive the analytical basis for it, define the nature of the requisite constitutive laws and related experimental data, and demonstrate that this concept is essential for the prediction of steam explosion energetics in large-scale premixtures in 2D geometries. We also provide the first numerical illustrations of this concept, implemented in the computer code **ESPROSE.m**. Further, we provide the first numerical results of steam explosions in large water pools, i.e., ex-vessel explosions. These results reveal two important mechanisms for explosion "venting" and thus for reducing the dynamic loads on adjacent structures. We conclude that, taken together, the "microinteractions" and "venting" make realistic predictions of steam explosion loads feasible and within reach in the near future.

INTRODUCTION

Now that the computation of realistic premixture conditions seems to be well within reach (Angelini et al., 1992; Denham et al., 1992), the possibility of predicting the detonation event itself, for use in safety analyses, cannot be overstated. Particular (and important) aspects of such predictions include: susceptibility of a given premixture to triggering, rate of escalation, peak pressures developed, and impulse delivered to the boundaries. These are new aspects of current interest, especially to advanced reactor designs (i.e., the passive ALWRs) in which one is concerned about direct explosion loading of the lower head, pedestal walls, and immediately adjacent containment pressure boundaries. In addition, this more in-depth understanding of the detonation process can be expected to further buttress previous energetics assessments focused on in-vessel missile generation (the alpha-mode containment failure) and carried out mainly by global energetics arguments (i.e., based on the quantities of fuel participating in an "explosive premixure" as in Medhekar et al., 1991, Turland et al., 1993 and Theofanous and Yuen, 1993).

The basic concept of thermal detonation was put forth about twenty years ago (Board and Hall, 1974), and it has remained unchanged in its basis since. In it, the basic feedback that sustains the detonation wave is derived from rapid fragmentation of coarsely premixed "fuel" behind the pressure wave of the explosion in the manner illustrated in Figure 1. As illustrated, the fragments are taken to mix homogeneously with the coolant. Subsequent work introduced a more detailed two-fluid formulation (Sharon and Bankoff, 1981), several fragmentation regimes (Bürger et al., 1984; Patel and Theofanous, 1981; Yuen et al., 1993; Kim and Corradini 1988), transient escalation from an initial trigger in a one-dimensional geometry (Bürger et al., 1993; Abolfadl and Theofanous, 1987; Fletcher and Thyagaraja, 1989; and Chu and Corradini, 1989) and also in a two-dimensional geometry (Medhekar et al., 1989), but the concept of homogeneous mixing of the fragmented debris with the coolant was retained throughout.

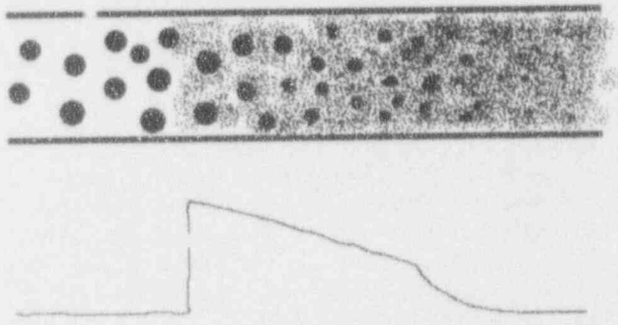

Figure 1. Schematic of current modeling of thermal detonation following the original Board and Hall concept.

Direct experimental evidence that this concept is incorrect has recently been made available (Yuen et al., 1992). In this study, the basic fragmentation/mixing morphology of exploding drops in a simulated detonation-wave environment was studied by quantitative X-ray radiography. This study revealed strong thermal effects on fragmentation and a mixing pattern that begins in the immediate vicinity of the drop and spreads, gradually involving more and more coolant and debris. Illustrative examples of these data are given here in Figure 2. The so-emerging concept of "mi-

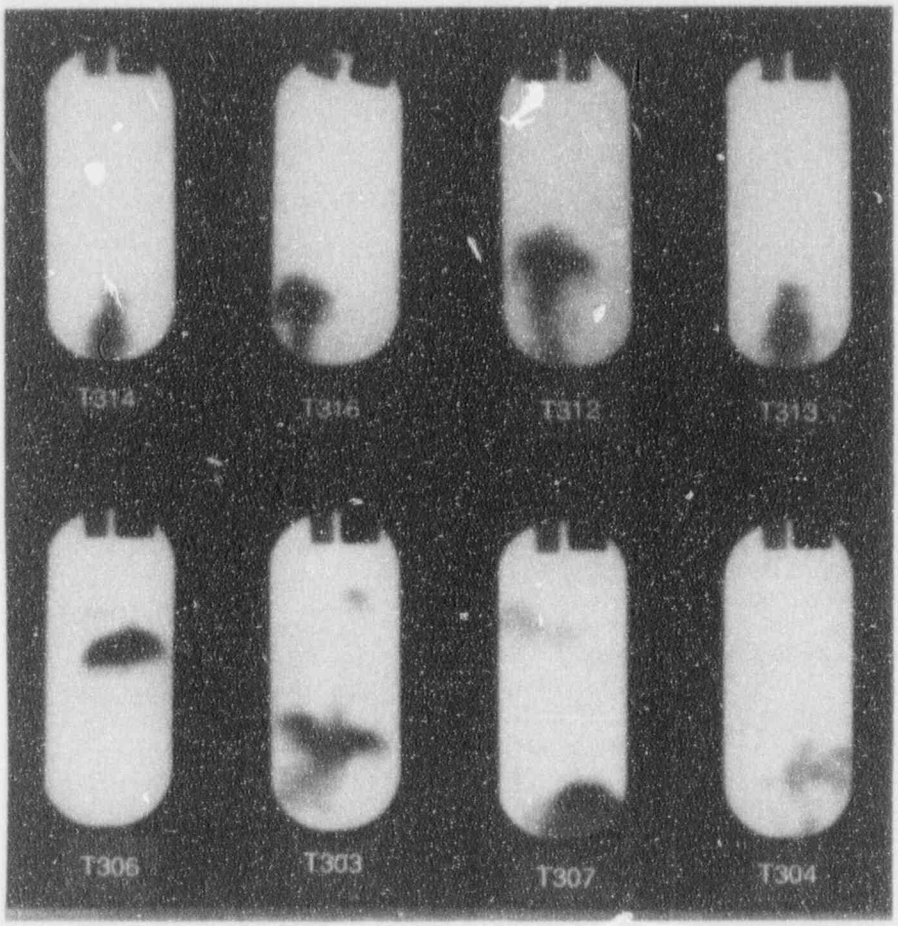

Figure 2. Example of fragmentation/mixing morphology of an exploding tin drop (1000 and 670 °C for the top and bottom rows, respectively) in a simulated explosion environment (200 bar), in the SIGMA facility (Yuen et al., 1992).

crointeractions" is schematically depicted in Figure 3. Having introduced this concept the main purpose of this paper is to show how it can be implemented in a multifield formulation, including consideration of the constitutive laws needed to characterize the microinteraction zone, and to provide the first illustrative numerical results. The code reflecting this new concept is called ESPROSE.m, where "m" stands for microinteractions.

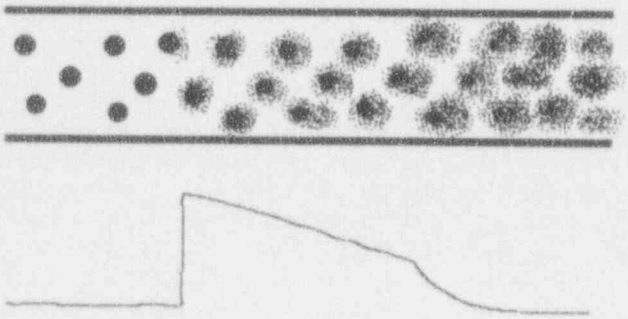

Figure 3. Schematic of the concept of "microinteractions" in a propagating large-scale explosion.

To further clarify the concept, we should point out that consideration of the microinteraction zone introduces non-equilibrium within the liquid (coolant) phase as a key aspect in the feedback process that allows a local (trigger) event to escalate to an explosion. Also, it is important to note that the coolant outside the microinteraction zone, and hence not thermally participating, is fully involved in the hydrodynamics, i.e., compression waves and associated velocity fields. It should now be clear that within the old computational frame "producing" an explosion would require artificially large amounts of fragmentation and even so, the time-signature of the realistic pressure pulse could not be reproduced. Furthermore, it should be clear that this problem cannot be fixed (even in 1D calculations) by increasing, artificially, the fuel volume fraction.

The above comments also imply a clear distinction between the microinteractions approach and other approaches accounting for non-equilibrium phase change (condensation) in the coolant. For example, in the approach employed in TEXAS (Chu and Corradini, 1989) or ESPROSE.a, the energy of the fragmenting debris or a specified fraction of

it, respectively, is taken to produce vapor, which is then allowed to condense at rates controlled by a heat transfer coefficient. This involves thermally the whole coolant mass with the fragmenting debris which is not what happens in reality. In particular, artificially low heat transfer coefficients must be utilized in order to reflect the limited thermal participation of the surrounding water implied in the microinteractions concept. Moreover, the appropriate amount of non-equilibrium is not known *appriori* and cannot (neither has it been attempted) be captured by means of "tuning" a heat transfer coefficient.

The two-dimensional feature of the ESPROSE code has been utilized in a first attempt at reflecting very roughly the limited coolant participation with the fragmenting debris in a precursor to this present effort (Yuen et al., 1992). Although a step in the right direction, this approach[a] is also open to criticism because it effectively fixes the quantity of water participating and hence, again it cannot reproduce the correct signature of an explosion. More importantly, this "remedy" is only possible in 1D geometries, i.e., the radial nodes are used to allow the required degree of contact between the melt and liquid coolant, as illustrated in Figure 4.

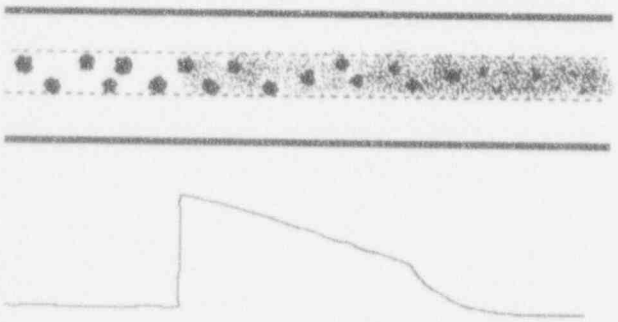

Figure 4. Illustration of the limited fuel-coolant contact afforded by ESPROSE.a. That is, using a 2D computational mesh for a quasi-1D geometry.

In fact, non-one-dimensional behavior is crucial in the consideration of large scale explosions, not only because realistic large scale premixtures are strongly non-one-dimensional (Angelini et al., 1993), but also because in reactor geometries the premixture zone is surrounded by significant quantities of water which provides the coupling medium between the explosion zone and the surrounding structures. A realistic consideration of the dynamic loads on these structures requires the dynamic coupling of this medium to the explosion zone, as schematically illustrated for the case of an ex-vessel explosion in Figure 5. This schematic makes evident two intuitively expected mechanisms of "venting"; one directly through the explosion zone and the other by "reflections" off the free pool surface as the pressure waves of the explosion "radiate" through the water pool toward the pool boundaries. Another purpose of this paper is to quantitatively illustrate these "venting" effects.

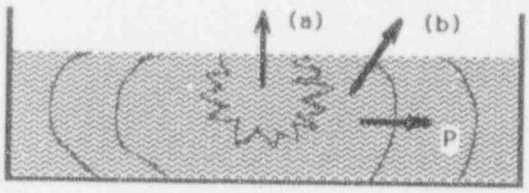

Figure 5. Illustration of the two "venting" mechanisms in ex-vessel explosions.

The timing of the developments described above in relation to this meeting allowed only the separate demonstration of the "microinteractions" and of "venting." The "microinteractions" concept was demonstrated in a 1D KROTOS-like geometry using ESPROSE.m, and the "venting" was illustrated in a 2D ex-vessel interaction geometry using ESPROSE.a. In the near future these two aspects are to be combined into a 2D ESPROSE.m capability which, together with the PM-ALPHA code (for premixing), will allow the first meaningful predictions of steam explosion loads in reactor geometries.

THE FIELD FORMULATION OF THE MICROINTERACTION ZONE CONCEPT

The original ESPROSE code (Medhekar et al., 1989) was based on a 3-fluid (3-field) formulation, the three fluids being "fuel particles," "steam" and a "water-debris" mixture. The field equations and constitutive laws were the same as those of PM-ALPHA (Amarasooriya et al., 1991; Angelini et al., 1992) supplemented by a debris continuity

$$\frac{\partial \rho'_{db}}{\partial t} + \nabla \cdot \rho'_{db} \mathbf{u}_\ell = F_r \qquad (1)$$

$$\frac{\partial \rho'_f}{\partial t} + \nabla \cdot \rho'_f \mathbf{u}_f = -F_r \qquad (2)$$

and a constitutive law for the fragmentation rate:

$$F_r = \frac{6\theta_f}{\pi \ell_f^3} \frac{dM}{dt} \qquad (3)$$

where

$$\frac{dM}{dt} = \frac{\pi \ell_f^2 \mid \vec{\mathbf{u}}_\ell - \vec{\mathbf{u}}_f \mid}{6 t_b^*} (\rho_f \rho_\ell)^{1/2} \qquad (4)$$

and the "fragmentation time" and the instantaneous and Bond numbers are defined by

$$t_b^* = 13.7 \ \mathrm{Bo}_i^{-1/4} \quad \text{and} \quad \mathrm{Bo}_i = \frac{3}{8} \frac{C_D \rho_\ell}{\sigma} \mid \mathbf{u}_\ell - \mathbf{u}_f \mid^2 \frac{\ell_f}{2} \qquad (5)$$

This instantaneous Bond number formulation was shown to be consistent with experimental data (from the SIGMA facility) where fragmentation is dominated by hydrodynamic

[a] This formulation also included an augmentation of the fragmentation rate to roughly reflect thermally-driven fragmentation (Yuen et al., 1992), and the assignment of a fraction of the thermal energy of the fragmenting debris to direct vapor production, as mentioned above. The ESPROSE code version reflecting these features is referred to as ESPROSE.a.

instabilities (Yuen et al., 1992). These comparisons also demonstrated that the numerical scheme captures well the shock features (steepness, speed) of the hydrodynamics. This aspect of the treatment presently includes an "artificial viscosity" in the manner discussed by von Neumann and Richtmyer (1950).

In the augmented version of this model (ESPROSE.a), we introduced an enhancement of the fragmentation rate [Eq. (3)] by a factor f_f to reflect the experimentally observed contribution of thermal fragmentation (Yuen et al., 1992), and modified the phase change model to allow some fraction, f_v, of the fragmenting debris energy to go directly to vapor production. This formulation,

$$J = \frac{1}{h_g - h_\ell}\{R_g(T_g - T_s) + R_\ell(T_\ell - T_s) + f_v F_r(I_f - I_{db}(T_\ell))\} \quad (6)$$

when $\alpha < 0.7$

$$\dot{Q}_{f\ell} = \eta_f(h_r + h_c)\pi\ell_f^2 Q_{\ell f}(T_f - T_\ell) + F_r(1 - f_v)I_f + f_v F_r I_{db}(T_\ell) \quad (7)$$

and when $\alpha \geq 0.7$

$$\dot{Q}_{f\ell} = \min(\eta_\ell \pi \ell_\ell^2, \eta_f \pi \ell_f^2)\sigma E_\ell E_g (T_f^4 - T_\ell^4) + (1 - f_v)F_r\{(1 - \alpha)I_f + \alpha I_f(T_\ell)\} + f_v F_r I_f(T_\ell) \quad (8)$$

$$\dot{Q}_{fg} = \eta_f h_c' \pi \ell_f^2 \phi_{fg}(T_f - T_g) + \alpha F_r(1 - f_v)(I_f - I_f(T_\ell)) \quad (9)$$

enhances the degree of interfacial non-equilibrium, but vapor is still allowed to condense, through a heat transfer coefficient [as seen in Eq. (6)], which thermally couples it to *all the water* in a computation cell. In other words, this formulation forces condensation for as long as there is any subcooling in the water, in the cell, taken all at the same temperature (T_ℓ). Regarding the factor f_f, we expect it to gradually decrease as pressure increases, and to essentially approach unity at supercritical pressures. The definition of the various exchange parameters is presented in a previous work (Medhekar et al., 1989).

By contrast, the concept of microinteractions is to allow for non-equilibrium within the liquid phase itself, and this is accomplished by introducing another field comprising all the liquid which is "too far" (outside the microinteraction zone) to thermally interact with the fragmenting debris. To fully appreciate the importance and need for this separate field (called here the "m-external" field, i.e., the coolant field external to the microinteraction zone) one needs to recall that typical premixtures are rather lean in fuel (typically less than 10% in a volume fraction), and as pressure builds up (in the explosion front) the liquid-to-vapor density ratio approaches unity—thus mixing induced by the large local velocities associated with evaporation at low pressures essentially disappears. This was clearly seen in the SIGMA simulations already at pressures of 100 to 200 bar, while the real interest in steam explosion energetics is for much higher pressures.

On the other hand, in the microinteraction zone the debris, some liquid in the vicinity entrained with it, and any vapor produced would be in such intimate contact that to a first approximation, they can be treated as an homogeneous mixture in thermodynamic equilibrium. In this approximation, then, the microinteraction zone is treated as a field. This field grows with time as it receives debris, from the fragmenting fuel drops (the "fuel" field), and liquid coolant from the "m-external field." Thus we arrive at a three-field formulation, the three fields (or "fluids") being "fuel particles," the "m-external field" and the "microinteraction zone." The equations are given in the appendix. A further elaboration could be made by separating further the microinteraction zone into two (debris-water and steam) or even three (debris, water, and steam) fields, which would also allow for departures from "local" equilibrium. The numerical implementation of the resulting 4- or 5-field model is quite feasible; however, the potential advantages of such an elaboration and therefore its need are best assessed after gaining some further experience with the 3-field microinteractions model, especially in regards to the constitutive treatment of the microinteraction zone, in relation to experiments run specifically for this purpose, as described next.

Along with the field equations given in the appendix, we specify the constitutive laws for mass transfer, at all two-field intrfaces. We distinguish between the case of fully-collapsed void immediately behind the propagating front and that in which a significant void remains. The former case is the most significant in terms of its positive feedback to the explosion, it typically arises in premixtures considered explosive ($\alpha < 30$ or 40%), and it is the only case investigated so far at the fundamental level (i.e., the SIGMA experiments described by Yuen et al., 1992). The latter case is basically dissipative (i.e., Medhekar et al, 1991; Fletcher, 1993) as its high compressibility tends to attenuate pressure waves and the low densities are ineffective to produce significant fragmentation rates. The emphasis at this stage of development is given in the former case, the latter case being treated in a more approximate fashion.

In the fully-collapsed void case, the initial volume fraction of the microinteraction field is essentially zero, and it grows as debris and entrained fluid from the m-external field enter it—the rates at which this is happening represent the key constitutive features of this model. For the fragmentation rate we use a generalization of Eqs. (3) and (4), including the thermal augmentation factor f_f. The detail is given in the appendix. We expect that the entrainment of the m-external field will depend on its relative velocity to the fuel field, and the amount of specific volume expansion (i.e., dilation due to thermal or phase-change effects) of the microinteraction zone. Further, we expect that these two mechanisms (rates) will interact and further data (than those presented by Yuen et al., 1992) in the SIGMA facility extending especially the range of conditions to higher melt temperatures and shock pressures would be required to open up the real fundamental understanding in this area.

Such work is currently in progress. The technical approach relies on the *simultaneous* use of several diagnostics including quantitative flash X-ray radiography (providing the debris fragmentation rates and growth of the microinteraction zone), high speed movies (giving an idea of the extent of phase change), pressure measurement in the immediate vicinity of the exploding drop (providing the transient thermal interaction feedback), and the final debris size distribution (providing another measure of the intensity of the explosion). The simultaneity of the transient measurements is emphasized because beyond the morphology the microinteraction model must also match the resulting thermal feedback. Finally, it is noted that by introducing steam bubbles into the shock tube we can obtain a wide range of liquid "flow" velocities and shock pressure combinations as appropriate in exploring the important regimes of escalating explosions. For the time being, the nature of the ESPROSE.m solution can be illustrated by making the volume of the entrained m-external fluid to be proportional to the volume of the fragmented fuel. The entrainment rate per fuel particle, $\dot{m}_e$, is thus given by

$$\dot{m}_e = f_e \frac{dM}{dt} \left(\frac{\rho_\ell}{\rho_f} \right) \tag{10}$$

where the factor f_e is parametrically fixed to various values, i.e., 1,2, ... 5.

For any region left with significant void behind the pressure front, this void is assigned, as an initial condition, to the microinteraction zone. In such regions fragmentation rates do not contribute significantly, but rather the behavior is controlled by the rates of condensation, i.e., vapor-liquid mixing which can also be viewed as an entrainment of the m-external field into the microinteraction zone. Under the intense condensation conditions behind a shock, we expect shattering of interfaces and large liquid subcoolings, i.e., enormous condensation rates. To bracket the behavior, we consider three different constitutive treatments in such regions (a) an entrainment rate given by Eq. (10), (b) an entrainment rate sufficiently large to incorporate all the m-external field to the microinteraction zone within a specified time constant τ_e, i.e.,

$$\dot{m}_e = \frac{m_\ell}{\tau_e} \tag{11}$$

where m_ℓ is the mass of liquid coolant (at any particular position, or computational call), and (c) a zero entrainment rate but an enhanced heat transfer coefficient, between the microinteraction and the m-external fields, to roughly represent transient condensation effects (i.e., $\frac{1}{\sqrt{t}}$ behavior) as well as shattering of interfaces.

The third and final important element of the constitutive treatment is in the drag laws of the "fuel" field. The treatment used previously in ESPROSE.a is maintained. It has been tested extensively with SIGMA experiments (Yuen et al., 1992) and will be expanded when additional experimental data become available.

QUASI-ONE-DIMENSIONAL EXPLOSIONS AND THE KROTOS EXPERIMENTS

Integral type explosion experiments are currently carried out in the KROTOS facility at the European Joint Research Center in ISPRA (Hohmann et al., 1993). These experiments involve the pouring of tin or aluminum oxide melts into a tube filled with water, the sudden release of a compressed gas volume at the bottom of the tube, and the measurement of the pressure transients of the resulting explosions along the length of the tube. The tube is 10 cm in diameter and 2 m long, thus the geometry is essentially one dimensional. The trigger is well-characterized by the expansion of the known volume and initial pressure of some compressed gas at the bottom of the tube. The melt is released in a controlled fashion from a well-known initial temperature, and the water temperature is uniform and known. Because of all these features, these experiments are very attractive for testing explosion concepts/models. This is especially so because the most recent KROTOS-28 test using aluminum oxide melts produced very energetic explosions and very high (supercritical) pressures. The main shortcomings currently are on the quantitative aspects of data-"prediction" comparisons, in that the local melt and steam volume fractions along the tube are not measured directly, and in that the range of the pressure transducers was exceeded in the latest and most interesting explosions. Even so, these are the best characterized experiments so far and it is worth pursuing their detailed understanding with diligence.

In a recent publication (Yuen et al., 1992) we consider KROTOS-21, a test with molten tin at 1000 °C. We concluded that this was a rather mild interaction, contributing to maintain the strong trigger imposed rather than to lead to a rapid escalation. Here, we consider the tests with aluminum oxide melts (KROTOS-26 and KROTOS-28).

Let us begin with an idealized case of arbitrarily specified, uniform melt and steam volume fractions—$\theta_f = 0.05$ and $\alpha = 0.01$, respectively—under the typical KROTOS trigger: the sudden release of a 12 MPa nitrogen gas of 15 cm^3. The ESPROSE.a calculation was run with $f_f = 1$, $f_v = 0.05$, and for the ESPROSE.m we used $f_f = 1$ and $f_e = 1$, 2, 4 and 6. The results are summarized in Figure 6. Note that ESPROSE.a calculates a relatively mild interaction, basically preserving the imposed trigger, while ESPROSE.m predicts rapid escalation to comparatively much larger pressures. Also note how strongly the factor f_e affects the "signature" of the explosion, as well as the peak pressure. This is inherent in the physics of the constitutive law for the microinteractions utilized here.

For KROTOS-26, the initial conditions were specified using the timing of the premature trigger, in relation to the start of the melt pour, the guidance from PM-ALPHA calculations and the speed of the pressure shock observed experimentally in the explosion. The specification used in an ESPROSE.a calculation is given in Figure 7. The calculation was carried out with $f_f = 5$ and $f_v = 0.05$. The results are given in comparison to the experimental data in Figure 8. The positions of the pressure transducer (K0 to K5) are

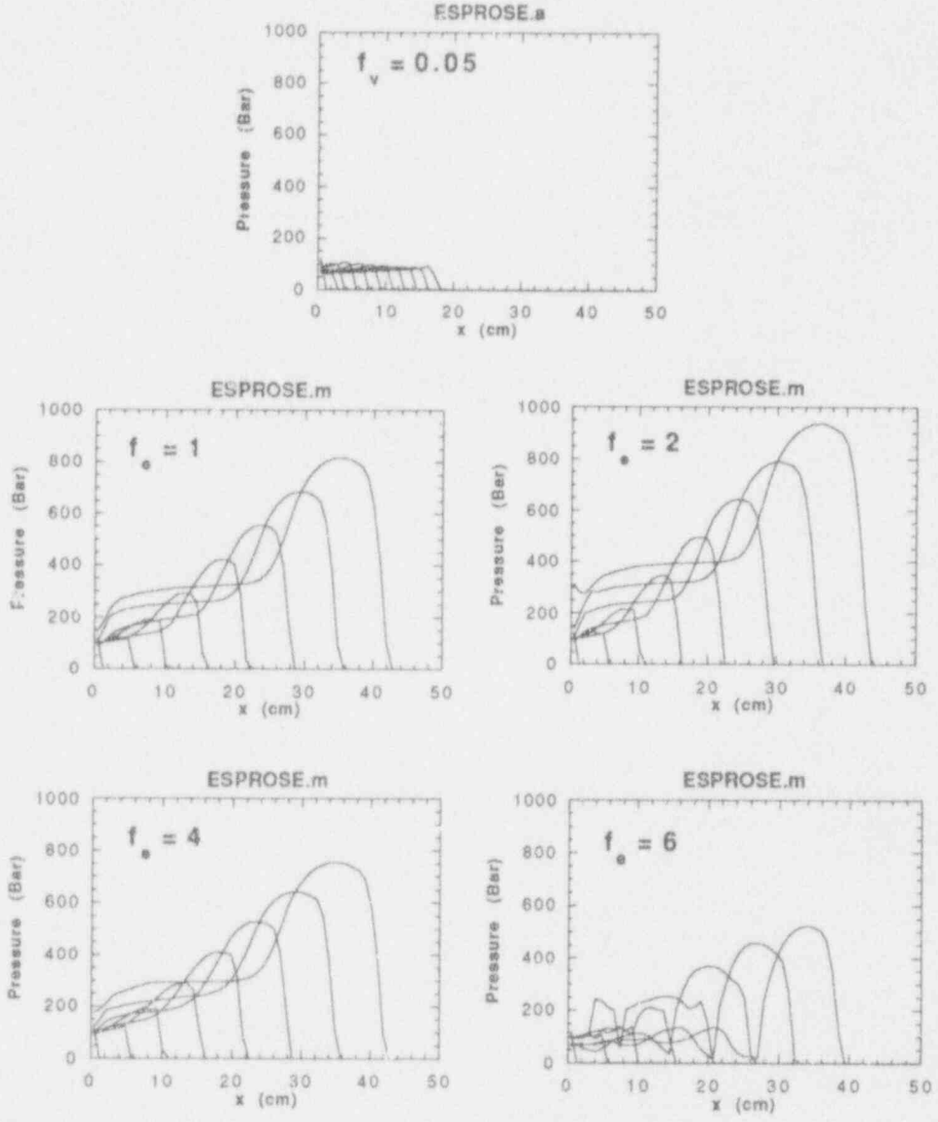

Figure 6. Illustration of the role of microinteractions in the escalation and propagation of steam explosions. These calculations refer to a KROTOS-like geometry and trigger with $\theta_f = 0.05$, $\alpha = 0.01$. All cases were run as 1D with $f_f = 1$. The f_v and f_e in the ESPROSE.a and ESPROSE.m models respectively are shown in each case.

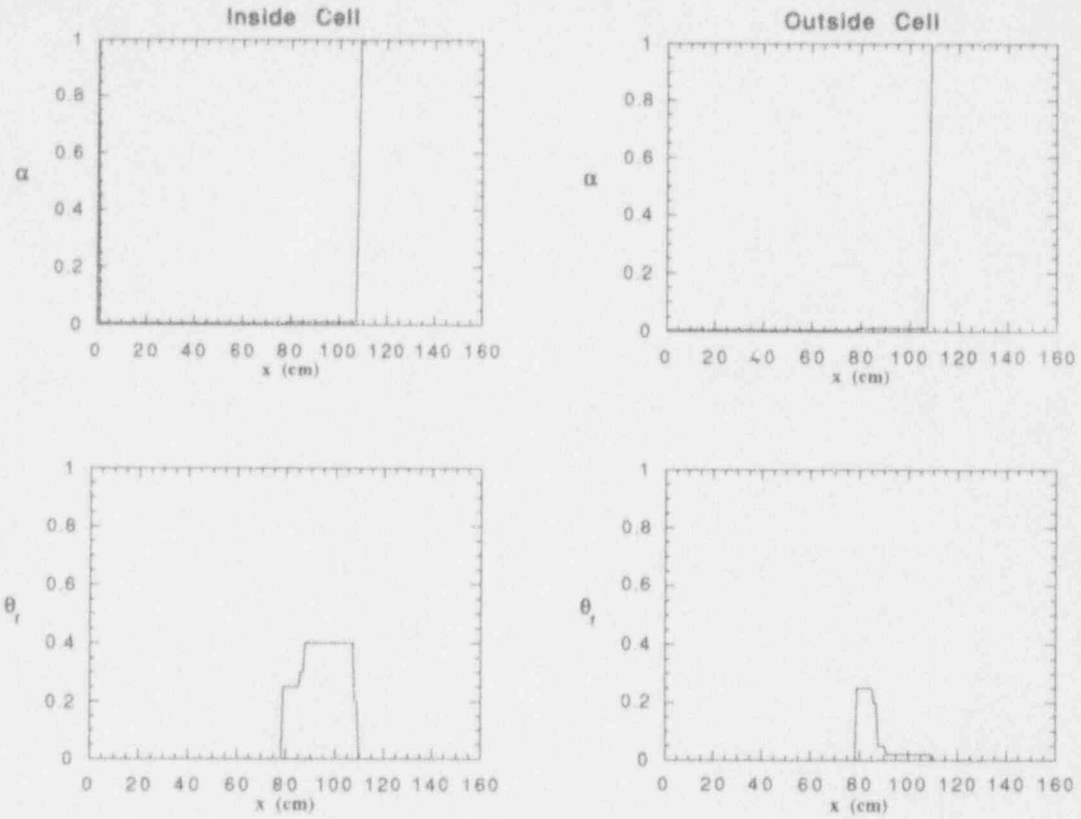

Figure 7. Initial conditions for the KROTOS-26 calculations.

described in Hohmann et al. (1993). Note that the trigger propagates essentially undiminished through the lower part of the shock tube ($\alpha = 0$), it triggers an explosion at the very top (K5), which then propagates downward. We note that the pressure amplitude at position K5 is reasonably well predicted. As the shock propagates downwards it seems to be attenuated at position K4, but drives the transducers out of scale at all lower positions. Given that K5 is the origin of the explosion, and that the melt did not penetrate below K4, the "topping-out" of the transducers K0 to K3 would appear to be suspect. So, this comparison is only of qualitative significance.

Much more interesting is the test KROTOS-28, in which the trigger functioned as intended—i.e., after the melt reached the bottom. For this case we ran both ESPROSE.a and ESPROSE.m calculations. The initial conditions were specified in the manner described above. For the ESPROSE.a run the initial conditions are shown in Figure 9, and the parameters f_f and f_v were set to 5 and 0.05, respectively. The results are compared to the experimental data in Figure 10. Note that the explosion was initiated at position K1 and escalated rapidly along the tube to pressures over 500 bar, "topping off" the transducers. The mechanical damage observed (Hohmann et al., 1993) seems to be consistent with such high pressures and pulse-widths. Note that even with the augmented treatment of ESPROSE.a and the relatively large value of $f_f = 5$ the explosion is grossly underpredicted. The ESPROSE.m calculation was run in 1D and with the 1D initial conditions from Figure 11a. The results are shown in Figure 11b. Because of the transducer cutoff, the comparison is only qualitative, but it is important that the microinteractions model predicts pressures well over 500 bar, as found in the experiment. In very rough terms the pulse widths are also comparable, indicating that a very energetic explosion is predicted as in the experiment. Clearly, this initial comparison is very promising for both the experiment and the calculation. To meet this promise the experiment should improve the reliability (and range) of the pressure measurements, and provide data that provide a better characterization of the premixture (i.e., melt and steam volume fraction distributions at the time of the trigger). At the same time, the calculations should be improved by the incorporation of new constitutive laws for microinteractions as they become available from the SIGMA experiment.

VENTING PHENOMENA IN 2D EXPLOSIONS

The purpose of this section is to quantitatively illustrate the "venting" processes mentioned in the introduction. The situations of interest are reactor cavities with diameters in the 6 to 10 meters range and pool depths of 1 to 3 meters. For these illustrations we chose the diameter of 6 meters and pool depths of 1 and 3 meters. The quantity of primary interest is the pressure pulse on the side walls.

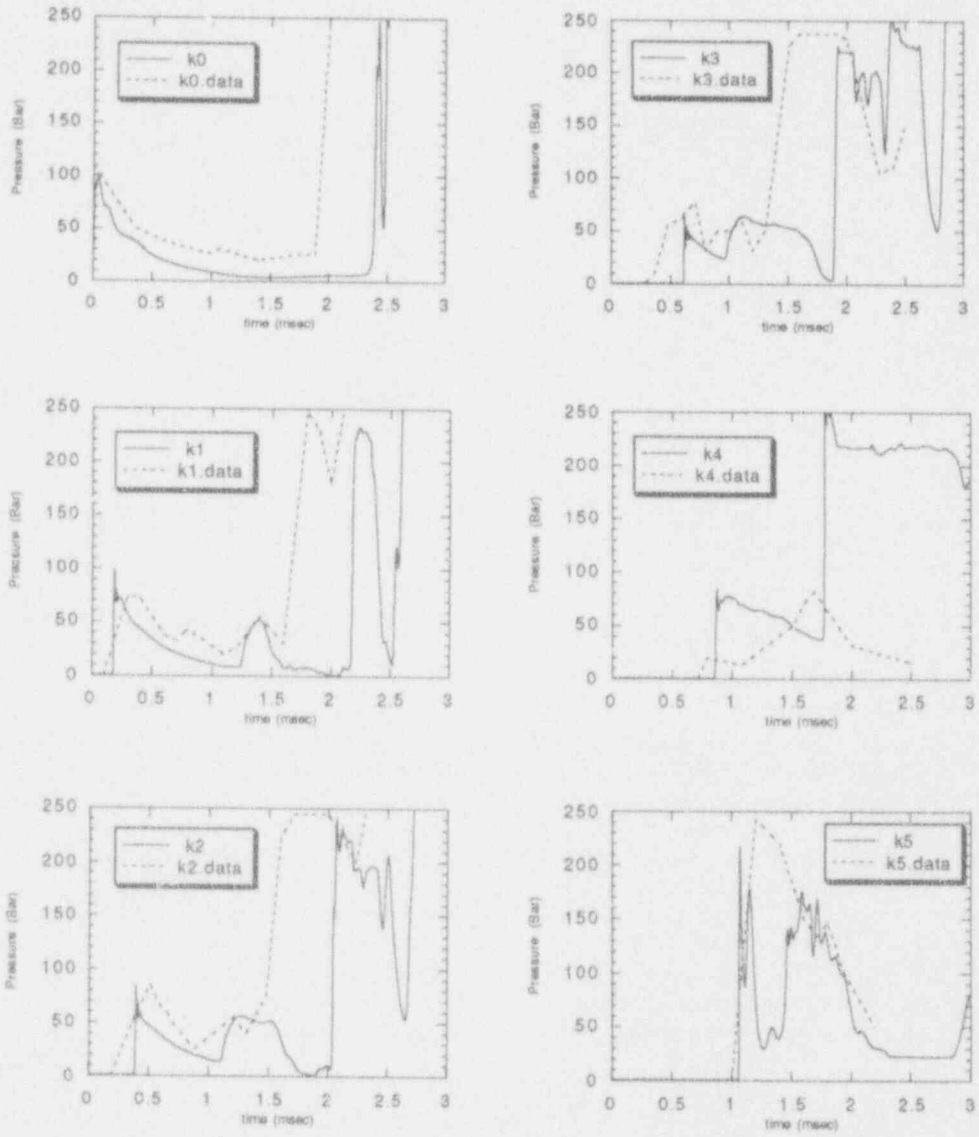

Figure 8. Comparison of an ESPROSE.a calculation of KROTOS-26 test with experimental data of pressures measured along the tube length.

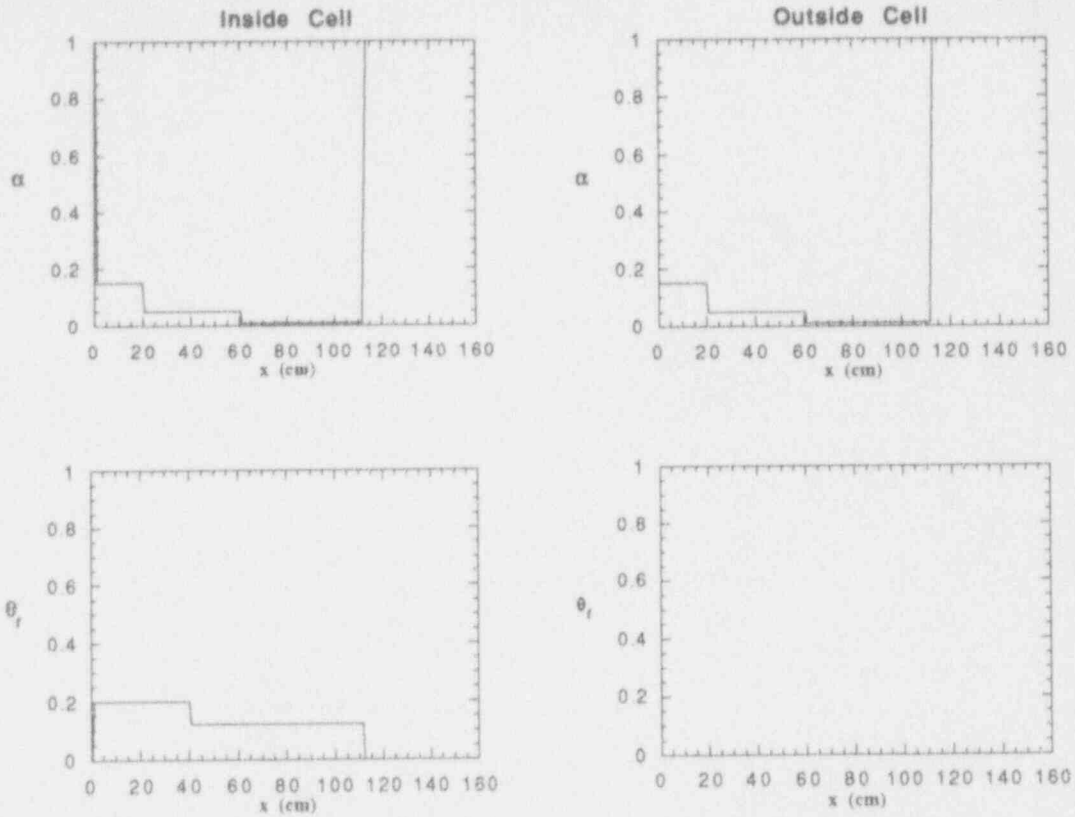

Figure 9. Initial conditions for the KROTOS-28, ESPROSE.a calculations.

The melt pouring conditions are very much system and scenario specific, thus we make no attempt to represent anything in particular here—for illustration purposes only, we assume a pour of 0.6 meters in diameter with velocities of 9.7 and 7.1 m/s at 0.2 and 0.4 m above the water surface ("inlet" to the computational flow field) for the 1 and 3 meter pool cases, respectively. In both cases the melt (UO_2 properties) volume fraction at the inlet was taken as 0.05, and the particle size was fixed as 1 cm. The premixing transient was calculated with PM-ALPHA and the explosions were triggered at the time the fuel reached the pool bottom, by suddenly releasing the pressure of saturated steam at 120 bar from one of the computational cells. The calculation was carried out using ESPROSE.a (with $f_f = 1$ and $f_v = 0.05$) because the 2D version of ESPROSE.m is, at this time, still being tested.

From the results of the previous section, we expect that ESPROSE.a will underestimate peak pressures in the explosion zone, thus we emphasize that these results are only illustrative of the "venting" in a separate-effects manner. On the other hand, we must also emphasize that the trigger employed in these calculations is quite energetic and not necessarily representing the true explosivity of these premixtures. Again, the idea is to focus on the "explosion venting" aspects of such geometries.

The initial conditions for the explosion in the 1-meter pool are depicted in Figure 12. The calculated pressure pulses along the side boundary are shown in Figure 13, and the dynamics of the explosion zone interacting with the surrounding fluid and the free surface can be surmised from Figure 14. For the 3-meter pool case the corresponding type of information is found in Figures 15, 16 and 17, respectively. The venting processes are quite evident in both cases from Figures 14 and 17, and they manifest themselves in Figures 13 and 16, by the relatively low pressure at the wall as compared to that in the explosion zone. It is also clear that this venting is more pronounced in the 1-meter case, as expected. In parallel with preparing the 2D version of ESPROSE.m, we are working toward a theory to generalize these 2D venting aspects for convenient future use.

CONCLUSIONS

- As in the case of premixing, propagation is a fundamentally non-1D phenomenon, dominated by microinteractions.
- "Venting" is a key feature of ex-vessel explosions, and it plays a key role in mitigating the dynamic loads on the side boundaries of "shallow" (1 to 3 meter) pools in reactor cavities.
- The quantitative prediction of steam explosions now depends on the formulation of adequate constitutive laws for the microinteractions. Relevant experiments (single-drop explosions in a simulated detonation front environment, i.e., sustained pressure pulse with a detailed diagnostics on the microinteraction zone) are currently in progress in the SIGMA facility.

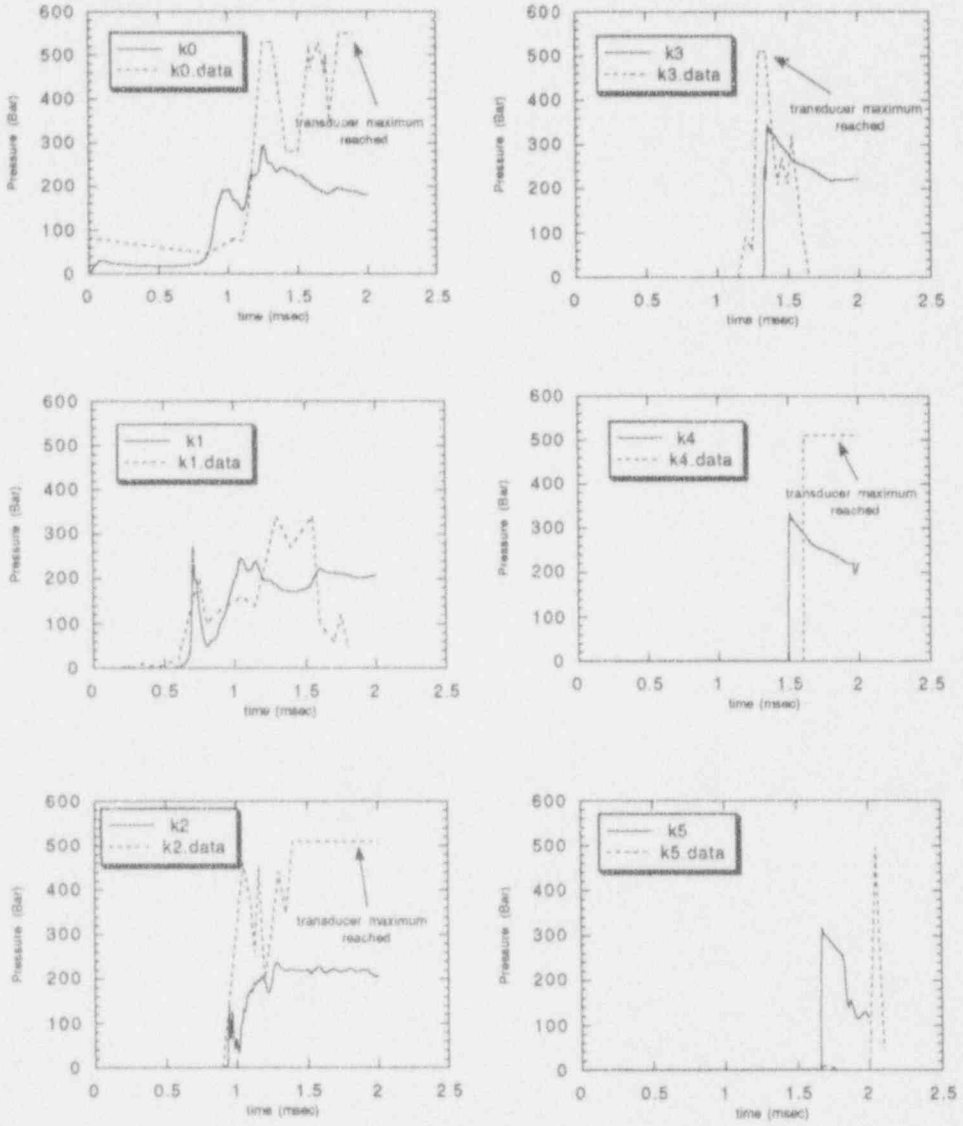

Figure 10. Comparison of an ESPROSE.a calculation of KROTOS-28 with experimental data of pressures measured along the tube length.

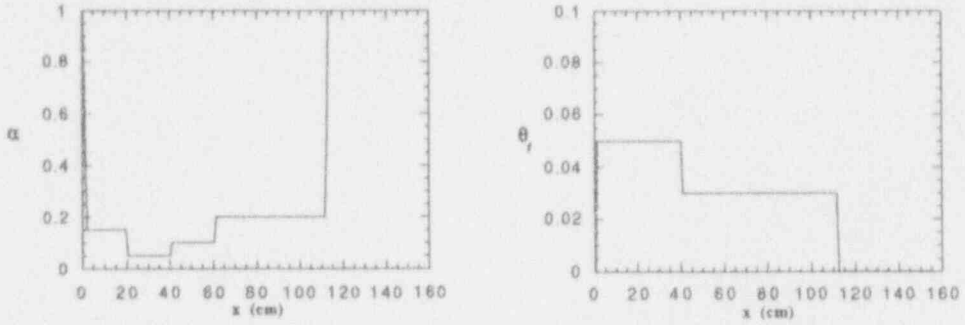

Figure 11a. Initial conditions for the KROTOS.28, ESPROSE.m calculations.

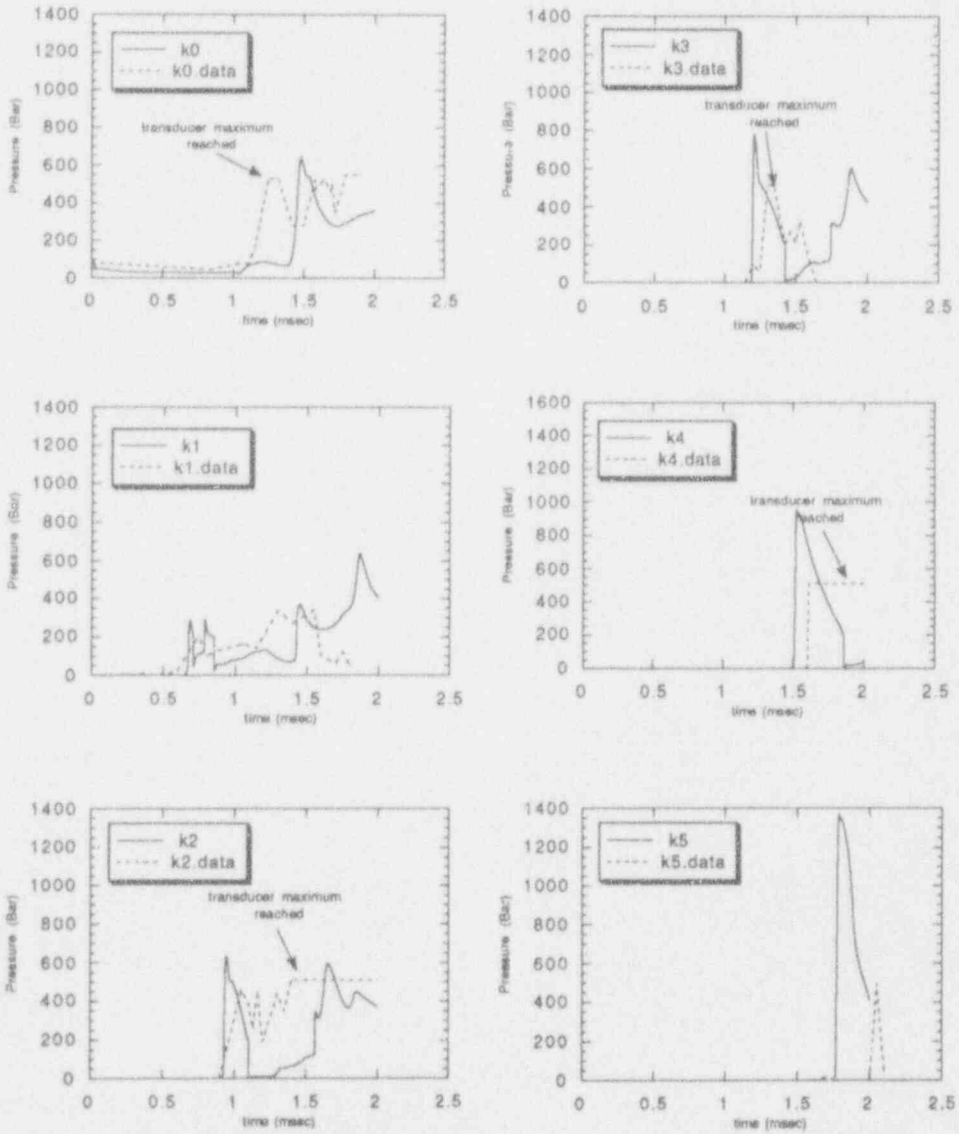

Figure 11b. Comparison of an ESPROSE.m calculation of KROTOS-28 with experimental data of pressures measured along the tube length.

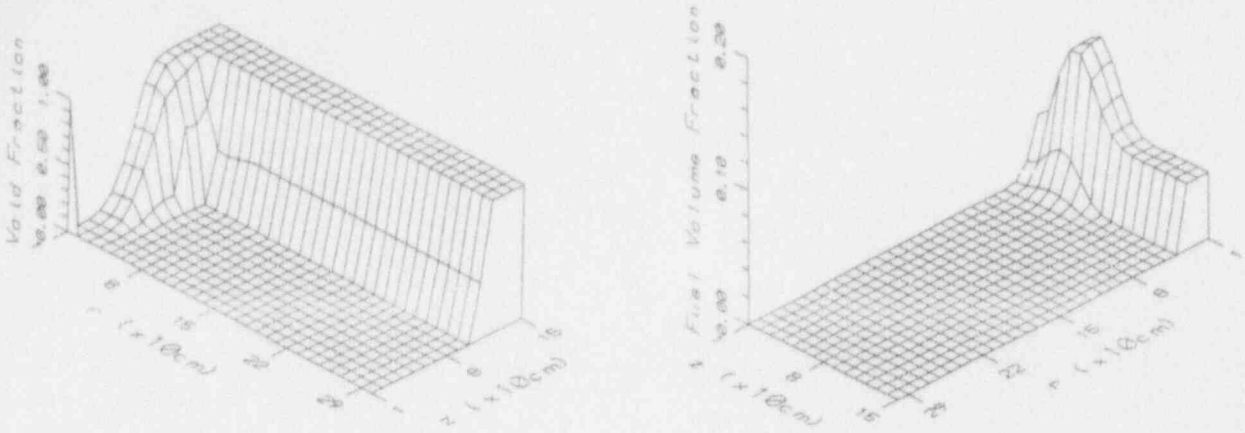

Figure 12. Initial conditions for the ex-vessel, 1-m deep pool, ESPROSE.a calculation.

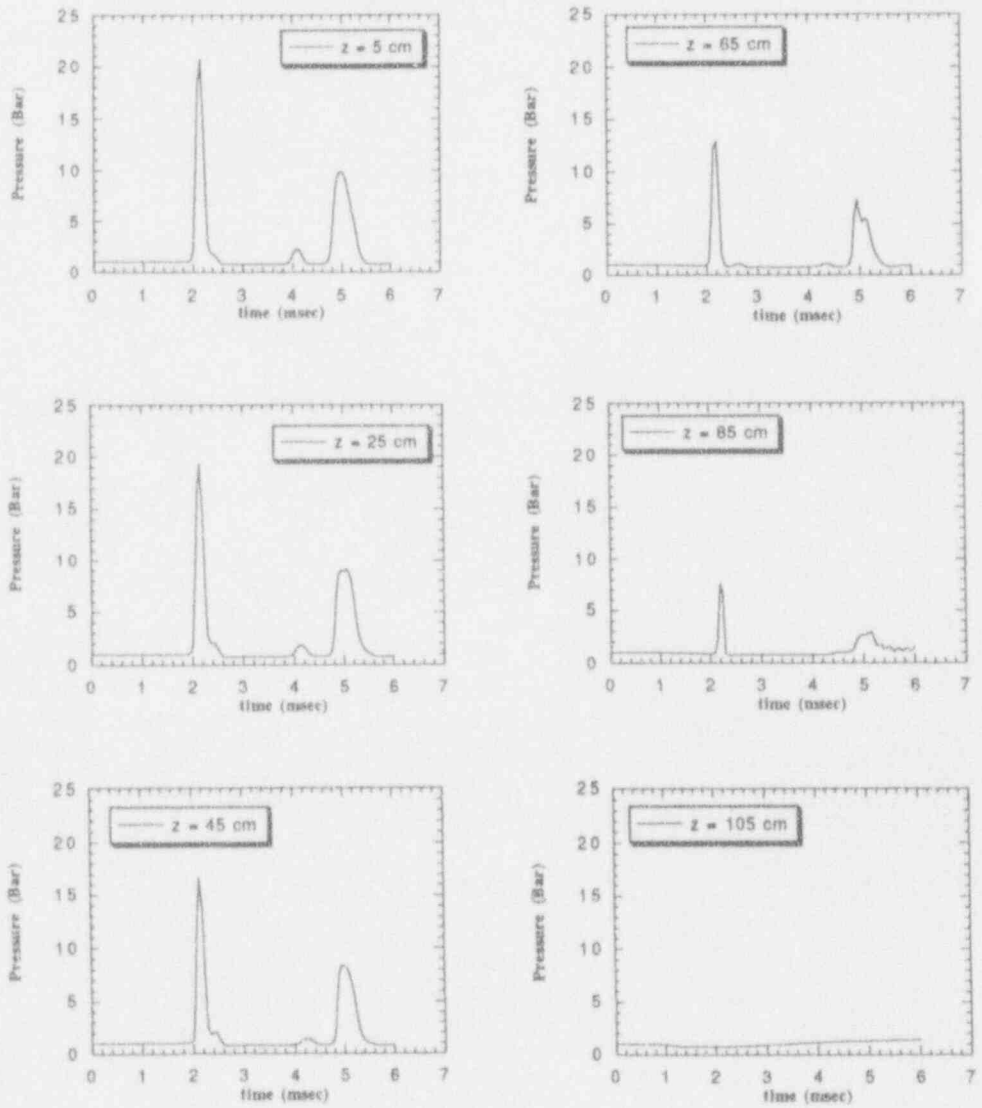

Figure 13. Calculated loadings on lateral pool boundary for a 1-m deep pool, ESPROSE.a with $f_f = 1$ and $f_v = 0.05$.

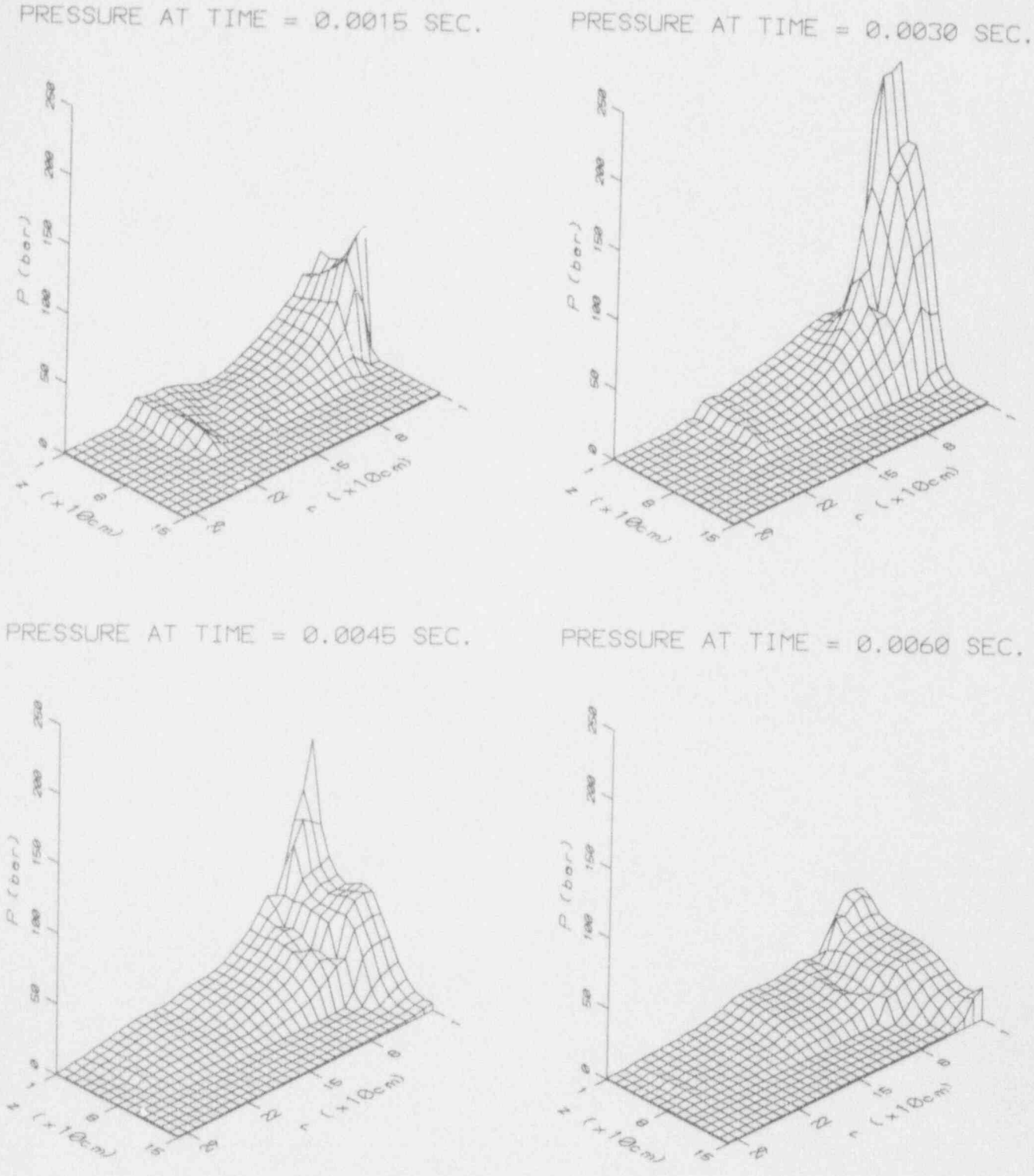

Figure 14. Calculated transient pressure distribution of an ex-vessel explosion for a 1-m deep pool using ESPROSE.a.

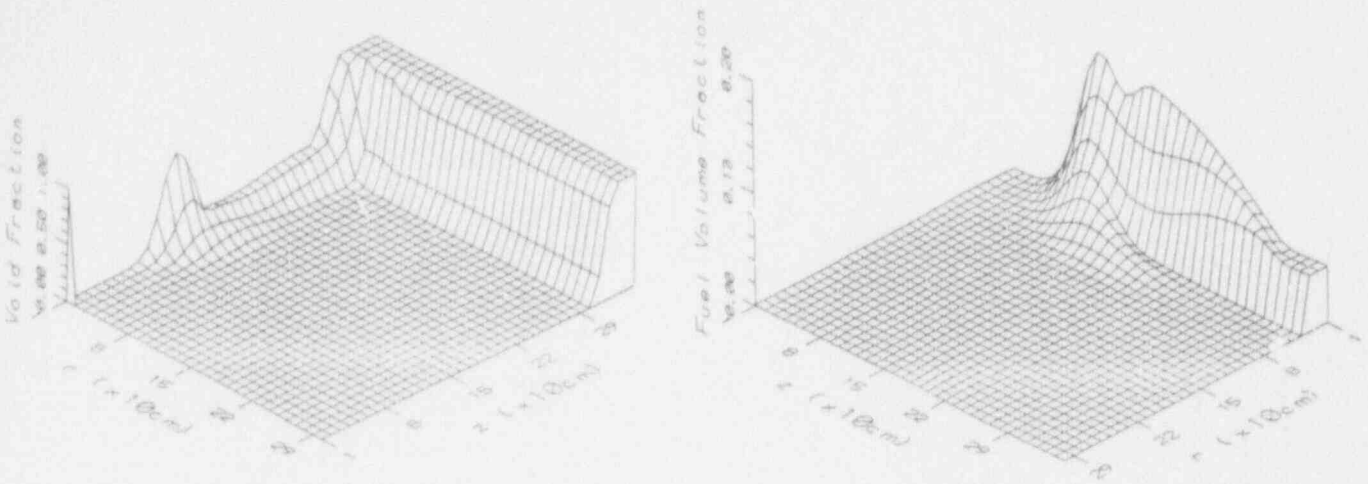

Figure 15. Initial conditions for the ex-vessel, 3-m deep pool, ESPROSE.a calculation.

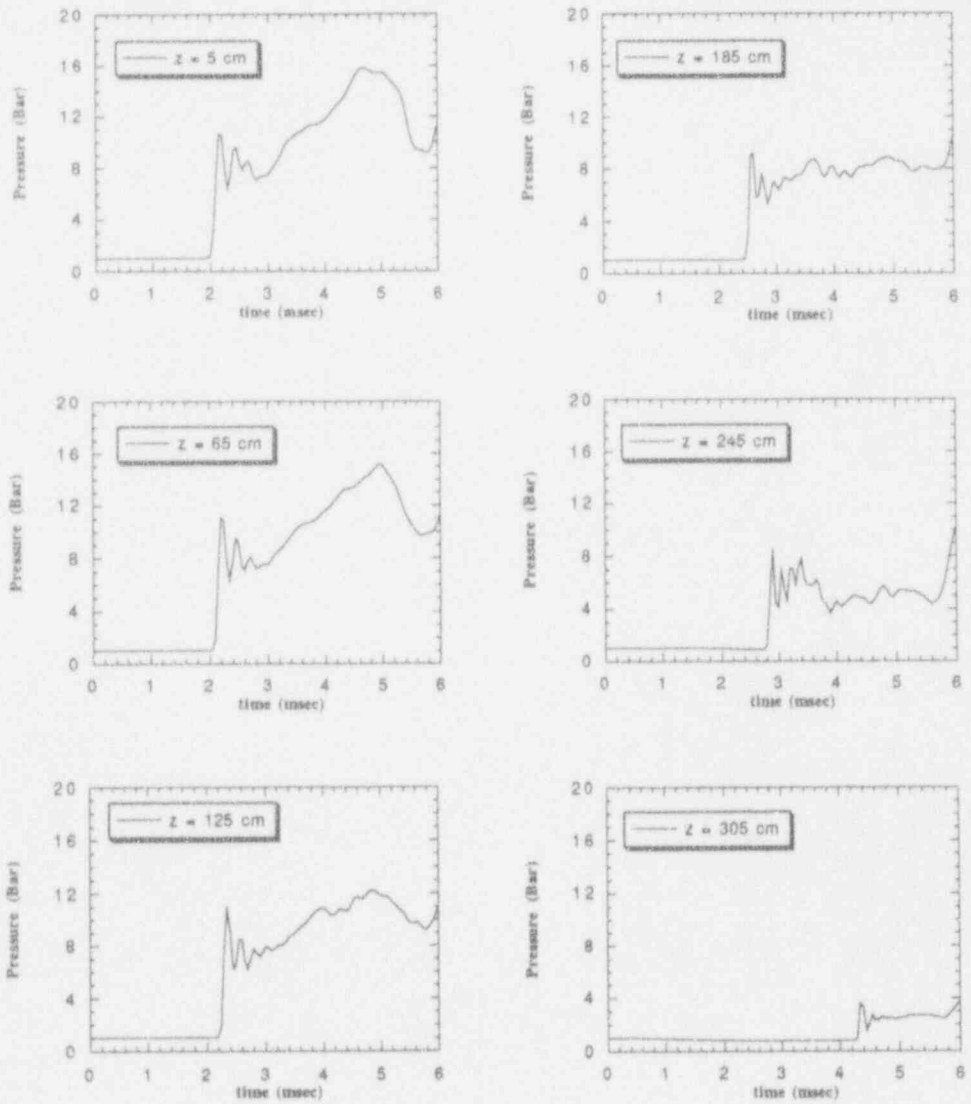

Figure 16. Calculated loadings on lateral pool boundary for a 3-m deep pool. ESPROSE.a with $f_f = 1$ and $f_e = 0.05$.

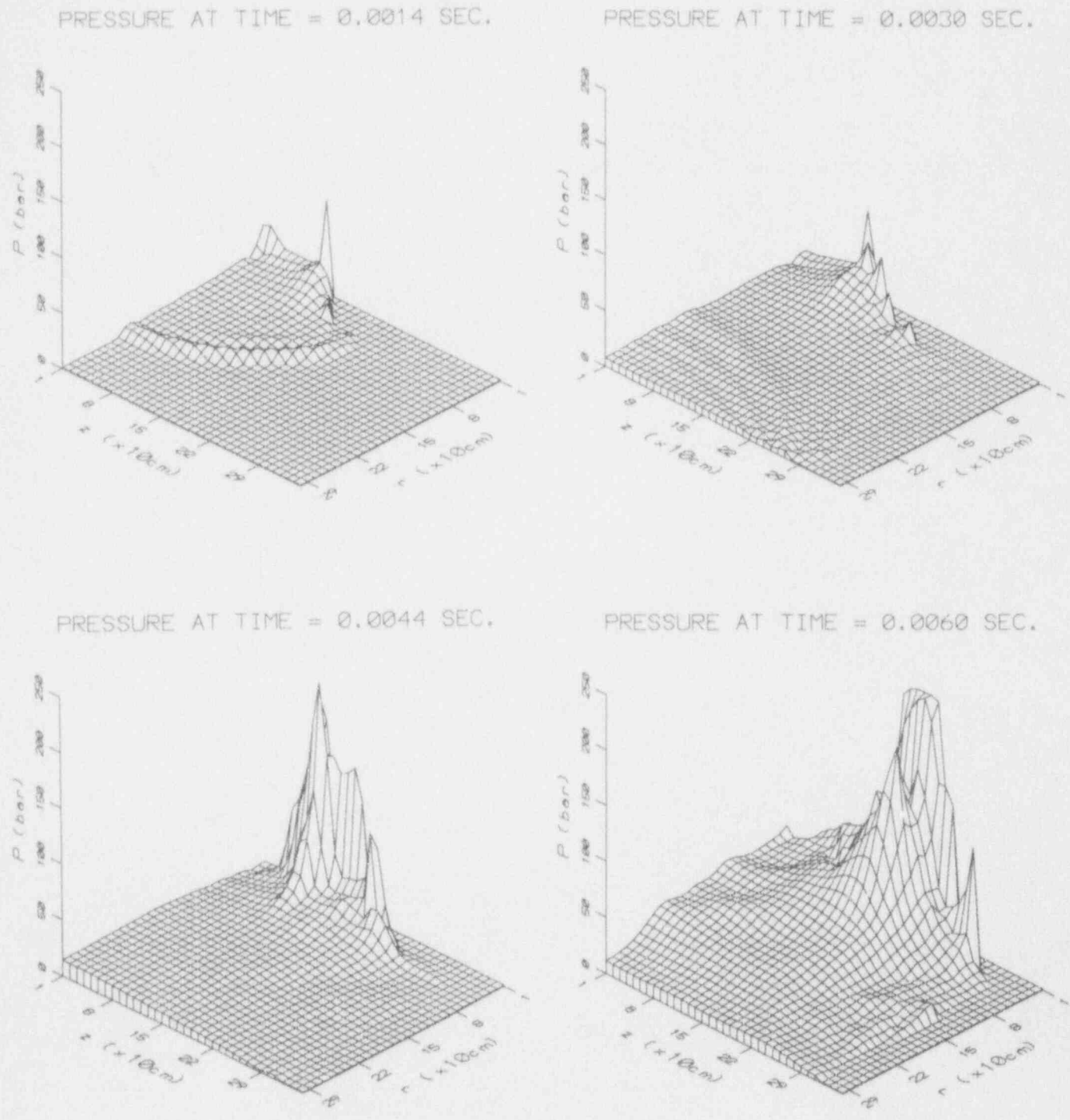

Figure 17. Calculated transient pressure distribution of an ex-vessel explosion for a 3-m deep pool using ESPROSE.a.

APPENDIX: FORMULATION OF ESPROSE.m FIELD MODEL

I. CONSERVATION EQUATIONS

There are four phases: namely, "micro-interaction" fluid, coolant liquid, fuel (melt) drops, and fuel debris. They will be referred to as m-fluid, liquid, fuel and debris respectively. Each phase is represented by one flow field with its own local concentration and temperature. The debris is assumed to be part of the m-fluid in thermal and hydrodynamic equilibrium. Thus we have four continuity equations, three momentum equations, and three energy equations. In the usual manner, the fields are allowed to exchange energy, momentum and mass with each other. With the definition of the macroscopic density ρ_i' of phase i,

$$\rho_i' = \theta_i \rho_i \qquad \text{for} \quad i = m,\ \ell,\ f, \text{and } db, \tag{A.1}$$

and the compatibility condition,

$$\theta_m + \theta_\ell + \theta_f + \theta_{db} = 1, \tag{A.2}$$

these equations can be written rather directly (Ishii, 1975).

• Continuity Equations.

m-Fluid:

$$\frac{\partial \rho_m'}{\partial t} + \nabla \cdot (\rho_m' \mathbf{u}_m) = E + J \tag{A.3}$$

Liquid:

$$\frac{\partial \rho_\ell'}{\partial t} + \nabla \cdot (\rho_\ell' \mathbf{u}_\ell) = -E - J \tag{A.4}$$

Fuel:

$$\frac{\partial \rho_f'}{\partial t} + \nabla \cdot (\rho_f' \mathbf{u}_f) - F_r \tag{A.5}$$

Debris:

$$\frac{\partial \rho_{db}'}{\partial t} + \nabla \cdot (\rho_{db}' \mathbf{u}_m) = F_r \tag{A.6}$$

• Momentum Equations.

m-Fluid:

$$\begin{aligned}\frac{\partial}{\partial t}((\rho_m' + \rho_{db}')\mathbf{u}_m) + \nabla \cdot ((\rho_m' + \rho_{db}')\mathbf{u}_m \mathbf{u}_m) = \\ - (\theta_m + \theta_{db})\nabla p - F_{m\ell}(\mathbf{u}_m - \mathbf{u}_\ell) \\ - F_{mf}(\mathbf{u}_m - \mathbf{u}_f) + E\mathbf{u}_\ell + F_r \mathbf{u}_f \\ + J(H[J]\mathbf{u}_\ell - H[-J]\mathbf{u}_m + (\rho_m' + \rho_{db}')\mathbf{g}\end{aligned} \tag{A.7}$$

Liquid:

$$\begin{aligned}\frac{\partial}{\partial t}(\rho_\ell' \mathbf{u}_\ell) + \nabla \cdot (\rho_\ell' \mathbf{u}_\ell \mathbf{u}_\ell) = \\ \theta_\ell \nabla p + F_{m\ell}(\mathbf{u}_m - \mathbf{u}_\ell) - F_{\ell f}(\mathbf{u}_\ell - \mathbf{u}_f) \\ - E\mathbf{u}_\ell - J(H[J]\mathbf{u}_\ell - H[-J]\mathbf{u}_m) + \rho_\ell' \mathbf{g}\end{aligned} \tag{A.8}$$

Fuel:

$$\begin{aligned}\frac{\partial}{\partial t}(\rho_f' \mathbf{u}_f) + \nabla \cdot (\rho_f' \mathbf{u}_f \mathbf{u}_f) = -\theta_f \nabla p + F_{mf}(\mathbf{u}_m - \mathbf{u}_f) \\ + F_{\ell f}(\mathbf{u}_\ell - \mathbf{u}_f) + \rho_f' \mathbf{g} - F_r \mathbf{u}_f\end{aligned} \tag{A.9}$$

• Energy Equations.

m-Fluid:

$$\begin{aligned}\frac{\partial}{\partial t}(\rho_m' I_m + \rho_{db}' I_{db}(T_m)) \\ + \nabla \cdot [(\rho_m' I_m + \rho_{db}' I_{db}(T_m))\mathbf{u}_m] = \\ - p\left[\frac{\partial}{\partial t}(\theta_m) + \nabla \cdot (\theta_m \mathbf{u}_m)\right] \\ + E h_\ell + J h_m \\ - R_{ms}(T_m - T_s) + \dot{Q}_{fm}\end{aligned} \tag{A.10}$$

Liquid:

$$\begin{aligned}\frac{\partial}{\partial t}(\rho_\ell' I_\ell) + \nabla \cdot (\rho_\ell' I_\ell \mathbf{u}_\ell) = \\ - p\left[\frac{\partial}{\partial t}(\theta_\ell) + \nabla \cdot (\theta_\ell \mathbf{u}_\ell)\right] \\ - E h_\ell - J h_\ell \\ + R_{\ell s}(T_\ell - T_s) + \dot{Q}_{f\ell}\end{aligned} \tag{A.11}$$

Fuel:

$$\frac{\partial}{\partial t}(\rho_f' I_f) + \nabla \cdot (\rho_f' I_f \mathbf{u}_f) = -\dot{Q}_{fm} - \dot{Q}_{f\ell} \tag{A.12}$$

In the above equation, $H(J)$ is the Heaviside step function that becomes unity for positive values of the argument and zero otherwise. When $T_m < T_s$, the m-fluid is liquid and J is set to be zero and T_s is an "equivalent" interface temperature given by

$$T_s = \frac{R_{ms} T_m + R_{\ell s} T_\ell}{R_{ms} + R_{\ell s}}$$

When $T_m > T_s$, J is an evaporation rate given by

$$J = \frac{1}{h_m - h_\ell}[R_{ms}(T_m - T_s) + R_{\ell s}(T_\ell - T_s)]$$

It should be pointed out that diffusive transport within each field (shear stresses and conduction) has been ignored in the above formulation—they are expected not to be important.

II: THE CONSTITUTIVE LAWS

The interfacial exchanges of momentum and heat are clearly regime dependent, and uncertainties remain even for simple two-phase flows. Only experiments specifically oriented to this problem and detailed local measurements will provide the basis for the appropriate assessment, particularly if one of the phases is the "micro-interaction" fluid. For now, our approach is to treat the m-fluid as a "pseudo" gas and utilize a similar set of constitutive laws as in a previous work (Medhekar et al., 1989).

For the mass transfer from the fuel, the fragmentation rate, F_r, is calculated based the instantaneous Bond number formulation as described in a previous work (Yuen et al., 1992). The relevant equations are

$$F_r = \frac{6\theta_f}{\pi \ell_f^3} \frac{dM}{dt} \qquad (A.13)$$

where

$$\frac{dM}{dt} = \alpha_m \left(\frac{dM}{dt}\right)_m + (1-\alpha_m)\left(\frac{dM}{dt}\right)_\ell \qquad (A.14)$$

with

$$\left(\frac{dM}{dt}\right)_i = \frac{\pi \ell_f^2 \mid \vec{u}_i - \vec{u}_f \mid}{6 t_{b,i}^*} (\rho_f \rho_i)^{1/2} \qquad \text{for} \quad i = m, \ell \qquad (A.15)$$

Equation (A.14) is a generalization of the single phase fragmentation rate utilized in the previous work (Yuen et al., 1992) with α_m being the "void fraction" of the m-fluid defined by

$$\alpha_m = \frac{\theta_m}{\theta_\ell + \theta_m} \qquad (A.16)$$

The "fragmentation time" and the instantaneous and Bond numbers for each phase are defined by

$$t_{b,i}^* = 13.8 \ \mathrm{Bo}_i^{1/4} \quad \text{and} \quad \mathrm{Bo}_i = \frac{3 C_D \rho_i}{8\sigma} \mid \mathrm{u}_i - \mathrm{u}_f \mid^2 \frac{\ell_f}{2} \qquad (A.17)$$

For the mass transfer between the m-fluid and liquid, the entrainment rate, E, is assumed to be directional proportional to the fragmentation rate in the preliminary calculations presented in this work. Specifically,

$$E = f_e F_r \frac{\rho_\ell}{\rho_f} \qquad (A.18)$$

with f_e being an empirical entrainment factor which can be varied parametrically.

NOMENCLATURE

Bo Bond number
C_D drag coefficient
$\frac{dM}{dt}$ fragmentation rate for a fuel drop
E entrainment rate
E_f emissivity of fuel particles
E_ℓ absorptivity of liquid droplets
F factor for interfacial momentum exchange
F_r fragmentation rate
f_e entrainment factor used by ESPROSE.m
f_f enhancement factor of fragmentation rate
f_v direct vaporization factor used in ESPROSE.a
g gravity
h specific enthalpy
h_c' heat transfer coefficient
I specific internal energy
J evaporation rate
ℓ length scale
$\dot{m}_e$ entrainment rate of microintraction fluid by a fuel drop
n number of fuel particles (or liquid droplets) per unit volume
p pressure
$\dot{Q}_{fg}$ heat transfer rate between fuel and vapor
$\dot{Q}_{f\ell}$ heat transfer rate between fuel and liquid
$R_{\ell s}$ heat transfer coefficient between liquid and the liquid/m-fluid interface
R_{ms} heat transfer coefficient between the m-fluid and the liquid/m-fluid interface
T temperature
t time
t_b^* fragmentation time
u velocity

Greek
α void fraction
α_m "void fraction" of microinteraction fluid
θ volume fraction
ρ microscopic density
ρ' macroscopic density
σ surface tension or Stefan-Boltzman constant
τ_e entrainment time constant used by ESPROSE.m

Subscripts
db debris
f fuel
g vapor (steam) used in ESPROSE.a
ℓ coolant (m-external fluid)
m microinteraction fluid
s saturation properties

ACKNOWLEDGMENT

The ESPROSE.a code utilized in the calculations presented in this paper is an advanced, developmental version of the ESPROSE code developed for the U.S. Nuclear Regulatory Commission under contract number 04-89-082.

REFERENCES

1. Abolfadl, M.A. and T.G. Theofanous (1987) "An Assessment of Steam-Explosion-Induced Containment Failure. Part II: Premixing Limits," *Nuclear Science and Engineering* **97**, 282.
2. Amarasooriya, W.H. and T.G. Theofanous (1991) "Premixing of Steam Explosions: A Three-Fluid Model," *Nuclear Engineering & Design* **126**, 23-39.
3. Angelini, S., E. Takara, W.W. Yuen and T.G. Theofanous (1992) "Multiphase Transients in the Premixing of Steam Explosions," Proceedings NURETH-5, Salt Lake City, UT, September 21-24, 1992, Vol. II, 471-478.

4. Angelini, S., W.W. Yuen and T.G. Theofanous (1993) "Premixing-Related Behavior of Steam Explosions," CSNI Specialists Meeting on Fuel-Coolant Interactions, Santa Barbara, CA, January 5-8.

5. Board, S.J. and R.W. Hall (1974) "Propagation of Thermal Expansions Part 2: A Theoretical Model," Berkeley Nuclear Labs, RD/B/N 3249.

6. Bürger, M. et al. (1984) "Description of Vapor Explosion by Thermal Detonation and Hydrodynamic Fragmentation Modeling," Int. Meet. of Thermal Nucl. Reactor Safety, Karsruhe, Sept. 1984.

7. Bürger, M., M. Buck, K. Müller and A. Schatz (1993) "Stepwise Verification of Thermal Detonation Models: Examination by Means of the KROTOS Experiments," CSNI Specialists Meeting on Fuel-Coolant Interactions, Santa Barbara, CA, January 5-8.

8. Chu, C.C. and M.L. Corradini (1989) "One-Dimensional Transient Fluid Model for Fuel/Coolant Interaction Analysis," *Nuclear Science and Engineering* **101**, 48-71.

9. Denham, M.K., A.P. Tyler and D.F. Fletcher (1992) "Experiments on the Mixing of Molten Uranium Dioxide with Water and Initial Comparisons with CHYMES Code Calculations," ANS Proceedings NURETH-5, Salt Lake City, UT, September 21-24, 1992, Vol. VI, 1667-1675.

10. Fletcher, D.F. (1993) "Propagation Investigations Using the CULDESAC Model," CSNI Specialists Meeting on Fuel-Coolant Interactions, Santa Barbara, CA, January 5-8.

11. Fletcher, D.F. and A. Thyagaraja (1989) "A Mathematical Model of Melt/Water Detonations," *Applied Mathematical Modelling* **13**, 333-350.

12. Hohmann, H., D. Magallon, H. Schins and A. Yerkess (1993) "FCI Experiments in the Aluminumoxide/Water System," CSNI Specialists Meeting on Fuel-Coolant Interactions, Santa Barbara, CA, January 5-8.

13. Ishii, M. (1975) *Thermo-Fluid Dynamic Theory of Two-Phase Flow*, Eyrolles, France.

14. Kim, H.J. and M.L. Corradini (1988) "Modelling of Small Scale Single Droplet Fuel Coolant Interactions," *Nuclear Science and Engineering* **98**, 16-29.

15. Medhekar, S., M. Abolfadl and T.G. Theofanous (1991) "Triggering and Propagation of Steam Explosions," *Nuclear Engineering and Design* **126**, 41-46.

16. Medhekar, S., W.H. Amarasooriya and T.G. Theofanous (1989) "Integrated Analysis of Steam Explosions," Proceedings Fourth International Topical Meeting on Nuclear Reactor Thermal-Hydraulics, Karlsruhe, FRG, Oct. 10-13, 1989, Vol. 1, 319–326.

17. Patel, P.D. and T.G. Theofanous (1981) "Hydrodynamics Fragmentation of Drops," *J. Fluid Mech.* **103**, 207-223.

18. Sharon, A. and S.G. Bankoff (1981) "On the Existence of Steady Supercriticalplane Thermal Detonations," *Int. J. Heat Mass Transfer*, **24**.

19. Theofanous, T.G., B. Najafi and E. Rumble (1987) "An Assessment of Steam-Explosion-Induced Containment Failure. Part I: Probabilistic Aspects," *Nuclear Science and Engineering*, **97**, 259-281. (Also, including peer review comments, in NUREG/CR-5030, 1989.)

20. Theofanous, T.G. and W.W. Yuen (1993) "The Probability of Alpha-Mode Containment Failure Updated," CSNI Specialists Meeting on Fuel-Coolant Interactions, Santa Barbara, CA, January 5-8.

21. Turland, B., D.F. Fletcher, K.I. Hodges and G.J. Attwood (1993) "Quantificaton of the Probability of Containment Failure Caused by an In-Vessel Steam Explosion for the Sizewell B PWR," CSNI Specialists Meeting on Fuel-Coolant Interactions, Santa Barbara, CA, January 5-8.

22. Yuen, W.W., X. Chen and T.G. Theofanous (1992) "On the Fundamental Microinteractions That Support the Propagation of Steam Explosions," ANS Proceedings NURETH-5, Salt Lake City, UT, September 21-24, 1992, Vol. II, 627–636.

23. von Neumann, J. and R.D. Richtmyer (1950) "A Method for the Numerical Calculations of Hydrodynamical Shocks," *J. Applied Physics* **21**, 232-237.

EFFECTS OF SURFACTANTS ON THE LIKELIHOOD AND SEVERITY OF STEAM EXPLOSIONS

M. G. Kowal,[a] M. F. Dowling, and S. I. Abdel-Khalik

Nuclear Engineering Program
George W. Woodruff School of Mechanical Engineering
Georgia Institute of Technology, Atlanta, GA 30332
Telephone (404) 894-3719 -- Fax (404) 894-3733

ABSTRACT

Dilute aqueous solutions of two surface active agents (surfactants) were tested for their ability to suppress spontaneous steam explosions. Nonylphenol polyethylene glycol ether (Tergitol NP-9), a non-ionic surfactant, and dodecylbenzene sulfonate sodium salt (Witconate-90), an ionic surfactant, were used to prepare aqueous solutions with surfactant concentrations of 5, 10, and 50 wppm. Twelve grams of tin metal at 800°C and atmospheric pressure was dropped into a vessel containing 6 liters of deionized water, or one of the listed solutions. The experiments were repeated a minimum of twenty times with each coolant to check for consistency and repeatability. The peak pressures recorded for each experiment were statistically analyzed and compared with those for deionized water. Additionally, particle size distribution of the fragmented debris were measured and statistically analyzed.

It was found that the surfactants do, indeed, mitigate the severity of vapor explosions. On average, the surfactant solutions resulted in a 65% reduction in average peak pressures when compared with the deionized water results. However, very little difference in the mitigating effect of the surfactant solutions was observed as the concentration was increased beyond 5 wppm. The particle size distribution results also indicated a mitigating effect on steam explosion severity, as a 19% reduction in participating melt mass fraction was observed when the surfactants were used. For the peak pressure and particle size distribution results obtained, statistical analyses showed that the differences between the water and the surfactant experiments were significant. When comparing the surfactant solutions amongst themselves, however, the differences were not statistically significant.

I. INTRODUCTION

Vapor explosions are energetic interactions which occur when a high temperature molten material comes into contact with a cold volatile liquid. Rapid heat transfer from the melt to the coolant, and the subsequent phase transition of the coolant, result in the formation of a vapor film between the volatile liquid and the melt. Shortly thereafter the vapor film collapses, causing the melt to fragment into small particles. This fragmentation significantly increases the surface area available for heat transfer, thus significantly increasing the heat transfer rate. As a result of this enhanced heat transfer, explosive vaporization of the liquid and highly destructive shock waves can occur.

One possibility for reducing the consequences of steam explosions during a nuclear accident is to identify an additive which can be injected into the emergency cooling water and reliably suppress the explosion. Recently, considerable interest has been generated in both the nuclear and aluminum industries in trying to identify such an additive, and both polymer and surfactant solutions have been studied.

Several studies have been performed which examined the effect of coolant viscosity on the likelihood and severity of steam explosions (see review in Reference 9). Most recently, Ip, Dowling, and Abdel-Khalik (1992) experimented with dilute solutions of four water-soluble polymers to examine their ability to suppress spontaneous vapor explosions. Two of these additives did not affect the surface tension of the coolant; the other two did not decrease it by more than 10% even at the highest concentrations examined. Their results suggested that dilute solutions of polymeric additives, particularly poly(ethylene oxide), may be used to completely suppress vapor explosions if, and only if, it can be assured that the concentration can be maintained above a threshold value. Their data indicated, however, that at lower concentrations, more violent, yet less frequent, explosions may result.

The effect of coolant surface tension on steam explosion severity has not been studied as extensively as has coolant viscosity. Surface tension reducing surfactants have, however, in a similar context, been studied to determine their effect on liquid-vapor interface stability, and for use in applications such as quenching of molten materials (Becker, 1991). The use of surfactants has been applied with satisfactory results for several years in the metallurgical industry in Norway (Becker, 1991). In this respect, small amounts of surfactants are added to water for the production of copper and ferrous alloy granulate by the quenching of molten metals.

The idea of using surfactants to suppress steam

[a] Present address: Northeast Utility Company, Hartford, CT.

explosions is based on their ability to form a layer of surfactant molecules at the coolant-vapor interface, and thus stabilize the vapor film which surrounds the melt. Becker states that the surfactant layer at the interface tends to decrease the surface tension of the bulk liquid, increase the coolant surface viscosity, increase the coolant surface density, and impose a rigid surface on the vapor bubble. Surfactants also affect the formation of new surface (for example, as bubbles grow within the liquid) since surfactant molecules migrate from the bulk of the liquid to the new interface at a finite rate (Kippenhahn and Tegeler, 1970).

Experimental data relevant to the effect of surfactants on liquid-vapor heat transfer and interface stability have been reported by Cary (1958), Yu (1985), Kippenhahn and Tegeler (1970), and Becker (1991). Steam explosion experiments involving surface tension reduction have been performed by Groenveld (1972), McCracken (1973), and Becker (1991).

Cary investigated the use of a polyvinyl alcohol solution as a quenching coolant for medium-carbon steel parts. The goal was to identify a quenching solution with a cooling rate between those of water and oil. Aqueous solutions of polyvinyl alcohol (500-3000 ppm by weight) resulted in a longer cooling time: quenching was complete in approximately 15 seconds in pure water, but the process took over 20 seconds in the alcohol solution.

Yu (1985) investigated the boiling heat transfer mechanism in the high temperature quenching process of aluminum ingot casting. Yu performed a quench test using a solution containing 0.2% of an unspecified surfactant which lowered the surface tension of deionized water from 5.5×10^{-2} N/m to 2.1×10^{-2} N/m at 98°C. Yu found that the surfactants retarded the boiling heat transfer rate. Based on these results, surfactants may also favorably influence the boiling heat transfer phenomena inherent in steam explosions.

Kippenhahn and Tegeler (1970) studied dynamic surface tension effects in surfactant solutions by observing the formation of air bubbles beneath the surface of the liquid. The effective surface tension acting on the bubble surface was correlated with the instantaneous rate of change of bubble surface area (the true area strain rate). In distilled water the surface tension was constant. In surfactant solution the effective surface tension increased as the true area strain rate increased, starting from the static surface tension and approaching the limiting value for pure water at higher rates. This effect was attributed to the finite rate at which surfactant molecules could migrate to the bubble surface from the bulk liquid.

Becker (1991) reviewed measurements of bubble rise velocities and presented data for new surfactants. In general, the addition of surfactants decreases the velocity of gas bubbles. This result was attributed to the increased rigidity of the interface (hence, increased drag) due to the surfactant molecules.

Groenveld (1972) used water droplets in combination with organic fluids instead of molten metal, to allow him to see any encapsuled drops. His results pointed to a possible way of preventing vapor explosions. He concluded that, "a surfactant which makes the interface inelastic should be added."

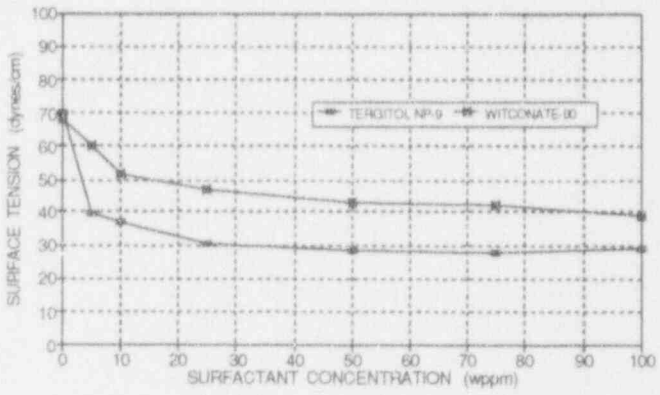

Figure 1: Surface Tension v. Concentration for Surfactants used in Present Investigation

McCracken (1973) obtained results which were in contradiction to the results obtained by Groenveld. McCracken experimented with surface tension by adding up to 50 drops of a detergent to water (sufficient to produce a good lather when stirred). His results indicated that the detergent had no effect on the percentage disintegration of the melt. He therefore concluded that the surface tension of the coolant was not a major factor in determining whether or not a vapor explosion takes place.

Most recently, Becker (1991) of the Royal Institute of Technology (Stockholm, Sweden) in a joint project with Sandia National Laboratory, carried out small-scale steam explosion experiments to study the effect of surfactants on hydrodynamic fragmentation and steam explosions. Both spontaneous explosions in a tin-water system and triggered explosions in a thermite-water system were performed. Detailed reports documenting the results of these experiments are expected to be published by Sandia National Laboratory in the near future. The information discussed here was obtained from Reference 3, which does not discuss all experiments performed.

The majority of the spontaneous tin-water experiments were performed by dropping 12 grams of molten tin at 650°C into a water/ethoxilated-nonyle-phenole solution. Although a few exceptions occurred, it was reported that the spontaneous steam explosions were generally mitigated or completely suppressed by the addition of 1-10 ppm of the surfactant to the water. At a water temperature of 50°C, 1 ppm and 5 ppm were sufficient to completely suppress the explosions. By use of a Hycam high-speed film (3000 f/s), Becker reported that explosions were mitigated at 20°C and 35°C. At 40°C, an enhancement of the steam explosion was observed for 5 ppm. In general, they concluded that for the tin-water experiments, small concentrations in the water mitigate steam explosions. Based on these results, Becker suggested that small amounts of surfactants be added to emergency cooling water in light water reactors under severe accident conditions (Becker, 1990).

Based on the above discussion, the purpose of this investigation was to examine further the effect of surfactants on the likelihood and/or severity of vapor explosions in molten tin/water systems. The surfactants used in this investigation were chemically identical to those used by Becker: nonylphenol polyethylene glycol ether (sold under the brand name Tergitol NP-9 by Union Carbide) and dodecylbenzene sulfonate sodium salt (Witconate-90, Witco Corporation). Figure 1 shows variation of static surface tension with concentration for the two surfactants used. These data were obtained using the DuNouy ring method.

II. EXPERIMENTAL APPARATUS AND PROCEDURES

A. Apparatus

The experimental apparatus was composed of three major systems: the furnace and melt release mechanism, the containment system, and the instrumentation and data acquisition system. Figure 2 contains a schematic diagram of the experimental apparatus.

1. Furnace and Melt Release Mechanism. Figure 3 provides a schematic diagram of the furnace and melt release mechanism. Tin samples were melted in an electrically heated muffle furnace mounted in the upper chamber of the vessel. The melt was held in a stainless steel crucible coated with boron nitride lubricant and had a 0.833 cm diameter hole in the bottom through which the melt could be dropped. A steel plug contained the melt during the heat-up process. A solenoid mechanism lifted this plug to release the melt. The drop distance of the melt (from bottom of the crucible to coolant surface) was approximately 25.5 cm.

2. Containment System. The containment vessel consisted of two large stainless steel crosses from a vacuum system separated by a large gate valve. Each cross had a

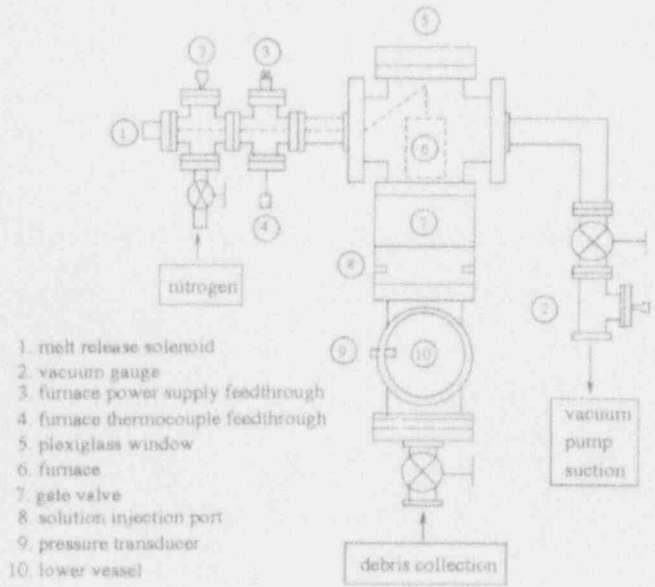

Figure 2: Schematic Diagram of Apparatus

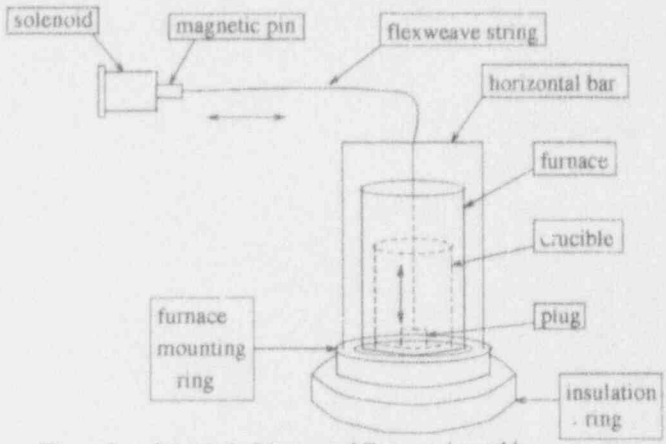

Figure 3: Schematic Diagram of Furnace Assembly and Dropping Mechanism

volume of approximately 7000 cm^3 with circular openings 13.75 cm in diameter on each side. The upper cross held the furnace assembly and could be evacuated to prevent oxidation of the tin during heating. The lower cross held the coolant solution and contained penetrations for the pressure transducers. Windows were installed on two opposite sides of the lower cross so that the explosions could be viewed and filmed. The volume of the coolant solution used (6 liters) reached a level slightly above the two window openings. To assist in the removal of debris from the lower vessel following each experiment, a plexiglass cone was placed at the bottom to funnel the debris into the drainage valve at the bottom.

3. Instrumentation and Data Acquisition. Piezoelectric crystal transducers (PCB Piezotronics) were used to measure the transient pressure history in the liquid coolant solution during the experiments. Two types of transducers were used: a wall mounted type and a hanging type. The wall mounted transducer (Model #HE102A06) had a sensitivity of 10.50 mV/psi with deviations from linearity less than 1.0% full scale. The rise time for a step increase in pressure was approximately 1 μsec. The hanging transducer (Model No. 138M09) had a sensitivity was 5.42 mV/psi with deviations from linearity less than 2.0% full scale and a risetime of 1.5 μsec. The transducers were mounted so that their sensing elements were at the same height in the experimental vessel (approximately 10 cm below the surface of the water, 6 cm from the central axis). The signal from each transducer was amplified and then digitally sampled at 100 kHz using an EGAA Computerscope data acquisition system from RC Electronics (Goleta, CA). Data acquisition was triggered when the pressure signal exceeded 0.08 psi.

4. Materials. High quality granulated tin metal from Fisher Scientific was used for all of the experiments. Iron and copper impurities were present at 0.001% levels, and lead was present at 0.008%.

Of the two surfactants used in this investigation, one was in a liquid form (Tergitol NP-9) and the other was in a powder form (Witconate-90). Each sample came in an air-tight container supplied by the manufacturer, and both were stored at room temperature during the course of the experiments.

Deionized water used for the coolant and to rinse the lower vessel between experiments came from a three cartridge water deionization unit. No degassing of the water was performed, but it was stored in large Nalgene jugs for one to two days prior to use.

B. Experimental Procedures

1. Surfactant Solution Preparation. For all experiments, six liters of pure deionized water from a clean plastic bucket outside of the steel containment vessel were drained through a short length of plastic tubing into the lower vessel. For the powdered surfactant (Witconate-90), the solution was prepared by placing the appropriate mass into the lower vessel before the water was added. The liquid surfactant (Tergitol NP-9) was injected into the water flow using a microliter syringe. (A small glass "T" with a serum bottle stopper (septum) on the perpendicular leg was inserted into the drain tube for this purpose.) In each case the turbulence of the water flowing into the lower experimental vessel provided the mixing. Solutions remained in the lower vessel for approximately 20 minutes prior to each melt drop.

2. Melt Dropping Procedure. Once the coolant solution for each experiment was prepared, the lower vessel ports were closed along with the gate valve between the upper and lower vessels. Tin metal (12.000±0.002 grams) was placed into the furnace crucible, and the upper vessel was sealed and evacuated using a roughing pump. The tin was then melted and heated to a temperature of 880-890°C, at which point the furnace was turned off and the tin cooled to the desired experimental temperature (800°C). During the latter part of the cool-down, the pump was shut off and the upper vessel repressurized to atmospheric pressure with nitrogen gas. The upper/lower vessel isolation valve was then opened, and the solenoid energized to release the melt. Solutions were all at room temperature (23°C) and atmospheric pressure.

Before energizing the solenoid, the melt was checked for oxidation through a window at the top. Data acquisition was triggered automatically by a pressure signal in the water exceeding 0.08 psi.

3. Debris Collection and Analysis. Following the experiment, the coolant solution and debris were drained from the lower vessel. The lower vessel was then thoroughly rinsed to ensure that all of the debris had been drained and to remove traces of surfactant. Extremely small amounts of debris sometimes remained on the wall of the lower vessel in spite of this rinsing procedure; these were collected by wiping with a piece of filter paper and the vessel was rinsed again to remove all traces of surfactant. The debris was then carefully filtered from the coolant and dried. On average, from the 12.0 grams of tin originally placed in the furnace, approximately 11.6 grams of explosion debris was retrieved. (Seperate experiments were done to verify that the differences were due to losses before the melt was dropped.)

To obtain the distribution of particle sizes a set of sieves on a vibration stand was used to sort the debris. The sieve series openings (in microns) were: 45, 75, 212, 354, 595, 841, 1000, 1410, 4760, and 12,700 μm. To assure good separation, the samples were shaken for 20 minutes (Allen, 1990, p.200). Differences in the sample mass before and after the separation were negligible (<1%).

III. EXPERIMENTAL RESULTS

Seven series of experiments, each utilizing a different coolant solution, were performed. The seven coolant solutions investigated included pure deionized water, and 5, 10, and 50 wppm solutions of both Tergitol NP-9 (NPGE) and Witconate-90 (Witco-90) surfactant. To check for consistency and repeatability, each series included a minimum of 20 experiments conducted under identical conditions. A total of 150 experiments were performed, and all resulted in a vapor explosion with debris fragmentation.

The experimental data consisted of digitized pressure signals for each experiment and particle size distributions for the fragmented metal debris from three of the experimental series (pure water, 5 wppm Tergitol NP-9 and 5 wppm Witconate 90). To determine whether differences in results for the various coolant solutions were statistically significant, the Mann-Whitney test (Conover, 1971) was applied.

A. Peak Pressure Results

Digitized pressure signals for each experiment were acquired through the use of two piezoelectric crystal pressure transducers and a data acquisition system. Except for a handful of experiments, pressure data were digitally sampled at 10 μsec intervals and collected for a period of 160 msec.

Figure 4 contains a typical pressure signal. In 4(a), the complete pressure history is given, while in 4(b) the plot is expanded about the pressure peak visible in 4(a). In general, the two pressure transducers produced consistent results with respect to the magnitude and timing of the pressure peaks. In many experiments, more than one pressure peak was observed, for example, in Figure 4 there is a second pressure fluctuation at approximately 45 msec. In some experiments, the peak pressures obtained during a second, or even a third pressure fluctuation were of significant magnitude. For a small number of experiments performed, the interaction was too weak to trigger the data acquisition system; a peak pressure value of zero was assigned to these experiments.

A summary of the average peak pressure results for the seven series of experiments performed is given in Table 1. This table provides the average, maximum, and minimum peak pressure values obtained for both the wall mounted and hanging transducers. It is apparent that the average peak pressures of the vapor explosions were reduced by both the Tergitol NP-9 (NPGE) and Witconate-90 coolant solutions compared to explosions in pure water. This difference in average peak pressures was not significantly affected by the concentration of the surfactant solution. Additionally, there was no sizeable difference between average peak pressures obtained in the Tergitol NP-9 and Witconate-90 surfactant solutions. In order to determine whether differences between solutions (or between the various concentrations of a surfactant) were statistically significant, the nonparametric Mann-Whitney statistical test

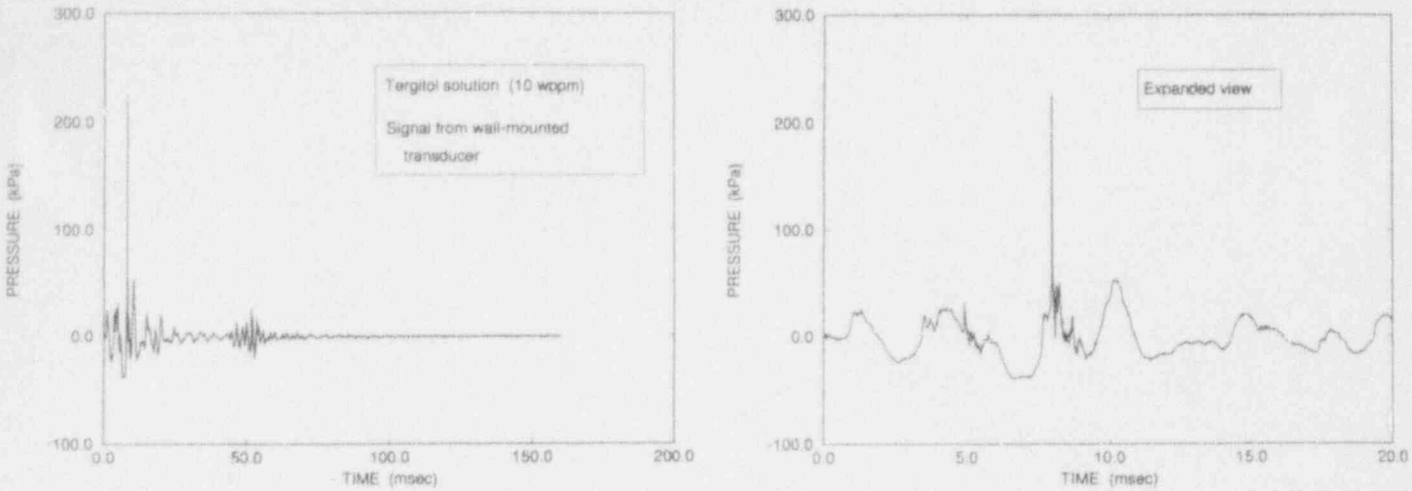

Figure 4: Typical Pressure Signal from Explosion

was applied.

The Mann-Whitney test is a "distribution free" statistical test which can be used to compare two data samples. A detailed description of the test can be found in Conover (1971). The results indicate that differences in average peak pressures from pure water experiments versus those from any of the surfactant solutions were statistically significant. When compared amongst themselves, however, the differences in the average peak pressures for the surfactants were not significant. In conjunction with these results, it was shown that the average peak pressure distribution functions for the pure water results versus any of the surfactant concentrations are dissimilar, while for the various surfactant concentration comparisons, the distribution functions are similar.

These distributions are illustrated in Figure 5, which shows only the results for experiments with pure water and 5 wppm surfactant solutions. For the pure water experiments, the peak pressures were randomly distributed over a broad range. For the 5 wppm solutions, the distribution of peak pressures had a narrower range and was concentrated from 0-105 kPa; for the 5 wppm surfactant solutions 80% of the acquired peak pressures fell into this range, whereas for pure water only 35% did. Similar results were found for the surfactant solutions with concentrations of 10 aad 50 wppm.

B. Particle Size Distributions

Particle size distribution measurement provides another method for comparing steam explosion severity. Intuitively, stronger, more powerful explosions would result in larger amounts of finely fragmented debris particles than would a weaker explosion. Size measurements were carried out for all of the experiments from the series utilizing pure water, 5 wppm Tergitol NP-9, and 5 wppm Witconate-90.

The results are presented in Table 2 and Figure 6 using the cumulative mass percentage; this curve facilitates comparisons of the total debris mass smaller than a given size. For each of the three series the average values (for the twenty experiments in each series) are plotted. In Table 2 standard deviations are also given. Figure 6 shows that there is a general shift in cumulative mass percentage towards larger particles in the surfactant solutions. The direction of this shift suggests a decrease in steam explosion severity due to the reduction in finely fragmented debris particles.

It is evident, however, due to the large standard deviations in Table 2, that depending upon which specific experiments were compared, it could be concluded that surfactants have either a positive or an adverse effect toward mitigating vapor explosions. Therefore, a statistical comparison of the particle size distributions was performed.

Table 1: Summary of Peak Pressure Results

	PEAK PRESSURES (kPa)					
	AVERAGE		MAXIMUM		MINIMUM	
	WALL	HANGING	WALL	HANGING	WALL	HANGING
WATER ONLY	213.39	171.40	509.86	456.57	0.00	0.00
NPGE(5wppm)	65.84	44.40	229.59	154.79	0.00	0.00
NPGE(10wppm)	76.39	49.43	340.74	225.59	0.00	0.00
NPGE(50wppm)	76.21	59.23	206.01	139.41	0.00	0.00
WITCO(5wppm)	74.35	72.19	235.66	267.24	0.00	0.00
WITCO(10wppm)	78.81	53.71	291.51	317.85	0.00	0.00
WITCO(50wppm)	69.82	35.58	259.93	132.65	0.00	0.00

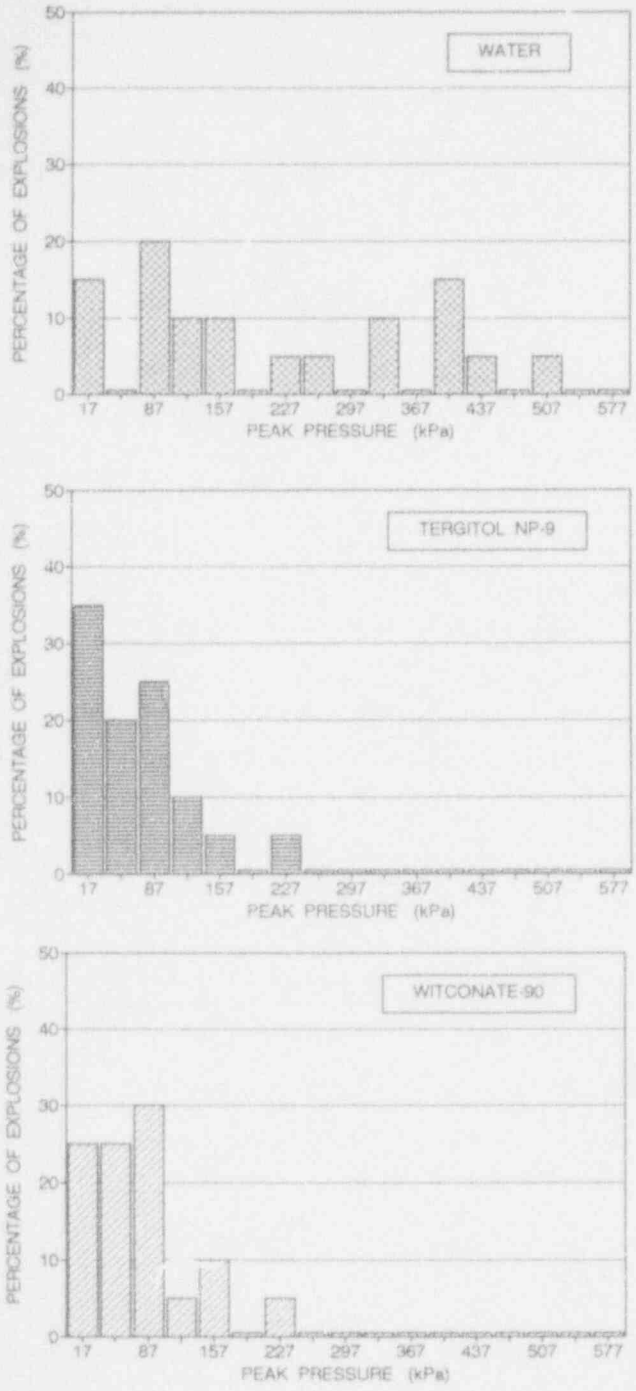

Figure 5: Histograms of Peak Pressures for Explosions in Pure Water and 5 wppm Surfactant Solutions. Each bar represents explosions in a range of 35 kPa centered on the values shown along the x-axis.

The Mann-Whitney test was applied again using the cumulative mass percentage of particles less than 354 μm as the data variable for each experiment. (This variable was selected based on previous experimental evidence which suggests that only a fraction of the molten metal participates in the vapor explosion. A cut-off value of 300 μm was used by Farawila and Abdel-Khalik (1990) in a previous analysis of steam explosion energetics, and 354 μm was the sieve size closest to this value used in this investigation.)

The Mann-Whitney test indicates that differences in the amount of debris smaller than 354 μm obtained from explosions in pure water compared to either of the 5 wppm surfactant solutions were statistically significant. Differences between the surfactant solutions, however, were not significant. Thus, on the basis of particle size distribution results only, it can be concluded that surfactants have a mitigating effect on vapor explosions. This confirms the conclusion based on the peak pressure results.

IV. DISCUSSION AND CONCLUSIONS

Spontaneous steam explosions of molten tin were carried out using coolant solutions of pure deionized water and solutions with concentrations of 5, 10, and 50 ppm by weight made with a non-ionic surfactant (Tergitol NP-9) and an ionic surfactant (Witconate-90). The relative severity of the explosions was determined by measuring and statistically comparing peak pressure values and also (for three of the experimental series) by comparing debris particle size distributions. Steam explosions and debris fragmentation occurred in all 150 experiments performed (for pure water, this is in agreement with Dullforce, 1976).

Both the peak pressure values recorded and the size distribution measurements performed on the debris indicate that small quantities of surfactants have a mitigating effect on spontaneous steam explosions of tin in aqueous solutions at room temperature. When the peak pressures of the twenty experiments performed with each solution are averaged, the values for the surfactant solutions are approximately 65% lower than that for pure water; the maximum peak pressure for each series is similarly reduced in the surfactant solutions (Table 1). On average, the total amount of fragmentation debris smaller than 354 μm was reduced in the surfactant solutions; this also implies that weaker explosions were occurring.

For spontaneous explosions comparison of one or two specific experiments does not suffice due to the range of the observed quantities even when experiments are performed under identical conditions. Statistical analysis of data sets from repeated experiments was required to ascertain the significance of the results. Using a non-parametric statistical test, it was found that the reductions referred to in the previous paragraph were indeed statistically significant and that the surfactants did mitigate the explosions on the average. Differences between solutions made with different surfactants or with different concentrations of surfactant were found to be statistically insignificant.

Based on the average peak pressure results, increasing the surfactant concentration beyond 5 wppm did not have a significant effect on explosion severity even though the additional surfactant further reduced the surface tension of the coolant. (Figure 1 shows the surface tension at various concentrations for the two surfactants used in the present investigation.) Intuitively, one might expect that the mitigating effect would continue to improve as the surface

tension decreased, but this was not the case; the differences in average peak pressure values for surfactant solutions with different concentrations were statistically insignificant. Since the difference between solutions made with different surfactants were also statistically insignificant, the fact that one additive was ionic and the other non-ionic was not important.

These results suggest that there may exist another mechanism other than simple reduction of static, macroscopic surface tension which mitigates the severity of the explosions. Possibly this is due to the limited ability of the surfactants to reduce the surface tension at the surface of a rapidly growing gas bubble (Kippenhahn and Tegeler, 1970); even as the concentration increases beyond 5 wppm the dynamic surface tension of a bubble expanding beneath the surface of the liquid is limited by the rate at which molecules can migrate from the bulk to the interface.

When considering the effect of static, macroscopic surface tension, it should also be noted that Figure 6 shows that the shift towards larger particles for the surfactant data occurs in the order which would be expected. As shown in Figure 1, 5 wppm of Tergitol NP-9 produces a lower surface tension than Witconate-90. Thus, it would be expected that Tergitol NP-9 would result in a more significant shift towards larger particles. Although particle size distribution analyses were not performed for the 10 and 50 wppm experiments, Figure 6 shows that this is the case for the 5 wppm experiments. Statistical analysis of the resulting participating melt fraction, however, indicated that the difference between the surfactants was not significant. This would also indicate that there is no significant difference in the mitigating effects of the ionic and non-ionic surfactants used.

Due to the very limited database regarding effects of surfactants and surface tension on vapor explosions, the results of the present investigation can only be compared to the recent work of Becker (1991), who concluded that surfactants mitigate and suppress steam explosions. In general, the results of the present investigation are in agreement with Becker's results for coolant at approximately 20°C with surfactant concentrations in the range of 0-10 wppm. The present investigation produced no evidence to confirm that surfactants can completely suppress steam explosions, as was indicated by Becker. When Becker observed complete suppression of the

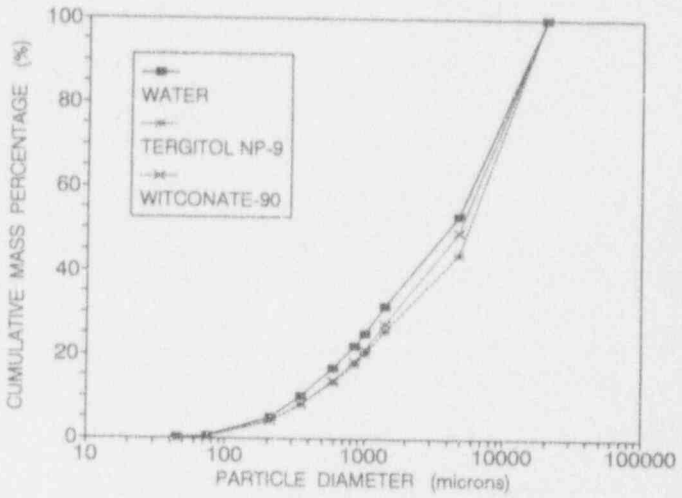

Figure 6: Averaged Cumulative Mass Percentages of Explosion Debris Sorted by Size for Experiments in Pure Water and in 5 wppm Surfactant Solutions

spontaneous explosions, however, the coolant temperature was higher (50°C). Higher coolant temperature by itself is known to mitigate steam explosions, and this additional factor may explain why the surfactant additives were able to completely suppress interactions in some of Becker's experiments.

Our results for the higher surfactant concentrations (above the critical micelle concentration, the concentration above which surface tension is no longer reduced) indicate that Becker's hypothesis that this concentration is a critical point above which the explosions will be stronger may be incorrect. Based on a few experiments carried out at 1000 wppm (far above the critical micelle concentration), Becker (1991) observed more violent explosions, and hypothesized that the micelles were the cause. In the present investigation, the experiments performed at 50 wppm were above the critical micelle concentration (see Figure 1) but did not result in significantly different average peak pressures compared to those from solutions with 5 and 10 wppm.

The particle size distribution analysis performed by Becker also supports our conclusion that comparing individual experiments does not provide any conclusive

Table 2: Averaged Cumulative Mass Percentage Data and Standard Deviations

PARTICLE SIZE	AVERAGE CUMULATIVE MASS (%)					
	WATER		NPGE (5 wppm)		WITCO-90 (5 wppm)	
(microns)	AVG	STND DEV	AVG	STND DEV	AVG	STND DEV
45 or less	0.122	0.096	0.101	0.069	0.119	0.106
75 or less	0.384	0.188	0.357	0.171	0.342	0.124
212 or less	4.973	1.619	4.094	2.086	4.120	1.423
354 or less	10.069	3.239	8.140	4.147	8.244	2.781
595 or less	16.782	5.272	13.508	6.984	13.787	4.367
841 or less	22.039	6.718	17.705	8.928	18.276	5.611
1000 or less	24.980	7.590	20.159	10.105	21.099	6.397
1410 or less	31.556	9.489	25.710	12.545	27.235	8.275
4760 or less	52.998	13.304	43.857	17.615	49.076	11.545
20000 or less	100.000	0.000	100.000	0.000	100.000	0.000

information regarding explosion severity. Only three experiments carried out by Becker could be compared: 0, 5, and 10 wppm concentrations of ethoxilated nonyle phenole solution at 40°C. Particle size analysis of these three experiments indicated that the strongest explosion was obtained at 5 wppm, and the weakest explosion at 0 wppm. This is not consistent with the general trend of his results at the other coolant temperatures tested, and also reinforces the need to perform many controlled experiments at identical conditions, and statistically compare their results.

Based on the results of this investigation, some insight into the effects of coolant surface tension versus viscosity can be advanced. In general, both parameters have been reported to mitigate vapor explosions. Total suppression of vapor explosions using viscous coolants at room temperature has also been reported by a number of experimenters (see Ip et al., 1992). Total suppression of vapor explosions by reducing coolant surface tension has only been reported by Becker (1991) at higher coolant temperatures. On the other hand, in solutions only slightly more viscous than water (and with negligible reduction of surface tension), Ip et al. observed peak pressures much larger than any recorded in pure water. In the present experiment, even the most dilute surfactant solutions (5 wppm) had the same effect as solutions with more surfactant, and Becker reports experiments with 1 wppm solutions which imply that there is no unexpected behavior at lower concentrations. The viscosities of the surfactant solutions were identical to that of pure water when measured with a Ubbelohde capillary viscometer.

Based on the results of this investigation, it is concluded that dilute solutions of surface active agents (surfactants) do have a mitigating effect on vapor explosions; however, no positive conclusions can be made regarding their ability to completely suppress explosions. Regarding the use of surfactants for practical application, at the present time, insufficient data exists regarding the effects of surface tension to propose any firm recommendations. The results indicate that surfactants may have potential for application in the nuclear industry, but due to the very limited database, must be investigated further.

V. RECOMMENDATIONS

The results of the present investigation indicate that surface active agents (surfactants) have a mitigating effect on vapor explosions. However, prior to recommending their use in applications such as severe nuclear accidents, it is recommended that additional investigations be performed under both small and large scale conditions, and over a wide range of surfactant concentrations. In conjunction with the surfactant additives, parameters such as ambient pressure, coolant solution temperature, melt mass, melt temperature, and melt/coolant mass ratios should be varied to determine their effects. Additionally, various ionic and non-ionic surfactants should be investigated. When considering the application of surfactants in severe nuclear accidents, all of these parameters are of significant importance.

For future experiments, it is recommended that efforts be taken to better control melt geometry. For this, single drop experiments can be performed, or metals with higher surface tension than tin can be used. High speed filming of the dropping melt and subsequent vapor explosions should also be performed. This would allow more consistent comparisons to be made, and would also provide a better understanding of the results obtained.

Based on the very limited knowledge of the effects of surfactants and reduced coolant surface tension on vapor explosions, investigation of any of the previously mentioned parameters would provide a significant contribution towards determining the practicality of utilizing surfactants to mitigate or suppress steam explosions during a severe nuclear accident.

REFERENCES

1. Allen T., *Particle Size Measurement*, Chapman and Hall, 1990.

2. Becker K. M., Engström, J. and MacBeth R. V., "Enhancement of Core Debris Coolability," KTH-NEL-51, Royal Institute of Technology, Stockholm, Sweden, May, 1990.

3. Becker K. M. and Lindland K. P., "The Effects of Surfactants on Hydrodynamic Fragmentation and Steam Explosions," KTH-NEL-50, Royal Institute of Technology, Stockholm, Sweden, May, 1991.

4. Cary P.E., Magnus E.O., and Herring W.E., "A New Quenchant for Steel," *Metal Progress*, March, 1958.

5. Conover W. J., *Practical Nonparametric Statistics*, John Wiley & Sons, Inc., 1971.

6. Dullforce T. A., Buchanan D. J. and Peckover R. S., "Self Triggering of Small-Scale Fuel-Coolant Interactions: I. Experiments," *J. Phys. D: Appl. Phys.*, **9**, 1295, 1976.

7. Farawila Y. M. and Abdel-Khalik S. I., "On the Calculation of Steam Explosion Conversion Ratios From Experimental Data," *Nuclear Science and Engineering*, **104**, 288-295, 1990.

8. Groenveld P., "Explosive Vapor Formation," *Transactions of the ASME, Journal of Heat Transfer*, 236, May 1972.

9. Ip B. M., Dowling M. F. and Abdel-Khalik S. I., "An Experimental Investigation of the Effects of Polymeric Additives on the Likelihood and Severity of Steam Explosions," Proceedings of the Fifth International Topical Meeting on Reactor Thermal Hydraulics, Salt Lake City, UT, September 21-24, 1992.

10. Kippenhahn C. and Tegeler D., "A Bubble Growth Experiment for the Determination of Dynamic Surface Tension," *AIChE Journal*, **16**, n.2, 314, 1970.

11. McCracken G. M., "Investigation of Explosions Produced by Dropping Liquid Metals into Aqueous Solutions," 1972 UKAEA Safety Research Bulletin of the Safety and Reliability Directorate, **11**, 20, 1973.

12. Yu H., "The Effect of Cooling Water Quality on Aluminum Ingot Casting," *Light Metals 1985*.

STEAM EXPLOSIONS OF SINGLE DROPS OF PURE AND ALLOYED MOLTEN ALUMINUM[a]

Lloyd S. Nelson
Sandia National Laboratories
Albuquerque, New Mexico 87185

ABSTRACT

Studies of steam explosion phenomena have been performed related to the hypothetical meltdown of the core and other components of aluminum alloy-fueled production reactors. Our objectives were to characterize the triggers, if any, required to initiate these explosions and to determine the energetics and chemical processes associated with these events. Three basic studies have been carried out with 1 to 10 g single drops of molten aluminum or aluminum-based alloys: untriggered experiments in which drops of melt were released into water, triggered experiments in which thermal-type steam explosions occurred, and one triggered experiment in which an ignition-type steam explosion occurred.

In untriggered experiments, spontaneous steam explosions never occurred during the free fall through water of single drops of pure Al or of the alloys studied here. Moreover, spontaneous explosions never occurred upon or during contact of the globules with several underwater surfaces. When Li was present in the alloy, H_2 was generated as a stream of bubbles as the globules fell through the water, and also as they froze on the bottom surface of the chamber.

The triggered experiments were performed with pure Al and the 6061 alloy. Bare bridgewire discharges and those focused with cylindrical reflectors produced a small first bubble that collapsed and was followed by a larger second bubble. When the bridgewire was discharged at one focus of an ellipsoidal reflector, a melt drop at the other focus triggered only very mildly in spite of a 30-fold increase in peak pressure above that of the bridgewire discharge without the reflector.

Experiments were also performed with globules of high purity Al in which the melt release temperature was progressively increased. Moderate thermal-type explosions were produced over the temperature range 1273 to 1673 K. At about 1773 K, however, one experiment produced a brilliant flash of light and bubble growth about an order of magnitude faster than normal; it destroyed the chamber. The exceptional vigor of this latter interaction was attributed to ignition of the metallic Al.

In both the triggered steam explosions with drops of high purity Al and untriggered experiments with drops of Al-Li, only a few tens of cm^3 of hydrogen per gram of metal were generated; the extent of metal-water reaction was only a few percent at most.

The information obtained from these studies with triggered and untriggered drops of molten aluminum-based alloys can be used directly in certain safety studies where hypothetical core or component meltdown occurs in a production reactor. Moreover, this information is consistent with recent advances in the understanding of single-drop steam explosion triggering and concepts of the development of larger scale steam explosions.

INTRODUCTION

The contact of aluminum-based melts with liquid water has been shown to be explosive in many experiments performed by the aluminum industry (Long, 1957; Hess and Brondyke, 1969; Nelson et al., 1988) and in several nuclear reactor-related experiments and accidents including NRX, SL-1, SPERT, etc. (Cronenberg and Benz, 1980) and recent field-scale experiments performed at Sandia National Laboratories (Rightley et al., 1993). In order to obtain quantitative information relating to the fuel-coolant interactions that might occur with aluminum-alloy fuel, a laboratory-scale experimental

[a]This work was supported by the Westinghouse Savannah River Company, Aiken, S. C., and was performed at Sandia National Laboratories, which is operated for the U.S. Department of Energy under contract Number DE-AC04-76DP00789.

study has been performed at Sandia National Laboratories. The overall objective of this research program is to provide an understanding of the mechanism of steam explosions with the melt compositions expected in several hypothetical core meltdown accident scenarios in production reactors. Our work is part of a larger safety study performed by the Savannah River Laboratory (Hyder, 1991).

Experiments were performed with 1 to 10 g melt globules released into water contained in a chamber with transparent walls. The melts were formed from high purity Al, the 6061 alloy (1.0 Mg, 0.6 Si, 0.25 Cu, 0.25 Cr), the 2090 alloy (2.25 Li, 2.74 Cu) and the "B" alloy, (3.1 Li) (all weight percent, balance Al). When desired, triggering was accomplished by introducing pressure and flow transients into the aqueous phase by the discharge of a capacitor through a submerged exploding bridgewire.

Spontaneous steam explosions never occurred without triggering transients during the free fall through water of single drops of pure Al or the alloys studied here. Moreover, spontaneous explosions never occurred upon or during contact of the globules with underwater aluminum, stainless steel, graphite or polymeric (polymethylmethacrylate or polycarbonate) surfaces.

Various triggering transients with peak pressures up to about 50 MPa produced mostly moderate thermal-type steam explosions with total bubble volumes <1 L. One experiment with a drop of pure Al at a high melt temperature, however, generated a flash of light and a huge bubble (>15 L) that destroyed the chamber. This vigorous interaction was attributed to an ignition-type steam explosion in which a portion of the Al burned.

Only small amounts of hydrogen were generated here, even from the Al-Li alloys (untriggered only). However, because of the apparatus damage, hydrogen could not be measured in the ignition-type steam explosion.

With proper theoretical interpretation, the information obtained from these studies with triggered and untriggered drops of molten Al and Al-based alloys can be used directly in certain safety studies where hypothetical core or component meltdown occurs in a nonpower reactor. Moreover, this information is consistent with recent advances in the understanding of single-drop steam explosion triggering and concepts of the development of larger scale steam explosions.

EXPERIMENTAL

Experiments were performed with 1 to 10 g melt globules released from either a tilting furnace (Al-Li alloys) or a resistance- or RF-heated bottom-drain crucible. Melt temperatures in the range 1000 to 1800 K could be achieved. Melting was performed under argon to minimize oxidation. The melt globules were released into deionized water contained in a 30 cm x 60 cm x 30 cm-deep chamber with transparent, 12.7 mm-thick Lexan walls. At various stages of the experiments, the bottom surface of the chamber was left unprotected or covered with plates of polymethylmethacrylate, graphite, Type 1100 aluminum or Type 316L stainless steel to protect against pyrolysis by the globules of hot melt. The melts were formed from high purity Al, the 6061 alloy (1.0 Mg, 0.6 Si, 0.25 Cu, 0.25 Cr), the 2090 alloy (2.25 Li, 2.74 Cu), and the "B" alloy, (3.1 Li) (all weight percent, balance Al). Diagnostics included high-speed photography (Hycam, 16-mm, 4000 fps), video imaging (VHS), collection of debris and analysis by sieving, X-ray diffraction or photomicrography, and estimation of gaseous H_2 by bubble analyses and a volumetric/mass spectrometric technique.

Further experimental details may be found in Nelson et al. (1992a, b, c).

Selected frames from the 16-mm films were analyzed with an automatic digitizing video analysis system. This system operated with hand-tracings from projected individual Hycam frames. Because the images were essentially circular, bubble volumes were estimated by assuming the images could be represented as the sum of many right circular cylindrical slices at all positions along the vertical axis of the bubble.

Triggering was accomplished by introducing pressure and flow transients into the aqueous phase by the discharge of a capacitor (7 to 63 μF at 3kV) through a submerged exploding bridgewire. The transients were produced either with a bare bridgewire in the water or by surrounding it with an ellipsoidal (see diagram in Figure 1) or cylindrical (the bridgewire was mounted through a hole centered in a standard 5.1 cm I.D. galvanized pipe cap threaded onto a 10 cm-long 5.1 cm I.D. galvanized pipe nipple; the axis of the resulting capped cylinder was placed horizontally in the water with the open end pointed toward the falling drop) reflector. By careful release into the water, the drop was caused to fall through the outer focus of the ellipsoid, at a given location across

the centerline of the cylinder or at predetermined distances from the bare exploding bridgewire to control the intensity and shape of the shock wave applied. The bare bridgewire produced about 2 μs-wide transients at the drop with peak pressures of 2-3 MPa or 1-2 MPa when the discharges occurred at 57 or 103 mm from the drop, respectively. When the ellipsoidal reflector was in place, the peak pressure was 30-60 MPa at the drop, with similar durations (see Nelson et al., 1992d). The transients produced with the cylindrical reflector were complex, with lower peak pressures and much longer times. A photodetector initiated the discharge as the melt globule fell past the desired triggering location in the water.

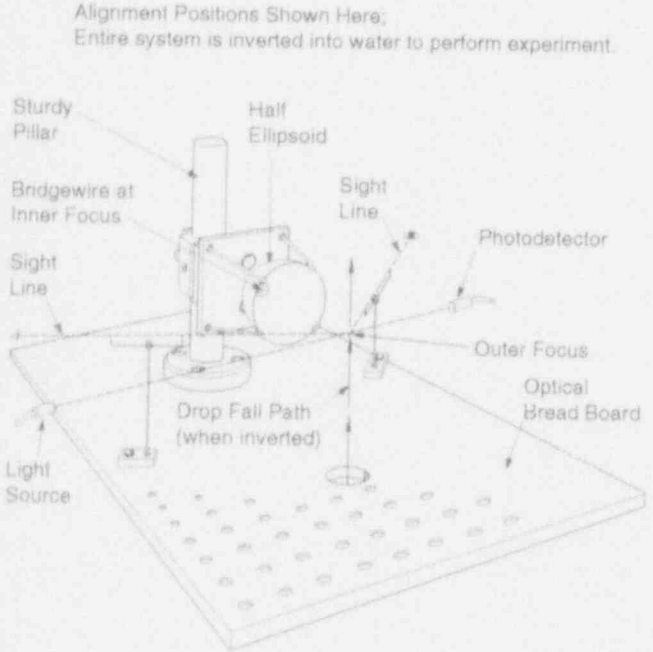

Figure 1. Schematic diagram of the ellipsoidal reflector mounted on the optical breadboard. The bridgewire is indicated at the center of the ellipsoid. The sight lines and the light source-photodetector beam are indicated schematically. Also, the upward pointing arrows indicate the path the melt drop will take when the unit is inverted over the water chamber.

An enclosed water chamber of similar dimensions (30 cm x 60 cm x 30 cm) was used to measure the generation of hydrogen with Al-Li alloy drops. It had a high speed gate valve at the top to admit the melt globule and provision to collect and analyze the cover gas quantitatively. A diagram of the apparatus is shown in Figure 2. (See Nelson et al., 1992c for more information.)

All experiments were performed at the local atmospheric pressure of 0.083-0.085 MPa. The water was always at room temperature, 293 to 298 K.

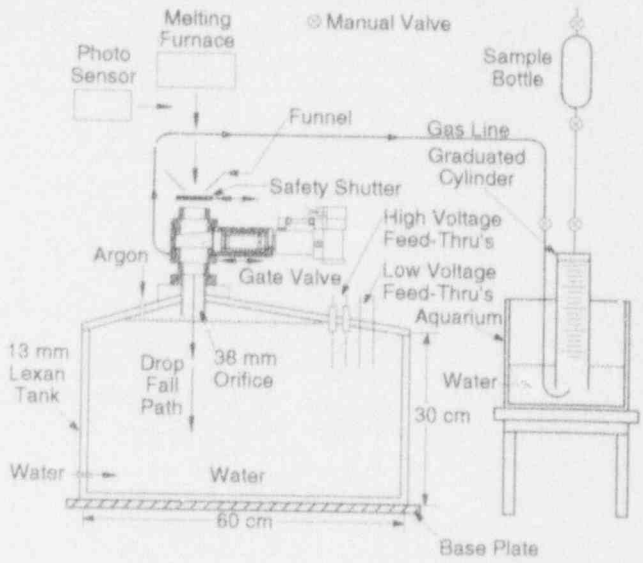

Figure 2. Schematic diagram of the system for collecting hydrogen generated during the interactions of molten globules of Al-Li alloy with liquid water.

RESULTS

Untriggered Experiments

The video and Hycam images recorded during these experiments showed the complete path of the molten metal globule as it fell through the water and after it contacted and eventually froze on the bottom surface of the chamber.

No bubbles were released from the globules of pure aluminum or the 6061 alloy, either during fall through the water or after contact with the bottom surface.

When a molten globule of either the 2090 or the "B" alloy was released into water, however, a stream of bubbles evolved as the melt passed downward through the water; each bubble rose separately and eventually burst through the water surface. The evolution of bubbles from both alloys continued after the melt globule struck either the stainless steel or the aluminum sheets placed in the bottom of the water chamber. The bubble formation decreased gradually as the melt globule cooled at the bottom of the chamber, eventually turning into a gentle effervescence of very fine bubbles that persisted many seconds after the globule had solidified.

A major objective of this work was to look for spontaneous steam explosions. In the absence of pressure and flow transient triggers, such explosions have never been observed in the laboratory during

free fall through room temperature water of single 1 to 10 g drops of pure Al or the 6011 alloy (Nelson et al., 1989, 1992a, b) or of the two Al-Li alloys studied (2090 and "B"). They have not occurred at the melt temperatures studied—1273 to 1773 K for pure Al and the 6061 alloy, 1273 K for the 2090 alloy and 973 to 1273 K for the "B" alloy. Nor have they occurred during or after contact of the pure Al or Al-Li globules with submerged aluminum or stainless steel surfaces. (The failure of drops of molten aluminum and its alloys to explode spontaneously should be compared to the behavior of drops of molten tin. Drops of this metal explode readily without triggering in the same melt and water temperature ranges studied here, e.g., T_{melt} = 1273 K, T_{H_2O} = 298 K [Dullforce et al., 1976].)

Triggered Experiments

Effect of Trigger Transient Characteristics. The triggered explosions of molten aluminum drops produced several cyclic bubble growths and collapses during 10 or 15 ms after application of the triggering transient. Typical bubble volume-time plots, produced from the Hycam films with the automatic video digitizing system, are shown in Figure 3. Each interaction produced a small (approximately 10^2 cm^3) first bubble that collapsed within 5 to 8 ms. After collapse, each of these bubbles was followed by growth of a second bubble that produced a combined volume that never exceeded approximately 1 L.

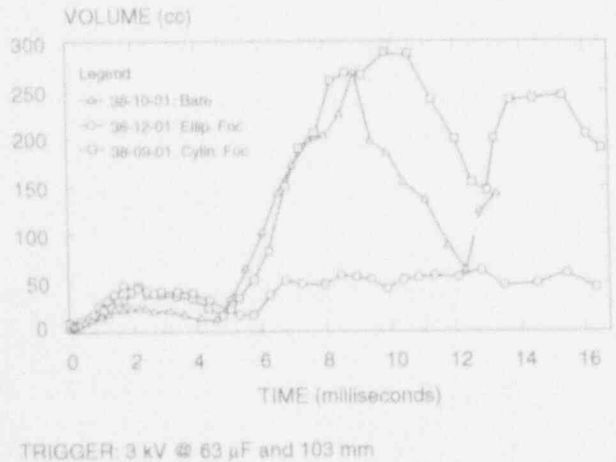

Figure 3. Steam explosion bubble volumes versus time for pure aluminum drops triggered with three different configurations: a bare (unfocused shock wave) bridgewire; a bridgewire placed at the inner focus of an ellipsoidal reflector; and a bridgewire placed in a cylindrical reflector.

Repetitive bubble formation-contraction cycles such as these have been observed in previous studies of single drop explosions (Nelson and Duda, 1982a,b). With flash X-ray and high speed photographic imaging, Ciccarelli (1991) has recently analyzed the first and second bubbles produced by similarly triggered explosions of drops of molten tin and a low melting alloy. His observations will be discussed below in greater detail.

The three plots in Figure 3 were generated with molten aluminum drops initiated by discharging a capacitor (63 µF at 3 kV) through identical bridgewires placed horizontally 103 mm away from the drop. The bridgewire was discharged "bare" in the water (triangles), inside the capped end of a 5.1 cm I.D. x 10 cm long pipe (squares), and at the inner focus of the ellipsoidal reflector shown in Figure 1 (the drop was at the outer focus at triggering time) (circles). From the plots presented in Figure 3, it can be seen that at a given distance from the exploding bridgewire and at a given discharge energy, the cylindrical reflector produced the most vigorous explosion while the unfocused shock wave produced the next most vigorous explosion; surprisingly, however, the ellipsoidal reflector produced only a very mild interaction, even though the peak pressure produced at the drop (approximately 30 MPa [Nelson et al., 1992d]) was an order of magnitude greater than that produced by the unfocused discharge or the discharge in the pipe (approximately 2 MPa).

When the bare bridgewire discharge was moved closer to the drop (to 57 mm), the explosion became more vigorous, as shown in Figure 4.

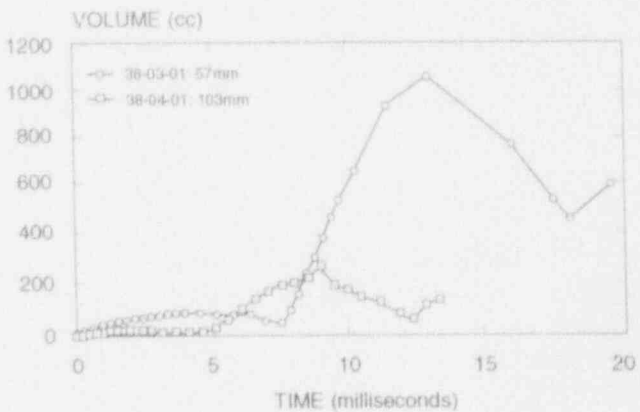

Figure 4. Steam explosion bubble volume versus time for pure aluminum drops at two different triggering distances.

Effect of Alloying. An effect of melt composition was observed when experiments with pure aluminum drops were compared with drops of the 6061 aluminum alloy. The pure aluminum drops exploded more vigorously than did the 6061 alloy drops when exposed to identical moderate triggering conditions with (7 μF at 3 kV) unfocused shock waves. This is shown in Figure 5. However, when the trigger strength was increased (to 63 μF at 3 kV), the explosive vigor of both the pure aluminum and the 6061 alloy was about the same. Thus it appears that the presence of a few weight percent of alloying materials may cause significant differences in the initiation threshold of single drops of molten aluminum.

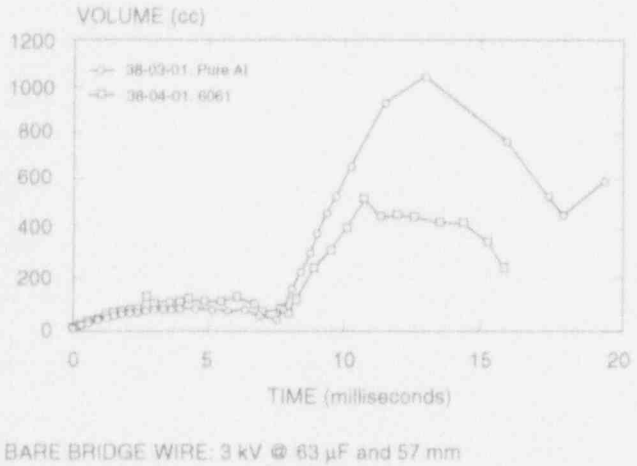

Figure 5. Steam explosion bubble volumes versus time for drops of pure aluminum and the 6061 alloy. Triggering conditions were the same in both experiments.

Effect of Melt Temperature. In another sequence of experiments, melt temperature was increased in 100 K steps from 1273 K to nominally 1773 K. Water temperature was nominally 298 K. Melt mass of pure aluminum was in the range 2 to 10 g. In all but one of over 30 successful experiments in this sequence, we observed only moderate explosions with small first bubbles followed by maximum second bubbles with total volumes ≤1 L. A typical volume-time plot for these interactions is shown in the lower curve in Figure 6. We regard these as thermal-type interactions similar to those shown in Figures 3, 4, and 5. However, in one experiment performed with approximately 10 g of melt at nominally 1773 K, the interaction became extremely vigorous, accompanied initially by a brilliant 1 ms-long flash of light. A huge bubble formed over the next 4 ms, larger in some dimensions than the 30 cm by 60 cm by 30 cm-deep water chamber. The bubble grew rapidly to 14 L before it broke the water surface. The 12.7 mm-thick Lexan walls of the water chamber were cracked or torn apart in several places by the explosive force of the interaction, causing uncontrolled flooding in which some of the debris, probably the finer particles, was lost. The volume-time relationship for this bubble until the chamber failed is shown as the upper curve in Figure 6. We regard this as an ignition-type steam explosion.[b] Note that both plots in Figure 6 indicate similar growth and collapse during the initial 8 ms of a small first bubble before the formation of a second larger bubble.

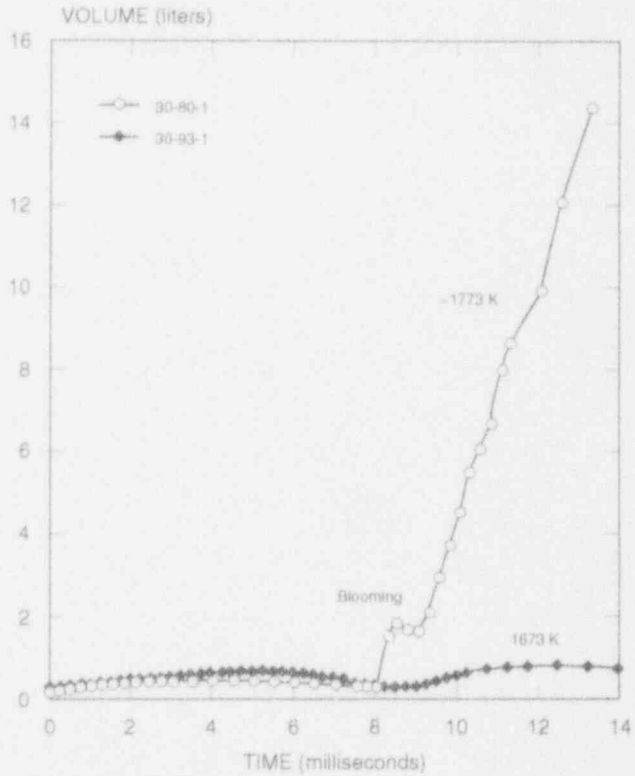

Figure 6. Comparison of the bubble volume-time relationships for the triggered ignition-type and thermal-type steam explosions of single drops of molten aluminum (30-93-1 and 30-80-1). The upper curve is for aluminum at a nominal temperature of 1773 K; the lower curve is for a nominal temperature of 1673 K. The blooming caused by the flash of light is indicated at about 8 ms.

[b]We use the term "ignition-type steam explosion" in a broad sense to indicate that the usual thermal processes are accompanied by metal combustion. In the more detailed view of the single drop explosions, it might be preferable to use the term "steam explosion-driven ignition."

In the debris recovered from the ignition-type steam explosion, there was no visually observable aluminum oxide present, and only trace amounts detectable by X-ray diffraction. Moreover, there were no apparent differences either in the metallic appearance or particle size distributions between debris recovered from the ignition-type and from comparable thermal-type steam explosions.

We have compared the growth of the second bubble in the ignition-type aluminum-water explosion with comparable bubbles produced by underwater explosion (Beck, 1989) of two commercially available high explosive (HE) exploding bridgewire detonators that contain 60 and 606 mg of PETN/RDX, Types RP-1 and RP-2, respectively. The volume-time plots for the three bubbles are shown in Figure 7 (the time scale is reset to zero at the flash of light for the aluminum bubble). Note that the explosions of the nominally 10 g of molten aluminum and 606 mg of HE produce similar bubble growth rates.

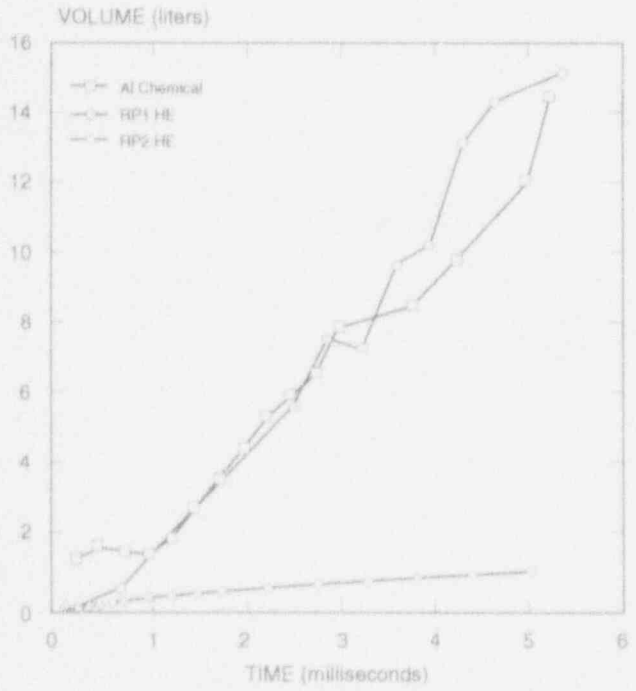

Figure 7. Comparison of bubble volumes versus time produced by an ignition-type steam explosion of a drop of molten pure aluminum (30-80-1) and exploding bridgewire detonators Types RP-1 and RP-2. The release temperature of the molten aluminum was nominally 1773 K.

We believe ours to be the first clear photographic observation of an ignition-type steam explosion of molten aluminum in the laboratory. The ignition of aluminum drops underwater has been photographed before, e.g., Tao et al. (1989), but never, to our knowledge, when initiated by a steam explosion. Moreover, this experiment shows many similarities to extremely energetic explosions with flashes of light observed with 10^1 to 10^2 kg of molten aluminum in field-scale experiments (Hess and Brondyke, 1969; Lemmon, 1980; Rightley et al., 1993).

(For further information about experiment 30-80-1, see Nelson et al., 1991, 1992b.)

Hydrogen Generation

Pure Aluminum. We explored the possibility that metal/water reactions had occurred during thermal-type steam explosions with molten pure aluminum drops. By examining our Hycam films carefully at late times, we discovered a single bubble that remained long after the steam explosion bubble had collapsed and disappeared. This appeared to be a bubble of permanent gas, presumably hydrogen. By measuring this bubble we were able to place approximate upper and lower bounds on the extent of metal/water reaction in thermal-type laboratory explosions.

We measured two such bubbles, one from an interaction in which the molten aluminum release temperature was 1243 K, and the other in which the melt release temperature was approximately 200 K higher, namely, 1468 K. The volumes of these bubbles were estimated to be 80 and 267 cm^3, respectively.

If we assume the bubbles contained only hydrogen, we can estimate both the total amount of hydrogen and the amount produced per gram of aluminum participating in the interaction if we can assume a temperature for the gas. Upper and lower limits can be placed on the temperature of the gas within the bubble, namely, the release temperature of the melt (assumes negligible heating from combustion) and the temperature of the water. The corresponding limiting values of the extent of metal/water reaction are compared for the two experiments in Table 1. These values are based on the assumption that the aluminum in the debris was not oxidized. Note that the estimated maximum extents of metal/water reaction are less than 1 percent for the 1243 K aluminum and less than 4 percent for the 1468 K aluminum melts. (Recent model oxidation predictions showed good agreement with the results of these experiments [Young and Nelson, 1991].)

The extent of aluminum/water reaction in the ignition-type explosion could not be estimated in this manner because of the early failure of the water chamber.

(Better estimates of gas temperatures in the bubbles, based on chemical heating of the gas seem unlikely because of the very small extent of the metal/water reactions.)

Table 1. Metal-Water Reaction for Steam Explosions of Pure Aluminum Drops Determined From Hycam Bubble Images

Experiment No.	38-3-1	38-6-1
T_{melt} (K)	1243	1468
V_{H_2}*(cm^3)	80	267
Debris Weight (g)	6.54	4.50
$\frac{V_{H_2}^*}{Al}\left[\frac{cm^3}{g}\right]$	12.3[a]	59.4[a]
Extent of Al-H_2O Reaction (%)	0.8[b] 0.2[c]	3.8[b] 0.8[c]

*Volume at local atmospheric pressure of 0.085 MPa
[a]Assumes aluminum is not oxidized
[b]Assumes H_2 is at T_{H_2O} (298 K)
[c]Assumes H_2 is at T_{melt}

Aluminum-Lithium Alloy

One goal of this program was to measure the hydrogen generated by the reaction between drops of molten Al-Li alloys and water. The experiments were performed without triggers applied to the water in order to investigate whether spontaneous initiation of steam explosions occurred with these alloys as discussed above. The drop sizes and melt temperatures were chosen to simulate globules that might form during hypothesized melting of certain Al-Li alloy components of aluminum alloy-fueled production reactors. We released into liquid water 1 to 10 g drops of "B" alloy (3.1 w/o Li, balance Al). Melt temperatures were in the range of 973 to 1273 K; water temperatures were in the range of 293 to 298 K.

A stream of hydrogen-containing bubbles was generated as each melt drop fell freely through the water and froze in contact with the bottom surface of the water chamber. (Streams of bubbles were never observed when drops of pure aluminum were released into water under essentially identical conditions. This is taken to indicate that the bubbling observed here is overwhelmingly caused by the presence of lithium in the melt and only slightly [if at all] by the persistence of steam generated by the hot globule.) The fast shuttering hydrogen-measuring apparatus shown in Figure 2 was used for studying the reaction between liquid water and single drops of molten aluminum-lithium alloy. Hydrogen generated during the interactions at several melt temperatures was collected quantitatively and measured by combining volumetric and mass spectrometric information; the results are presented in Figure 8. This figure shows total volume of hydrogen (STP) increased from about 2 to 9 cm^3/g of melt as initial melt temperature increased from 973 and 1273 K. There were no signs of runaway temperature increases as in the ignition-type interaction, however, even though the formation of hydrogen indicated that some underwater "combustion" had been occurring.

The amounts of hydrogen shown in Figure 8 indicate that the extent of the metal-water reaction for the untriggered "B" alloy drops was always relatively small (the measured H_2 corresponded to an extent of reaction of at most 0.7 percent, if both the Al and Li in the alloy are assumed to react). (We have no information about the effect a triggered steam explosion might have on the amount of hydrogen generated from Al-Li melts.)

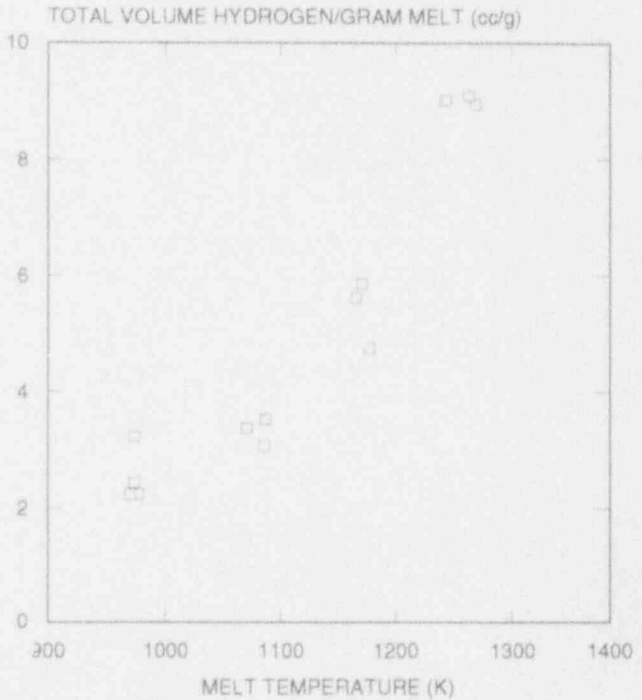

Figure 8. Total volume of hydrogen at STP generated from approximately 5 g globules of aluminum-3.1 w/o lithium ("B") alloy released into water as a function of melt temperature. Analyses were performed by a combined volumetric/mass spectrometric technique.

DISCUSSION

Comparisons with the McGill Drop Triggering Studies

The experiments recently described by Ciccarelli (1991) of McGill University provide significant insight into the behavior of the single drops of molten aluminum studied here. Ciccarelli studied hot drops (973 K) of molten tin and of a molten low temperature alloy (Cerrolow) released into water at 312 K. His drops were triggered with capacitor discharges through underwater bridgewires similar to ours; he used a variety of discharge energies that produced peak pressure transients between about 1 and 20 MPa at the drops. Ciccarelli compared high speed photographs of the drop explosions with simultaneously recorded flash X-ray images. He reported cyclic bubble growth and collapse patterns similar to ours shown in Figures 3 through 6 (without ignition).

Ciccarelli analyzed the small first bubble followed by the larger second bubble in the first two cycles. He concluded that the small first bubble was primarily a thermal event that produced fingers of melt extending radially outward from the drop. These were caused by Rayleigh-Taylor instabilities produced during the rapid generation and outward flow of steam from the melt surface. After the modest first bubble collapsed, it then reinflated due to heat transfer from the drastically fragmented melt fingers produced during growth of the first bubble. The second bubble was larger than the first, due to the greater amount of heat transferred from the particles that had greater total surface area than the fingers produced during the first bubble inflation cycle.

He also showed that a triggering shock wave was needed to produce the initial contact between the melt globule and the liquid water which initiates the thermal growth of melt fingers. Ciccarelli also showed that for his initial conditions, the peak pressure of the shock wave generated by the triggering source was not an important parameter once it exceeded about 2 MPa at the drop (at least up to approximately 20 MPa; see Ciccarelli's Figure 29).

Ciccarelli also studied the effect of increasing the water flow across the drop during the triggering event. This was accomplished by firing his triggering source (bridgewire or, to produce extreme values, a blasting cap) at the bottom of a capped water-filled pipe. The source was initiated when the melt drop passed a predetermined point above the pipe. He learned that at water flows greater than about 50 m/s, than the inflation of the second bubble could be strongly altered. The high water flow tended to strip the melt fingers from the parent drop during the first bubble inflation and essentially "blow away" the bubble before the collapse could occur. We never achieved water flows in this regime, however; instead, with our triggers, we always produced flows in the range of a few meters per second rather than his several tens of meters per second.

If, indeed, our aluminum drops behave similarly to Ciccarelli's tin and Cerrolow drops (our drops were exposed to flow conditions with Weber numbers of about the same magnitude as Ciccarelli's slower flows), then we can speculate about what is occuring during the triggering and bubble growth phases. Ciccarelli's observations strongly suggest that our aluminum drops also produce the Rayleigh-Taylor fingers during the growth and collapse of the first small bubble. The resulting porcupine-like configuration then apparently is strongly fragmented during the first collapse and likewise presents both higher surface area and fresh unoxidized surfaces at the start of the second inflation.

We speculate that the differences observed in our work for triggering of the pure aluminum and the 6061 aluminum alloy (see Figure 5) may be related to changes in the surface properties caused by the alloying. Thus the formation of the Rayleigh-Taylor instabilities may be sensitive to changes in melt surface tension and wettability produced by small amounts of alloying components. Also, the finger formation and breakup may be strongly affected by alloy composition via the rates and structure of the oxide skin growth that accompany the increased surface area of the drop (cf. Kahl and Fromm, 1985) and by the possible changes in heat transfer related to the nature of these skins (cf. Moreaux et al., 1975). However, when the triggering level was increased, we were able to obtain essentially similar explosive behavior and override the alteration in the finger formation caused by the changes in surface properties.

We may also speculate that the increase in the vigor of the interaction when the bridgewire-to-drop distance was decreased from 103 to 57 mm (see Figure 4) was caused by exceeding the threshold shock wave peak pressure needed to adequately initiate the initial thermal interaction and the first bubble growth. Our triggering peak pressures at these distances essentially straddle the threshold indicated by Ciccarelli (1991) (his figure 29).

It is important to note that our single ignition-type experiment performed with pure aluminum at high melt temperatures (nominally 1773 K) apparently underwent the same initial small bubble growth, accompanied by Rayleigh-Taylor fingers as in the thermal-type explosions (see Figure 6). The millisecond-long flash of light seems to have occurred just

as the bubble collapsed and produced the highly disturbed particles from breakup of the melt fingers. (A similar ignition upon bubble collapse was observed for very small drops generated by capacitor discharges through aluminum wires [Tao et al., 1989].) The nature of the transition of the hot melt particles to the ignited state is not known from observations of our films. However, it apparently involves the highly increased surface area and fresh metal surface of the melt particles at the disruption of the fingers. It is interesting to speculate what might happen if high velocity triggering conditions similar to Ciccarelli's were applied to a molten aluminum drop at high temperature.

It is necessary to point out that triggering conditions were somewhat different in the tin and Cerrolow experiments performed by Ciccarelli and in our aluminum drop experiments. First, our melt drops were larger than Ciccarelli's namely 1 to 10 g of Al compared to his 0.5 g drops. This caused our first bubbles to be larger and to collapse later. But more importantly, Ciccarelli had to increase his water temperature to 312 K to prevent spontaneous triggering of the tin drops (compare with the temperature interaction zone of Dullforce et al., [1976]), whereas our Al drops never triggered spontaneously even at the much colder water temperature of 298 K. Using the larger Al drops in our experiments primarily seemed to increase the time scale of the interactions, namely to increase Ciccarelli's approximately 1 ms to 5 to 8 ms times for our first bubbles to collapse. The effects of increasing the time scale and bubble volume of the initial thermal event are not known at the time.

Focused Versus Unfocused Shock Waves

As these studies began, conventional wisdom was that the significant parameter governing triggering of single drops of a molten material was the maximum pressure of the shock wave produced by the triggering source. Thus when we began to examine the effects of placing our underwater bridgewater discharge within an ellipsoidal reflector, we expected significantly increased triggering effects. With this relatively simple modification of our triggering device, we were able to produce peak pressures at least an order of magnitude greater than the 2 or 3 MPa transients produced by the unfocused discharges, namely, on the order of 30 to 60 MPa (Nelson et al., 1992d). We learned rapidly, however, that the apparent increase in peak pressure did not offer a significant increase in the triggering capability of the discharge (see Figure 3). Instead, it seemed that triggering with the focused shock wave was less effective than with the bare bridgewire placed at the same distance without the reflector. (Similar decreased triggering effectiveness of focused shockwaves has also been observed for thermite drops [Nelson et al., 1992d].)

It is now known, however, that apparently the peak pressure of the initiating shock wave is not an important parameter in determining the nature of the steam explosion of a single drop. Thus Ciccarelli varied his shock wave pressure at the drop over an order of magnitude (2 to 20 MPa) and found little change in the growth of the first small bubble. Apparently, the thermal interaction requires only a minimal shock wave to start the interaction, but then is essentially independent of the magnitude after it passes the threshold (at least over the range 2 to 20 MPa).

This statement does not explain, however, the actual reduction in the second and subsequent bubble growth shown in Figure 3 when the focusing reflector is placed around the bridgewire.

The reason for the differences between triggering with focused and unfocused shock waves may be related to the hypothesis advanced by Beck (1989) and summarized in Figure 9. This hypothesis suggests that the triggering of a single drop is caused by the diffraction of the planar shock wave around the drop, focusing in the wake at the opposite side of a drop. Thus the boiling film is induced to move toward the drop and impact it from both sides to achieve efficient triggering. When the focused shock wave is used, however, the diffracting wave cannot form and focus at the other side of the drop. Thus film collapse occurs only at a localized portion of the drop's surface and triggering becomes less efficient.

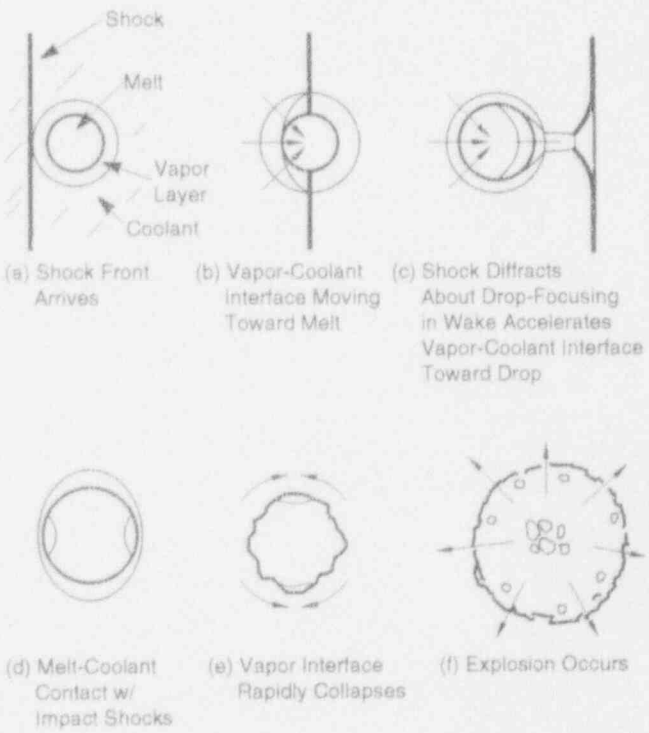

Figure 9. Illustration of possible prompt explosion trigger mechanism for single drops of melt dispersed in water. This mechanism is due to Beck (1989).

Mass of Al Involved in the Ignition-Type Steam Explosion

This section summarizes and offers additional thoughts on our laboratory experiment 30-8-1 in which a clear photographic image of an ignition-type steam explosion of molten aluminum was recorded. This experiment has been described above and by Nelson et al., (1991, 1992b). The discussion in this section is based on the following preliminary observations (Nelson et al., unpublished results, 1992):

- Bubbles that grow with the same initial rates (i.e., same dV/dt slopes) ultimately appear to achieve the same maximum volumes. This has been demonstrated for various capacitor discharge-produced bubbles that have grown almost as large as 1 liter.

- The light-emitting combustion of aluminum in water seems to liberate bubble (pressure-volume) energies in the range of 6 to 12 J/mg. This range of values has been determined from several underwater capacitor discharges through strips of aluminum foil of known weight (up to 14 mg). (These chemical energies have been corrected for the purely electrical bubble energies by performing side experiments with similar capacitor discharges focused through fine gold or tungsten wires submerged in water where the chemical component of the bubble growth is negligible; these nonchemical bubble energies are < 20 percent of those produced when the aluminum strips are present.) Our work follows the lead of Lee (1991), who obtained about 15 J/mg with carefully tuned electrical discharge circuits. (Conventional high explosives generate about 4 J/mg [Rightley et al., 1993].)

To utilize these preliminary relationships, we note that the complete bubble from the detonator achieves a maximum volume of about 31 L in about 13 ms. If we can assume from the first observation that the maximum bubble volume for the ignition-type steam explosion also would have been 31 L, the maximum pressure-volume energy release would have been 2670 J. (We assume that during the initial bubble growth, there is no difference between condensable and noncondensable inflating gases.)

Using the second observation, that the energy release for aluminum in an underwater ignition-type event lies at the range 6 to 12 J/g, we estimate that the total amount of aluminum that participated in the ignition type steam explosion was 0.22 to 0.44 g. This is only 3 to 6 percent of the 8 g of debris recovered after the experiment and after the failure of the apparatus. If the value of 15 J/g reported by Lee (1991) is a more accurate value, then the total amount of aluminum that reacted according to this analysis would have been only 0.18 g, or about 2 percent of the 8 g.

The estimate that only a few percent of the metal participated in the ignition-type steam explosion is consistent with the virtual absence of oxidized aluminum in the debris recovered from the ignition-type steam explosion experiment. Aluminum oxide could not be observed visually and was detected only in trace amounts by X-ray diffraction. There was no appreciable difference from the debris recovered from comparable thermal-type steam explosions.

Temperature Thresholds for Ignition-Type Explosions

It is interesting to compare data obtained from the literature for the temperatures at the onset of underwater ignition of molten aluminum as a function of metal mass. Nine ignition temperature thresholds are shown as a function of metal mass in Figure 10. These data are taken from reports by Baker (1965), Hess and Brondyke (1969), Higgins and Schultz (1957), Lemmon (1980), Rengstroff et al. (1969), Rightley et al. (1993); Tao et al. (1989) and from this work.

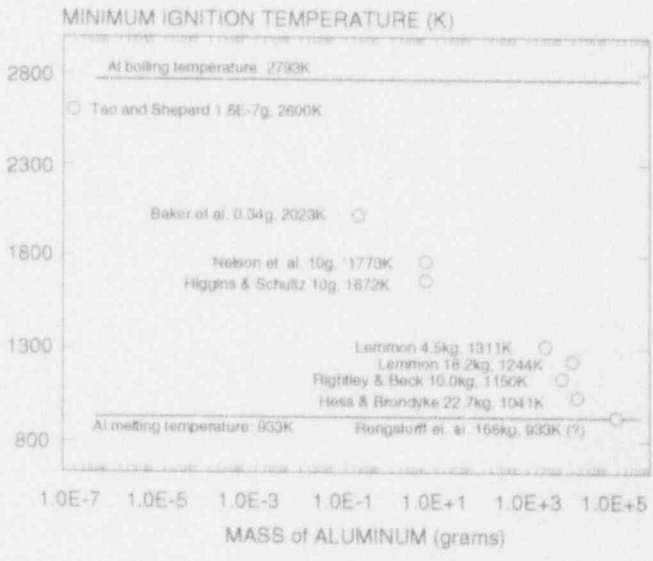

Figure 10. Plot of melt release temperatures for onset of underwater ignition of molten aluminum plotted as a function of mass of molten metal. Note the steady decrease in ignition temperature as melt mass increases.

It can be seen from this figure that as melt mass increases, the threshold ignition temperature decreases until at approximately 10^5 g (and presumably above), it approaches the melting temperature of aluminum. In addition to its impact on nuclear reactor safety, this plot may have great significance for the metal-working industries, where large quantities of molten aluminum are often handled just above the melting temperatures in close proximity to liquid water.

CONCLUSIONS

The work described here forms part of an experimental safety study related to aluminum alloy-fueled production reactors. However, the observations also should provide considerable information for the aluminum industry in which significant property damage, loss of production and personnel injury and fatalities are still caused by ignition-type steam explosions (Epstein and Miller, 1987).

The information summarized here indicates that aluminum differs from other low melting metals in that single drops fail to initiate spontaneously, compared for example to molten tin in the same water temperature and melt temperature ranges (Dullforce et al., 1976). And with one exception, all triggered interactions of aluminum drops were relatively mild and produced only small energy conversion and metal/water reactions. Even with the aluminum-lithium alloy without triggering, the generation of hydrogen was small. Unfortunately we were not able to study the aluminum-lithium alloys in a triggered mode.

Many aspects of the oxidative behavior of molten aluminum in contact with liquid water fell beyond the scope of this work, for example, the possible stabilization of the melt by the addition of small amounts of hydrogen to the film boiling layer, the changes of surface temperature when the melt contacts the water, the possible transition from diffusion flame to detonation as ignition occurs, and, above all, in experiment 30-80-1, why the ignition occurs not at the initial contact of melt with water but after the first collapse of the vapor bubble subsequent to the first thermal explosion. Clearly, further studies are required.

We feel the information presented here should have significant impact on ongoing theoretical efforts to extend the understanding of both thermal- and ignition-type steam explosions to large scale, propagating events.

ACKNOWLEDGEMENTS

I gratefully acknowledge the participation of the many collaborators involved in the work summarized here. They are named as co-authors of the three major reports covering the work here (Nelson et al., 1992a,b,c). In addition I thank M. L. Hyder of the Savannah River Laboratory and my colleagues K. D. Bergeron, M. Berman, B. W. Marhsall, Jr., K. O. Reil, and S. E. Slezak for valuable discussions and support of the concepts studied in this report.

REFERENCES

Baker, L., Jr., 1965, "Metal-Water Reactions," Nuclear Safety, 7, 25-34.

Beck, D. F., 1989, Sandia National Laboratories, Albuquerque, NM, personal communication.

Ciccarelli, G., 1991, Investigation of Vapor Explosions with Single Molten Metal Drops in Water Using Flash X-ray, Thesis, Department of Mechanical Engineering, McGill University, Montreal, Quebec, Canada.

Cronenberg, A. W., and Benz, R., 1980, "Vapor Explosion Phenomena With Respect to Nuclear Reactor Safety Assessment," in Advances in Nuclear Science and Technology, J. Lewins and M. Becker, editors, Plenum Press, New York, NY.

Dullforce, T. A., Buchanan, D. J., and Peckover, R. S., 1976, "Self-Triggering of Small-Scale Fuel-Coolant Interactions: I. Experiments," Journal of Physics D: Applied Physics, 9, 1295-1303.

Epstein, S. G., and Miller, R. E. 1987, "Causes and Prevention of Molten Aluminum-Water Explosions, "Light Metals 1987, The Metallurgical Society of AIME, Warrendale, PA, 693-698.

Hess, P. D., and Brondyde, K. J., 1969, "Cause of Molten Aluminum-Water Explosions and Their Prevention," Metal Progress, 95, 93-100.

Higgins, H. M., and Schultz, R. D., 1957, The Reaction of Metals With Water and Oxidizing Gases at High Temperatures, IDO-28000, Aerojet-General Corporation, Azusa, CA.

Hyder, M. L., 1991, "The Severe Accident Analysis Program for the Savannah River Nuclear Production Reactors," Nuclear Safety, 32, 502-510.

Kahl, W., and Fromm, E., 1985, "Examination of the Strength of Oxide Skins on Aluminum Alloy Melts," Met. Trans. B, 16B, 47-51.

Lee, W. M., 1991, "Metal/Water Chemical Reaction Coupled to a Pulsed Electrical Discharge", Journal of Applied Physics, 69, 6945-6951.

Lemmon, A. W., Jr., 1980. "Explosions of Molten Aluminum and Water," Light Metals 1980, C. J. McMinn , ed., The Metallurgical Society of AIME, Warrendale, PA, 817-836.

Long, G., 1957, "Explosions of Molten Aluminum in Water -- Cause and Prevention," Metal Progress, 71, 107-112.

Moreaux, F., Chevrier, J. C., and Beck, G., 1975, "Destabilization of Film Boiling by Means of a Thermal Resistance, " Intl. J. Multiphase Flow, 2, 183-190.

Nelson, L. S., and Duda, P. M., 1982a, Steam Explosion Experiments With Single Drops of Iron Oxide Melted With a CO_2 Laser, NUREG/CR-2295, SAND81-1346, Sandia National Laboratories, Albuquerque, NM.

Nelson, L. S., and Duda, P. M., 1982b, "Steam Explosion Experiments With Single Drops of Iron Oxide Melted With a CO_2 Laser," High Temperatures-High Pressures, 14, 259-281.

Nelson, L. S., Eatough, M. J. and Guay, K. P., 1988, "Why Does Molten Aluminum Explode at Underwater or Wet Surfaces?" in Light Metals 1989, edited by P. G. Campbell, The Minerals, Metals & Materials Society, Warrendale, PA. 951-961.

Nelson, L. S., Duda, P. M., and Hyndman, D. A., 1991, "Thermal- and Ignition-Type Steam Explosions of Single Drops of Molten Aluminum," Transactions of the American Nuclear Society, 64, 378-379.

Nelson , L. S., Fuketa, T., Eatough M. J., Vigil, F. J., and Duda, P. M., 1992a, The Triggering of Steam Explosions of Single Drops of Pure and Alloyed Molten Aluminum, SAND90-0131, Sandia National Laboratories, Albuquerque, NM.

Nelson L. S., Duda, P. M., and Hyndman, D. A., 1992b, Thermal and Ignition-Type Steam Explosions of Single Drops of Molten Aluminum, SAND91-1354, Sandia National Laboratories, Albuquerque, NM.

Nelson, L. S., Duda, P. M., and Hyndman, D. A., 1992c, Interactions Between Drops of Molten Al-Li Alloys and Liquid Water, SAND91-2191, Sandia National Laboratories, Albuquerque, NM.

Nelson, L. S., Fuketa, T., Eatough, M. J., Vigil, F. J., Szklarz, D. D., Wong, C. C., and Hyndman, D. A., 1992d, Steam Explosions of Single Drops of Thermite-Generated Melts: 25 and 50 Weight Percent Aluminum-Iron Oxide Initial Mixtures, SAND90-0511, Sandia National Laboratories, Albuquerque, NM.

Rengstroff, G. W., Lemmon, Jr., A. W., and Hoffman, A. O., 1969, Review of Knowledge on Explosions Between Molten Aluminum and Water, Battelle Memorial Institute, Columbus, OH. Report to the Aluminum Association, April 11.

Rightley, M. J., Beck, D. F., and Berman, M., 1993, NPR/FCI EXO-FITS Experiment Series Report, SAND91-1544, Sandia National Laboratories, Albuquerque, NM. In preparation.

Tao, W. C., Frank, A. M., Sheherd, J. E., and Clements, R. E., 1989, "The Fundamentals of Metal Combustion in Composite Explosives Revealed by High speed Micro Photography, "Proceeding of the Ninth (International) Symposium on Detonation, Portland, OR, August 28-September 1.

Young, M. F., and Nelson, L. S., 1991, "Oxidation of Molten Fuel Simulant Drops Under Film Boiling Conditions," paper presented at the International Topical Meeting on Safety of Thermal Reactors, Portland, OR, July 21-25, 1991. Proceedings published by the American Nuclear Society, LaGrange Park, IL, 319-323.

STUDIES ON FUEL COOLANT INTERACTIONS DURING CORE MELT ACCIDENT OF NUCLEAR POWER PLANTS

N.Yamano, J.Sugimoto, Y.Maruyama and K.Soda
Japan Atomic Energy Research Institute
Tokai-mura, Ibaraki-ken, Japan 319-11
Telephone (292) 82-5871 -- Facsimile (292) 82-5570

ABSTRACT

Two series of experiments to investigate FCIs have been performed at JAERI. In the melt drop steam explosion experiments, melt simulating the molten core was dropped into a pool of water. Spontaneous steam explosion was suppressed when the falling melt was dispersed by an artificial device or the ambient pressure was increased to 1.6 MPa. In the molten core coolability experiments, water was poured onto the melt. Melt eruption which might have led to an explosive interaction was observed when subcooled water was poured through a pipe nozzle. The eruption was not found when the water was at near saturation temperature or supplied through a spray nozzle. Heat transfer characteristics from the melt to the overlying water was evaluated. Size distribution of the debris was investigated in the both experiments.

I. INTRODUCTION

The containment of a nuclear power plant plays an important role to minimize accidental release of fission products to the environment as the last physical barrier(OECD/CSNI,1989). Therefore maintaining the containment integrity is crucial to minimize the consequence of a severe accident. It has been known that the containment integrity would be challenged in a severe accident due to thermal and mechanical loads exceeding the design limit of the containment(Soda, 1990). It is considered that one of such extreme loads may be caused by "fuel-coolant interactions (FCI)" when the molten core consisting of fuels and core component materials contacts with coolant. In particular energetic FCI which is referred as "steam explosion" is considered to be one of the threats to the containment integrity due to its destructive force (Ginsberg et al., 1985 and Theofanous et al., 1987).

In order to reduce the possibility of the loss of the containment integrity during a severe accident, various measures have been proposed to mitigate the accident consequence and those measures are called "accident management". Intentional supply of the coolant to the molten core either in the reactor vessel or in the containment is considered as one of such accident management measures to terminate the severe accident. However adding water to the molten core may generate an energetic steam explosion and cause a severe damage to the reactor vessel or the containment. Therefore experimental investigation for verification of effectiveness of water addition is needed before such accident management is adopted in the severe accident.

In order to clarify the phenomena which would threaten the containment integrity and to establish the accident management measures, ALPHA (Assessment of Loads and Performance of Containment in a Hypothetical Accident) program was initiated at JAERI(Japan Atomic Energy Research Institute) in 1990 (Soda et al., 1991). The ALPHA program consists of four test items; melt coolant interaction, molten core concrete interaction, FP aerosol behavior and penetration leak characterization. The melt coolant interaction test of the ALPHA program has been performed in order to quantify loads to the containment during FCI and evaluate coolability of the molten core (Sugimoto et al., 1992a). Two series of experiments have been performed in the melt coolant interaction test; melt drop steam explosion experiments in which simulated molten core was dropped into water pool and molten core coolability experiments in which water was poured on to simulated core melt. Major findings from these experiments are described in the present paper.

II. MELT DROP STEAM EXPLOSION EXPERIMENTS

Since several early experiments in the melt drop steam explosion experiments were presented at NURETH-5 conference (Sugimoto et al., 1992b), results of the experiments including new ones performed after the presentation are mainly described in this paper.

A. Experimental Apparatus

Schematic diagram of the melt drop steam explosion experiments is shown in Figure 1. Molten core simulant generated in the melt generator was dropped into the water pool located inside the model containment vessel.

The model containment vessel has an inner diameter of 3.9 m, a height of 5.7 m and an inner volume of 50m^3. Several viewing windows are provided in the vessel for visual observation during the experiments. The vessel was pressurized by nitrogen in several experiments.

Melt was generated in the melt generator by thermite

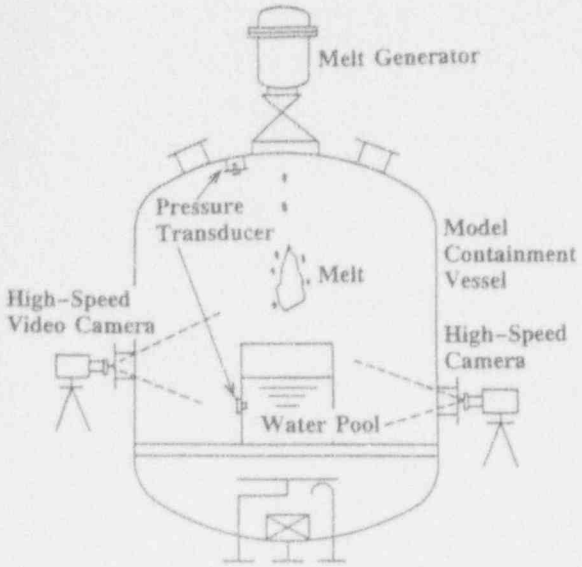

Figure 1. Schematic diagram of melt drop steam explosion experiments

reaction of iron oxides (FeO and Fe_2O_3) and aluminum. The melt generator was placed on the top of the model containment vessel. The maximum capability of generating melt by the melt generator is 100 kg. In this paper the experimental results with either 10 kg or 20 kg of melt are presented. The diameter of the orifice at the bottom of a crucible in the melt generator was 200 mm for both 10 kg and 20 kg of melt experiments. Two layers of the thermite was installed in the melt generator: the upper layer for generating the melt and the lower layer as the melt dropping device. Four kg of MgO powder was inserted between the two layers as thermal insulator. The two layers of the thermite and MgO powder were placed on a glass plate which plugged the orifice at the bottom of the crucible. The lower layer of the thermite was electrically ignited after confirming that all of the thermite in the upper layer was melted. Exothermic reaction of the lower layer of the thermite broke the glass plate and the melt (upper layer) was dropped with MgO powders within 0.8 sec. It took about 12 s to complete the thermite reaction in the upper layer and 20 s to drop the generated melt after the initiation of the thermite reaction in the upper layer.

The melt was dropped into the water pool which was placed inside of the model containment vessel. Two kinds of the water pool were used as shown in Figures. 2 and 3, respectively. One was the cylindrical water pool made of carbon steel and the other was the box-shaped transparent water pool made of acrylic panels. The cylindrical water pool has the inner diameter of 1 m and the height of 1.2 m while the transparent water pool has the cross section of 0.88 m x 0.88 m and the height of 1.2 m. In the present experiments, water of 1 m in depth was held in these pools which corresponded to 0.785 m^3 in the cylindrical pool and 0.774 m^3 in the transparent pool.

In some of the experiments, the dispersion device as shown in Figure 3 was placed at the top of the transparent water pool. Essential part of the device was a grid of 63 cm x 63 cm which was fixed at the center of the steel frame. The grid was made of steel wire of 2 mm in diameter and the pitch of the grid was 25 mm. The device was installed at the top of the pool so that the grid plane was located horizontally at 10 cm above the water surface.

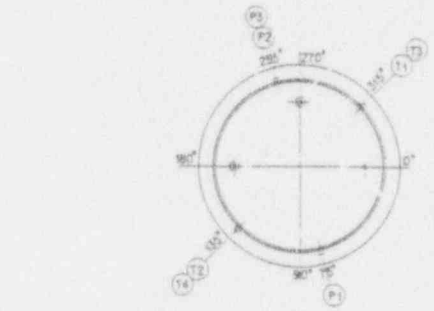

T:Temperature
P:Pressure

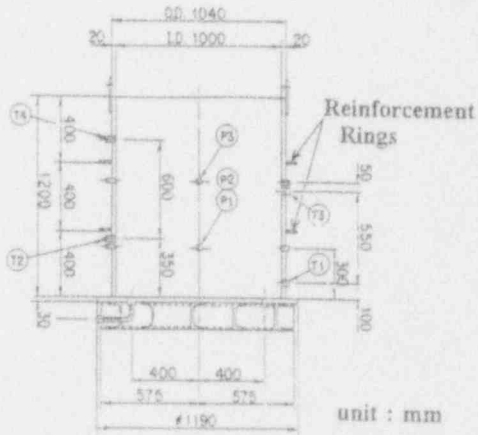

Figure 2. Steel water pool

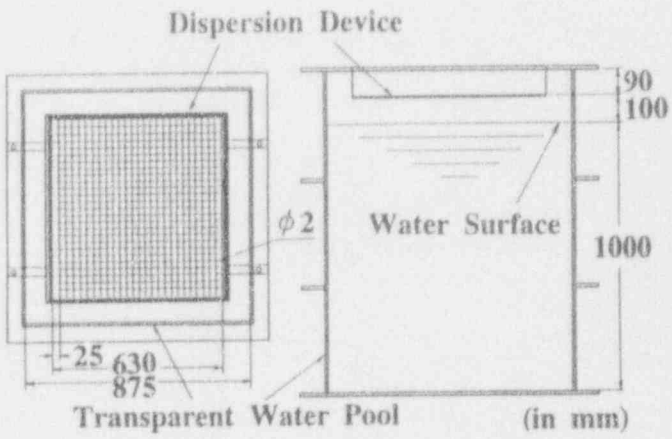

Figure 3. Transparent water pool and dispersion device

Instrumentation of the melt drop steam explosion experiments is summarized in Table 1. Measured data were recorded by the high-speed recording system with sampling rate of up to 1 MHz and the low-speed recording system with sampling rate of up to 100 Hz. A high-speed 16 mm camera and a high-speed video camera were used in the experiments to qualitatively and quantitatively investigate the phenomena of the steam explosion.

Table 1 Summary of Instrumentation

Item	Detector	
Pressure in water pool	Strain gauge transducer	3
Pressure in model containment	Strain gauge transducer	1
Temperature in melt generator	Thermocouple	4
Water temperature in water pool	Thermocouple	4
Temperature in model containment	Thermocouple	2
Water level in water pool	Differential pressure	1
Water level in model containment	Differential pressure	1
Thermite burn condition	Melt detector	5
Visual observation	High-speed camera	1
	High-speed video	1

B. Experimental Conditions

The experimental conditions of the melt drop steam explosion experiments are summarized in Table 2. The experiment performed in the air at atmospheric pressure using 20 kg of the melt was chosen as the base case and repeated three times in STX002, STX003 and STX005. The atmosphere was replaced by nitrogen in STX009 and pressurized to 1.6 MPa in STX008. Ten kg of the melt was used in STX001 and STX010. The falling melt was dispersed by the dispersion device which was placed at about 10 cm above the water surface in STX006 and STX011. The initial water temperature was room temperature in all the experiments, but it was slightly varied as shown in Table 2. The melt temperature was measured with a pyrometer in an independently conducted separate experiment. The measured temperature at the melt surface was about 2700 K. It should be noted that it was surface temperature and bulk temperature of the melt was estimated to be between 2700 K and 3450 K which is calculated by assuming adiabatic heating up of the thermite. The melt was dropped from the melt generator into the water pool. The traveling distance of the melt was 3.5 m. It was estimated from the analysis of photos taken by the high speed video camera that the melt reached the entry velocity of 8.0 m/s at the surface of the water pool.

C. Experimental Results

1. Visual observations

Spontaneous steam explosion was observed in all of the experiments in the case when 20 kg of the melt was dropped into the water pool at atmospheric pressure and no dispersion device was used as shown in Table 2. Time sequential events of the steam explosion was recorded with the high-speed 16 mm camera. Photo of the steam explosion of STX005 which was taken by the camera with 4,000 frames/s was presented in the NURETH-5 paper (Sugimoto et al., 1992b) as an example.

At the beginning several fragments of molten thermite which was used as the dropping device fell into the water with the MgO powder followed by the melt. Although some of the melt was dispersed in the air, most of the melt entered water as a lump. The shining melt which was surrounded with steam bubble sank in water. Suddenly the brightness of the melt was locally lost at some point when explosion was triggered. The dark region then rapidly expanded over the whole melt, which indicated shock front propagation and rapid heat transfer from the melt to the surrounding water.

Table 2 Summary of Melt Drop Steam Explosion Experiments

Run No.	Melt Mass (kg)	Pressure (MPa)	Atmos-phere	Water Temp.(K)	Water pool	Explosion (Yes/No)	Comment
STX002	20	0.1	Air	289	Steel	Yes	Data not Recorded
STX003	20	0.1	Air	292	Steel	Yes	
STX005	20	0.1	Air	300	Acrylic	Yes	
STX009	20	0.1	N_2	289	Acrylic	Yes	Nitrogen Atmosphere
STX001	10	0.1	Air	293	Steel	No	
STX010	10	0.1	Air	297	Acrylic	Yes	
STX008	20	1.6	N_2	288	Acrylic	No	High Pressure (N_2)
STX006	20	0.1	Air	298	Acrylic	No	Dispersion Device
STX011	20	0.1	Air	290	Acrylic	Yes (Mild)	Dispersion Device (Locally Broken)

The propagation velocity of shock front was estimated as in the order of 400 to 800 m/s from the change of the color in the photos. It was also estimated that the expansion velocity was about 60 to 80 m/s at first, and later decreased to 50 m/s due to the resistance of the water. It was observed that the expansion wave of the steam explosion took near spherical shape.

It should be mentioned that the shape of the melt entering the water was almost spherical according to the observation with the high-speed video. The estimated melt mass entered the water when the trigger occurred was roughly 80 % of the melt according to this observation.

Although surface of the melt was surrounded with steam bubbles, it was not discerned that the melt was fragmented in the water in the cases the spontaneous steam explosion occurred such as in STX005. However it was clearly observed that the melt was dispersed in the wide range of the water in STX006 in which the dispersion device was used and no spontaneous explosion occurred.

The trigger of the spontaneous steam explosion was identified near the surface of water in both STX005 and STX009, but it was observed at the lower front of the melt in the water pool in STX010. More experimental data will be required to decide whether the melt mass has influence on the trigger location or not.

2. Thermal-hydraulic behavior

The variance of pressure was measured with several pressure transducers located at the bottom and the side walls of the water pool. Figure 4 shows the pressure history measured at P1 of the Figure 2 in STX003 as an example. The initial pressure peak was higher than 10 MPa and the peak width was about 1 ms. These values are in the same order of magnitude obtained in the intermediate scale experiments at SNL (Mitchell et al. 1986). The oscillatory and decreasing behavior of the pressure response was probably due to the reflection of the pressure wave in the water pool.

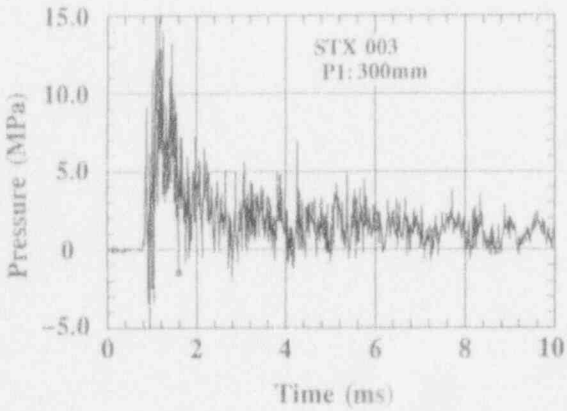

Figure 4. Pressure history measured at the wall of steel water pool (at P1 in STX003)

Ambient pressure in the model containment vessel increased about 8 kPa after the steam explosion as shown in Figure 5. It should be noted that the pressure was measured with a pressure transducer with relatively slow response and recorded by the low-speed recording system. Therefore pressure peak is not seen in the figure. The pressure increase was much smaller than that obtained in the SNL's experiments, in which the pressure increase was in the order of 100 kPa. This is probably because the volume of the model containment vessel is about ten times larger than the vessel used in the SNL's intermediate experiments.

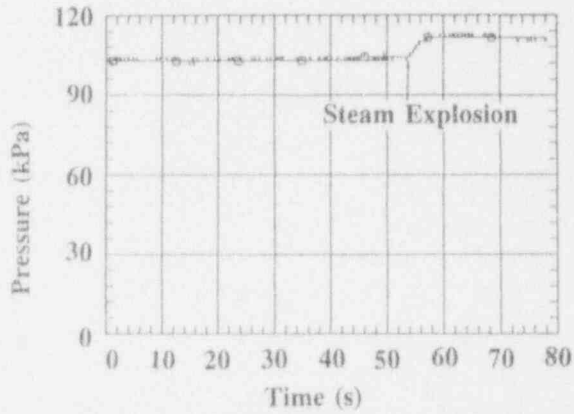

Figure 5. Pressure in model containment vessel (STX003)

3. Debris particle sizes

The size distribution of debris measured with automatic sieve in test STX003 is shown in Figure 6. It should be noted that it was difficult to remove MgO powders from the debris. Since most of MgO powders are larger than 1 mm in diameter, fraction of particles larger than 1 mm tends to be overestimated. The debris size varies from about 10 microns to several 1,000 microns when the steam explosion took place. The debris sizes were much larger for the experiment without steam explosion, in which many debris particles were in the order of several mm. This of course is the result of the fragmentation process caused by the steam explosion. It is noted that the debris particles had much smoother surface when steam explosion took place, indicating that the fragmentation process took place when the melt temperature was still high.

The average diameter of debris remained in the steel water pool was a little larger than that of debris outside of the steel water pool as shown in Figure 6. In particular debris with diameter less than 20 microns was mostly found outside of water pool. This may suggest that the debris effectively contributed to the steam explosion tended to be ejected outside of the steel water pool and that the debris not contributed to the steam explosion tended to be remained inside the steel water pool.

4. Parametric effects on the occurrence of spontaneous steam explosion

mass of melt

The results of the melt drop steam explosion experiments are also summarized in Table 2. The spontaneous explosion occurred in all of the four experiments when 20 kg of the melt was dropped without the dispersion device at the atmospheric pressure

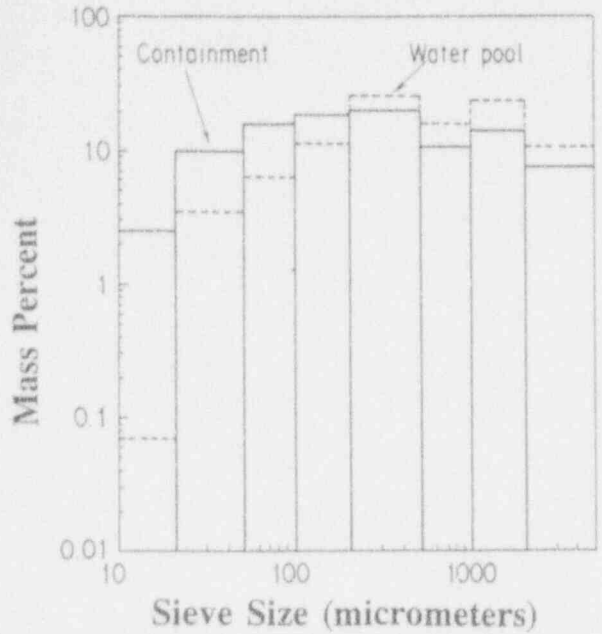

Figure 6. Debris size distribution (STX003)

condition. The spontaneous steam explosion did not occur when the mass of the melt was 10 kg in STX001, while it occurred in STX010 which was performed at the same condition except water pool. It is reported that there exists a minimum critical mass for the spontaneous steam explosion in the experiments (Corradini et al., 1988) with several to several tens kg of melt. Although such minimum critical mass could depend on the geometry, it is revealed that the critical mass is less than 10 kg according to the present experiments at the atmospheric pressure and low water temperature conditions. It may be understood that the difference of the reproducibility of the spontaneous explosion for the experiments with 20 and 10 kg of the melt indicates that the occurrence of steam explosion tend to be more uncertain when the melt mass decreases to the minimum critical mass. However, the reproducibility for 10 kg experiment may have to be examined further before the understanding of the phenomena.

The scaling problem is the most essential part in applying the test results to an actual situation. A careful scaling analysis is inevitable based on the physical understanding of the fuel-coolant interaction phenomena. The experimental data of the melt-coolant interaction test of ALPHA program would be utilized for that purpose.

dispersion device

In the experiment of STX006, the spontaneous steam explosion was suppressed by using the dispersion device shown in Figure 3. It was designed to disperse the melt into finer debris with 2.5 cm gap grid before entering the water. However the spontaneous steam explosion occurred in STX011 which was performed at almost same condition as STX006. Observations with high speed 16 mm camera showed that the melt was not completely dispersed in the water in STX011. The fact found by the posttest observation that the dispersal device was locally broken in STX011 while it was less damaged in STX006 implies the difference of initial mixing condition in the water for the both experiments.

The debris size distribution is compared for STX005(steam explosion), STX008(non steam explosion) and STX011(steam explosion with the dispersion device) in Figure 7. When the steam explosion did not occur as in STX008, the debris size was mostly over mm in range. On the other hand once the steam explosion occurred it was in the order of several tens or hundreds of microns as shown in the figure. It is also shown that the debris has larger size distribution in STX011 than in STX005, which indicates that the steam explosion was less energetic when the dispersal device was used.

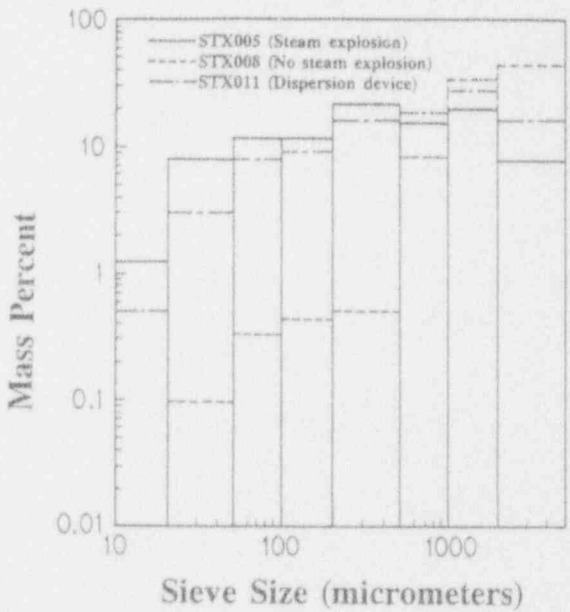

Figure 7. Comparison of debris size distribution among STX005, STX008 and STX011

Although the effect of disperse of the melt on steam explosion occurrence is not fully understood at present, there may be several possible explanations. The dispersion device enhanced the steam generation by increasing the melt surface area available for heat transfer and the resultant water depletion was probably realized in the mixing zone. It may be possible that propagation and/or growth of pressure wave was depressed in the high void region. The other explanation is that the dispersion device enhanced mixture of the melt with air and the dispersed melt in the water was wrapped with steam including noncondensable gas. It is known that noncondensable gas content in the vapor film significantly suppress the occurrence of the steam explosion (Corradini et al., 1988).

There is a possibility that the dispersion device realizes "optimized" coarse mixing condition which leads to more energetic steam explosion. Several experiments with the dispersion device by varying grid gap sizes or using external trigger will be required to understand the effect of the device on

the occurrence of spontaneous steam explosion.

ambient pressure

The steam explosion was suppressed by the high ambient pressure of 1.6 MPa. Effect of ambient pressure on the occurrence of the spontaneous steam explosion was reported with some experiments (Mitchell et al.,1981). However the data were limited to 5.4 kg of melt and pressure at 1.09 MPa. The present experiment confirmed that the extended evidence was obtained using 20 kg of melt up to 1.6 MPa. It is considered that the high ambient pressure affect the premixing behaviors, since the film boiling heat transfer is strongly influenced by the ambient pressure. However the detailed mechanism of this effect is not fully understood and needs further investigation.

III. MOLTEN CORE COOLABILITY EXPERIMENTS

A. Experimental Apparatus

The conceptual diagram of the molten core coolability experiments is shown in Figure 8. The experiments were performed in the model containment vessel of the ALPHA facility. The same thermite was used to simulate molten core as in the melt drop steam explosion experiments. The high temperature melt was generated and held in the interaction vessel, typical structure of which is illustrated in Figure 9. An MgO crucible was placed in a carbon steel cover, and the gap between them was filled with MgO powder as a thermal insulator. Several thermocouples were provided to measure temperature of the bottom and the side walls of the MgO crucible and the overlying water. Dimensions of the MgO crucibles are listed in Table 3. The steel water pool in the melt drop experiments was used in order to hold overflow water from the interaction vessel. Water was poured onto the melt surface through the water supply system with a pipe nozzle or a spray nozzle.

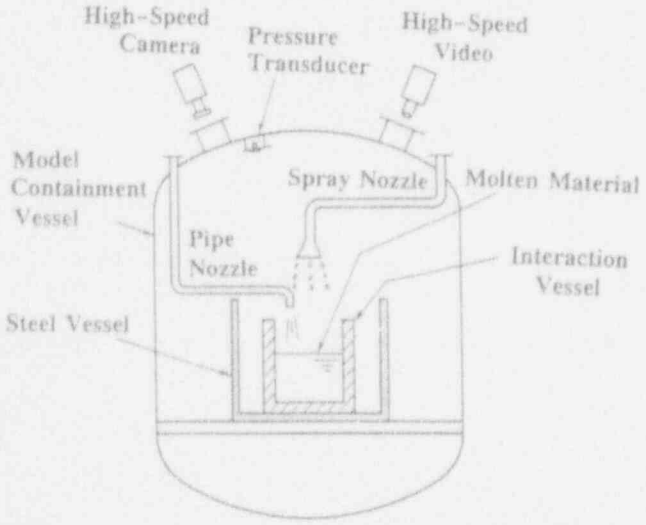

Figure 8. Conceptual diagram of molten core coolability experiments

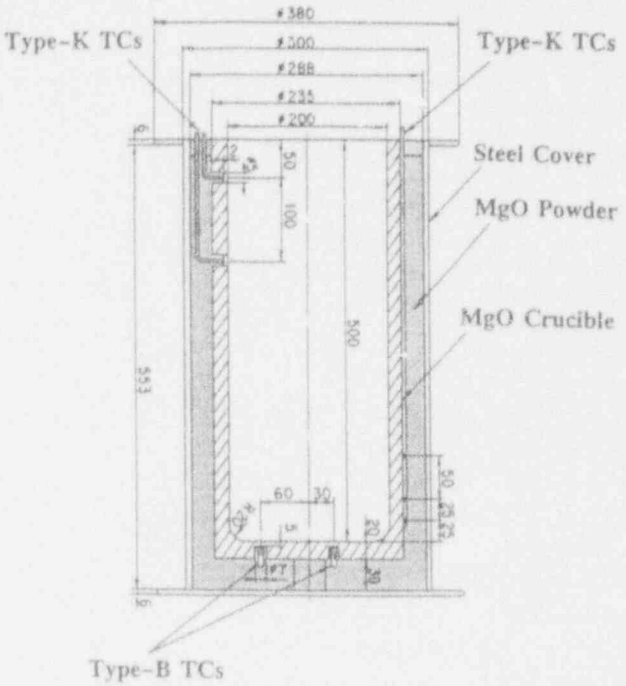

Figure 9. Typical structure of interaction vessel

Table 3. Dimensions of MgO crucibles

Run No.	Inner Diameter Top (m)	Inner Diameter Bottom (m)	Outer Diameter (m)	Height (m)	Depth (m)
ACM002	0.2	0.2	0.235	0.52	0.5
ACM003	0.2	0.2	0.235	0.52	0.5
ACM004	0.1	0.1	0.12	0.515	0.5
ACM005	0.2	0.2	0.235	0.52	0.5
ACM006	0.355	0.355	0.42	0.535	0.5
ACM007	0.2	0.194	0.235	0.370	0.348
ACM008	0.345	0.33	0.395	0.495	0.460

B. Experimental Conditions

1. General conditions

The experimental conditions of the molten core coolability experiments are summarized in Table 4. Depth of the thermite melt was set at about 8 cm in the experiments. Ten kg of thermite was used in the interaction vessels with an inner diameter of about 0.2 m for ACM002, ACM003, ACM005 and ACM007. Smaller or larger inner diameter interaction vessels were provided for ACM004, ACM006 and ACM008 in order to investigate the effect of contact surface area between the melt and water. Water was poured onto the melt surface through a pipe nozzle in the all experiments except ACM003, in which a spray nozzle was employed.

Table 4. Summary of major experimental conditions of molten core coolability experiments

Run No.	Melt Mass (kg)	Melt Surface Diameter(m)	Water Pouring Mode	Nozzle Inner Diameter (mm)	Inlet Water Temperature (K)	Duration of Thermite Reaction[1](s)	Water Pouring Timing[3](s)
ACM002	10.0	0.2	Pipe Nozzle	16.7	288	17	36
ACM003	10.0	0.2	Spray Nozzle	–	283	19	26
ACM004	2.5	0.1	Pipe Nozzle	8.0	293	10–15[2]	34[4]
ACM005	10.0	0.2	Pipe Nozzle	16.7	373	19	28
ACM006	31.5	0.355	Pipe Nozzle	32.9	297	23	31[4]
ACM007	10.0	0.196	Pipe Nozzle	16.7	296	14	32
ACM008	30.0	0.333	Pipe Nozzle	16.7×3	299	17	35

1) Evaluated from measured temperature in the bottom wall of the MgO crucibles
2) Estimated from the separate tests
3) Elapsed time from ignition of thermite
4) Time interval between thermite ignition and activation of an orifice flow meter

The nozzle exit was located at about 0.3 m above the center of the melt surface. In case the pipe nozzle was used, water fell down from the downward nozzle at the superficial velocity ranged between 0.46 and 0.66 m/s at the exit of the nozzle. In case the spray nozzle was used, some water flowed down on the side wall of the crucible while some water directly fell on the surface of the melt as droplets.

With respect to the inlet water temperature, saturated water was supplied only in ACM005 and subcooled water was used for the other experiments. Water supply was initiated at around 30 s after ignition of thermite. As shown in Figure 10, water mass flux based on the melt surface area was varied in the similar manner in all the experiments except ACM004 and ACM005, in which that was kept at constant values during the experiments.

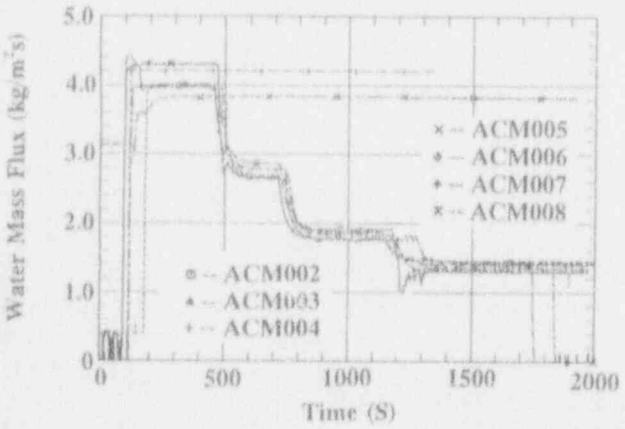

Figure 10. Water mass flux poured onto melt based on top surface area of melt

2. Melt conditions

Temperature of the melt surface at water pouring was estimated from the results of the two separate tests using 3 kg of thermite. Depth of the molten thermite in the separate tests was set as the same level as that of the molten core coolability experiments. The top surface temperature of the melt was measured using a pyrometer assuming an emissivity of 0.4 which is the emissivity of solid aluminum oxide at around 1800 K (Touloukian). Duration of the thermite reaction was also measured in the separate tests by detecting a signal of type-K thermocouple failure at the bottom of the thermite layer. From the separate tests, the top surface temperature of the melt was approximately 2700 K at the thermite reaction completion and 2450 K at around 30 s after the thermite ignition. However, it must be mentioned that bulk temperature of the melt would be much higher than the surface temperature because of a large temperature gradient at the surface of the melt due to heat transfer to the environment. Assuming an adiabatic condition, temperature of the thermite melt would reach about 3450 K if all of energy released from the thermite reaction is used to heat up the melt.

Duration of the thermite reaction in the molten core coolability experiments was evaluated from the measured temperature of the bottom wall of the MgO crucibles. The evaluated thermite reaction time is also listed in Table 4. It was slightly longer than the measured value in the separate tests, which ranged 10 to 15 s. It can be seen in Table 4 that the thermite reaction had completed to produce the high temperature melt before adding water onto the melt. Due to the large density difference between the immiscible thermite reaction products (aluminum oxide and iron), it was anticipated that a stratified state of the melt must have been quickly established after the thermite reaction completion.

C. Results and Discussions

1. Post test observations

The post test observations were made for the solidified melt and dispersed debris. It was found that solidified oxides (alumina) whose typical thickness was 6 through 8 cm overlay on the about

4 cm thick metallic materials (iron). Rough surfaces were observed at the top of the solidified oxides. In some experiments, it was found that spherical particles of several millimeters in diameter accumulated on the solidified melt. It is considered that these particles were formed when the melt erupted into water. Fine fragmented particles with smooth surface were found in ACM002. It is considered that these particles were generated by an explosive melt/water interaction as described later in 3.

2. Heat transfer characteristics

The melt was cooled by the overlying water in the molten core coolability experiments. The temperature history of the water pool is shown in Figure 11. Until the water level approached thermocouples to measure temperature of the overlying pool water, the temperature exceeded saturation temperature because the thermocouples detected high temperature gas products from the thermite reaction and/or radiation from the melt. The pool water temperature decreased gradually with time, starting with the saturation temperature, as the water was continuously poured and the water level rose. The overlying water temperature in ACM004 showed the largest subcooling due to constant and relatively higher water mass flux than the other experiments as is seen in Figure 11.

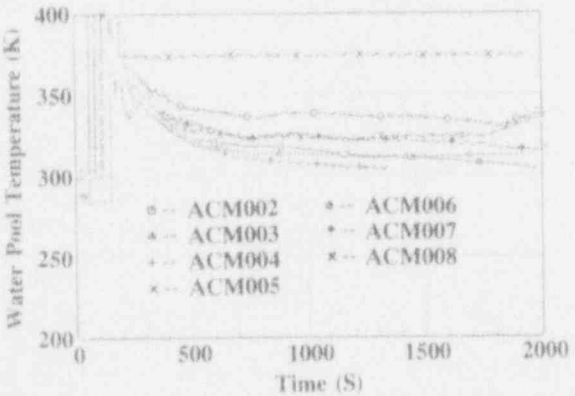

Figure 11. Water temperature in overlying pool

Heat flux at the top surface of the melt was calculated from the measured pool water temperature by assuming that the overlying water was well-mixed and vaporization of the water was negligible. The energy balance for the water pool can be written as,

$$q = \frac{\rho C_{pw}}{A_s}\left[w(T_p - T_0) + V_p \frac{dT_p}{dt}\right]. \qquad (1)$$

The calculated heat flux at the top surface of the melt is shown in Figure 12 for all the experiments except ACM005. Heat flux could not be calculated for ACM005, in which saturated water was poured, since no instrumentation was provided for steam generation rate.

The calculated heat flux decreased with time, reducing the surface temperature of the melt. Since heat transfer rate at the melt surface is influenced by many parameters such as the melt temperature, water temperature in the overlying pool, surface

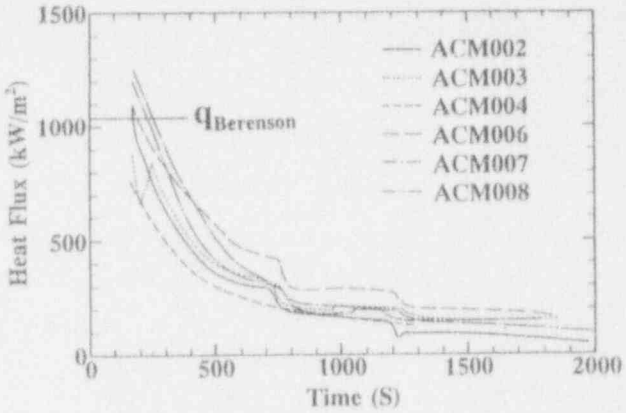

Figure 12. Evaluated heat flux from melt to overlying water. $q_{Berenson}$ shows the calculated heat flux with Berenson's flat plate film boiling correlation by assuming the melt surface is at the melt solidification temperature(2320 K).

roughness, detailed analyses considering convection and phase change in the melt and heat loss through the wall should be required to interpret the observations in all the experiments. However qualitative characteristics can be obtained by comparing the experiments with same configuration, i.e, ACM002, ACM003 and ACM007. Heat flux for both ACM002 and ACM003 was evaluated to be smaller than that for ACM007 in the early period. The pool water temperature was also lower in both ACM002 and ACM003 than in ACM007. As mentioned in later section, an explosive interaction between the melt and the water occurred in ACM002 to disperse the melt out of the interaction vessel. The dispersion of the melt decreased the total enthalpy in the melt, which resulted in relatively high temperature reduction rate. It is supposed that the melt surface was effectively cooled down by water droplets in ACM003 where a spray nozzle was used. It was observed in ACM003 that film flow along the side wall surface was established together with spray droplets dispersion onto the top surface of the melt. From the visual observation of ACM003, vigorous steam was generated immediately after the water addition.

The heat flux at the melt surface can be defined as,

$$q = h(T_m - T_s). \qquad (2)$$

The heat transfer coefficient depending on the melt surface temperature must be more valuable information for general discussion on the molten core coolability. Unfortunately, the melt surface temperature could not be measured during cooling phase by the overlying water pool in the experiments. However assuming that the stratified state was quickly established in the melt consisting of aluminum oxide in the upper layer and iron in the lower layer and that the melt surface temperature decreased to near the solidification temperature of aluminum oxide (2320 K) during the initial short period in the cooling phase after the water level approached thermocouples for the overlying water pool, the heat transfer coefficient can be determined from the calculated heat flux. It is indicated in Figure 12 that the heat flux ranged between 800 and 1200 kW/m^2 for all the experiments during the corresponding period, from which the heat transfer coefficient is calculated to be 410 through 620 W/(m^2•K). Since the pool water temperature was near saturation temperature as

shown in Figure 11 in the early cooling phase, the Berenson's flat plate film boiling correlation (Berenson, 1961) for saturated coolant including the effect of radiation heat transfer can be applied in this case. The heat transfer coefficient calculated from the Berenson's correlation was 530 W/(m^2•K) at the melt surface temperature of 2320 K with an emissivity of aluminum oxide of 0.4. Though the Berenson's correlation was developed for the surface temperature condition near the minimum film boiling point, it seems that the correlation would be applicable under high surface superheat condition encountered in the present experiments.

3. Occurrence of Explosive Interaction

An explosive interaction between the melt and the overlying water was observed only in ACM002. The pressure increase in the model containment vessel atmosphere shown in Figure 13 indicated this phenomenon. Such explosive interaction was also observed in the steam explosion experiments with a stratified geometry performed at Sandia National Laboratories (Berman, 1986). The steam explosion was observed in the SNL experiments, however, only when water was fed onto the molten thermite just after the completion of the thermite reaction, and no steam explosion was observed in the case that water was poured at about 5 s after the thermite reaction completion due to the formation of thin crust at the melt surface. In ACM002, on the other hand, water was poured at about 19 s after the thermite reaction completion and the explosive event occurred at about 9 s after water pouring, during which about 3.6 cm depth of water was accumulated over the stable interfacial vapor film.

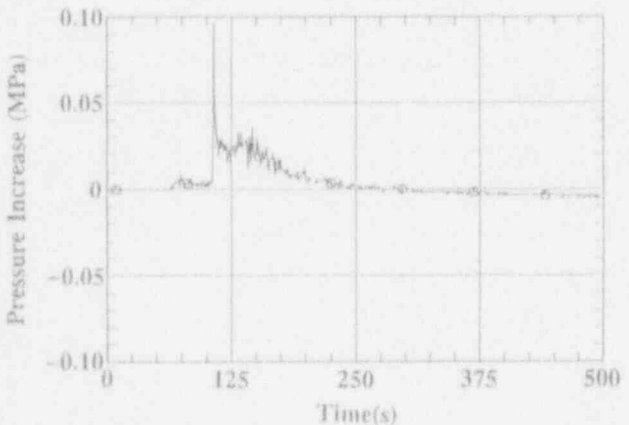

Figure 13. Pressure increase in model containment vessel atmosphere caused by explosive interaction in ACM002

Immediately before the occurrence of the explosive interaction, consecutive eruptions of the melt took place as shown in Photo. 1. Although additional information concerning the melt–water interactions must be accumulated, the eruptions would be an important phenomena to establish an adequate coarse mixing configuration and trigger to produce an energetic event in stratified geometries. Bang and Corradini(1991) observed two types of the spontaneous triggering from the high-speed films in their vapor explosion experiments in a stratified geometry; (a) vapor film collapse due to minimum film boiling dynamics and (b) vapor film destabilization due to an internal pressure source near the interface. In the present experiments, latter type of the spontaneous triggering by the eruptions is considered to cause the subsequent explosive interaction.

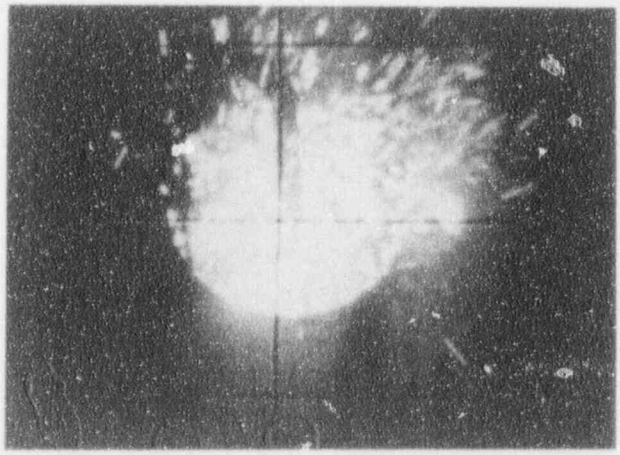

Photo 1. Eruption observed in ACM002

It is supposed that the eruptions were resulted from the direct contact between the melt and the overlying water through the vapor film. In the experiments performed by Greene et al.(1990, 1988) liquid–liquid contacts were observed when water was poured onto such liquid metals as lead, bismuth and Wood's metal under surface superheat conditions up to about 600 K. It was also visually confirmed in the Greene's experiments that liquid metal jets penetrated into the overlying water layer, which would be the corresponding phenomena to the eruption in the present study.

Several eruptions were observed in the other molten core coolability experiments. The eruption timing for all the experiments is summarized in Table 5. In addition to ACM002, the multiple eruptions were identified in ACM004, ACM007 and ACM008. However, from the visual observations, scale of these eruptions were clearly much smaller in comparison with the eruptions observed in ACM002. No eruption was observed in ACM003 and ACM005, in which water was poured through a spray nozzle or at saturated temperature, respectively. Visual observation was not possible in ACM006 due to scattering of the external light source by vigorous generation of aerosols during the thermite reaction. However a lot of particles with smooth surface were found on the solidified melt and it suggested that there might have been the eruptions. The eruptions were observed only in the case that subcooled water was poured onto the melt through a pipe nozzle. It is considered that localized destabilization of the interfacial vapor film would be caused by the mixing of the subcooled water in the overlying pool. In ACM003, stable crust must have been quickly formed at the melt surface because of the effective cooling by spray droplets.

The dispersed debris due to the explosive interaction in ACM002 was collected and size distribution was measured by the automatic sieve. The result of size distribution measurement is shown in Figure 14 along with data obtained from the melt drop steam explosion experiment (STX005). It can be seen that a less

Table 5. Summary of time difference between water pouring and eruptions

Run No.	Time Difference between Water Pouring and Eruptions (s)
ACM002	9 (Double)
ACM003	No Eruptions
ACM004	2, 8
ACM005	No Eruptions
ACM006	Unsuccessful Visual Observation
ACM007	31, 33, 35
ACM008	14, 17, 20

fraction was occupied by smaller size particles in ACM002 than in STX005. It is indicated that the explosive interaction occurred in ACM002 would be milder than the steam explosion observed in STX005.

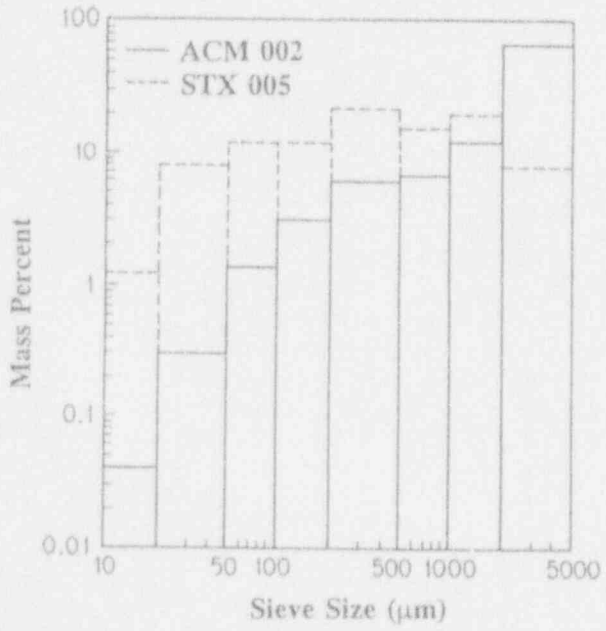

Figure 14. Comparison of debris particle size disribution in ACM002 and STX005

IV. APPLICABILITY TO ACCIDENT SITUATIONS

Since the scale of the experimental facility is much smaller than the actual nuclear reactor geometry, the results of the experiments can not be directly applied to the accidental situation of a nuclear reactor. We consider that it will not be possible to estimate the occurrence and the consequence of the steam explosion in the reactor accident before the reasonably mechanistic model of the steam explosion is established. However it is also considered that some of the results obtained in the experiments suggest candidates of the accident management measures.

In the melt drop steam explosion experiments, the spontaneous steam explosion did not occur when ambient pressure was increased up to 1.6MPa. Therefore, increasing ambient pressure is expected to be hopeful candidate for the prevention of the steam explosion. Spontaneous steam explosion was suppressed when the falling melt was forced to disperse by the dispersal device in two experiments; no explosion occurred in STX008 and less energetic explosion was obtained in STX011. Although more experiments are needed to confirm the effect and specify appropriate dispersed condition, artificially dispersing the molten core should be considered as one of the candidates of prevention and/or mitigation of the steam explosion.

In the molten core coolability experiments, explosive interaction was found only in one experiment and it was estimated that the explosive interaction was less energetic comparing with the steam explosion in the melt drop steam explosion experiments. The results of the experiments also indicate water injection mode(by a pipe nozzle or by a spray nozzle) may have strong influence on the FCI phenomena. Although more confirmation experiments and/or understanding phenomena are needed, the results suggest that the adding water onto molten core is a hopeful accident management measure if water is provided in a proper way.

V. CONCLUSIONS

In order to investigate fuel-coolant interaction which would occur when molten core contacts water during severe accidents of LWRs, two series of experiments were performed in the melt-coolant interaction test of the ALPHA program: melt drop steam explosion experiments and molten core coolability experiments. The melt generated by thermite reaction of aluminum and iron oxide was used as molten core simulant in the both experiments.

The melt was dropped into a pool of water by varying amount of melt, ambient pressure and dispersal condition of the melt in the melt drop steam explosion experiments. The following findings were obtained from the experiments:

(1) Spontaneous steam explosion was observed in all the experiments when 20 kg of the melt was dropped without dispersing by the device at the atmospheric pressure. When the mass of the melt was 10 kg, the spontaneous steam explosion was found in one of two experiments.
(2) The spontaneous steam explosion was triggered near the surface of the water for the experiments with 20 kg of the melt and triggered at the lower front of the melt for the experiment with 10 kg.
(3) The spontaneous steam explosion did not occur when the ambient pressure was increased to 1.6 MPa.
(4) The dispersion device is expected to have suppressing effect on the occurrence of the spontaneous steam explosion; no explosion and less energetic explosion were observed in the two experiments with this device.
(5) When the spontaneous steam explosion occurred, the size distribution of debris particles varied from several 10 to 1,000 microns.

The present results suggests the possibility that the spontaneous steam explosion can be prevented when the ambient pressure is high or the appropriate device for fragmenting the melt is used.

The molten core coolability experiments were performed by pouring water onto molten thermite to evaluate the coolability of the high temperature molten core including the occurrence of the explosive event. The following findings were obtained from the experiments:

(1) Heat transfer characteristics between the melt and the overlying water were investigated.
(2) Heat transfer coefficient during short period in the cooling phase was determined and compared with the Berenson's horizontal flat plate film boiling correlation for saturated coolant. The Berenson's correlation appeared to be applicable even under high surface superheat conditions.
(3) The occurrence of the explosive event was observed at about 9 seconds after water pouring onto the melt surface. This event might have been caused by the large scale eruption of the melt into the overlying water layer.
(4) From the comparison of the debris particle size distribution between the molten core coolability experiments and melt drop steam explosion experiments, it is considered that the explosive event in a stratified geometry was less energetic than that in the melt drop steam explosions.

NOMENCLATURE

A_s : Top surface area of melt (m^2)
C_{pw} : Specific heat of water (J/(kg•K))
T_i : Inlet water temperature (K)
T_m : Temperature at the top surface of melt (K)
T_p : Temperature of overlying water pool (K)
T_s : Water saturation temperature (K)
V_p : Volume of overlying water pool (m^3)
h : Heat transfer coefficient ($W/(m^2•K)$)
q : Heat flux (W/m^2)
t : Time (s)
w : Volumetric flow rate (m^3/s)
ρ : Density of water (kg/m^3)

ACKNOWLEDGEMENTS

We would like to gratefully acknowledge the excellent work in preparation of the experiments and operation of the test facilities by the stuffs of the Safety Facility Engineering Services Division in JAERI led by Mr. Hideo Itoh.

REFERENCES

1. Bang, K.H. and Corradini, M.L.(1991) "Vapor Explosions in a Stratified Geometry", Nucl. Sci. Eng. Vol. 108, 88–108.
2. Berenson, P.J.(1961) "Film Boiling Heat Transfer from a Horizontal Surface", J. Heat Transfer, Vol. 83, 351–358.
3. Berman, M.(1986) "Light Water Reactor Safety Research Program Semiannual Report, October 1983–March 1984", SAND85–2500, Sandia National Laboratories.
4. Corradini, M.L. et al.(1988) "Vapor Explosions in Light Water Reactors: A Review of Theory and Modeling", Prog. Nucl. Energy, Vol. 22, 1.
5. CSNI (1989) "The Role of Nuclear Reactor Containment in Severe Accident", OECD/NEA, Paris.
6. Ginsberg, T. et al.(1985) "A Review of the Current Understanding of the Potential for the Containment Failure Arising from In–Vessel Steam Explosions", NUREG–1116.
7. Greene, G.A. et al.(1986) "The Effect of Water in Film Boiling over Liquid–Metal Melts", Trans. Am. Nucl. Soc., Vol. 53, 360–362.
8. Greene, G.A. et al.(1988) "Phenomenological Studies on Molten Core–Concrete Interactions", Nucl. Eng. Des., Vol. 108, 167–177.
9. Mitchell, D.E. et al.(1981), "Intermediate Scale Steam Explosion Phenomena: Experiment and Analysis", SAND81–0124.
10. Mitchell, D.E. et al.(1986) "Steam Explosion Experiment at Intermediate Scale: FITS–B Series", SAND83–1057.
11. Soda, K.(1990), "Containment Research Overview", Proc. The Second International Conference – Containment Design and Operation –, Oct. 1990, Toronto, Canada.
12. Soda, K. et al.(1991), "Recent Development and Results from Severe Accident Research in Japan", NUREG/CP –0119, Vol.2, Proc. 19th Water Reactor Safety Meeting, Oct. 1991, Bethesda.
13. Sugimoto, J. et al.(1992a), "Steam Explosion Experiment in the ALPHA Program –Phenomena and Estimation of Energy Conversion Ratio–", JAERI–M 92–035, March(1992)(In Japanese).
14. Sugimoto, J. et al.(1992b), "Fuel–Coolant Interaction Experiments in ALPHA Program", Proc. Fifth International Topical Meeting on Reactor Thermal Hydraulics, Sept. 1992, Salt Lake City, UT, Vol.3, 890–897,
15. Theofanous, T.G. et al.(1987) "An Assessment of Steam–Explosion–Induced Containment Failure Part I: Probabilistic Aspects", Nucl. Sci. Eng., Vol.97, 259–281.
16. Touloukian, Y.S. (edit),"Thermophysical Properties on High Temperature Solid Materials", vol.4

STUDIES ON FUEL–COOLANT INTERACTIONS DURING A REACTIVITY INITIATED ACCIDENT OF NUCLEAR POWER PLANT

Toyoshi FUKETA, Norihiro YAMANO
Japan Atomic Energy Research Institute
Tokai-mura, Ibaraki-ken, 319-11 Japan
FAX 81-292-82-6160

Akira INOUE
Tokyo Institute of Technology
Meguro-ku, Tokyo 152 Japan
FAX 81-3-3729-1875

ABSTRACT

During a reactivity initiated accident (RIA) a large and prompt amount of energy is deposited within fuel rods. Consequent fuel melting and rod failure can lead to a fine dispersal of fuel melt in coolant, resulting in a violent thermal interaction between the fuel melt and coolant (i.e. fuel/coolant interaction--FCI). The generation of destructive forces during FCIs under RIA conditions have been demonstrated by the in-pile experiment program in Japan Atomic Energy Research Institute. The FCIs in an RIA have been also studied in Tokyo Institute of Technology by out-of-pile experiments and analytical modeling. The outlines and primary results of the both programs are described and discussed in this paper.

I. INTRODUCTION

The behavior of reactor fuels during off-normal and postulated accident conditions is being studied to provide a data base for the Japanese regulatory guide for reactivity initiated accidents (RIAs) in the Nuclear Safety Research Reactor (NSRR) Program at the Japan Atomic Energy Research Institute (JAERI). Numerous experiments have been performed to evaluate the thresholds, modes, and consequences of fuel rod failure in terms of the energy deposition, the coolant conditions, and the irradiation history of the fuel. As a part of this program, a series of experiments with high energy deposition has been conducted to evaluate the destructive forces generated by molten fuel/coolant interactions (FCIs) during reactor power excursion(Fujishiro and Fuketa, 1989; Fuketa and Fujishiro, 1992). In the NSRR experiment, a single LWR fuel rod contained in a test capsule, is subjected to a large power burst. Molten fuel is ejected into the coolant through a breach in the cladding. To study the effects of coolant and fuel conditions on the molten fuel fragmentation, the experimental conditions including an amount of deposited energy, coolant subcooling, fuel/coolant ratio and fuel rod internal pressure have been varied extensively in the NSRR program. The melting and fragmentation of the fuel during severe reactivity transients have also been investigated using an out-of-pile technique(Inoue et al., 1991, 1992) in Tokyo Institute of Technology. Since number of difficulties concerning the handling of radio active materials, visual observation during transients, etc. exist in in-pile experiments, out-of-pile techniques are effective measure to investigate the detailed phenomena during FCIs in an RIA. The results obtained in the out-of-pile experiment were compared with the analytical predictions based on the surface stretch model.

II. IN-PILE EXPERIMENT

A. Experimental Method

The NSRR is a modified TRIGA-ACPR (Annular Core Pulse Reactor) of which the salient features include a large pulsing power capability that allows the moderately enriched fuel to be heated by nuclear fission to a temperature above the melting point of UO_2, and a large (22 cm diameter) dry irradiation space located in the center of the reactor core that can accommodate a sizable experiment. In the in-pile experiments, PWR type fresh fuel rods, which were segmented to an overall length of 279 mm, were used. A schematic diagram of a test fuel rod is shown in Fig. 1. The fuel rod contained fourteen UO_2 pellets, and had a fuel stack length of 135 mm. In some experiments, 5% enriched and unenriched UO_2 pellets were installed in both ends of fuel stack. The major specifications of the test fuel rod are summarized in Table 1. A test fuel rod was installed in the irradiation capsule as illustrated in Fig. 2(a). In the experiment with pre-pressurized fuel rod, the double capsule system was used. The internal vessel used in the double capsule system is also shown in Fig. 2(b). These capsules contained stagnant water at atmospheric pressure and ambient temperature. The pressure pulses generated at fuel failure were measured with a strain gauge type fast response transducer installed at the bottom of the internal vessel. The plenum pressure was measured at the upper flange of the vessel. A good index of the severity of mechanical energy generation is the thermal to mechanical energy conversion ratio, a ratio of mechanical energy generated to the nuclear energy deposition in the fuel. The thermal to mechanical energy conversion ratio η is then defined as:

$$\eta = \frac{K_e}{m_f c Q} \qquad (1)$$

In the experiment with single capsule system, mechanical energy was estimated from the kinetic energy of the water slug:

$$K_e = \frac{1}{2} m_w u^2 \qquad (2)$$

The velocity of the water slug was measured by the float

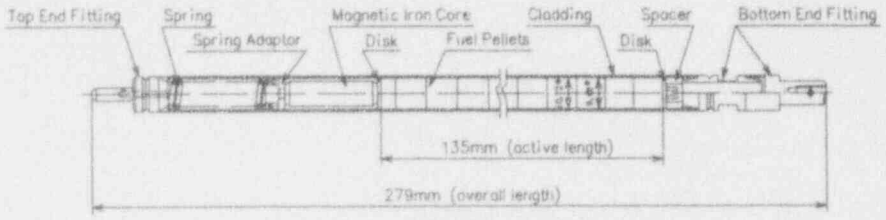

Fig. 1 Schematics of the test fuel rod

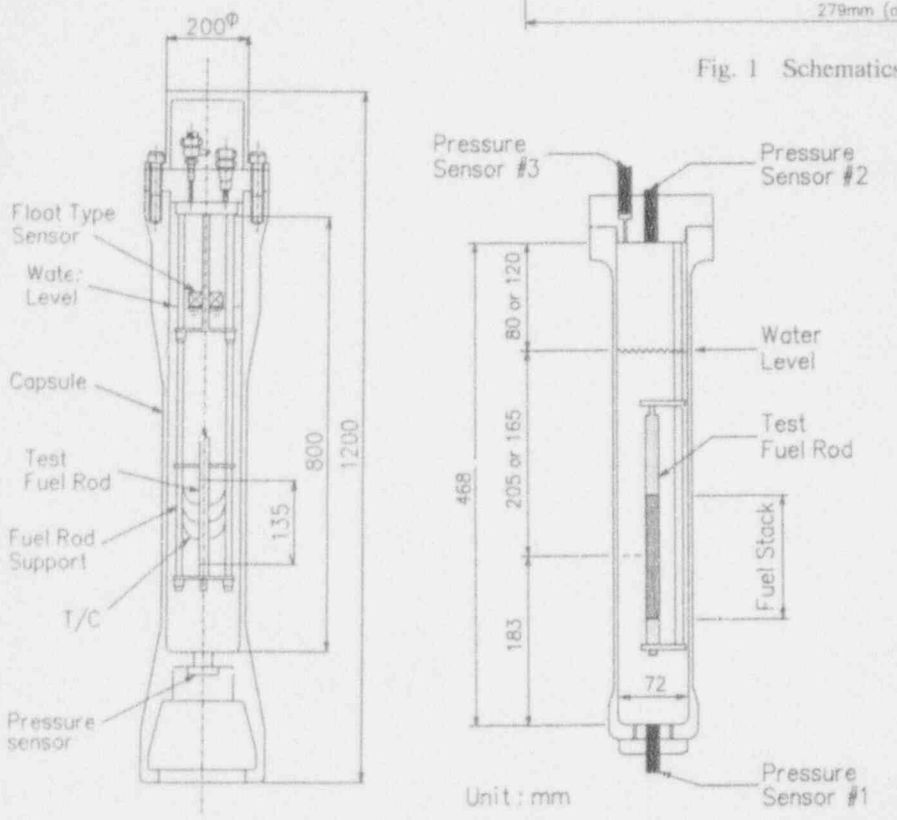

(a) Single capsule system (b) Inner vessel of double capsule system

Fig. 2 Schematic diagram of the test capsule

Table 1 Specifications of the test fuel rod

UO_2 pellets	
Diameter	9.29 mm
Length	10 mm
Density	95% TD
Enrichment	10 and 20%
Shape	Chamferred
Cladding	
Material	Zircaloy-4
Wall thickness	0.62 mm
Outer diameter	10.72 mm
Radial gap	
Pellet-cladding	0.095 mm
Element	
Overall length	279 mm
Active fuel length	135 mm
Number of pellets	14
Fill gas	Helium
Gap volume	3.0×10^{-6} m^3
Initial internal pressure	0.1 to 8.5 MPa

type sensor as shown in Fig. 2(a). In the experiment with double capsule system, mechanical energy was estimated from the energy used to compress the gas in the capsule upper plenum. The mechanical energy, K_e, was calculated by the following equation, assuming adiabatic compression of plenum gas:

$$K_e = -\int_{V_{gas,0}}^{V_{gas,1}} P_{gas}\,dV = \frac{P_{gas,0}V_{gas,0}}{\kappa_g - 1}\left[\left(\frac{P_{gas,1}}{P_{gas,0}}\right)^{\frac{\kappa_g - 1}{\kappa_g}} - 1\right] \quad (3)$$

The energy used in deforming the wall of test capsule was neglected since the deformation was well within the elastic domain.

B. Results and Discussion

Threshold for Mechanical Energy Generation Fuel damage in an RIA depends on the energy deposition in the fuel rods since the energy is supplied to rod almost adiabatically by the prompt power excursion. Figure 3 compares the post-test appearance of fuel rods in relation to energy deposition. In the energy deposition range beyond 0.46 kJ/g·UO_2, onset of departure from nucleate boiling (DNB) occurred. The cladding surface temperature reached a maximum of over 1100 K, and film boiling continued for a few to about ten seconds. Oxidation of cladding surface was observed over the full length of the pellet stack. The amount of oxidation increased as the fuel enthalpy became higher. Incipient fuel failure occurred at an energy deposition of about 0.9 kJ/g·UO_2 due to brittle fracture of the cladding with circumferential cracks. The cladding surface temperature approached the melting point of Zircaloy (2110 K) during the transient and variations in cladding wall thickness were observed in the failed fuel rods. No mechanical energy was generated in this mode of fuel failure. When the energy deposition exceeded 1.4 kJ/g·UO_2, the failure mode changed from that of incipient failure. Molten UO_2 was expelled into coolant and both fuel and cladding formed small particles as shown in the top row in Fig. 3. The fragmentation of a fuel rod caused pressure generation and jumping of the water column above the fuel rod region in a capsule. Figure 4 shows the peak pressure measured at the bottom of the capsule and the measured mechanical energy conversion ratio as a function

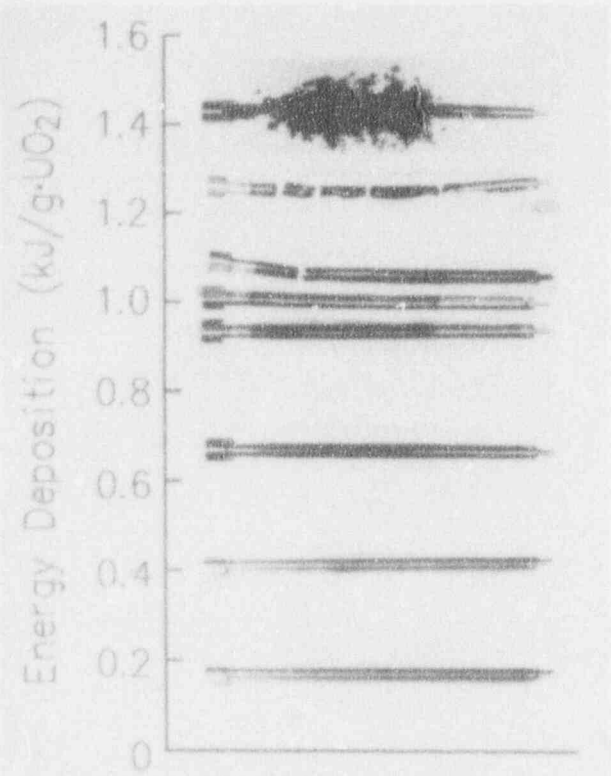

Fig. 3 Appearance of post-test fuel rods related with energy deposition

of energy deposition. The data are from the experiments with a coolant temperature of 293 K and non-pressurized fuel rods. The peak pressure and the conversion ratio increased exponentially with energy deposition over the range of 1.36 to 2.09 kJ/g·UO_2. The mechanical energy was strongly dependent on the fuel fragmentation and the conversion ratio was well correlated to the mean diameter of the fuel fragment(Tsuruta et al., 1985).

Hydrogen Generation The amount of hydrogen generated during the transient was estimated by the pressure increase of capsule plenum gas(Inabe and Fuketa, 1992). The estimated amount of hydrogen is plotted in Fig. 5 as a function of energy deposition. The generated hydrogen increased linearly with energy deposition. The increase of hydrogen generation due to the occurrence of fuel fragmentation can be observed, but this effect is not vigorous. This fact suggests that the most of hydrogen is generated from cladding oxidation and the oxidation of UO_2 is not significant.

Effect of Coolant Subcooling To study the effects of coolant conditions, experiments were conducted with different coolant subcooling. Fuel rods were subjected to the energy depositions of about 1.7 kJ/g·UO_2 and 2.0 kJ/g·UO_2. The coolant subcooling temperatures were varied from 10 K to 80 K under atmospheric pressure conditions. Figure 6 shows the plot of the peak pressure and the mechanical energy conversion ratio as a function of coolant subcooling temperature. With an energy deposition of 1.7 kJ/g·UO_2, the conversion ratio decreased as the coolant

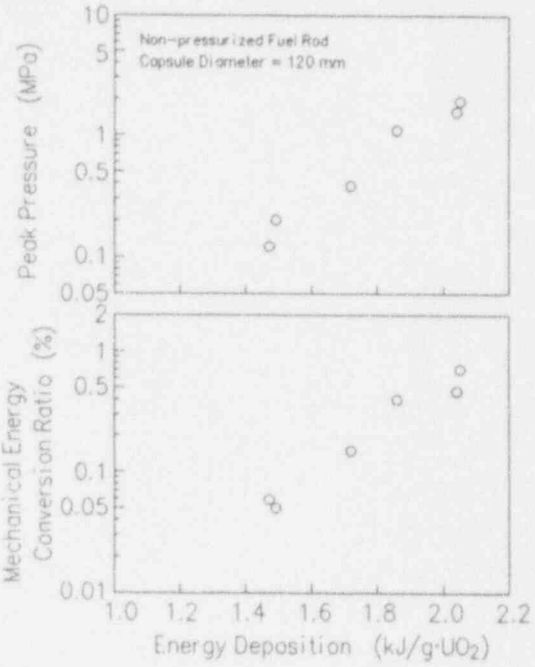

Fig. 4 Peak pressure and mechanical energy conversion ratio versus energy deposition

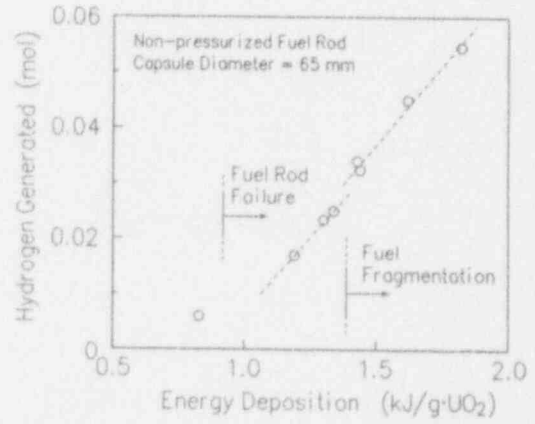

Fig. 5 Hydrogen generation as a function of energy deposition

temperature was increased but the effect was not significant when the energy deposition was raised to 2.0 Kj/g·UO_2. The decrease of the conversion ratio at 1.7 kJ/g·UO_2 coincided with an increase of the mean diameter of the fuel fragments, which suggests that the reduced fuel fragmentation resulted from the lower conversion ratio. It is thought that reducing the coolant subcooling temperature caused vapor blanketing around the ejected molten fuel which might have prevented the contact between the fuel and the coolant and suppressed the development of fuel fragmentation. The different results at the higher energy deposition level indicate that, in this case, the fragmentation developed even under vapor blanketing conditions. With an energy deposition of 2.0 kJ/g·UO_2, the fuel become completely molten during the rapid power transient and a

part of it was vaporized by the end of the energy insertion. Under these conditions, the molten fuel could have been ejected into the coolant at a greater velocity because of the higher rod internal pressure, and this extensive fragmentation occurred even with very little subcooling.

Effect of Water/Fuel Ratio The test fuel rod was supported in a flow shroud and the amount of the water

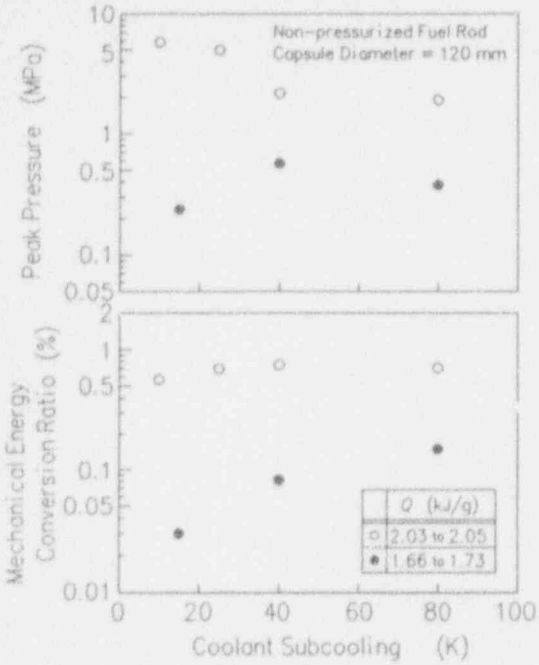

Fig. 6 Peak pressure and mechanical energy conversion ratio versus coolant subcooling

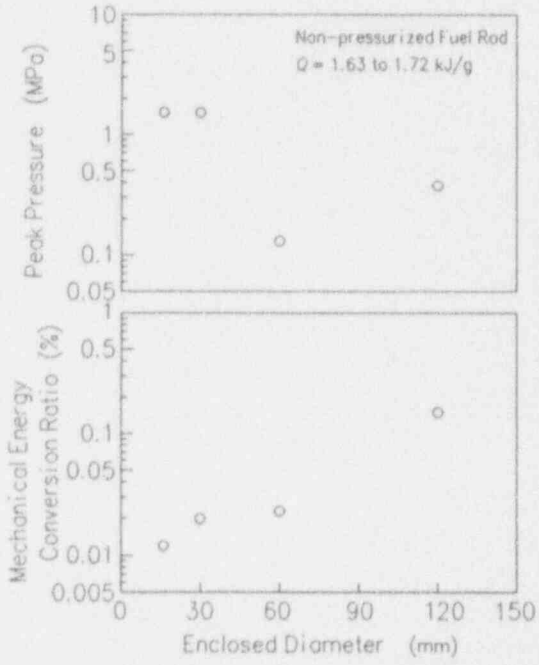

Fig. 7 Peak pressure and mechanical energy conversion ratio versus enclosed diameter

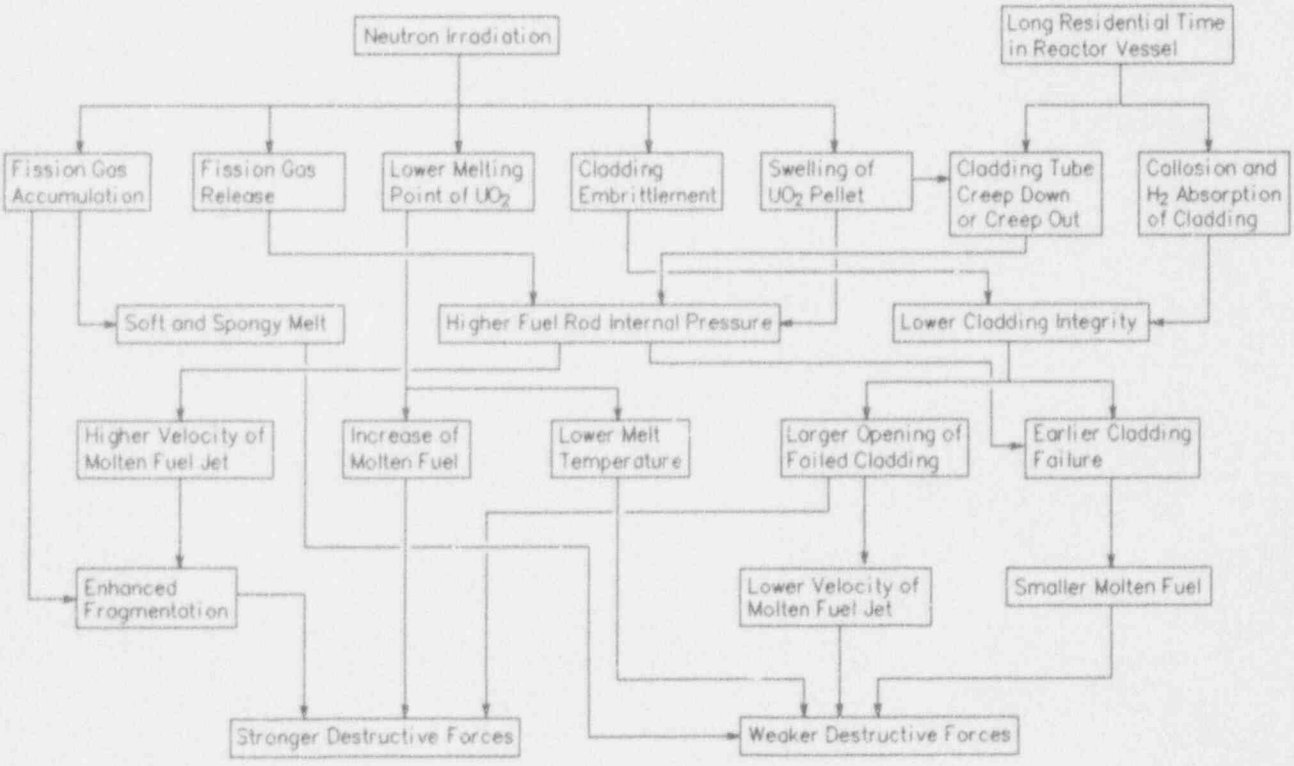

Fig. 8 Possible burnup effects on FCIs in an RIA

around the test rod was controlled. By employing arrangements of 16 mm, 30 mm and 60 mm diameter shrouds, or with no shroud present (equivalent to an enclosed diameter of 120 mm), the water to fuel cross-sectional ratio was varied from 1.6 to 170. Figure 7 is a plot of the peak pressure and the mechanical energy conversion ratio versus enclosed diameter. The conversion ratio varied by a factor of ten for the range of enclosed diameters studied. Fragmentation is assumed to occur during the course of mixing of the molten fuel jet with the coolant. It follows that the mixing length and thus the fragmentation are both influenced by the enclosed diameter.

Effect of Fuel Rod Internal Pressure The RIA studies are now being focused on the effects of irradiation history on the fuel rod. Figure 8 illustrates possible factors concerning the influence of fuel burnup on generation of destructive forces during a severe RIA. In the NSRR program, the experiment with pre-irradiated fuel has been initiated from 1989 and the energy deposition level will be increased to cause an FCI by 1994. Although the experimental data of FCIs in the experiment with pre-irradiated fuels are not available at present, the experiment with pressurized fresh fuel rod also gives important insights on the behavior of burnup fuel rods under high energy deposition, since fission gas accumulation in the irradiated fuel rods is of primary concern. Figure 9 shows the maximum value of pressure measured at the bottom of the capsule as a function of the initial internal pressure of the fuel rod. The effect of the initial fuel rod internal pressure on the peak pressure for fuel enriched to 20% can be seen from the figure only for the test which had a violent secondary interaction. However, an increase in fuel rod internal pressure results in an increase of the peak pressure for the experiments with 10% enriched fuel. In the experiments with fuel rods having a high initial internal pressure, it is presumed that the jet of fuel expelled from the opening in the failed cladding was accelerated by the pressurized plenum gas in the fuel rod. The mode of mixing of the fuel with the coolant may be affected strongly by the velocity of this fuel jet.

Figure 10 shows the influence of the initial internal pressure of the fuel rod on the thermal to mechanical energy conversion ratio. Most of the data ranged below 0.2% in the figure. The conversion ratios exceeded 0.25% only in three of the tests. These were the two experiments with a fuel enrichment of 10% and high fuel rod internal pressure (7.0 MPa or higher) and also the 20% enriched experiment where the generation of a secondary interaction was observed. The effect of the internal pressure of the fuel rod on the thermal to mechanical energy conversion ratio is more apparent in the experiments with 10% enriched fuel than in the experiments with 20% enriched fuel. Since the fuel used in a commercial reactor has an enrichment much less than 10%, it can be expected that the accumulation of gaseous fission products leading to increased pressure in a fuel rod would affect the intensity of FCIs during an RIA. It should be noted that the accumulation of gaseous fission products in irradiated fuel results not only in the increase of the plenum gas pressure of the fuel rod, but also results in the increased pressure inside the fuel pellets. In the NSRR experiments with irradiated fuel rods, a considerable effect of fission product accumulation on fuel pellet swelling. It could be expected that the accumulation of gaseous fission products, especially in grain boundaries, might have a significant potential to cause vigorous fragmentation. It should also be noted that the fission gas produces soft, spongy melts which might have a contrary effect.

Debris Particle Size Distribution Knowledge of the debris particle size is important in various areas of the safety evaluation of nuclear reactors. In the computer modeling of the damage potential of FCIs, the debris particle size is frequently an input parameter. Knowledge of the debris particle size is also needed to assess the likelihood that finely dispersed core debris will settle. Fission product decay heat might cause such settled fuel debris to remelt and thus cause damage to the core structures or containment. Finally, aerosol sizes must be known to establish mobility, respirability and clean-up capability(Vaughan, 1979). The fragmented fuel debris were sieved to obtain particle size distributions in this study. Since this debris was radioactive, the variation of mesh size was restricted to seven. The mesh openings for the sieves were 4, 2, 1, 0.5, 0.25, 0.125 and 0.074 mm.

To quantify debris particle size distributions, Rosin-Rammler's law was used as the fitted

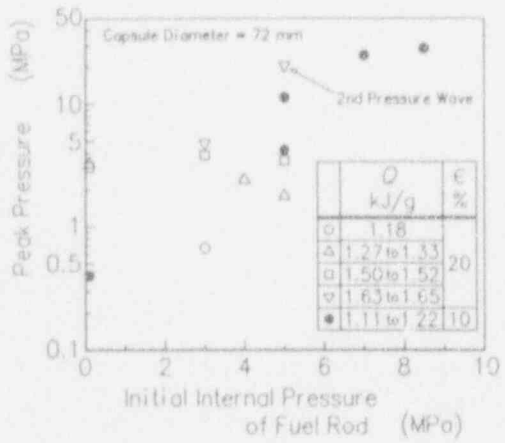

Fig. 9 Peak pressure versus initial internal fuel rod pressure

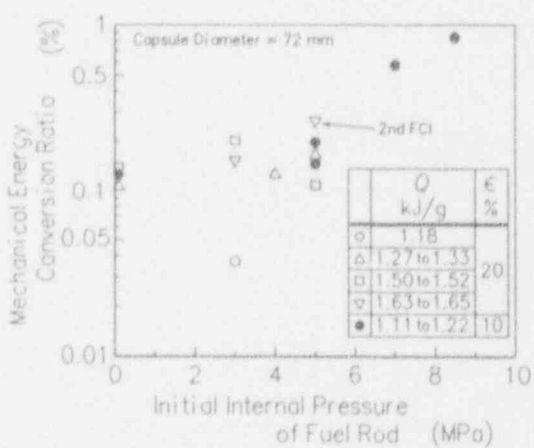

Fig. 10 Mechanical energy conversion ratio versus initial internal fuel rod pressure

function(Tsuruta et al., 1985). In Rosin–Rammler's law, the distribution function is given by:

$$R(D_p) = 1 - \exp\left[-\left(\frac{D_p}{D_e}\right)^n\right] \quad (4)$$

where $R(D_p)$ denotes the mass fraction of the fragments smaller than the diameter D_p, and D_e and n are the parameters of size and of deviation, respectively. For each experiment, the sieved particle size distribution was fitted by Rosin–Rammler's distribution function using a least-squares algorithm. In each experiment, the fraction of collected debris to the mass of fuel ranged from 70% to 98%. In obtaining the parameters D_e and n, it was assumed that diameters of uncollected debris particles were smaller than 0.25 mm. Rosin–Rammler's distribution was then applied to the experimental data, including the masses of particles having diameters below 4, 2, 1, 0.5 and 0.25 mm. Good applicability of Rosin–Rammler's function to the debris particle size distribution is obtained in the experiments.[2] The distribution parameter n ranged from 0.22 to 1.17 in this study. When n becomes larger, Rosin–Rammler's distribution approaches the lognormal distribution. For the case when n is three or higher, the lognormal distribution should be used for the fitted function. Another possible fitted distribution is the upper limit lognormal (ULLN) distribution(Fletcher, 1988). It should be noted that the ULLN distribution needs three parameters concerning particles; maximum size, location and scale. Therefore, Rosin–Rammler's distribution was used in this study because of its simplicity and wide applicability.

As an index for fragmentation, specific surface area S_w, defined as the total surface area of the particles per unit mass, is derived by the integration of the fitted distribution as follows:

$$S_w = \phi \frac{n}{\rho D_e^{\,n}} \int_{D_{p,min}}^{D_{p,max}} D_p^{\,n-2} \exp\left[-\left(\frac{D_p}{D_e}\right)^n\right] dD_p + \frac{1-\exp\left[-\left(\frac{D_{p,min}}{D_e}\right)^n\right]}{\rho} \frac{\phi}{D_{p,min}} \quad (5)$$

The geometric factor for fragmented debris particles, ϕ, is assumed to be six, which means particles are spherical and dense. This assumption allows a conservative estimate of the surface area to be derived from the debris particle size distribution. Porous debris has been observed in many steam explosion experiments. In this study, numerous porous debris was also observed. However, the spherical, dense particle assumption has been used for many studies because of the difficulty in estimating the particle geometry factor. Therefore, although the absolute values of the debris particle surface area are subject to uncertainty, it may be of value to compare the data with this series of experiments. As for $D_{p,max}$, the diameter when $R(D_p)$ becomes 99.9% was adopted. $D_{p,min}$ = 0.001 mm was also assumed. This value seemed to be realistic from the observation of debris by a scanning electron microscope. Another possible index for the degree of fuel fragmentation is the volume–surface mean diameter D_s, defined as the ratio of the total volume of fragments to the total surface. D_s can be related to the specific surface area S_w, as follows:

$$D_s = \frac{\phi}{\rho S_w} \quad (6)$$

The correlation between the specific surface area of the debris and the peak pressure measured at the bottom of the test capsule during the experiments for the effect of fuel rod internal pressure is shown in Fig. 11. The results indicate that higher peak pressure correlates with larger specific surface area, that is, finer debris. Figure 12 shows the correlation between the specific surface area of the debris and the thermal to mechanical energy conversion ratio. When the specific surface area is more than 3000 mm^2/g,

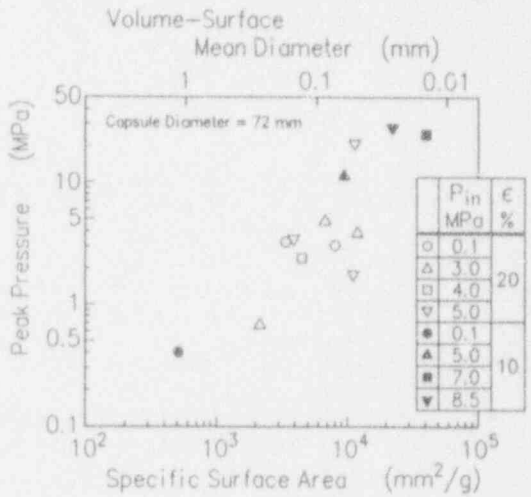

Fig. 11 Peak pressure as a function of specific surface area of fuel debris

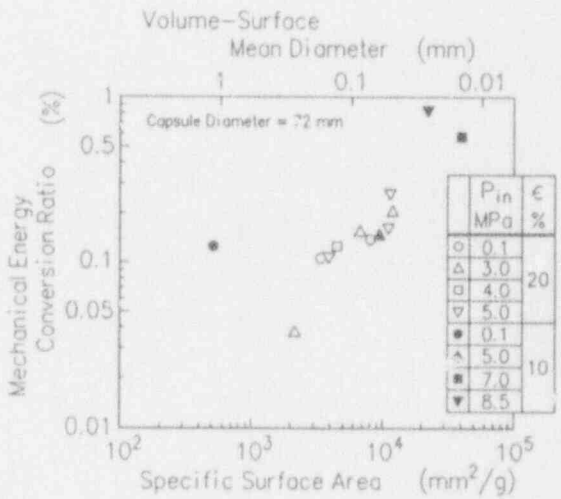

Fig. 12 Mechanical energy conversion ratio as a function of specific surface area

the conversion ratio is also well correlated with the surface area. Therefore, the specific surface area of the fragmented fuel would serve as a good measure of the peak pressure and conversion ratio, which in turn gives a good indication of the intensity of FCIs.

III. OUT-OF-PILE EXPERIMENT

A. Experimental System

The loop used in the out-of-pile experiment is illustrated in Fig. 13. A test vessel of 80 mm in inner diameter and 1000 mm in length is filled with stagnant water. A small preheater at the bottom part of the vessel controls initial water temperature. The upper part of the vessel is connected to a separator by a glass pipe of 10 mm in inner diameter and 500 mm in length. Inertia force of efflux water from the test vessel is mainly controlled by the length of the glass tube. At the exit of the glass tube, a small impact tube is installed to measure efflux velocity of water. On both sides of the test vessel, windows are set to observe transient phenomena around the heated rod by a high speed camera. A piezo-electric type pressure transducer with the response time of less than 1 μs is mounted on the wall of the vessel. A stainless steal rod with diameter of 4 mm and length of 100 mm is installed at the center of the vessel. The rod is transiently heated by large electric current produced by discharge from a power condenser bank of 2000 μF. The discharge time is about 4 ms. This value is almost equivalent to the width of reactor power in the pulse irradiation of the NSRR. In the out-of-pile experiment, the electric power input is shut down when the rod is dispersed. Even in reactor transients the additional heat generation in dispersed fuels by fission and disintegrations of fission products is negligible after the loss of the fuel rod geometry. Therefore, the out-of-pile experiment can well simulate boiling phenomena around the dispersed melt. Though the temperature of the heated rod

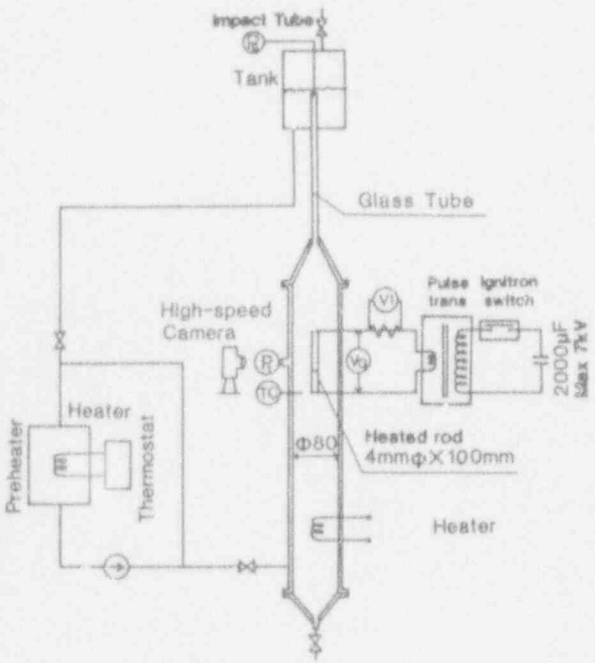

Fig. 13 Out-of-pile experiment loop

was not measured in the experiment, it was ascertained in the preliminary experiment that the average temperature estimated from the input energy under the adiabatic condition was almost equivalent to the temperature measured by the resistance method. Therefore, heat transfer from the rod surface to the ambient water is negligible in comparison with the heat capacity of the heated rod. As the heat capacity of the stainless steel is about 0.49 J/g·K, the input energy density of 750 J/g·SS is roughly correspond to the temperature rise of 1530 K. The initial pressure and water subcooling were varied from 0.1 MPa to 0.3 MPa and from 5 K to 110 K, respectively. The input energy density ranged from 650 J/g·SS to 950 J/g·SS.

In the out-of-pile experiment, the mechanical energy is obtained as follows;

$$K_e = \int_0^{\infty} v(t)(p_t(t) - p_0)A\,dt \qquad (7)$$

where efflux velocity, v(t), is obtained by;

$$v(t) = \int_0^{t} \frac{p_t(t) - p_0}{\rho_l L_t}\,dt \qquad (8)$$

Then the conversion ratio in the out-of-pile experiment is defined as a ratio of mechanical energy, K_e, to total energy input by the Joule heating.

B. Results and Discussion

Pressure Generation The heated rod becomes molten with the input energy density of 650 J/g·SS or higher. A series of photographs taken by the high speed camera and the corresponding pressure history are shown in Fig. 14. In the pressure plot, the history measured in the experiment with lower input energy density, resulting in non-melting of the heated rod, is also shown by a broken line. During a nucleate boiling stage, pressure peaks recorded in the experiment with the high input energy density, i.e. the melting case, are less than 0.2 MPa, and notable difference can not be seen in comparison with the non-melting case. However, pressure increases rapidly to ten times higher value comparing with that of non-melting case when the melting occurs. With the large input power resulting in the heated rod melting, both nucleate and film boiling periods become very short (1 ms) and the temperature of the rod reaches to the melting point for short time. Then, the upper end of the heated rod is broken at 1.4 ms after the initiation of heating, and an electric spark is generated (Photo (b)). Pressure reaches the maximum at 2.8 ms between photos (c) and (d) in the early stage of fragmentation and dispersion of the melting rod. By the hoop stress caused by the electric current, the heated rod is deformed and broken at both ends and at the center. In these observations melting metal is ejected and dispersed like a water jet. It can be noted that the melting and the fragmentation process in the early stage has an important role for generation of an intensive pressure peak.

Peak Pressure Relations between the peak pressure and the input energy density in two different subcoolings are

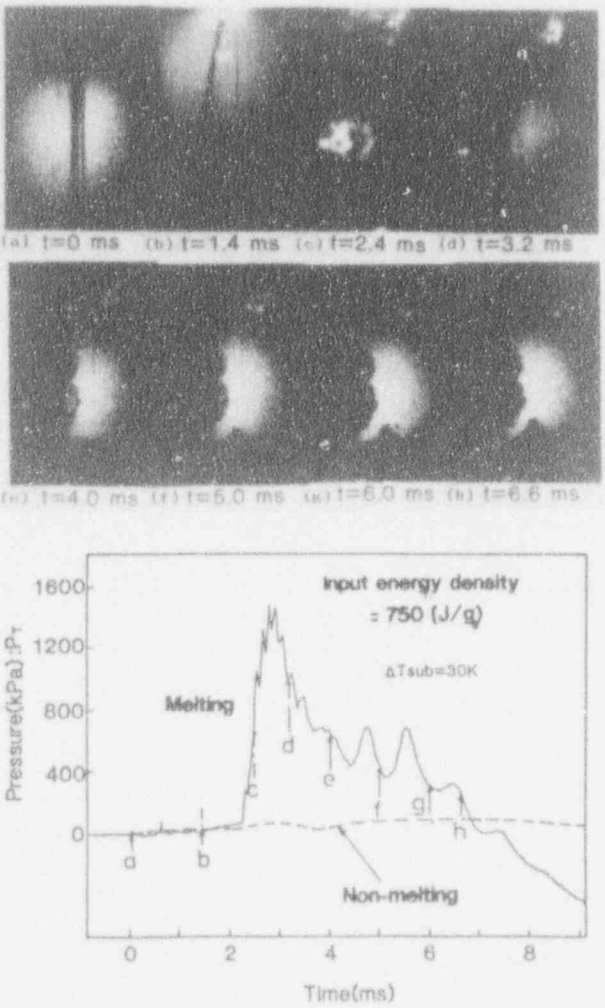

Fig. 14 Photograph by high speed camera and the corresponding pressure history

shown in Fig. 15. The peak pressure increases monotonically with the increase of the input energy density up to 950 J/g·SS. The effect of water subcooling on maximum peak pressure are shown in Fig. 16. In the case of input energy density of 830 J/g·SS, maximum of the peak pressure appears at water subcooling of 25 K. The results indicate that there is the most suitable subcooling to generate the peak pressure.

Mechanical Energy Conversion Ratio Figure 17 shows the experimental result of the mechanical energy conversion ratio as a function of the input energy density. The conversion ratio increased with the input energy density both in the two different water subcooling conditions. Maximum value of the conversion ratio obtained in the experiment is approximately 0.01%. This value is considerably small in comparison with melt drop type experiments. One possible reason is that the pressure measured at the wall of the test vessel is not equal to that generated in the vapor film. If pressure propagates as a cylindrical acoustic wave, the measured pressure must be multiplied by $(r_w/r_f)^{0.5} = 4.5$, because the pressure decays

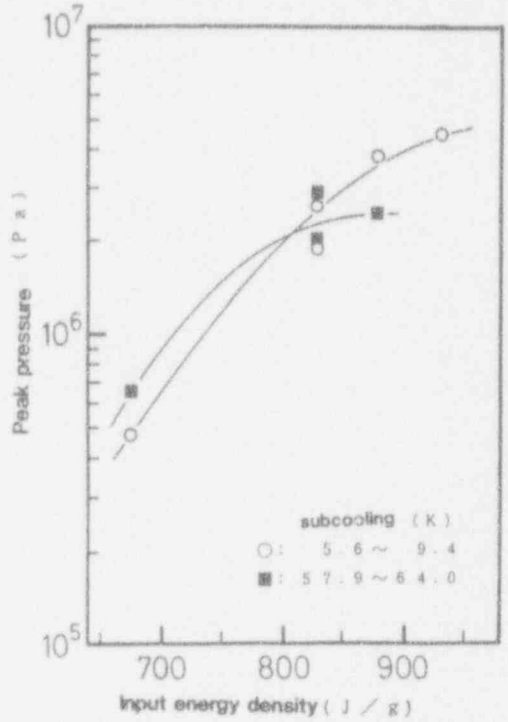

Fig. 15 Peak pressure versus input energy density

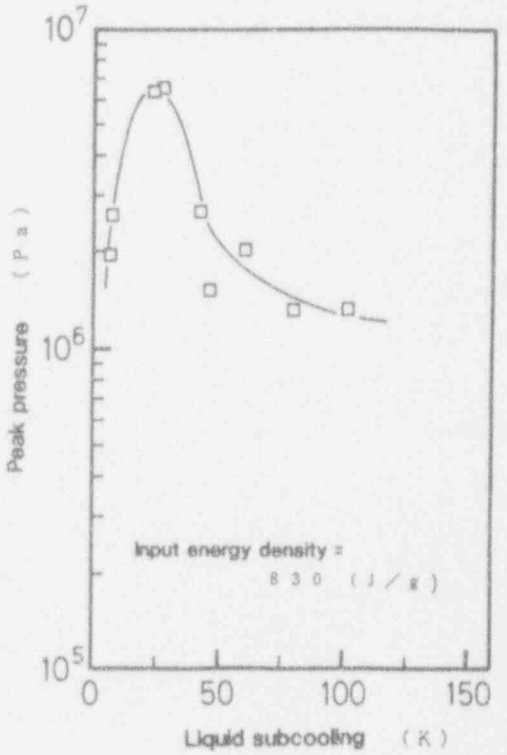

Fig. 16 Peak pressure versus coolant subcooling

inversely proportional to square root of the distance from the cylindrical pressure source in the heated rod to the wall. Here, r_f and r_w are radii of the heated rod and the test vessel, respectively. Considering this correction, maximum

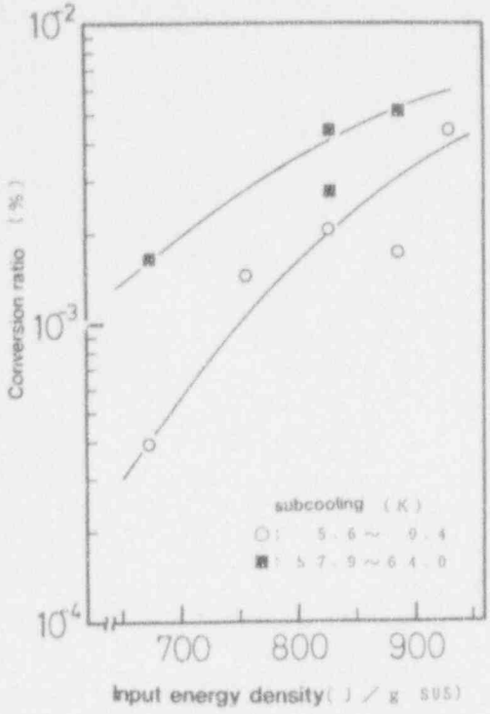

Fig. 17 Mechanical energy conversion ratio versus input energy density

conversion ratio obtained in the experiment becomes about 0.045%.

Debris Particle Size Distribution The size distribution of the debris fragmented during the out-of-pile experiment is shown in Fig. 18. The mass ratio of particles with less than 100 μm in diameter to the total mass ranged 30% to 70%. Because only limited data are available at this stage, it is difficult to discuss the influence of test conditions to the fragmentation. However, it can be seen that the large subcooling condition results in the production of finer debris.

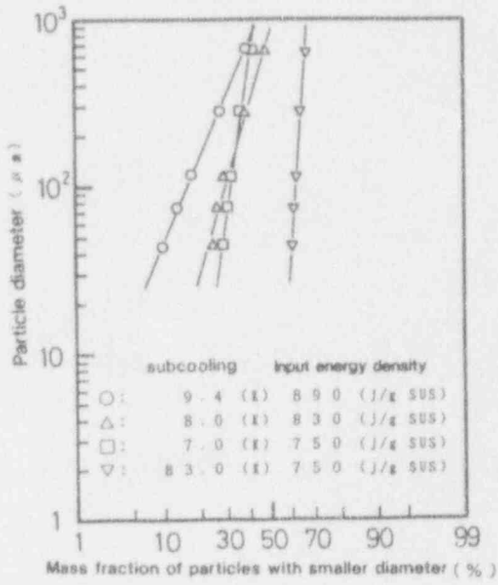

Fig. 18 Debris particle size distribution obtained in out-of-pile experiments

IV. ANALYSIS

A. Model

According to the observation by a high speed camera in the out-of-pile experiment, fragmentation process of the heated rod can be described as the following manner.

1) Formation of thermal boundary layers in both solid and liquid
2) Incipient boiling and onset of nucleate boiling
3) Transition from nucleate boiling to film boiling
4) Melting and fragmentation of the heated rod
5) Cooling of the dispersed particle

The model was formulated under the following assumptions.

1) One dimensional heat transfer model
2) Film boiling directly follows the incipient boiling since the duration of nucleate boiling is very short.
3) Interface between vapor and liquid is kept at the saturation temperature

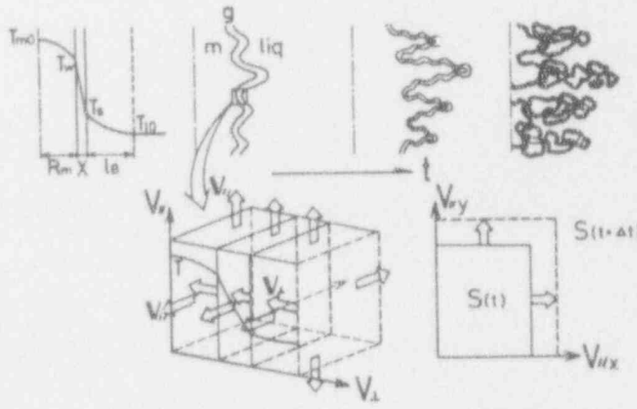

Fig. 19 Conceptual description of surface stretch model

4) Superheated vapor in the vapor film follows to the ideal gas law

During the melting and dispersion processes of the heated rod, two mechanisms can play a leading role with respect to enhancement of heat transfer. One is the increase of heat transfer area due to the fragmentation, and the other is decrease of thicknesses of thermal boundary layer and vapor film due to the stretch of surface. Schematics of surface stretch model proposed in this study is shown in Fig. 19.

The interface stretching rate $\dot{S}/S$ during fragmentation can be described as follows. The continuity equation is described as;

$$\nabla \cdot V = \nabla_{//} \cdot V_{//} + \nabla_{\perp} \cdot V_{\perp} = 0 \qquad (9)$$

where, subscripts of // and ⊥ denote components of parallel

and normal directions to the surface. As describing in Fig. 19, the stretching rate becomes;

$$\nabla_{//} \cdot V_{//} = \frac{\dot{S}}{S} \tag{10}$$

Then from Eq. (9),

$$\nabla_{\perp} \cdot V_{\perp} = -\frac{\dot{S}}{S} \tag{11}$$

As temperature gradient in the stretching direction is negligible;

$$\nabla_{//} T = 0 \tag{12}$$

then an energy balance equation is described as follows;

$$\frac{\partial T}{\partial t} + (V_{\perp} \cdot \nabla_{\perp})\, T = \nabla_{\perp}(\kappa \nabla_{\perp} T) + \frac{\dot{Q}}{\rho C_p} \tag{13}$$

When Eq. (13) is integrated over thickness δ of thermal boundary layer or vapor film, the following equation is obtained.

$$\frac{\partial \bar{T}}{\partial t}\delta + [V_{\perp} T]_0^{\delta} - \int_0^{\delta} T\,[\nabla_{\perp} \cdot V_{\perp}]\, dr_{\perp} = \nabla_{\perp}(\kappa \nabla_{\perp} T) + \frac{\dot{Q}}{\rho C_p} \tag{14}$$

where T is the averaged temperature across δ. When one side of the boundary layer or the vapor film is fixed, velocity of the other side become;

$$V_{\perp}(\delta) = -\frac{\delta \dot{S}}{S} \tag{15}$$

Then, Eq. (14) becomes,

$$\frac{\partial \bar{T}}{\partial t} + [\bar{T} - T(\delta)]\frac{\dot{S}}{S} = \frac{\kappa}{\delta}[\nabla_{\perp} T(\delta) - \nabla_{\perp} T(0)] + \frac{\dot{Q}}{\rho C_p} \tag{16}$$

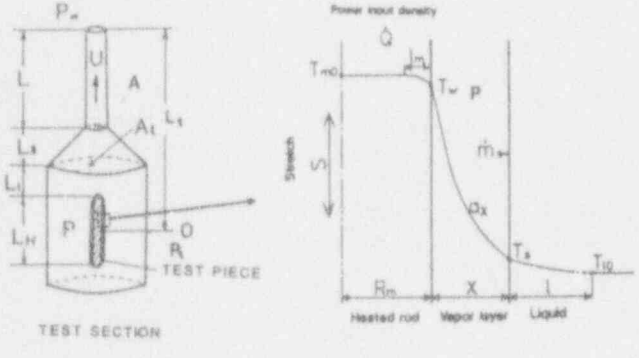

Fig. 20 Heat transfer model around heated rod

The effect of heat transfer due to surface stretch is described by the second term of left hand side in this equation. In the proposed model including the surface stretch concept, it is assumed that the cylindrical heated rod elongates axially according to the surface stretch function, S(t)/S(0). Figure 20 illustrates the heat transfer model during the film boiling stage. The second order temperature profiles are assumed in the thermal boundary layers of the heated rod and liquid and in vapor film. Then, the boundary layer integral method is applied. The proposed model consists of;

1) Energy equations of the thermal boundary layers in the heated rod and the liquid,
2) Mass and energy equations of vapor film during film boiling,
3) Momentum equation of the efflux liquid,
4) State equation of the vapor and saturation condition at the vapor/liquid interface,
5) Equations of mass and energy fluxes at the metal/vapor and vapor/liquid interfaces,
6) Empirical correlations concerning the superheat of incipient boiling(Okuyama, 1986), and
7) Surface enhancement function.

The details of the formulation are presented in Ref.(Inoue et al., 1992). To get the surface enhancement function S(t), it is necessary to know the dynamics of fragmentation. Though numerous possible mechanisms have been proposed in terms of fragmentation, pressure induced fragmentation seems most applicable to the current study since there are many pressure pulse sources, boiling and/or condensation, around the melting rod. Several fragmentation models based on the boundary layer stripping, the Taylor instability and the entrapment by the micro jet have been investigated. However, they are applicable to fragmentation under larger pressure shock or pulse. Therefore, the surface enhancement function was derived from the following consideration. It is assumed for the fragmentation process that the melting metal which has initial surface area of $\Delta S(0)$ per unit length of the heated rod is successively divided by instability as described in Fig. 19. When an initial spherical particle with radius of R_{m0} is divided successively into n particles with radius of r_i after i times division,

$$R_{m0}^3 = n r_1^3 = n^2 r_2^3 = \cdots = n^i r_i^3 \tag{17}$$

When the growth rate due to the surface instability can be assumed as a constant c, the fragmentation time, Δt_i, of particle with radius of r_{i-1} can be described as follows;

$$\Delta t_i = \frac{r_{i-1}}{c} = R_{m0}\frac{n^{-(i-1)/3}}{c} \tag{18}$$

When the average radius of particle becomes r_b after k times division, the fragmentation time τ_b becomes,

$$\tau_b = \sum_{i=1}^{k} \Delta t_i \frac{R_{m0}}{c}\left(\frac{1-n^{-k/3}}{1-n^{-1/3}}\right) = \frac{R_{m0}-r_b}{c(1-n^{-1/3})} \tag{19}$$

and time needed for i times division, t_i is,

$$t_i = \frac{R_{m0}}{c}\left(\frac{1-n^{-i/3}}{1-n^{-1/3}}\right) = \frac{R_{m0}-r_i}{c\,(1-n^{-1/3})} \tag{20}$$

From Eqs.(19) and (20),

$$r_i = r(t_i) = R_{m0} n^{-1/3} = R_{m0}\left(1 - \frac{R_{m0} - r_b}{R_{m0}\tau_b} t_i\right) \quad (21)$$

The number of particles $n(t_i)$ at time t_i(s) becomes from Eq. (17),

$$n(t_i) = n^i = \left(\frac{R_{m0}}{r(t_i)}\right)^3 \quad (22)$$

and total surface area, $S(t_i)$ at t_i is,

$$S(t_i) = 4\pi r(t_i)^2 n(t_i) L_H = S(0)\left(1 - \frac{R_{m0} - r_b}{R_{m0}\tau_b} t_i\right)^{-1} \quad (23)$$

$$for \quad 0 < t_i < \tau_b$$

and

$$S(0) = \Delta S(0) L_H = 4\pi R_{m0}^2 L_H \quad (24)$$

where L_H and R_m are described in Fig. 20 and R_{m0}, r_b and τ_b are the initial radius of heated rod, final radius of the fragmented particles and the fragmentation time, respectively. The final radius r_b and the fragmentation time τ_b are set at 50 μm and 3 ms from the post test examination on debris. The set of equations is solved numerically by the Runge-Kutta scheme with variable time mesh.

B. Numerical Results and Comparison with experimental data

Pressure Trace The numerically predicted pressure history is compared with the experimental data in Fig. 21. The first small peak is generated by the transient boiling around the pre-melting heated rod and the second large peak is caused in the period of melting and fragmentation of the heated rod. Since the relatively small surface enhancement function is used in this calculation in order to have good agreement with respect to maximum pressure, the pressure peak of the analysis appears much later than that recorded in the experiment. However, the analysis with the larger surface enhancement function results in generation of the higher pressure. The transient histories of the input energy density, surface enhancement rate, pressure and efflux velocity in the analysis are illustrated in Fig. 22.

Peak Pressure and Mechanical Energy Figure 23 shows the analytical and experimental results of the peak pressure as a function of the input energy density. Although the analysis predicts higher peak pressure than the experimental data, the dependency on the input energy density is well described by the analysis. Relation between the mechanical

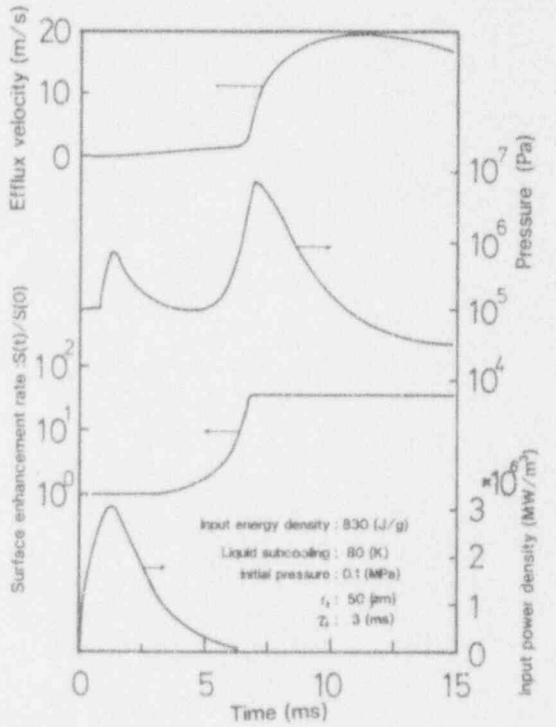

Fig. 22 Transient histories of parameters in the analysis

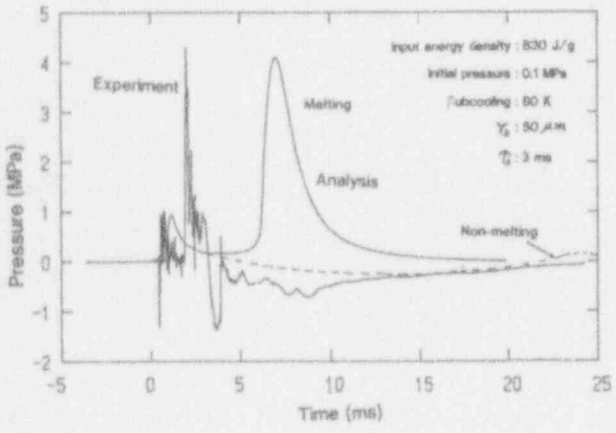

Fig. 21 Pressure histories during transient

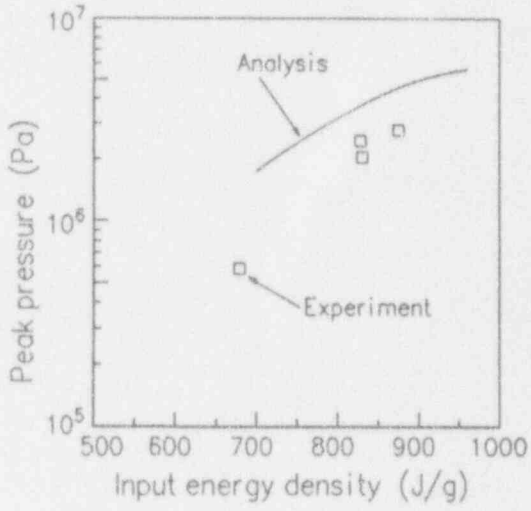

Fig. 23 Peak pressure versus input energy density

energy and the input energy in the conditions of water subcooling of 60 K and initial pressure of 0.1 MPa is shown in Fig. 24. The analytical result of the mechanical energy shows the similar trend as the experimental data, but the calculated mechanical energy is about ten times higher than the experimental data. As it can be seen in pressure histories in Fig. 21, time span of the second peak in the analytical result is much wider than the peak recorded in the experiment. In the analysis, it is assumed that the whole heated rod is melt and fragmented at same time. On the other hand, the peak pressure appears in the experiment when the both ends and the center of the heater rod are melt and fragmented, as shown in Fig. 14. This difference could result in the relatively large discrepancy between the analysis and the experiment. As shown in Fig. 25, the conversion ratio shows the same trend as the mechanical energy. As noted previously, maximum value of the conversion ratio obtained in the experiment is approximately 0.01%, and it becomes about 0.045% by employing the correction concerning pressure decay during propagation. In the analysis, maximum conversion ratio becomes near 0.1%

Parameter sensitivity Sensitivities of the water subcooling, fragmentation time and particle size to peak pressure and mechanical energy generation are examined in the analysis. Each effect is shown in Fig. 26(a), (b) and (c), respectively. In the analysis, the superheat temperature of the transition to film boiling increases with the water subcooling. Then the larger subcooling results in the increased heat flux from the melt to the water and in the higher pressure peak. On the other hand, the duration time of the pressure generation decreases in the large subcooling condition due to the large condensation rate of steam. The mechanical energy is derived from the integration of the pressure with respect to time, so the larger subcooling results in the lower mechanical energy. The decreases of the fragmentation time and particle size cause the higher pressure and the larger mechanical energy.

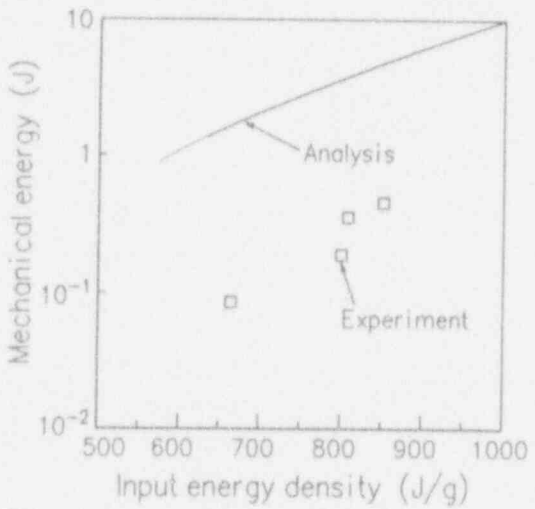

Fig. 24 Mechanical energy versus input energy density

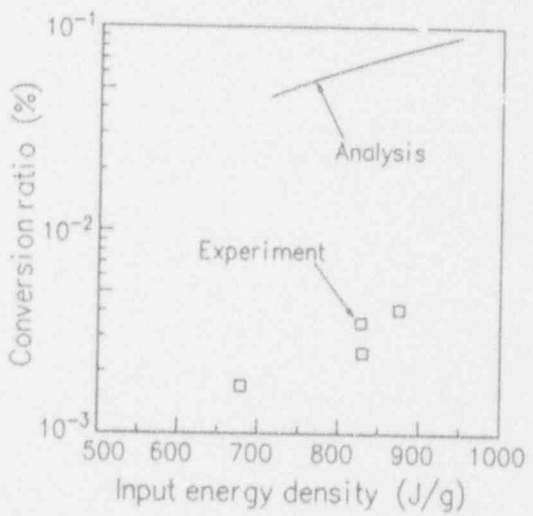

Fig. 25 Mechanical energy conversion ratio as a function of input energy density

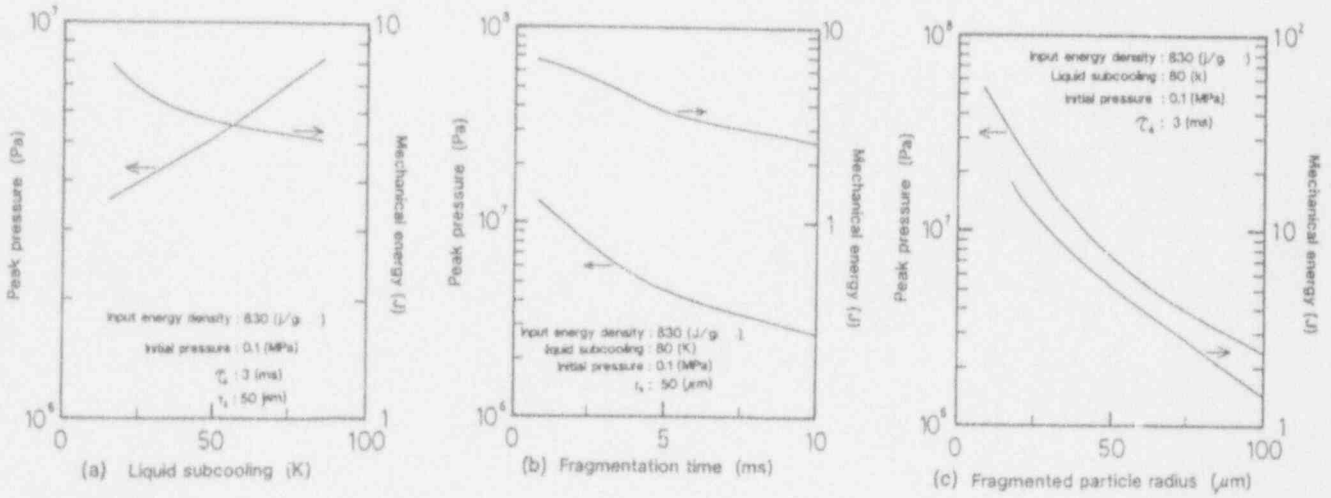

Fig. 26 Sensitivities of coolant subcooling, fragmentation time and fragmented debris radius on mechanical energy

V. SUMMARY

The generation of destructive forces during FCIs in a severe RIA was demonstrated through the in-pile experiments with a LWR uranium dioxide fuel. Transient behavior of the rod during a severe power transient was also investigated in the out-of-pile experiment by the Joule heating of a stainless steal rod. The analytical model including surface stretch during melting and fragmentation was developed, and its applicability to the out-of-pile experiment was discussed.

The effects of the energy deposition, coolant conditions and fuel rod internal pressure on the generation of destructive forces were extensively investigated in the NSRR experiments. The results are summarized as follows:

(a) For non-pressurized fresh fuel rods, threshold enthalpy for the initiation of FCIs is about 1.4 kJ/g·UO_2. Breach of the cladding and resultant ejection of molten fuel into the coolant seems to be major mechanism for this condition.

(b) The increase of hydrogen generation due to the occurrence of fuel fragmentation can be observed, but this effect is not vigorous. It is thought that the most of hydrogen is generated from cladding oxidation.

(c) Decreasing the coolant subcooling reduces the mechanical energy conversion ratio but this effect is not important for large energy depositions of around 2.0 kJ/g·UO_2.

(d) The mechanical energy conversion ratio decreases when the water/fuel ratio is decreased, possibly because of the reduced mixing length of molten fuel jet in the coolant.

(e) Intense pressure waves, which had a peak pressures higher than 24 MPa, are measured in experiments with highly pressurized fuel rods. It is expected that a hydrodynamic effect results in enhanced mixing of the molten fuel with the coolant.

(f) The effect of the fuel rod internal pressure is more apparent in experiments with fuel enriched to 10% than in experiments with 20% enriched fuel. An intensive FCI can be expected in the case of irradiated fuel rods in a commercial reactor, which will have a lower enrichment and increased pressure due to the accumulation of the gaseous fission products.

(g) The intensity of the destructive forces are well correlated with the specific surface area of debris by using Rosin-Rammler's fitted distribution. The specific surface area of the fragmented fuel would serve as a good measure of the peak pressure and conversion ratio, which in turn gives a good indication of the intensity of FCIs.

The simultaneous acquisition of visual appearance of melting and dispersion of the heated rod and transient pressure history was realized in the out-of-pile experiment. The results obtained in the out-of-pile experiment and the analysis are summarized as follows;

(h) The increase of the input energy results in the generation of the higher pressure peak and the larger mechanical energy.

(i) There is the most suitable coolant subcooling to generate the higher peak pressure.

(j) An analytical model considering surface stretch during melting and fragmentation was proposed. Though the analysis describes the peak pressure, it has considerable discrepancy with the experimental data concerning mechanical energy. Further improvement of the model is needed.

NOMENCLATURE

A	=	Horizontal cross-section area of the out-of-pile test vessel (m^2)
c	=	Factor for unit justification
C_p	=	heat capacity at constant pressure (J/g·K)
D_e	=	Size parameter of the Rosin-Rammler's distribution (mm)
D_p	=	Diameter of the fragmented fuel debris (mm)
$D_{p,max}$	=	Maximum particle diameter for the integration of the fitted distribution (mm)
$D_{p,min}$	=	Minimum particle diameter for the integration of the fitted distribution (mm)
D_s	=	Volume-surface mean diameter (mm)
K_e	=	Mechanical energy generated by FCIs (J)
L_t	=	Length of glass tube (m)
m_f	=	Mass of fuel (g)
m_w	=	Mass of water slug (kg)
n	=	Distribution parameter of Rosin-Rammler's distribution
p_t	=	Pressure in the out-of-pile test vessel (Pa)
p_0	=	Pressure in
P_{gas}	=	Pressure of the capsule plenum gas (Pa)
$P_{gas,0}$	=	Initial pressure of the capsule plenum gas (Pa)
$P_{gas,1}$	=	Peak pressure of the capsule plenum gas (Pa)
P_{in}	=	Initial internal pressure of the fuel rod (MPa)
Q	=	Deposited energy per unit mass of UO_2 fuel (kJ/g)
$\dot{Q}$	=	Input power density in the out-of-pile experiment (W/m^3)
r_b	=	Radius of fragmented particles (m)
r_f	=	Radius of the heated rod in the out-of-pile experiment (mm)
r_w	=	Radius of the test vessel in the out-of-pile experiment (mm)
$R(D_p)$	=	Rosin-Rammler's distribution function of the mass below a given size
R_{m0}	=	Initial equivalent radius of melting metal (m)
S	=	Surface area in interface (m2)
S_w	=	Specific surface area of the fragmented fuel debris (mm^2)
T	=	Temperature (K)
u	=	Velocity of water slug (m/s)
$V_{gas,0}$	=	Initial volume of capsule plenum gas (m^3)
$V_{gas,1}$	=	Volume of capsule plenum gas at $P_{gas}=P_{gas,1}$ (m^3)
$V_\perp$	=	Velocity vector of vertical direction to surface (m/s)
$V_{/\!/}$	=	Velocity vector of parallel direction to surface(m/s)
δ	=	Thickness of boundary layer or vapor film (m/s)
ε	=	Fuel enrichment (%)
η	=	Thermal to mechanical energy conversion ratio (%)
κ	=	Thermal diffusivity coefficient (m^2/s)
κ_g	=	Specific heat ratio of capsule plenum gas
ρ	=	Density (kg/m^3)
ρ_f	=	Density of the fragmented fuel debris (g/mm^3)
ρ_l	=	Liquid density (kg/m^3)
τ_b	=	Fragmentation time (s)
ϕ	=	Geometry factor of the fragmented fuel debris

REFERENCES

Fletcher, D. F., (1988) "The Particle Size Distribution of Solidified Melt Debris from Molten Fuel–Coolant Interaction Experiment", *Nuclear Engineering and Design.*, *105*, 313–319.

Fujishiro, T. and Fuketa, T., (1989) "NSRR Experimental Results on Fuel/Coolant Interaction during a Severe Reactivity Initiated Accident", Proc. 4th Int. Topical Meeting on Nuclear Reactor Thermal-Hydraulics(NURETH–4), Karlsruhe, Germany, October 10–13, 1992, Vol.1, 297–303.

Fuketa, T. and Fujishiro, T., (1992) "Generation of Destructive Forces During Fuel/Coolant Interactions Under Severe Reactivity Initiated Accident Conditions", Proc. 5th Int. Topical Meeting on Nuclear Reactor Thermal-Hydraulics(NURETH–5), Salt Lake City, Utah, September 21–24, 1992, Vol.3, 753–761.

Inabe, T. and Fuketa, T., (1992) "Hydrogen Generation Measurement Tests", *Annual Progress Report on the NSRR Experiments 20*, Reactivity Accident Research Laboratory and NSRR Operation Division, Japan Atomic Energy Research Institute, JAERI–M 92–049, 35–37. (in Japanese)

Inoue, A., Shinano, M. and Hirabayashi T.,(1991) "Fundamental Study on Thermo–Hydraulic Behaviors of a Fuel Channel during a Severe Power Transient", Proc. 1st JSME/ASME Joint Int. Conf. Nuclear Engineering(ICONE–1), Tokyo, Japan, November 4–7, 1991, Vol.2, 227–233.

Inoue, A., Aritomi, M., Takahashi, M. and Shinano, M., (1992) "Experimental and Analytical Study on Vapor Explosion of Melting Heated Rod During A Severe Power Transient", Proc. 5th Int. Topical Meeting on Nuclear Reactor Thermal–Hydraulics (NURETH–5), Salt Lake City, Utah, September, 21–24, 1992, Vol.3, 762–771.

Okuyama, K., (1986) "Study on Transient Boiling Phenomena and Enhancement of Critical Heat Flux during Very High Heat Generation", Ph.D Thesis, Tokyo Institute of Technology.

Tsuruta, T., Ochiai, M. and Saito, S., (1985) "Fuel Fragmentation and Mechanical Energy Conversion Ratio at Rapid Deposition of High Energy in LWR Fuels", *Journal of Nuclear Science and Technology*, *22*–9, 742–754.

Vaughan, G. J., (1979) "Some Theoretical Considerations Concerning Molten Fuel–Coolant Interaction Debris Size", 4th CSNI Specialist Meeting on Fuel–Coolant Interaction in Nuclear Reactor Safety, Bournemouth, April 2–5, 1979.

SAFETY ISSUES RELATED TO

FUEL–COOLANT INTERACTIONS IN BWR'S

T. Okkonen, J. Hyvärinen, K. Haule
Finnish Centre for Radiation and Nuclear Safety (STUK)
P.O. Box 268, SF–00101 HELSINKI, Finland
Telephone Int–358–0–7082354, Fax Int–358–0–7082392

ABSTRACT

The need to understand the physics of fuel–coolant interactions (FCI's) is due to the fact that all severe accidents of light water reactors involve hot material (fuel) attacking water (coolant), or vice versa. In this paper, the boiling water reactors (BWR's) are examined. In addition to the steam explosion loads after core melt pouring into a water pool, FCI's are related to other mechanisms that may threaten containment of a severe accident. The two examples analysed in this paper are the effect of in–vessel coolant behaviour on BWR core degradation and recriticality, and the sensitivity of BWR containments to steam and non–condensible gas generation. As an overall conclusion, gas generation, coolant hydraulics and melt quenching during FCI's play a crucial role in the progression, and the success in management, of a severe BWR accident.

I. PRELUDE

If the contact between fuel and coolant is lost in a light water reactor core, the fuel begins to heat up and without restoration of sufficient cooling will start melting. After such initiation of a so–called severe accident, the reunion of molten material (fuel) and water (coolant), if available, becomes the major driving force for the plant response. In this paper, some risks caused by fuel–coolant interactions (FCI's) in severe accidents of boiling water reactors (BWR's) are discussed. Whether the fuel–coolant contact results in a vast explosion, rather benign gas generation or something in between, the subsequent loads may threaten containment integrity and lead to radioactive releases to the environment.

First in chapter II, the characteristic BWR features relevant to this paper are described. Chapter III includes brief notes on steam explosions. Chapters IV and V are outcome of investigations on accident progression and management actions, for which the FCI phenomena can have a major influence. The effect of coolant behaviour on core degradation and recriticality and the effect of gas generation on containment pressurization, are examined. Chapter VI contains selected accident management considerations, and in chapter VII a summary is given.

II. BWR CHARACTERISTICS

Examples of the FCI–related BWR features are shown below. Features 1 and 5 cause a melt–coolant contact in the pressure vessel (in–vessel) or in the containment (ex–vessel). Features 2–4 make the plant sensitive to FCI effects, such as steam and non–condensible gas (NCG) generation and in–vessel coolant behaviour.

(1) The pressure vessel region (lower plenum) below the core is large in volume.
(2) The metallic control rods can melt and relocate at a lower temperature than fuel.
(3) The core includes a large amount of metals.
(4) The containment is typically small in volume.
(5) In some plant designs, the containment pedestal below the vessel is flooded with water.

For the numerical examples, the fuel parameters of table 1 are used as representing a typical BWR. The selected pressure vessel volumes are shown in figure 1 and they correspond to a 2200 MWt BWR with internal circulation pumps.

The containment volumes of figure 1 have to be viewed as exemplary. In fact, the lower volume ranges resemble older BWR containments (eg. Mark I) and the upper ranges some evolutionary designs (eg. Advanced BWR). The containment design pressure is typically 4–6 bar (40–70 psig) and the failure pressure, depending on prevailing temperature, about twice the design limit.

Table 1. Fuel materials of a BWR.

Materials (kg)	Heat cap (MJ/K)	Heat of fusion (GJ)	Hydrogen prod. *) (m^3)
a 2200 MWt BWR			
UO_2 100'000	40.0	27.4	
Zr 45'000	16.7	10.1	26'500
(ZrO_2 60'900)	32.8	43.0	
a 3300 MWt BWR			
UO_2 140'000	56.0	38.4	
Zr 63'000	23.3	14.2	37'100
(ZrO_2 85'100)	46.0	60.2	

*) If zirconium is fully oxidized. H_2 volume based on (1 bar, 50 °C).

If filtered venting is used to control containment pressurization, it is activated above the design and below the failure pressure. While the basic idea of the pressure suppression into a water pool is the same for all BWR containments, topological and volumetric deviations from figure 1 do exist.

III. STEAM EXPLOSIONS

In most BWR accident sequences, coolant is present in the pressure vessel regions below the core when the fuel begins to melt. After the pressure vessel failure, some containment designs offer a flow path, or an erosive wall, through which molten corium could contact suppression pool water. In some designs, the pedestal is deliberately flooded during an accident in

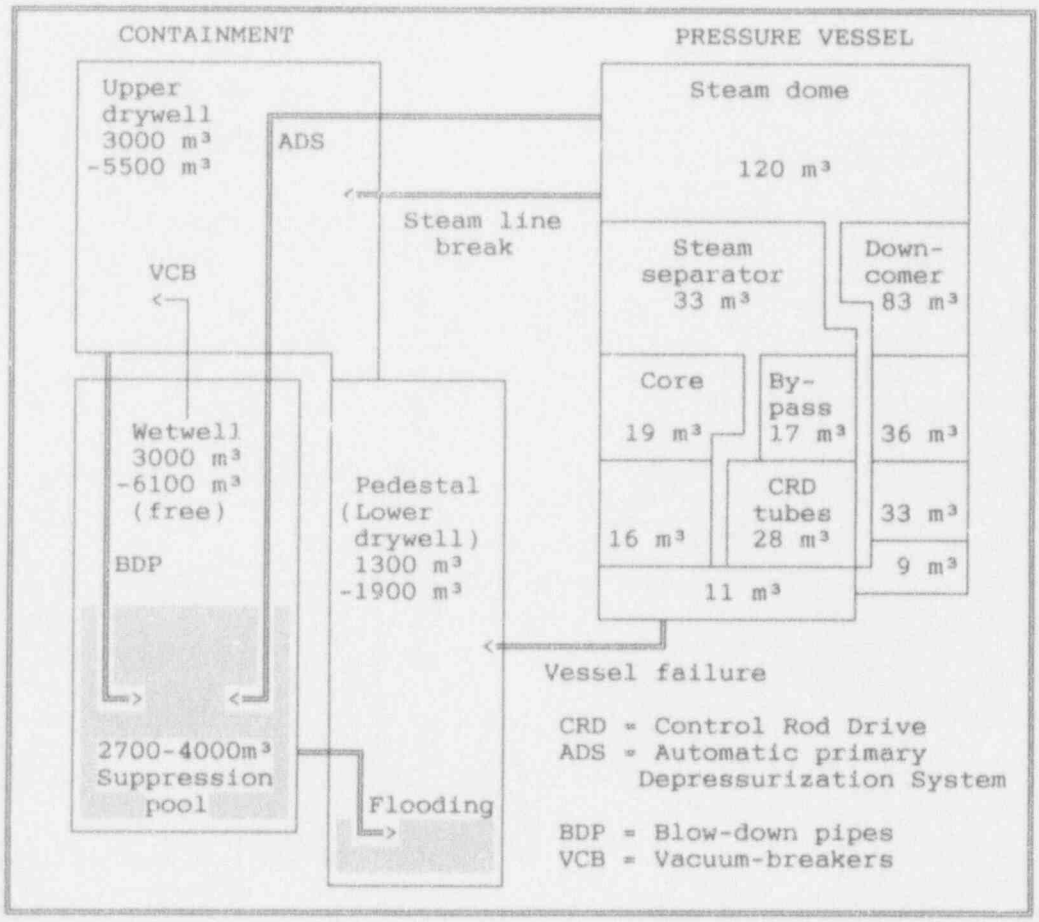

Figure 1. A schematic example of a BWR vessel and containment.

order to enhance corium cooling and to prevent basemat penetration. Filling the containment by water spray is used, design-specifically, to stabilize plant state in the long term. If the pressure vessel were submerged in water, the corium might even be retained inside the pressure vessel. In addition, all the time during an accident, the restoration of core and containment cooling is strived for. For all these scenarios, energetic FCI's called steam explosions are possible either in the pressure vessel or in the containment – after melt pouring into a water pool (pouring mode), coolant covering a molten corium pool (stratified mode) or coolant flowing into the core (reflood mode).

In general, an in-vessel steam explosion strong enough to damage the pressure vessel and containment is considered unlikely (Theofanous et al, 1987), while the uncertainties involved have not allowed universal agreement. In the probability assessments, experimental data and analytical results on fuel-coolant premixing, explosion propagation and vessel's capability are combined with specialist judgment. The lower plenum of a BWR vessel is densely occupied by control rod guide tubes and a coherent, core-wide melt relocation seems unlikely due to numerous (separate) core support plates. These features can limit the potential of fuel-coolant premixing, and the kinetic energy of a steam-explosion-induced water-melt slug may be dissipated by the vessel internals. As a result, a containment failure due to a missile from a slug-ruptured pressure vessel head is estimated even less likely in a BWR than is indicated by the studies focused on PWR's.

The ex-vessel steam explosions have not been studied as extensively as the in-vessel threats, although the conditions in the containment (the fuel-to-water mass ratio, water pool height, water subcooling, containment pressure) could be more favourable for an energetic interaction. The capability of suppression pool columns and surrounding structures to withstand steam explosion loads, after melt pouring into the pool, has been examined (Frid and Torell, 1989; Greene et al, 1992). The possibility of an ex-vessel steam explosion endangering containment integrity has been considered remote (Unger et al, 1989; Frid et al, 1991). Yet the recent experimental results (Alsmeyer, 1992) support the need for more careful, plant-specific studies on stratified interactions, too.

Despite the low probability of a containment failure due to a steam explosion, several specialists have concluded that the potential for an early containment failure and significant radioactive releases calls for further research. The large scales of reactor applications necessitate the development and experimental validation of analytical models on fuel-coolant premixing and explosion propagation. In the following chapters, some other FCI interests than the pouring mode explosions are discussed.

IV. FCI-INDUCED CORE REFLOOD

A. General

In most BWR accident sequences there is a water pool in the vessel lower plenum when the core begins to melt. In this chapter the interest is in cases, where the water level is close to core bottom and melt-coolant contact could lead to inherent core reflood due to effective steam production and subsequent coolant level swelling. Examples of such accident sequences are listed in table 2, which applies for the vessel designs with internal circulation pumps; breaks under the core are thus unlikely.

Table 2 does not include those station blackout cases, in which the primary depressurization is activated late after a significant part of the core has dried out and flashing lowers the coolant level substantially below core bottom. Such an action may be beneficial with regard to the inherent reflood and, in fact, appears to be used in most emergency operating procedures of BWR's. The applied delay between core top uncovery and primary pressure relief cannot be stretched further, in order to avoid coolant swelling and steaming at elevated fuel temperatures and, more importantly, the vessel breach at high pressure.

The reflood of an overheated core is related to several safety concerns: enhanced gas production, resultant containment pressurization (chapter V), fission product release – and reactivity problems, which involve large uncertainties in core melt progression, relocation and in melt-coolant behaviour. Extreme consequences, that is, dispersion of molten fuel into coolant due to excessive fission power generation and a subsequent "burst mode" steam explosion may result, if water enters fast a core region of intact fuel and absent control rods. This chapter is devoted to such concerns, with the special focus on FCI-driven slug penetration into the core. The reactivity-induced fuel fragmentation and the potential fuel-coolant loads have been studied by Fujishiro and Fuketa (1989, 1992) and by Inoue et al (1992); the application of their results, to the consequences of recriticality, is deferred to later papers.

B. Hydraulics

In addition to the lower plenum water inventory, its void fraction must be evaluated to assess the extent of FCI-induced core reflood. In this section, the

Table 2. Severe BWR accident sequences, with large water inventories in the vessel lower plenum when core melt relocation begins.

Initiating event	Operability of core cooling	Timing for (ADS) primary depress.	Primary pressure
statior blackout	none	none	high
small breek LOCA	none	none	medium
station blackout	none	early	low
small break LOCA	none	early	low
large break LOCA	none	irrelevant	low
transient	late failure	early	low
small break LOCA	late failure	early	low
transient	late recovery	early	low
station blackout at refueling shutdown	late failure	irrelevant	low

potential of coolant level swelling is first examined with simple steady-state curves, and then an attempt is made to capture slug generation by using a one-dimensional two-phase flow code. These studies are restricted to averaged conditions over the vessel lower plenum, though separating between the volumes inside and outside the control rod guide tubes. A more detailed assessment would have to address also multidimensional effects.

Figure 2 depicts the steady state void fraction of a saturated water pool. The critical heat flux is obtained with the correlations of Kutateladze and Zuber, and the void fraction with the generalized void fraction correlation of Chexal and Lellouche (Chexal et al, 198x) for a vertical channel with stagnant water. At low pressures, a void fraction of 40 % is reached even if the steaming rate is controlled by critical heat flux against the flow area. At 1 bar, a void fraction of 55 % is caused by a superficial steam velocity of 2 m/s, which corresponds to a saturated steam flow rate of 5 kg/s through a 4 m² flow area, typical for a BWR lower plenum outside the guide tubes. Such a steaming rate can be induced, for example, by molten steel particles of total-mass/diameter 150kg/1cm or 15kg/1mm, assuming a 1 MW/m² melt-to-coolant heat flux. These crude heat transfer examples neglect the feedback from coolant voiding, which may be outweighed by heat fluxes higher than assumed. The averaged, steady-state approach leaves out also local, multidimensional and inertial effects.

At low pressures the void fraction of the lower plenum pool outside the guide tubes can climb high already with moderate steaming rates, caused by small masses of fragmented core melt or massive melt jets spread across the vessel lower head. (The high void fractions are, of course, no news for those investigating steam explosion premixtures.) On the other hand, steady-state estimates are not bounding, if the steaming rate becomes high enough to push coolant upwards as a slug. The transient slug generation has been examined by using a one-dimensional two-phase flow code, RELAP5/MOD2. The goal is to find the worst scenario with regard to the recriticality concerns by mapping out the obtainable core coolant densities as functions of released energy and the release rate.

The RELAP5 analyses have been performed using a standard 2200 MWt BWR input deck. The pressure vessel nodalization scheme is depicted in figure 1; the downcomer, lower plenum and core regions consist of pipe components of roughly ten volumes each. In the lower plenum, the flow areas in and out of the control rod guide tubes are modelled separately, as are also the active and bypass channels (in and out of the cans) in the core. The loss of separation between active and bypass channels in a degraded core is not modelled and thus the bypass remains empty in the analyses. This is not a major drawback, since the actual interest is in the peak, core-average coolant density.

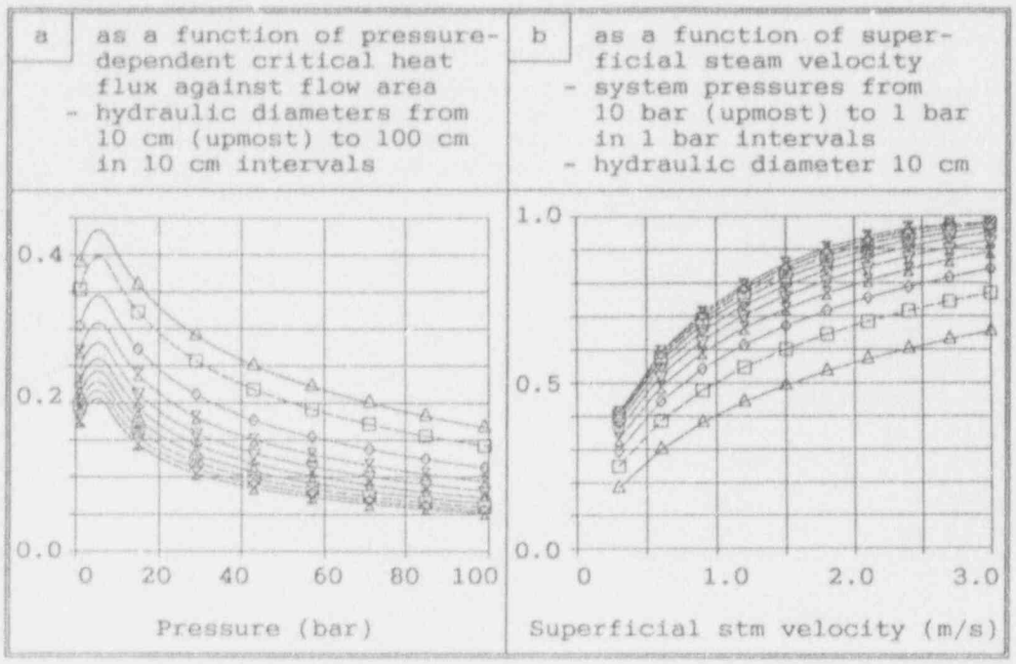

Figure 2. The void fraction of a saturated pool with stagnant water.

The initial conditions correspond to a situation where the core has been uncovered long enough to reach fuel temperatures of about 1400 K so that the control rods are beginning to melt. It is assumed that the whole lower plenum and the downcomer up to core bottom are almost full of saturated water. Other parts of the system are occupied by more or less superheated steam. As boundary conditions, a constant 1.5 % core power, an opening of all safety valves and a 2.0 bar containment backpressure are assumed. The melt heat release is modelled as direct heating into the lowest node of lower plenum. The melt-to-coolant power is determined from a pressure-dependent critical heat flux table and a preset melt surface area, and the duration of heating by a predefined cut-off level for the total heat release. The total energies, 1.3 to 2.5 GJ, correspond to a range of 4-8 tonnes of solidifying melt or 1-2 tonnes of melt quenching to the coolant temperature. The rate of heat release extends from 200 to 2500 MW, and the release periods from 0.5 to 12 seconds.

The results of the calculations are summarized in figure 3. The maximum core coolant densities given there prevail for at least one second, to allow enough time for the reactor power to escalate in case the criticality is reached; the actual peaks can be 50 to 100 kg/m³ higher. The densities refer to active channels and are averaged over the core height. The lower core is less voided during slugging, after which the non-vaporized part of core coolant drains back to lower plenum.

At heat release rates below 300 MW, slug formation does not occur, the pressurization of lower plenum is moderate, and the core is flooded with two-phase mixture which gives maximum core coolant densities well below nominal conditions. This is consistent with the (bounding) flooding criterion of table 3, when the effects of lower plenum pressurization and steam escape to the downcomer are taken into account. With a 1 MW/m² fuel-to-coolant heat flux, the 300 MW power corresponds to fragmented fuel particles of total mass/diameter 8tn/2.0cm or 1tn/2.5mm. While the fuel-to-coolant heat flux is assumed as critical and increases with pressure, the power of figure 3 refers to the average over the heat release period.

At higher powers, slugs form and the core coolant density maxima and the peak lower plenum pressures increase. The density maxima saturate at 900 MW heating power at a level of 600 kg/m³. This is way over nominal in the active core channels, and roughly nominal when averaged over the whole core with an empty bypass channel. The peak lower plenum pressures reach 20 bar. The durations of the slugging and pressure peaks are in the order of a second, implying high dynamical loads on the vessel internals and starting to shorten as the power exceeds 2000 MW. With a 1 MW/m² fuel-to-coolant heat flux, the 900 MW power models fragments of total mass/diameter 8tn/6.7mm or 1tn/0.83mm, and 2000 MW even finer (explosive) fragmentation.

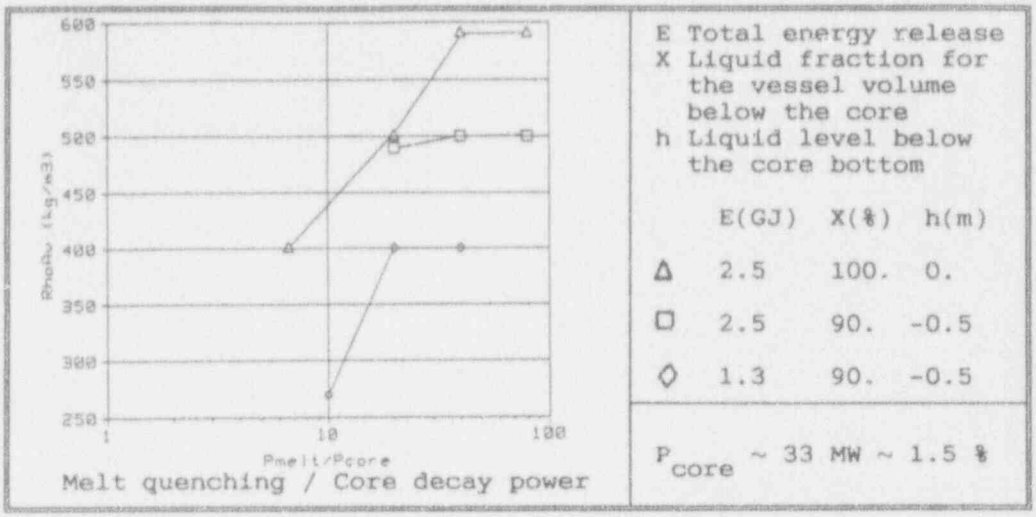

Figure 3. The maximum coolant density inside fuel cans as a function of heat release rate into the bottom head.

Table 3. Flooding in a channel with saturated water (l) and steam (g). Flow area 5 m².

$$Ku_g = j_g \cdot \left[\frac{\rho_g^2}{\sigma g(\rho_l - \rho_g)} \right]^{1/4} \quad (1a)$$

$$Ku_g > 3.2 \; ; \; \text{flooding} \quad (1b)$$

Ku	Kutateladze number (-)
j	superficial velocity (m/s)
ρ	density (kg/m³)
σ	surface tension (kg/s²)
g	acceler. due to gravity (m/s²)
Q	mass flux (kg/m²s)
F	mass flow rate (kg/s)
P	vaporization power (MW)

p (bar)	j_g (m/s)	Q_g (kg/m²s)	F_g (kg/s)	P (MW)
1.0	20.2	11.9	59.7	135.
2.0	14.3	16.1	80.7	178.
5.0	8.93	23.8	119.	251.
10.0	6.17	31.7	159.	320.
20.0	4.04	42.5	213.	399.

During rapid steaming, slug formation will occur also in the downcomer as part of the generated steam is vented through the recirculation pumps. RELAP5 captures this phenomenon, too. The largest downcomer slugs weigh about 20 tonnes but move relatively slowly, rising up to the steam line elevation in about two seconds before gradually disintegrating and falling down. The internal recirculation pumps act as turbines, driven by the steam that escapes from the lower plenum and as reverse pumps after the termination of lower plenum heating. Steam venting into the downcomer also contributes to the saturation of obtainable core-average coolant densities, which decrease with the pre-slugging vessel water inventory as shown in figure 3.

For the FCI-induced slug penetration into the core, maximum coolant densities about nominal when averaged over the whole core, and well above nominal in lower core regions, were obtained. The coolant density peaks prevailed for at least one second and the minimum time periods between slug entrance and peak density were less than one second, yielding coolant penetration velocities above 1 m/s. These results indicate a potential of reactivity concerns, when they are compared to the power excursion characteristics of the following section.

C. Recriticality

A degraded BWR core can become recritical if refilled with unborated water, since the metallic control rods melt at a lower temperature than the ceramic fuel. In contrast to the recriticality due to recovery of emergency core cooling, the FCI-induced "inherent" reflood can keep the core critical only temporarily. On the other hand, FCI's may push the coolant into the core faster than the rather quiet coolant level rise after the core cooling reactivation.

Figure 4 shows the effective multiplication factor for a 2200 MWt BWR core, control rods outdrawn (Anttila, 1990). The same is derived into table 4, again using the results of Anttila, for different fuel burn-ups and average coolant densities, core being full of

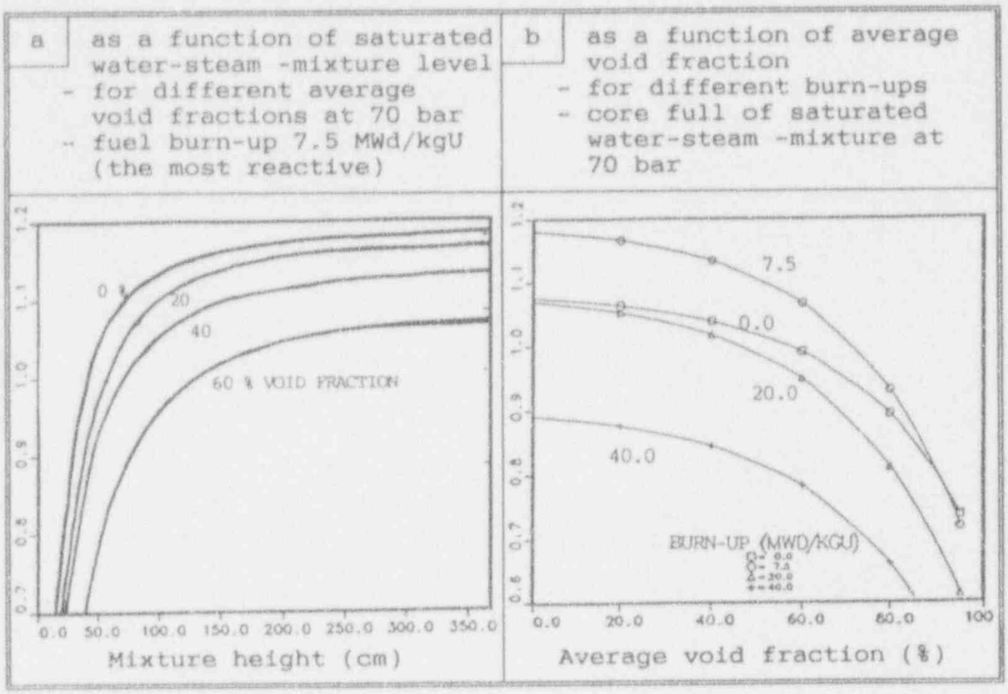

Figure 4. The effective multiplication factor of a 2200 MWt core.

saturated water-steam mixture. The coolant void fraction and density are averaged over the active channels (inside) and the bypass (outside the cans). Table 4 shows also the relation between average coolant density and void fraction for various pressures, and the void fraction in active fuel channels that yields a given core-average void fraction, with the inter-assembly bypass either full or empty of water. This "active" bypass contains 30 % of the moderator volume in the active core without control rods. Although the xenon behaviour and the doppler effect can cause further complications, there exists a potential of superprompt-criticality with intact fuel lengths higher than 1 m and average void fractions below 60 %, if a degraded core without control rods is reflooded with unborated water.

Table 4. The effective multiplication factor of a 2200 MWt core, without control rods, at a fuel temperature of 1500 K.

Average coolant density (kg/m³)				
	740.	599.	458.	318.
Pressure (bar)	Average void fraction (saturation) (%)			
70.	0.	20.	40.	60.
20.	13.	30.	47.	63.
2.	21.	36.	51.	66.
Burn-up (MWd/kgU)	Effective multiplication factor			
0.	1.08	1.06	1.04	0.991
7.5	1.15	1.17	1.13	1.07
20.	1.07	1.05	1.02	0.949
40.	0.891	0.877	0.845	0.783

Density (kg/m³)		
p(bar)	Water	Steam
70.	740.	36.
20.	850.	10.
2.	940.	1.1

Void fraction with
(a) bypass solid
(b) bypass empty

Core average	Active channel	
(%)	(a)	(b)
20.	29.	-
40.	57.	14.
60.	86.	43.

For fast refloods, the reactivity insertion may lead to a rapid, adiabatic fuel enthalpy rise without feedback from the fuel-to-coolant heat transfer and subsequent coolant voiding. In this case, only the doppler effect due to fuel heatup can react fast enough to cut the power peak. From the NSRR experiments (Fujishiro and Fuketa, 1989), the threshold enthalpy for fresh fuel dispersion is 1.36 MJ/kgUO_2, which is essentially the enthalpy of molten UO_2. The enthalpy difference of UO_2 between the control rod melting temperature (1500 K) and the molten state of UO_2 (at 3100 K) is 1 MJ/kgUO_2, including the heat of fusion 0.27 MJ/kgUO_2. For initial fuel temperatures higher than 1500 K, energy depositions somewhat lower than 1 MJ/kgUO_2 may cause fuel melting and dispersion.

As a rough estimate, the formulae for a superprompt-critical fission power peak (Lewis, 1977) are used in table 5. From figure 4a, the derivative of the effective multiplication factor with respect to the coolant level is of the order of 0.0035 1/cm (0.001-0.006 1/cm) or 0.625 \$/cm near the criticality, for the most reactive fuel. Using this in table 5 the reactivity insertion rate, that yields a certain average energy deposition (E), is translated into a rate of coolant level rise (v) in the core. It is worth emphasizing that the peak energy deposition is several times higher than the average of table 5. The superprompt-critical equations are applicable since the transition from criticality to prompt-criticality requires only a few centimeters' increase in coolant level.

For cases where the recriticality is caused by core cooling systems' recovery, the coolant penetration rate into the core has been estimated by assuming the maximum coolant injection rate spread over the total cross-sectional flow area of the core or vessel. However, there may exist a mechanism for a faster local reflood, if a water pool forms on top of the core and suddenly slumps down into some part of the core.

Table 5. A superprompt-critical fission power peak ($P_m >> P_o$).

$$\rho' = \{ 2\omega\Lambda \cdot [\ln(\omega/(\mu \cdot P_o)) - 1] \}^{1/2} \sim (\omega\Lambda)^{1/2} \quad (2a)$$

$$E = 2 \cdot \rho'/\mu \sim (\omega\Lambda)^{1/2}/\mu \quad (2b)$$

$$t' = \rho'/\omega \quad (2c)$$

$$P_m = \omega \cdot \ln(P_m/P_o)/\mu \quad (2d)$$

ρ'	peak reactivity in excess of prompt-critic.	(-)
ω	reactivity insertion rate	(1/s)
Λ	prompt neutron life time	($50 \cdot 10^{-6}$ s)
μ	absolute value of doppler coefficient	(10^{-7} kgUO_2/J)
P_o	power when prompt-criticality is reached	(W/kgUO_2)
P_f	normal operation power	(22000 W/kgUO_2)
E	average energy deposition during the peak	(J/kgUO_2)
t'	time from prompt-critic. to peak reactivity	(s)
P_m	peak power	(W/kgUO_2)

E (MJ/kgUO_2)	ω (1/s)	ω (\$/s)	ρ' (-)	ρ' (\$)	t' (s)	P_m/P_f (-)	v (cm/s)
$P_o/P_f=10^{-10}$							
1.	0.892	159.	0.0500	8.92	0.0561	13200.	255.
0.5	0.234	41.8	0.0250	4.46	0.107	3310.	66.9
0.25	0.0616	11.0	0.0125	2.23	0.203	833.	17.6
$P_o/P_f=10^{-20}$							
1.	0.495	88.5	0.0500	8.92	0.101	12500.	142.
0.5	0.127	22.7	0.0250	4.46	0.196	3130.	36.4
0.25	0.0327	5.84	0.0125	2.23	0.382	784.	9.4

v = the rate of coolant level rise, based on the reactivity increase against coolant level 0.0035 1/cm (0.625 \$/cm).

As obvious from the previous section, such a fast coolant level jump near the criticality may be induced also by FCI's, should core melt relocations coincide with, and temporarily accelerate, the core reflood front. These ingredients, related to recovery actions, are not explored in detail in this paper. It is merely suggested that the potential for unsteadiness may aggravate the recriticality transient during core refill.

A coolant penetration rate of 25 cm/s into a configuration of 4X4 fuel bundles of one-third height was assumed by Scott et al (1990); the coolant injection corresponded to the maximum after core cooling recovery. A reactivity worth of 10 $, the difference between an average void fraction of nominal 40 % and solid 0 % (see table 4), was then added in the 5 seconds' reflood time, the reactivity insertion rate being 2 $/s or 0.08 $/cm. The average energy deposition was estimated to be 0.080 MJ/kgUO_2 and the maximum 0.31 MJ/kgUO_2. A certain coolant penetration rate was estimated to give a reactivity insertion rate 7.8 times lower than figure 4 does, and the doppler coefficient was weighted 1.3 times higher. Combining these and equation (2b), the same unborated coolant injection rate lead to an average energy deposition $1.3(7.8)^{1/2}$ =3.6 times lower than in table 5. In fact, the peak value of Scott et al (1990) is close to the average of table 5 with the upper prompt-critical power.

As an order-of-magnitude estimate, the coolant penetration rate causing fuel melting and dispersion into coolant is around, or somewhat above, 25 cm/s. At the moment, the limit cannot be set higher, especially if a lightly-voided slug rushes into the core. This is due to the results obtained above and the most complicated phenomena and their coupling involved: neutronics, fuel-to-coolant heat transfer, coolant hydraulics - and all in a complicated geometry of a degraded core.

In light of the hydraulic analyses of the previous section, the maximum obtainable reactivities (above prompt-critical), the residence times of corresponding coolant masses in core (at least a second), as well as the maximum coolant penetration rates (above 1 m/s), seem to warrant concern. A more detailed study of the phenomena and mitigation aspects of the BWR recriticality is justified.

D. Core melt behaviour

In the sections above, the FCI-induced reflood and recriticality potentials have been examined only from the hydraulics' and neutronics' point of view. Of course, the way core behaves during melt progression affects both the boundary and initial conditions of the FCI's in the vessel lower plenum. Unfortunately, no well-supported scenario exists and large uncertainties disturb detailed analyses on the late-phase core melt progression.

At the time of melt relocation down to the vessel lower plenum, most of the core may be molten and supported by a crust. Alternatively, there may still be intact, overheated fuel without control rods left especially in the core periphery. In this case, if the coolant rushed into the core as a result of melt-coolant contact, intact fuel and also core debris might become critical. At SNL (USA), experiments and analyses are underway, for example, to examine how relocating metallic melts behave in the lower BWR core regions: do they solidify and block the flow routes or do they penetrate into the lower plenum water pool (Gauntt and Schmidt, 1992). No experiments or experiences on the full-scale BWR core melt progression, addressing the radial effects, are available, though some aspects of the TMI-2 accident may apply also to BWR's. Analytical tools, with insights from small-scale and separate-effect studies, must be used to obtain the initial and boundary conditions of FCI's.

Also the way core melt penetrates and fragments into the lower plenum water pool is important. Melt fragmentation in contact with water, and FCI's in general, have been studied for the steam explosion purposes, and several experimental programs are underway. If core melt relocates down as a jet, the penetration length, before significant fragmentation occurs, affects the boundary conditions of the FCI hydraulics. In the afore-described RELAP5 analyses, the heat was effectively released into the lowermost lower plenum volume. The melt may fragment higher, although the formulae of Schneider et al (1992) and the resuls of Sienicki et al (1992) indicate several meters' penetration, before complete breakup and quenching of a 10cm-diameter jet. Due to the jungle of guide tubes in a BWR vessel lower plenum, the formation and spreading of melt fragments, and their further (fine) fragmentation in case of explosion triggering and propagation, may differ from those in PWR's .

For coolant level swelling, it is important to know the location of most effective steam generation. Both the radial coherence and axial extent of inherent core reflood depend on the coolant void fraction profile and on the energety of fuel-coolant contact and slug dynamics in the vessel lower plenum. For an in-depth assessment, premixing and explosion propagation codes, as well as experimental results, could be utilized.

V. CONTAINMENT PRESSURIZATION

In this chapter, the direct pressurization of an inerted BWR containment, due to steam and NCG production, is discussed. In cases, where molten core material contacts coolant, gas generation during FCI's drives the flows in containment and affects the extent of NCG production. The distribution of NCG's is important when analysing containment pressurization. This is because the volume of hydrogen (at atmospheric pressure), that could be produced from the oxidization of all core metals, is far greater than the containment volume of a typical BWR (see table 1).

In a Loss Of Coolant Accident (LOCA) with a break from the primary system into the containment drywell, the in-vessel gas generation may fill the drywell with steam and pack NCG's into the wetwell atmosphere through blow-down pipes (see fig. 1). In the worst case, the available space for NCG's is only the free volume of wetwell. Special concerns arise, if an overheated core or corium pool is attacked by coolant because of operator actions. Experiments have shown that flooding a hot core with water produces quickly large amounts of NCG's. The containment integrity may be threatened especially in LOCA's with substantially delayed activation of emergency core cooling. However, if the drywell spray is reactivated, it can mitigate containment pressurization (Lin and Lehner, 1991).

In the station blackout cases without primary breaks, all steam and NCG's produced in the primary system are blown straight into the suppression pool via the depressurization system. In this case, NCG's are distributed nearly uniformly into the containment through the wetwell vacuum-breakers, which pass the gases when the pressure in wetwell exceeds the pressure in drywell (in a LOCA, the situation is vice versa). With no major primary breaks, inoperability of primary depressurization system would be of concern due to the vessel breach at elevated pressure and, consequently, high mass and energy release rates (packing power) into the drywell. If high-temperature fluid contents of the primary system are relieved by a high-pressure vessel breach, also the hydrodynamic suppression pool loads add to the spectrum of containment challenges (Lin and Lehner, 1991).

After the pressure vessel failure the molten core materials can produce steam and NCG's in the pedestal, if this is flooded. In figure 1, the blow-down pipes exit from the upper drywell, which again brings the possibility of a drywell filled with steam. In some containment designs, the blow-down pipes exit from the pedestal and most of the NCG's in the upper drywell at the time of vessel breach could be stratified up there, due to the buoyancy of hydrogen. In all the designs with a flooded pedestal, NCG's produced during the ex-vessel melt-coolant-concrete interactions may be blown into the wetwell atmosphere, at least partially.

The partial pressure of NCG's (nitrogen and hydrogen), for a uniform and wetwell-packed distribution, is calculated into table 6 using the lowermost containment volumes of figure 1. Hydrogen production is taken as an equivalent oxidation fraction of either all core zirconium or only cladding. The partial pressure of NCG's is evaluated at a temperature of 50 °C, initial conditions assumed as 1 bar, 50 °C and the whole containment fully nitrogen-inerted. The drywell steam masses at the partial pressure of NCG's are also listed for situations, in which the drywell is full

Table 6. The conditions of a BWR containment (NCG pressures at 50°C).

Condition	2200 MWt core Core Zr oxidized 40 % 70 % 100 % Cladding oxidized 72 % 126 % 180 %			3300 MWt core Core Zr oxidized 40 % 70 % 100 % Cladding ozidized 72 % 126 % 180 %		
Uniform gas distr						
H_2 pressure (bar)	1.45	2.54	3.63	2.03	3.56	5.08
NCG pressure (bar)	2.45	3.54	4.63	3.03	4.56	6.08
All NCG's in WW						
H_2 pressure (bar)	3.54	6.19	8.84	4.95	8.66	12.4
NCG pressure (bar)	5.97	8.62	11.3	7.38	11.1	14.8
Satur temp (°C)	159.	174.	185.	167.	184.	198.
DW steam mass (kg)	13600.	19200.	24800.	15600.	24400.	32200.
Assumed free volumes: drywell (DW) 4300 m³, wetwell (WW) 3000 m³.						

of saturated steam and all NCG's are accumulated into the wetwell. From table 6 it can be seen, that if large amounts of NCG's were produced and packed into the wetwell atmosphere, the containment pressure could climb high, up to design and failure pressures, typically from 4 to 12 bar (from 40 to 160 psig). For wetwell free volumes larger than 3000 m^3, the maximum partial pressure of hydrogen is lowered according to the volume ratio.

FCI's are related to the pressurization of a BWR containment, as described above, in several ways. If hot and unoxidized metals meet water, NCG's are generated (Marshall Jr, 1988; Young et al, 1988). The steam production efficiency, including the effects of inherent core reflood, determines the rate of containment pressurization. The time and mode of a vessel failure, dependent on fuel quenching during the in-vessel FCI's, affect the release rate of primary mass and energy.

VI. ACCIDENT MANAGEMENT ITEMS

If the accident management actions caused a significantly increased likelihood of destructive FCI's, they could be brought under scrutiny and mitigative measures would have to be found, for example the use of coolant additives (Kim et al, 1989; Becker and Lindland, 1991; Ip et al, 1992). Currently, the benefits of, for example, the following actions seem to outweigh the low probability of a large explosion:

Action	Potential benefits
Primary system depressurization	No vessel breach at high system pressure
Core cooling recovery trials	Corium retained inside the vessel
Pedestal flooding	Core-concrete interactions arrested
Containment water-filling	Long-term plant stabilization

A fuel-coolant premixture is more susceptible to explosion triggering at low pressures (Corradini, 1991), but a containment failure due to an in-vessel steam explosion is considered unlikely (chapter III).

The recovery of coolant injection into the vessel is always strived for. The outcome of such an action may change, if core melt slumping causes a lower head failure and coolant leakage out from the vessel. The remains of the core may experience an extended time period of steam and hydrogen generation, without fast refill and quenching. If coolant boration is used to prevent core recriticality, the coolant escape out from the vessel is of concern.

The ex-vessel benefits are still somewhat uncertain and the on-going experiments (MACE, WETCOR and BETA) aim at assessing the coolability of an ex-vessel debris bed covered by a water pool due to late pedestal flooding. The likelihood of an explosion-induced containment failure on one hand, and the formation of a coolable debris bed on the other, may depend on the timing of pedestal flooding, whether before or after the vessel breach. The recommendations could turn out controversial, though it appears non-trivial to avoid the pouring mode FCI's even with late flooding, that is, if late melt relocations should occur. Further inter-dependences arise, if limited-scale steam explosions produce tiny particles worsening the coolability of debris. The benefits of coolant injection on top of the corium pool, with regard to pouring mode explosions, are not clear either: stratified explosions have occurred (Alsmeyer, 1992).

Filling the containment with water may lead to geometries not experienced inside the vessel. A sub-cooled ocean with a depth and cross-sectional area up to 20 m and 100 m^2, respectively, may be available for a late melt attack from the vessel. The effects may be further amplified if the in-vessel volcano expels its lava after a delayed lower head failure preceded by external vessel flooding (Hodge et al, 1991). The conservation of a large mass of molten corium may also result in degradation of the vessel's capability to withstand fuel-coolant loads, in case of late coolant injection into an internally dried-out vessel.

FCI's play a dominant role when assessing the potential merits and concerns, as well as the success, of various severe accident management measures and procedures.

VII. FINALE

The need to understand the physics of fuel-coolant interactions (FCI's) is due to the fact that all severe accidents involve hot core material (fuel) attacking water (coolant), or vice versa. In this paper the boiling water reactors (BWR's) were discussed. The main idea was to highlight important FCI-related safety issues other than the direct loads caused by pouring mode steam explosions.

In some accident sequences the in-vessel-FCI's can have an important feedback effect on core degradation. If the water level is close to the core bottom at the time of melt relocation, the melt-coolant contact may lead to an inherently induced or accelerated core reflood due to effective coolant steaming and subsequent level swelling. The core reflood is related to several safety concerns: enhanced steam and hydrogen production, fission product release, containment pressurization and reactivity problems. The first analyses presented justify a detailed study of the phenomena and mitigation aspects related to the BWR recriticality in a severe accident. If further analyses (or plant design or modifications) cannot preclude severe consequences of an FCI-aggravated power transient, mitigative measures should be available whether the operators succeed in core cooling recovery (FCI-accelerated reflood front) or not (FCI-induced slug penetration into the core).

When molten core materials meet the coolant, steam and non-condensible gases (NCG's) are generated. The containment volume of most BWR's is small compared to the amount of hydrogen that may be produced by the oxidation of core metals. If the steaming rates are high during FCI's and gases are driven to the suppression pool via drywell, most of the NCG's can be packed into the wetwell atmosphere. As a result, the containment pressure could reach venting, leak or failure pressures early into the accident. In the accident management considerations, the mechanisms for fast containment pressurization have to be accounted for. The capacity, activation criteria and operator instructions related to the containment venting, if used, have to be carefully assessed. For the future containment designs, the associated problems should be eliminated by the combination of containment design and accident management.

In addition to the explosion characteristics, also gas production, melt jet quenching and fragmentation, as well as coolant behaviour, during benign FCI's affect the progression, and the success in management, of a severe BWR accident. Since it is not possible to avoid fuel-coolant contact and, in fact, it is strived for during an accident by recovery trials, the fuel-coolant loads remain somewhat generic in nature and FCI's among the key phenomena in severe BWR accidents.

REFERENCES

H. Alsmeyer (1992), Melt Attack and Penetration of Radial Concrete Structures Cooled by Outside Water, Trans. of the 20th WRSIM, Bethesda, Maryland, Oct. 21-23, 1992, NUREG/CP-0125, USNRC (USA), Oct. 1992

M. Anttila (1990), Recriticality Potential in a Severe Accident at TVO Plant, in Finnish, YDI013/90, VTT (Finland), May 21, 1990

K.M. Becker, K.P. Lindland (1991), The Effects of Surfactants on Hydrodynamic Fragmentation and Steam Explosions, KTH-NEL-50, KTH (Sweden), Dec. 1989, Revised Edition Apr. 1991

B. Chexal, et al (1989), A Void Fraction Correlation for Generalized Applications, Proc. of 4th Int. Top. Mtg on Nucl. R. Th.-Hydr., NURETH-4, Karlsruhe, FRG, Oct. 10-13, 1989

M.L. Corradini (1991), Vapor Explosions: A Review of Experiments for Accident Analysis, Nuclear Safety, Vol. 32, No. 3, July-September 1991

W. Frid, P-Å. Torell (1989), An Assessment of Structural Response of Condensation Pool Columns in a BWR/Mark II Containment to Loads Resulting from Steam Explosions, Proc. of 4th Int. Top. Mtg on Nucl. R. Th.-Hydr., NURETH-4, Karlsruhe, FRG, Oct. 10-13, 1989

W. Frid (editor), et al (1991), Containment Severe Accident Thermohydraulic Phenomena, RAMA III Final Report, RAMA III 89-04, SKI (Sweden), Aug. 1991

T. Fujishiro, T. Fuketa (1989), NSRR Experimental Results on Fuel/Coolant Interaction During a Severe Reactivity Initiated Accident, Proc. of 4th Int. Top. Mtg on Nucl. R. Th.-Hydr., NURETH-4, Karlsruhe, FRG, Oct. 10-13, 1989

T. Fuketa, T. Fujishiro (1992), Generation of Destructive Forces During Fuel/Coolant Interactions Under Severe Reactivity Initiated Accident Conditions, Proc. of the 5th Int. Top. Mtg On R. Th. Hydr., NURETH-5, Salt Lake City, Utah, Sept. 21-24, 1992

R.O. Gauntt, R.C. Schmidt (1992), Metallic Melt Relocation Under BWR Dry-Core Accident Conditions, Trans. of the 20th WRSIM, Bethesda, Maryland, Oct. 21-23, 1992, NUREG/CP-0125, USNRC (USA), Oct. 1992

S.R. Greene, et al (1991), BWR Mark II Ex-Vessel Corium Interaction Analysis, NUREG/CR-5623, USNRC (USA), Nov. 1991

S.A. Hodge, et al (1991), External Flooding of a BWR Reactor Vessel as a Late Accident Mitigation Strategy, Letter Report ORNL/NRC/LTR-91/9, ORNL (USA), Aug. 27, 1991

A. Inoue (1992), et al, Experimental and Analytical Study on Vapor Explosion of Melting Heated Rod During a Severe Power Transient, Proc. of the 5th Int. Top. Mtg On R. Th. Hydr., NURETH-5, Salt Lake City, Utah, Sept. 21-24, 1992

B.M. Ip, et al (1992), An Experimental Investigation of the Effects of Polymeric Additives on the Likelihood and Severity of Steam Explosions, Proc. of the 5th Int. Top. Mtg On R. Th. Hydr., NURETH-5, Salt Lake City, Utah, Sept. 21-24, 1992

H. Kim, et al (1989), Single Droplet Vapor Explosion: Effect of Coolant Viscosity, Proc. of 4th Int. Top. Mtg on Nucl. R. Th.-Hydr., NURETH-4, Karlsruhe, FRG, Oct. 10-13, 1989

E.E. Lewis (1977), Nuclear Power Reactor Safety, John Wiley & Sons

C.C. Lin, J.R. Lehner (1991), Identification and Assessment of Containment and Release Management Strategies for a BWR Mark I Containment, NUREG/CR-5634, USNRC (USA), Sept. 1991

B.W. Marshall Jr. (1988), Hydrogen Generation During Fuel Coolant Interactions: Results from the FITS-D Series, SAND88-1335C, SNL (USA), June 1988

J.P. Schneider, et al (1992), Breakup of Metal Jets Penetrating a Volatile Liquid, Proc. of the 5th Int. Top. Mtg On R. Th. Hydr., NURETH-5, Salt Lake City, Utah, Sept. 21-24, 1992

W.B. Scott, et al (1990), Recriticality in a BWR Following a Core Damage Event, NUREG/CR-5653, USNRC (USA), Dec. 1990

J.J. Sienicki, et al (1992), Analysis of Melt Arrival Conditions on the Lower Head in U.S. LWR Configurations, Proc. of the 5th Int. Top. Mtg On R. Th. Hydr., NURETH-5, Salt Lake City, Utah, Sept. 21-24, 1992

T.G. Theofanous, et al (1987), An Assessment of Steam-Explosion-Induced Containment Failure, Nuclear Science and Engineering: **97**, 259-326 (1987)

H.E. Unger, et al (1989), Ex-vessel Melt/Water Interaction, Int. Sem. on Fission Product Transport Processes in Reactor Accidents, Dubrovnik, Yugoslavia, May 22-26, 1989

M.F. Young, et al (1988), Hydrogen Generation During Fuel/Coolant Interactions, Nuclear Science and Engineering: **98**, 1-15 (1988)

QUANTIFICATION OF THE PROBABILITY OF CONTAINMENT FAILURE CAUSED BY AN IN-VESSEL STEAM EXPLOSION FOR THE SIZEWELL B PWR

B.D. Turland, D.F. Fletcher, K.I. Hodges
SRD, AEA Technology,
Culham Laboratory, Oxon., OX14 3DB, UK.
Tel. (44) 235-521840 — Fax (44) 235-464143

G.J. Attwood
AEA Reactor Services,
Winfrith Technology Centre, Dorchester,
Dorset, DT2 8DH, UK. Tel. (44) 305-251888

ABSTRACT

AEA Technology has provided an assessment of the probability of α-mode containment failure for the Sizewell B PWR. After a preliminary review of the methodologies available it was decided to use the probabilistic approach described in the paper, based on an extension of the methodology developed by Theofanous et al. (1987). The input to the assessment is 12 probability distributions; the bases for the quantification of these distributions are discussed.

The α-mode assessment performed for the Sizewell B PWR has demonstrated the practicality of the event-tree method with input data represented by probability distributions. The assessment, itself, has drawn attention to a number of topics, which may be plant and sequence dependent, and has indicated the importance of melt relocation scenarios.

The α-mode failure probability following an accident that leads to core melt relocation to the lower head for the Sizewell B PWR has been assessed as a few parts in ten-thousand, on the basis of current information. This assessment has been the first to consider elevated pressures (6 MPa and 15 MPa) besides atmospheric pressure, but the results suggest only a modest sensitivity to system pressure.

I. INTRODUCTION

A pre-operational safety report (POSR) has been completed for the Sizewell B PWR, a 1300 MWe reactor of Westinghouse design currently being constructed in the UK. The POSR contains a probabilistic safety assessment of the response of the plant to severe accidents. As part of this process it was necessary to quantify the probability of containment failure induced by an in-vessel steam explosion. AEA Technology provided an independent assessment of the probability of containment failure by this mechanism (α-mode failure) given a core-melt accident. The assessment is summarised in this paper. Unlike previous published studies, three system pressures were considered: 0.1 MPa, 6.0 MPa and 15 MPa. Generic accident sequences without significant operator intervention were considered for each system pressure.

After a preliminary review of the methodologies available it was decided to use a probabilistic approach, and the methodology developed by Theofanous et al. (1987) was used as the starting point. This was developed and adapted for the current study (see Section II). The input to the assessment is 12 probability distributions; the bases for the quantification of these distributions are summarised in Section III. Results for the low pressure evaluation are presented in Section IV, while those for higher pressures are summarised in Section V. Finally the methodology and results are discussed.

II. METHODOLOGY

The methodology used is based on that of Theofanous et al. (1987), who split the α-mode failure process into a number of events, each of which was represented by a probability distribution. This allows the use of results of mechanistic models, where they are available, and expert judgement, where mechanistic models are not available, knowledge is incomplete, or there is a stochastic nature to the process.

For the AEA assessment a Monte Carlo approach is used with an individual event followed through the event tree, and appropriate distributions sampled. (The Monte Carlo approach has previously been applied to much simpler event trees by Corradini and Swenson (1981) and Berman, Swenson and Wickett (1984).) An individual melt relocation event may (i) fail to cause a steam explosion (no effective trigger), (ii) cause a steam explosion that does not fail the containment, or (iii) give an α-mode failure event. By following many individual events through the tree, with random sampling of the distributions, the probability of α-mode failure can be evaluated. (It is not the purpose of this paper to discuss the meaning of 'probability' in this context, but the methodology is consistent with both a 'frequentist' and 'degree of confidence' interpretation.)

The tree-structure developed by Theofanous et al. was modified so that the following additional features could be considered: melt relocation, triggering, stratified explosions, and venting of the steam explosion through the core region. The revised tree is shown in Figure 1 and it is described briefly below. Input distributions are indicated by italics in the text; their quantification is described in the following Section.

- First the distribution representing *the amount of melt relocating* is sampled. Distributions giving *the melt flow rate* (conditional on the amount of melt relocating) and on *the time to first base contact* are then used to establish the time periods for the interaction, which are used to determine the quantities of melt and its configuration (in transit through the lower head (referred to as 'in the mixture') or settled out and segregated from any remaining water (referred to as 'in the pool')) should a trigger occur.

- Triggering is treated by sampling *a cumulative distribution which represents the likelihood of triggering:* (i) in the early stages of the interaction, (ii) before base contact, (iii) before all the melt has reached the base of the vessel, and (iv) after all the melt is in the base of the vessel. A non-zero probability can be given for the lack of an effective trigger.

- The equivalent mass involved in the explosion is evaluated taking all the melt in transit in the lower head and multiplying that in the pool by an *'equivalence factor'* to represent the likelihood that only a small fraction of melt in the pool would participate in the interaction. A distribution for *the specific thermal energy of the melt* is then sampled, and using a distribution for *the conversion efficiency of the mixture*, the explosion energy is evaluated. The explosion energy is considered to be the kinetic energy imparted to a slug as the mixture expands down to atmospheric pressure, without 'leakage' from the high pressure region (see below).

- At this point, the tree developed for the assessment included a distribution for the *effective pressure on the lower head* conditional on the explosion energy and a distribution for the *effective pressure to fail the lower head*. These distributions were included so that credit for lower head failure in reducing the energy in the upward moving slug could be claimed. However, when this topic was reviewed (see below) it was concluded that it was premature to claim any credit for lower head failure.

- *The kinetic energy that the slug has when it impacts the upper core support plate* is evaluated using a conditional distribution based on the calculated explosion energy (and system pressure). (The original tree had the option of an alternative conditional distribution for those cases in which the lower head was predicted to fail.) *The energy required to crush and fail structures in the upper head* is then evaluated as a function of the impacting slug energy, which leads to the energy in the material (the slug plus remains of the upper internals) impacting the upper head.

- The distribution of the likely *energy required to the fail the upper head* is sampled and compared with that evaluated for the event under consideration.

- If the vessel is predicted to fail, then containment failure is considered. First a *missile energy* dependent on the slug energy prior to vessel failure is sampled; this is then compared with the distribution of *missile energies likely to fail the containment.*

It is important to realise that any tree structure represents a compromise. In practice, it is not possible to include every event that one can think of as a series of distributions, or to allow for too many dependencies in conditional distributions, as the tree would become too cumbersome. The tree inevitably contains 'pinch points' at which detailed information is lost. The intention was that the results should not be adversely affected by the particular choice made. One option considered was having a loop in the tree for multiple explosions; instead these may be allowed for through the 'efficiency' and 'equivalence' distributions.

The input to the assessment consists of the 12 probability distributions indicated above, which may depend on the system pressure and previously calculated quantities. The probability of containment failure is evaluated using Monte Carlo sampling (the usual sample size is 5 million) by the SEEP code which contains a representation of the tree structure and performs the sampling, the simple arithmetic and the logical operations required.

The SEEP code plots the input distributions generated for the variables (thus providing valuable self-checking) and the distribution for those cases that do give α-mode failure. This feature allows the sensitivity of containment failure to the variable in question to be examined readily; where the shape of the overall distribution and that for events that lead to containment failure are similar, there is little sensitivity to the variable; where the shapes of the distributions differ significantly, there is great sensitivity.

III. QUANTIFICATION OF THE DISTRIBUTIONS

In most cases the intention has been to construct best-estimate distributions. Where very little information is available, a more conservative approach has been adopted. The bases for the distributions are outlined below (the sub-sections correspond to the bullet points in Section II).

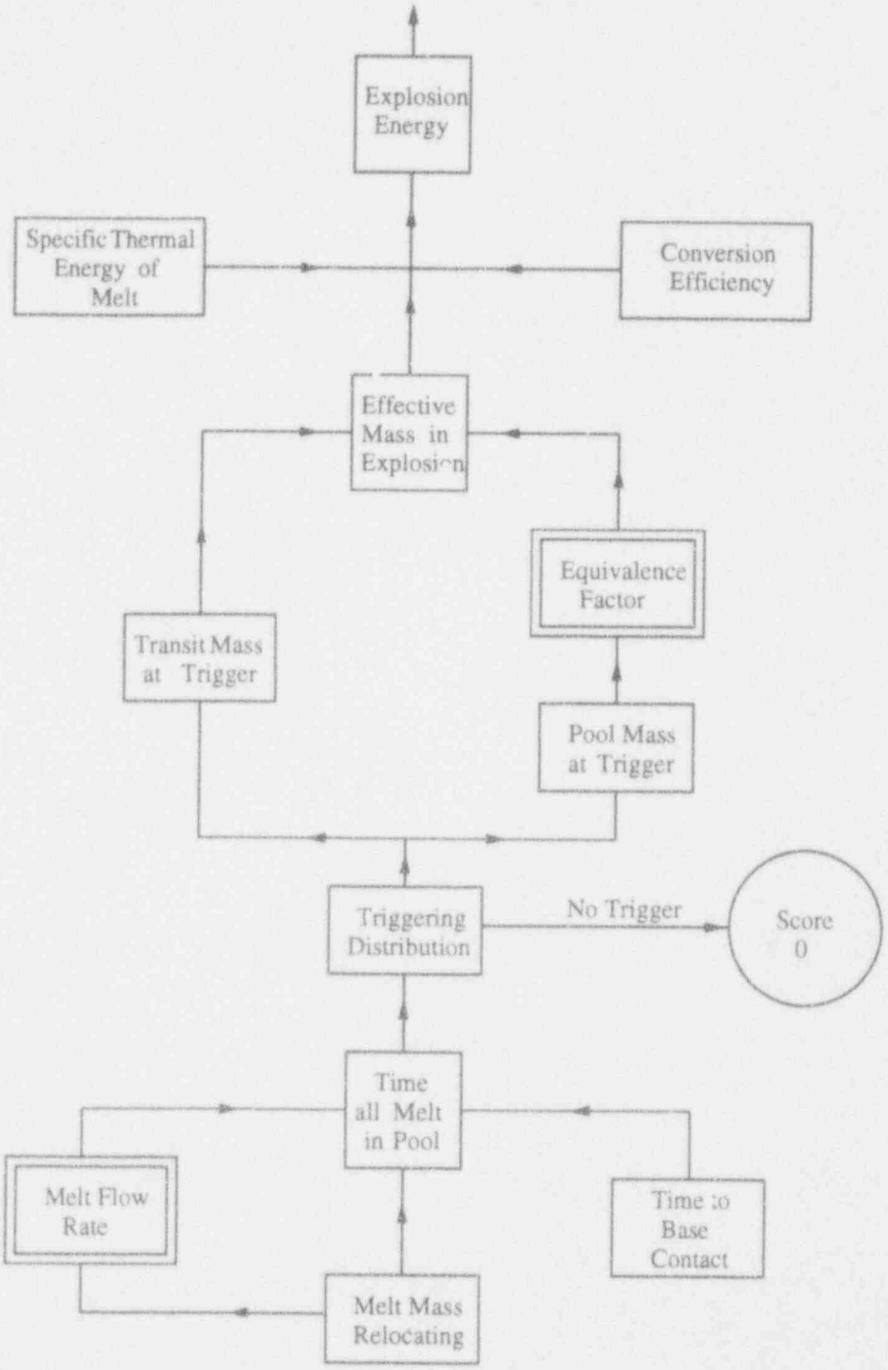

Figure 1: The tree structure used in the assessment. Rectangles represent probability distributions that are sampled; double-edged rectangles represent conditional probability distributions, square boxes represent calculated distributions and diamonds indicate decision points.

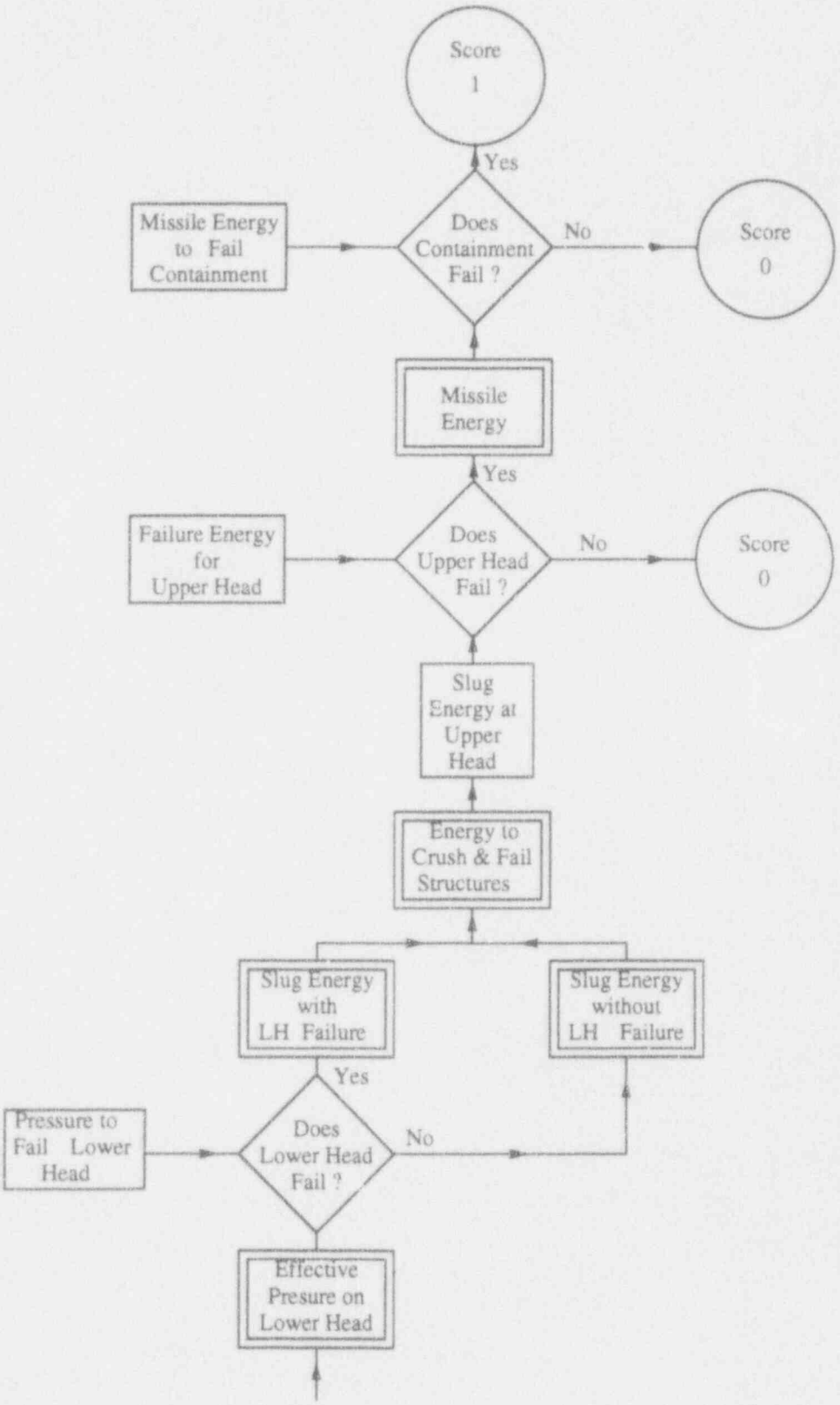

Figure 1 continued.

A. Melt Relocation

Two routes for melt relocation are identified: via the core region, and through the bypass (as at TMI-2). The current generation of severe accident progression codes are unable to make predictions of the relocation pathway. However, they tend to predict the formation of in-core blockages (supported by experimental data), and a relatively uniform heat-up across the core. Thus the core debris is predicted to have access to the bypass region before failure of the lower crust. (The Sizewell B design is such that there are holes in the baffle plates, so, although these are expected to fail, this is not essential for melt to have access to the bypass.) One feature of the Sizewell B design is that the holes in the horizontal former plates are smaller in diameter (11.2 mm) than those at TMI-2, thus making blockage of the holes more likely. Calculations have been performed with a UK-upgrade of the PLUGM code (Pilch and Mast, 1984) for melt relocation through the former plates and through intact lower fuel bundles. These indicate that for passage through the former plates the melt should have a superheat of at least 150 K. This is the range expected when the lateral crust fails. Melt relocation was quantified using a mini-event tree, where the probability of melt access to the bypass was assessed at 0.9, and a probability of 0.6 was then assigned to melt relocation through the bypass region; other pathways were also considered. On the basis of this assessment, it was concluded that in about 60% of the cases melt would enter the lower head through the outer holes in the lower core plate. This plate was not expected to ablate significantly and the total area of the flow holes is only about 3×10^{-2} m^2, whilst the flow area through the former plates is about one-tenth of this value. Thus, the expected melt flow rates are low (typically 150 kg/s). Because the top of the core relocates first, lower amounts of mass are associated with this relocation pathway (10 to 60 tonnes).

The melt flow rate for downward relocation through the core is more difficult to judge, as the area of the pour is unknown (lumped parameter codes are useless for this purpose as they inevitably fail whole sectors of structures). Melt may relocate following failure of a supporting crust (held on fuel pin stubs), or by failure of the lower fuel assembly nozzle. Failure of the lower core plate itself is not expected as (i) it is independently supported from beneath, (ii) the design also includes a secondary core support structure, which would support the core on the lower head should the core barrel fail, and (iii) the holes in it are sufficiently wide that if melt passes through the much smaller holes in the lower fuel nozzles it will not re-freeze and form a crust at the lower core plate. It was judged that the most likely failure is either that of one fuel nozzle plate, or a small area of crust. The judgement was made that 60% of these cases had pour areas less than 0.04 m^2, giving mass flow rates of less than 1500 kg/s. The upper 5% of the distribution has flow rates greater than 7.2 te/s, with the top 1% of the distribution between 18 te/s and 72 te/s. Downward relocation through the core is typified by large amounts of melt relocating (40 to 100 tonnes).

The distribution for time to base contact (after passage through the lower core plate) was based on a number of CHYMES (Fletcher and Thyagaraja, 1991) calculations, consideration of data from the Winfrith MIXA tests (Denham et al., 1992; Fletcher and Denham, 1993), and bounding calculations for both an unperturbed jet and a 10 mm diameter droplet travelling at its terminal velocity through water. The resulting distribution for time to base contact has a minimum time of 0.4 s, a mean of 1.15 s and a maximum value of 1.9 s.

B. Triggering

Triggering, either its ease or its absence, has been used as an argument against large scale steam explosions occurring. Thus it should be included in any assessment. However, a review by one of the authors [DFF] concluded that relatively wide distributions should be adopted to take account of the uncertainty in triggering. The main points of the review were:

- There are no developed and validated models of triggering that can be used with any degree of confidence.
- Model predictions indicate that triggering becomes more difficult at higher pressure and higher melt temperature.
- Permanent gas can affect the triggering process, small quantities inhibiting it, but rapid gas evolution leading to spontaneous explosions.
- Experimental data show clearly the random nature of the triggering process.
- Spontaneous explosions which occur on contact can be suppressed by a small increase in pressure (as little as 5–10 bars).
- There is no clear evidence for a triggered explosion above 3 MPa without the injection of cold water.
- The claims for inevitable early triggering cannot be substantiated by the experimental data (particularly the scaling of likelihood with the amount of mass involved).

As noted above the time over which a trigger could occur was split into 4 periods. Values of p_1 - p_4 are

given in Table I, where p_1 is the probability that it occurs in the initial interaction, p_2 is the probability it occurs before first contact with the bottom of the vessel, p_3 is the probability it occurs before the melt has fully settled and p_4 is the probability it occurs at all. Thus $p_4 - p_3$ is the probability of a stratified explosion being triggered once all the melt is in a pool, while $1-p_4$ is the probability that there is no trigger.

Table I The pressure dependence of parameters in the triggering distribution.

Pressure (MPa)	p_1	p_2	p_3	p_4
0.1	0.2	0.3	0.6	0.7
6.0	0.02	0.05	0.15	0.2
15.0	0.01	0.04	0.08	0.1

C. Explosion Yield

Three further distributions require quantification before the explosion yield can be calculated: the 'equivalence factor' for melt in the pool, the specific thermal energy of the melt, and the conversion efficiency of the mixture.

The 'equivalence factor' is used to account for the contribution to the explosion of melt residing in the pool. This may arise because of (i) a stratified explosion at the interface with overlying water, (ii) because melt from the pool is lofted into the water by an earlier stratified or conventional steam explosion, or (iii) as the result of entrapped water again leading to part of the pool being 'blown' back into the water. A review of experimental data for stratified explosions indicated that, although they can occur, they are a much weaker phenomenon than explosions involving pre-mixed melt and water (e.g. experiments at McGill University on stratified explosions gave only a 0.07% conversion ratio when based on the total thermal energy of the melt (Ciccarelli et al., 1991)). The data also suggest that only very thin layers, typically ~10 mm deep, are involved in the explosion. The energy required to generate a mixture of droplets following an initial interaction was considered, and it was concluded that a stratified explosion is not able to explosively mix more melt on a millisecond timescale, but may be able to throw some melt upwards in a pre-mixed state. With these considerations, a distribution, conditional on the melt-mass in the pool, was constructed based on a layered model for the melt-pool; the top 100 mm having an equivalence factor in the range 0.05 to 0.5, with a best-estimate of 0.2; a second 100 mm layer with an equivalence factor between 0.01 and 0.2, with a best-estimate of 0.05; and the remainder of the melt with an equivalence factor between 0.002 and 0.01, with a best-estimate of 0.005.

The specific thermal energy of the melt was based on an evaluation for partially oxidised core debris; using MATPRO phase diagrams (Hohorst, 1990) a melting range of 2600 K to 2900 K was determined. Based on considerations of natural convection, a melt superheat between 0 and 300 K was used. With these assumptions a triangular distribution for the specific thermal energy of the melt was specified, with a lower bound of 1.21 GJ/te, a mean and mode of 1.37 GJ/te and an upper bound of 1.53 GJ/te. These values are somewhat larger than those of previous workers (e.g. Theofanous et al., 1987) because of allowance for ZrO_2, which has about twice the specific enthalpy of UO_2.

The distribution for the efficiency with which the thermal energy of the melt in transit can be converted to mechanical energy of the slug was based on the following considerations:

- Table B.1 of Corradini et al. (1988) provides a summary of large scale experimental programmes, including the measured conversion ratios. These range from 0.3% to 3%.
- Experiments with prototypic material at Winfrith, both at the 0.5 kg and larger scales up to 24 kg, indicate a conversion efficiency, *for the material that was finely fragmented*, of 4%, when there was no sub-cooling (Bird, 1984). This value decreases with sub-cooling, but is independent of pressure up to 1 MPa ambient pressure (although the melt mass participating increased).
- The CHYMES code (Fletcher and Thyagaraja, 1991) has been used to predict the distribution of melt and coolant for a large pour under reactor conditions. Typically, only a small part of the melt is in a region of good mixture; much of it is in a steam rich region. This picture is supported by experimental data (Fletcher and Denham, 1993; Angelini et al., 1992). At present it is not possible to define what type of mixture will support propagation. However, even if an explosion could propagate through them, the regions of 'weak mixture' cannot contribute to the explosion with high efficiency. Calculations have been performed for the maximum energy yield assuming that each cell in the CHYMES prediction produces the Hicks-Menzies yield, with vapour blanketing assumed. These calculations indicate that the upper bound efficiency for large pours is ~20% at early times in the pour, falling to ~8% when vapour production becomes significant. Somewhat larger efficiencies are possible for low melt pour rates (e.g. 3 te/s).

- In attempting to extrapolate experimental efficiencies to the plant-scale, the calculations referred to above suggest that efficiency will go down with scale. However the low values for efficiency in the experiments may be due, in part, to condensation, which may not be as efficient in the plant, and to a lack of tamping. In the latter case, with the large steam production predicted for the mixing phase at plant-scale, it may well be that there is less tamping at plant-scale than in some of the experiments.

It was decided to bias the efficiency distribution to the experimental data, and to use a different distribution for the two high pressure cases, as these are significantly less dispersive than the atmospheric pressure case. For the high pressure cases 85% of the probability lies between 2% and 8% efficiency, with the top 1% of the probability spread between 15% and 20% efficiency. For the low pressure cases 85% of the probability lies between 2% and 5% efficiency, with the top 1% of the probability spread between 10% and 15% efficiency. It is emphasised that this efficiency applies to all the melt in transit at the time of the trigger (plus the 'equivalent' mass of melt from any pool that has formed).

D. Lower Head Failure

As indicated in Section II the event tree developed for the assessment had two distributions associated with lower head failure. The intention was to claim credit for lower head failure as a mitigative event, eliminating many of the events which would otherwise fail the upper head, as was done in the study by Theofanous et al. (1987). However, our review of this topic led us to the view that there was insufficient evidence to support strong claims for lower head failure. The static pressure that the Sizewell B lower head can sustain is estimated to be about 65 MPa; some additional work would be required to justify this figure for the penetrations, but these are, in general, areas of low stress rather than stress enhancers. Thus it is anticipated that only explosions with dynamic pressures in excess of this value would fail the lower head. Elsewhere it has been widely assumed that explosions with an energy greater than about 1 GJ would lead to lower head failure (Corradini and Swenson, 1981; Theofanous et al., 1987). However, this criterion was based on calculations which use very high explosion pressures, typically 500 MPa, obtained from idealised thermodynamic models (Theofanous et al., 1987). There is no evidence for such high pressures, and experiments and more realistic modelling suggest that explosion pressures would more likely be in the range 40–80 MPa for 1 GJ of mechanical energy. When models for propagation are better validated, it may be possible to substantiate claims in this area, but currently the distributions for lower head failure are not used. With these lower explosion pressures, the threat to the upper head arises as a slug may integrate the work done in the expansion and then load the upper head on a shorter timescale.

E. Energy Loss Processes

As noted in Section II, the energy yield of the explosion used in this study is the kinetic energy a slug would acquire if the mixture region expanded down to 0.1 MPa without leakage. However, in practice it is hard to identify a coherent slug tamping the whole explosion, as (i) calculations typically indicate much steam in the region above the mixture; (ii) there may be relatively intact fuel assemblies at the periphery of the core; (iii) the downcomer is expected to contain highly voided water; and (iv) the core debris is unlikely to be a single liquid, but could contain substantial solid remains (remains of the lower crust, upper and lower fuel pins etc). A simple lumped parameter model was developed to scope the effect of leakage from the explosion region. The explosion region was treated as a zone of high pressure gas, and the gas in the upper head and steam generators was treated as a second well-mixed gas volume. Work was performed on a slug located between the two regions by the pressure forces, but leakage over a fixed cross-sectional area was also allowed. The flow rate through the leak was calculated assuming simple or choked flow as appropriate. The effect of the leak is to reduce the driving pressure on the slug and thus the kinetic energy it acquires. A series of runs were performed using explosion pressures in the range 25–100 MPa, explosion volumes in the range 5–20 m^3, a slug mass of 55 te, with no leakage and with 1 m^2 leakage. For the 0.1 MPa case, without leakage, the slug kinetic energy at impact with the upper core support plate (UCSP) is between 40% and 70% of the energy yield (because the high pressure region has not been able to expand fully); the leakage further reduces the kinetic energy by a factor of about 2. For the high pressure sequences, the simple model demonstrates that the explosion yield must be greater than a finite quantity (0.2 GJ at 6 MPa; 0.5 GJ at 15 MPa, with no leakage) for the slug to reach the UCSP. These values increase significantly (1.0 GJ at 6 MPa; 1.5 GJ at 15 MPa) when leakage is assumed. These values were used to create conditional distributions; the results for 1 m^2 leakage form the lower bound, those for no leakage the upper; a triangular distribution with its mode at the lower bound was used, as it is believed that a 1 m^2 area of leakage underestimates that available.

The slug will be resisted by the upper core plate (a 76 mm thick plate above the core) and upper plenum structures, including the UCSP (the most substantial structure above the core). Figure 2 shows an outline of the upper part of the Sizewell B reactor. For the assessment, the energy absorbed in above-core structures was first

evaluated by scaling the assessments of Theofanous et al. (1987), followed by more detailed evaluations for the UCSP. The independent analysis performed supports the scenario outlined in Theofanous et al., i.e. the upper internal structures are crushed and remove energy from the slug prior to significant loading of the upper head. The one assumption made by Theofanous et al. for the behaviour of upper internal structures that seems unlikely is that the upper core plate and the lower parts of the guide tubes and support columns remain at a low temperature. Radiation heat transfer from the degrading core and natural circulation heat transfer (most significant at high pressures) are likely to heat the lower parts of these structures significantly. The energy required to crush the structure between the upper core plate (if it retains its strength) and the UCSP is estimated to be 330 MJ for the Sizewell B design. Consideration was given to the energy losses by friction in these structures if the upper core plate has been melted away (as suggested by some plant calculations). Depending on the length of structures with which the slug interacts (1 m or 2.13 m — their full length) and the assumed friction factor (0.002 to 0.2) the energy loss varies from only 1% of the initial slug energy to 24%.

Additional energy loss processes, not considered by Theofanous et al., were identified. These are 50 MJ to buckle the support ring of the UCSP, and between 70 MJ and 110 MJ for plastic deformation of the UCSP prior to its failure.

Considerable energy losses were claimed by Theofanous et al. for radial venting of the slug prior to UCSP failure. The degree of venting depends on whether the slug occupies the region out to the core barrel, and the relative ease of distortion of the core barrel compared with that of the UCSP and its support ring. For the assessment, the analysis of Theofanous et al. was supported by simple coefficient of restitution arguments that also show a significant energy loss (as much as 50%) as the slug and UCSP combine into a single upwardly moving mass.

The energy required to fail the mountings of the UCSP was estimated to be 35 MJ, while that required to crush the support and guide tubes between the UCSP and the upper head was estimated to be between 55 MJ and 90 MJ.

In using these estimates to form a distribution for the energy loss, it was borne in mind that all the calculations are derived from axisymmetric models, and that in reality, with some parts of structures collapsing earlier than others, the total dissipation might be reduced. Following Theofanous et al. the kinetic energy (E_I) of the slug and UCSP after UCSP failure was written in the form

$$E_I = 0.66(E_S - E_{\text{crush}}) - 90 \quad \text{MJ}$$

where E_S is the energy of the slug at the UCSP, without losses, and E_{crush} is sampled from a triangular distribution with a range 0–500 MJ and a mean of 250 MJ (this covers the energy absorbed prior to impact with the UCSP, the deformation of the support ring and the plastic deformation of the UCSP). The factor of 0.66 allows for the radial venting of the slug, while the 90 MJ is a conservative estimate of the failure energy of the UCSP and the subsequent crushing of guide and support tubes in the upper head.

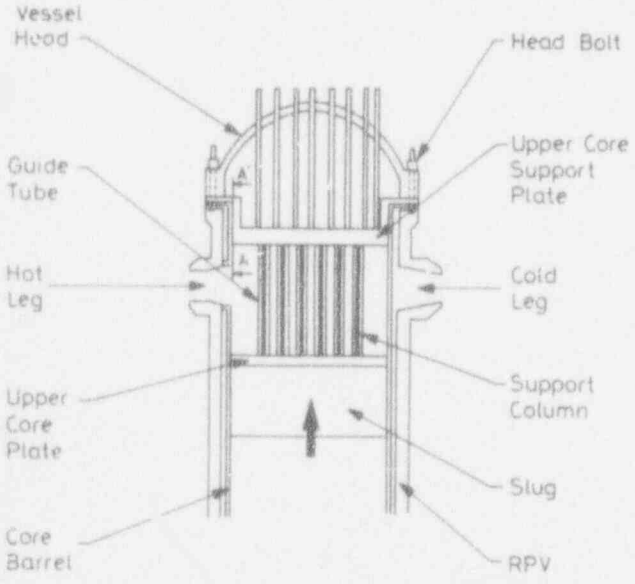

Figure 2. A schematic representation of the upper internal structures of the reactor.

F. Upper Head Failure

Finite element calculations have been performed for the upper head loading using the ABAQUS code (Attwood, 1993). These calculations were two-dimensional and contained a distributed representation of the studs (including the pre-load) which secure the upper head to the vessel flange. Both static (pressure loads) and dynamic loads, represented by 'lumped masses', over an assumed area of impact (the impact ring) and over the upper head out to a diameter corresponding to that of the UCSP were considered. Energy dissipation by plastic deformation was calculated for failure strains of 12% (taken as the lower limit) and 20% (taken as the upper limit). These calculations showed that:

- In all cases the head material would fail before the studs, and the strains in the studs were insignificant.
- When the dynamic load was applied over an impact ring, for a slug with energy at impact of 144 MJ

there was significant distortion of the upper head, but it did not exceed 12% plastic strain. It was considered that for slightly higher slug energies the 12% limit would have been reached. When this slug energy was applied over most of the upper head, failure was predicted with the lower and upper bounds for energy dissipated as 91 MJ and 99 MJ, respectively; the predicted failure was at the very top of the upper head, so no missile would have been produced.

- For a large slug energy at impact (917 MJ) failure was predicted for the ring loading case with the energy dissipated lying between 120 MJ and 290 MJ. With the load spread across most of the upper head the energy dissipated had lower and upper bounds of 170 MJ and 250 MJ, respectively.

On the basis of these calculations, and supporting hand calculations, it was decided to use a triangular distribution for the energy dissipated during failure of the upper head over the range 100–300 MJ with a mean of 200 MJ. If the sampled dissipation energy is greater than the slug energy at impact (E_I, above), the upper head survives, and the containment remains intact.

G. Containment Failure

Because of the blow-down forces on the upper head for the sequences at elevated pressure, it is conservatively assumed that, for the 6 MPa and 15 MPa evaluations, failure of the upper head inevitably leads to containment failure. For the low pressure evaluation, the energy of the missile is compared with that likely to cause penetration of the containment.

The energy of the missile is evaluated in a similar manner to that of Theofanous et al. A factor for the reduction in kinetic energy of the upwardly moving upper head missile and slug (after allowing for the dissipation in failing the upper head) is sampled based on coefficient of restitution arguments. The distribution for this factor is triangular on the range 0.3 to 0.6, with a mean of 0.45.

The energy the missile and slug require to fail the containment is the sum of the potential energy required to raise the missile to the containment dome, and the energy then required to perforate the structure. The energy required to lift the estimated mass of 224 te to the containment roof is 100 MJ. Specific formulae exist for the perforation velocity for the Sizewell B containment. For a hard missile, these give required energies between 22 MJ, assuming a 2 m diameter missile, and 54 MJ, if the missile diameter is that of the vessel. As the missile will deform on impact these values are believed to be conservative. The distribution for the missile energy required to fail the containment was selected to be uniform, bounded by 120 MJ and 160 MJ.

IV. RESULTS FOR 0.1 MPa SYSTEM PRESSURE

The distributions outlined above for the system pressure of 0.1 MPa were input into the SEEP code and a sample size of 20 million was used. Examples of some of the probability distributions generated by the random sampling are shown as plots of probability density in Figure 3. These show the input distributions for melt mass relocating, time to first base contact and conversion efficiency, as reproduced by the sample; these distributions are clearly well-represented.

Figure 4 shows two of the distributions generated from this input by SEEP: the effective mass in the explosion (there is an off-scale spike at zero, representing core-relocation events that do not lead to the triggering of a steam explosion), and the slug energy on impact with the upper head (again there is a large off-scale spike at zero, representing cases where the slug does not reach the upper head).

The code also produces distributions for those events that lead to containment failures. Figure 5 shows these distributions for the same variables as Figure 3. At this system pressure none of the cases where the melt enters the lower head through the bypass lead to containment failure, so there are no melt masses relocating less than 40 te in Figure 5(a). Comparing Figure 5(b) with Figure 3(b) for the time of first base contact, shows the effect of basing the trigger time on the time to first base contact: here, longer times put more melt into the mixture, and so, on average, give rise to more energetic events. Comparison of Figure 5(c) with Figure 3(c) indicates that, in this assessment, relatively low efficiency events contribute significantly to α-mode failure.

Figure 6 is the analogue of Figure 4 for those cases that fail the containment. Figure 6(a) shows the effective masses in the explosion; these clearly correspond to large pours and late triggers (note the difference in scale between Figures 6(a) and 4(a)). Figure 7 shows two additional distributions for the events that gave α-mode failure — those for the mechanical energy release and the final missile energy. It is seen that the majority of failures come from mechanical energy releases of between 1.5 GJ and 5 GJ, and that there are a substantial number of cases where the predicted missile has significantly more energy than that needed to perforate the containment.

The probability of containment failure was estimated to be 2.7×10^{-4} conditional on there being an accident leading to core-melt relocation. (Although this, and other probabilities of α-mode failure are given to two significant figures here, the authors view the assessment as being indicative to about one-half of an order of magnitude.)

(a)

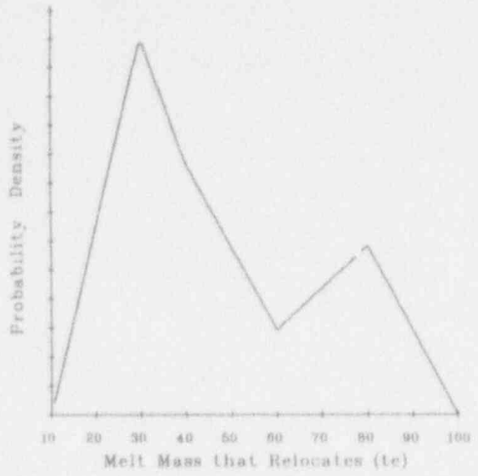

(b)

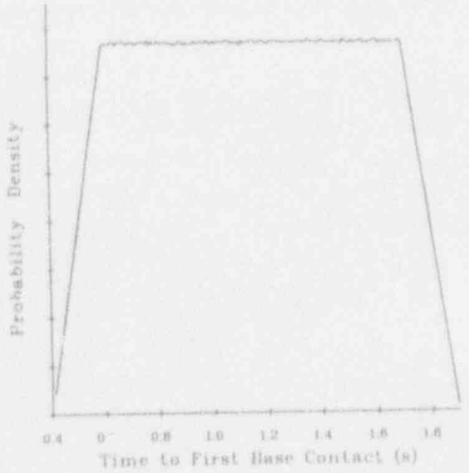

(c)

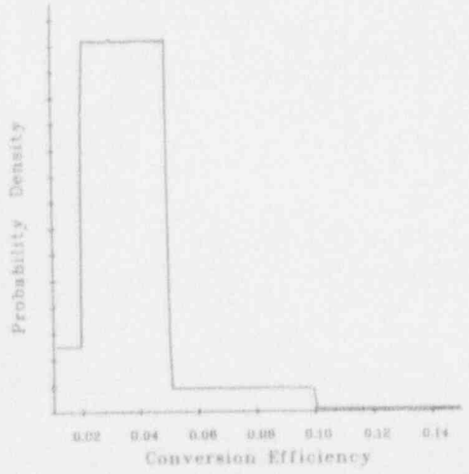

Figure 3. Examples of the independent distributions output by SEEP.

V. RESULTS FOR ELEVATED PRESSURES

Using a sample of 5 million, and the distributions outlined above, the estimated probability of α-mode failure is 5.7×10^{-4} at 6 MPa and 1.9×10^{-4} at 15 MPa, both conditional on there being an accident leading to core melt relocation. In general, the detailed results follow a similar trend to those outlined above for the low pressure sequence. Although triggering a steam explosion at 6 MPa is considered significantly less likely than at 0.1 MPa, the probability given to higher efficiencies and the assumption that all upper head failures lead to containment failure have led to the α-mode failure probability being a factor of 2 higher at the higher pressure. The reduction in probability for 15 MPa is simply the result of the lower probability of triggering.

(a)

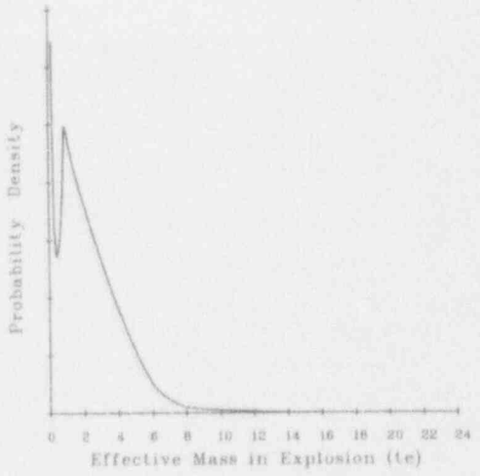

(b)

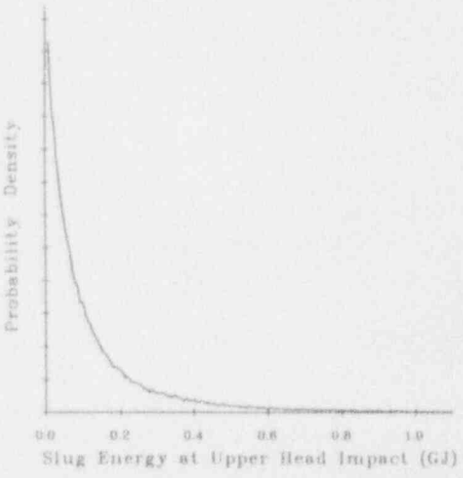

Figure 4. Examples of the derived distributions output by SEEP.

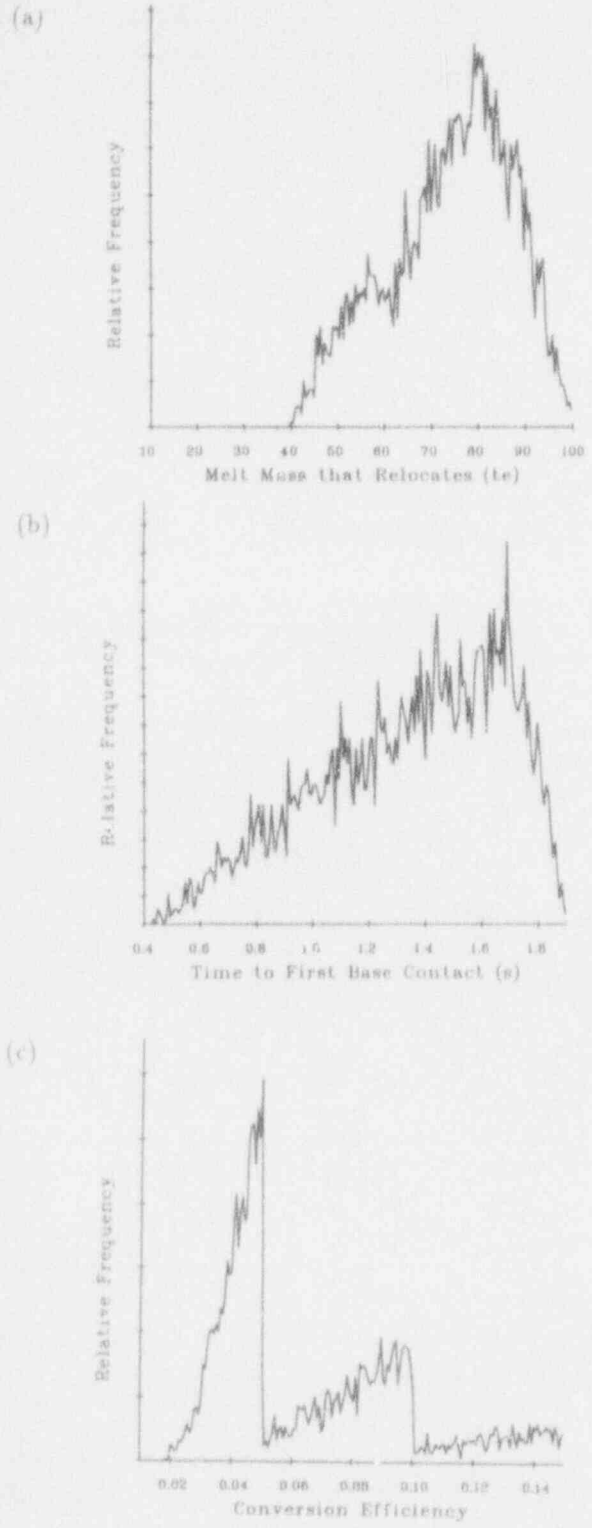

Figure 5. Distributions of the variables shown in Figure 3 for the events which fail the containment. The sample size in these and subsequent Figures is 2.7×10^{-4} of the original sample size.

VI. DISCUSSION

The results presented above show many features in common with earlier analyses (e.g. those of the US Steam Explosion Review Group (1985) and of Theofanous et al., (1987)). The overall probability of α-mode failure is also in line with most previous studies. As is evident by a comparison of the papers of Theofanous et al. (1987) and the present assessment, which were performed for similar plants, there are a number of differences in how the available evidence has been interpreted as probability distributions. Broadly, Theofanous et al. place most emphasis on 'limits to mixing' and lower head failure, while our assessment claims significant credit for slow melt pours, the range of triggering times, and lower conversion efficiencies (partly another way of using the 'limits to mixing' argument).

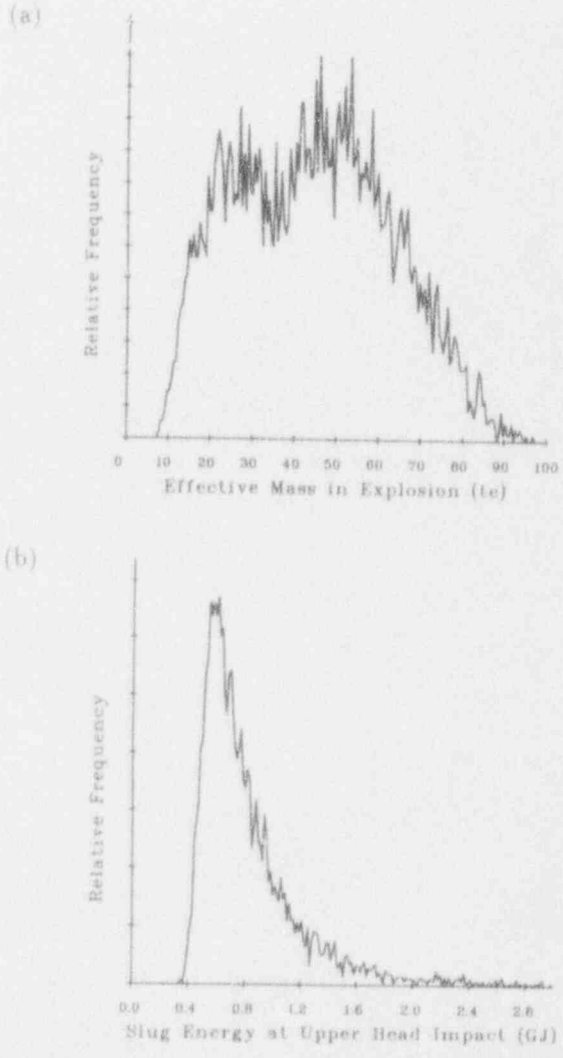

Figure 6. Distributions of the variables shown in Figure 4 for the events which fail the containment.

Clearly some of the distributions are poorly known, and with improved knowledge the assessed probability may change significantly. Given that the present study is 'best-estimate', the authors acknowledge that with improved knowledge the assessed probability may rise by a modest amount. However, if the improved knowledge is able to truncate some of the distributions (e.g. those for efficiency or triggering) or provide greater confidence where conservative assumptions are now made (e.g. for lower head failure) then a substantial reduction in the assessed probability of α-mode failure is a realistic expectation. These improvements are generally dependent on an improved knowledge of core-melt behaviour, an improved knowledge of the physics of the steam explosion process, and an improved ability to apply these in plant calculations (particularly in the coupling between the explosion region, the 'slug' and the rest of the vessel's contents).

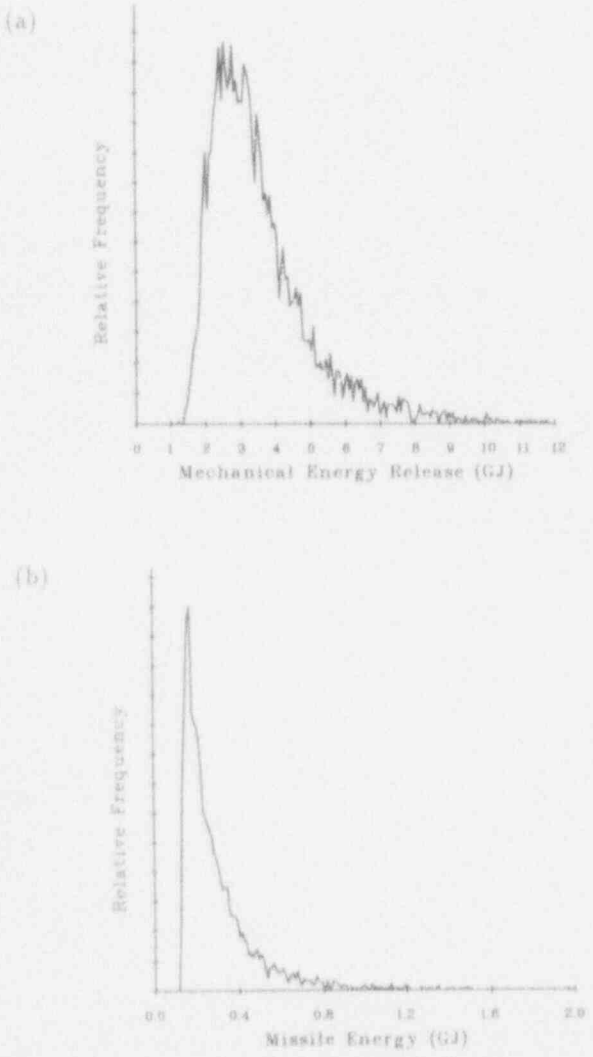

Figure 7. The distributions of mechanical energy and missile energy for those events which fail the containment.

We believe that the most likely area in which improvements can be made is that of propagation, as this would provide substantial support to 'limits to mixing' arguments and delineate better the conditions under which the lower head will fail (Fletcher, 1993).

If one is required to make a probabilistic assessment of events such as α-mode failure, there are significant advantages in the type of methodology used in the present assessment (based on the earlier work of Theofanous et al.). A relatively detailed event tree, and the use of distributions, allow the relevant experts (who vary for different parts of the assessment) to make judgements relatively unbiased by the (anticipated) end-result and include outliers that they believe should be considered. The presentation of the distributions allows a peer review process, so that some arguments are not over-deployed. The present study demonstrates the practicality of Monte Carlo methods even for relatively complex event trees and low probability events. The evaluations were performed on a UNIX work station with a few hours cpu time. Structured Monte Carlo methods would reduce the number of evaluations, but require care when the final outcome is dependent on the tail of a number of distributions (biasing in the sampling can be introduced to improve the resolution); however this technique seems more appropriate when complex models are being used as part of the evaluation.

We believe that it would be beneficial for the steam explosion community to consider what is the optimum tree for the α-mode assessment and agree definitions of the terms commonly used, such as 'efficiency' and 'explosion yield'. This would further the development of a consensus on this issue.

The α-mode assessment performed for the Sizewell B PWR has demonstrated the practicality of the event-tree method with input data represented by probability distributions. It has also drawn attention to a number of topics, which may be plant and sequence dependent (e.g. the melt relocation route and dissipation and failure mechanisms). The study has indicated the importance of melt relocation scenarios. This, perhaps, appears more pronounced than might have been anticipated, because very low probabilities based on a combination of triggering, low overall conversion efficiencies (less than a few %) or the ameliorating effects of lower head failure, do not appear to be justified at present, given the uncertainty in these areas. One topic we considered during the study and were unable to quantify (apart from developing the concept of 'leakage') was the question of whether or not a coherent slug forms. The absence of a slug would further reduce the probability of α-model failure.

In summary, the α-mode failure probability following an accident that leads to core melt relocation to the lower head for the Sizewell B PWR has been assessed as a few

parts in ten-thousand, on the basis of current information. This is consistent with a number of evaluations for other plants. The Sizewell B assessment has been the first to consider elevated pressures, but the results suggest only a modest sensitivity to system pressure.

ACKNOWLEDGEMENTS

This work was supported by Nuclear Electric plc, and permission to publish this paper is gratefully acknowledged. The authors appreciate the contributions to the study made by P R D Watkins, who first demonstrated the practicality of the Monte Carlo method, by M P Owens who performed the PLUGM calculations, and by H F Devonshire and D M O'Gara, who performed the initial structural calculations. They also thank their colleagues in AEA Technology and Nuclear Electric for many stimulating discussions throughout the course of this work.

REFERENCES

Angelini, S., Theofanous, T.G., Takara, E. and Yuen, W.W., (1992) *Multiphase Transients in the Premixing of Steam Explosions.* Proc. 5th Int. Topical meeting on Reactor Thermal Hydraulics (NURETH–5), Salt Lake City, 21–24 September, 1992, 471–478.

Attwood, G.J., (1993) *Structural assessments of possible steam-explosion-induced damage to a PWR.* Paper submitted to 12th International Conference on Structural Mechanics in Reactor Technology, Stuttgart, 15–20 August, 1993.

Berman, M., Swenson, D.V. and Wicket, A.J., (1984) *An uncertainty study of PWR steam explosions.* NUREG/CR–3369.

Bird, M.J., (1984) *An Experimental Study of Scaling in Core Melt/Water Interactions.* Paper presented at the 22nd National Heat Transfer Conference, Niagara Falls, 5–8 August, 1984.

Ciccarelli, G., Frost, D.L. and Zarafonitis, C., (1991) *Dynamics of Explosive Interactions between Molten Tin and Water in Stratified Geometry.* Prog. Astronaut. Aeronaut., **134**, 307–325.

Corradini, M.L., Kim, B.K. and Oh, M.D., (1988) *Vapour Explosions in Light Water Reactors: A Review of Theory and Modelling.* Prog. Nucl. Energy, **22**, 1–117.

Corradini, M.L. and Swenson, D.V., (1981) *Probability of Containment Failure due to Steam Explosions Following a Postulated Core Meltdown in an LWR.* NUREG/CR–2214.

Denham, M.K., Tyler, A.P., and Fletcher, D.F. (1992) *Experiments on the Mixing of Molten Uranium Dioxide with Water and Initial Comparison with* CHYMES *Code Calculations.* Proc. 5th Int. Topical meeting on Reactor Thermal Hydraulics (NURETH–5), Salt Lake City, 21–24 September, 1992, 1667–1675, (1992).

Fletcher, D.F., (1993) *Propagation Investigations using the* CULDESAC *Model.* Paper to be presented at the CSNI Specialist Meeting on Molten Fuel Coolant Interactions, Santa Barbara, 5–8 January, 1993.

Fletcher, D.F. and Denham, M.K., (1993) *Validation of the* CHYMES *Mixing Model.* Paper to be presented at the CSNI Specialist Meeting on Molten Fuel Coolant Interactions, Santa Barbara, 5–8 January, 1993.

Fletcher, D.F. and Thyagaraja, A., (1991) *The* CHYMES *Coarse Mixing Model.* Prog. Nucl. Energy, **26**, 31–61.

Hohorst, J.K. (ed.), (1990) *SCDAP/RELAP5/MOD2 Code Manual, Volume 4: MATPRO — A Library of Material Properties for Light Water Reactor Accident Analysis.* Idaho National Engineering Laboratory report EGG–2555 [NUREG/CR–5273].

Pilch, M. and Mast, P.K., (1984) *PLUGM — A Coupled Thermal-Hydraulic Computer Model for Freezing Melt Flow in a Channel.* Sandia National Laboratories report SAND82–1580 [NUREG/CR–3190].

SERG, (1985) *A Review of the Current Understanding of the Potential for Containment Failure arising from In-Vessel Steam Explosions.* US Nuclear Regulatory Commission, NUREG/1116.

Theofanous, T.G. et al., (1887) *An Assessment of Steam Explosion Induced Containment Failure.* Nucl. Sci. & Eng., **97**, 259–325, (4 parts).

STEAM EXPLOSION RESEARCH AT KERNFORSCHUNGSZENTRUM KARLSRUHE

H. Jacobs
Kernforschungszentrum Karlsruhe, Institut für Neutronenphysik und Reaktortechnik
Postfach 3640, D-7500 Karlsruhe 1, ☎ +49 (7247) 82-2443

ABSTRACT

A research program has been set up at Kernforschungszentrum Karlsruhe with the aim to determine realistic upper bounds to the loads on components of the containment of a large pressurized water reactor in case of a core melt down accident. This research is part of an attempt to find out whether the containments of such reactors can in the future be built in such a way that even the consequences of core melt down accidents are limited to the plant itself. After a short outline of the motivation for this venture, the plans of research correlated to in-vessel steam explosions are discussed.

I. INTRODUCTION

The steam explosion research at Kernforschungszentrum Karlsruhe (KfK) is part of a research program that aims at finding out whether nuclear power stations that might be built in the next century can be equipped with containments that nominally withstand even severe, i. e. core melt down accidents. With the presently most important reactor types, i. e. pressurized water reactors (PWR's) and boiling water reactors (BWR's), early containment failure following a severe accident is the potential source of the largest possible releases of radioactivity and thus constitutes the so-called remaining risk. All attempts to quantify the probability of occurrence of early containment failure have led to very small numbers and therefore this risk is widely accepted as tolerable. Still, with respect to future nuclear power stations, new reactor designs are studied in many places in the world with the aim of further reducing this risk. The mostly adopted approach is to further reduce the probability of a core melt down, e. g. by reducing the reactor size and providing it with largely passive safety features. The approach taken by KfK in collaboration with civil engineers from the University of Karlsruhe is different, see Hennies et al. (1989), Krieg et al. (1992), and Eibl et al. (1992). We are looking at large PWR's giving electrical power of over 1 GW because of the extensive and good experience with this reactor type. Also, in addition to all precautions taken to prevent a core melt down, we want to provide the reactor with a containment that fulfills the traditional functions of a containment and is able to prevent release of large masses of radioactivity even in the case of a core melt down accident.

The basic reason behind all activities with the aim of further improving the safety of nuclear power stations is the concern that the large consequences of an early containment failure following a severe accident may not be acceptable, although they have, at present already, an extremely small probability of occurrence. The dimension of the problem may be illustrated with the help of Figure 1 (Ehrhardt and Hasemann, 1991). Here the evacuation area is shown as a function of the fractions of the total inventories of cesium, iodine, and tellurium that are released after the melt down of a typical large PWR in Germany. In case of an early containment failure these fractions are estimated at 50...90 %, see GRS (1990), and thus the area that would have to be evacuated would be of the order of 2000...5000 km^2. In Central Europe with its high population density a million and possibly several millions of people would be affected. This would constitute a national (in Central Europe most probably a multinational) catastrophe. Even worse, displacement of so many people would simply be impossible. Thus, one could not even think of satisfactory countermeasures.

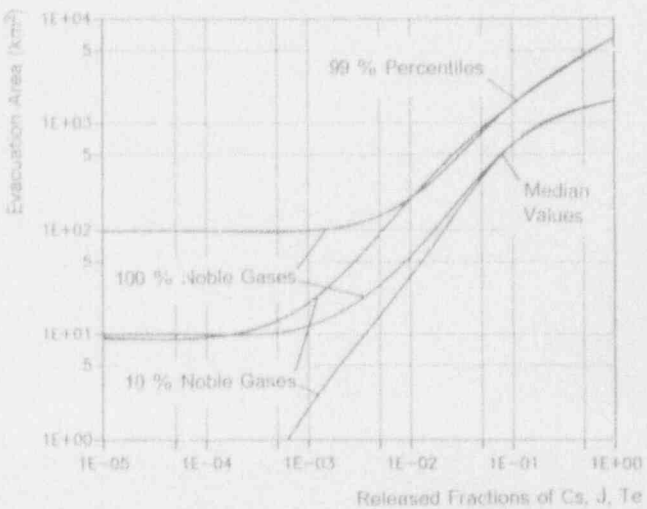

Figure 1: Evacuation area as function of released fractions of total inventories of cesium, iodine, and tellurium.

There are additional concerns on the side of KfK. On the one hand, the probabilities of occurrence of a core melt down accident and even more those of early containment failure are already now so small that their merit and even their interpretation are sometimes questioned. On the other hand, even sticking to those numbers, the overall risk would increase if the total power provided by nuclear energy globally would increase. Furthermore, the maximum consequences could still increase due to higher radioactive inventories caused by higher burnup or higher thermal power of single plants.

The containment solution offers an advantage in this situation. If a containment can be designed to withstand all loads resulting from severe accidents, catastrophical consequences outside the fence of nuclear power plants can be excluded altogether, at least nominally. Of course, absolute safety is impossible and there will remain a certain probability that the containment fails to perform as designed. However, this probability can be made very small independent of all measures taken inside the building to avoid the demand. The containment thus adds another substantial and quite obvious safety factor to any level of safety that is achieved by designing the reactor system against core melt down. Also, an improved containment should not add to the complexity of the reactor system and thus would not make it more prone to failure. One might even hope that the obvious, real, and qualitative reduction of the remaining risk provided by this containment could help to gain new public acceptance.

In case of a core melt down accident, unacceptably large radioactivity releases could result in the first place from early containment failure due to an in-vessel steam explosion, hydrogen burn or detonation, or high-pressure failure of the reactor pressure vessel (RPV) but also from basemat melt-through or a containment by-pass. Correspondingly, KfK has set up activities in the following fields:

- Determine sufficiently realistic (i. e. not too pessimistic) upper bounds to the loads on inner and outer containment structures due to steam explosion, hydrogen burn or detonation, and high-pressure failure of the RPV.
- Contribute (in collaboration with University of Karlsruhe) to the development of design concepts that allow to cope with these maximum loads.
- Develop core catcher concepts.
- Develop design ideas for safe long-term decay heat removal.

In most of these fields the French Commissariat à l'Energie Atomique and KfK have established a close cooperation and in some of them the two organizations will participate in Europe-wide so-called 'Reinforced Concerted Actions on Reactor Safety' that are organized and partially supported financially by the Commission of the European Communities. The problem of by-pass sequences is, at present, left to the designers of the reactor system.

In the following, only the activities aiming at determining upper bounds to containment loads due to steam explosions are described. At the moment these activities are concentrated on in-vessel steam explosions. However, the data to be collected and the tools to be developed will also allow a better quantification of loads due to ex-vessel steam explosions.

II. THE SITUATION AT OUTSET

Research into steam explosions has been carried out since more than 20 years. It has lead to a general qualitative understanding of the preconditions, the processes involved, and the consequences. The most important general conclusion is that there is no simple (back-of-an-envelope) argument to exclude early containment failure due to a steam explosion (often called α-mode failure) altogether. Attempts to quantify the probability of occurrence of such containment failure have (almost) unanimously resulted in 'small enough' values (SERG, 1985; Theofanous et al., 1987; GRS, 1990; Turland et al., 1993) but the data base for this conclusion is poor, e. g. Jacobs (1989). This has mainly two reasons: Firstly, all experiments available until now (or conceivable) involve melt masses that are smaller than those possibly available in a core melt accident by orders of magnitude, see Corradini (1991). And secondly, the detailed processes involved in steam explosions are not yet understood well enough or sufficiently amenable to modelling so that a reliable extrapolation from small scale experiments to the reactor accident case could be performed, see Corradini et al. (1988). At any rate, there are not sufficient quantitative data available for arriving at useful upper limits to loads on containment structures.

Past research into steam explosion has however led to the identification of a worst case scenario, i. e. the sequence of events that most likely leads to an early containment failure. This will be discussed in the next section. Past research has also identified phenomena that tend to prevent early containment failure due to steam explosions:

- the enormous load carrying capability of the RPV,
- the autocatalytic separation of melt and water that limits the interacting masses, and
- an energy conversion efficiency that is limited to some value between 10 and 20 %.

Sufficient quantification of these phenomena should allow to reduce the conservatisms in the determination of upper load limits to such an extent that really (practically) useful upper limits can be arrived at.

III. THE REFERENCE SCENARIO

The identification of uppermost loads requires a quantification of all phenomena on the critical path, i. e. the sequence of events that most likely leads to threats to the containment. This worst case or reference scenario has been worked out most clearly by Theofanous et al. (1987) and important parts of it have been studied mechanistically, thus providing valuable insight into the problem, in the SIMMER calculations by Bohl (1990). The scenario presently underlying the KfK research plans is described in the following.

The sequence starts with establishing the trivial preconditions of a steam explosion, i. e. assembly of large pools of core melt and water. This process is illustrated in Figures 2a and 2b. Figure 2a shows a partial core melt down similar to the final state of the TMI-2 core, Broughton et al. (1989), while Figure 2b represents a total core melt down. As discussed in the next paragraph, it would be helpful if melt relocation into the lower plenum would always start prior to total core melt down.

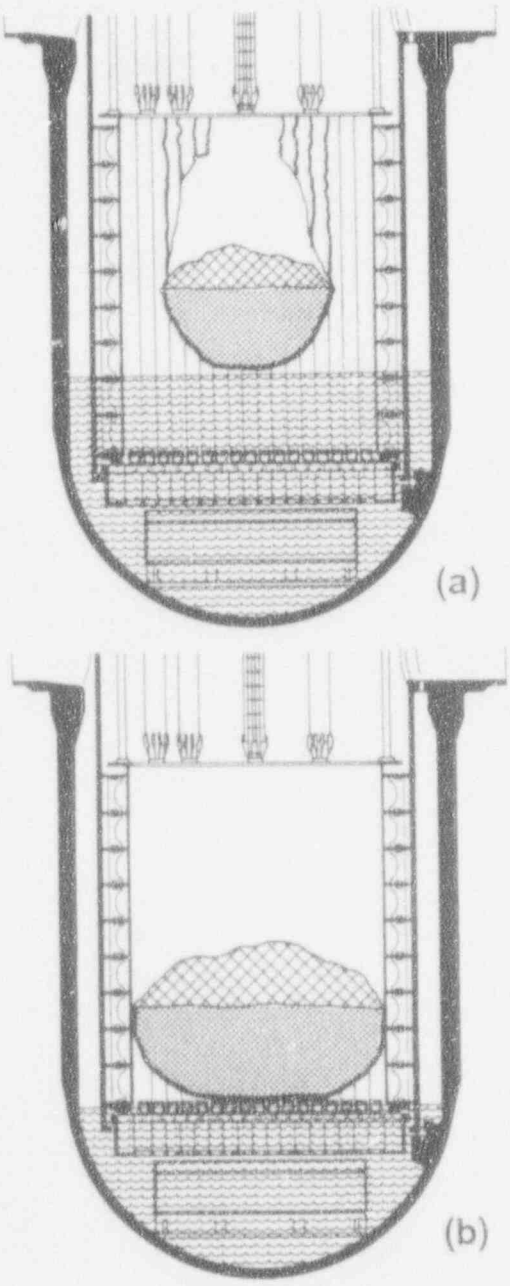

Figure 2: Schematic representation of possible core states from which melt relocation into lower plenum can occur:
a) partial core melt down
b) complete core melt down

Next, according to the present understanding of steam explosions, melt and water must be 'premixed' coarsely, e. g. Jacobs (1989), Courtaud et al. (1993). Essentially this means that the melt must flow from the core area into the lower plenum and be mixed with the water after having been broken up into relatively large lumps or drops. (The inverse process, i. e. mixing water into the melt, appears to be impossible or at least too ineffective, in practice.) During this phase the thermal interaction of melt and water is kept at a non-explosive level by a relatively small melt surface and separation of the materials by film boiling. Still, the radiative heat flux is enormous and produces a lot of vapor that is expected to remove liquid water from the mixing zone and thus inherently (autocatalytically) limit the masses that can mix and participate in the steam explosion. In this process the circumstances of melt relocation from the core into the lower plenum play an important role. The fact that melt relocation into the lower plenum occurred already when only part of the core was molten down in TMI-2, could be interpreted as an indication that it would always occur in such an early stage of core melt down. It would be very helpful if that could be proven to be true, because with a partially molten core (Figure 2a as compared to Figure 2b) the available melt mass is smaller and in addition the lower hydrostatic head in the melt pool and the longer and probably more complicated flow path of the melt (like in TMI-2) would reduce the rate of melt transport into the lower plenum. However, as long as such mitigating effects cannot be assured we must account for the most unfavorable possibility. The probably most pessimistic way of melt relocation is a large central pour as illustrated in Figure 3.

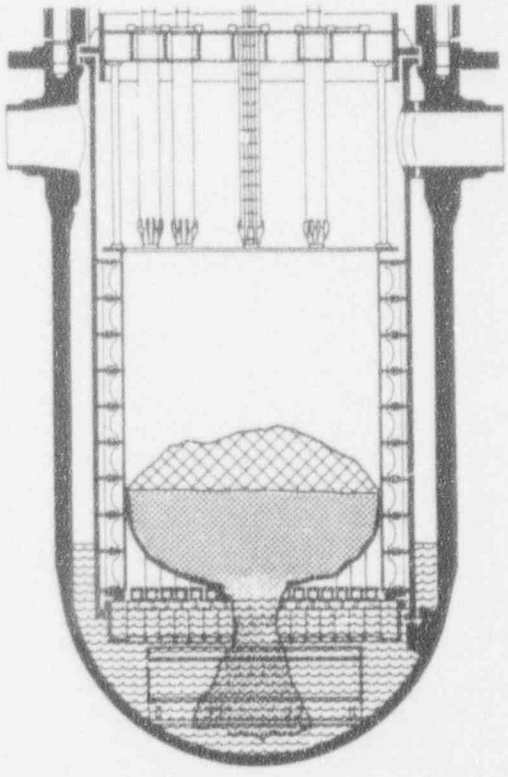

Figure 3: Schematic representation of melt relocation in a large central pour

When premixing has formed a mixture of melt and water a trigger or more clearly a trigger wave that is running through the whole mixture can start the intensive thermal interaction. The trigger wave starts fine scale fragmentation of the melt throughout the mixing zone and initiates the high heat transfer rates that are able to superheat the water with respect to the initial pressure so that the pressure rises and the mixing zone starts to expand rapidly.

During a very short (few milliseconds) initial period of the expansion phase, the structures surrounding the interaction zone (primarily RPV lower head and lower grid plate) may be loaded by high precaures on the order of 100..1000 bar. This might lead to lower head failure as indicated in Figure 4a. At the same time the interaction zone starts to expand and thus tranfers mechanical energ, to any mobile materials in its vicinity. Most important with respect to early containment failure is kinetic energy that is collected in materials moving upwards. Here the pessimistic assumption is that the materials moving upwards form a single coherent slug as shown schematically in Figure 4b.

The impact of the upwards moving slug against the upper vessel head could conceivably detach the vessel head or a part of it from the RPV and thus create a large missile that could pierce the outer containment, as illustrated in Figure 4c. However, prior to the impact with the vessel head the slug (or, more generally, the materials moving upwards) must destroy the structures above the core that have (probably to a large extent) survived the core melt down. This mechanical interaction is expected to dissipate a lot of the kinetic energy of the materials moving upwards before they impact on the vessel head.

In order to check whether there was a realistic chance to design a containment against the maximum loads from steam explosions, a rough quantitative estimate of the mechanical energies involved was required. As a starting point of this quantification, an explosion energy of 3 GJ has been postulated, which is a mere guess. This value is twice as high as the upper limit (the meaning of which was somewhat different) that was derived in the German Risk Study, Phase B, GRS (1990). It was chosen sufficiently high so that there seemed to be a chance to prove (in the future) that it was an upper limit, while, at the same time, undue conservatism had to be avoided. In fact, the 3 GJ were chosen so high that after the analysis by Theophanous et al. (1985) the mitigating effect of lower head failure could be taken into account and the worst case without lower head failure was covered.

The analysis by Theophanous et al. (1987) was used as well for evaluating the missile energy that finally results from the assumed explosion. In doing so, always their most pessimistic assumptions have been adopted. So, the figures given below represent

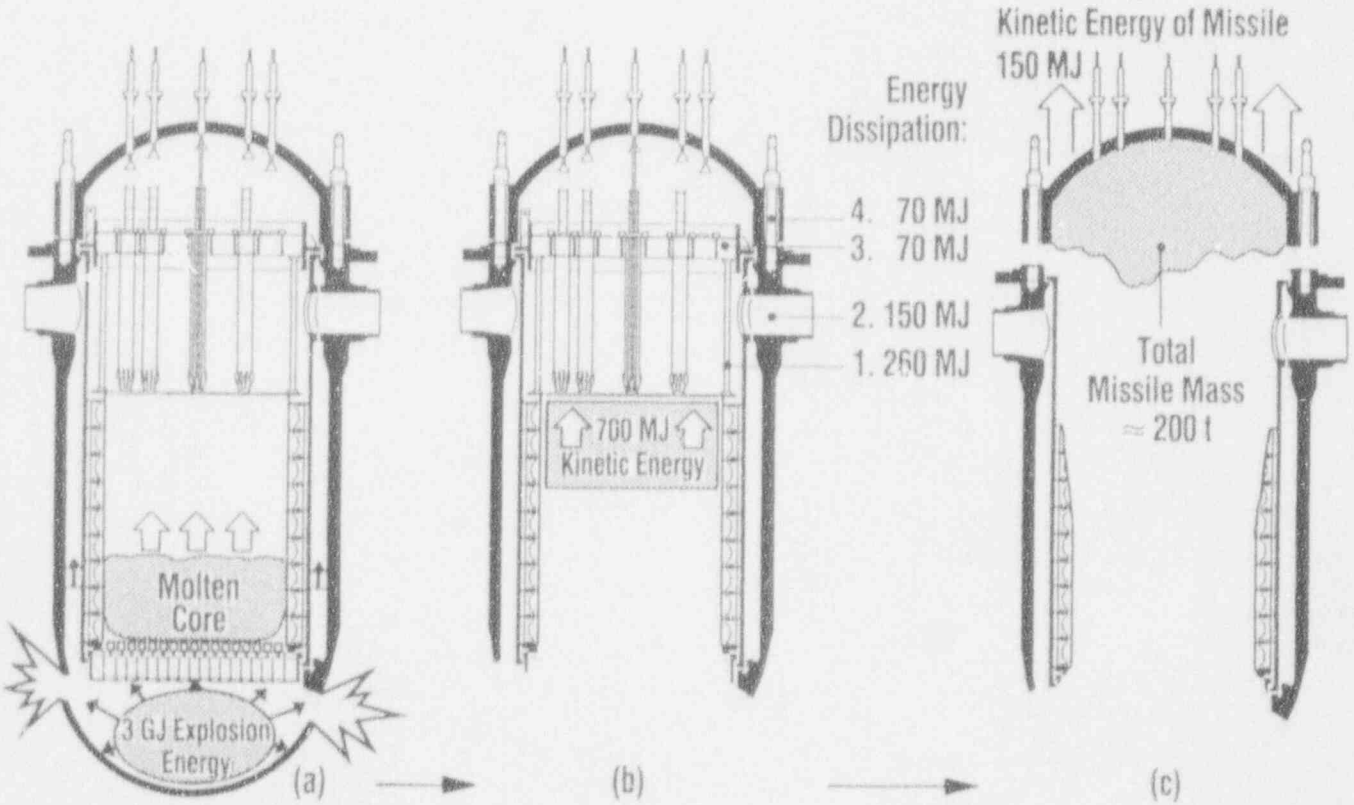

Figure 4: Schematic representation of the consequences of an energetic in-vessel steam explosion

the worst case. With 3 GJ of explosion energy, the kinetic energy of an assumed slug that is accelerated upwards is 700 MJ. Out of this, 260 MJ are absorbed during deformation of the upper internal structures (support columns and control rod guide tubes) and 34 % of the remaining energy, i. e. 150 MJ, are dissipated by venting into the hot legs and by core barrel straining that are caused by a transient pressure increase below the upper core support plate. Failure of this plate consumes another 70 MJ.

With these energy losses the energy remaining at slug impact against the vessel head is 220 MJ. Failure of the weakest part, the bolts, consumes (at least) 70 MJ. The maximum kinetic energy of a missile would thus be 150 MJ. This energy would be sufficient to penetrate the outer containment, but design studies have shown that such a missile could be intercepted by a missile shield at the top of the reactor cavity, Hennies et al. (1989).

In the above cited study of upper vessel head failure, Theofanous et al. (1987) assumed that the forces in the vessel head bolts quickly rise beyond the bolts' carrying capabilities so that failure is sure. This assumption appears to us to be overly pessimistic. We envisage that the (mostly liquid) materials that move upwards have partly to penetrate through the structures above the core, partly they will distort those structures and move them out of the way, and partly they will carry with them debris of those structures. Consequently, they will interact with the upper head not as a single slug but as a series of individual jets that are interspersed with pieces of solid debris of different sizes. It is thus conceivable that the center of gravity of these masses will travel a certain distance before their mean velocity is equilibrated with the velocity of the potential missile, i. e. the vessel head. Such a protracted mechanical interaction would lead to much reduced forces on the vessel head. And in the light of the about 1500 MN that the bolts of a typical large (German Konvoy type) PWR can carry, there is a good chance that vessel head failure will not occur in load cases as defined above, Krieg and Jacobs (1989). However, the limitations to the forces on the vessel head that are suggested by the above consideration must be proven, of course, before they can be relied on.

It should be understood that the above reference scenario will have to be modified if it turns out that it does not cover a more pessimistic case that reasonably should be taken into account. There are, e. g. indications that, at least for the RPV of a large German PWR, failure of the lower vessel head cannot be assured in the range of explosion energies here discussed, Krieg and Göller (1992). These authors find that the lower head doesn't fail when exposed to a parametrically assumed very pessimistic pressure history (for the resulting deformation see Krieg et al., 1992) while, at the same time, the deformation work absorbed by the vessel amounts to well over 1 GJ. However, the energy absorbed by the vessel can amount to only a few tenths of the explosion energy. Thus, it is uncertain whether failure can be expected with an explosion energy of a few gigajoules. This problem is further pursued and if it should finally turn out that lower head failure cannot be relied on, such failure could not be considered when determining energy partition. As a consequence, the energy of the upwards moving slug could increase to such an extent that design against the resulting missile could become practically impossible. In that case either a smaller maximum explosion energy will have to be proven or additional mitigating effects that have not been taken into account in the above scenario will have to be included. The energy of the materials moving upwards could e. g. be further reduced by an early breakup of the one single slug that would allow venting of the interaction zone into the upper part of the RPV. These very provisional remarks are added here in order to stress the fact that the above described scenario and even more the numbers given are in no way considered as being settled but serve as a guide for initiating the right research.

IV. KFK RESEARCH PROGRAM

According to the above described scenario and the usual way to conceptually subdivide the evolution of large scale steam explosions, the following key phenomena of early containment failure due to steam explosions can be identified:

1. Assembly of melt and water pools
2. Melt/water premixing
3. Explosion trigger
4. Explosion energy release
5. Slug formation and vessel head loading
6. Missile movement and containment breach

The main activities at KfK are concentrated on three of these phenomena: premixing, energy release, and vessel head loading. Above all, important experimental studies are or will be devoted to these topics and these will be decribed first.

With respect to melt/water premixing two different series of experiments are in preparation. The first of these are the particle/water intermixing (PWI) experiments in which large amounts (on the order of 10^5) of approximately spherical, hot (up to 2500 K), and solid particles are used to simulate the melt. The main purpose of this type of experiments is a detailed verification of the multifield multiphase hydridynamics code that will be used for analysis of the reactor case (see below) with respect to heat transfer and multiphase drag under conditions that are as representative as possible and especially in the high temperature range up to about 2500 K that has not been studied experimentally before. The particles simulate the drops of melt after its breakup. They have the advantage that shape, size, and surface area of the hot material are known and that no further fragmentation and therefore no steam explosion can occur. Thus, these experiments can be performed in the laboratory and a large number of parameters like density and temperature of the particles, vessel geometry, scale, and ambient pressure can be studied. In order to allow for sufficiently high temperatures, e. g. molybdenum spheres will be used. High speed movies will be used to register the basic behaviour, and the vapor production rate will be determined with the help of vortex flow meters. The main problem at present is to develop

enough quantitative measurement devices determining e. g. local void for being able to perform detailed and local code comparisons. At present preexperiments using a single sphere of 15 mm diameter that is equipped with a thermocouple are conducted mainly to develop measurement techniques (e. g. using pyrometers) and experimental procedures, Meyer and Rehme (1993).

In the second series of experiments, the large scale coarse mixing (LSCM) experiments, the premixing of actual melts with saturated water shall be studied in a simulation of the reactor case that is as realistic as possible. The experiments will typically be performed at 1/5 reactor size, see Figure 5 for a first concept of the test rig, Peppler et al. (1993). Aluminum thermite will be used in place of the core melt. It is intended to utilize 20...100 kg of melt that consists mainly (about 80 w-%) of alumina. In this case, more violent events (even explosions) cannot be ruled out a priori. Therefore these tests will be performed at open air at a blasting site close to Karlsruhe. The instrumentation will consist mainly of optical recordings and steam flow measurements. But if the necessary equipment will become available, local measurements as mentioned above will be performed as well. In preparation of this experiment series, exploratory experiments have been performed in which about 4 kg of molten alumina supplied from an already available melt injector have been released into boiling water in a strong container that was open at the top. These experiments are being evaluated at present.

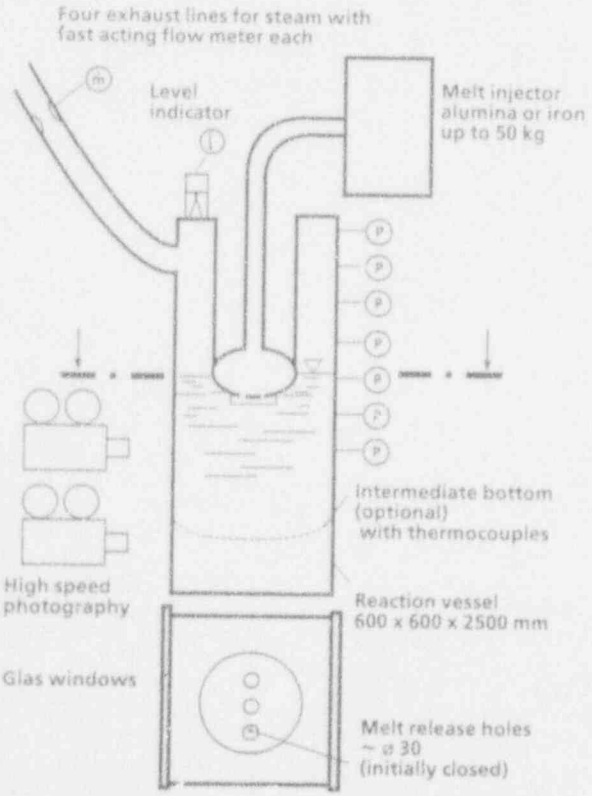

Figure 5: Basic lay-out of a first test rig for melt/water premixing

The extrapolation involved in transferring data from the experimental scale to the actual reactor scale is a special problem. It may therefore become necessary that in addition one of the premixing experiments described above is performed at a scale beyond 1/5 reactor size. This decision will be taken when data will be available that allow to determine how well the code is able to extrapolate.

With respect to mechanical energy release the steam explosion energy conversion (SEEC) experiments are under consideration. In these experiments the maximum possible energy conversion under conditions typical of an in-vessel steam explosion shall be actually measured. This means that the explosions must be contained with the only exception of a movable piston. The motion of this piston will be used to determine the energy release. The pressure time history, of course, will be measured as well. It is again intended to use molten alumina that is prepared in a thermite reaction as a simulant of the core melt. The requirement of containing the explosions will probably limit the melt masses to about 20 kg.

In a fourth series of experiments (BERDA) the vessel head loading will be studied. These will be model experiments at 1/10 reactor scale. They will simulate the impact of the materials that have been accelerated upwards on the upper internal structures and the vessel head. They will thus demonstrate the energy dissipation by the upper internal structures and the characteristics of the loads on the vessel head. In these experiments the load will be simulated by accelerating a molten pool of some high density low melting point alloy by an air gun with a piston of almost 40 cm diameter. For more details see Krieg et al. (1992).

Apart from the experiments, a code is required with which the knowledge and data gained from the experiments can be transferred to the reactor case. In our understanding this requires a multiphase code with at least three velocity fields that allow to describe the individual motions of melt, liquid water, and gas in at least two dimensions. The availability of such a code is considered as the essential progress in modeling capability that in the first place allows to start on determining upper limits to loads from steam explosions. The appearance of such codes also makes the essential difference between the situation today (or in a few years when these codes will be better tested and verified) and the situation in which the Steam Explosion Review Group (1985) found itself.

At KfK the transient three dimensional three field multiphase code IVA3 has been developed by Kolev (1992). As developed, this code has two variants. In one of them two phase flow in a heated 'porous' structure as e. g. a reactor core can be modelled and in that case the third field is used to describe the droplets moving separately within the steam core of annular flow. In the variant to be used in connection with steam explosions the three fields describe gas (steam and possibly noncondensable gas), liquid water, and the melt. The code assumes equal pressures in all three fields locally and uses

flow regimes to model the exchange terms with respect to energy and momentum. Some more details are given in Jacobs (1993) which also describes some part of the effort to validate the code.

The code is still being assessed and will certainly need further development. The first aim is to qualify the code for analysis of the premixing phase. This will need further development of the largely mechanistic models of melt breakup and exchange of heat and momentum with the two phase water that are already available in the code, see also Jacobs (1993). The code shall also be enabled to describe the propagation and expansion phases of the steam explosion. To this end (probably parametric) models of (local) explosion triggering, fine scale fragmentation, and heat transfer during a steam explosion will have to be added to the code. All these models will be verified with the help of sufficiently representative experiments performed at KfK and (hopefully) elsewhere in the world. The code will as well be compared with other codes of this type available.

After having been fully qualified, the code will be used to determine the most pessimistic way in which the core melt can be mixed with water and the upper limit of the melt mass that can be mixed. In doing so we will only partially rely on some (rather arbitrary) mixing criterion but will use combined calculations of premixing and explosion expansion to determine the upper limit of the kinetic energy associated with materials that are accelerated upwards. This task might require to account at least in an approximate manner for structural responses of the RPV (and the structures supporting the core). This would mean a further development of the code but could be done e. g. like in Bohl (1990).

Besides the main activities described above there are also smaller activities in two fields: One is the investigation of the mechanical behaviour of RPV and structures supporting the core as already mentioned. This is done by applying standard structural mechanics methods, see Krieg et al. (1992). The second is the investigation of the initial conditions of steam explosions, especially premixing. These include e. g. the melt configuration when relocation into the lower plenum occurs and the primary system pressure at that time. The tool to be used is SCDAP/RELAP5, see e. g. Allison et al. (1991). As already discussed in section III, it would be very helpful if it could e. g. be proven that the configuration from which relocation into the lower plenum occurs looks more like shown in Figure 2a than in Figure 2b. However, it is uncertain whether the size of a molten pool is really limited to some value as represented in Figure 2a and even more whether such a finding can be arrived at with sufficient reliability during the next few years. Still the problem must be pursued. Unfortunately the strict limitations in available manpower force this activity to be a smaller one at present. In the long run, a complete description of the processes leading to core melt discharge into the lower plenum is required. The first task which is in work at the moment, Sengpiel (1993), is validating and further developing the SCDAP code by comparison of calculations with severe fuel damage experiments (the KfK out-of-pile experiments CORA and the French experiments PHEBUS FP).

Two of the key phenomena that were listed above will essentially not be attended to. These are first the trigger and second missile movement and containment breach. With respect to the trigger there doesn't seem to be a chance to prove that there are circumstances in which no trigger occurs at all or that it occurs very early. So, this point will have to be covered conservatively, i. e. we will have to assume that the trigger occurs in the most unfavorable moment. If missile movement should be found to constitute a threat to the containment, it will be the task of civil engineers to develop proper countermeasures.

V. CONCLUDING REMARKS

The aim of steam explosion research at KfK is to determine the resulting maximum loads on containment structures. As these shall be used as design criteria, they must not be overly pessimistic. For practical purposes the task is broken up into two parts: determine the maximum explosion energy and determine what the resulting large missile(s) may look like. In detail the individual tasks are:

1. Determine the premixing configuration that results in the maximum energy release.
2. Determine whether the resulting pressure-time history leads to lower head failure with certainty, possibly, or certainly not.
3. If lower head failure is at least possible, determine its maximum kinetic energy (as function of distance travelled so that the design can be adjusted).
4. Determine the worst case mass, composition, and kinetic energy of the materials accelerated upwards (without taking credit of lower head failure if that cannot be assured).
5. Determine worst case loads on the vessel head.
6. Determine whether vessel head bolts fail, i. e. whether the vessel head or the whole vessel are to be accelerated by the materials moving upwards.
7. Determine the kinetic energy of the missile (assuming an inelastic impact).

Finally it will be necessary to determine the influence of the primary system pressure on the above evaluations. However, arriving at useful upper load limits with elevated system pressures might prove to be difficult. On the one hand it seems to be clear that the inherent limitation to premixing is less effective at elevated pressures. On the other hand elevated pressures may not be sufficient to reduce the explosion yield to such an extent that large premixed masses can be tolerated. This is indicated by experimental results that show the most energetic interaction in the one case out of a series in which the ambient pressure was raised to 10 bar, Bird (1984). Also, triggering of a steam explosion has been observed at an ambient pressure of about 50 bar, Edwards et al. (1988). The most dangerous situation might arise in the range of 10...20 bar and the most favorable solution to the problem (from the present point of view) would be to assure that the pressure on the long run (prior to melt relocation

into the lower plenum) drops well below that pressure range. In any case, ambient pressures of a few bars will have to be considered and this will require experimental data with respect to premixing and energy conversion obtained under such conditions.

ACKNOWLEDGEMENT

The auther is grateful to Dr. Lisa Väth for thoroughly reviewing this manuscript.

REFERENCES

Allison, C. M., C. H. Heath, L. J. Siefken, and J. K. Hohorst, 1991, SCDAP/RELAP5/MOD3 Code Development and Assessment, Proc. 19th Water Reactor Safety Information Meeting, Bethesda, USA, October 28-30, 1991, US Nuclear Regluratory Commission Report NUREG/CP-0119, pp. 199-210

Bird, M. J., 1984, An experimental study of scaling in core melt/water interactions, 22nd Natl. Heat Transfer Conf., Niagara Falls, USA, August 1984

Bohl, W. R., 1990, An Investigation of Steam-Explosion Loadings with SIMMER-II, Los Alamos National Laboratory Report LA-10639-MS, March 1990

Broughton, J. M., Pui Kuan, D. A. Petti, and E. L. Tolman, 1989, A Scenario of the Three Mile Island Unit 2 Accident, Nuclear Technology **87** (1989) 34-53

Corradini, M. L., B. J. Kim, and M. D. Oh, 1988, Vapor Explosions in Light Water Reactors: A Review of Theory and Modelling, Progress in Nuclear Energy, Vol. 22, pp. 1-117

Corradini, M. L., 1991, Vapor Explosions: A Review of Experiments for Accident Analysis, Nuclear Safety **32** (1991) 337-362

Courtaud, M., M. Réocreux, P. Hofmann, and H. Jacobs, 1993, In-Vessel Core-Melt Progression Phenomena, Proc. of ENS Topcl. Mtg. Towards the Next Generation of Light Water Reactors, The Hague, Netherlands, April 25-28, 1993, to be published

Edwards, A. J., J. B. Knowles, and R. B. Tattersall, 1988, Molten Fuel Studies at Winfrith, U K Atomic Energy Authority Report AEEW-R 2301, January 1988

Ehrhardt, J. and I. Hasemann, 1991, private communication

Eibl, J., F. H. Schlüter, T. Klatte, W. Breitung, F. Erbacher, B. Göller, R. Krieg, W. Scholtyssek, and J. Wilhelm, 1992, An Improved Design Concept for Next Generation PWR Containments, Proc. of Fifth Workshop on Containment Integrity, Washington, USA, May 12-14, 1992, US Nuclear Regluratory Commission Report NUREG/CP-0120 (SAND92-0173), pp. 337-363

Gesellschaft für Reaktorsicherheit (GRS), 1990, Deutsche Risikostudie Kernkraftwerke, Phase B, Verlag TÜV Rheinland, Köln

Hennies, H. H., G. Kessler, and J. Eibl, 1989, Improved Containment Concept for Future PWRs, in: Safety of Nuclear Installations: Future Direction, Proc of Int. Wurkshop on the Safety of Nuclear Installations of the Next Generation and Beyond, Chicago, USA, August 28-31, 1989, International Atomic Energy Agency Report IAEA-TECDOC-550, pp. 361-371

Jacobs, H., 1989 Steam explosions during light water reactor meltdown accidents, Proc. of 3rd Int. Seminar on Containment of Nuclear Reactors, Los Angeles, CA, August 10 - 11, 1989, pp. 302-320

Jacobs, H., 1993, Analysis of Large-Scale Melt-Water Mixing Events, Proc. of CSNI Spec. Mtg. on Fuel Coolant Interactions, Santa Barbara, USA, January 5-8, 1993, to be published

Krieg, R. and B. Göller, 1992, private communication

Krieg, R., H. Alsmeyer, G. Jacobs, H. Jacobs, J. Eibl, F. H. Schlüter, T. Klatte, 1992, Extreme Loadings of Inner Structures of Next Generation PWR Containments, Proc. of Fifth Workshop on Containment Integrity, Washington, USA, May 12-14, 1992, US Nuclear Regluratory Commission Report NUREG/CP-0120 (SAND92-0173), pp. 323-335

Meyer, L. and K. Rehme, 1993, private communication

Peppler, W., F. Huber, and H. Will, 1993, private communication

Sengpiel, W., 1993, private communication

Steam Explosion Review Group (SERG), 1985, A Review of the Current Understanding of the Potential for Containment Failure from In-Vessel Steam Explosions, U.S. Nuclear Regulatory Commission Report, NUREG-1116, June 1985

Theofanous, T. G. et al., 1987:
T. G. Theofanous, B. Najafi, and E. Rumble, An Assessment of Steam-Explosion-Induced Containment Failure. Part I: Probabilistic Aspects, Nucl. Sci. Eng. **97** (1987) 259-281
M. A. Abolfadl and T. G. Theofanous,
An Assessment of Steam-Explosion-Induced Containment Failure.
Part II: Premixing Limits, Nucl. Sci. Eng. **97** (1987) 282-295;
W. H. Amarasooriya and T. G. Theofanous,
An Assessment of Steam-Explosion-Induced Containment Failure.
Part III: Expansion and Energy Partition, Nucl. Sci. Eng. **97** (1987) 296-315;
G. E. Lucas, W. H. Amarasooriya, and T. G. Theofanous, An Assessment of Steam-Explosion-Induced Containment Failure. Part IV: Impact Mechanics, Dissipation, and Vessel Head Failure, Nucl. Sci. Eng. **97** (1987) 316-326.

Turland, B. D., D. F. Fletcher, K. I. Hodges, and G. J. Attwood, 1993, Quantification of the Probability of Containment Failure Caused by an In-Vessel Steam Explosion for the Sizewell B PWR, Proc. of CSNI Spec. Mtg. on Fuel Coolant Interactions, Santa Barbara, USA, January 5-8, 1993, to be published

THE PROBABILITY OF ALPHA-MODE CONTAINMENT FAILURE UPDATED

T.G. Theofanous and W.W. Yuen
Center for Risk Studies and Safety
University of California, Santa Barbara, CA 93106
Tel. (805) 893-4900 — Fax (805) 893-4927

ABSTRACT

Since the original quantification of the likelihood of α failure in NUREG/CR-5030, major experimental and analytical developments have taken place. By taking advantage of these developments, we believe it is possible to reduce the substantial conservatisms in the original quantification, and to thus conclude that even vessel failure by steam explosions may be regarded as physically unreasonable. We have illustrated how this can be done within the original framework, as well as in a complementary framework that takes advantage of current integral analysis capabilities. On this basis, the α-failure issue is now ripe for final resolution; what is needed is a complete set of calculations supporting a revised quantification of CR1 and CR3 and a final review step in the ROAAM process.

INTRODUCTION

Since its definition and initial quantification in WASH-1400, the α-mode containment failure has maintained a unique place in risk analyses of nuclear reactors and related safety research. It involves an energetic fuel-coolant interaction that takes place in the lower plenum of a pressurized water reactor (PWR): the generation of an internal missile that loads the upper head of the reactor vessel to failure, the generation of an external missile, and containment boundary (upper dome) impact. The energetic interaction presupposes a massive pour of molten corium from a crucible-held geometry into the lower plenum; the energetics of the internal missile depend on a number of dissipative phenomena associated with the momentum and structural interactions leading up to and including upper head loading and failure; and the external missile (the detached vessel head or portion of it) must destroy or "sweep-away" the missile shield before it can begin to rise toward impacting the containment. The problem is significant because it gives rise to the possibility of "early" containment failure, and it has become an "issue" because the complex phenomenology has been addressed variably and on occasion with conflicting results.

In interesting contrast to most other major containment integrity "issues" (in severe accidents), the α failure has evolved as a rather benign one, that is, more as a matter of omission rather than one of commission. In other words, more as a result of failure to deliver a definitive (generally agreeable) closure rather than as a result of explicitly specified and generally accepted active concerns on it. This is quite evident in the first systematic evaluation of it by an *ad hoc* panel of experts, the Steam Explosions Review Group (SERG, 1985), some eight years ago, as well as in the latest quantification of it as a part of the NUREG-1150 study two years ago. Specifically, in SERG, we find panel member assessments that, with only a few exceptions, agree that α failure is of adequately low likelihood not to pose serious containment integrity concerns, while the NUREG-1150 expert panel on this issue agreed that these SERG assessments were appropriate and made use of an aggregate (based on arithmetic averaging) of them in the quantification. The NUREG-1150 results indicate that the probability of α failure (conditional on core melt) is under 1%, with an upper bound (95^{th} percentile) estimate of "a few" percent. The reasons for further attention on this issue can be listed as follows:

1. *Quality and Robustness of Assessments.* Individual assessments in SERG were based on widely variable reasoning and to a great extent on judgment.

2. *Treatment of Outliers.* Individual SERG assessments of probability varied over many orders of magnitude, including some extremely small as well as some rather large (the few exceptions noted above) values.

3. *Interpretation of Results.* The SERG-aggregate mean value of 0.8% and the above-quoted NUREG-1150 result (under 1%) may mean different things to different people, and not necessarily always a negligible concern.

It is worth noting that these specific, quantitative, concerns were framed in the context of the scenario described above; it can be expected that their resolution will provide the impetus and help address explicitly other less tangible aspects of this issue, including multiple explosions and other (than pouring) modes of contact, especially as they arise in consideration of accident management actions (Theofanous, 1991).

An initial step toward resolving the concerns listed above was made five years ago (Theofanous et al., 1987, to be referred to as NUREG/CR-5030) under an approach formalized later as the Risk-Oriented Accident Analysis Methodology (ROAAM) — Theofanous and Yan (1991). Meanwhile, the methodology has been employed to the

resolution of two other major issues—Mark-I Liner Attack (Theofanous et al., 1991) and Direct Containment Heating (Pilch et al., 1992)—while new data and calculations anticipated by, and relevant to, the original quantification have recently become available. Guided by the methodological insights from these further applications of ROAAM, our purpose here is to re-examine the NUREG/CR-5030 quantification, in light of these new data and calculations, with an eye toward an ultimate resolution.

OVERVIEW OF THE ORIGINAL QUANTIFICATION AND THE NEW DEVELOPMENTS

The probabilistic framework employed in NUREG/CR-5030 is shown (in current notation and with the practically unimportant limit of molten core available omitted) in Figure 1, and it can be understood in terms of the explosion scenario described in the early part of the introduction section, with the help of Figures 2 and 3. Of critical importance to the quantification, is the "upper-central" portion of this framework including, in particular, the quantification of premixtures (CR1) and of the energy partition associated with lower head failure (CR3). Indeed, these also happened to be the focus of the criticism received in the review process, as documented in NUREG/CR-5030, and accordingly, these will be the focus of the present reexamination here. In passing, we note that the overall framework and, in general, the approach, has been well received; moreover, a similar approach has been taken in addressing this issue within the licensing proceedings of the Sizewell plant in the UK. The details of this study are to be made openly available soon (Turland et al., 1993), but it is our understanding that the results indicate an adequately low likelihood (of containment failure) for licensing purposes. This can be taken as generally reinforcing of the NUREG/CR-5030 conclusion that such failures are "physically unreasonable," but the extent of actual synergism obtained can only be understood after a detailed comparative study of the two quantifications.

Premixing, in NUREG/CR-5030, was quantified strictly on the basis of computations. In particular, a two-fluid model was used to compute the transient penetration of fuel particles in a locally homogeneous steam-water mixture, allowing for two-dimensional motions and to thus demonstrate the water-depletion phenomenon envisioned by Henry and Fauske (1981). Assuming that fuel surrounded by highly voided coolant (say, 50 to 70%) cannot effectively participate in an explosion, limits to the quantities of fuel premixed (and thus able to explode) could be obtained for arbitrarily large pours. The resulting quantification, allowing for highly generous margins above the quantities deduced from such computations to judgementally cover uncertainties, is shown in Figure 4. Important subsequent developments include: a new and more general three-fluid formulation and computer code, the PM-ALPHA, that confirms the conservative nature of the original quantification (Amarasooriya and Theofanous, 1991); a comparative study of reactor-scale premixing calculations between PM-ALPHA and the independently developed CHYMES code (Fletcher, 1992); and the MAGICO (Angelini et al, 1992) and MIXA (Denham et al., 1992) experiments designed specifically for comparisons with the PM-ALPHA and CHYMES codes predictions, respectively. At a much larger scale, the FARO Quenching Test series is now also beginning to produce the first results. We will argue that these developments provide the firm basis needed to drastically reduce the conservatism built in the quantification of Figure 4.

Energy partition, during the early yield phase of the explosion, in NUREG/CR-5030, was based on what was thought to be a conservative treatment of explosion energetics in combination with the structural response of the lower head. The simple idea was that an explosion energetic enough to produce an upper-head-threatening missile should be able to fail the lower head that contained it in the first place; such failure provides downward relief and thus significant mitigation of energy in the upward-directed missile. The quantification is reproduced in Figure 5. The "break" in slug energy due to lower head failure is seen to occur at ~1 GJ of total mechanical energy release, and this is consistent with other independent studies. Still, the mechanism depends on the time scale of the energy release, and it can, therefore, be (it has been) questioned in a quantification based on equilibrium thermodynamics that bypasses the dynamic aspects of the interaction. It is now possible to account for these dynamic aspects and thus address this question directly. Several developments have contributed to this new capability, including: experience with several independent one-dimensional detonation codes (Medhekar et al., 1991; Fletcher and Thyagaraja, 1991; Bürger et al., 1993), single-drop fragmentation data under conditions relevant to an established detonation wave (Yuen et al., 1992), the first quantified experimental demonstration of a strong detonation with $A\ell_2O_3$ melts (Hohmann et al., 1993) as compared to mild ones obtained with tin melts in previous works, and an experimentally-tested analysis tool, the ESPROSE code, that when interfaced with PM-ALPHA can follow the triggering and escalation of an explosion in two dimensions from realistic premixtures and in relevant reactor geometries (Yuen and Theofanous, 1993). We will argue that these developments provide a firm basis for the consideration of lower head integrity, and the related energy partition question, under physically meaningful explosions in the lower plenum.

With this integral capability at hand, from a methodological standpoint, the question arises as to whether the lower-central portion of the framework affected should be condensed into one single operation, as illustrated in Figure 6. This structure is attractive because it captures in a consistent manner the "size" of the explosion in terms of premixture characteristics and respective level of energetics. In the original quantification, this could be done only in a preliminary way, by making the conversion ratio a function of the energy stored in the premixture (CR2). Also, this approach continues to capture the main variable characterizing the "massiveness" of the melt pour. In particular, we note that this is adequate to reflect "side" versus "bottom" pours as well as other variables in accident characteristics such as system pressure or lower plenum subcooling by defining an appropriate set of splinter scenarios (Theofanous and Yan, 1991). An important disadvantage of such a condensation, on the other hand, is that it could detract

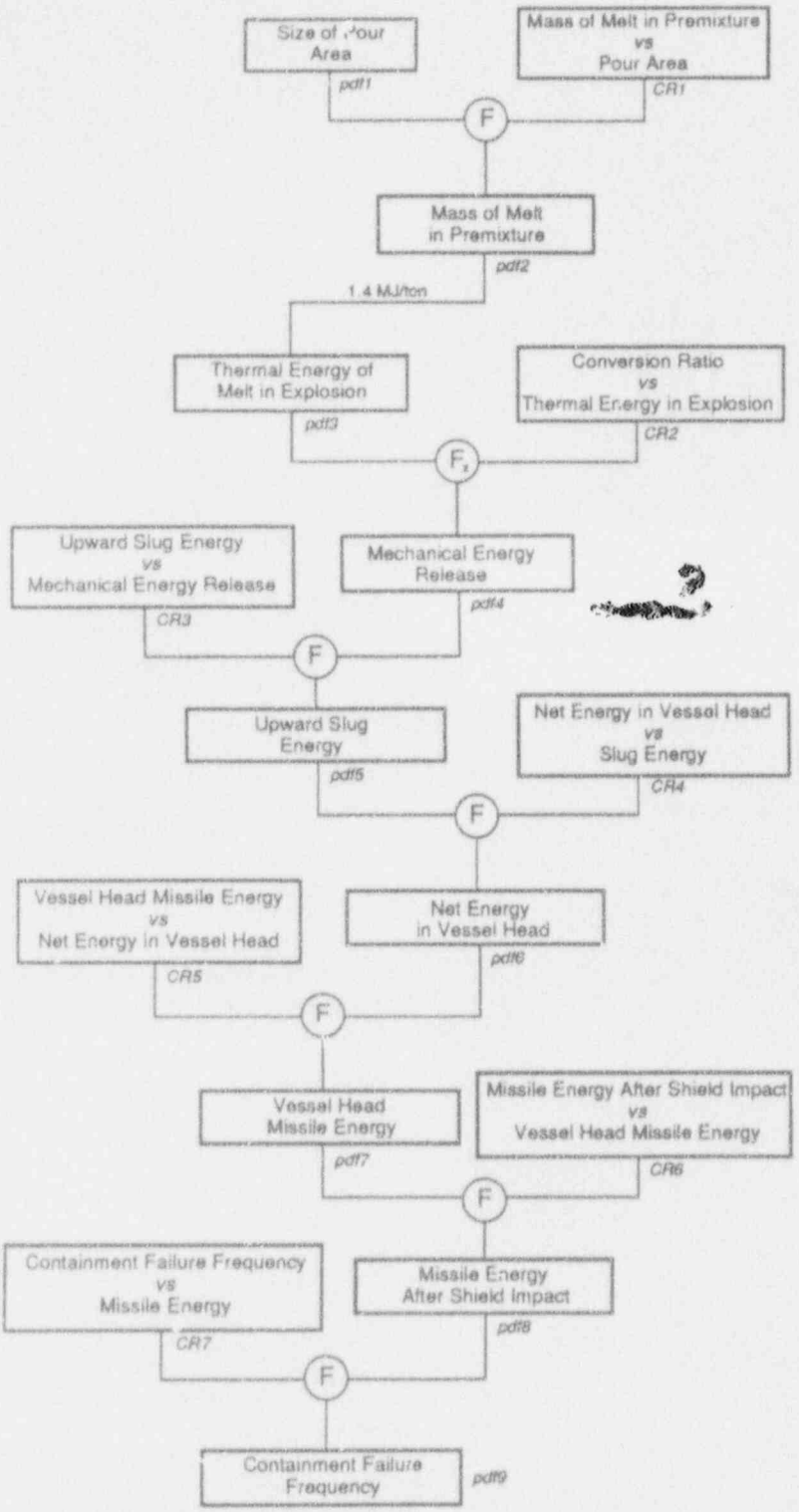

Figure 1. Probabilistic framework for the assessment of α failure as proposed in NUREG/CR-5030. pdf and CR refer to "probability density function" and "causal relation" in the ROAAM terminology.

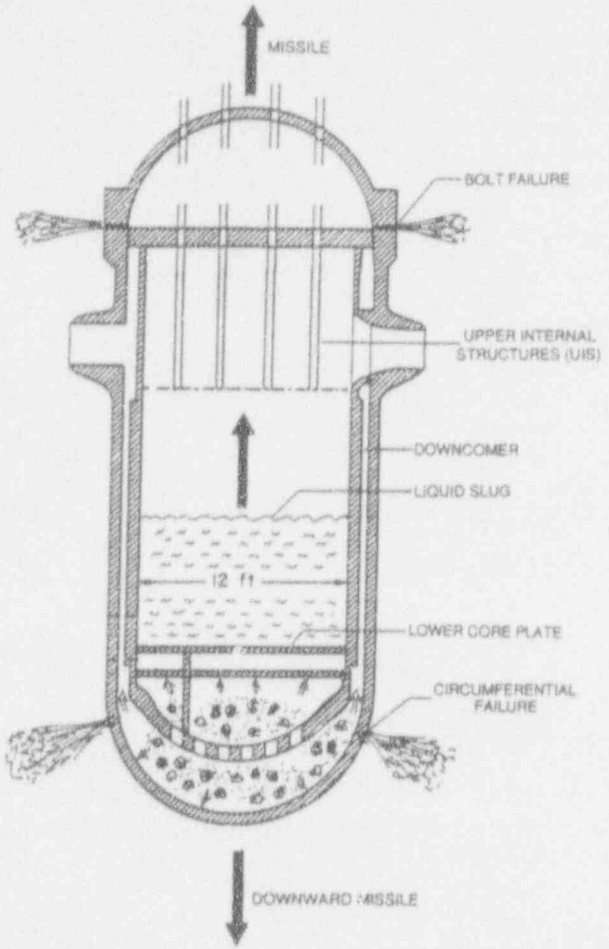

Figure 2. Key mechanisms and terminology for a steam explosion event (in-vessel portion).

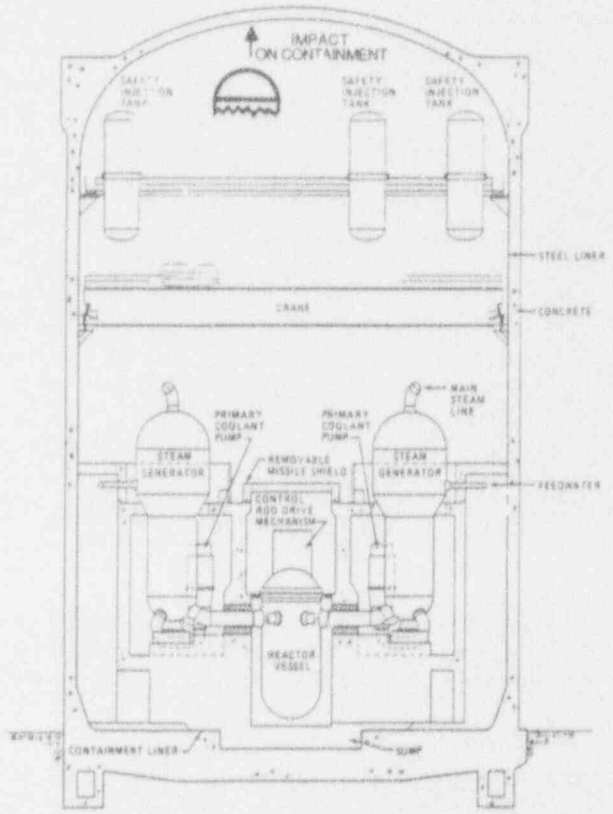

Figure 3. Geometry relevant to the ex-vessel portion of a steam explosion event in a large dry containment.

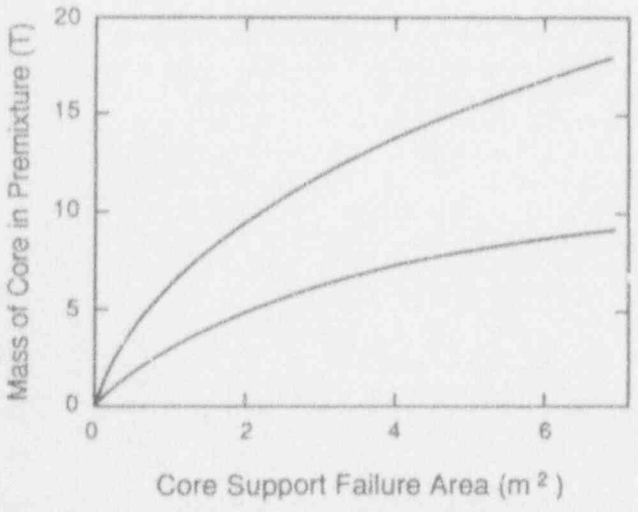

Figure 4. CR1 according to NUREG/CR-5030. A flat distribution was assumed between the 5 and 95% limit lines shown. The point refers to a calculation presented later on in this paper.

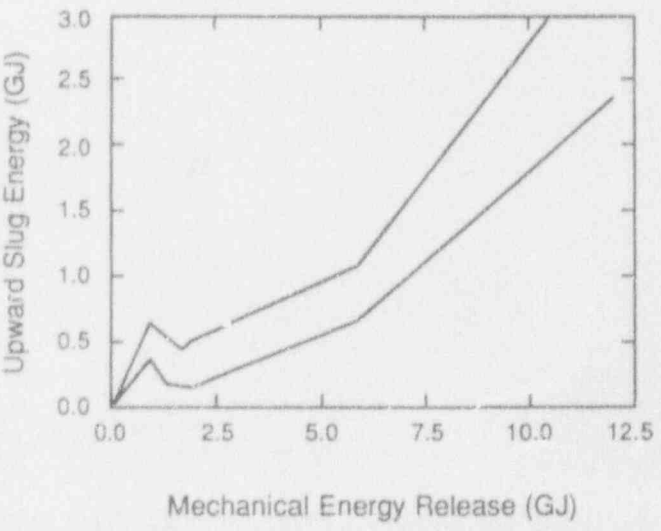

Figure 5. CR3 according to NUREG/CR-5030. A normal distribution is assumed between t' = 5 and 95% limit lines shown.

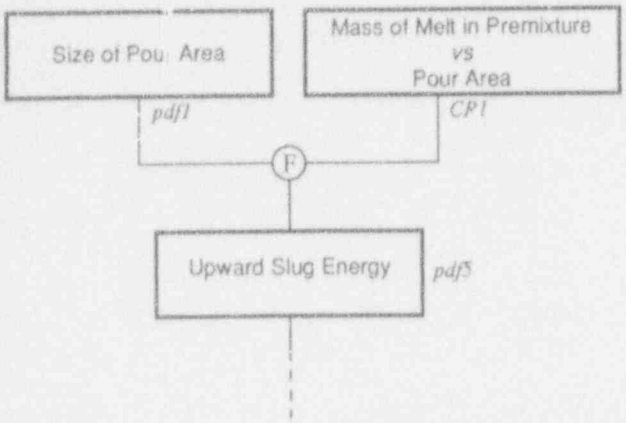

Figure 6. A condensed version of the upper-central portion of the probabilistic framework in NUREG/CR-5030, making use of currently available integral analysis capability.

from one of the key aims of ROAAM; that is, allowing for as many independent quantifications of each component of the framework as possible. For example, an independent contribution to the quantification of premixing could not be made to the condensed framework. Conversely, the breakdown of the results from integral analyses, for the purposes of the original framework, should always be possible while still retaining the essential features of consistency (or dependencies). For these reasons, we propose the condensed framework as a complement to rather than as a substitute for the original one.

QUANTIFICATION OF PREMIXING

The fundamental parameter in quantifying a premixture is the void fraction. From a bounding equilibrium thermodynamics standpoint (i.e., Hicks–Menzies), the implied working-fluid depletion drastically reduces the thermal-to-mechanical energy conversion (Amarasooriya and Theofanous, 1987), while from an explosion dynamics standpoint, it interferes with both the triggering and the escalation processes. This interference is further augmented by two-dimensionality (Medhekar et al., 1989; Yuen and Theofanous, 1993), and vice versa, two-dimensionality is essential to the prediction of void fraction distributions (Angelini et al., 1993). Accordingly, this discussion and a related experimental program are focused on void fractions.[a] The analysis tool is PM-ALPHA, and its performance against these experiments has been presented in a companion paper (Angelini et al., 1993). The only other comparable analysis tool available at this time is CHYMES, and the first comparisons of its predictions, with those made previously by PM-ALPHA for reactor-scale premixing calculations, have just been published (Fletcher, 1992). Melt volume fraction distributions were very consistent, and even premixed-mass transients up to the melt contact time with the lower head were found to be in excellent agreement; however, disturbingly large discrepancies on the spatial evolution of the steam volume fractions were also noted. The author attributed these discrepancies to differences in the drag laws employed in these two codes but offered no specific recommendations for resolution. To us, these discrepancies became a significant cause of concern, especially in light of our opinion of the importance of void fractions, as detailed above, and the prior use of PM-ALPHA to quantify premixing for the actual assessment of α failure.

In fact, the cause could be traced to an organic difference between the two codes: CHYMES cannot allow for the presence of subcooling, while PM-ALPHA does. More specifically, in CHYMES, the local rate of boiling is taken as a local latent heat requirement; i.e., in CHYMES's notation (Fletcher and Thyagaraja, 1991),

$$\dot{m}_s = 6\alpha_m\alpha_w h(T_m - T_{sat})/(L_m h_{fg}) \qquad (1)$$

where the α's are the melt and water volume fractions, h is the heat transfer coefficient, h_{fg} is the latent heat of vaporization, and L_m is a melt length scale used to estimate the heat transfer area. By contrast, in PM-ALPHA, boiling occurs at the rates necessary to bring the water locally to saturation. In practical terms, this means that the water cannot sustain any significant amount of superheat, which is, of course, the physically meaningful behavior. Moreover, CHYMES cannot allow for condensation, while in PM-ALPHA, steam is allowed to condense, as it should, if it happened to flow through a subcooled water region. [The complete constitutive package can be found in Angelini et al., 1993.] The importance of subcooling is not limited to scenarios with an initially "cold" pool of water; gravitational head in deep pools (as the one in the lower head) implies a non-negligible subcooling even in "saturated" cases, but more importantly, even modest increases in pressure due to the limited venting area from the lower plenum (the area leading into the downcomer) can produce, through the induced subcooling, a most significant feedback effect on boiling. In the absence of this feedback, as in CHYMES, the calculation in a sense "runs away," since any large quantities of steam are taken to escape, not accounting for the higher and higher pressure increases required to actually deliver this escape. To demonstrate this as the root-cause of the discrepancy under investigation, we ran PM-ALPHA with only the one change needed to make it mimic the CHYMES phase-change formulation; namely, we used Eq. (1) for boiling and set the condensation rate identically to zero. The current comparison with CHYMES is shown, side-by-side with the comparison produced by Fletcher (1992), in Figure 7. Note the remarkable agreement even at the "microscopic" level, i.e., the shape of the 0.7 contours. The pressure field responsible for these important differences is shown in Figure 8. In a vice-versa comparison, we ran PM-ALPHA with CHYMES's drag laws; as shown in Figure 9, the differences are rather minor. Clearly, CHYMES's "run-away" boiling rates pushed the calculation

[a] Note: "void fraction" refers the "steam content" to the "coolant volume," while "steam volume fraction" refers the "steam content" to the total (three-phase) mixture volume.

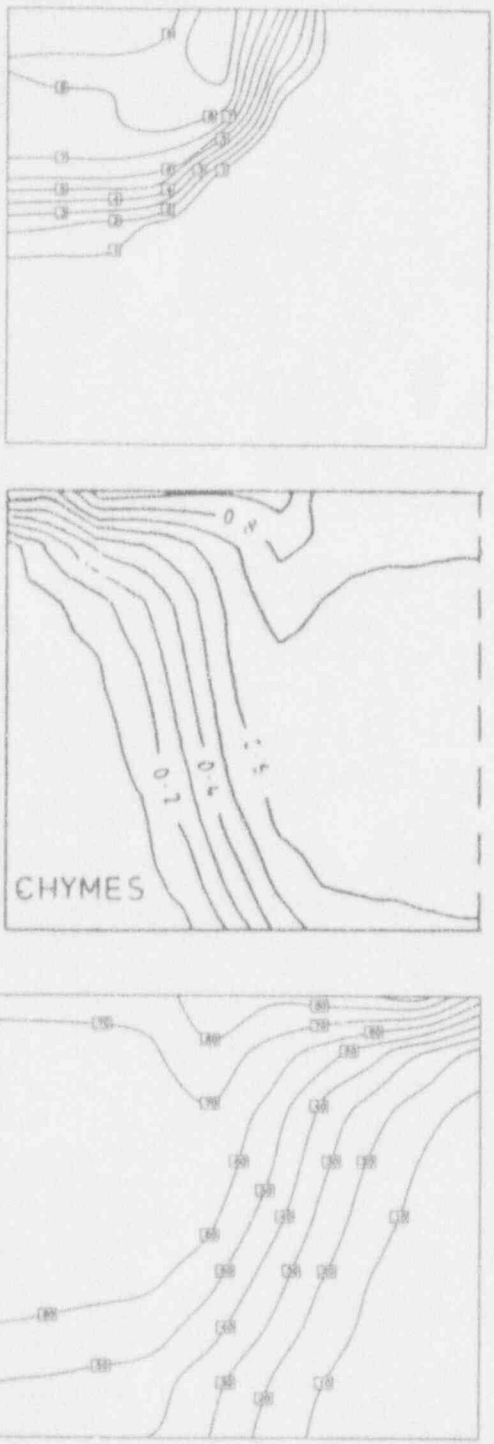

Figure 7. A side-by-side comparison of calculated steam volume fraction distributions at 0.5 s, for the premixing problem of Amarasooriya and Theofanous (1991), predicted by PM-ALPHA (a), CHYMES (b), and PM-ALPHA modified to mimic CHYMES' boiling model (c).

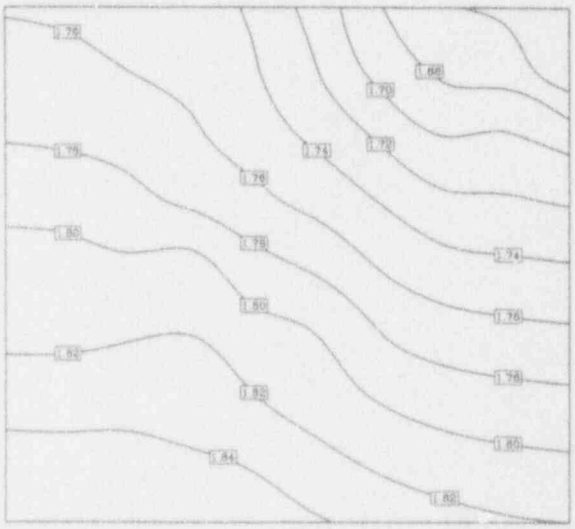

Figure 8. The calculated pressure field at 0.5 s into the premixing transient.

into a regime that accentuated these drag-related differences in Fletcher's comparisons.

Further insights into "what is important" were obtained from a series of related calculations made within the same context. In particular, we investigated fuel emissivity, gravitationally-induced subcooling, and condensation. The results are summarized in Table 1 and the figures indicated on this table. We conclude that only the treatment of subcooling is the essential difference regarding the practical aspects of application to reactor conditions, while in every other aspect, CHYMES provides indirect support to PM-ALPHA for both the numerics as well as the formulation of premixing of steam explosions.

With the numerical and physical aspects of the three-fluid formulation in PM-ALPHA well scrutinized, we are prepared to take the next major step in the quantification of premixing. In this, we persist in the fixed-particle size treatment; we expect that the real behavior can be captured/bounded by appropriate parametric variations of particle sizes, and this is all that is possible until a reasonably defensible approach to accounting for melt breakup behavior becomes available. For the particular calculation reported here, we chose the case considered above (fuel pour diameter 1.60 m, inlet velocity 1 m/s, inlet void melt fraction 0.5, melt temperature 2500 °C, and pressure 0.1 MPa), except for modifying the shape of the liquid pool boundary into the hemispherical shape of the lower head (same maximum depth). To better resolve the curved portion of the boundary, the grid size was reduced by a factor of 3 (a 30 by 27 mesh). Otherwise, aspects of accuracy and convergence (time step, spatial discretization, convergence criteria in the numerical iteration) are well at hand and need not be elaborated here. A sample of the main results, including a couple of snapshots (at times of mid- and full-penetration of the water pool by the melt front) of melt and steam volume fraction distributions and the premixed-mass transient,

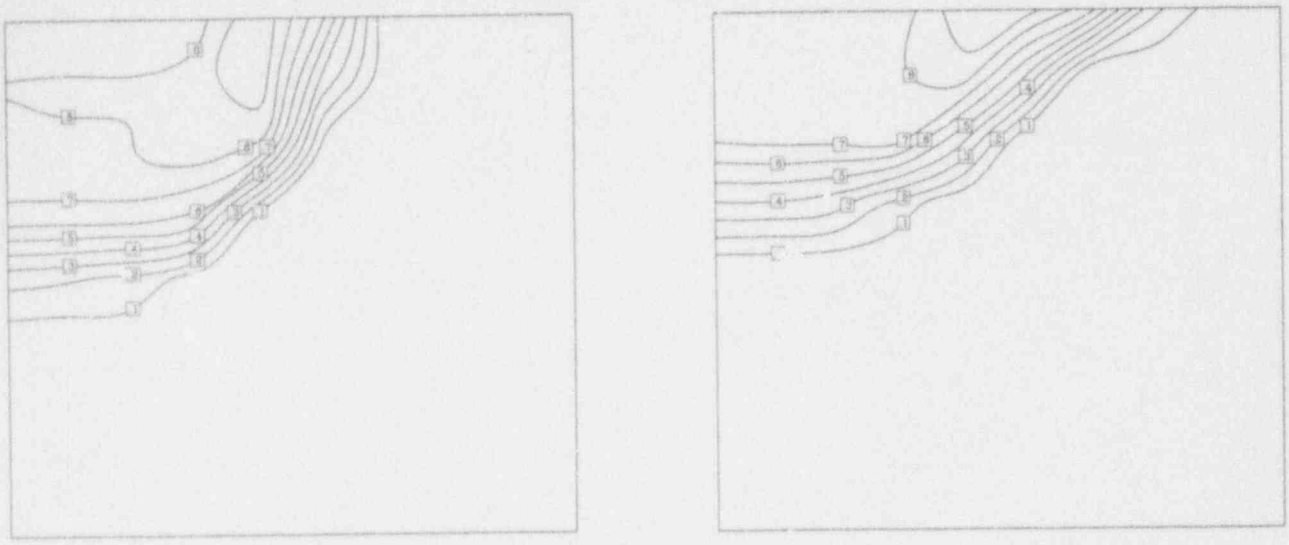

Figure 9. The effect of drag laws in the calculation of premixing. (a) PM-ALPHA, (b) PM-ALPHA with CHYMES' drag laws.

Table I

Sensitivity to Various Treatments in the CHYMES and PM-ALPHA Formulations, Deduced by Making the Change Indicated to the PM-ALPHA Code

CASE	PARAMETER OR PROCESS	PM-ALPHA BASE VALUE	CHYMES VALUE FOR SENSITIVITY	COMMENTS
I	Fuel Emissivity	0.7	0.85	Slight Effect See Figure 10
II	Condensation	Allowed	Set to Zero in Addition to Case I Change	Moderate Effect: Spreading of the Void Near Top See Figure 11
III	Gravitational Subcooling	Allowed	Set to Zero in Addition to Case I, II Changes	Negligible Effect

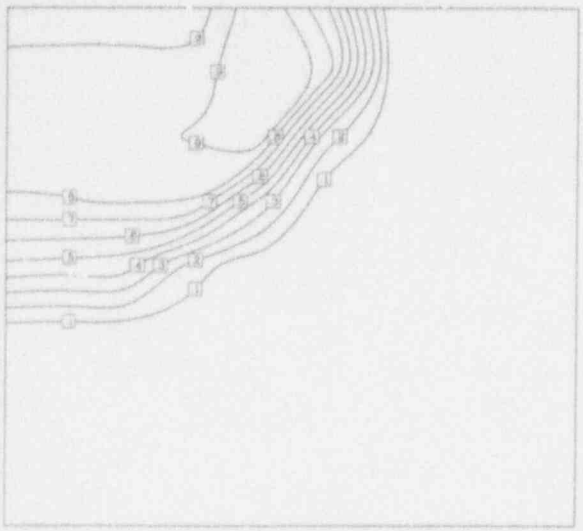

Figure 10. The calculated steam volume fraction for the premixing problem of Amarasooriya and Theofanous (1991), with increased particle emissivity.

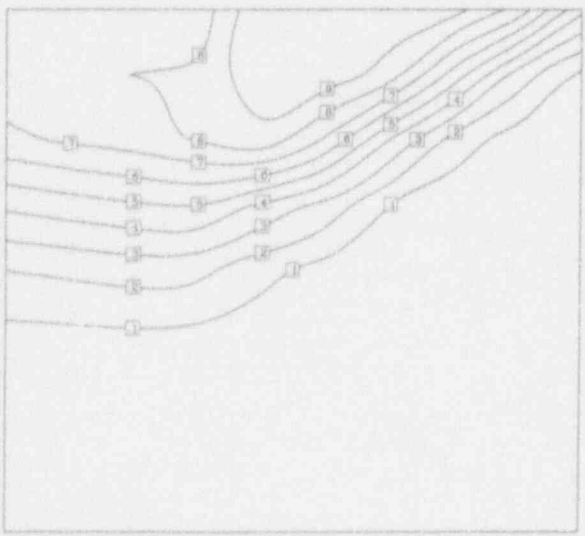

Figure 11. The calculated steam volume fraction for the premixing problem of Amarasooriya and Theofanous (1991), with increased particle emissivity and zero condensation

are shown in Figures 12 through 14. Again, we notice the familiar fuel spreading and mixing zone voiding patterns. The premixed mass is seen to depart early enough from the total quantity of melt poured to reach a peak value of ~2.5 tons at about the time that the melt front touches the lower head (~1 s). Shown in Figure 4, this calculation provides an indication of the very large degree of conservatism embodied in the NUREG/CR-5030 quantification. A systematic set of calculations for the complete requantification of premixing are currently in progress, but we expect both 5 and 95% bounds to be reduced by at least a factor of 2. Within the context of the original quantification, the impact of such a reduction is in revealing further significant margins, as discussed in Section 4, and thus to further confirm the NUREG/CR-5030 conclusion that α failure is "physically unreasonable."

QUANTIFICATION OF ENERGY YIELD

With 1.3 GJ/ton and a conservatively bounding conversion ratio of 20%, the 2.5-ton premixture found in the particular PM-ALPHA calculation of Section 3 implies a mechanical energy release of 0.65 GJ, that is, a value way too small to threaten the lower head. Conversely, for an energy yield of 1.5 GJ, we would need a mass of ~6 tons which, based on the discussion of Section 3, cannot be anticipated to be physically possible under any circumstances relevant to reactor accidents. Clearly, only a small portion (the one under 1.5 GJ) of the CR3 quantification in Figure 5 is relevant, and by reference to the NUREG/CR-5030 quantification of CR4 reproduced here as Figure 15, it is rather clear that the upper head is not threatened either.

In fact, based on our experience of the effects of water depletion and two-dimensionality, we expect that the above estimates are highly conservative and that the real margins to vessel failure are even larger. This is illustrated below by an integral calculation that accounts for the dynamics of the energy conversion process, along the lines of the alternative framework of Figure 6. [A systematic set of calculations along these lines needed to quantify pdf7 in this framework are underway.]

Using ESPROSE.a, the premixture of Figures 12 and 13 was triggered by means of suddenly releasing the contents of a computational cell pressurized (by steam) to 12 MPa. The timing of the trigger corresponds to melt arrival and contact of the lower head; its location is taken at the bottom of the axis of symmetry; and its magnitude is chosen to ensure a strong initial escalation (based on experience with the KROTOS $A\ell_2O_3$ calculations discussed by Yuen and Theofanous, 1993). In this calculation, we chose the fragmentation (f_f) and vaporization (f_v) parameters (see reference above) as 1.0 and 0.05, respectively, and the calculation was run with all flow paths, in or out of the lower plenum, sealed, and all boundaries rigid. This maximizes the loads on the lower head and, in particular, it provides an upper bound estimate of the impulse that could be delivered if the explosion was constrained from above by a hydrodynamic mass (i.e., a slug of material) instead. The results are summarized in Figures 16 and 17.

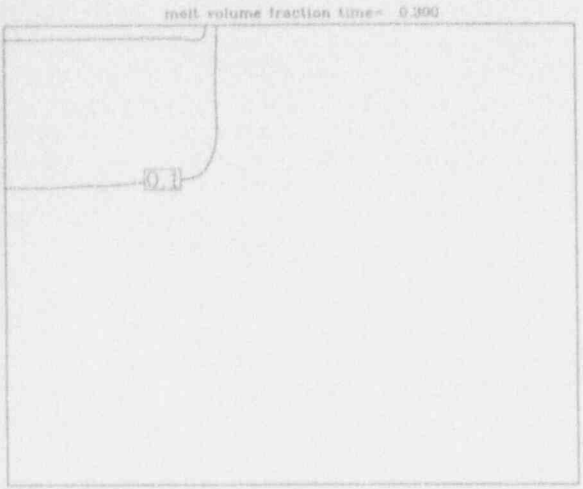

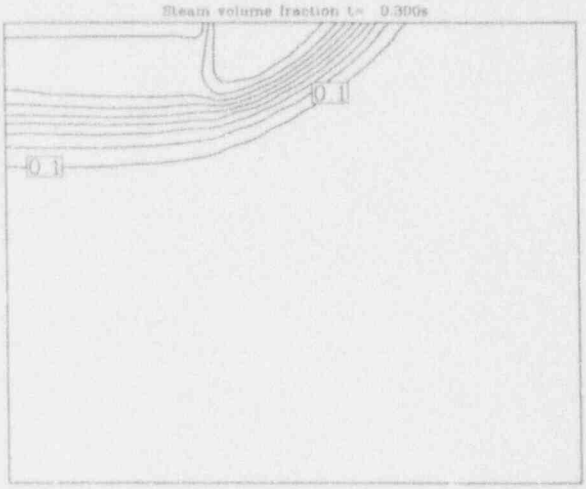

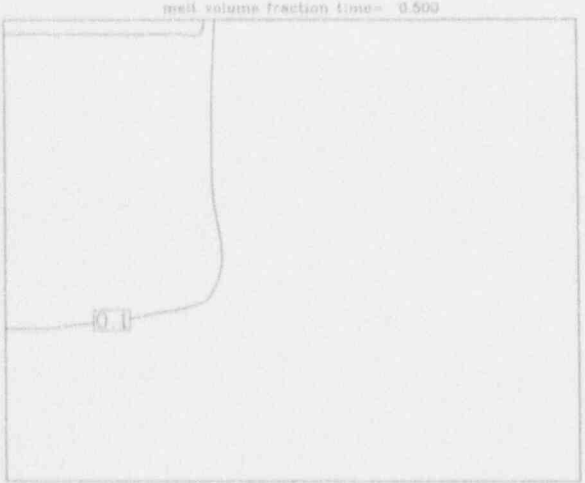

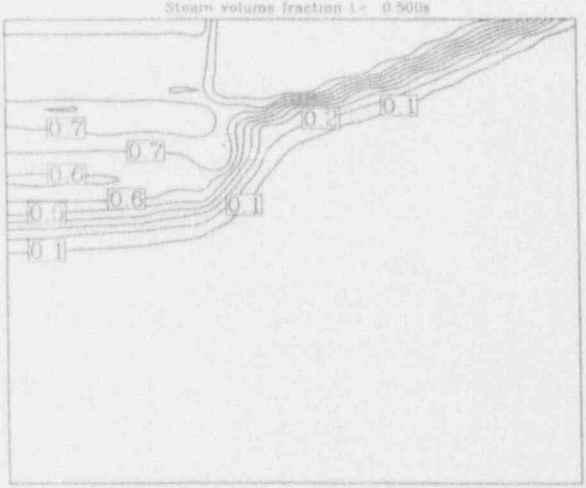

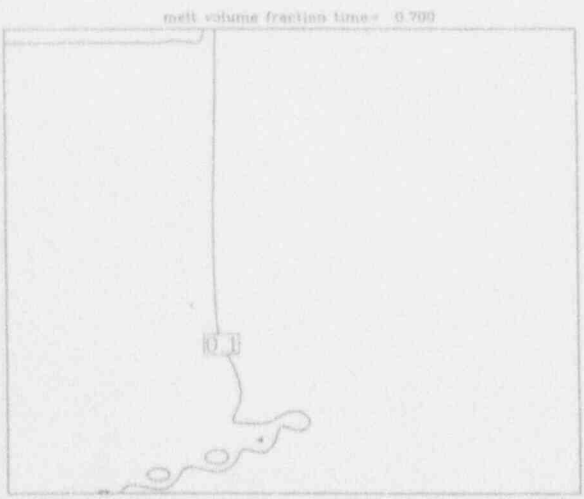

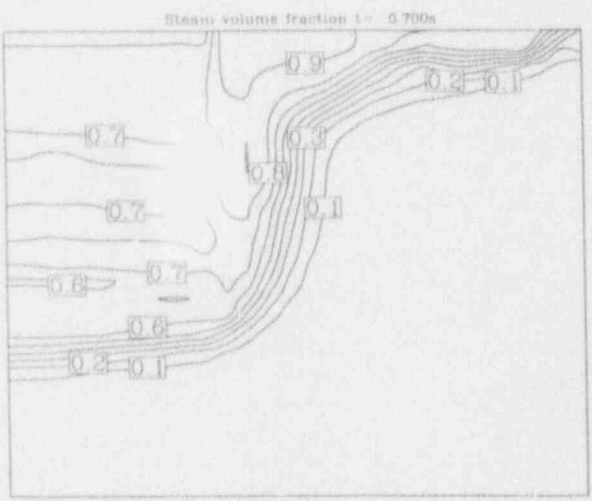

Figure 12. Calculated melt volume fraction distribution at different times into the transient.

Figure 13. Calculated steam volume fraction distribution at different times into the transient.

1

IMAGE EVALUATION TEST TARGET (MT-3)

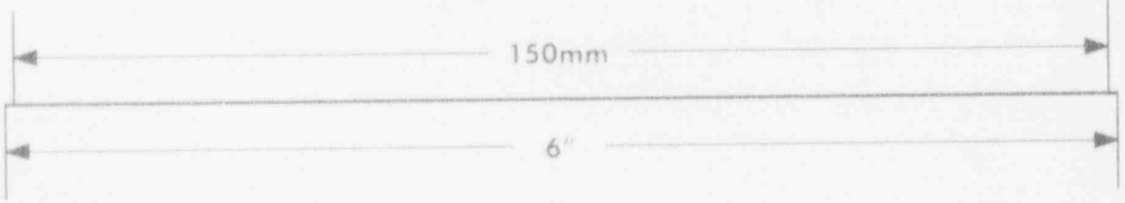

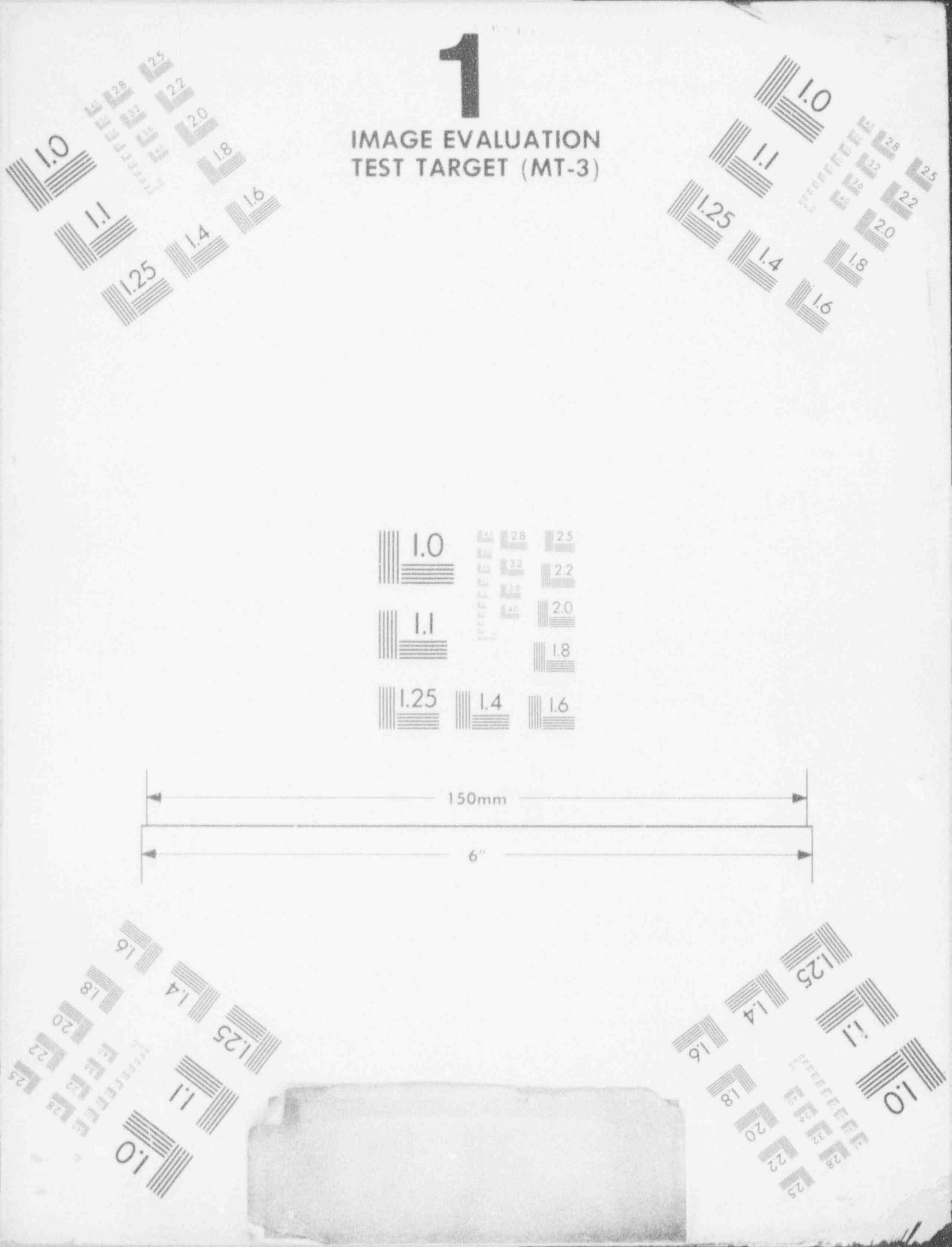
1
IMAGE EVALUATION
TEST TARGET (MT-3)
1.0
1.1
1.25
1.4
1.6
1.8
2.0
2.2
2.5
2.8
3.2
3.6
4.0
150mm
6"

1

IMAGE EVALUATION
TEST TARGET (MT-3)

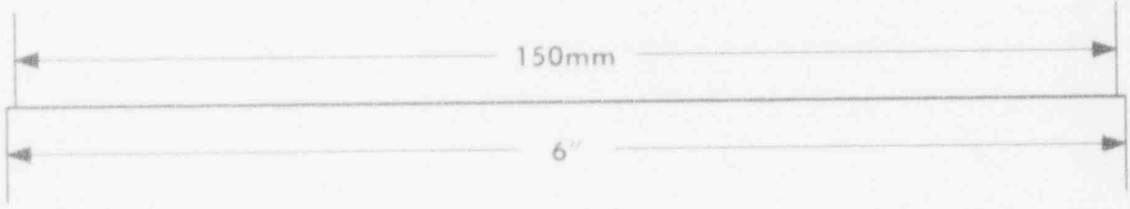

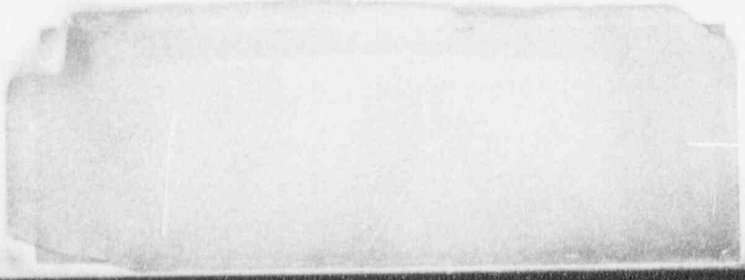

1

IMAGE EVALUATION
TEST TARGET (MT-3)

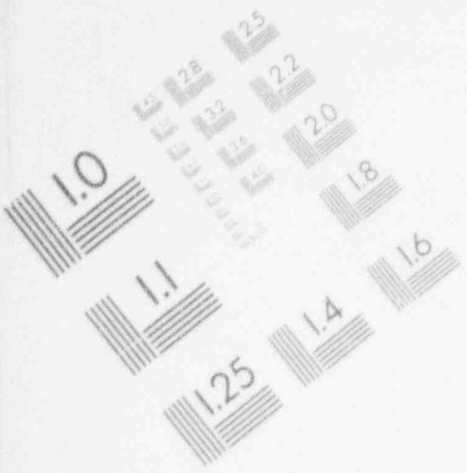

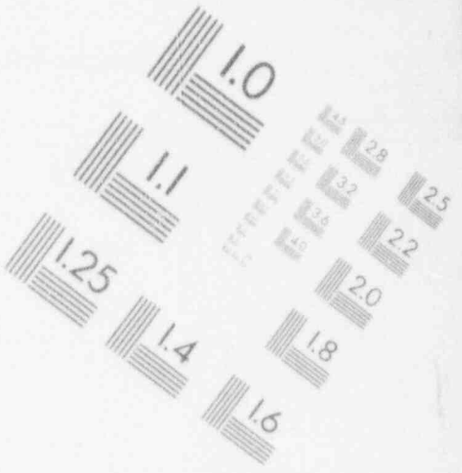

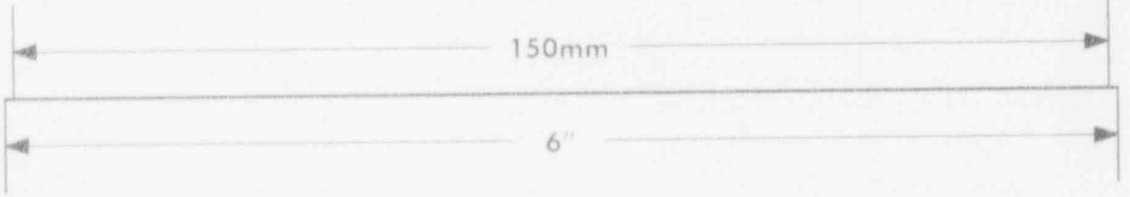

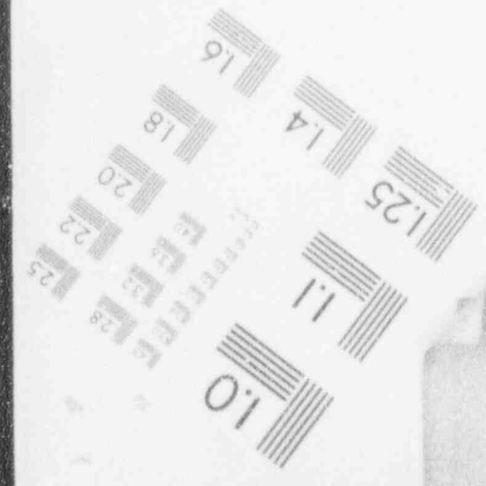

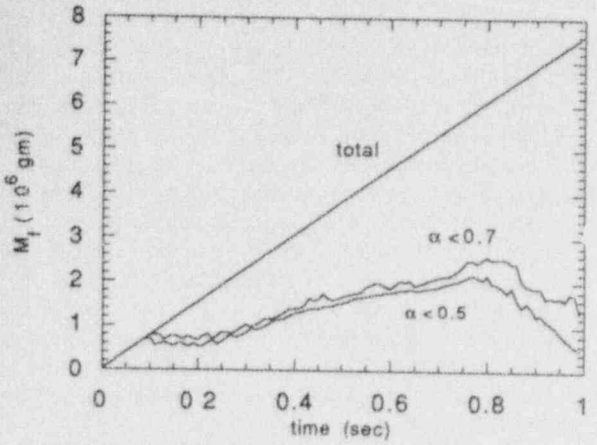

Figure 14. Premixed mass transient compared to the total quantity of melt poured.

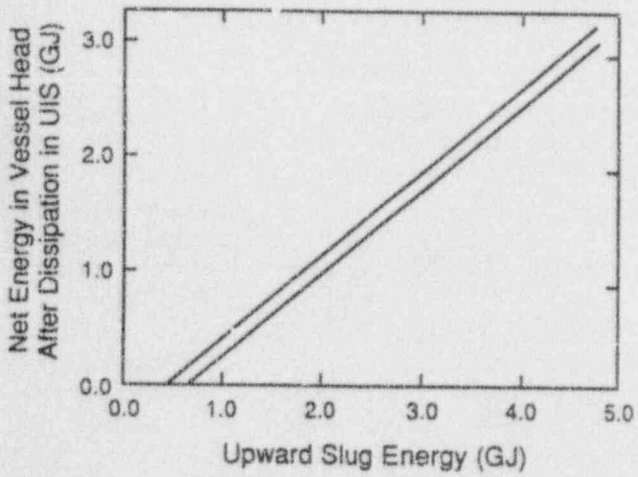

Figure 15. CR4 according to NUREG/CR-5030.

The basic results of this calculation, i.e., the evolution of the pressure field, are summarized in Figure 16. Some particular results, the pressure transients at five points along the lower head, are shown in Figure 17. We note the generically benign character of this calculated explosion; an initial trend to escalate seems to die out rather quickly as the wave encounters the highly voided mixing zone, while a larger amplitude wave is seen to propagate *around* the periphery of the mixing zone where there is fuel but the void is low. Further, we see that this wave is reinforced by reflections off the curved boundary of the lower head in a complicated wave interaction pattern that exhibits the effect of void in the mixing zone. A sample of wall pressure pulses is provided in Figure 17. Again, we note that the pressure pulses are rather low and clearly of no consequence to lower head integrity. These results are presently tested against a new model, ESPROSE.m (Yuen and Theofanous, 1993), that effects unique opportunities for representing the basic physics of the steam explosion phenomenon.

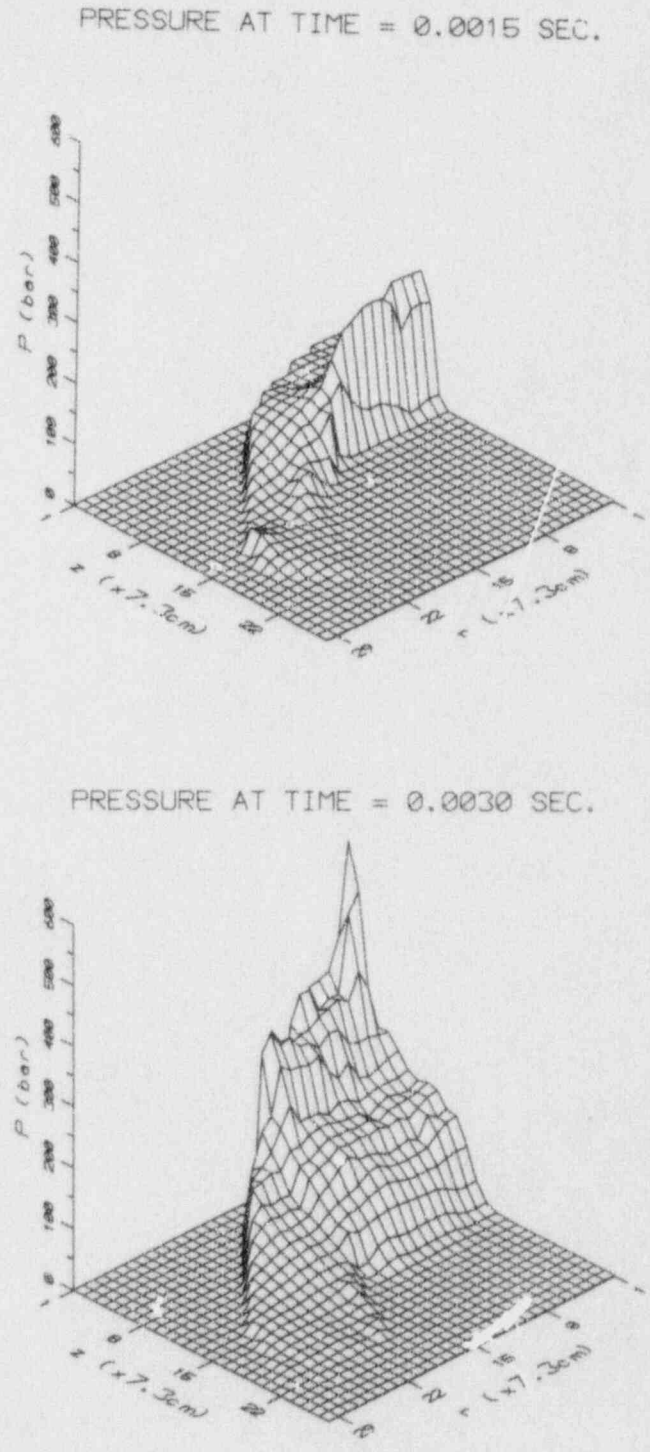

Figure 16. Evolution of an explosion in the lower head under total confinement.

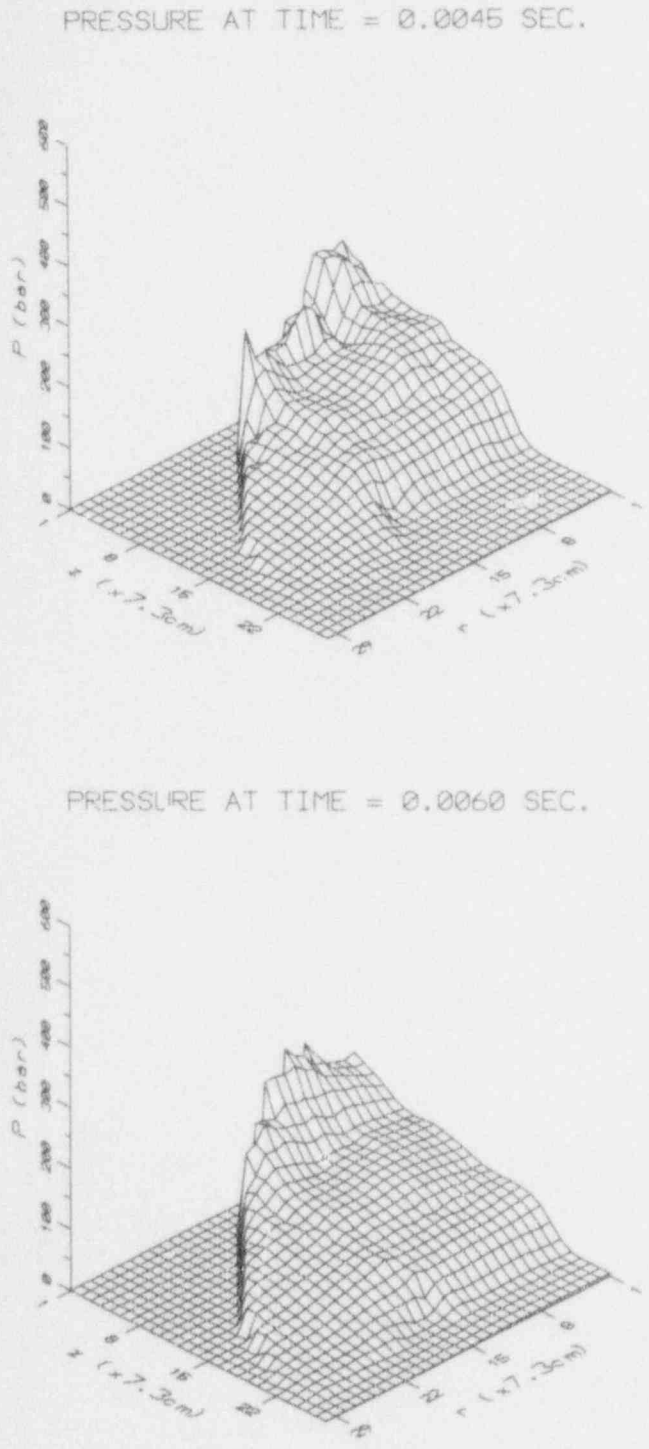

Figure 16. Cont.

CONCLUSIONS

Since the original quantification of the likelihood of α failure in NUREG/CR-5030, major experimental and analytical developments have taken place. By taking advantage of these developments, we believe it is possible to reduce the substantial conservatisms in the original quantification, and to thus conclude that even vessel failure by steam explosions may be regarded as physically unreasonable. We have illustrated how this can be done within the original framework, as well as in a complementary framework that takes advantage of current integral analysis capabilities. On this basis, the α-failure issue is now ripe for final resolution; what is needed is a complete set of calculations supporting a revised quantification of CR1 and CR3 and a final review step in the ROAAM process.

ACKNOWLEDGMENTS

The ESPROSE.a code is an advanced, developmental version of the ESPROSE code, which together with PM-ALPHA and related premixing calculations reported here were supported by the U.S. Nuclear Regulatory Commission under contract number 04-89-082.

REFERENCES

1. Amarasooriya, W.H. and T.G. Theofanous (1991) "Premixing of Steam Explosions: A Three-Fluid Model," *Nuclear Engineering & Design* **126**, 23-39.

2. Amarasooriya, W.H. and T.G. Theofanous (1987) "An Assessment of Steam-Explosion-Induced Containment Failure. Part III: Expansion and Energy Partition," *Nuclear Science and Engineering*, **97**, 296-315.

3. Angelini, S., W.W. Yuen and T.G. Theofanous (1993) "Premixing-Related Behavior of Steam Explosions," CSNI Specialists Meeting on Fuel-Coolant Interactions, Santa Barbara, CA, January 5-8, 1993.

4. Angelini, S., E. Takara, W.W. Yuen and T.G. Theofanous (1992) "Multiphase Transients in the Premixing of Steam Explosions," Proceedings NURETH-5, Salt Lake City, UT, September 21-24, 1992. Vol. II, 471–478.

5. Bürger, M., M. Buck, K. Müller and A. Schatz (1993) "Stepwise Verification of Thermal Detonation Models: Examination by Means of the KROTOS Experiments," CSNI Specialists Meeting on Fuel-Coolant Interactions, Santa Barbara, CA, January 5-8, 1993.

6. Denham, M.K., A.P. Tyler and D.F. Fletcher (1992) "Experiments on the Mixing of Molten Uranium Dioxide with Water and Initial Comparisons with CHYMES Code Calculations," ANS Proceedings NURETH-5, Salt Lake City, UT, September 21-24, 1992, Vol. VI, 1667-1675.

7. Fletcher, D.F. (1992) "A Comparison of Coarse Mixing Predictions Obtained from the CHYMES and PM-ALPHA Models," *Nuclear Engineering and Design*, **135**, 419-425.

8. Fletcher, D.F. and A. Thyagaraja (1991) "The CHYMES Coarse Mixing Model," *Progress in Nuclear Energy*, **26** No. 1, 31-61.

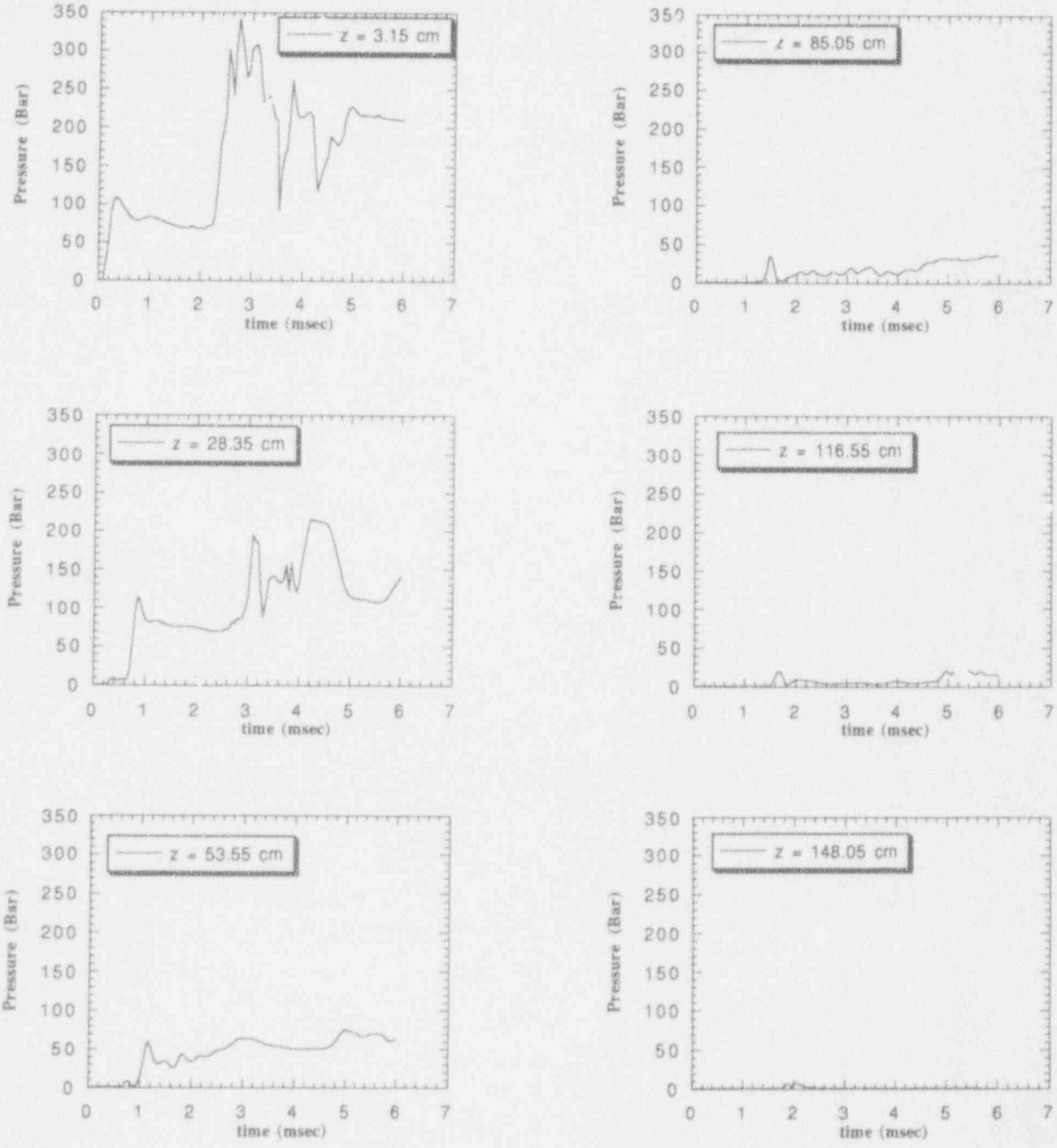

Figure 17. Transient loadings at various positions along the containing boundaries of the explosion in Figure 16.

9. Henry, R.E. and H.K. Fauske (1981) "Required Initial Conditions for Energetic Steam Explosions," *Fuel-Coolant Interactions, HTD-V19*, American Society of Mechanical Engineers.

10. Hohmann, H., D. Magallon, H. Schins and A. Yerkess (1993) "FCI Experiments in the Aluminumoxide/Water System," CSNI Specialists Meeting on Fuel-Coolant Interactions, Santa Barbara, CA, January 5-8, 1993.

11. Medhekar, S., M. Abolfadl and T.G. Theofanous (1991) "Triggering and Propagation of Steam Explosions," *Nuclear Engineering & Design* **126**, 41-49.

12. Medhekar, S., W.H. Amarasooriya and T.G. Theofanous (1989) "Integrated Analysis of Steam Explosions," Proceedings Fourth International Topical Meeting on Nuclear Reactor Thermal-Hydraulics, Karlsruhe, FRG, Oct. 10-13, 1989, Vol. 1, 319–326.

13. Pilch, M., H. Yan, M. Allen and T.G. Theofanous (1993) "The Probability of Containment Failure by Direct Containment Heating," to be published as a NUREG/CR report by the U.S. Nuclear Regulatory Commission.

14. Steam Explosion Review Group (1985) "A Review of Current Understanding of the Potential for Containment Failure Arising from In-Vessel Steam Explosions," NUREG-1116, U.S. Nuclear Regulatory Commission.

15. Theofanous, T.G. (1991) "The Role of Fuel-Coolant Interactions in Severe Accident Management," Appendix A in NUREG/CR-5682, U.S. Nuclear Regulatory Commission.

16. Theofanous, T.G., W.H. Amarasooriya, H. Yan and U. Ratnam (1991) Failure in a Mark-I Containment," NUREG/CR-5423, U.S. Nuclear Regulatory Commission.

17. Theofanous, T.G., B. Najafi and E. Rumble (1987) "An Assessment of Steam-Explosion-Induced Containment Failure. Part I: Probabilistic Aspects," *Nuclear Science and Engineering*, **97**, 259-281. (Also, including peer review comments, in NUREG/CR-5030, 1989.)

18. Theofanous, T.G. and H. Yan (1991) "ROAAM: A Risk-Oriented Accident Analysis Methodology," Proceedings, International Conference on Probabilistic Safety Assessment and Management (PSAM), Beverly Hills, CA, February 4-7, 1991, Vol. 2, 1179–1185.

19. Turland, B., D.F. Fletcher, K.I. Hodges and G.J. Attwood (1993) "Quantificaton of the Probability of Containment Failure Caused by an In-Vessel Steam Explosion for the Sizewell B PWR," CSNI Specialists Meeting on Fuel-Coolant Interactions, Santa Barbara, CA, January 5-8, 1993.

20. Yuen, W.W., X. Chen and T.G. Theofanous (1992) "On the Fundamental Microinteractions That Support the Propagation of Steam Explosions," ANS Proceedings NURETH-5, Salt Lake City, UT, September 21-24, 1992, Vol. II, 627–636.

21. Yuen, W.W. and T.G. Theofanous (1993) "The Prediction of Two-Dimensional Detonations and Resulting Damage Potential," CSNI Specialists Meeting on Fuel-Coolant Interactions, Santa Barbara, CA, January 5-8, 1993.

PROCEEDINGS CSNI SPECIALISTS MEETING ON FUEL-COOLANT INTERACTIONS

AUTHOR INDEX

PROCEEDINGS OF THE CSNI SPECIALISTS MEETING ON FUEL-COOLANT INTERACTIONS

LIST OF PARTICIPANTS

Australia

Mr. Greg Storr
Australian Nuclear Science and Technology
Organisation (ANSTO)
PMB 1, MENAI 2234, NSW

Austria

Dr. Gert Sdouz
Austrian Research Center Seibersdorf
Energy and Engineering
A-2444 Seibersdorf

Belgium

Dr. Dries Gryffroy
AiB-Vinçotte
Nuclear Safety Analysis Department
Section: Mid-Term Project
Koningslaan 757
B-1060 Brussels

Dr. Jean Snoeck
Senior Engineer
Tractebel
Avenue Ariane, 7
B-1200 Bruxelles

Canada

Professor David Frost
Mechanical Engineering Department
McGill University
817 Sherbrooke St. W.
Montreal, Que, H3A 2K6

Prof. Susan McCahan
Department of Mechanical Engineering
University of Toronto
5 Kings College Road
Toronto, Ontario M5S 1A4

Dr. Vijay I. Nath
Senior Safety Analyst
AECL - CANDU
Sheridan Park Research Community
Mississauga, Ontario, L5K 1B2

Dr. Jack Veeder
AECL
Chalk River Laboratories
Chalk River, Ontario, K0J 1J0

Prof. James E.S. Venart
Director, Fire Science Center
University of New Brunswick
P.O. Box 4400
Frederickton, N.B., E3B 5A3

CEC

Dr. Hermann Hohmann
Commission of the European Communities
Joint Research Centre
Safety Technology Institute - TP 421
I - 21020 Ispra (VA) Italy

Dr. Daniel Magallon
Commission of the European Communities
Joint Research Centre
Safety Technology Institute - TP 421
I - 21020 Ispra (VA) Italy

Finland

Mr. Timo (Juhani) Okkonen
STUK (Finnish Centre for Radiation and Nuclear Safety)
P.O. Box 268
SF-00101, Helsinki

Dr. Harri Tuomisto
Densio Design Engineer
Imatran Voima Oy
P.O. Box 112
SF-01601 Vantaa

France

Dr. Georges Berthoud
CEA - CENG
STR/LML
85 X 38041 Grenoble Cedex

Mr. Gerard Cenerino
Institut De Protection et de Surete Nucleaire
Department de Protection de l'Environment et des
Installations
IPSN/CEA, BP6, 92265
Fonteney-Aux-Roses Cedex

Dr. Michel Gabillard
Gaz de France
Research and Development Division - CERMAP
Roche Maurice B.P. 1140
44024 Nantes Cedex 01

Germany

Mr. Manfred Bürger
Institut für Kernenergetik und Energiesysteme
University of Stuttgart
Pfaffenwaldring 31
D-7000 Stuttgart 80

Prof. Enno Hicken
Director, Institute for Safety Research and Reactor Technology
Forschungszentrum Jülich GmbH
Postfach 1913
D-5170 Jülich

Dr. Helmut Jacobs
Kernforschungszentrum Karlsruhe GmbH (KfK)
Institut für Neutronenphysik und Reaktortechnik
3640, D-7500 Karlsruhe

Dr. Leonhard Meyer
Kernforschungszentrum Karlsruhe GmbH
Inst. für Neutronenphysik und Reaktortechnik
Postfach 3640, W-7500 Karlsruhe

Dr. Wilhelm Peppler
Kernforschungszentrum Karlsruhe GmbH
Inst. für Reaktorsicherheit
Postfach 3640, D-7500 Karlsruhe

Dr. Klaus Trambauer
Gesellschaft für Anlagen
und Reaktorsicherheit (GRS) mbH
Forschungsgelände
D-W-8046 Garching

Italy

Mr. Marino Valisi
ENEL-CRTN
Via Monfalcone N.15 - 20132
Milano

Japan

Prof. Mamoru Akiyama
Nuclear Engineering Department
University of Tokyo
7-3-1 Hongo, Bunkyo-ku
Tokyo 113

Mr. Norihiro Yamano
Research Engineer
Severe Accident Research Laboratory
Department of Fuel Safety Research
Japan Atomic Energy Research Institute
2-4 Sirakata-Sirane, Tokai-mura
Ibaraki-ken, 319-11

Sweden

Mr. Gunnar Jung
Vattenfall AB
S-162 87 Vällingby

Mr. Yngve S. Waaranperä
ABB Atom AB
Department RP
S-721 63 Västerås

United Kingdom

Dr. David F. Fletcher
Section Leader - Computational Fluid Mechanics
26B/D5 SRD (Culham Office)
Culham Laboratory
Abingdon, Oxon OX14 3DB

Dr. Brian D. Turland
Section Leader - Severe Accidents
D5/45 SRD (Culham Office)
Culham Laboratory
Abingdon, Oxon OX14 3DB

United States

Prof. Said Abdel-Khalik
Nuclear Engineering Program
Georgia Institute of Technology
Atlanta, GA 30332-0225

Mr. Steve Additon
Tenera L.P.
7272 Wisconsin Avenue
Bethesda, MD 20814-4836

Dr. Ali-Reza Behbahani
U.S. Nuclear Regulatory Commission
NL/N
Washington, DC 20555

Ms. Carol Buchholz
GE Nuclear Energy
175 Curtner Avenue
San Jose, CA 95125

Dr. Dae Cho
Argonne National Laboratory
9700 South Cass Avenue, Bldg. 208
Argonne, IL 60439

Prof. Michael Corradini
Department of Nuclear Engineering
University of Wisconsin
1500 Johnson Drive
Madison, WI 53706

Prof. Vijay K. Dhir
University of California, Los Angeles
38-137E
405 Hilgard Avenue
Los Angeles, CA 90024-1597

Dr. Farouk Eltawila
U.S. Nuclear Regulatory Commission
5650 Nicholson Lane, MS NLN344
Rockville, MD 20852

Dr. Hans Fauske
Fauske & Associates, Inc.
16W070 W. 83rd Street
Burr Ridge, IL 60521

Dr. Theodore Ginsberg
Brookhaven National Laboratory
Building 197D
Upton, NY 11973

Dr. Robert E. Henry
Fauske & Associates, Inc.
16W070 W. 83rd Street
Burr Ridge, IL 60521

Dr. Herbert Isbin
2815 Monterey Parkway
St. Louis Park, MN 55416

Prof. Bill Kerr
University of Michigan
2009 Hall Avenue
Ann Arbor, MI 48104

Dr. David Leaver
Pole Star
4 Main Street
Los Altos, CA 94022

Dr. Mati Merilo
Electric Power Research Institute
3412 Hillview Avenue
Palo Alto, CA 94304

Dr. Lloyd S. Nelson
Sandia National Laboratories
Reactor Safety Experiments Department 6423
Albuquerque, NM 87110

Dr. James J. Sienicki
Argonne National Laboratory
9700 South Cass Avenue
Argonne, IL 60440

Mr. Michael Snodderly
Reactor Systems Engineer
U.S. Nuclear Regulatory Commission
Washington, DC 20555

Dr. Bruce W. Spencer
Manager, Engineering Development Laboratories
Argonne National Laboratory
9700 South Cass Avenue, Building 206
Argonne, IL 60440

Dr. Rusi P. Taleyarkhan
Martin Marietta Energy Systems, Inc.
Oak Ridge National Laboratory
P.O. Box 2009
Bldg. 9104-1
Oak Ridge, TN 37831-8057

Prof. T.G. Theofanous
Department of Chemical and Nuclear Engineering
Director, Center for Risk Studies and Safety
University of California, Santa Barbara
Santa Barbara, CA 93106

Dr. Charles Tinkler
U.S. Nuclear Regulatory Commission
5650 Nicholson Lane
Rockville, MD 20852

Dr. Robert W. Wright
Office of Research
U.S. Nuclear Regulatory Commission
5650 Nicholson Lane
Rockville, MD 20852

Prof. Walter W. Yuen
Mechanical and Environmental Engineering
University of California, Santa Barbara
Santa Barbara, CA 93106

OECD

Mr. Heikki L.O. Holmström
OECD Nuclear Energy Agency (NEA)
Le Seine St. Germain
12 Boulevard des Iles
F-92130 Issy-Les-Moulineaux

NRC FORM 335 (2-89) NRCM 1102, 3201, 3202

U.S. NUCLEAR REGULATORY COMMISSION

BIBLIOGRAPHIC DATA SHEET

(See instructions on the reverse)

1. REPORT NUMBER (Assigned by NRC. Add Vol., Supp., Rev., and Addendum Numbers, if any.)

NUREG/CP-0127
NEA/CSNI/R(93)8

2. TITLE AND SUBTITLE

Proceedings of the CSNI Specialists Meeting on Fuel-Coolant Interactions

3. DATE REPORT PUBLISHED

MONTH: March YEAR: 1994

4. FIN OR GRANT NUMBER

5. AUTHOR(S)

N/A

6. TYPE OF REPORT

7. PERIOD COVERED (Inclusive Dates)

8. PERFORMING ORGANIZATION – NAME AND ADDRESS (If NRC, provide Division, Office or Region, U.S. Nuclear Regulatory Commission, and mailing address; if contractor, provide

Organized by

OECD Nuclear Energy Agency

Center for Risk Studies and Safety
University of California, Santa Barbara, CA

9. SPONSORING ORGANIZATION – NAME AND ADDRESS (If NRC, type "Same as above"; if contractor, provide NRC Division, Office or Region, U.S. Nuclear Regulatory Commission, and mailing address.)

Division of Systems Research
Office of Nuclear Regulatory Research
U.S. Nuclear Regulatory Commission
Washington, DC 20555-0001

10. SUPPLEMENTARY NOTES

11. ABSTRACT (200 words or less)

A specialists meeting on fuel-coolant interactions was held in Santa Barbara, CA from January 5-7, 1993. The meeting was sponsored by the United States Nuclear Regulatory Commission in collaboration with the Committee on the Safety of Nuclear Installation (CSNI) of the OECD Nuclear Energy Agency (NEA) and the University of California at Santa Barbara.

The objectives of the meeting are to cross-fertilize on-going work, provide opportunities for mutual check points, seek to focus the technical issues on matters of practical significance and re-evaluate both the objectives as well as path of future research

12. KEY WORDS/DESCRIPTORS (List words or phrases that will assist researchers in locating the report.)

Fuel Coolant Interactions (FCI), steam explosion, vapor explosion, premixing, fragmentation, triggering, accident management, explosion propagatio...

13. AVAILABILITY STATEMENT

unlimited

14. SECURITY CLASSIFICATION

(This Page) unclassified

(This Report) unclassified

15. NUMBER OF PAGES

16. PRICE

Federal Recycling Program

UNITED STATES
NUCLEAR REGULATORY COMMISSION
WASHINGTON, D.C. 20555-0001

120555139531 1 1AN
US NRC-OADM
DIV FOIA & PUBLICATIONS SVCS
TPS-PDR-NUREG
P-211
WASHINGTON DC 20555